IEEE TRANSACTIONS ON

PLASMA SCIENCE

A PUBLICATION OF THE IEEE NUCLEAR AND PLASMA SCIENCES SOCIETY

AUGUST 2000 VOLUME 28 NUMBER 4 ITPSBD (ISSN 0093–3813)

SPECIAL ISSUE ON LASER AND PLASMA ACCELERATORS

Guest Editorial ..... *P. Muggli and T. M. Antonsen, Jr.* 1054

SPECIAL ISSUE PAPERS

Laser Propagation, Channeling, and Guiding

Investigation of a Channeling High-Intensity Laser-Beam in Underdense Plasmas ..... *Z. Najmudin, A. E. Dangor, A. Modena, M. R. Salvati, C. E. Clayton, C. N. Danson, D. F. Gordon, C. Joshi, K. A. Marsh, V. Malka, P. Muggli, D. Neely, and F. N. Walsh* 1057

Extending Plasma Accelerators: Guiding with Capillary Tubes ..... *B. Cros, C. Courtois, G. Malka, G. Matthieussent, J. R. Marquès, F. Dorchies, F. Amiranoff, S. Rebibo, G. Hamoniaux, N. Blanchot, and J. L. Miquel* 1071

Interaction of Ultraintense Laser Pulses with an Underdense, Preformed Plasma Channel ..... *V. Malka, J. Faure, J. R. Marquès, F. Amiranoff, C. Courtois, Z. Najmudin, K. Krushelnick, M. R. Salvati, and A. E. Dangor* 1078

Measurement of Forward Raman Scattering and Electron Acceleration from High-Intensity Laser-Plasma Interactions at 527 nm ..... *Z. Najmudin, R. Allott, F. Amiranoff, E. L. Clark, C. N. Danson, D. F. Gordon, C. Joshi, K. Krushelnick, V. Malka, D. Neely, M. R. Salvati, M. I. K. Santala, M. Tatarakis, and A. E. Dangor* 1084

Propagation of Intense Laser Pulses Through Inhomogeneous Ionizing Gas Profiles ..... *N. E. Andreev, M. V. Chegotov, M. C. Downer, E. W. Gaul, N. H. Matlis, A. A. Pogosova, and A. R. Rundquist* 1090

Wakefield Generation by Elliptically Polarized Femtosecond Laser Pulse in Ionizing Gases ..... *N. E. Andreev, M. V. Chegotov, and M. E. Veisman* 1098

On the Effect of Long-Wavelength Electron Plasma Waves on Large-Angle Stimulated Raman Scattering of Short Laser Pulse in Plasmas ..... *N. E. Andreev and S. Yu. Kalmykov* 1106

Proposed Beatwave Experiment at RAL with the Vulcan CPA Laser ..... *D. Neely, J. L. Collier, R. Allott, C. N. Danson, S. Hawkes, Z. Najmudin, R. J. Kingham, K. Krushelnick, and A. E. Dangor* 1116

Beam Dynamics, Acceleration, and Control

Scaling of Accelerating Gradients and Dephasing Effects in Channel-Guided Laser Wakefield Accelerators ..... *R. F. Hubbard, P. Sprangle, and B. Hafizi* 1122

Experimental Verification of Laser Photocathode RF Gun as an Injector for a Laser Plasma Accelerator ..... *M. Uesaka, K. Kinoshita, T. Watanabe, J. Sugahara, T. Ueda, K. Yoshii, T. Kobayashi, N. Hafz, K. Nakajima, F. Sakai, M. Kando, H. Dewa, H. Kotaki, and S. Kondo* 1133

Inverse Cerenkov Acceleration and Inverse Free-Electron Laser Experimental Results for Staged Electron Laser Acceleration ..... *L. P. Campbell, C. E. Dilley, S. C. Gottschalk, W. D. Kimura, D. C. Quimby, L. C. Steinhauer, M. Babzien, I. Ben-Zvi, J. C. Gallardo, K. P. Kusche, Jr., I. V. Pogorelsky, J. R. Skaritka, A. van Steenbergen, V. E. Yakimenko, D. B. Cline, P. He, Y. Liu, and R. H. Pantell* 1143

(Contents Continued on Page 1053)

IEEE TRANSACTIONS ON PLASMA SCIENCE

The IEEE Nuclear and Plasma Sciences Society is an organization, within the framework of the IEEE, of members with principal professional interest in the field of plasma science. All members of the IEEE are eligible for membership in the Society and will receive this TRANSACTIONS upon payment of the annual Society membership fee of $15.00 plus an annual subscription fee of $10.00. For information on joining, write to the IEEE at the address below. *Member copies of Transactions/Journals are for personal use only.*

ADMINISTRATIVE COMMITTEE

Society Officers

President
I. ALEXEFF
Univ. of Tenn.
Elec. Eng. Dept.
Knoxville, TN 37996
(423) 974-5467
I.alexeff@ieee.org

Vice President
P. S. WINOKUR
Sandia Nat. Labs.
P. O. Box 5800, MS 1083
Albuquerque, NM 87185
(505) 844-3013
winokup@sandia.gov

Secretary
A. M. DAWSON LARSEN
Stanford Linear
Accelerator Ctr.
P.O. Box 4349
Stanford, CA 94309
(650) 926-2748
FAX: (650) 926-5124
amlarsen@slac.stanford.edu

Treasurer
E. J. LAMPO
Univ. of Calif.
Lawrence Berkeley
Laboratory, 80-101
Berkeley, CA 94720
(510) 486-6779
FAX: (510) 486-4102
lampo@lbl.gov

Past President
R. J. JASZCAK
Duke Univ. Medical Ctr
Dept. Radiology/Nuclear Medicine
DUMC 3949 (161D, Bryan Res. Bldg.)
Durham, NC 27710
(919) 684-7685
FAX: (919) 684-7122
rjj@dec3.mc.duke.edu

Technical Committee Chairmen

(see directory)

Computer Applications in Nuclear and Plasma Sciences
T. KOZLOWSKI

Fusion Technology
R. J. FOLEY

Nuclear and Medical Imaging Sciences
J. S. KARP

Nuclear Instruments and Detectors
W. M. BUGG

Particle Accelerator Science and Technology
M. A. ALLEN

Plasma Science and Applications
V. M. AYRES

Pulsed Power Science and Technology
P. TURCHI

Radiation Effects
K. G. KERRIS

Radiation Instrumentation
G. F. KNOLL

Functional Committee Chairmen

Conference Policy
R. S. LARSON
L. COSTRELL

Awards
P. CLOUT

Chapter Development
V. G. PRICE

Continuing Education
G. ALLEY

Transnational
E. HEIJNE

Finance
H. L. FLESCHER

Fellow Candidate Evaluation
F. J. WALTER

Membership
V. G. PRICE

Newsletter
W. K. DAWSON

Nominations
R. F. JASZCZAK

Publications
S. J. GITOMER

Students and Careers
K. A. CONNER

NPSS Liaison Representatives in IEEE Committees

Medical Imaging Transactions Steering Committee
A. B. BRILL
R. P. JASZCZEK

Membership Development
V. G. PRICE

Professional Activities Council for Engineers (PACE)
J. R. FORSTER

Sensors Council
W. W. MOSES

NPSS Liaison Representatives to IEEE-USA Committees

Aerospace Research and Development Policy
K. LABEL

Distinguished Lecturer Program
V. G. PRICE

Energy Policy
N. R. SAUTHOFF

Engineering Research and Development Policy
D. M. NEWBERRY
P. S. WINOKUR

TAB New Technology Directions Committee
P. S. WINOKUR

Social Implications of Technology
R. S. LARSEN

Standards
J. R. FORSTER

TAB Awards and Recognition Committee
P. CLOUT

IEEE TRANSACTIONS® ON PLASMA SCIENCE

S. J. GITOMER, *Editor*

Associate Editors

I. ALEXEFF
R. L. BOXMAN
R. J. COMMISSO
S. H. GOLD
A. HIROSE
T. C. KATSOULEAS
H. KUEHL
M. J. KUSHNER
G. S. NUSINOVICH
A. L. PERATT
G. L. ROGOFF
E. SCHAMILOGLU
K. H. SCHOENBACH
J. L. SHOHET
P. K. SHUKLA

J. DRUMMOND, *Founding Editor (1973–1978)*

E. J. POWERS, JR., *Editor (1979–1983)*

THE INSTITUTE OF ELECTRICAL AND ELECTRONICS ENGINEERS, INC.

Officers

BRUCE A. EISENSTEIN, *President*
JOEL B. SNYDER, *President-Elect*
DAVID J. KEMP, *Secretary*
DAVID A. CONNER, *Treasurer*
LYLE D. FEISEL, *Vice President, Educational Activities*
MICHAEL S. ADLER, *Vice President, Publication Activities*
ANTONIO BASTOS, *Vice President, Regional Activities*
DONALD C. LOUGHRY, *President, Standards Association*
ROBERT A. DENT, *Vice President, Technical Activities*
MERILL W. BUCKLEY, *President, IEEE USA*
WILLIAM G. GJERTSON, *Director, Division IV—Electromagnetics and Radiation*

Executive Staff

DANIEL J. SENESE, *Executive Director*

DONALD CURTIS, *Human Resources*
ANTHONY DURNIAK, *Publications*
JUDITH GORMAN, *Standards Activities*
CECELIA JANKOWSKI, *Regional Activities*
PETER A LEWIS, *Educational Activities*
RICHARD D. SCHWARTZ, *Business Administration*
W. THOMAS SUTTLE, *Professional Activities*
MARY WARD-CALLAN, *Technical Activities*
JOHN WITSKEN, *Information Technology*

IEEE Periodicals

Transactions/Journals Department

Staff Director: FRAN ZAPPULLA
Editorial Director: DAWN M. MELLEY
Production Director: ROBERT SMREK
Transactions Manager: GAIL FERENC
Electronic Publishing Manager: STEPHEN COHEN
Managing Editor: JEFFREY E. CICHOCKI

IEEE TRANSACTIONS ON PLASMA SCIENCE (ISSN 0093–3813) is published bimonthly by The Institute of Electrical and Electronics Engineers, Inc. Responsibility for the contents rests upon the authors and not upon the IEEE, the Society/Council, or its members. **IEEE Corporate Office:** 3 Park Avenue, 17th Floor, New York, NY 10016-5997. **IEEE Operations Center:** 445 Hoes Lane, P.O. Box 1331, Piscataway, NJ 08855-1331. **NJ Telephone:** +1 732 981 0060. **Price/Publication Information:** Individual copies: IEEE members $10.00 (first copy only), nonmembers $20.00 per copy. (Note: Add $4.00 postage and handling charge to any order from $1.00 to $50.00, including prepaid orders.) Member and nonmember subscription prices available on request. Available in microfiche and microfilm. **Copyright and Reprint Permissions:** Abstracting is permitted with credit to the source. Libraries are permitted to photocopy for private use of patrons, provided the per-copy fee indicated in the code at the bottom of the first page is paid through the Copyright Clearance Center, 222 Rosewood Drive, Danvers, MA 01923. For all other copying, reprint, or republication permission, write to Copyrights and Permissions Department, IEEE Publications Administration, 445 Hoes Lane, P.O. Box 1331, Piscataway, NJ 08855-1331. Copyright © 2000 by The Institute of Electrical and Electronics Engineers, Inc. All rights reserved. Periodicals Postage Paid at New York, NY and at additional mailing offices. **Postmaster:** Send address changes to IEEE TRANSACTIONS ON PLASMA SCIENCE, IEEE, 445 Hoes Lane, P.O. Box 1331, Piscataway, NJ 08855-1331. GST Registration No. 125634188. Printed in U.S.A.

REPORT DOCUMENTATION PAGE

Form Approved OMB No. 0704-0188

Public reporting burden for this collection of information is estimated to average 1 hour per response, including the time for reviewing instructions, searching existing data sources, gathering and maintaining the data needed, and completing and reviewing this collection of information. Send comments regarding this burden estimate or any other aspect of this collection of information, including suggestions for reducing this burden to Department of Defense, Washington Headquarters Services, Directorate for Information Operations and Reports (0704-0188), 1215 Jefferson Davis Highway, Suite 1204, Arlington, VA 22202-4302. Respondents should be aware that notwithstanding any other provision of law, no person shall be subject to any penalty for failing to comply with a collection of information if it does not display a currently valid OMB control number. **PLEASE DO NOT RETURN YOUR FORM TO THE ABOVE ADDRESS.**

1. REPORT DATE *(DD-MM-YYYY)*	2. REPORT TYPE	3. DATES COVERED *(From - To)*
	FINAL TECHNICAL REPORT	02/01/99 - 01/31/00

4. TITLE AND SUBTITLE
"Theoretical Support Program for Plasma-Based Concepts for Future High Energy Accelerators"

5a. CONTRACT NUMBER
n/a

5b. GRANT NUMBER
#N00014-99-1-0285

5c. PROGRAM ELEMENT NUMBER
n/a

6. AUTHOR(S)
Thomas C. Katsouleas

5d. PROJECT NUMBER
n/a

5e. TASK NUMBER
n/a

5f. WORK UNIT NUMBER
n/a

University of Southern California
Dept. of Electrical Engineering/Electrophysics
3737 Watt Way
Los Angeles, Ca. 90089-0271

9. SPONSORING / MONITORING AGENCY NAME(S) AND ADDRESS(ES)

Office of Naval Research
Dr. Charles W. Roberson
ONR Code 331, Ballston Tower
800 N. Quincy Street
Arlington, VA 22217-5660

Office of Naval Research
Carol Colwell
Regional Office, San Diego
4520 Executive Drive, Ste#300
San Diego, CA. 92121-3019

10. SPONSOR/MONITOR'S ACRONYM(S)
ONR

11. SPONSOR/MONITOR'S REPORT NUMBER(S)

12. DISTRIBUTION / AVAILABILITY STATEMENT
Unlimited

13. SUPPLEMENTARY NOTES
n/a

14. ABSTRACT

The purpose of this grant was to support a workshop entitled "International Workshop on 2nd Generation Plasma Accelerators". The attached proceedings of that meeting have now been published as a Special Issue of IEEE Transactions on Plasma Science (August 2000, Volume 28, Number 4).These proceedings serve as a summary of the workshop and hence an appropriate summary report of the results of the grant.

15. SUBJECT TERMS
Laser Propagation, Plasma Accelerators, Laser Pulses, Acceleration, Laser-Beam

16. SECURITY CLASSIFICATION OF:			17. LIMITATION OF ABSTRACT	18. NUMBER OF PAGES	19a. NAME OF RESPONSIBLE PERSON
Unclassified					
a. REPORT	b. ABSTRACT	c. THIS PAGE	Unlimited Unclassified		19b. TELEPHONE NUMBER *(include area code)*
FINAL					

USC
UNIVERSITY
OF SOUTHERN
CALIFORNIA

February 16, 2001

Dr. Charles Roberson,
Program Manager
US Office of Naval Research
800 N. Quincy Street
Arlington, VA 22217-5660

School of Engineering
Electrical Engineering
Electrophysics

Tel: (213) 740-0194
Fax: (213) 740-8677
Email: katsoule@usc.edu
3737 Watt Way, PHE
Los Angeles, Ca. 90089
MC0271

Dear Dr. Roberson:

This letter and the attached proceedings are submitted as a final technical report for Grant #N00014-99-1-0285. We apologize for the delay; however, the proceedings of the workshop supported by this grant have just now been published by the IEEE Transactions on Plasma Science. They offer the most complete account of the activity of the workshop. As seen in the Table of Contents, there are 30 submissions that address a broad range of topics advancing the field of laser and plasma-based accelerators. This was a highly successful meeting, arguably the most productive in the series of four related workshops. The success of the meeting has prompted plans for a follow-on meeting in 2001 hosted by Ecole Polytechnique in France. Please note that ONR was the sole sponsor of the workshop through this grant and is duly acknowledged in the Editorial preceding the Special Issue papers.

Sincerely,

T. Katsouleas /tc

Tom Katsouleas
Private Investigator

TK/tc

University of
Southern California
Los Angeles,
California 90089

(Contents Continued from Front Cover)

Adiabatic Plasma Buncher ..... M. Ferrario, T. C. Katsouleas, L. Serafini, and I. Ben Zvi 1152
Transverse Stability of the Electron Beam in the Wiggler Plasma Wave Accelerator ..... V. Petrillo and C. Maroli 1159
Energy Spread in Plasma-Based Acceleration ..... A. Reitsma, R. Trines, and V. Goloviznin 1165
Laser Wakefield Acceleration of Short Electron Bunches ..... N. E. Andreev and S. V. Kuznetsov 1170

Novel Acceleration Schemes

Ion Acceleration Regimes in Underdense Plasmas .....
F. Pegoraro, S. V. Bulanov, F. Califano, T. Zh. Esirkepov, T. V. Lisejkina, N. M. Naumova, H. Ruhl, and V. A. Vshivkov 1177
Ultrahigh-Intensity Laser-Produced Plasmas as a Compact Heavy Ion Injection Source .....
..... *K. Krushelnick, E. L. Clark, R. Allott, F. N. Beg, C. N. Danson, A. Machacek, V. Malka,*
Z. Najmudin, D. Neely, P. A. Norreys, M. R. Salvati, M. I. K. Santala, M. Tatarakis, I. Watts, M. Zepf, and A. E. Dangor 1184
Optical Guiding of a Radially Polarized Laser Beam for Inverse Cherenkov Acceleration in a Plasma Channel .....
..... *P. Serafim, P. Sprangle, and B. Hafizi* 1190
Acceleration and Compression of Charged Particle Bunches Using Counterpropagating Laser Beams .....
..... *G. Shvets, N. J. Fisch, and A. Pukhov* 1194

Theory and Computation

Photon Kinetics for Laser-Plasma Interactions .....
..... *L. O. Silva, W. B. Mori, R. Bingham, J. M. Dawson, T. M. Antonsen, Jr., and P. Mora* 1202
Study of Propagation of Ultraintense Electromagnetic Wave Through Plasma Using Semi-Lagrangian Vlasov Codes ..
..... *F. Huot, A. Ghizzo, P. Bertrand, E. Sonnendrücker, and O. Coulaud* 1209
A Ponderomotive Guiding Center Particle-in-Cell Code for Efficient Modeling of Laser-Plasma Interactions .....
..... *D. F. Gordon, W. B. Mori, and T. M. Antonsen, Jr.* 1224

REGULAR ISSUE PAPERS

Fluid-Like Transport Variables in a Kinetic, Collisionless Plasma Near a Surface with Ion and Electron Reflection ....
..... *P.-S. Wei and F.-B. Yeh* 1233
Distribution Functions of Positive Ions and Electrons in a Plasma Near a Surface ... *P.-S. Wei, F.-B. Yeh, and C.-Y. Ho* 1244
Temporal Characteristics of Runaway Electrons in Electron-Neutral Collision-Dominated Plasma of Dense Gases. Monte Carlo Calculations ..... *K. I. Bakhov, L. P. Babich, and I. M. Kutsyk* 1254
Current Sheath Dynamics and X-Ray Emission Studies from Sequential Dense Plasma Focus Device .....
..... *R. Gupta, S. R. Mohanty, R. S. Rawat, and M. P. Srivastava* 1263
Fundamental Properties of Inert Gas Mixtures for Plasma Display Panels ..... *G. Veronis, U. S. Inan, and V. P. Pasko* 1271
Experimental Investigation of Ion Parameters in a Cathodic Arc Plasma Operated with Nitrogen Gas .....
..... *D. Grondona, H. Kelly, A. Márquez, F. O. Minotti, and J. Zebrowski* 1280
Electron Mobility in Mixtures of Optically Excited Sodium Vapor, Molecular Nitrogen, and Heavy Inert Gases .....
..... *N. A. Gorbunov, O. V. Krylova, and I. Smurov* 1287
Feasibility Study on Frozen Inert Gas Plasma MHD Generator ..... *H. Kobayashi and Y. Okuno* 1296

TECHNICAL NOTES

Chopping Effect Observed at Cathodic Arc Initiation ..... *A. Anders* 1303
A Note on the Possible Electrostatic Disruption of Bacteria ..... *D. A. Mendis, M. Rosenberg, and F. Azam* 1304

ANNOUNCEMENTS

Pulsed Power/Plasma Science 2001 (PPPS-2001) 1307

20010302 089

Editorial

MANY GROUPS around the world are working on plasma accelerators, and since publication of the last special issue on laser- and plasma-based accelerators (IEEE TRANSACTIONS ON PLASMA SCIENCE, Volume 24, 1996), a great deal of progress, both experimental and theoretical, has been made. The processes that affect laser pulses as they propagate through gas and plasma and the key requirements for guiding laser pulses and generating coherent plasma wakefields are better understood. Researchers are focusing attention on the study of the production, control, and quality of the particle beams accelerated by plasma wakefields. A strong component of the effort is devoted to the development of new theories and computational tools to predict and understand the outcome of experiments and to design future accelerators. At the same time, novel schemes for laser and plasma acceleration of charged particles are being proposed and analyzed. The progress has generated a considerable amount of excitement in the plasma-based accelerator community, and the full range of research is evident in the contributions to this special issue. Many of this issue's contributors met at the ICFA International Workshop on 2nd Generation Laser and Plasma Accelerators, held June 27 through July 2, 1999, in Kardamyli, Greece. There, working groups addressed the challenges of laser and plasma acceleration of charged particles in an environment particularly conducive to achieving progress.

The contributions to this special issue have been divided into four general topics. However, classification like this is always difficult, and a number of papers span several of the topic areas. The first topic, addressed by eight papers, is the propagation, focusing, and guiding of intense laser pulses. Four of these papers report new experimental results, and it is clear that plasma accelerator experiments are becoming increasingly well diagnosed and understood. Two papers by the Imperial College group report the investigation of self-channeling of intense radiation, the generation of stimulated Raman scattered radiation, and subsequent particle acceleration in the self-modulated regime. Their results are very impressive: energy gain in excess of 100 MeV, accelerating gradient larger than 100 GeV/m, and laser beam self-guiding over many Raleigh lengths. These results show the need for more controlled experiments, leading to the generation of electron beams with parameters suitable for applications such as high-energy physics accelerators. These issues were addressed at the workshop and discussed in some of the other contributions. Among the proposed guiding schemes, the excitation of a single electromagnetic mode in a capillary (Cros *et al.*), and the propagation in a preformed plasma channel (Malka *et al.*) seem very promising. The difficulty to overcome in these experiments is the coupling of the high-intensity laser beam into the channel, through the plasma generated by ionization at the channel entrance. This problem is considered theoretically in a paper submitted by an Institute for High Temperatures, Russian Academy of Science–University of Texas collaboration (Andreev *et al.*). Other important issues considered are the generation of a laser wakefield in the presence of ionization (Andreev *et al.*) and the effect of the laser wakefield on stimulated Raman scattering (Andreev and Kalmykov). Improvements to existing acceleration schemes are being considered to take full advantage of the available laser power. For example, in the Plasma Beat Wave Accelerator (PBWA), overcoming the plasma frequency detuning resulting from various phenomena (motion of the plasma ions, relativistic detuning, etc.) can be achieved by careful tailoring of the driving laser pulse along the laser amplifier chain (Neely *et al.*). The maximum energy attainable in an experiment can be increased by the use of a laser pulse of higher frequency (frequency-doubled) laser pulse exciting a plasma wave with a larger phase velocity (Najmudin *et al.*).

With the maturing of the field, more attention is being devoted to the study of beam dynamics, acceleration, and control, which is the second main topic of the special issue. The general requirements on a laser wakefield accelerating section are reviewed and analyzed by computer calculation in the contribution of Hubbard and Sprangle. More detailed theoretical beam dynamics studies appear in the contributions of Petrillo and Maroli, Reitsma and Trines, and Andreev and Kuznetsov. The injection of short electron bunches into the plasma wave at the appropriate time (or phase) is necessary to produce low-emittance, low-energy spread electron beams required for the generation of subpicosecond electron bunches, produced with a typical timing jitter of less than 100 fs with respect to the plasma wave. Subpicosecond electron bunches have to be produced and injected into the plasma wave at the appropriate time (or phase) with a typical timing jitter of less than 100 fs (with respect to the plasma wave) to produce the low-emittance, low-energy spread electron beams suitable for high-energy physics and other applications. The RF gun (Uesaka *et al.*), the inverse free electron laser buncher (IFEL, Campbell *et al.*), and the DC gun (Ferrario *et al.*) with sophisticated timing jitter compensation/elimination systems are good candidates to reach the goal. Note that although no paper on this subject is published in this issue, "all optical" injector schemes are also presently investigated to reach the same goal. The staging of multiple accelerator cells is necessary to reach the energies required for high-energy physics applications. It is also required to overcome the cell length limitation imposed by the laser natural divergence, and by the dephasing between the accelerated particles and the plasma wave. Plasma accelerators operate at plasma densities larger than 10^{14} cm^{-3}, corresponding to accelerating structures at frequencies above 100 GHz, and subpicosecond accelerating "buckets" in the plasma wave. The staging and synchronization can be achieved by the excitation of the different accelerator components (electron gun or buncher, and multiple acceleration cells) by laser pulses originating from the same laser chain (Campbell *et al.*).

Success in the realization of particle acceleration by plasma wakefields has stimulated further interest in novel acceleration schemes, the third main topic of this special issue. The schemes and tools developed for electron acceleration can be used for the

Publisher Item Identifier S 0093-3813(00)09278-X.

0093–3813/00$10.00 © 2000



Fig. 1. Group picture of the participants to the Kardamily workshop.

production of other high-energy particles (Pegoraro *et al.*). Of particular interest is the development of proton or ion sources as injectors suitable for more conventional accelerating structures (Krushelnick *et al.*). Also, demonstration of acceleration of positrons by plasmas is of utmost importance for plasma accelerators to play a significant role in future electron–positron TeV colliders. New approaches to producing a longitudinal accelerating field are also being proposed and refined. In particular we note the progress in the inverse Cerenkov accelerator (Serafim *et al.*) in which the axial electric field of a channel-guided laser pulse could be used to achieve energy gain. In addition, an alternative scheme for exciting plasma wakefields (Shvets *et al.*) using counterpropagating laser pulses is presented.

Numerical simulation of laser and plasma acceleration has been a key tool used in gaining understanding of experiments and testing new concepts since the field originated, and it constitutes the fourth main topic of this special issue. It is not surprising, then, that development of improved modeling techniques continues at a rapid pace. This special issue presents three contributions describing new numerical algorithms. It is interesting to note that the proposed methods offer completely different solutions to essentially similar problems. For example, the contribution of Silva *et al.* proposes simulation of the laser propagation via particle techniques, whereas that of Huot *et al.* proposes simulation of the electron plasma response via the solution of the Vlasov equation. The paper by Gordon *et al.* proposes a ponderomotive guiding center, particle-in-cell code to describe the laser–plasma interaction. Such a code offers the possibility of more rapid simulation of interactions in which the laser propagates many plasma periods.

Plasma accelerator experiments have produced a wealth of physics results, crucial for the understanding and the development of the plasma accelerator. Theory and simulation have played an essential role in developing new concepts and studying existing ones. Many issues that will determine the realization of plasma-based accelerators remain unresolved. However, the enthusiasm and the creativity displayed during the 1999 Workshop and in the contributions to this special issue lead us to believe that solutions to the unresolved problems will be found.

ACKNOWLEDGMENT

The authors would like, in the name of all of the participants to the Kardamyli workshop (see Fig. 1), to thank Prof. T. Katsouleas (USC) for organizing such an exciting workshop. They would like to thank the Office of Naval Research (ONR) and Dr. C. Roberson for sponsoring the workshop.

They would also like to thank Governor D. Drakos, I. Marabeas, V. Tatareas, S. Katsouleas, S. Mistry, the local organizing team, and the people of Kardamyli for making the workshop possible. Finally, the Guest Editors thank the authors and referees who contributed so generously to this Special Issue, and they thank S. Gitomer for his tolerance toward the "Amateur Editors."

PATRICK MUGGLI, *Guest Editor*
University of Southern California
Department of EE-Electrophysics
Los Angeles, CA 90089 USA

THOMAS M. ANTONSEN, JR., *Guest Editor*
University of Maryland
Institute for Plasma Research
College Park, MD 20742 USA



Patrick Muggli received the B.S. and Ph.D. degrees from the Centre de Recherche en Physique des Plasmas, Ecole Polytechnique Fédérale de Lausanne, Switzerland, in the fields of plasma physics and high-power microwave sources.

He was a Swiss National Science Foundation post-doctoral fellow at the Electrical Engineering Department of the University of California, Los Angeles. He worked on frequency upshiftting of electromagnetic radiation using plasmas, and on photoemission processes. He joined the University of Southern California (USC), Los Angeles, and his research topics include all aspects of plasma-based radiation sources, and plasma-based particle accelerators. He is currently an Assistant Research Professor at USC.

Dr. Muggli is the USC representative to the Coalition for Plasma Science.



Thomas M. Antonsen, Jr. (M'87) was born in Hackensack, NJ, in 1950. He received the B.S. degree in electrical engineering in 1973, and the M.S. and Ph.D. degrees in 1976 and 1977, all from Cornell University, Ithaca, NY.

He was a National Research Council Post Doctoral Fellow at the Naval Research Laboratory in 1976–1977, and a Research Scientist in the Research Laboratory of Electronics at MIT from 1977 to 1980. In 1980, he moved to the University of Maryland where he joined the faculty of the Departments of Electrical Engineering and Physics in 1984. He is currently a Professor of physics and electrical engineering. He has held visiting appointments at the Institute for Theoretical Physics (UCSB), the Ecole Polytechnique Federale de Lausanne, Switzerland, and the Institute de Physique Theorique, Ecole Polytechnique, Palaiseau, France. His research interests include the theory of magnetically confined plasmas, the theory and design of high power sources of coherent radiation, nonlinear dynamics in fluids, and the theory of the interaction of intense laser pulses and plasmas. He is the author and coauthor of more than 180 journal articles and coauthor of the book *Principles of Free-electron Lasers*. He has served on the editorial board of *Physical Review Letters*, *The Physics of Fluids*, and *Comments on Plasma Physics*.

Prof. Antonsen was selected as a Fellow of the Division of Plasma Physics of the American Physical Society in 1986.

Investigation of a Channeling High-Intensity Laser Beam in Underdense Plasmas

Z. Najmudin, A. E. Dangor, A. Modena, M. R. Salvati, C. E. Clayton, C. N. Danson, Daniel F. Gordon, C. Joshi, *Fellow, IEEE*, K. A. Marsh, V. Malka, Patrick Muggli, D. Neely, and F. N. Walsh

***Abstract*—The interaction of an intense short pulse laser ($>5 \times 10^{18}$ Wcm^{-2}) with underdense plasma was extensively studied. The beam is found to be highly susceptible to the forward Raman scattering instability. At sufficiently high growth rates, this can lead to wavebreaking with the resultant production of a high flux of accelerated electrons ($>10^{11}$ for E $>$ 2 MeV). Some electrons are found to be accelerated well above the dephasing energy, up to 94 MeV. Self-scattered images intimate the presence of high-intensity channels that extend more than 3.5 mm or 12 Rayleigh lengths. These filaments do not follow the axis of laser propagation, but are seen to be emitted within an $f4$ cone centered around this axis. Spectra of the self-scattered light show that the main contribution of the scattering is *not* from light captured within these filaments. But there is evidence for self-phase modulation from effects such as ionization and relativistic self-focusing. However, no clear correlation is observed between channel length and the number or energies of accelerated electrons. Evidence for high intensities within the channels is given by small-angle Thomson scattering of the plasma wave generated therein. With this method, the intensity is found to be of the order of 10^{18} Wcm^{-2} greater than 12 Rayleigh lengths from focus.**

***Index Terms*—Electromagnetic propagation in plasma media, electromagnetic scattering electron accelerators, plasma waves.**

I. Introduction

THE advent of high-intensity short pulse laser systems has reignited interest in many possible applications of high-power lasers. The most noteworthy of these include the fast-igniter scheme for inertial-confinement fusion (ICF) [1], generation of coherent short wavelength radiation [2]–[4], and production of large amplitude plasma waves for next-generation particle accelerators [5]. The interactions are characterized by rapid ionization (through the large intrinsic electric field of the laser) [6], [7], susceptibility to instabilities (because of the increased intensity-dependent growth rates) [8], [9], and the nonlinear response to the laser of the plasma. The nonlinearity can manifest either through relativistic effects [10], [11] or through modification of the plasma via the ponderomotive force (or light pressure) of the extremely intense laser pulse [12]. An example of this is in the hole-boring creation of a guiding channel [13], which is of vital importance in the fast-igniter scheme.

Rapid ionization through optical field ionization (OFI) is particularly important for the generation of large amplitude plasma waves, because through the use of a uniform gaseous medium, we can create a plasma with an almost uniform initial density [14]. The plasma wave formed can thus be of constant (plasma) frequency. Such a medium is also ideal for the study of instabilities in this high-intensity regime, because it presents a long scale length over which the instability can grow [15]–[17], and allows us to distinguish the signatures of many different density regimes [18]. Particularly significant has been the first optical observation of the forward Raman scatter (FRS) instability [10], [19]. This four wave process generally has a smaller growth rate than does the three-wave Raman processes, which are possible off the axis of the laser propagation (i.e., the light is scattered out of the cone of the laser beam). Hence, until the use of high-intensity lasers, FRS was only significant at density close to the quarter-critical surface of laser–solid interaction [20]. With laser intensities that can routinely reach relativistic intensities (i.e., the quiver velocity of the electrons in the laser field is close to the speed of light), the growth rate of FRS is close to its maximum [9] and thus allows a laser pulse to exhibit FRS at much lower densities. FRS studies are difficult with long pulses (trying to offset the lower growth rate with a longer growth time), because on time scales $\gg$1-ps ion motion can destroy the favorable phase matching for FRS'. FRS is particularly interesting, because the scattering process generates a large amplitude plasma wave that travels with the laser pulse at close to the speed of light. This plasma wave can be responsible for the acceleration to relativistic energies of trapped electrons from within the plasma [19]. This can have serious implications not only as a possible compact source of high-energy electrons, but also in ICF schemes in which the generation of such high-energy particles can have significance to the distribution of energy into the compressed fuel pellet.

The nonlinear optical properties of an underdense plasma when subjected to an intense laser pulse [21] can be as substantial as in solid–laser interaction. This is because a high-intensity laser pulse modifies the refractive index of the plasma as it travels through it. This can be achieved primarily in three ways, ionization [22], [23], plasma blow-out [24], [25], and relativistic effects [10], [26]. All three effects can modify the prop-

Manuscript received October, 2 1999; revised February 20, 2000. This work was supported by EPSRC, with the aid of EPSRC visiting fellowships.

Z. Najmudin, A. E. Dangor, A. Modena, and M. R. Salvati are with Blackett Laboratory, Imperial College, SW7 2BZ, London, U.K. (e-mail: zn1@ic.ac.uk).

C. E. Clayton, C. Joshi, and K. A. Marsh are with the Department of Electrical Engineering, University of California at Los Angeles, Los Angeles, CA 90095 USA.

C. N. Danson, D. Neely, and F. N. Walsh are with Central Laser Facility, Rutherford Appleton Laboratory, Chilton, Didcot, OX11 OQX Oxon, U.K.

D. F. Gordon is with the Naval Research Laboratory, Washington, DC 20375 USA.

V. Malka is with LULI, École Polytechnique-Université Pierre et Marie Curie, 91128 Palaiseau Cedex, France.

P. Muggli is with the Department of EE-Electrophysics, University of Southern California, Los Angeles, CA 90089 USA.

Publisher Item Identifier S 0093-3813(00)07242-8.

0093–3813/00$10.00 © 2000 IEEE

agation of the laser pulse, and they can result in spectral modification of the pulse. (All of the effects can be termed generally as manifestations of self-phase modulation of the laser beam.) Ionization, which tends to decrease the refractive index on axis, where intensity and, hence, OFI rates are highest, can act to defocus the laser beam. Plasma blow-out, which is caused by the transverse ponderomotive pressure of the intense laser pulse, and relativistic effects, which make the electrons quivering at velocities close to c seem more massive, increase the refractive index, hence, making the plasma act like an optical fiber. If the focusing caused by these two effects can overcome the natural diffraction of the laser beam, the laser beam waist will be reduced compared with its size were it focusing in vacuum. These two effects acting concurrently (because both occur naturally at high intensities in a plasma) are generally termed together as relativistic self-focusing [11], [27]. If the beam reaches such a size where the self-focusing effect is exactly balanced by natural diffraction, the beam can reach an equilibrium state, where it is said to be channeling. A simple treatment for a perfect Gaussian beam that only considers these two combined effects shows that channeling occurs at a critical laser power for relativistic self-focusing $P_{cr} \approx 17(\omega_0/\omega_p)^2$ GW. Indeed, if this threshold is exceeded, the beam size should be reduced. For nonideal beams, this threshold is weakly dependent on intensity [28]. Relativistic channeling has long been conjectured as a possible means of increasing the interaction length of plasma-based accelerator schemes and increasing the gain length of X-ray laser schemes, as well as providing the hole-boring path for the fast igniter concept.

This paper describes a series of experiments performed with the CPA:Vulcan laser [29], which provides 30 J in an 1-ps laser pulse at 1.054 μm. When focused with an $f4.5$ focusing optic, it produces a four times diffraction limited spot of around 20-μm diameter. This corresponds to on-target intensities of up to 5×10^{18} Wcm^{-2}. At such intensities, the normalized vector potential (which at low intensities is equal to the ratio of classic quiver velocity of the electrons in the laser field to the speed of light) is $a_0 \approx 2$. Hence, such a laser should be highly susceptible to the phenomena discussed above. The setup for the experiment is described in Section II. The results of the different diagnostics are detailed in Section III. In particular, emphasis is given to propagation, as measured by several forms of imaging, and to modulational instabilities of the laser pulse that give rise to fast electron production. We conclude with a summary in Section IV.

II. Experiment

The laser was focused onto the edge of a collimated flow of gas from a supersonic gas jet. The gas jet had been diagnosed previously by interferometric techniques [30], [48]. These measurements confirm a relatively uniform density profile over a range similar in size to the gas jet orifice. This type of nozzle is also characterized by a sharp gas–vacuum boundary ($\sim$500 μm), which helps to minimize ionization-induced refraction of the laser pulse. The gas jet had backing pressures up to 100 bar of either He or H_2, which gave plasma densities up to 5×10^{19} cm^{-3}, over a distance of 3.5 mm, the bore size of the gas jet used in these experiments. The laser beam travels in vacuum after being (grating) compressed [29] to 1 ps to the edge of the gas jet, to mitigate the pulse degradation that would result from the resulting high B-integral. For the same reason, the beam is focused with a ($f4.5$) reflective off-axis parabola.

The interaction is diagnosed in several ways. The transmitted beam is spectrally resolved to look for signs of FRS. The intensity of this transmitted light is reduced by allowing some of the light to leak through a pellicle with a high-reflection coating around 1 μm. This is to ensure that the spectrum is not modified by self-phase modulation as it passes through the collection optics. The FRS spectrum is also used to ascertain the density of the interaction on each shot. This is possible because the FRS spectrum produces a satellite separated from ω_0 by ω_p ($\omega_s = \omega_0 \pm \omega_p$). Because the group velocity of the plasma wave off which the FRS scatters is relativistic, there is minimal thermal correction to the plasma frequency. So $\omega_p^2 = (n_e e^2/\epsilon_0 m_e)$, where n_e is the electron plasma density. The density obtained in this way agrees well with double the number of neutrals obtained for the same gas jet backing pressure as obtained by interferometry (because both helium and hydrogen gases have two electrons per neutral). The error in the density obtained by this method is close to 6% over the whole density range considered here. The electron spectrum resulting from electrons trapped in the FRS-generated plasma wave is also recorded. Holes were made in the collection optics of the transmitted laser beam, so that both electron and laser spectra could be made simultaneously without unwelcome scattering of the electrons.

Direct evidence of the large amplitude plasma wave is obtained by small-angle collective Thomson scattering of a 527-nm probe beam. The probe beam of a size ($\approx$5 mm) sufficient to fully illuminate the whole plasma was injected nearly orthogonal (74°) to the direction of propagation of the driving CPA laser pulse. It was also orthogonal to the plane of polarization of the driver beam to minimize spurious signal from self-generated second harmonic, caused by relativistic Thomson scattering or density/intensity gradients within the plasma [31]. The Thomson scattered signal was taken at 3.5° ± 1.5° to the probe beam (77.5° from the direction of propagation of the laser).

For proper wavematching, $\omega_s = \omega_0 - \omega_p$, and $\vec{k}_s = \vec{k}_0 - \vec{k}_p$, where the subscripts $s, 0$, and p refer to the scattered, incident and plasma wave. Because $\omega \approx ck$ for all of the waves in the case of a plane infinite relativistic plasma wave, scattering is only permissible in exactly the same direction as the incident laser [32], as shown in Fig. 1(a). However, in our experiment, the plasma wave is constrained to the order of 10 μm by the focal spot size of the laser. Hence, the relativistic plasma wave has a radial component to the wave vector comparable to k_p, because for $n_e = 1 \times 10^{19}$ cm^{-3}, λ_p is also around 10 μm. This allows resonant Thomson scattering off-axis, as is shown in Fig. 1(b). By focusing the probe and the scattered beams, it is possible to spatially isolate the undeviated probe beam and to dump its energy on a razor blade, reducing spurious light from this unscattered component. The scattered light is then reimaged onto the slit of an imaging spectrometer, providing a spatially resolved profile of the plasma wave, along the direction of the driver beam.

To complete the diagnostics, there are three imaging channels, one schlieren and two imaging self-scatter of the driving beam. The schlieren channel provides information about the

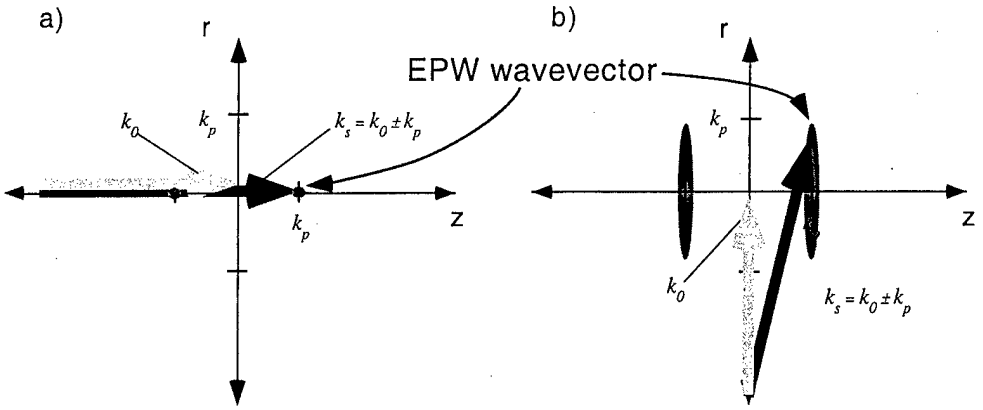


Fig. 1. Thomson scattering k-vector matching (a) for infinite plane waves (with k-vector $\pm k_p$) wavematching is only valid in the exact forward direction from the fast wave $k_p \approx \omega_p/c$. (b) For a plasma wave constrained to a focal spot on the order of the plasma wave length, the wave has a spread in radial k vector $\approx k_p$, which allows direct scattering off this fast wave at greater angles, allowing spatial monitoring of the wave.

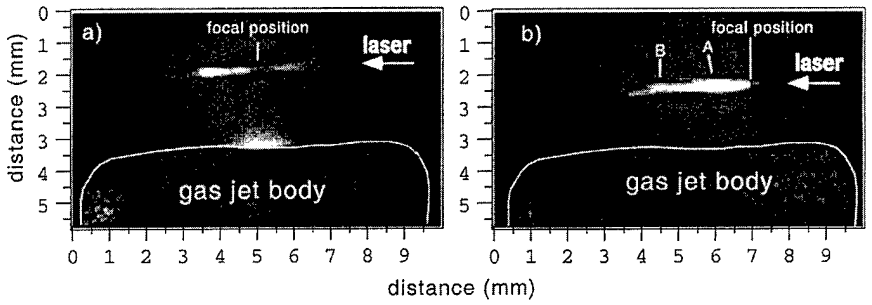


Fig. 2. Images showing self-Thomson scattered images of propagation of a 25-TW laser in underdense plasma, when focused (a) at the center of the jet (orifice size = 3.5 mm), and (b) 0.5 mm from the edge of the jet. Direction of the laser is right to left, and the extent of the gas is marked by the faint (time-integrated) background glow of the unionised. A and B indicate branching of the filaments.

density channels within the plasma by reimaging light refracted by these density channels. This is done by putting a wire stop at a virtual focus of the probe beam (which has been previously split from the small-angle Thomson scattering signal), so that only those rays deviated by density gradients may pass the stop. The self-scattering imaging channels were placed; one at 30° to the incident laser in the plane of polarization of the laser, and the other orthogonal to both drive laser and its polarization. For the imaging channel at 30°, a transmission grating of spacing 2 l/mm was placed in the beam at a point where the beam was collimated, in order to give a spectrally resolved image away from the (zero-order) transmitted image. The self-scattered light orthogonal to the plane of polarization was also spectrally resolved. However, in this case, the image was split with a beam splitter, and reimaged onto the slit of a standard high dispersion spectrometer/charge-coupled device (CCD) system.

III. Results

A. Imaging of Self-Scattering

Two images are presented in Fig. 2, for 25 TW focused either at the center or the edge of the jet. The resolution of these images is limited to 45 μm by the pixel size of the CCD cameras used. Both show a beam diverging away from focus in roughly the expected cone angle ($f4.5 \approx 16°$). The image with the focus at the center of the jet shows plasma over the whole length of the jet, 1.75 mm either side of focus. At this edge of the gas jet, the expected intensity in vacuum would be $\approx 1 \times 10^{16}$ Wcm^{-2}, just above the threshold value for double ionization of helium, the gas used for these shots. Also note that the image shows a minimum in scattering intensity close to focus. This (as explained by Gibbon *et al.* [33]) is because of volumetric effects; simply, there are fewer scatterers at focus because of the small focal spot size. The image with the focus at the edge of the jet also shows Thomson scattered light over the whole length of the gas jet. However, in this case, the other edge is now 3.5 mm from focus, where the expected vacuum intensity would be 2.5×10^{15} Wcm^{-2}. Though this is sufficient to singly ionize helium, it is below the OFI threshold required for full ionization of He atoms. It is therefore surprising that the scattering intensity does not show a marked diminution at this distance from focus.

The spectrum of the transmitted beam (Fig. 3) is also significantly different, even though in both cases, the beam is unstable to FRS. When focused at the center of the jet, the spectra shows narrow satellites sat on top of a spectrally wide, blue-shifted shoulder of the original laser frequency. When focused at the edge of the jet, though, the anti-Stokes lines of the Raman spectra become much broader and often display modulations of the satellite. The blue-shifted shoulder is greatly reduced. (Note in both cases the longer wavelength Stokes satellite cannot be seen clearly because of the reduced efficiency of the silicon-based detector used. The fact that the Stokes signal is observed at all when focusing at the edge of the jet is presumably because of its greater spectral width.) The greater width and modulations

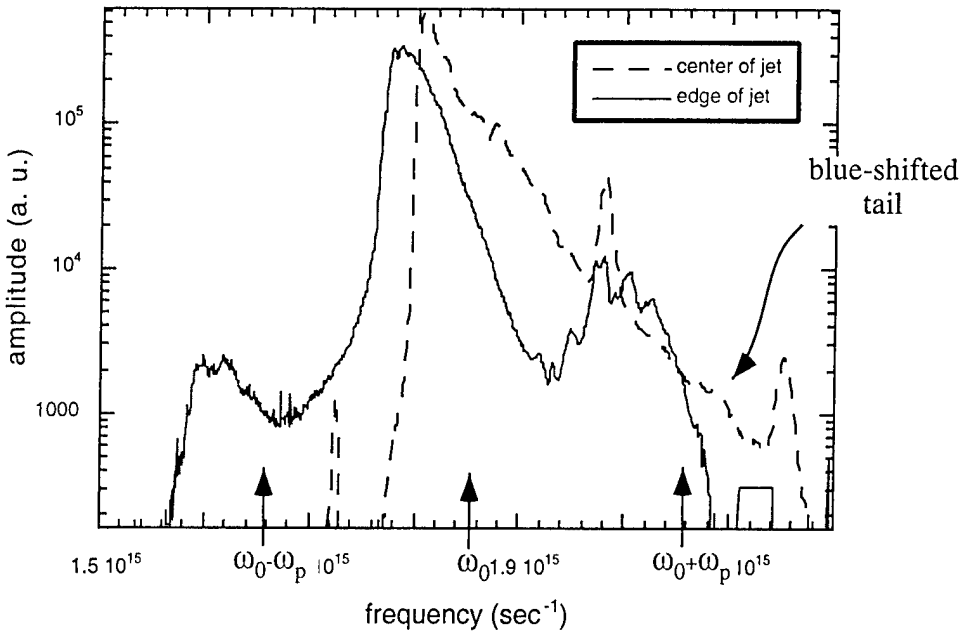


Fig. 3. Two transmitted light spectra for a 25-TW laser beam focused in helium, creating an underdense plasma of density 1.3×10^{19} cm^{-3}, one with the focus at the center of a 3.5-mm gas jet, and the other at the edge of the jet.

of the satellite, with the focus at the edge of the jet, point to wavebreaking of the Raman-induced plasma wave and, hence, indicate a greater growth rate for FRS [10]. This manifests in the electron spectra, which in this case register electrons accelerated up to 50.7 ($\pm$1.8) MeV because of the wavebreaking. However, when focused at the center of the jet, no electrons are detected above 20 MeV.

These results are not surprising when we consider the density n_e at which ionization-induced refraction becomes important, for light of wavelength λ (and critical density n_{cr}) is given by $n_e/n_{cr} > \lambda/z_r$. We can calculate the Rayleigh length, defined as twice the length over which the laser intensity drops by a factor of 2, using the simple expression $z_r = 2\sqrt{2}fd$, where f is the f-number of the focusing optics and d is the focal spot diameter. The expression comes from purely geometrical assumptions and is reasonable for nondiffraction-limited laser beams. Taking $f = 4.5$ and $d \doteq 20$ μm, the Rayleigh length in our condition is $z_r = 260$ μm. For $\lambda = 1$ μm light, we find that ionization-induced defocusing becomes important for $n_e \approx 4 \times 10^{18}$ cm^{-3}. Above this density, we can expect that the maximum vacuum intensity will not be reached. This is indeed apparent in the Raman spectra with the focus at the center of the jet, where the anti-Stokes amplitude actually decreases above this density. In fact, at a density of only 1.8×10^{19} cm^{-3}, the Raman satellites are completely "washed out" by the rising blue-shifted tail of the driver frequency. The blueshift is generated by ionization and the resultant time-dependent decrease in refractive index, similar to the spatial dependence, which causes ionization-induced defocusing. Hence, it is a good indicator of the importance of ionization in the interaction [23]. The Raman spectra, when focused at the edge of the jet, exhibits a greatly reduced ionization blue-shift, and so indicates an alleviation of ionization-induced diffraction effects. This shows the importance of good positioning of the focal position. Indeed, we find that movements as small as 250 μm either side of an optimum position can reduce the maximum number of accelerated electron by orders of magnitude. This also demonstrates the importance of having a (supersonic) gas jet with a sharp vacuum–gas interface.

Also interesting to note in Fig. 2(b), which shows an image with the focus at the edge of the jet, is that the filament not only propagates forward, but also has filament branching away from the main filament, marked in the figure as A. Indeed, the main filament seems to terminate into two filaments moving away at an angle of around 10°, at position B. This lateral movement of laser energy, which does not necessarily occur from the initial focal position, was seen often when the beam shows signs of channeling. Simulations of channeled beams (with slightly different parameters) have shown such lateral movement can result from the termination of transverse oscillations of the beam center because of "hosing instabilities" [34], [35]. In these simulations, it is seen that this lateral filamentation can be seeded by kinking of the electron beams generated by the interaction, which are subject to transverse center of beam instabilities. Sideways motion of a high-intensity beam would of course have serious implications for applications of whole beam self-channeling.

Figs. 4 and 5 show a series of images of shots taken with fixed density and increasing intensity (Fig. 4), and with fixed intensity and increasing density (Fig. 5). The ratio of laser power over critical power for self-focusing P/P_{cr} is presented for each shot, which is proportional to laser power/electron density. In all cases, the laser was focused at the same position, 500 μm from the edge of the gas jet (i.e., $x = 4.75$ mm in the figures). As we can see for a fixed plasma density of 1.4×10^{19} cm^{-3}, as the laser power is increased, the length of the scattered signal increases. Indeed, at a laser energy of 4.6 J ($P/P_{cr} = 3.8$—for which $a_0 \approx 1$), we see intense scattering only near

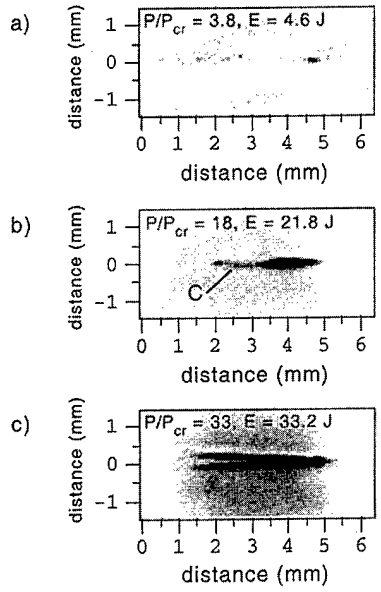


Fig. 4. Self-scattered images of laser propagating in a gas jet at a plasma density of 1.4×10^{19} cm^{-3}, for increasing on target laser energy and correspondingly P/P_{cr}. Direction of the laser is right to left, and the extent of the gas is marked by the faint (time-integrated) background glow of the unionized gas. C indicates the branching of a filament.

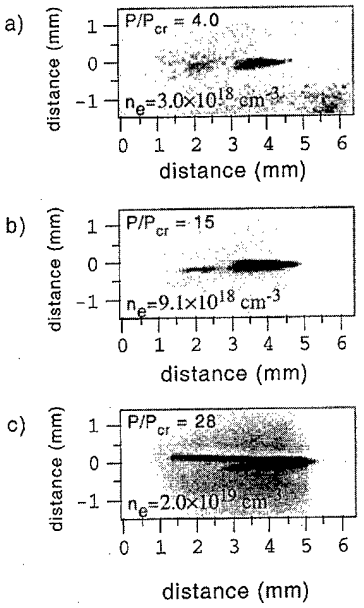


Fig. 5. Self-scattered images of propagation of a 25-TW laser in various densities of gas jet. Direction of the laser is right to left, and the extent of the gas is marked by the faint (time-integrated) background glow of the unionised gas.

focus [Fig. 4(a)]. With increasing energy, the scattering region increases, in a volume closely representing the $f4$ cone of the laser beam, until the laser energy is about 15 J, where the length of this cone no longer increases. However, signs of a thinner region of scattering extending away from this cone are apparent [e.g., the filament marked C in Fig. 4(b)]. For P/P_{cr} around 15, this filament extends by over 2 mm; all the way to the other edge of the gas jet, as seen in Fig. 4(b). As mentioned before, to maintain intensities above the ionization threshold, for the first ionization of helium, the intensity must be greater than 2.5×10^{15} Wcm^{-2}. In reality, the intensity in these filaments must be rather higher, not only because we do not see any Thomson scattered signal for beam energies less than 3 J, but also because we must be close to relativistic intensities to be subject to the plasma nonlinearities that cause these extended filament [36]. The laser power in the filament must be above P_{cr}. Because the original power of the laser beam is many times P_{cr}, this is not unreasonable. However, the fact that it takes powers many times P_{cr} to see these extended filaments suggest that much of the laser energy is not trapped into a long filament, as is evidenced by the $(f4)$ cone of scattered light naturally diffracting away from the vacuum focal position. Fig. 4(b) shows the filament branching into two close to its end, as in Fig. 2(b), (marked C in the figure). This branching is even more apparent in Fig. 4(c), which shows two clearly separated filaments, both of high-intensity, propagating all the way from close to focus to the other edge of the jet. Many such instances of these multiple filaments are observed at $P/P_{cr} > 20$, though most tend to remain within the cone angle of the original laser beam.

Fig. 5 shows the Thomson scattered images for a variety of densities (again represented as a function of P/P_{cr}), for a fixed laser power of around 25 TW. Generally, the features are similar to those at corresponding values of P/P_{cr} for fixed density and increasing intensity (Fig. 4). In particular for $P/P_{cr} \approx 10$–15, a clear filament can be observed, extending beyond a broader conical region of emission, where the laser appears to be diffracting naturally. At yet higher densities (and, therefore, P/P_{cr}), multiple filaments are again seen to form that can extend over the whole length of the gas jet. However, a major difference is observed at lower densities, i.e., closer to the critical power for relativistic self-focusing. Though the first sign of scattering is roughly at the same value of P/P_{cr}, the shape of the scattering region is different to that at low intensity. At low densities [Fig. 5(a)], we still see the conical shape of the laser beam diffracting naturally. However, with the equivalent P/P_{cr} at lower energy and higher density [Fig. 4(a)], we see a more intense, but much shorter scattering region. The difference in intensity of scattering is expected, because of the $n_e^2 \cdot I$ dependence of Thomson scattering. The difference in length of the scattering signals can be explained by the rate of ionization, which is different in the two cases. Because the intensities are well above the threshold values for tunnel ionization, the ionization rates and, hence, rate of ionization-induced defocusing is almost independent of the laser intensity. However, it does depend linearly on the density of plasma created, because the path difference between two rays traveling in ionized and nonionized parts of the jet is proportional to $\Delta n_e \cdot \partial l$. Therefore, at higher density, ionization defocusing can reduce significantly the distance over which the beam defocuses, as we appear to observe in Fig. 4(a). It also explains why it is necessary to be many times the critical power for relativistic self-focusing for us to see signs of self-channeling. As a result of the relatively high densities required in the self-modulated wakefield, as in our experiments ($>1 \times 10^{19}$ cm^{-3}), it is difficult to envisage channeling in such a scheme at powers close to P_{cr}, without the aid of a plasma-producing prepulse.

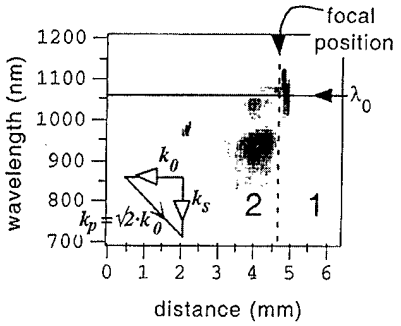


Fig. 6. Spectrally dispersed self-scattered images of propagation of a 33-TW 1.054-μm laser in plasma of density 1.4×10^{19} cm^{-3} (orifice size = 3.5 mm), viewed orthogonally to the direction of propagation. The laser travels from right to left and is focused at the marked position where $x = 4.75$ mm. Inset shows the wavevector matching for this angle of scattering.

B. Spectra of Self-Scattered Images

Most studies of self-channeling of laser pulses have relied on the Thomson scattering images to infer propagation lengths of the interaction. However, despite the large amount of qualitative data we can obtain from these images, we must be wary in interpreting these images, as is demonstrated by spectral dispersion of these images. Fig. 6 shows a typical spectrum of one of the Thomson scattered images, taken with a transmission grating placed in front of the image forming lens, so that there is combined spatial and spectral information. The image was taken at $P/P_{cr} \approx 30$; (density = 1.4×10^{19} cm^{-3}, laser power = 33 TW). The figure shows some surprising features. Firstly, in the region marked 2 in the figure, the spectra shows a prominent blue satellite. A similar feature to the red side is not seen, because of the insensitivity of the Si-based CCD camera used, above 1.1 μm. For Thomson scattering to be in this collective regime with clearly separated satellites, the relation $k_p \lambda_d < 1$ must hold. In the case of viewing orthogonal to the laser propagation, $k_p \approx \sqrt{2} k_0$, as shown in the inset of Fig. 6. This would suggest that the temperature of the scattering plasma is less than 3.5 keV. Indeed, the satellite, just beyond the focus, shows no discernible Bohm–Gross shift to the plasma frequency ($\omega_{\mathrm{BG}}^2 = \omega_p^2 + v_{\mathrm{th}}^2 k^2$), suggesting that it is much colder than this. The Thomson scattering nature of this light is confirmed by variations in density or intensity, which show the scattering is proportional to $n_e^2 \cdot I$, as expected in the collective regime. Noticeably, this blue satellite appears to start slightly beyond the focal position, and its length is the same as that of the bright cone of naturally unchanneled light seen in Figs. 4 and 5. Indeed, it is difficult to view the scattered light from the longer length filaments because the scattering is much dimmer, except close to where they terminate, where they show the same behavior as for the uncaptured light closer to the vacuum focal position [for example, as in Figs. 4(b) and 5(b)].

As can be seen, the satellite shows a marked shift to the blue further into the gas jet. This second "burst" of scattering has a Bohm–Gross shift that corresponds to a temperature of around 450 eV. Also of interest is the ion feature; the scattering close to the wavelength of the driver pulse λ_0, in particular, at the highest powers (or highest density because the spectra are similar for similar values of P/P_{cr}). As we can clearly see, this feature seems to blue shift as the scattering comes from later in the propagation of the pulse. This blue-shifting could well be the result of ionization-induced self-phase modulation of the driver pulse. However, it is surprising that all of the scattered light becomes blue-shifted (without any λ_0 component), considering that most of the light at λ_0 detected in the forward scatter is unshifted (despite a strong blue-shifted tail from ionization). Recent higher resolution probing of this interaction [37] has showed that though much of the laser light is captured into a channel of a high f-number, a good amount of light leaks away from this cone, perhaps because of ionization-induced refraction [38] early in the pulse, or intense Raman side scatter [15], [16]. This light would then be subject to further ionization (because it travels through as yet nonionized gas), and further blueshifting. This simple picture could be complicated by the bulk motion of the plasma.

Another interesting feature is the broad bright burst of scattering centered on λ_0, right at the start of the scattering region (marked 1 in the figure). The position of this scattering in the gas jet does not change and is very close to where we expect the vacuum focus position to be. The scattering only appears at the highest powers or densities (i.e., for $P/P_{cr} > 30$). Noticeably, it begins about 200–300 μm before the electron feature. The $1/e$ width of this feature is found to be 50.5 (± 1.0) nm, which corresponds to an electron temperature of around 350 eV, were this from incoherent Thomson scattering. But for any form of heavily damped scattering, we can expect that $k_p \lambda_d > 1$. This gives an upper bound for the plasma density in *this* region of $n_e < 1.3 \times 10^{18}$ cm^{-3}, suggesting that we are seeing scattering from close to the vacuum–gas interface. The sharp appearance of this scattering indicates that some form of stimulated process is involved; otherwise, incoherent scattering should scale with density and laser intensity and should be proportional in scattering intensity to the strength of the rest of the scattered signal (at least in changes of density and intensity). This type of scattering, where the plasma waves are heavily damped, is often referred to as stimulated Compton scattering. This demonstrates that self-scattering in these high-intensity interactions can be from different regimes, in different parts of the interaction, and is not necessarily Thomson scattering. It seems, therefore, that we must take great care in defining the properties of a self-channeling beam from only the images of scattered light.

C. High-Resolution Self-Scattering Spectra

Thomson scattered images were also obtained orthogonal to both the beam and the plane of polarization. This is the direction in which the scattering should be maximized. The images seen were qualitatively the same as those taken slightly off the plane of polarization, shown in Figs. 2, 4, and 5. Again, these images were spectrally dispersed. This was done by imaging the Thomson scattered light on to the slit of an imaging spectrometer, thus, giving higher spectral resolution, coupled to the spatial information. The slit was aligned along the direction of propagation of the laser. Fig. 7 shows a density scan of these spatially resolved spectra, for a variety of P/P_{cr}. Again, a series done with varying intensity are qualitatively similar, for the corresponding value of P/P_{cr}, except at the low intensity, where

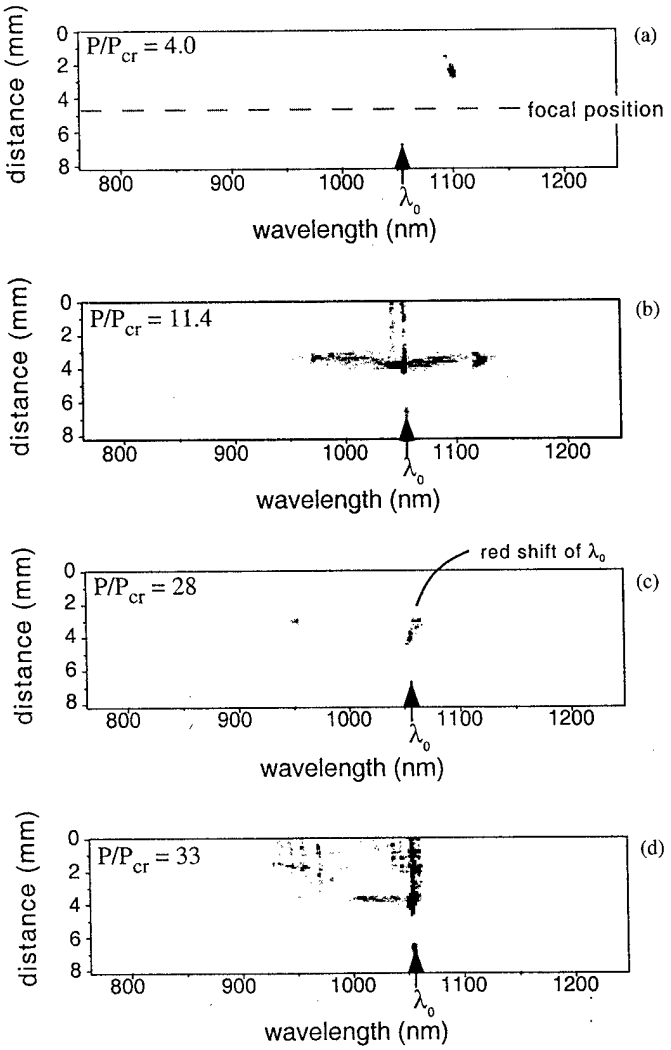


Fig. 7. Spatially resolved high-resolution Thomson scattering spectra in direction mutually orthogonal to direction of propagation of laser beam and its polarization for varying P/P_{cr}: (a) $P/P_{cr} = 4.0$ ($n_e = 3.0 \times 10^{18}$ cm^{-3}, $E_{\rm las} = 27.2$ J), (b) $P/P_{cr} = 11.4$ ($n_e = 7.5 \times 10^{18}$ cm^{-3}, $E_{\rm las} = 30.9$ J), (c) $P/P_{cr} = 28$ ($n_e = 2.0 \times 10^{19}$ cm^{-3}, $E_{\rm las} = 27.6$ J), (d) $P/P_{cr} = 33$ ($n_e = 1.4 \times 10^{19}$ cm^{-3}, $E_{\rm las} = 33.2$ J). Direction of the laser is upward. The focus is the same at $x = 4.75$ mm on the spatial axis.

the feature is smaller, because of ionization defocusing. For the lowest density case [Fig. 7(a)], the feature seems to have moved further along the direction of propagation of the laser (by over 1.5 mm). This gradual moving of the scattering feature away from focus as the density is reduced is seen in all of the Thomson scatter diagnostics. This indicates that ponderomotive reduction of the plasma density close to focus is more significant at the lowest densities. This is as expected because the space-charge restoring force will be less in this case. Noticeably, for all shots of low P/P_{cr}, there is an absence of the blue satellite, but the red satellite is clearly visible. This would suggest that in these shots, a three-wave stimulated scattering process was in action. However, for increasing density, the blue satellite does appear, as shown by the almost symmetrical feature in Fig. 7(b). The scattering, hence, appears to mirror the FRS (as we shall see later). Unfortunately, once more the Stokes (red) satellite is lost at densities greater than 1×10^{19} cm^{-3}, because of the detector response. On some, though not all, shots, at high P/P_{cr}, the scattering feature is seen to extend all the way to the edge of the jet [as shown in Fig. 7(d)]. The scattering then shows a preference for the blue side of λ_0, as seen in the other imaging channels. However, the higher dispersion shows a curious feature, the presence of strong modulations in the broad-shifted blue satellite. The modulations are neither regular nor related to characteristic oscillations of the interaction. Strong modulation of ionization-induced blue-shifted light [39] has been observed previously, and it could be that it is just this blue-shifted light that is being rescattered. This extended modulated feature is not seen on all shots [e.g., Fig. 7(c)], because it depends on the angle of the filament created on the shot and, hence, is not seen when the filament is misaligned from the (200 μm) slit of the spectrometer used.

There is scattered light close to λ_0 along the whole length of the scattered signal in Fig. 7(d). This is in contrast to the scattering profile in Fig. 6, which showed only light to the blue side of λ_0. Noticeably, the λ_0 light is slightly shifted close to focus, but this time to the red. This is clearer on Fig. 7(c), where there is no light from the filament passing into the spectrometer, and a shift of approximately 10 nm is observed. Such a shift could result from any process that acts to rapidly increase the refractive index of the laser beam as it travels through the gas jet. A simple estimate gives the wavelength shift of the fundamental frequency λ_0 as $\Delta\lambda/\lambda_0 = -L/2n_e w_p^2/w_0^2\, d/dt\,(n_e/\gamma)$, where L is the interaction length, and the Lorentz factor γ, given in terms of the normalized vector potential, is $\gamma = (1 + a_0^2/2)^{1/2}$. Red shifts can result from processes that act to decrease the effective plasma density n_e/γ, such as relativistic or ponderomotive blow-out effects. From the shape of the red-shifting in Fig. 7(c), which takes place gradually as the light travels close to 1 mm in the gas jet, we can see that the red-shifting takes place on the time scale that it takes the pulse to traverse this distance. Calculating the change in density required over this distance to obtain such a shift, we obtain $\Delta(n_e/\gamma) \approx n_e$. If only density changes were responsible for this change, this would imply total cavitation of the plasma. This seems unlikely because we would then expect a rapid decrease in the strength of the signal as the number of scatterers is reduced. Indeed, simulations show that the hot plasma temperatures within self-focusing filaments serve to prevent total cavitation [41]. Hence, the focal spot size must also be changing, giving evidence of an increase in intensity within the filaments.

The plasma channels left behind by the filaments are clearly observed by schlieren images of the plasma, which serve to highlight high-density gradients caused by ionization of the laser channels, by ponderomotive expulsion, and by thermal expansion of the plasma. A particularly long and straight channel extending over the whole length of the gas jet is shown in Fig. 8.

D. Small Angle Resonant Thomson Scattering

As described before, a frequency-doubled probe beam was injected to the CPA driver at 74°. The scattering of this probe beam at an angle of 3.5° has a component corresponding to the scattering from a wave whose wavenumber k_p is equal to that of

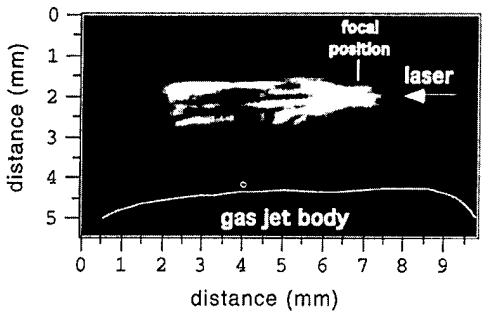


Fig. 8. Schlieren image delineating sharp density gradients in a plasma created by propagation of a 29-TW laser in a gas jet, giving a plasma density of $n_e = 1.4 \times 10^{19}$ cm^{-3}. Direction of the laser is right to left.

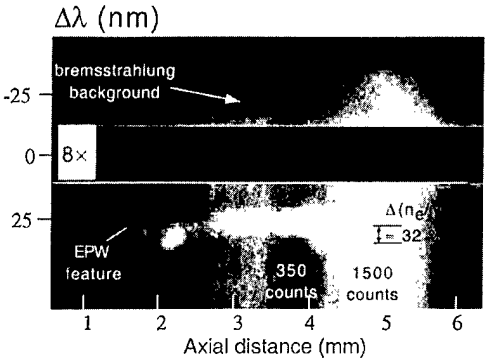


Fig. 9. Small-angle Thomson scattering image of an electron plasma wave (EPW), generated by a 28-TW beam in a plasma of density 1.9×10^{19} cm^{-3}. The laser travels from right to left (and is focused at $x = 4.75$ mm). Spurious scattered light at 527 nm has been attenuated to emphasize the ω_p shifted light caused by the EPW. The spectrally broadbands of background light are from bremsstrahlung radiation.

the FRS-generated "fast" plasma wave. Fig. 9 shows this light that has been reimaged at the slit of an imaging spectrometer. The resulting image is gated with a gated-optical imager with a gate time of 1 ns. Without the gating, the scattering signal would be obscured by recombination lines of helium in this part of the spectrum. The horizontal direction, therefore, gives spatial information, whereas the vertical is spectral. A bright feature is seen at the wavelength of the probe (527 nm). This is despite the presence of a notch filter, which attenuates this light by 10^2. This is mostly stray scattering from the optics used, as can be seen by the uniformity of this signal across the whole field. We do not expect to see much scattering from ion wave-type oscillations because the phase velocity of the waves detected at this angle would be too high. The feature below, shifted by $\approx$30 nm, is the collective scattering from the electron plasma wave ($\omega_s = \omega_0 - \omega_p$). Notice that no corresponding feature is observed to the blue side of 2ω, because it is prohibited by the wavematching conditions. The scattering has a bursting nature (i.e., strongly modulated in intensity), similar to some of the self-scattered images of the driver beam. The signal on this shot is particularly impressive because it extends over the whole length of the gas jet, 3.5 mm or more than 12 Rayleigh lengths from focus. Indeed, we can detect the profile of the gas jet, with a dip in density in the middle and sharply falling density at the edges of the gas jet. The lower plasma frequency at the center of the gas jet caused by lower gas density was confirmed by taking lower intensity shots focused at the center of the jet. These shots reproduce the lower density in their FRS spectra, and so exclude the effect of nonlinear processes, such as a relativistic or ponderomotive reduction in the effective plasma frequency. Indeed, the FRS spectra on the same shot as Fig. 9 has two anti-Stokes satellites at the two frequencies corresponding to the two different density regions of the jet. A limit for the extent of cavitation can be obtained by looking at the width of the scattered satellite near focus in Fig. 9. It is found to be about 12.5 nm or about 33% of ω_p. So the reduction in density is not more than $\approx$50%. At the other edge of the jet, the satellite is even narrower, so that cavitation is even less significant in this part of the filament.

Recent simulation results have shown that a beam subjected to FRS undergoes many complex processes. In particular, pulse erosion of the front of the pulse is vital for generating a large amplitude plasma wave that serves to seed the interaction [15], [41]. As the laser beam propagates through the plasma wave, wavebreaking within the pulse as well as self-phase modulation causes the phase within the pulse to become incoherent. The bulk of the pulse is also susceptible to other instabilities (hosing, ponderomotive, ion motion) [5]. These effects reduce the effectiveness of the main part of this (relatively long) laser pulse in plasma wave generation. However, at the same time, the front end can become so deeply eroded that at relativistic laser intensities, the front edge generated plasma wave can be of the order of the wavebreaking limit. Indeed, we can estimate the amplitude of the plasma wave because on many shots, it is possible to observe the second harmonic of the plasma wave scattered into the diagnostic ($\omega_s = \omega_0 - 2\omega_p$). These are shots where the background from bremsstrahlung is low. At a large amplitude, the harmonic content of the plasma wave is an indicator of its nonlinearity, which is directly dependent on its amplitude. We estimate that the plasma wave amplitude is 40% ($\pm$20) [26]. This is consistent with the wave amplitude observed in particle-in-cell (PIC) simulation [43] and is generally limited by beam loading of the electron plasma wave (EPW). The wakefield generated by a step function increase in intensity is given by $\delta n_e/n_0 = (1/2)a_0^4(1 + a_0^2)$, where the maximum normalized vector potential a_0 is related to the laser intensity I by $\Delta a_0 = (0.86 \cdot \lambda\ [\mu\text{m}] \cdot I^{1/2}[\times 10^{18}\ \text{Wcm}^{-2}])$. This gives us an estimate for the intensity of the laser filament, which was observed for greater than 12 Rayleigh lengths from focus, at 8×10^{17} Wcm^{-2}. Indeed, because the plasma wave amplitude is limited by beam loading effects, it is conceivable that the intensity in the filament is greater than this.

When the maximum possible vacuum intensity is reduced to this intensity (by reducing the laser energy by a factor of 6 from the maximum possible vacuum intensity of 5×10^{18} Wcm^{-2}), the EPW scattered signal actually drops below the level observable by this diagnostic. Though, as we have already said, the vacuum focused intensity is never reached because of ionization-induced defocusing. Though other high-intensity effects, such as observation of intensity-dependent plasma frequency and half-harmonic Raman spectra, have been observed previously [10], spatially resolved Thomson scattering is the first positive indication of high-intensity effects within the filament of a channeling laser beam, and that these intensities persist over

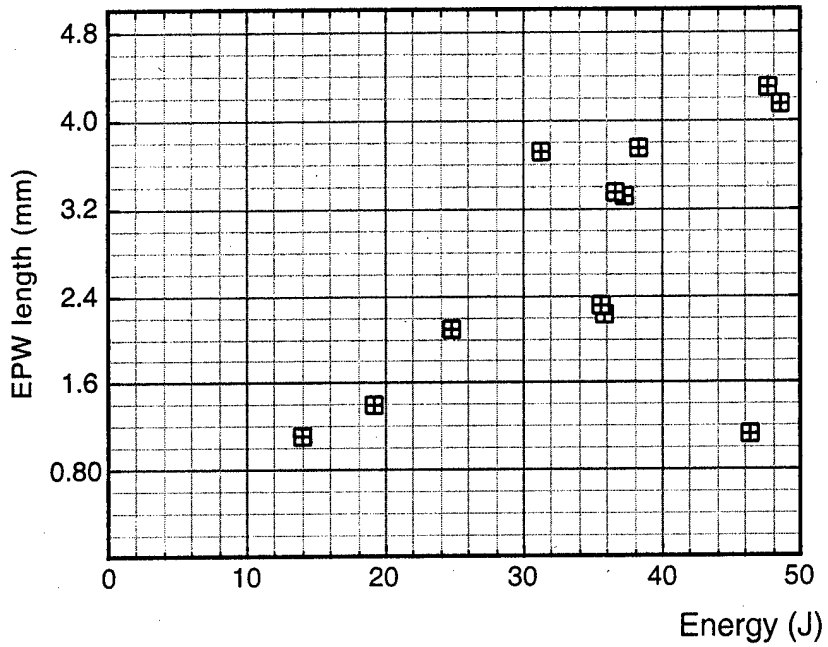


Fig. 10. Length of small-angle Thomson scattering image of an electron plasma wave as a function of incident laser energy in a 1-ps pulse, for a plasma of density 1.4×10^{19} cm^{-3}.

12× the Rayleigh length is a clear verification of relativistic self focusing.

Also of interest in Fig. 9 is the spectrally broadband of light that appears over the whole spectrum but is spatially modulated. Because recombination light is not significant over the time range observed (≈1 ns), this light must be caused by laser-induced bremsstrahlung. The efficiency of bremsstrahlung emission is proportional to the number density of ions and electrons, but is very weakly dependent on temperature for plasma temperatures above 4 eV. For our plasma, just the above-threshold ionization heating of the first electron of helium should be well above this energy, so that the scattering observed is almost independent of temperature. Therefore, the large fluctuations of bremsstrahlung along the direction of propagation of the laser beam are the result of fluctuations in the number of scattering centers. This could be because of a decreasing number density caused by ponderomotive blow-out; however, the scattering from the plasma wave does not decrease where the bremsstrahlung intensity decreases. A severely cavitated channel is unlikely to support a large amplitude plasma wave; hence, it is unlikely that this is the reason for the changes in bremsstrahlung intensity. The number of scatterers is also dependent on the beam size, because a larger number are involved in the bremsstrahlung process, which is dependent only on photon number, not intensity. The varying intensity is, therefore, an indicator of varying spot size. As indicated in the figure, a variation of intensity from around 1500 counts to 350 counts per pixel corresponds to a doubling of the spot size. In fact, it is then remarkable that the spot size remains so constant over such long distances; e.g., for the first ≈1.5 mm at the front of the gas jet in this figure, the spot size would not be changing by more than 10%.

The length of the plasma wave scattered feature does not extend over the whole gas jet on all shots. Indeed, it is usually smaller. Fig. 10 shows the variation of the Thomson scattered feature with intensity. Evidently, as the laser energy is increased, the channel length increases, though the shot-to-shot variation is high. A similar increase in length is also observed with increasing density (up to the maximum allowed for our gas jet). This suggests that the efficiency of channel creation is roughly proportional to P/P_{cr}.

E. Forward Raman Scattering

This interaction is characterized by its susceptibility to FRS. This is manifest in the modulation of the transmitted laser spectrum at multiples of the plasma frequency. Also characteristic is production of high fluxes of electrons ($>10^8$ in an $f60$ cone) that result from the transition to turbulence of the daughter EPW generated by the FRS. This chaotic behavior is termed wavebreaking, and it occurs when the EPW amplitude $\Delta n_e/n_0$ is close to unity, i.e., when charge sheets are able to overlap in the longitudinal wave, such that electrons from one oscillation period cross over to the next period and, thus, feel a large accelerating force rather than the returning force of their harmonic motion. This behavior is clear in the spectra of the transmitted light, in which the first satellite (shifted at ω_p from ω_0) becomes broad and modulated as its amplitude reaches close to that of the fundamental frequency light. Fig. 11 shows the number of electrons detected in energy channels between 23 and 29 MeV as a function of plasma frequency. Also plotted are the amplitudes of the anti-Stokes satellite versus the transmitted light at the fundamental frequency. As can be seen, the satellite height rises rapidly as ω_p (and, thus, density) is increased, until at a density close to 1×10^{19} cm^{-3} ($\omega_p/\omega_0 \approx 0.1$), it reaches close to unity. At this density, the electron signal at this energy increases even more rapidly, to a maximum of around 10^6 electrons/megaelectronvolts for some shots. This rapid increase in electron numbers corresponds to wavebreaking.

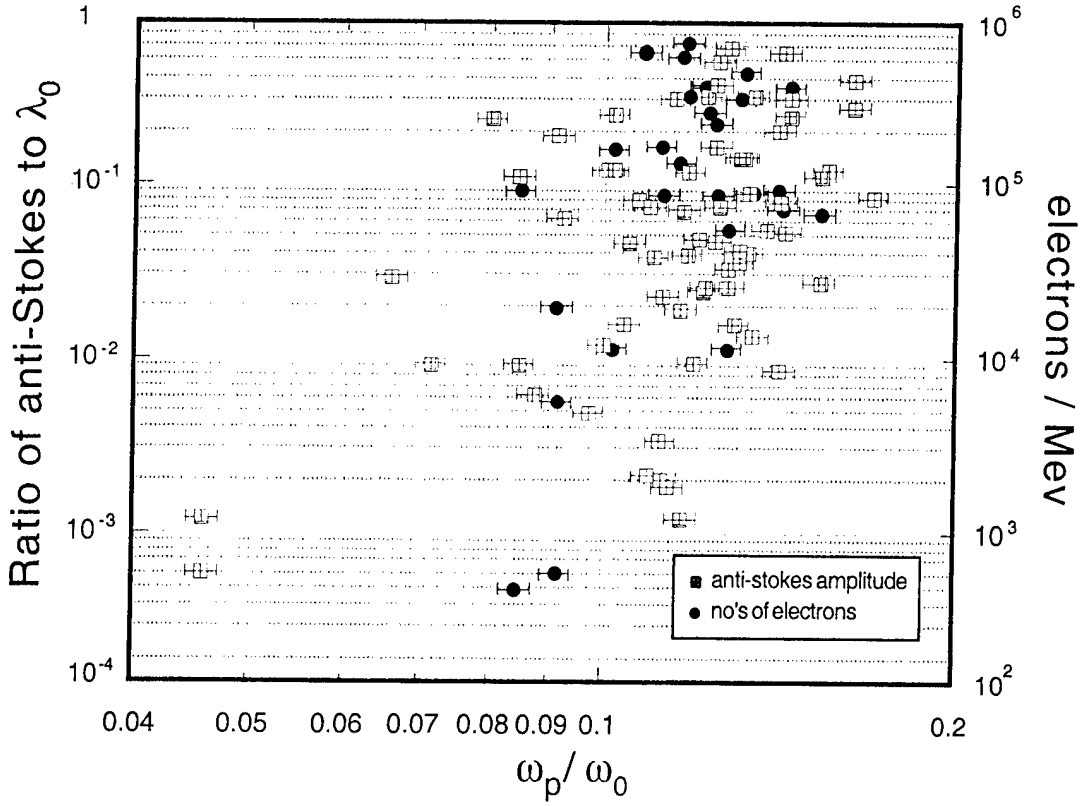


Fig. 11. Ratio of anti-Stokes to fundamental frequency of transmitted beam as a function of plasma frequency, and numbers of electrons detected in an $f60$ cone between 23 and 29 MeV as a function of plasma frequency, for shots with laser power in the range 22 to 30 TW.

Some electron energy spectra are shown in Fig. 12 for shots at the same laser power and plasma density, which exhibited different channel lengths in the image and Thomson scattering channels. The dephasing energy is given by $W_{\max} \approx 2\gamma_{\rm ph}(1 + \epsilon\gamma_{\rm ph})m_e c^2$ (valid in the limit $\epsilon\gamma_{\rm ph} > 1$) [42]. In these shots, the Lorentz factor $\gamma_{\rm ph} = 8.5$ ($n_e = 1.4 \times 10^{19}$ cm^{-3}), and as found previously, the EPW amplitude ($\epsilon = (\delta n_e/n_0)$) is measured to be 0.4. Hence, the expected maximum energy gain would be 55 MeV. As can be seen, the highest energy observed is 90 MeV. In fact, a further doubling of the density produces very little change in the spectrum observed, despite an almost $4\times$ reduction in the maximum expected energy gain. The extra acceleration is not caused by nonlinear steepening of the wake amplitude because then we would measure higher values of ϵ with our Thomson scattering diagnostic. Indeed, PIC simulations show that wake amplitudes never exceed our measured value because of beam loading effects [43]. These simulations also exhibit the same enhanced acceleration. The effect is attributed to the high current of electrons that are accelerated by the EPW. The leading part of the (micro) bunch of accelerated electrons can form a plasma wakefield in which to accelerate trailing electrons, so creating a staged acceleration process. However, this simple picture can be complicated by many other effects, such as self-generated focusing fields [44], relativistic effects [5], incoherent plasma dynamics [45], and a nonlinear group velocity of light in the plasma wave [46].

Also of note in Fig. 12 is that neither the electron energies nor, more surprisingly, the electron numbers increase with increasing channel length. The former is evidently a result of the most energetic electrons being close to their (modified) dephasing energies, because the dephasing length $L_d = 2\gamma^2\lambda_p/\pi \approx 400$ μm is less than the length of the channel. The number of electrons accelerated might be thought to increase with an increase in the amount of plasma over which the plasma wave grows. In fact, it decreases. Although very few shots are observed with the longest channel lengths, there can be many explanations as to why this happens; it could just be that the filaments are misaligned with our rather narrow electron spectrometer entrance and so results in decreased signal observation. Also, an increased channel length means the presence of longer lengths of transverse electric fields that could act to deflect many electrons. It seems at any rate that the number of trapped electrons within the filaments is not particularly great.

FRS is a four-wave process, because a downshifted Stokes line cannot directly couple to the pump laser and a seed relativistic plasma wave caused by the wavematching conditions. Hence, in FRS, the upshifted and downshifted Raman components should be created with equal amplitude. Fig. 13 shows the variation in intensity of the Stokes and anti-Stokes Raman satellite as a function of density. As can be clearly seen, this is not the case, especially at low densities ($\omega_p/\omega_0 < 0.08$), where the Stokes satellite is much greater in amplitude than is the anti-Stokes component. As density increases, the anti-Stokes component increases in amplitude relative to the Stokes component. Indeed, it appears as if the Stokes component is falling in amplitude. However, our collecting system is far from ideal for this measurement, because we use an Si-based CCD camera

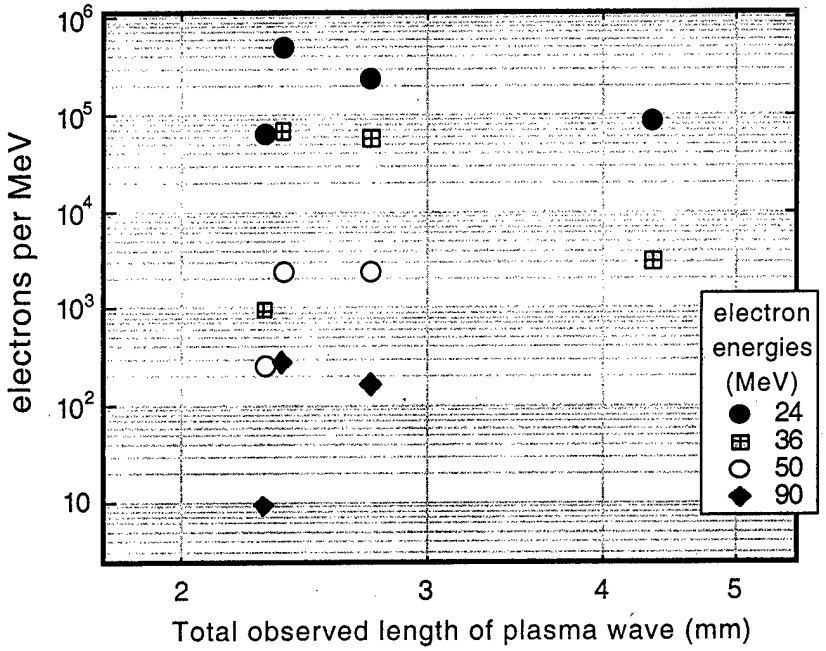


Fig. 12. Numbers of electrons accelerated to four given energies as a function of electron plasma wave length (as measured by small-angle Thomson scattering), on four shots with power between 25- and 30-TW beam in a plasma of density of 1.4×10^{19} cm^{-3}.

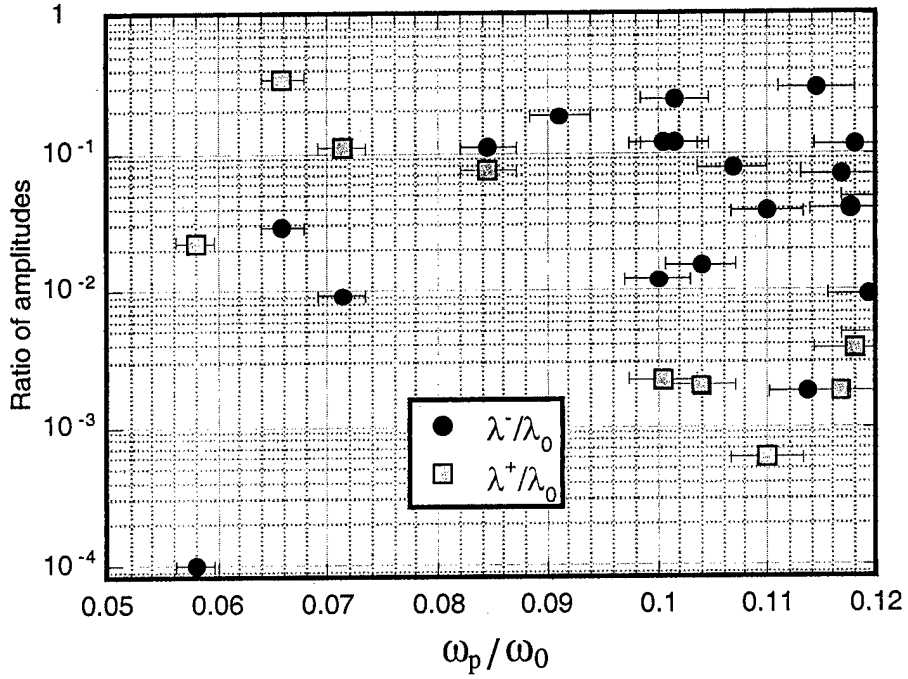


Fig. 13. Ratio of Stokes (λ^+) and anti-Stokes (λ^-) lines in the transmitted Raman spectra to the transmitted laser energy at λ_0, plotted as a function of plasma frequency.

as the detector, which has a serious fall in sensitivity beyond ≈1100 nm, so that our detection system is almost blind to the Stokes satellite for densities greater than 1×10^{19} cm^{-3}. These findings seem to be confirmed, though, when the detection is performed with a (bolometric) thermal imager with a sensitivity up to ≈2 μm. However, because of the low dynamic range of this detector and the associated large error, these data are not presented here. It seems clear then that the four-wave process is preceded by a three-wave process, which preferentially amplifies the Stoke satellite. A similar dependence with intensity is also observed, with the Stokes satellite greater in amplitude than the anti-Stokes at low laser powers, but with the anti-Stokes amplitude rising most rapidly until at high powers (>15 TW for $n_e = 1.5 \times 10^{19}$ Wcm^{-2}), they are approximately equal in amplitude. Theoretical studies of FRS show that there are clear regimes for which either the three-wave, four-wave nonresonant (where both Stokes and anti-Stokes grow, but the former has a higher growth) or four-wave resonant (where Stokes and

anti-Stokes grow equally) are dominant. Indeed, as we increase intensity, the scattering evolves from three-wave to four-wave nonresonant to four-wave resonant, in that order [9], [47]. So the observed trend of larger Stokes leading to equal Stokes and anti-Stokes amplitude is as expected. However, with increasing density, the opposite should happen, because the plasma wave wavenumber decreases, so that the mismatch in wavematching decreases. Hence, we would expect the Stokes and anti-Stokes to be more equal in amplitude with decreasing density, opposite to what is observed. The reason may well be because of the influence of Raman sidescatter. Three-wave processes are allowed off-axis; however, for the four-wave process, the amount of mismatch increases at angles away from direct forward scattering. Three-wave small-angle sidescatter also has a relatively high growth rate, and it can be amplified over as much length as direct forward scattering because of the large range of angles occupied by our laser beam because of the high f-number focusing optic ($\approx f4$). Because it can then propagate with the driver laser beam, it will be detected in the transmitted beam spectrum and can act as a supplementary seeding mechanism for four-wave FRS.

IV. Conclusion

The dynamics of a high-intensity short pulse laser propagating in an underdense plasma has been characterized through the simultaneous use of several different diagnostics. Importantly though, none of the reported high-intensity effects is observed if the laser beam has to propagate through nonionized gas before focus. This is because of ionization-induced refraction that prevents the laser beam from focusing as tightly as possible in vacuum. Hence, to observe high-intensity effects, it is necessary to focus the laser to the edge of a gas jet with a sharp gas–vacuum interface. Even in this case, the effect of ionization-induced refraction is still evident, in that it takes laser powers several times the theoretical value to observe effects such as relativistic self-focusing (though of course this is exacerbated by the far-from-ideal beam quality that such high-power systems possess).

The beam focused to high intensity at the edge of the jet is found to be susceptible to FRS. The growth of FRS increases rapidly with density but only weakly with intensity, as expected for FRS at relativistic intensities ($a_0 \sim 1$). At sufficiently high density, this can lead to the FRS satellites becoming comparable in amplitude to the fundamental frequency. This, correlated with the observation of a high flux of accelerated electrons ($>10^{11}$ for $E > 2$ MeV), indicates wavebreaking of the FRS's daughter relativistic plasma wave. Some electrons are found to be accelerated well above the dephasing energy, up to 94 MeV, suggesting that the accelerating plasma wave has been modified by beam-loading effects.

Images of the self-scattered light of the propagating beam orthogonal to the beam show signs of channeling away from focus. However, these are only apparently over any extended length for powers many times the critical power for relativistic self-focusing. At yet higher ratios of laser power to critical power, the beam breaks into more than just one filament. Spectral examination of this self-scattered light shows that it is mostly from cold plasma and, hence, is indicative only of the interaction of light at low intensities escaping from the side or end of any self-guided channels. At the highest densities and intensities, stimulated Compton scattering is also observed at 90° to the laser propagation, but only close to the vacuum–gas interface. Hence, it is difficult to fully characterize a channeling laser beam through only self-scattered images.

High intensities within the guided channel can be directly ascertained through small-angle Thomson scattering of an orthogonal probe beam. This allows us to measure the plasma wave generated in the filament at the end of the gas jet away from focus. On some shots, it is found to be as great as at the start of the jet, which from simple wakefield theory suggest intensities of the order of 10^{18} Wcm^{-2}. That these channels are formed by relativistic self-focusing is supported by observing the fundamental of the self-scattered light, which often shows a red-shifting, consistent with the increasing refractive index caused by an intensity increase. Though schlieren images show density gradients are present after the laser beam passes, it is clear that the channel is not fully cavitated; otherwise, it would not be able to support a relativistic plasma wave. Though the length and direction of the filaments varies greatly shot to shot, the accelerated electron signal is not found to depend greatly on the channel length. Hence, the filaments contribute little to the electron acceleration process.

Acknowledgment

The authors would like to thank W. Mori and K.-C. Tzeng for helpful discussions and suggestions.

References

[1] M. Tabak, J. Hammer, M. E. Glinsky, W. L. Kruer, S. C. Wilks, J. Woodworth, E. M. Campbell, M. D. Perry, and R. J. Mason, "Ignition and high-gain with ultrapowerful lasers," *Phys. Plasmas*, vol. 1, p. 1626, 1994.

[2] Z. H. Chang, A. Rundquist, H. W. Wang, M. M. Murnane, and H. C. Kapteyn, "Generation of coherent soft X rays at 2.7 nm using high harmonics," *Phys. Rev. Lett.*, vol. 79, p. 2967, 1997.

[3] P. A. Norreys, M. Zepf, S. Moustaizis, A. P. Fews, J. Zhang, P. Lee, M. Bakarezos, C. N. Danson, A. Dyson, P. Gibbon, P. Loukakos, D. Neely, F. N. Walsh, J. S. Wark, and A. E. Dangor, "Efficient extreme UV harmonics generated from picosecond laser-pulse interactions with solid targets," *Phys. Rev. Lett.*, vol. 76, p. 1832, 1996.

[4] C. Spielmann, N. H. Burnett, S. Sartania, R. Koppitsch, M. Schnurer, C. Kan, M. Lenzner, P. Wobrauschek, and F. Krausz, "Generation of coherent X-rays in the water window using 5-femtosecond laser pulses," *Science*, vol. 278, p. 661, 1997.

[5] E. Esarey, P. Sprangle, J. Krall, and A. Ting, "Overview of plasma-based accelerator concepts," *IEEE Trans. Plasma Sci.*, vol. 24, p. 252, 1996.

[6] S. Larochelle, A. Talebpour, and S. L. Chin, "Non-sequential multiple ionization of rare gas atoms in a Ti:Sapphire laser field," *J. Phys. B*, vol. 31, p. 1201, 1998.

[7] M. V. Ammosov, N. B. Delone, and V. P. Krainov, "Tunnel ionization of complex atoms and atomic ions in an alternating electromagnetic field," *Sov. Phys. JETP*, vol. 64, p. 1191, 1987.

[8] C. A. Coverdale, C. B. Darrow, C. D. Decker, W. B. Mori, K. C. Tzeng, K. A. Marsh, C. E. Clayton, and C. Joshi, "Propagation of intense subpicosecond laser-pulses through underdense plasmas," *Phys. Rev. Lett.*, vol. 74, p. 4659, 1995.

[9] W. B. Mori, C. D. Decker, D. E. Hinkel, and T. Katsouleas, "Raman forward scattering of short-pulse high-intensity lasers," *Phys. Rev. Lett.*, vol. 72, p. 1482, 1994.

[10] A. Modena, Z. Najmudin, A. E. Dangor, C. E. Clayton, K. A. Marsh, C. Joshi, V. Malka, C. B. Darrow, and C. Danson, "Observation of Raman forward scattering and electron acceleration in the relativistic regime," *IEEE Trans. Plasma Sci.*, vol. 24, p. 289, 1996.

[11] C. E. Max, J. Arons, and A. B. Langdon, "Self-modulation and self-focusing of electromagnetic waves in plasmas," *Phys. Rev. Lett.*, vol. 33, p. 209, 1974.
[12] S. C. Wilks, W. L. Kruer, M. Tabak, and A. B. Langdon, "Absorption of ultra-intense laser-pulses," *Phys. Rev. Lett.*, vol. 69, p. 1383, 1992.
[13] M. Zepf, M. Castrocolin, D. Chambers, S. G. Preston, J. S. Wark, J. Zhang, C. N. Danson, D. Neely, P. A. Norreys, A. E. Dangor, A. Dyson, P. Lee, A. P. Fews, P. Gibbon, S. Moustaizis, and M. H. Key, "Measurements of the hole boring velocity from doppler-shifted harmonic emission from solid target," *Phys. Plasmas*, vol. 3, p. 3242, 1996.
[14] A. E. Dangor, A. K. L. Dymoke-Bradshaw, A. Dyson, T. Garvey, I. Mitchell, A. J. Cole, C. N. Danson, C. B. Edward, and R. G. Evans, "Generation of uniform plasmas for beatwave experiments," *IEEE Trans. Plasma Sci.*, vol. PS15, p. 161, 1987.
[15] T. M. Antonsen and P. Mora, "Self-focusing and Raman-scattering of laser-pulses in tenuous plasmas," *Phys. Rev. Lett.*, vol. 69, p. 2204, 1992.
[16] C. D. Decker, W. B. Mori, T. Katsouleas, and D. E. Hinkel, "Spatial temporal theory of Raman forward scattering," *Phys. Plasmas*, vol. 3, p. 1360, 1996.
[17] C. J. McKinstrie and E. J. Turano, "Spatiotemporal evolution of parametric instabilities driven by short laser pulses: Two-dimensional analysis," *Phys. Plasmas*, vol. 4, p. 3347, 1997.
[18] B. Quesnel, P. Mora, J. C. Adam, S. Guerin, A. Heron, and G. Laval, "Electron parametric instabilities of ultraintense short laser pulses propagating in plasmas," *Phys. Rev. Lett.*, vol. 78, p. 2132, 1997.
[19] A. Modena, Z. Najmudin, A. E. Dangor, C. E. Clayton, K. A. Marsh, C. Joshi, V. Malka, C. B. Darrow, C. Danson, D. Neely, and F. N. Walsh, "Electron acceleration from the breaking of relativistic plasma-waves," *Nature*, vol. 377, p. 606, 1995.
[20] C. Joshi, T. Tajima, J. M. Dawson, H. A. Baldis, and N. A. Ebrahim, "Forward Raman instability and electron acceleration," *Phys. Rev. Lett.*, vol. 47, p. 1285, 1981.
[21] W. B. Mori, "The physics of the nonlinear optics of plasmas at relativistic intensities for short-pulse lasers," *IEEE J. Quant. Electron.*, vol. 33, p. 1942, 1997.
[22] A. J. Mackinnon, M. Borghesi, A. Iwase, M. W. Jones, G. J. Pert, S. Rae, K. Burnett, and O. Willi, "Quantitative study of the ionization-induced refraction of picosecond laser pulses in gas-jet targets," *Phys. Rev. Lett.*, vol. 76, p. 1473, 1996.
[23] S. C. Rae, "Spectral blueshifting and spatial defocusing of intense laser-pulses in dense gases," *Opt. Commun.*, vol. 104, p. 330, 1994.
[24] K. Krushelnick, A. Ting, C. I. Moore, H. R. Burris, E. Esarey, P. Sprangle, and M. Baine, "Plasma channel formation and guiding during high intensity short pulse laser plasma experiments," *Phys. Rev. Lett.*, vol. 78, p. 4047, 1997.
[25] S. Y. Chen, G. S. Sarkisov, A. Maksimchuk, R. Wagner, and D. Umstadter, "Evolution of a plasma waveguide created during relativistic-ponderomotive self-channeling of an intense laser pulse," *Phys. Rev. Lett.*, vol. 80, p. 2610, 1998.
[26] C. E. Clayton, K. C. Tzeng, D. Gordon, P. Muggli, W. B. Mori, C. Joshi, V. Malka, Z. Najmudin, A. Modena, D. Neely, and A. E. Dangor, "Plasma wave generation in a self-focused channel of a relativistically intense laser pulse," *Phys. Rev. Lett.*, vol. 81, p. 100, 1998.
[27] P. Sprangle, C. M. Tang, and E. Esarey, "Relativistic self-focusing of short-pulse radiation beams in plasmas," *IEEE Trans. Plasma Sci.*, vol. 15, p. 145, 1987.
[28] X. L. Chen and R. N. Sudan, "Necessary and sufficient conditions for self-focusing of short ultraintense laser-pulse in underdense plasma," *Phys. Rev. Lett.*, vol. 70, p. 2082, 1993.
[29] C. N. Danson, J. Collier, D. Neely, L. J. Barzanti, A. Damerell, C. B. Edwards, M. H. R. Hutchinson, M. H. Key, P. A. Norreys, D. A. Pepler, I. N. Ross, P. F. Taday, W. T. Toner, M. Trentelman, F. N. Walsh, T. B. Winstone, and R. W. W. Wyatt, "Well characterized 10^{19} Wcm^{-2} operation of VULCAN—An ultra-high power Nd:glass laser," *J. Mod. Opt.*, vol. 45, p. 1653, 1998.
[30] R. Bruckner, "Etude de l'ionization laser de jets de gaz haute densite," Ph.D. dissertation, Universite d'Orleans, 1994.
[31] V. Malka, A. Modena, Z. Najmudin, A. E. Dangor, C. E. Clayton, K. A. Marsh, C. Joshi, C. N. Danson, D. Neely, and F. N. Walsh, "Second harmonic generation and its interaction with relativistic plasma waves driven by forward Raman instability in underdense plasmas," *Phys. Plasmas*, vol. 4, p. 1127, 1997.
[32] A. K. Lal, D. Gordon, K. Wharton, C. E. Clayton, K. A. Marsh, W. B. Mori, C. Joshi, M. J. Everett, and T. W. Johnston, "Spatio-temporal dynamics of the resonantly excited relativistic plasma wave driven by a CO_2 laser," *Phys. Plasmas*, vol. 4, p. 1434, 1997.
[33] P. Gibbon, P. Monot, T. Auguste, and G. Mainfray, "Measurable signatures of relativistic self-focusing in underdense plasmas," *Phys. Plasmas*, vol. 2, p. 1305, 1995.
[34] P. Sprangle, J. Krall, and E. Esarey, "Hose-modulation instability of laser-pulses in plasmas," *Phys. Rev. Lett.*, vol. 73, p. 3544, 1994.
[35] G. Shvets and J. S. Wurtele, "Instabilities of short-pulse laser propagation through plasma channels," *Phys. Rev. Lett.*, vol. 73, p. 3540, 1994.
[36] F. Vidal and T. W. Johnston, "Electromagnetic beam breakup: Multiple filaments, single beam equilibria, and radiation," *Phys. Rev. Lett.*, vol. 77, p. 4852, 1996.
[37] Z. Najmudin, K. Krushelnick, E. L. Clark, M. Salvati, M. I. K. Santala, M. Tatarakis, A. E. Dangor, V. Malka, D. Neely, R. Allott, and C. Danson, "Hosing, sausaging, filamentation and sidescatter of a high-intensity short-pulse laser in an under-dense plasma," presented at the IFSA, Bordeaux, France, 1999.
[38] T. M. Antonsen and Z. Bian, "Ionization induced scattering of short intense laser pulses," *Phys. Rev. Lett.*, vol. 82, p. 3617, 1998.
[39] M. Ciarrocca, J. P. Marangos, D. D. Burgess, M. H. R. Hutchinson, R. A. Smith, S. C. Rae, and K. Burnett, "Spectral and spatial modifications to an intense 1 μm laser-pulse interacting with a dense argon gas," *Opt. Comm.*, vol. 110, p. 425, 1994.
[40] K. C. Tzeng and M. W. B. Mori, "Suppression of electron ponderomotive blowout and relativistic self-focusing by the occurrence of Raman scattering and plasma heating," *Phys. Rev. Lett.*, vol. 81, p. 104, 1998.
[41] C. D. Decker, W. B. Mori, K. C. Tzeng, and T. Katsouleas, "Evolution of ultra-intense, short-pulse lasers in underdense plasmas," *Phys. Plasmas*, vol. 3, p. 2047, 1996.
[42] D. Gordon, K. C. Tzeng, C. E. Clayton, A. E. Dangor, V. Malka, K. A. Marsh, A. Modena, W. B. Mori, P. Muggli, Z. Najmudin, D. Neely, C. N. Danson, and C. Joshi, "Observation of electron energies beyond the linear dephasing limit from a laser-excited relativistic plasma wave," *Phys. Rev. Lett.*, vol. 80, p. 2133, 1998.
[43] K. C. Tzeng, W. B. Mori, and T. Katsouleas, "Electron beam characteristics from laser-driven wave breaking," *Phys. Rev. Lett.*, vol. 79, p. 5258, 1997.
[44] L. Gorbunov, P. Mora, and T. M. Antonsen, "Magnetic field of a plasma wake driven by a laser pulse," *Phys. Rev. Lett.*, vol. 76, p. 2495, 1996.
[45] D. W. Forslund, J. M. Kindel, W. B. Mori, C. Joshi, and J. M. Dawson, "2-dimensional simulations of single-frequency and beat-wave laser-plasma heating," *Phys. Rev. Lett.*, vol. 54, p. 558, 1985.
[46] C. D. Decker and W. B. Mori, "Group-velocity of large-amplitude electromagnetic-waves in a plasma," *Phys. Rev. Lett.*, vol. 72, p. 490, 1994.
[47] S. Guerin, G. Laval, P. Mora, J. C. Adam, A. Heron, and A. Bendib, "Modulational and Raman instabilities in the relativistic regime," *Phys. Plasmas*, vol. 2, p. 2807, 1995.
[48] V. Malka, C. Coulaud, J. P. Geindre, V. Lopez, Z. Najmudin, D. Neely, and F. Amiranoff, "Characterization of neutral density profile in a wide range of pressure of cylindrical pulsed gas jet," *Rev. Sci.*, vol. 71, p. 2329, 2000.

Z. Najmudin, photograph and biography not available at the time of publication.

A. E. Dangor, photograph and biography not available at the time of publication.

A. Modena, photograph and biography not available at the time of publication.

M. R. Salvati, photograph and biography not available at the time of publication.

C. E. Clayton, photograph and biography not available at the time of publication.

C. N. Danson, photograph and biography not available at the time of publication.

Daniel F. Gordon, received the B.S., M.S., and Ph.D. degrees in electrical engineering from the University of California, Los Angeles, in 1991, 1995, and 1999, respectively.

He is currently a National Research Council research associate at the Naval Research Laboratory, Washington, DC. His research interests are in high intensity, short pulse, laser-plasma interactions, plasma based accelerators, and computer modeling.

C. Joshi (M'83–SM'88–F'93), photograph and biography not available at the time of publication.

K. A. Marsh, photograph and biography not available at the time of publication.

V. Malka, photograph and biography not available at the time of publication.



Patrick Muggli received the B.S. and Ph.D. degrees from the Centre de Recherche en Physique des Plasmas, Ecole Polytechnique Fédérale de Lausanne, Switzerland, in the fields of plasma physics and high-power microwave sources.

He was a Swiss National Science Foundation postdoctoral fellow at the Electrical Engineering Department of the University of California, Los Angeles. He worked on frequency upshiftting of electromagnetic radiation using plasmas, and on photoemission processes. He joined the University of Southern California (USC), Los Angeles, and his research topics include all aspects of plasma-based radiation sources, and plasma-based particle accelerators. He is currently an Assistant Research Professor at USC.

Dr. Muggli is the USC representative to the Coalition for Plasma Science.

D. Neely, photograph and biography not available at the time of publication.

F. N. Walsh, photograph and biography not available at the time of publication.

Extending Plasma Accelerators: Guiding with Capillary Tubes

B. Cros, C. Courtois, G. Malka, G. Matthieussent, J. R. Marquès, F. Dorchies, F. Amiranoff, S. Rebibo, G. Hamoniaux, N. Blanchot, and J. L. Miquel

Abstract—**In order to extend plasma accelerators, the laser beam has to be guided inside gas or plasma over a distance of the order of the dephasing length, which is typically much larger than the diffraction length z_R of the laser. A capillary tube can be used as a waveguide for high-intensity laser pulses over distances well in excess of z_R. Experimental demonstration of monomode guiding over 100 z_R of 10^{16} W/cm^2 pulses has been obtained in evacuated capillary tubes (45–70-μm inner diameter). A drop of transmission has been observed when the intensity of the amplified spontaneous emission (ASE) is high enough to ionize the capillary tube entrance. Propagation in helium gas-filled (10–40 mbar) capillary tubes has been studied at intensities up to 10^{16} W/cm^2; a plasma column with on-axis density of the order of 10^{17} cm^{-3} has been created on a length of the order of 4 cm. The use of a capillary tube for an extended accelerator is discussed for the case of linear, resonant excitation of plasma waves by laser wakefield.**

Index Terms—**Guiding, plasma accelerator.**

I. Introduction

SINCE the original idea [1] of using a plasma as a medium able to sustain high-amplitude longitudinal electric fields, plasma accelerators have been extensively studied. The three possible schemes (for a review, see [2]) to excite plasma waves by laser, beat wave, wakefield [3], [4], and self-modulated wakefield, have been demonstrated experimentally as well as the acceleration of injected electrons [5]. In order to go beyond a proof of principle experiment, a way of extending the length of the plasma accelerator has to be achieved. The maximum energy gain of electrons injected into the accelerating structure is proportional to the amplitude of the electric field and to the interaction length. A physical limitation for the interaction length is the dephasing length, i.e., the distance over which the electrons overtake the plasma wave and stop gaining energy. In previous experiments, the plasma length was limited to a few Rayleigh lengths, which is the diffraction length of the laser beam used to excite the plasma wave. Extending a plasma accelerator, therefore, requires a guiding mechanism for the laser beam so that high-intensity propagation can be achieved over a distance much larger than the Rayleigh length.

Various mechanisms, based on a modification of the transverse profile of the refractive index of the plasma, have been proposed to guide a high-intensity laser pulse inside a plasma. For sufficiently high laser power, the refractive index can be modified by the laser pulse and lead to relativistic or ponderomotive self-channeling [6]. Alternatively, Durfee *et al.* [7] have demonstrated that a long laser pulse can create a plasma channel [8], [9] in which a short laser pulse can be guided over more than 70 z_R. The guiding of an intense (10^{16} W/cm^2) laser pulse has also been demonstrated in a plasma channel created by a slow capillary discharge [10]. In all of these schemes, the guiding conditions impose the plasma density and its spatial profile. However, many applications need plasma parameters very different from those required by laser guiding and would benefit from a guiding structure existing independently of the plasma.

The use of hollow capillary tubes as a guiding structure is attractive for laser interaction over long distances with a relatively low-density plasma. In this scheme, the laser pulse is guided by the capillary tube inner wall and the plasma can be provided by the ionization of a gas filling the capillary tube. Guiding of high-intensity laser pulses in capillary tubes has been observed in a few experiments [11]–[13]. Jackel *et al.* [11] have observed multimode guiding of a picosecond pulse, characterized by a complex transverse intensity profile and a slow group velocity; in the same experiment, they also observed inner wall breakdown at high intensity. Monomode guiding [13] is more appropriate for laser–plasma accelerators because a smooth transverse profile and a high group velocity can be achieved with this mode of propagation. Furthermore, the damping is minimized, allowing guiding over a long distance of high-intensity pulses without wall breakdown.

The paper is organized as follows. Section II summarizes the properties of the monomode propagation for a Gaussian beam inside a capillary tube, and experimental results in evacuated and gas-filled capillary tubes are presented. Some experimental limitations of the coupling of intensities higher than 10^{17} W/cm^2 to capillary tubes are described in Section III. Finally, the parameters of an extended laser accelerator are discussed in Section IV.

II. Characteristics of Monomode Guiding

A. Analytical Model

In vacuum, a capillary tube can be modeled as a wave guide of cylindrical symmetry with a core of inner radius a and di-

Manuscript received October 7, 1999; revised January 2, 2000. This work was supported in part by the Université Paris XI, under a BQR contract.

B. Cros, C. Courtois, G. Malka, and G. Matthieussent are with the LPGP, UMR 8578 CNRS, Université Paris XI, 91405, Orsay, France.

J. R. Marquès, F. Dorchies, F. Amiranoff, and S. Rebibo are with the LULI, UMR 7605 CNRS-CEA, Université Paris VI, Ecole Polytechnique, 91128 Palaiseau Cedex, France.

G. Hamoniaux is with the LOA, ENSTA, Ecole Polytechnique, 91128 Palaiseau Cedex, France.

N. Blanchot is with the CEA/CESTA, 33114 Le Bart, France.

J. L. Miquel is with the CEA/DAM-Ile de France, 91680 Bruyères Le Chatel, France.

Publisher Item Identifier S 0093-3813(00)07245-3.

0093–3813/00$10.00 © 2000 IEEE

electric constant $\varepsilon = 1$ and a wall made of dielectric material characterized by a dielectric constant $\varepsilon_w > 1$. The calculation of the fields inside this type of waveguide can be found in [14] and is summarized here.

The propagation of the laser beam inside an evacuated capillary tube can be analyzed by assuming that the electromagnetic field is a superposition of modes with a dependance along the propagation axis as $\exp(-ik_z z)$. Maxwell's equations are solved, taking into account continuity conditions at the interface of each medium and assuming the fields go to zero at infinity. Thus, we obtain a general dispersion relation that can be simplified and solved approximately when the wavelength of the incident beam is much smaller than the tube radius ($\lambda_0 \ll a$) and when the perpendicular wavenumber inside the capillary tube $k_{\perp m}$ is much smaller than the perpendicular wavenumber inside the tube wall $k_{\perp w}$, which can be written as $(|\varepsilon k_0^2 - k_z^2|)^{1/2} \ll (|k_z^2 - k_0^2\varepsilon_w|)^{1/2}$. For each mode, the dispersion relation is solved at zero order in $k_{\perp m}$; the first-order solution is related to a first-order perturbation of the longitudinal wavenumber and allows us to determine the amount of damping.

Apart from the transverse electric and magnetic modes, hybrid modes, with all electric and magnetic components different from zero, are also a solution of the problem. The coupling of the incident beam to eigenmodes inside the capillary tube can be treated mathematically as a mapping of the incident electromagnetic field on an orthogonal system of modes. In the case of our experiments, the incident beam is linearly polarized and its intensity profile along the radius can be approximated by a Gaussian function. The mapping of this incident beam on the system of modes is different from zero for hybrid modes of the type EH_{1m}, which electric components can be written, in cylindrical coordinates (z, r, ψ) and for $r < a$, as

$$E_z = -E_0 J_1(k_{\perp m} r)\cos\varphi \tag{1}$$

$$E_r = -E_0 \frac{k_z}{k_{\perp m}} J_0(k_{\perp m} r)\sin\varphi \tag{2}$$

$$E_\psi = E_0 \frac{k_z}{k_{\perp m}} J_0(k_{\perp m} r)\cos\varphi \tag{3}$$

with $\varphi = \omega_0 t - k_z z - \psi$, ω_0 is the pulsation of the incident electromagnetic wave in vacuum, and J_ν is the Bessel function of integer order ν. $k_{\perp m}$ is the transverse wave vector associated to the mth root, $\alpha_{0,m}$, of the equation $J_0(k_{\perp m} a) = 0$, which value increases with the value of the integer index m. These expressions of the fields have been obtained at the zero-order approximation. Note that under the assumptions $k_0 a \gg 1$ and $k_{\perp m} \ll k_0$, $E_r, E_\psi \gg E_z$, so that the electromagnetic field is quasi-transverse (the same type of relation holds between the magnetic components). The group velocity, $v_{gm} \simeq c\varepsilon^{-1/2}(1 - k_{\perp m}^2/\varepsilon k_0^2)^{1/2} \equiv c[1 - (\alpha_{0,m}\lambda_0)^2/4\pi^2 a^2]^{1/2}$, remains close to the free-space velocity of light in vacuum c and decreases when m is increased; the relativistic factor associated to this group velocity is $\gamma_{gm} = 2\pi a/(\lambda_0 \alpha_{0,m})$. For example, for typical parameters such as $\lambda_0 = 0.8\ \mu$m and $a = 25\ \mu$m, $\gamma_{g1} = 81$ and $\gamma_{g2} = 35$; after propagating inside a capillary tube 10 cm long, these two modes will be separated by a time delay of the order of 100 fs, which is of the order of magnitude of the incident pulse duration in the experiment. In order to keep the pulse duration short, it is then necessary to couple the incident beam to only one mode. Then, for capillary tubes up to 1 m long, the group velocity dispersion related to the incident pulse spectral width ($\Delta\lambda = 10$ nm) produces a time delay smaller than 1 fs and can be neglected.

The beam propagating along the Oz-axis is exponentially damped with a characteristic coefficient (imaginary part of the longitudinal wavenumber) given by

$$k_{zi,m} \simeq -\Im\left[\frac{\alpha_{0,m}^2}{2k_0^2 a^3}\frac{\varepsilon + \varepsilon_w}{\sqrt{\varepsilon - \varepsilon_w}}\right]. \tag{4}$$

Note that for waveguides such that $\varepsilon > \varepsilon_w$, as is the case usually for solid core fibers, no damping occurs. The beam intensity is divided by e after a length of propagation equal to $z_d/2 = k_{zi}^{-1}$. The damping coefficient increases with mode number and is strongly dependent on the capillary tube radius. The spatial contrast, or ratio of the intensity on the tube wall to the intensity on axis, can be expressed as

$$\frac{I(r=a)}{I(r=0)} \simeq J_1^2(\alpha_{0,m})\left|\frac{\alpha_{0,m}\lambda_0}{4\pi a}\frac{\varepsilon + \varepsilon_w}{\sqrt{\varepsilon - \varepsilon_w}}\right|^2. \tag{5}$$

For the above parameters and glass walls ($\varepsilon_w = 2.25$), $z_d = 11.5$ cm and $I(r=a)/I(r=0) \simeq 10^{-4}$. This analysis shows that most of the incident beam energy will propagate over the longest possible distance inside the capillary tube when the energy of the incident beam is transferred to the fundamental mode or EH_{11}-mode.

This coupling occurs at the entrance plane of the capillary tube, where the incident beam is focused. Assuming a Gaussian incident beam with an electric field $E(r) \propto \exp(-r^2/w_0^2)$, the best entrance coupling into the EH_{11}-mode is obtained for $w_0/a = 0.64$ [15]. In this model, 98% of the incident energy is then transferred to the fundamental mode, inducing a quasi-perfect monomode guiding of the laser beam.

B. Experimental Results

The laser beam coupling and guided propagation have been studied experimentally inside glass capillary tubes.

1) Experimental Arrangement: Experiments have been performed at the Laboratoire d'Optique Appliquée with a Ti : Sa laser system. An energy up to 30 mJ is delivered with a 10-Hz repetition rate and a pulse duration of 120-fs full-width at half maximum (FWHM); the light is linearly polarized and the central wavelength is $\lambda = 0.8\ \mu$m. The experimental setup is shown in Fig. 1. The beam enters a vacuum chamber and is focused by a $f/8$ plano-convexe $\mathrm{M_gF_2}$ lens on the entrance plane of a collinear capillary tube. A small part (less than 1%) of the beam is sent before focusing to a calibrated photodiode and to a second-order single-shot autocorrelator for incident energy and pulse duration measurement. The capillary tube is mounted on a target support with five degrees of freedom (the $x - y - z$ translations and the $\theta_x - \theta_y$ rotations). A $f/4$ $\mathrm{M_gF_2}$ lens images the output plane of the tube on the slit of an imaging spectrometer. The output beam is split into three parts: 96% of the output energy is sent to a calorimeter, 2% is sent to an autocorrelator, and the remaining 2% is sent to a spectrometer coupled to a 16-bit

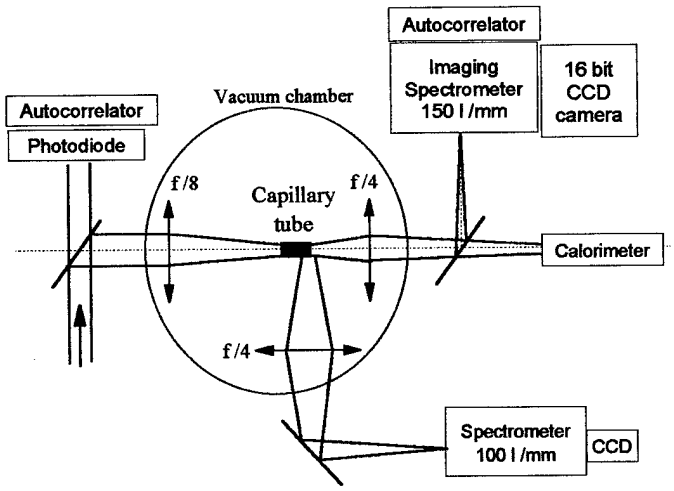


Fig. 1. Experimental setup.

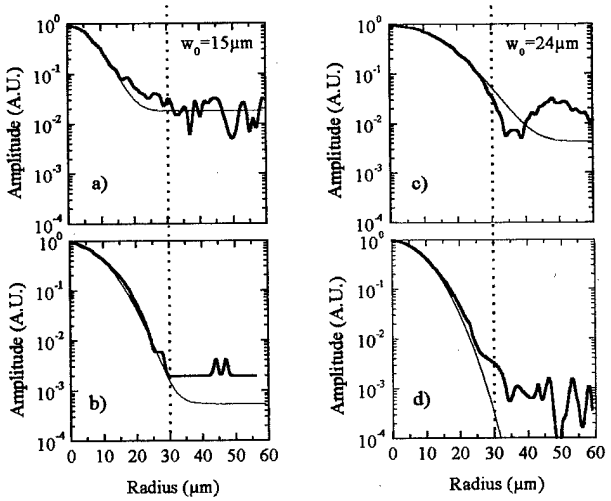


Fig. 2. Energy spatial repartition along the radius (a) on the entrance and (b) output plane of a capillary tube $a = 30\ \mu$m and $L = 5.4$ cm. Experimental measurement (bold line) and Gaussian fit (thin line); the dotted line is the interface $r = a$.

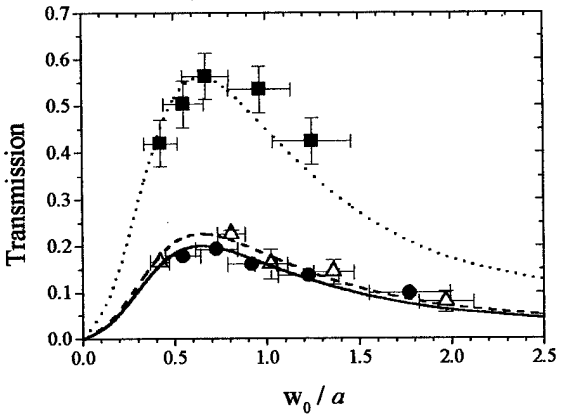


Fig. 3. Measured and theoretical (lines) transmission as a function of w_0/a for tubes with $a = 35\ \mu$m and $L = 8.3$ cm (squares and dotted line), $a = 22.5\ \mu$m and $L = 5.4$ cm (triangles and dashed line), and $a = 25\ \mu$m and $L = 8.3$ cm (circles and plain line). Theoretical curves are obtained with $C = 0.97, 0.87$, and 0.84, respectively.

charge-coupled device (CCD) camera. The specular reflection of the spectrometer grating gives the image of the laser spot, whereas the first order gives its spectrum.

2) In Vacuum: Evidence of monomode guiding is obtained by measuring the spatial repartition of the transmitted energy. The coupling of the incident beam to a capillary tube $a = 30\ \mu$m and $L = 5.4$ cm has been studied by varying the beam size before focusing. For spot size radii w_0 of the incident beam in the range 14—46 μm ($w_0/a = 0.56$–1.84), only the mode EH_{11} has been observed at the output plane of the capillary tube; this is illustrated in Fig. 2. The dotted line is the position of the capillary wall. The left-hand side panels [Fig. 2(a) and (b)] show the beam intensity profile (a) at the entrance of the capillary tube (incident focal spot), fitted by a Gaussian function with $w_0 = 15\ \mu$m, and (b) at the output plane of the capillary tube. The right-hand side panels [Fig. 2(c) and (d)] correspond to a larger spot size at the input plane (c), but the output intensity profile (d) is similar to (b). Note that the contrast at the output of the capillary tube is independant of w_0 and is better than 10^{-3} for $r > a$, in agreement with the theoretical value of 10^{-4}. The measurement of the contrast is limited experimentally by the light scattered through the capillary tube wall.

The transmission in energy T (ratio of output energy to the total incident energy in the focal spot) is plotted in Fig. 3 as a function of the ratio w_0/a for three values of the tube radius. The transmission is maximum when $w_0/a \simeq 0.6$, as expected for the coupling of the incident beam into the mode EH_{11}. For an incident Gaussian beam with $w_0/a = 0.64$, the analytical model predicts that 98% of the incident energy is coupled to the mode EH_{11}. The maximum transmission can be written as $T = C\exp[-2L/z_d]$, where C is the coupling coefficient at the tube input plane. The continuous curves in Fig. 3 are the theoretical curves normalized at $w_0/a = 0.64$ to the maximum transmission, computed for a value of C determined experimentally as the percentage of the total energy of the incident focal spot contained in a disk of radius equal to a; here, the measured values of C are 97% for $a = 35\ \mu$m, 87% for $a = 22.5\ \mu$m, and 84% for $a = 25\ \mu$m. A good agreement is obtained with experimental points, indicating that the damping length is close to the theoretical value of the fundamental mode. The fraction of the incident energy coupled to higher order modes has a contribution to the transmission smaller than the experimental error bars.

The damping characteristic length has been obtained experimentally by measuring the transmission as a function of the capillary tube length for a given incident beam and capillary tube radius. The capillary tube length has been changed by cutting the tube from the output end so that the entrance plane does not change with capillary tube length. The energy transmission as a function of the capillary tube length is shown in Fig. 4 for two values of tube radius, $a = 25\ \mu$m and $35\ \mu$m. The experimental results are fitted by decreasing exponential functions; their extrapolation at $L = 0$ gives values of $C = 84\%$ (respectively, 81%) corresponding to the measured percentage of energy in a disk of radius 35 μm (25 μm) of the focal spot imaged in the absence of capillary tube. The best fits give damping lengths $z_d = 36 \pm 5$ cm (12 ± 1 cm), close to the theoretical values for the fundamental mode in each case: $z_{d1} = 31.5$ cm (11.5 cm).

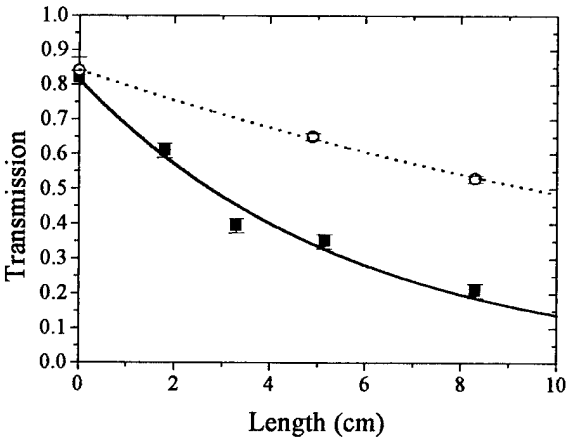


Fig. 4. Energy transmission measured as a function of capillary tube length for two values of capillary tube radius: $a = 35\ \mu$m (circles) and $a = 25\ \mu$m (squares). The curves are exponential fits of the type $T = C\exp(-2L/z_d)$.

The energy transmission factor has been measured for different incident energies. It remains constant within 15% fluctuations up to the maximum energy available in this experiment, corresponding to an input intensity of 5×10^{16} W/cm^2. For a capillary tube 10 cm long with $a = 25\ \mu$m, the transmission is typically of 20%, so that an intensity larger than 10^{16} W/cm^2 has been guided over 100 z_R ($z_R \simeq 1$ mm).

In vacuum, no modification of the output pulse duration and spectrum caused by the guided propagation has been measured experimentally. This is in agreement with the theoretical model, which predicts time delays (compared with free-space propagation) of the order of 1 fs, smaller than shot-to-shot pulse duration fluctuations.

3) In Gas: In this section, we present results relative to the propagation of the laser beam in a capillary tube filled with gas or plasma. The setup is the same as previously, and the interaction chamber is filled with helium gas at a pressure up to 40 mbar. The output of the capillary tube is imaged at 90° of the laser axis on a spectrometer: the observation of the recombination spectral line (586.7 nm) of helium is the signature of plasma at the exit of the tube [13]. For an incident energy higher than 20 mJ and gas pressure lower than 20 mbar, this spectral line is always observed at the output of capillary tubes with $a = 25\ \mu$m and $L = 1.2$ to 4 cm, showing that ionization occurs over a length much longer than the diffraction length and that the output intensity is larger than 10^{15} W/cm^2 (ionization threshold [16] of helium). This is also confirmed by the measurements of energy, pulse duration, and waist of the output beam.

The spectrum of the transmitted light through a capillary tube 4 cm long is compared with a spectrum obtained without capillary tube in Fig. 5, for a helium gas pressure of 10 mbar. The corresponding spectra in vacuum are also plotted (thin line) as reference spectra. Whereas the 10-mbar spectrum of unguided light remains similar to the vacuum spectrum, the spectrum at the output of the capillary tube for a pressure of 10 mbar exhibits a blue shift and a broadening. The spectral blue shift is induced by the rapid ionization of gas in the front of the laser pulse. As each temporal slice of the laser pulse sees a different electron density variation, the spectral blue shift of each slice results in a spectral broadening of the transmitted spectrum. These effects

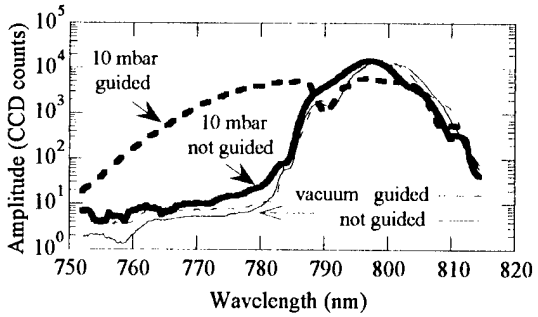


Fig. 5. Spectra of the light transmitted through a capillary tube with $a = 25\ \mu$m and length $L = 4$ cm. The spectra are normalized to the same integral.

are important only when the pulse is guided and confirm that ionization occurs over a length much larger than $2z_R$.

We observed that the transmission decreases when the laser ionizes the gas. For example, for a tube with $L = 1.2$ cm, the transmission decreases from 50% ± 5% under vacuum to 30% ± 5% in 20 mbar of helium, and to only 10% ± 5% in 40 mbar. In addition, when the tube length is increased to 4 cm, the transmission under vacuum is divided by 2.5 (20% ± 5%), whereas it is divided by 6 (5% ± 2%) at 20 mbar, indicating that not only the coupling factor, but also the damping length in the tube is affected by ionization. The laser energy loss caused by the ionization of gas over the length of the capillary tube can be neglected: the total ionization of helium gas contained in a capillary tube of 25 μm inner radius uses 6.6 μJ·cm^{-1}·mbar^{-1}, or 0.5 mJ for $L = 4$ cm and a pressure of 20 mbar.

The input and output pulse duration were also measured for different gas pressures and capillary tube lengths. For example, with a 4-cm long capillary tube, the pulse duration under vacuum (160 ± 40 fs) decreases to 65 ± 15 fs for a pressure of 20 mbar. Pulse shortening occurs because of refraction, which prevents the rear of the pulse to enter the capillary tube and propagate to the end of the capillary tube.

III. High-Intensity Guiding Limitation

Monomode guiding of ultrashort laser pulses of intensities from 10^{13} to 3×10^{18} W/cm^2 has been studied in glass capillary tubes in vacuum. The experiment was performed with the 100-TW P102 laser system at CEA Limeil Valenton [17], [21], which delivers pulses of 20 J in 500 fs (FWHM) at a wavelength of 1.06 μm. The laser pulse is focused at the center of a vacuum chamber by an $f/3$ on-axis parabola. The focal spot has a waist $w_0 = 10\ \mu$m (five times diffraction limit), so that the maximum intensity at the entrance of the capillary tube is 10^{19} W/cm^2. Three micrometric translations and two rotations allow the alignment of the capillary tube on the propagation axis of the laser. After focus, 0.8% of the transmitted light is reflected by a glass plate to a $f/3$ doublet that images (with a magnification of 30) the output plane of the capillary tube on a 12-bit CCD camera. The focal spot in the absence of a capillary tube is imaged by moving the doublet backward on the axis, of a distance equal to the capillary tube length. A fast diode has been used on some shots to measure the temporal contrast caused by amplified spontaneous emission (ASE), which is of the order of 10^7 in intensity at 2 ns before the maximum intensity. For this

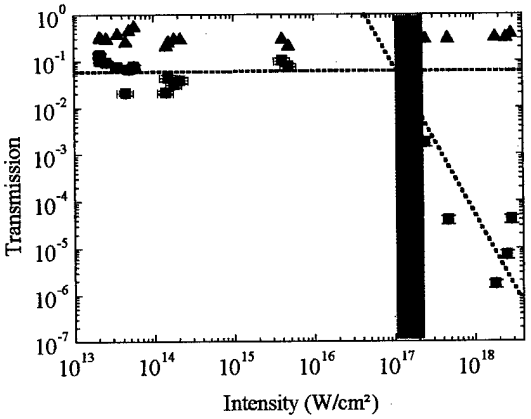


Fig. 6. Energy transmitted through a capillary tube with $a = 15$ μm and length $L \simeq 1$ cm as a function of the maximum incident intensity; measured transmission (squares) and theory (triangles).

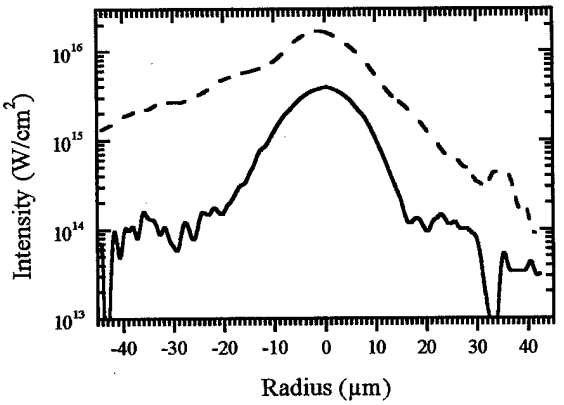


Fig. 7. Energy repartition at the input (dashed line) and output (plain line) planes of the capillary tube ($a = 15$ μm, $L = 1$ cm).

experiment, 15-μm inner radius capillary tubes are used to optimize coupling to the fundamental mode ($w_0/a \sim 0.67$). The damping length of the EH_{11}-mode is then $z_d = 14.3$ mm, and capillary tubes in the range 8 to 12 mm have been used.

Fig. 6 shows the transmission as a function of the maximum intensity at the entrance of the capillary tube. Squares are experimental values of the transmission obtained by analyzing 12-bit CCD camera images on two shots, without and with capillary tube. The transmission is computed as the ratio of energy in a disk of radius 15 μm at the output of the capillary tube to the incident energy. Triangles are the theoretical values of transmission given by $T = C\exp(-2L/z_d)$, where C is the coupling constant, defined as the percentage of energy of the incident beam coupled to the fundamental mode at the entrance plane ($L = 0$) of the capillary tube; for theoretical values, $C = 1$; i.e., 100% of the incident beam energy is coupled to the fundamental mode. The dispersion of transmission for the theoretical points results from the use of different capillary tube lengths. The transmission curve presents two tendencies. An approximately constant transmission of 6% followed by a transmission drop for intensities larger than a threshold value of around 10^{17} W/cm^2. In the range of constant transmission, the difference between theory and experiment comes mainly from a low coupling on the fundamental mode. For $I > 10^{17}$ W/cm^2, the transmission drops to 10^{-6}, well below the predicted theoretical value.

The spatial contrast was measured on 12-bit CCD camera images. Fig. 7 shows for a maximum intensity of the order of 10^{16} W/cm^2, the intensity distribution in the entrance plane of the capillary tube (dashed line, focal spot of the incident beam) and in the output plane (plain line) of the capillary tube. Fig. 7 corresponds to a transmission of the order of 6%. The incident focal spot exhibits pedestals, leading to an intensity on the capillary tube front wall ($r > 15$ μm) of the order of 25% of the maximum intensity. At the exit of the capillary tube, the measured contrast is of the order of 400 (resolution limited by noise level), so that the capillary tube acts as an efficient spatial filter. For higher incident intensity, the focal spot pattern is similar to Fig. 7.

The transmission drop occuring at intensities above 10^{17} W/cm^2 can be explained by the ionization of the entrance wall of the capillary tube. Before going into details, note that for a normal incident laser pulse, the ionization intensity threshold of fused silica is of the order of 10^{13} W/cm^2 for 500-fs pulses, and of the order of 10^{10} W/cm^2 for nanosecond pulses [18], [19].

In our conditions (focal spot with 25% contrast at $r = a$), ionizing the front wall of the capillary tube with the 500-fs pulse only requires an on-axis intensity of around 10^{14} W/cm^2. However, the plasma expands at a speed of the order of 10^7 cm/s, leading to a 50-nm expansion in 500 fs, so that the large transmission drop cannot be explained by the ionization produced by the short pulse.

A transmission drop can occur if the plasma expands and fills the capillary tube before the short pulse arrival. As indicated previously, the temporal contrast between the short component of the laser pulse and the nanosecond part (ASE) is of 10^7 at 2 ns before the laser maximum. The nanosecond component will create a plasma on the front wall of the capillary tube ($r > 15$ μm) when the intensity on the wall becomes larger than 10^{10} W/cm^2. Such an intensity is reached 2 ns before the pulse maximum as soon as the maximum intensity reaches 1 to 2×10^{17} W/cm^2 (gray area in Fig. 6), which is where the transmission drop occurs. When the short component of the pulse arrives at the capillary tube entrance, the plasma has already expanded to a size larger than 100 μm, blocking the capillary tube entrance.

IV. Prospect for an Extended Laser Accelerator

Using the expression of (1)–(3) for the electric field spatial repartition as a source term, the excitation of the plasma wave in the wake of the laser beam can be computed analytically in the linear regime. Inside a capillary tube, the longitudinal E_{pz} and transverse E_{pr} electric field components of the plasma wave can be expressed as

$$E_{pz} \simeq k_p \phi_{p0} J_0^2(k_\perp r)\cos(\omega_p t - k_p z)e^{-2k_{zi}z} \quad (6)$$

$$E_{pr} \simeq k_\perp \phi_{p0} J_0(k_\perp r) J_1(k_\perp r)\sin(\omega_p t - k_p z)e^{-2k_{zi}z} \quad (7)$$

with

$$\phi_{p0} = 0.2\,\frac{e}{\varepsilon_0}\,\frac{E_n}{mc^2}\,\frac{\lambda_0^2}{a^2\lambda_p}\,e^{-\omega_p^2\tau^2/(16\ln 2)}$$

where E_n is the laser energy in the entrance plane of the capillary tube and k_p is the wavenumber of the plasma wave. It has

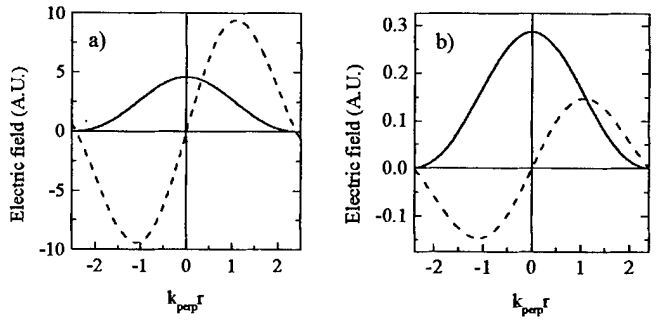


Fig. 8. Transverse profiles of the longitudinal (plain line) and radial (dashed line) electric fields of the plasma wave inside a capillary tube with (a) $a = 0.125\lambda_p$ and (b) $a = 0.5\lambda_p$.

been assumed that 98% of the incident Gaussian beam is coupled to the capillary tube and that the focal spot size is such that $w_0 = 0.64a$. Equations (6) and (7) are approximate expressions in which small terms of order $k_\perp^2/k_z^2$ and k_{zi}/k_p have been neglected. The transverse characteristics of the electric fields of the plasma wave inside the capillary tube are similar to those obtained in a two-dimensional model [20] for unguided laser pulses. The transverse profiles of these fields are plotted in Fig. 8 for two values of the tube radius a. In each case, the relationship $w_0 = 0.64a$ is imposed, and the plasma density and the incident beam energy are the same, so that only the tube radius is varied. In Fig. 8(a), the tube radius is small compared with the plasma wavelength ($a = 0.125\lambda_p$) and the radial component of the electric field becomes larger than the longitudinal component for $k_\perp r \simeq 1$. For the case $a \geq 0.5\lambda_p$ [Fig. 8(b)], the radial field remains smaller than the longitudinal field over the whole capillary tube radius.

In the case of a linear, resonant wakefield, a set of parameters for an extended accelerator is now discussed. A low value of the plasma density is suitable to allow propagation of the laser beam with a damping length similar to the one in vacuum inside the capillary tube. Typically, an electron density $n_e = 3.4 \times 10^{17}\,\mathrm{cm}^{-3}$ corresponds to a plasma wavelength $\lambda_p = 56\ \mu\mathrm{m}$, and for a resonant wakefield ($2\pi c\tau/\lambda_p = 4\sqrt{\ln 2}$), $\tau = 100$ fs, where τ is the pulse duration (FWHM in intensity). The plasma wave remains in the linear regime as long as the longitudinal electron density perturbation ($\delta n_z/n \simeq -\varepsilon_0 e^{-1} k_p E_{pz}/n$) remains of the order of 1; this value corresponds to a limit for the longitudinal electric field of the order of 56 GV/m (maximum value on axis). The transverse component of the density perturbation, $\delta n_\perp/\delta n_z \sim 0.3\lambda_p^2/a^2$, will remain smaller than the longitudinal component for large enough focal spots, giving the condition on the tube radius $a > 0.55\lambda_p$.

Assuming a maximum distance of acceleration L_{acc}, for injected electrons equal to half the dephasing length $L_{\mathrm{acc}} = 0.5\lambda_p^3\lambda_0^{-2}$, with the above parameters $L_{\mathrm{acc}} = 8.8$ cm. Choosing a capillary tube length L, i.e., a plasma length, equal to L_{acc}, the maximum energy gain, $\Delta W_{\max} = eLE_{z\max}$ is equal to 4.9 GeV. The capillary tube length should be smaller than the characteristic damping length z_d, given by (4); the condition $z_d > L_{\mathrm{acc}}$ is equivalent to $a > 0.4\lambda_p$ for glass capillary tubes. The choice of the value of the tube radius now determines completely the maximum intensity or laser energy needed to excite the maximum electric field. Typically, $a = \lambda_p$ corresponds to a laser energy of 4.8 J ($I = 2.5 \times 10^{18}\ \mathrm{W/cm}^2$).

V. Conclusion

We have demonstrated experimentally that a capillary tube used as a waveguide in vacuum allows us to propagate high-intensity pulses (10^{16} W/cm^2) over distances of the order of 10 cm, much larger than the diffraction length. When the capillary tube is filled with gas, plasma columns up to 4 cm long with an electron density on axis of the order of 10^{17} cm^{-3} have been achieved. For incident intensities higher than 10^{17} W/cm^2, the coupling of the laser beam to a capillary tube can be prevented by plasma creation on the front plane of the capillary tube. The value of the intensity threshold is related to the level of ASE before the main pulse and to the spatial quality of the focal spot. The coupling could then be improved by increasing the incident beam quality (temporal and spatial contrast improved by frequency doubling the incident beam) or by using a tapered coupler. The above estimations show that a few gigaelectronvolts energy gain over a few centimeters long plasma is expected in the resonant, linear wakefield scheme inside a capillary tube; such an experiment should be feasible in the near future.

Acknowledgment

The authors would like to acknowledge the help of the technical staff of P102.

References

[1] T. Tajima and J. M. Dawson, "Laser electron accelerator," *Phys. Rev. Lett.*, vol. 43, pp. 267–270, 1979.

[2] E. Esarey, P. Sprangle, J. Krall, and A. Ting, "Overview of plasma-based accelerator concepts," *IEEE Trans. Plasma Sci.*, vol. 24, pp. 252–288, 1996.

[3] J. R. Marquès, J. P. Geindre, F. Amiranoff, P. Audebert, J. C. Gauthier, A. Antonetti, and G. Grillon, "Temporal and spatial measurements of the electron density perturbation produced in the wake of an ultrashort laser pulse," *Phys. Rev. Lett.*, vol. 76, pp. 3566–3569, 1996.

[4] C. W. Siders, S. P. Le Blanc, D. Fisher, T. Tajima, M. C. Downer, A. Babine, A. Stepanov, and A. Sergeev, "Laser wakefield excitation and measurement by femtosecond longitudinal interferometry," *Phys. Rev. Lett.*, vol. 76, pp. 3570–3573, 1996.

[5] F. Amiranoff, S. Baton, D. Bernard, B. Cros, D. Descamps, F. Dorchies, F. Jacquet, V. Malka, J. R. Marquès, G. Matthieussent, P. Miné, A. Modena, P. Mora, J. Morillo, and Z. Najmudin, "Observation of laser wakefield acceleration of electrons," *Phys. Rev. Lett.*, vol. 81, pp. 995–998, 1998.

[6] C. E. Clayton, K. C. Tzeng, D. Gordon, P. Muggli, W. B. Mori, C. Joshi, V. Malka, Z. Najmudin, A. Modena, D. Neely, and A. E. Dangor, "Plasma wave generation in a self-focused channel of a relativistic intense laser pulse," *Phys. Rev. Lett.*, vol. 81, pp. 100–103, 1998.

[7] C. G. Durfee III, J. Lynch, and H. M. Milchberg, "Development of a plasma waveguide for high-intensity laser pulses," *Phys. Rev. E*, vol. 51, pp. 2368–2389, 1995.

[8] V. Malka, E. De Wispelaere, F. Amiranoff, S. Baton, R. Bonadio, C. Coulaud, R. Haroutunian, A. Modena, D. Puissant, C. Stenz, S. Hüller, and M. Casanova, "Channel formation in long laser pulse interaction with a helium gas jet," *Phys. Rev. Lett.*, vol. 79, pp. 2979–2982, 1997.

[9] S. P. Nikitin, T. M. Antonsen, T. R. Clark, Y. Li, and H. M. Milchberg, "Guiding of intense femtosecond pulses in preformed plasma channels," *Opt. Lett.*, vol. 22, pp. 1787–1789, 1997.

[10] Y. Ehrlich, C. Cohen, A. Zigler, J. Krall, P. Sprangle, and E. Esarey, "Guiding of high intensity laser pulses in straight and curved plasma channel experiments," *Phys. Rev. Lett.*, vol. 77, pp. 4186–4189, 1996.

[11] S. Jackel, R. Burris, J. Grun, A. Ting, C. Manka, K. Evans, and J. Kosakowskii, "Channeling of terawatt laser pulses by use of hollow waveguides," *Opt. Lett.*, vol. 20, pp. 1086–1088, 1995.

[12] M. Borghesi, A. J. Mackinnon, R. Gaillard, O. Willi, and A. A. Offenberger, "Guiding of a 10-TW picosecond laser pulse through hollow capillary tubes," *Phys. Rev. E*, vol. 57, pp. R4899–R4902, 1998.
[13] F. Dorchies, J. R. Marquès, B. Cros, G. Matthieussent, C. Courtois, T. Vélikoroussov, P. Audebert, J. P. Geindre, S. rebibo, G. Hamoniaux, and F. Amiranoff, "Monomode guiding of 10^{16} W/cm^2 laser pulses over 100 Rayleigh lengths in hollow capillary dielectric tubes," *Phys. Rev. Lett.*, vol. 82, pp. 4655–4658, 1999.
[14] E. A. J. Marcatili and R. A. Schmeltzer, "Hollow metallic and dielectric waveguides for long distance optical transmission and lasers," *Bell Syst. Tech. J.*, vol. 43, pp. 1783–1809, 1964.
[15] R. L. Abrams, "Coupling losses in hollow waveguide laser resonators," *IEEE J. Quant. Electron.*, vol. QE-8, pp. 838–843, 1972.
[16] S. Augst, D. Strickland, D. D. Meyerhofer, S. L. Chin, and J. H. Eberly, "Tunneling ionization of noble gases in a high-intensity laser field," *Phys. Rev. Lett.*, vol. 63, pp. 2212–2215, 1989.
[17] N. Blanchot, C. Rouyer, C. Sauteret, and A. Migus, "Amplification of sub-100-TW femtosecond pulses by shifted amplifying Nd : glass amplifiers: Theory and experiments," *Opt. Lett.*, vol. 20, pp. 395–397, 1995.
[18] D. Du, X. Liu, G. Korn, J. Squier, and G. Mourou, "Laser-induced breakdown by impact ionization in SiO_2 with pulses widths from 7 ns to 150 fs," *Appl. Phys. Lett.*, vol. 64, pp. 3071–3073, 1994.
[19] M. Lenzner, J. Krüger, S. Sartania, Z. Cheng, CH. Spielmann, G. Mourou, W. Kautek, and F. Krausz, "Femtosecond optical breakdown in dielectrics," *Phys. Rev. Lett.*, vol. 80, pp. 4076–4079, 1998.
[20] L. M. Gorbunov and V. I. Kirsanov, "Excitation of plasma waves by an electromagnetic wave packet," *Sov. Phys. JETP*, vol. 66, pp. 290–294, 1987.
[21] C. Rouyer, N. Blanchot, I. Allais, E. Mazataud, J. L. Miquel, M. Nail, A. Pierre, C. Sauteret, and A. Migus, "Production and characterization of intensities above 2×10^{19} W/cm^2, obtained with 30-TW 300-fs pulses generated in a Ti : sapphire/Nd-doped mixed-glass chain," *J. Opt. Soc. Am. B*, vol. 13, pp. 55–58, 1995.

B. Cros, photograph and biography not available at the time of publication.

C. Courtois, photograph and biography not available at the time of publication.

G. Malka, photograph and biography not available at the time of publication.

G. Matthieussent, photograph and biography not available at the time of publication.

J. R. Marquès, photograph and biography not available at the time of publication.

F. Dorchies, photograph and biography not available at the time of publication.

F. Amiranoff, photograph and biography not available at the time of publication.

S. Rebibo, photograph and biography not available at the time of publication.

G. Hamoniaux, photograph and biography not available at the time of publication.

N. Blanchot, photograph and biography not available at the time of publication.

J. L. Miquel, photograph and biography not available at the time of publication.

Interaction of Ultraintense Laser Pulses with an Underdense, Preformed Plasma Channel

V. Malka, J. Faure, J. R. Marquès, F. Amiranoff, C. Courtois, Z. Najmudin, K. Krushelnick, M. R. Salvati, and A. E. Dangor

***Abstract*—We report on experimental results regarding the propagation of ultraintense laser pulses in a preformed plasma channel. In this experiment, the long (4-mm) fully ionized plasma channel created by the amplified spontaneous emission (ASE) was measured by interferometry before and after the propagation of the short laser pulse. Forward spectra show a cascade of Raman satellites, which merge with one another when the laser power was increased up to critical power for relativistic self-focusing P_c. The number of filaments measured by interferometry increases when the laser power increases. High conversion efficiency ($\approx$10%) of second harmonic generation was observed in the interaction.**

***Index Terms*—Laser particale acceleration and plasma guiding, laser plasma interaction, relativistic self-focusing.**

I. Introduction

THE propagation over a long distance of high-intensity laser beams in a plasma is crucial for laser plasma acceleration schemes [1]–[3], X-ray laser [4], high harmonics generation [5], and in inertial confinement fusion (ICF) with the fast ignitor scheme [6]. All of these schemes depend on the interaction length, which is typically limited by laser diffraction, to a few times the Rayleigh length. Various mechanisms can help to overcome this limitation. Relativistic and ponderomotive self-channeling are the natural way to do this, but they are not easy to obtain. Self-guiding in a preformed channel seems to be the most promising method to achieve propagation lengths of the order of several times the Rayleigh length. Recent experiments have proven the feasibility of this idea [7]–[11]. Intense electromagnetic waves propagating in an underdense uniform plasma can also excite intense relativistic plasma waves via the self-resonant wakefield instability (SRWI) [12]–[14] suitable for particle acceleration [15]–[19]. The maximum energy that an electron can get from the relativistic plasma waves (RPW) is proportional to the product of the RPW amplitude and the dephasing length (the length over which electrons stay in an accelerating arch of the relativistic plasma waves). In order to obtain the maximum energy from the waves, the electron must travel in a long and intense RPW. To achieve this with laser schemes, the laser pulse needs to be guided at high intensity. The interaction of an intense laser pulse with an underdense plasma is also of interest in the "fast ignitor" fusion concept. In this scheme, it is required to deliver a short, intense laser pulse to the (imploded) dense laser-fusion capsule. The intense pulse must propagate through a very long (a few millimeters) region of underdense plasma, and this propagation may be hampered by forward Raman scattering (FRS). Review papers on plasma guiding and plasma based accelerators can be found in [3] and [20].

In this paper, we present some recent experimental results on the propagation and the interaction of a short and intense laser pulse in a well-defined preformed plasma channel. Propagation was studied from interferograms, whereas interaction was studied from the FRS spectra. We also show that the second harmonic light is generated in the plasma channel and scattered

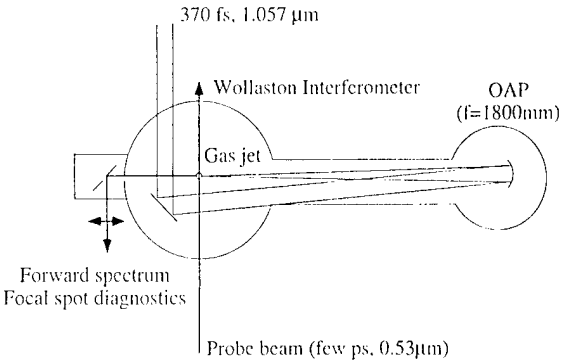


Fig. 1. Experimental setup.

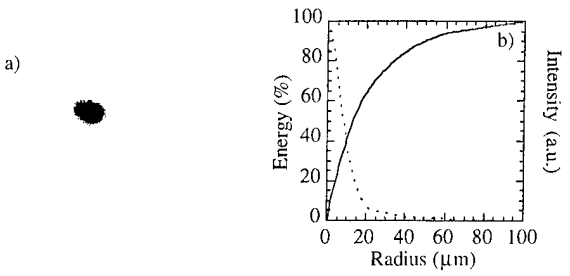


Fig. 2. (a) Focal spot image. (b) Fraction of energy contained inside a circle of radius r.

Manuscript received September 30, 1999; revised January 31, 2000. This work was supported by the EPSRC, the Human Capital and Mobility Program, and the European TMR, under Contract ERBFMGECT950044.

V. Malka, J. Faure, J. R. Marquès, and F. Amiranoff are with LULI, UMR 7605, CNRS-CEA, Ecole Polytechnique-Université Pierre et Marie Curie, 91128 Palaiseau Cedex, France.

C. Courtois is with LPGP, UMR 8578, CNRS, Université Paris XI, 91405 Orsay, France.

Z. Najmudin, K. Krushelnick, M. R. Salvati, and A. E. Dangor are with Imperial College, SW7 2BZ, London, U.K.

Publisher Item Identifier S 0093-3813(00)08795-6.

0093–3813/00$10.00 © 2000 IEEE

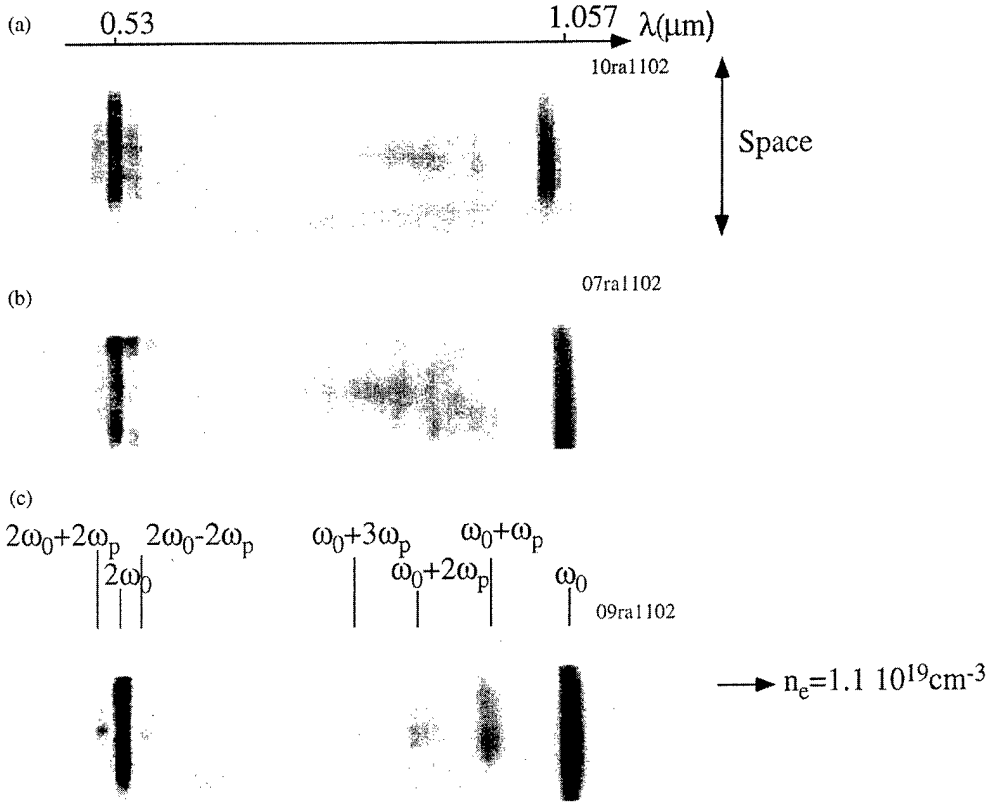


Fig. 3. Images of forward transmitted spectra obtained with a backing pressure of 60 bars, for a given energy of 10 J and for 370 fs (a), 3 ps (b), and 7 ps (c).

off the RPW, as evidenced by the observation of Stokes and anti-Stokes satellites in the forward Raman spectra.

II. Experimental Results

The experiment described here was performed at LULI with the TW laser operating at 1.057 μm in the chirped-pulse amplification (CPA) mode. In this configuration, the laser provided up to 10 J (on target) in 370-fs pulses. The laser beam was focused onto the edge of a gas jet with a $f/22$ off-axis parabola after propagation in vacuum. The experimental setup is presented in Fig. 1. The focal spot was imaged with 12 × magnification on to an 8-bit charge-coupled device (CCD) camera with 5-μm spatial resolution. The laser distribution at full energy (10 J) at the focal plane is a Gaussian function with a waist (FWHM) of 20 μm. In Fig. 2, we present the focal spot image [Fig. 2(a)] and the fraction of energy contained inside a circle with of radius r [Fig. 2(b)]. This corresponds to typical powers of 20 TW and to on-target intensities I_o of the order of 2×10^{18} W/cm^2. The measured Rayleigh length was 2 mm. To avoid refraction induced by ionization processes [21], [22], the laser beam was focused onto the sharp edge of a 4-mm diameter laminar plume of helium gas from a pulsed, supersonic gas jet located 2 mm below the focal region. The nanosecond prepulse, generated by using amplified spontaneous emission (ASE), with an estimated intensity of few 10^{14} W/cm^2 is intense enough to fully collisionally ionize helium and to create a channel over the whole length of the helium gas jet (4 mm). The electron density in the gas jet was controlled by changing the backing pressure of the jet. The neutral density

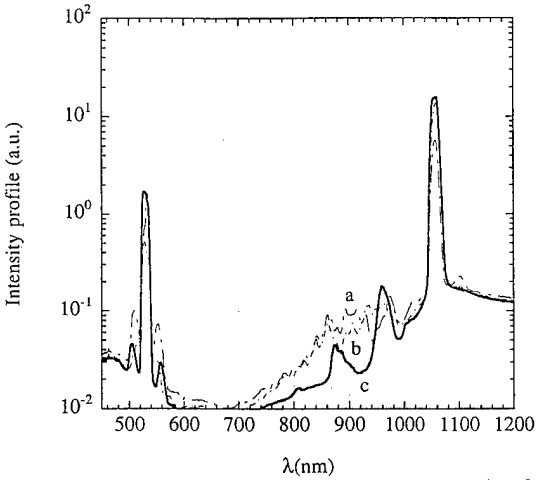


Fig. 4. On-axis corrected intensity profiles of spectra presented in Fig. 3.

profile was characterized before the experiment [23]. The interaction density was measured through the frequency shift ($n\omega_p$) of the anti-Stokes sidebands created by FRS, whereas the electron density profile is deduced from interfograms obtained from a green (0.53-μm) probe beam propagating at 90° to the laser axis, with a few picoseconds pulse duration.

The spectrum of the light transmitted in the forward direction was measured in the full $f/5$ cone angle and imaged at the entrance of an imaging spectrometer (100 lines/mm). This light was reflected by a silicate plate with a surface flatness of $\lambda/10$. The spectrum was detected with a 16-bit silicon CCD camera. A

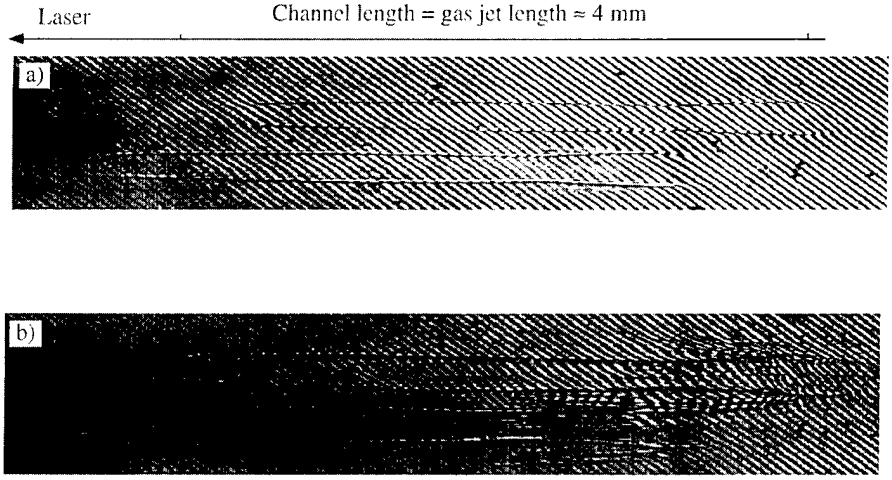


Fig. 5. Interferograms recorded 2 ps before [Fig. 4(a)] and 13 ps after [Fig. 4(b)] the main beam. The parameters are the same as those of Fig. 2(a).

bright blackbody source placed at the focal position of the pump laser was used to measure the overall transmission function of the optics and the spectral response of the CCD camera. This was used to correct the measured spectrum. Fig. 3 shows typical recorded forward spectra obtained with a backing pressure of 60 bars, for a given energy of 10 J and for 370 fs [Fig. 3(a)], 3 ps [Fig. 3(b)], and 7 ps [Fig. 3(c)]. The on-axis electron density deduced from frequency shift $n\omega_p$ of the anti-Stokes sidebands of the pump laser is 1.1×10^{19} cm^{-3} and corresponds to a critical power for relativistic self-focusing (as defined for an uniform plasma) of $P_c = 1.7$ TW. The Stokes satellites are not visible on these spectra because of the poor efficiency of the silicon CCD above 1.1 μm. The ratio between the laser power P_L and the critical power are then 17 [Fig. 3(a)], 2 [Fig. 3(b)], and 0.8 [Fig. 3(c)]. In the second harmonic, both Stokes and anti-Stokes satellites are visible. The electron density deduced from the position of the peaks of the satellites at $2\omega_0 \pm \omega_p$ is in agreement with those deduced at $\omega_0 + n\omega_p$. We observe that when P_L/P_c was increased, the satellites become broader and then merge with one another. In Fig. 4, we present the on-axis intensity profiles of these spectra after the overall spectral response was taken into account.

To obtain interferograms, the probe beam was sent into a Wollaston interferometer and recorded with a 8-bit CCD camera. Interferograms presented in this paper correspond to time-integrated images of the plasma, recorded 2 ps before [Fig. 5(a)] and 13 ps after [Fig. 5(b)] the interaction beam. The plasma expansion is sufficiently slow to obtain, in most cases, well-defined fringes in spite of the duration of the probe pulse. The interferogram in Fig. 5 is obtained with the same parameters as those of Fig. 3(a). Each picture contains two identical images. In the first case, when the probe beam arrives before the TW laser pulse, we obtain an interferogram of the plasma created by the ASE. In this picture, the laser propagates from the right to the left. In the picture, we see the sharp shift in the fringes, which indicates a plasma-vacuum boundary. The radial plasma size is about 300 μm in diameter, and the plasma covers the whole length (4 mm) of the gas jet. The plasma length is limited by the dimension of the gas jet. The plasma expands radially over a distance of about 100-μm radius and is homogenous over the whole gas jet length. Fringes are clearly visible, and it is reasonable to suppose that the plasma is axisymmetric. We can then use Abel inversion to retrieve the radial density profile as presented in Fig. 6. The electron density increases from 1×10^{19} cm^{-3} on axis to 4×10^{19} cm^{-3} at a radius of 100 μm. The on-axis electron density deduced from this interferogram is in good agreement with those deduced from the forward spectra. In the second case [Fig. 5(b)], we also observe [11], [24] at the beginning of the interaction zone, short filaments outside of the laser propagation axis that propagate over a distance of $\approx$1 mm. A main filament stays on the laser propagation axis over 3 mm. In this case, we cannot deduce the electron density profile using Abel inversion because the axisymmetric assumption is not justified. In the lower power case, only one long filament was observed.

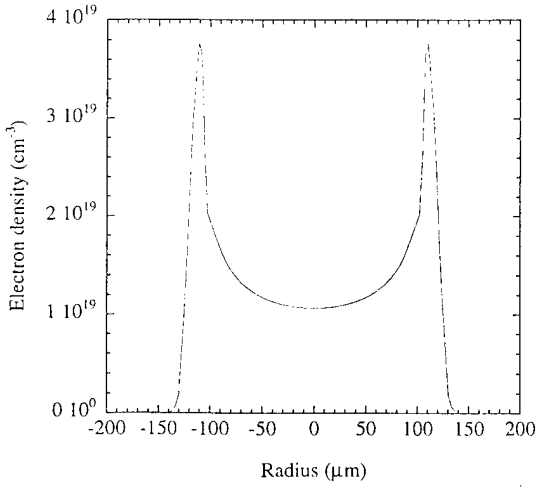


Fig. 6. Radial electron density deduced from the interferogram of Fig. 5(a).

In Fig. 7, we present an image obtained at $2\omega_0$, at 90°, to the laser propagation axis in that we see a long green filament that propagates over 3 mm. We point out here the fact that the TW laser beam is perfectly aligned along the channel center, because

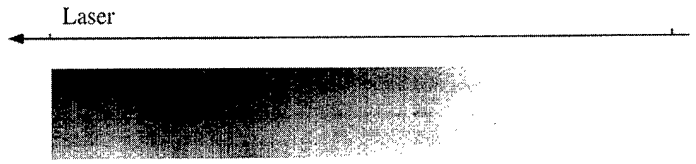


Fig. 7. Second harmonic side images [same parameters as Fig. 2(a)].

the creation beam (ASE beam) is perfectly aligned with the TW laser beam.

III. Discussion

In the experiments described in this paper, the RPW is excited by an intense pulse via the self-modulated wakefield SMW instability. In this regime, the strong electromagnetic pump wave (ω_o, k_o) decays into a plasma wave (ω_p, k_p) and two forward-propagating electromagnetic cascades at the Stokes $(\omega_o - n\omega_p)$ and anti-Stokes $(\omega_o + n\omega_p)$ frequencies [12]–[14], [25], [26]. Here, $\omega_p = (4\pi n_e e^2/\mathrm{m})^{1/2}$ is the plasma frequency and n is a positive integer. The signature of such a process is then visible in the presence of Stokes and anti-Stokes satellites in the spectrum of the transmitted light. We can estimate of the RPW amplitude, if we assume that the ratio of the harmonic Raman satellites is proportional to the harmonic content of the scattering plasma wave. The harmonic amplitude of the scattering μ_m as a function of the plasma wave amplitude $\partial n/n_0$, is given by [27]

$$(\mu_m/\mu_0) = (m^m/2^{m-1} \cdot m!) \cdot (\delta n/n_0)^m$$

where m is the number of the harmonic. Hence, the ratio between second and first harmonics is simply equal to the plasma wave amplitude. Values up to 6% were measured in the low laser power case. In the other cases, the satellites are so broad that is difficult to estimate this ratio.

In the high-power case, the main difference in the forward spectra near the propagation axis (where the electron density is constant) appears in the broadening of the Raman satellites. This is not surprising if we consider that the temporal envelope of the plasma wave is an increasing exponential function (at least at the beginning of the instability) $\exp(\Gamma t)$, where γ is the growth rate of the instability. The spectrum of such a wave has a width that is proportional to Γ. Furthermore, Γ scales as $I^{1/2}$ in the weakly relativistic limit. Hence, for the low-power case, the laser intensity is low and $\Gamma/\omega_p \ll 1$. This gives a narrow spectral peak at ω_p on the spectrum. This is as we observe on Fig. 3(c): in the high-power case, the intensity is larger, so is γ/ω_p, making the spectral peak wider. Physically, we can understand that when the growth rate becomes comparable to ω_p, the plasma wave can oscillate at nonresonant frequencies. Out of the propagation axis, the broad satellite [see the bottom of the Fig. 3(a)] could also be the signature of the propagation of light filaments in the high electron density region of the channel, as observed in the interferograms. These side beamlets can be produced in the self-focusing regime [28] or by Raman side scattering [29]. In the low laser power case $(P_L/P_C < 1)$, the laser beam is self-guided by the plasma channel that satisfied the guiding condition.

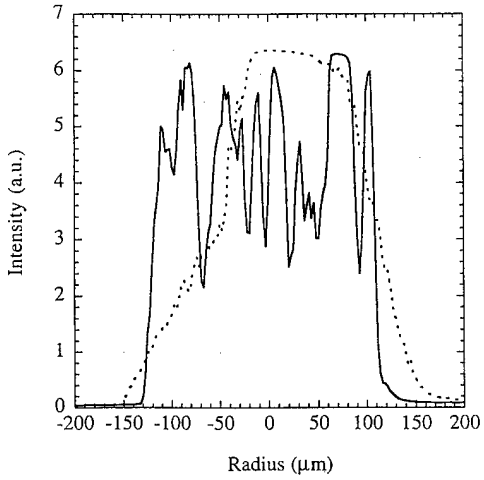


Fig. 8. Radial intensity profiles obtained from the forward Raman spectra at $2\omega_0$ and at ω_0 [same parameters as Fig. 2(c)].

In previous experiments [30] ($I_o \approx 5 \times 10^{18}$ W/cm^2 and $f/3$ focusing), second harmonic light was observed in the forward direction with a conversion efficiency of 10^{-3}. The laser pulse was focused into the helium gas jet, whereas in the present case, the short pulse laser interacts directly with the preformed plasma. The measured second harmonic conversion efficiency in the cone angle of the laser is defined as the ratio between the integral signal at $2\omega_0$ and ω_0 is of the order of 10%. The main mechanism to generate second harmonic is the presence of density gradients in the plasma. Physically, this is because of the laser-induced quiver motion of the electrons across a density gradient, which gives rise to a perturbation δn in the electron density at the laser frequency ω_o (as can be seen from the continuity equation). This density perturbation, coupled with the quiver motion of the electrons v_{osc} produces a source current J at the second harmonic frequency: $J = \delta n^* v_{osc} \propto \cos^2(\omega_0 t) \propto \cos(2\omega_0 t)$. For the transverse electron density gradient, the currents are phased to radiate predominantly in the forward direction. In this experiment, the source of the density gradient is mainly caused by relativistic or ponderomotive [31] self-focusing rather than laser ionization processes. This is shown by the observation (see Fig. 6) of the long filaments at $2\omega_0$ inside the plasma channel. Another confirmation of the production of second harmonic from density gradients appears clearly in the radial distribution measured in the forward spectra at $2\omega_0$. This distribution contains many hot spots, whereas the fundamental is homogeneous, as presented in Fig. 8. As mentioned in previous experiments [30], [32], the laser light is frequency-doubled passing the interaction region and scattered by the plasma wave, giving Stokes and anti-Stokes satellites at $2\omega_0 \pm \omega_p$.

IV. Conclusion

In conclusion, we have presented experimental observations of the propagation of an ultraintense laser pulse in a preformed plasma channel. Propagation was investigated by using interferometry. In the high laser power case, many filaments produced at the beginning of the interaction zone were observed because of Raman side scattering or to beam breakup. Forward spectra shows a cascade of Raman satellites, which merge with one another, in the high laser power case. We also report on the observation of the forward scattering of second harmonic ($2\omega_0$) light from relativistic electron plasma waves driven by FRS. The generation of the second harmonic light is consistent with the presence of radial electron density gradients resulting from the radial ponderomotive force.

Acknowledgment

The authors wish to thank the LULI technical staff for their excellent support during the experiment, and A. Solodov and P. Mora for very useful discussions.

References

[1] T. Tajima and J. Dawson, "Laser electron accelerator," *Phys. Rev. Lett.*, vol. 43, pp. 267–270, 1979.

[2] A. Modena, A. E. Dangor, Z. Najmudin, C. E. Clayton, K. Marsh, C. Joshi, V. Malka, C. B. Darrow, C. Danson, D. Neely, and F. N. Walsh, "Electron acceleration from the breaking of relativistic plasma waves," *Nature*, vol. 377, pp. 606–608, 1995.

[3] E. Esarey, P. Sprangle, J. Krall, and A. Ting, "Overview of plasma-based accelerator concept," *IEEE Trans. Plasma Sci.*, vol. 24, pp. 252–288, 1996.

[4] P. B. Corkum, N. H. Burnett, and F. Brunel, "Above-threshold ionization in the long-wavelength limit," *Phys. Rev. Lett.*, vol. 62, pp. 1259–1263, 1989.

[5] X. F. Li, A. L'Huillier, M. Ferray, L. A. Lompre, and G. Mainfray, "Multiple Harmonic generation in rare gases at high laser intensity," *Phys. Rev. A*, vol. 39, pp. 5751–5760, 1989.

[6] M. Tabak, J. Hammer, M. E. Glinsky, W. L. Kruer, S. C. Wilks, J. Woodworth, E. M. Campbell, M. D. Perry, and R. J. Mason, "Ignition and high gain with ultrapowerful lasers," *Phys. Plasmas*, vol. 1, pp. 1626–1634, 1994.

[7] C. G. Durfee III and H. M. Milchberg, "Light pipe for high intensity laser pulses," *Phys. Rev. Lett.*, vol. 71, pp. 2409–2412, 1993.

[8] C. G. Durfee III, J. Lynch, and H. M. Milchberg, "Development of a plasma waveguide for high-intensity laser pulses," *Phys. Rev. E*, vol. 51, pp. 2368–2389, 1995.

[9] Y. Ehrlich, C. Cohen, A. Zigler, J. Krall, P. Sprangle, and E. Esarey, "Guiding of intensity laser pulses in straight and curved plasma channel experiments," *Phys. Rev. Lett.*, vol. 77, pp. 4186–4189, 1996.

[10] K. Krushelnick, A. Ting, C. I. Moore, H. R. Burris, E. Esarey, P. Sprangle, and M. Baine, "Plasma channel formation and guiding during high intensity short pulse laser plasma experiments," *Phys. Rev. Lett.*, vol. 78, pp. 4047–4050, 1997.

[11] C. E. Clayton, D. Gordon, K. A. Marsh, C. Joshi, V. Malka, Z. Najmudin, A. Modena, A. E. Dangor, D. Neely, and C. Danson, "Observation of self-channeling of relativistically-intense laser light in a very underdense plasma.," *Phys. Rev. Lett.*, vol. 1, pp. 100–103, 1998.

[12] N. E. Andreev, L. M. Gorbunov, V. I. Kirsanov, A. A. Pogosova, and R. R. Ramazashvili, "Self-resonant wake-field generation by intense laser pulse in plasmas," *JETP Lett.*, vol. 55, pp. 571–574, 1992.

[13] T. M. Antonsen and P. Mora, "Self-focusing and raman-scattering of laser-pulses in tenuous plasmas," *Phys. Rev. Lett.*, vol. 69, pp. 2204–2207, 1992.

[14] P. Sprangle, E. Esarey, J. Krall, and G. Joyce, "Propagation and guiding of intense laser-pulses in plasmas," *Phys. Rev. Lett.*, vol. 69, pp. 2200–2203, 1992.

[15] A. Modena, A. E. Dangor, Z. Najmudin, C. E. Clayton, K. Marsh, C. Joshi, V. Malka, C. B. Darrow, and C. Danson, "Observation of Raman forward scattering in the relativistic regime," *IEEE Trans. Plasma Sci.*, vol. 24, pp. 289–295, 1996.

[16] C. A. Coverdale, C. B. Darrow, W. L. Kruer, and S. V. Bulanov, "Modulations in Raman backscatter spectra due to interaction of short-pulse high-intensity laser with underdense plasma," *Phys. Rev. Lett.*, vol. 74, pp. 4659–4663, 1995.

[17] D. Gordon, K. C. Tzeng, C. E. Clayton, A. E. Dangor, V. Malka, K. A. Marsh, A. Modena, W. B. Mori, P. Muggli, Z. Najmudin, and C. Joshi, "Observation of electron energies beyond the linear dephasing limit from laser-excited relativistic plasma wave," *Phys. Rev. Lett.*, vol. 80, pp. 10–13, 1998.

[18] D. Umstadter, S. Y. Chen, A. Maksimchuk, G. Mourou, and R. Wagner, "Nonlinear optics in relativistic plasmas and laser wake field acceleration of electrons," *Science*, vol. 273, pp. 472–475, 1996.

[19] C. I. Moore, A. Ting, K. Krushelnick, E. Esarey, R. F. Hubbard, B. Hafizi, H. R. Burris, C. Manka, and P. Sprangle, "Electron trapping in self-modulated laser wakefields by Raman backscatter," *Phys. Rev. Lett.*, vol. 79, pp. 3909–3912, 1997.

[20] W. P. Leemans, C. W. Widers, E. Esarey, N. E. Andreev, G. Shvets, and W. B. Mori, "Plasma guiding and wakefield generation for second-generation experiments," *IEEE Trans. Plasma Sci.*, vol. 24, pp. 331–350, 1996.

[21] V. Malka, E. D. Wispelaere, J. R. Marquès, R. Bonadio, F. Amiranoff, F. Blasco, C. Stenz, P. Mounaix, G. Grillon, and E. Nibbering, "Stimulated Raman backscattering instability in short pulse laser interaction with helium gas," *Phys. Plasmas*, vol. 3, pp. 1682–1688, 1996.

[22] P. Monot, "Interaction laser-gaz en champ intense," Thèse de doctorat, de l'université Paris-sud, Centre d'Orsay, 1993.

[23] V. Malka, F. Amiranoff, C. Coulaud, J. P. Geindre, V. Lopez, Z. Najmudin, and D. Neely, "Mesure des profils de densités d'atomes dans des jets de gaz à géométrie cylindrique," Rapport d'activite du LULI, vol. NTIS PB99-130973, 1998.

[24] Z. Najmudin, C. Clayton, A. E. Dangor, C. Danson, D. Gordon, C. Joshi, V. Malka, K. Marsh, A. Modena, P. Muggli, D. Neely, and F. N. Walsh, "Investigation of a channelling high intensity laser beam in underdense plasmas," *IEEE Trans. Plasma Sci.*, vol. 28, pp. 1057–1070, Aug. 2000.

[25] D. W. Forslund, J. M. Kindel, and E. L. Lindman, "Theory of stimulated scattering processes in laser-irradiated plasmas," *Phys. Fluids*, vol. 18, pp. 1002–1023, 1975.

[26] W. B. Mori, C. D. Decker, D. E. Hinkel, and T. Katsouleas, "Raman forward scattering of short-pulse high-intensity lasers," *Phys. Rev. Lett.*, vol. 72, pp. 1482–1485, 1994.

[27] F. F. Chen, "Excitation of large amplitude plasma waves," *Phys. Scripta*, vol. T30, pp. 14–21, 1990.

[28] F. Vidal and T. W. Johnston, "Electromagnetic beam breakup: Multiple filaments, single beam equilibria, and radiation," *Phys. Rev. Lett.*, vol. 77, pp. 1282–1285, 1996.

[29] J. T. M. Antonsen and P. Mora, "Self-focusing and Raman scattering of laser pulses in tenuous plasmas," *Phys. Fluids B*, vol. 5, pp. 1440–1452, 1993.

[30] V. Malka, A. Modena, Z. Najmudin, A. E. Dangor, C. E. Clayton, K. A. Marsh, C. Joshi, C. Danson, D. Neely, and F. N. Walsh, "Second harmonic generation and its interaction with relativistic plasma waves driven by forward Raman instability in underdense plasma," *Phys. Plasmas*, vol. 4, pp. 1127–1131, 1997.

[31] C. E. Max, J. Arons, and A. B. Langdon, "Self-modulation and self-focusing of electromagnetic waves in plasmas," *Phys. Rev. Lett.*, vol. 33, pp. 209–212, 1974.

[32] K. Krushelnick, A. Ting, H. R. Burris, A. Fisher, C. Manka, and E. Esarey, "Second harmonic generation of stimulated Raman scattered light in underdense plasmas," *Phys. Rev. Lett.*, vol. 73, pp. 3681–3684, 1995.

V. Malka, photograph and biography not available at the time of publication.

J. Faure, photograph and biography not available at the time of publication.

J. R. Marquès, photograph and biography not available at the time of publication.

F. Amiranoff, photograph and biography not available at the time of publication.

C. Courtois, photograph and biography not available at the time of publication.

Z. Najmudin, photograph and biography not available at the time of publication.

K. Krushelnick, photograph and biography not available at the time of publication.

M. R. Salvati, photograph and biography not available at the time of publication.

A. E. Dangor, photograph and biography not available at the time of publication.

Measurement of Forward Raman Scattering and Electron Acceleration from High-Intensity Laser–Plasma Interactions at 527 nm

Z. Najmudin, R. Allott, F. Amiranoff, E. L. Clark, C. N. Danson, Daniel F. Gordon, C. Joshi, *Fellow, IEEE*, K. Krushelnick, V. Malka, D. Neely, M. R. Salvati, M. I. K. Santala, M. Tatarakis, and A. E. Dangor

***Abstract*—High-intensity laser–plasma interaction experiments were performed using high-power laser pulses (greater than 8 TW) at a wavelength of 527 nm. These pulses were focused to intensity greater than 10^{18} W/cm^2 into underdense helium plasma at a density of $n_e \leq 5 \times 10^{19}$ cm^{-3}. Systematic examination of the forward Raman scattering instability was performed by measuring the spectrum of the forward scattered light. It was found that the three-wave instability occurs first, which then proceeds to a nonlinear regime involving four-wave processes. Measurements of the accelerated electron spectrum suggest that higher phase velocity plasma waves are generated than when using lower frequency light.**

***Index Terms*—Electron accelerator, electromagnetic scattering by plasma media, plasma waves.**

I. Introduction

THE emergence of high-power short pulse laser systems around the world has generated interest in the interaction of high-intensity laser light with plasmas because of the many potential applications of this technology [1]. It has also allowed a comprehensive experimental study of the fundamental physics, which can occur during these interactions, and in particular permits examination of high-intensity laser scattering instabilities. The forward stimulated Raman scattering (FRS) instability has long been studied in connection with laser-driven inertial confinement fusion (ICF), because of a consequence of FRS is the generation of large amplitude plasma waves [2]. This instability involves the scattering of laser photons from electron plasma waves and, subsequently, the transfer of energy from the laser beam to these waves. As this wave is then damped, energetic plasma electrons are produced that preheat the fuel in ICF and can reduce the efficiency of compression.

Manuscript received October 2, 1999; revised February 20, 2000. This work was supported in part by EPSRC (U.K.), EU (Europe), and DoE (U.S.)

Z. Najmudin, K. Krushelnick, M. Salvati, M. I. K. Santala, M. Tatarakis, and A. E. Dangor are with Imperial College, SW7 2BZ, London, U.K. (e-mail: zn1@ic.ac.uk).

R. Allott, C. N. Danson, and D. Neely are with Central Laser Facility, Rutherford Appleton Laboratory, Chilton, Didcot, OX11 OQX Oxon, U.K.

F. Amiranoff and V. Malka are with LULI, École Polytechnique-Université Pierre et Marie Curie, 91128 Palaiseau Cedex, France.

E. L. Clark is with the Radiation Physics Department, AWE plc, RG7 4PR, Aldermaston, U.K., and the Imperial College, SW7 2BZ London, U.K.

D. F. Gordon is with the Naval Research Laboratory, Washington, DC 20375 USA.

C. Joshi is with the Department of Electrical Engineering, University of California at Los Angeles, Los Angeles, CA 90095 USA.

Publisher Item Identifier S 0093-3813(00)07241-6.

Experimental studies of FRS at high density [3], where the growth rate is greatest, tend to be incomplete because measurements are difficult in this regime. In addition, there are other factors aside from FRS, that can contribute to plasma heating under these conditions. Theoretical calculations of FRS indicate that the growth rate of the instability is a maximum for incident electromagnetic radiation having a normalized vector potential a_o about equal to one [4], [5]. (The normalized vector potential at frequency ω is given by $a_o = eE_{\rm laser}/m_e\omega c$, where $a_o \approx 1$ corresponds to an intensity of 0.89×10^{18} W/cm^2 for a laser wavelength of 1 μm.) Therefore, intense short pulse lasers, which can easily produce such intensities, permit more systematic studies of this instability. Indeed, many experiments have been performed with high-power Nd:Glass laser systems ($\lambda \approx 1.05\,\mu$m), which clearly show the characteristics of FRS, i.e., a forward scattered spectrum with satellite lines separated from the fundamental by multiples of the electron plasma frequency [6]–[9]. The production of significant numbers of suprathermal electrons has also been measured. These electrons can be produced when the plasma wave generated by the FRS decays through wave-breaking, so that a significant number of electrons can become trapped and accelerated in relativistic plasma waves. Experimentally, beams of electrons with a normalized emittance as low as 0.4π mm mrad [9] and having an energy spectrum up to 94 MeV [10] have been observed. This emittance is an order of magnitude brighter than comparable state-of-the-art photo-injectors, and therefore, such experiments have been a source of much interest for particle accelerator applications.

Thus, FRS can be an interesting high-brightness source of moderately relativistic electrons. Acceleration to high energy is a result of the high phase velocity of the plasma wave at low plasma densities (close to c). Indeed, because the plasma wave must be in phase with modulations of the laser pulse energy for the wave to grow: The phase velocity of the plasma wave is equal to the group velocity of light in the plasma. For a plasma frequency ω_p much less than the laser frequency ω_o, the Lorenz factor of the plasma wave is given by $\gamma_\phi \approx \omega_o/\omega_p$. Hence, we can see that the maximum acceleration increases as the ratio ω_o/ω_p increases. A simple estimate of the maximum acceleration energy is given by

$$W_{\max} = 4\gamma_\phi^2 m_e c^2 \varepsilon \tag{1}$$

where ε is the ratio of plasma wave density variations to initial plasma density [11]. This estimate has been observed to be ex-

0093–3813/00$10.00 © 2000 IEEE

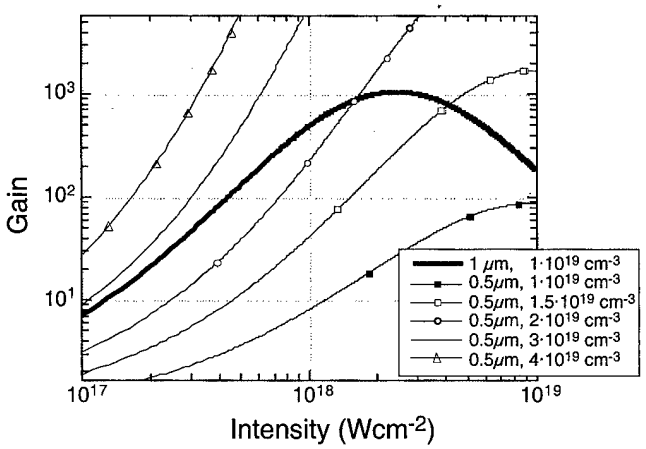


Fig. 1. Gain of FRS for either 1 μm at $n_e = 1 \cdot 10^{19}$ cm^{-3} or 0.5 μm at a variety of densities as a function of intensity for a 1-ps square pulse in the linear regime.

ceeded in experiments performed with 1.054-μm laser light at electron densities around $1 \cdot 10^{19}$ cm^{-3}, which have resulted in measured electron energies up to 94 MeV [10]. These higher-than-expected energies are also observed in simulation [12] and are found to be the result of a staged acceleration process. In essence, a large current of accelerated electrons, generated by wavebreaking, outrun the plasma wave. These electrons set up a (nonresonant) higher phase velocity plasma perturbation, which itself can accelerate the tail of this accelerated bunch to even higher energy. However, in the absence of such beam loading effects, (1) does hold. So, increasing the phase velocity of the plasma wave, either by reducing plasma density or by increasing the frequency of the driving laser pulse, leads to an increase in maximum possible acceleration energy.

Fig. 1 shows the gain of FRS [5] as a function of intensity for a 1-μm driver beam at an electron density of $1 \cdot 10^{19}$ cm^{-3}. This is the density close to which wavebreaking has been observed in previous experiments performed at 1 μm. Also plotted on the same graph is the gain with a 0.5-μm driving laser beam at several different plasma densities. We can see that at intensities less than $1 \cdot 10^{18}$ Wcm^{-2}, it is possible to match the growth rate at 1 μm by increasing the density to between 2-3 $\cdot 10^{19}$ cm^{-3} with a 0.5-μm driver (i.e., up to a $\sqrt{3}$ increase in plasma frequency). Because the Lorenz factor, γ_ϕ of the plasma wave created by FRS is proportional to ω_0/ω_p, doubling the driver frequency results in an increase in phase velocity ($>2/\sqrt{3}$). Also, because from (1) we find that the maximum possible accelerated energy of electrons is proportional to γ_ϕ^2, this should increase modestly by more than $4/3$.

The FRS growth rate for 1 μm actually has a maximum, at intensities close to $1 \cdot 10^{18}$ Wcm^{-2} ($a_{\max} \approx 1.4$). This is a result of the relativistic mass increase of electrons quivering in the electric field of the laser at intensities where $a_0 > 1$, which reduces the effective plasma frequency ($\omega_p \propto m_e^{-1}$). However, for $\lambda = 0.5$ μm, the FRS growth rate does not reach its maximum until intensities close to $1 \cdot 10^{19}$ Wcm^{-2}. At such high intensities, it would be possible with a second harmonic driver to obtain equivalent growth rates at almost the same densities, resulting in significantly higher maximum acceleration energies. Hence, frequency doubling of a high-intensity laser beam can be of interest when using short pulses as drivers for a plasma-based source of high-energy particles.

II. Experiment

The experiment was performed with the VULCAN CPA laser [13]. This system produces up to 30 J of infrared energy at 1.054 μm, in a stretched large bandwidth pulse. The pulse was subsequently recompressed with a pair of gratings (to about 900 fs) and frequency doubled, using a 4-mm thick KDP crystal, which generates up to 9 J at 527 nm in a 800-fs pulse [14].

This high power beam is transported in vacuum and focused with a $f5$ off-axis parabolic mirror to a spot of approximately 30-μm diameter, thus giving an on-axis intensity of around $1 \cdot 10^{18}$ Wcm^{-2}. The spot is six times the diffraction limit at this wavelength. This is worse than the beam quality at 1 μm and is because frequency doubling magnifies the initial phase distortions on the beam as a ratio of the laser wavelength [14]. The beam was then focused to the edge of a supersonic jet of helium. A supersonic gas jet is used to give a sharp vacuum/gas interface, so as to prevent problems caused by ionization-induced defocusing, which can significantly reduce the intensity of the interaction [15], [16]. The primary diagnostics in these experiments were measurements of the transmitted laser spectrum (for FRS), as well as an electron spectrometer to measure the energy of electrons generated by the FRS plasma wave. The FRS also serves as a measurement of the plasma density in the interaction, because its spectrum is characterized by lines separated from the driver frequency by ω_p, the plasma frequency. In the case of scattering off a relativistic plasma wave, as is the case for FRS, the thermal correction to the Bohm–Gross frequency is negligible. Therefore, the plasma frequency is simply proportional to the square root of the plasma density, $\omega_p = \sqrt{n_e e^2/\varepsilon_0 m_e}$. The density obtained in this way is in good agreement with interferometric measurements of the gas jet [17]. The electrons were dispersed using an electron spectrometer in the standard Browne and Buechner [18], [19] arrangement and measured using six silicon detectors, placed in the focal plane of the spectrometer. The total electron signal through the spectrometer, which had an acceptance of $f60$, was estimated by integrating the spectrum obtained, after removing the signal obtained on background shots. The background shots were obtained by firing with the same parameters but with the spectrometers B field set to zero.

Another advantage of performing laser–plasma interaction experiments using a laser with a wavelength of 527 nm is that conventional silicon-based CCD detectors, which are used for measuring the spectrum of scattered light in these experiments, have a much higher sensitivity in this wavelength region than around 1000 nm.

III. Results

Satellites caused by FRS were clearly observed in the spectrum of the transmitted beam. A typical FRS spectrum with multiple satellites on either side of the fundamental frequency is shown in Fig. 2. Fig. 3 shows the experimental measurements of the ratio of the upshifted and downshifted satellites as a function of density. At low densities, the scattering is dominated by

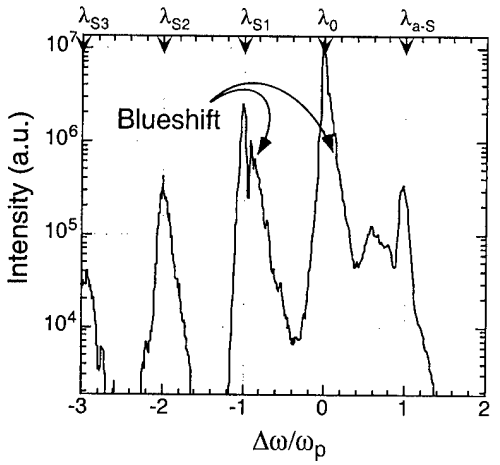


Fig. 2. Typical FRS spectra shows cascading. Plasma density was $4.6 \cdot 10^{19}$ cm^{-3}, average $|a_0| = 0.32$. λ_x refers to the expected wavelength of the different EM waves, where the subscript x is replaced by S, 0, a-S corresponding to Stokes, fundamental, and anti-Stokes lines, and the number refers to the order of the harmonic.

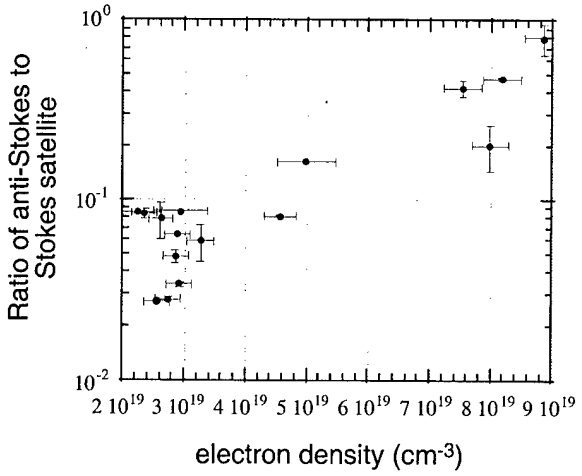


Fig. 3. Ratio of Stokes to anti-Stokes satellite in FRS spectra as a function of density.

the red satellite. This is commonly observed in FRS spectra because the FRS passes through several regimes having different characteristics. At low intensities—hence, early, in the interaction—the scattering is essentially three wave. In effect, the electromagnetic pump wave, of frequency ω_0, decays into a plasmon ω_p and a daughter wave ω^-, as given by $\omega_0 = \omega_p + \omega^-$. Initially, this process has a higher growth rate in sidescattered directions, but because of the large spread in wavenumber $\mathbf{k}$ of a tightly focused laser beam, some frequency-shifted photons can scatter into the cone of the laser beam and be further amplified. Plasma waves generated by this process can act as a seed for a four-wave process, in which both downshifted ω^- and upshifted ω^+ satellites are resonant or near-resonant. Several authors describe how one expects the scattering to progress in time from the three wave to the nonresonant four wave, where both satellites grow but the downshifted satellite still dominates, and finally, to the resonant four wave, where both red satellite and blue satellite should grow with equal amplitude [4], [20].

Fig. 3 shows the relative amplitude between anti-Stokes and Stokes lines as a function of density. By varying density, we can increase the relative growth rates and so affect the transition between these regimes. In the figure, we see that the anti-Stokes increases in amplitude relative to the Stokes with increasing density. This suggests that the transition between three wave and four wave occurs earlier for higher densities. This may seem surprising because the blue satellite is not exactly matched to the forward going plasma wave, and at higher densities, this mismatch would tend to increase. This would imply that the efficiency of the four-wave scattering processes ought to be reduced at higher density, resulting in a decrease in amplitude of the anti-Stokes compared with the Stokes, contrary to what is observed.

Evidence of the temporal behavior described above is apparent in the spectrum shown in Fig. 2. As can be seen, the laser light transmitted at the fundamental frequency has an extended width to the blue side. This has been reported by many authors and is the result of (optical field-induced) tunnel ionization. The extremely high ionization rates, which are experienced in these interactions, result in a dramatic increase in density and a corresponding decrease in refractive index. As the ionization state of the medium changes during the laser pulse, the decreasing refractive index retards the front of the pulse, causing a phase-shift as a function of distance into the pulse. Essentially, the contours of equal phase are brought closer together, resulting in a shift to shorter wavelength [15], [16]. In these experiments, the target gas was helium, which is completely stripped at an intensity of around $1 \cdot 10^{16}$ Wcm^{-2}. Hence, we expect that most of the ionization and ionization-induced blueshifting will take place early in the pulse, as soon as this intensity is reached. Noticeably, in Fig. 2, the red Stokes satellite has a blue shift similar to the fundamental frequency profile. No significant asymmetry is seen in the anti-Stokes satellite. It is evident, therefore, that the downshifted (red) satellite is produced throughout the duration of the laser pulse, including early times when ionization effects are significant. The blue satellite only achieves prominence later and is scattered from the later part of the laser pulse and, therefore, remains unshifted in frequency. The blue-shifted tail of the Stokes satellite was very reproducible and occurred on all of the spectra obtained in these experiments.

Also noticeable in the spectra is the presence of satellites at multiples of the plasma frequency. This cascading of laser energy to other scattered frequencies is a sign of a feedback mechanism between the scattered electromagnetic waves and the plasma. Hence, we can treat the increasing signal of the higher ω_p harmonics as a measure of increasing plasma wave amplitude. Fig. 4 shows the ratio of the second to first satellites for both blue and red sides of the fundamental. On the red side, there is a gradual exponential increase in this ratio, which, as expected, shows the distribution of energy to the higher harmonics as the created wave, and hence, the nonlinear feedback becomes larger. However, on the blue side, the behavior is completely different. Indeed, the ratio of the second satellite to the first actually decreases. In fact, not only does the first-order blue satellite grow much more rapidly than does the others, but also

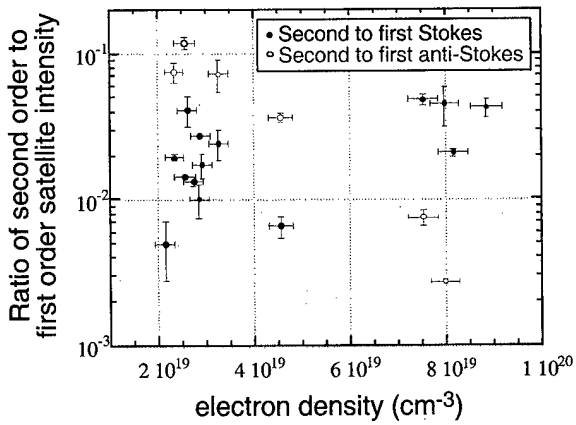


Fig. 4. Ratio of second to first Stokes and anti-Stokes lines as a function of density.

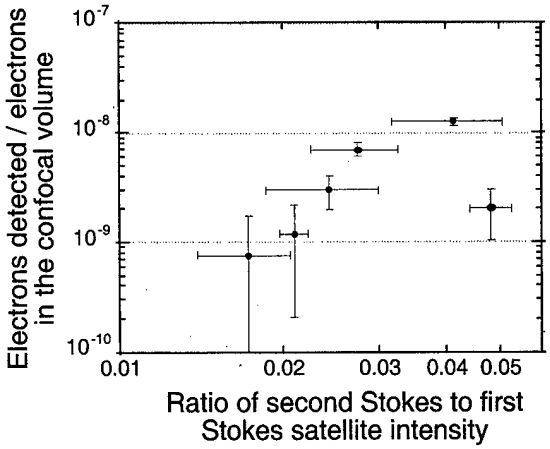


Fig. 5. Total number of detected electrons versus the ratio of second to first Stokes lines.

the second satellite actually decreases slightly in amplitude with increasing density. This implies that the cascading process is much less efficient for satellites of increasing photon energy, perhaps because of the increasing mismatch of wave-vectors at shorter wavelength.

We can make an estimate of the plasma wave amplitude, if we assume that the ratio of the harmonic Raman satellites is proportional to the harmonic content of the scattering plasma wave. This supposes that the generated sideband acts as a Thomson scattering probe for the self-generated plasma wave, though of course this is a great simplification considering the stimulated nature of this interaction. The harmonic content of the plasma wave μ_m as a function of the plasma wave amplitude $\delta n/n_0$ is given by [21]

$$(\mu_m/\mu_0) = (m^m/2^{m-1} \cdot m!) \cdot (\delta n/n_0)^m$$

where m is the number of the harmonic. Hence, the ratio of scattered intensity between second and first harmonics is simply equal to the square of the plasma wave amplitude. Values up to 0.05 were measured within our experimental parameters. Fig. 5 shows the total electron signal, measured above 5 MeV for a fixed setting of the dispersing magnet, plotted against this ratio of amplitudes of second to first Stokes line of the FRS. This value is obtained by interpolating the electron spectra between the values measured by the diodes and integrating. Hence, this number only corresponds to the electrons passing through the $f60$ acceptance angle of the spectrometer. The shot-to-shot variation of electron numbers is great and can vary by as much as an order of magnitude. However, clearly, as the plasma wave amplitude becomes larger, the total number of electrons trapped and accelerated also becomes larger, as expected. There is though, a surprising drop in electron number at the very highest value ($\approx$0.05), especially beause the maximum detected energy does not change greatly over these shots.

For our measurements of accelerated electrons, it was found that through the careful use of copper shielding in front of the silicon electron detectors, it is possible to eliminate stray lower energy electrons in the higher energy channels. With this method of shielding low-energy electron noise, the maximum electron energy measured with these parameters was 18 MeV.

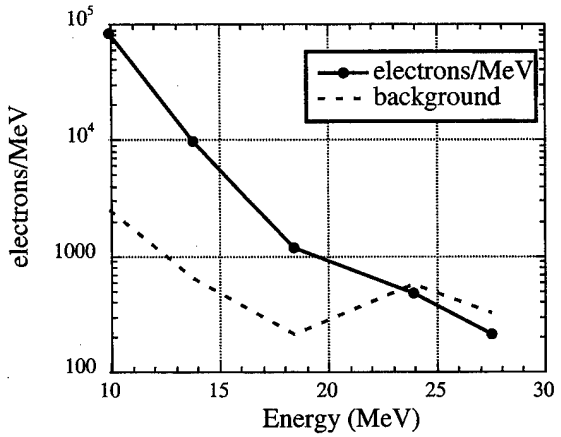


Fig. 6. Typical electron signal with background noise shown on same graph. Plasma density was $8.2 \cdot 10^{19}$ cm^{-3}, average $|a_0| = 0.33$.

For the particular shot shown in Fig. 6, the measured plasma wave amplitude was 0.02 and the density was $8 \cdot 10^{19}$ cm^{-3}. With these parameters, we can estimate the maximum energy of trapped electrons outrunning the plasma wave. Using (1), we obtain an expected maximum energy of 14 MeV, which is less than, but surprisingly close to, the measured value. Indeed two-dimensional considerations [10] have suggested that our estimate should be half this value, because acceleration is expected over only one-quarter of the plasma wave length, rather than the full half, which has an accelerating gradient, as has been taken for (1). This is because over only one-quarter of the plasma wave is the electric field of the wakefield both accelerating and focusing electrons. Hence, it seems that we underestimate the amplitude of the plasma wave by not taking into account volume and temporal integration of the scattering to the higher harmonics. However, the clear increase in electron numbers with increasing nonlinearity of the Raman scattering verifies that plasma wave excitation and self-trapping is the method of fast electron generation in this case [6]. This is confirmed by comparing the numbers of accelerated electrons above 5 MeV with increases in the Stokes amplitude, which shows an order of magnitude increase for modest increase (doubling) in anti-Stokes level, and agrees

well with the observation of simulation [12]. Of course, the fact that background electrons can be trapped and accelerated at plasma wave amplitudes well below the wave breaking limit [2] suggests that the plasma is extremely hot (on the order of kiloelectronvolts). It has been suggested that it is the influence of lower phase velocity stimulated scattering (in particular, Raman backscatter) that can provide sufficient heating to allow these electrons to be trapped [22], [23].

IV. Discussion

The experiments described here are the first high-intensity laser–plasma interaction experiments performed in the underdense regime using frequency doubled light at 527 nm. It is apparent from the observed forward-scattered spectra that the FRS instability initially begins in the three-wave mode, seeded by noise in the plasma. This mode then produces plasma waves that can couple with the two scattered electromagnetic waves sufficiently to excite the four-wave process, resulting in a significant amount of light being scattered into the anti-Stokes satellite.

The significance of the anti-Stokes satellite grows rapidly as the electron density or the laser intensity increases. Although theoretical understanding of the nonlinear evolution of the Raman scattering instability generally accepts that this is the process by which the four-wave scattering occurs, this is the first experimental evidence to confirm that the three-wave process always occurs first, and thus serves to seed the growth of four-wave processes and the subsequent cascading to higher order satellites.

With the nonideal beam used in this experiment ($6 \times$ diffraction limit), we were able to trap and accelerate electrons to 18 MeV. It is envisaged that with an optimized frequency doubled driver, offering intensities up to 1×10^{19} Wcm^{-2} [24], future experiments at 527 nm will offer plasma-based electron acceleration to yet higher energies.

References

[1] M. D. Perry and G. Mourou, "Terawatt to petawatt subpicosecond lasers," *Science*, vol. 264, p. 917, 1994.

[2] A. Modena, Z. Najmudin, A. E. Dangor, C. E. Clayton, K. A. Marsh, C. Joshi, V. Malka, C. B. Darrow, C. Danson, D. Neely, and F. N. Walsh, "Electron acceleration from the breaking of relativistic plasma-waves," *Nature*, vol. 377, p. 606, 1995.

[3] C. Joshi, T. Tajima, J. M. Dawson, H. A. Baldis, and N. A. Ebrahim, "Forward Raman instability and electron acceleration," *Phys. Rev. Lett.*, vol. 47, p. 1285, 1981.

[4] T. M. Antonsen and P. Mora, "Self-focusing and Raman-scattering of laser-pulses in tenuous plasmas," *Phys. Rev. Lett.*, vol. 69, p. 2204, 1992.

[5] W. B. Mori, C. D. Decker, D. E. Hinkel, and T. Katsouleas, "Raman forward scattering of short-pulse high-intensity lasers," *Phys. Rev. Lett.*, vol. 72, p. 1482, 1994.

[6] C. A. Coverdale, C. B. Darrow, C. D. Decker, W. B. Mori, K. C. Tzeng, K. A. Marsh, C. E. Clayton, and C. Joshi, "Propagation of intense subpicosecond laser-pulses through underdense plasmas," *Phys. Rev. Lett.*, vol. 74, p. 4659, 1995.

[7] A. Modena, Z. Najmudin, A. E. Dangor, C. E. Clayton, K. A. Marsh, C. Joshi, V. Malka, C. B. Darrow, and C. Danson, "Observation of Raman forward scattering and electron acceleration in the relativistic regime," *IEEE Trans. Plas. Sci.*, vol. 24, p. 289, 1996.

[8] A. Ting, C. I. Moore, K. Krushelnick, C. Manka, E. Esarey, P. Sprangle, R. Hubbard, H. R. Burris, R. Fischer, and M. Baine, "Plasma wakefield generation and electron acceleration in a self-modulated laser wakefield accelerator experiment," *Phys. Plasmas*, vol. 4, p. 1889, 1997.

[9] R. Wagner, S. Y. Chen, A. Maksimchuk, and D. Umstadter, "Electron acceleration by a laser wakefield in a relativistically self-guided channel," *Phys. Rev. Lett.*, vol. 78, p. 3125, 1997.

[10] D. Gordon, K. C. Tzeng, C. E. Clayton, A. E. Dangor, V. Malka, K. A. Marsh, A. Modena, W. B. Mori, P. Muggli, Z. Najmudin, D. Neely, C. Danson, and C. Joshi, "Observation of electron energies beyond the linear dephasing limit from a laser-excited relativistic plasma wave," *Phys. Rev. Lett.*, vol. 80, p. 2133, 1998.

[11] E. Esarey, P. Sprangle, J. Krall, and A. Ting, "Overview of plasma-based accelerator concepts," *IEEE Trans. Plasma Sci.*, vol. 24, p. 252, 1996.

[12] K. C. Tzeng, W. B. Mori, and T. Katsouleas, "Electron beam characteristics from laser-driven wave breaking," *Phys. Rev. Lett.*, vol. 79, p. 5258, 1997.

[13] C. N. Danson, J. Collier, D. Neely, L. J. Barzanti, A. Damerell, C. B. Edwards, M. H. R. Hutchinson, M. H. Key, P. A. Norreys, D. A. Pepler, I. N. Ross, P. F. Taday, W. T. Toner, M. Trentelman, F. N. Walsh, T. B. Winstone, and R. W. W. Wyatt, "Well characterized 10(19) Wcm(2) operation of VULCAN—An ultra-high power Nd:glass laser," *J. Modern Opt.*, vol. 45, p. 1653, 1998.

[14] D. Neely, C. N. Danson, R. Allott, F. Amiranoff, J. L. Collier, A. E. Dangor, C. B. Edwards, P. Flintoff, P. Hatton, M. Harman, M. H. R. Hutchinson, Z. Najmudin, D. A. Pepler, I. N. Ross, M. Salvati, and T. Winstone, "Frequency doubling of multi-terawatt picosecond pulses," *Laser Part. Beams*, vol. 17, p. 281, 1999.

[15] A. J. Mackinnon, M. Borghesi, A. Iwase, M. W. Jones, G. J. Pert, S. Rae, K. Burnett, and O. Willi, "Quantitative study of the ionization-induced refraction of picosecond laser pulses in gas-jet targets," *Phys. Rev. Lett.*, vol. 76, p. 1473, 1996.

[16] S. C. Rae, "Spectral blueshifting and spatial defocusing of intense laser-pulses in dense gases," *Opt. Commun.*, vol. 104, p. 330, 1994.

[17] V. Malka, F. Amiranoff, C. Coulaud, J. P. Geindre, V. Lopez, Z. Najmudin, and D. Neely, "Characterization of neutral density profile in a wide range of pressure of cylindrical pulsed gas jet," *Rev. Sci. Inst.*, vol. 71, p. 2329, 2000.

[18] H. A. Enge, *Deflecting Magnets*. New York: Academic, 1977.

[19] J. J. Livingood, *The Optics of Dipole Magnets*. New York: Academic, 1969.

[20] S. Guerin, G. Laval, P. Mora, J. C. Adam, A. Heron, and A. Bendib, "Modulational and Raman instabilities in the relativistic regime," *Phys. Plasmas*, vol. 2, p. 2807, 1995.

[21] F. F. Chen, "Excitation of large amplitude plasma waves," *Physica Scripta*, vol. T30, p. 14, 1990.

[22] E. Esarey, B. Hafizi, R. Hubbard, and A. Ting, "Trapping and acceleration in self-modulated laser wakefields," *Phys. Rev. Lett.*, vol. 80, p. 5552, 1998.

[23] K. C. Tzeng and W. B. Mori, "Suppression of electron ponderomotive blowout and relativistic self-focusing by the occurrence of Raman scattering and plasma heating," *Phys. Rev. Lett.*, vol. 81, p. 104, 1998.

[24] D. Neely, C. N. Danson, R. Allott, J. L. Collier, A. E. Dangor, C. B. Edwards, M. H. R. Hutchinson, Z. Najmudin, D. A. Pepler, I. N. Ross, and T. Winstone, "Achieving frequency doubled intensities of 10^{19} Wcm^{-2}," presented at the IFSA99, Bordeaux, France, 1999.

Z. Najmudin, photograph and biography not available at the time of publication.

R. Allott, photograph and biography not available at the time of publication.

F. Amiranoff, photograph and biography not available at the time of publication.

E. L. Clark, photograph and biography not available at the time of publication.

C. N. Danson, photograph and biography not available at the time of publication.

Daniel F. Gordon, received the B.S., M.S., and Ph.D. degrees in electrical engineering from the University of California, Los Angeles, in 1991, 1995, and 1999, respectively.

He is currently a National Research Council research associate at the Naval Research Laboratory, Washington, DC. His research interests are in high intensity, short pulse, laser-plasma interactions, plasma based accelerators, and computer modeling.

C. Joshi (M'83–SM'88–F'93), photograph and biography not available at the time of publication.

K. Krushelnick, photograph and biography not available at the time of publication.

V. Malka, photograph and biography not available at the time of publication.

D. Neely, photograph and biography not available at the time of publication.

M. R. Salvati, photograph and biography not available at the time of publication.

M. I. K. Santala, photograph and biography not available at the time of publication.

M. Tatarakis, photograph and biography not available at the time of publication.

A. E. Dangor, photograph and biography not available at the time of publication.

Propagation of Intense Laser Pulses Through Inhomogeneous Ionizing Gas Profiles

Nikolai E. Andreev, Mikhail V. Chegotov, Michael C. Downer, Erhard W. Gaul, Nicolas H. Matlis, Alla A. Pogosova, and Andy R. Rundquist

***Abstract*—By simultaneously and self-consistently solving Maxwell's equations, the Ammosov–Delone–Krainov (ADK) field ionization equation, and the relativistic cold plasma equations, we have investigated the propagation of intense, ultrashort laser pulses through spatially inhomogeneous longitudinal gas gradients. Along with highly accurate calculations of the spatial and temporal beam profiles of the pulse at the end of various gradients, we have also determined simple scaling rules for the location of the vacuum–gas interface in order to minimize the pulse distortion at the focus. We show the benefits of using either preionized or low-Z gases, and we discuss the implications of this work for plasma-channel laser wakefield acceleration.**

***Index Terms*—Laser ionization, laser propagation, laser pulse distortion, laser wakefield acceleration, plasma.**

I. Introduction

SIMULATIONS of intense laser pulse propagation in underdense plasmas [1]–[4] often assume fully ionized plasma as an initial condition. However, experiments often require the laser pulse first to ionize a gas, or to propagate through neutral gas end regions before reaching preionized plasma. The resulting ionization-induced distortions [5]–[11] of propagating pulses depend strongly on gas species, spatial profile of the gas, and focus geometry. From Maxwell and hydrodynamic equations and the Ammosov–Delone–Krainov (ADK) model of tunnel ionization [12], we derive a system of three-dimensional (3-D) equations for the slowly varying amplitude of a short, intense laser pulse propagating through an ionizing gas. We then simulate the propagation of 30-fs, 5-TW, 0.8-μm pulses through inhomogeneous longitudinal profiles of neutral H, He, Ne, and Ar gas tailored to reach final plasma density ($n_e = 2 \times 10^{18}$ cm^{-3}) upon complete outershell ionization, thus, enabling resonant laser wakefield [13], [14] generation with only mild relativistic self-focusing ($P < P_{\rm crit}$). The results show that the laser pulse can propagate stably over several Rayleigh lengths, reach peak focused intensity equal to or greater than the vacuum value, and generate a smoothly structured wakefield if the pulse intensity exceeds the threshold for complete outershell ionization at the entrance to the gas medium. If this simple criterion is not met, the pulse severely defocuses for the discussed ranges of gas pressure and pulse power.

Manuscript received November 1, 1999; revised April 3, 2000. This work was supported by the Department of Energy, under Grants DEFG03-96-ER40954 and DEFG03-97-ER54439, and the Russian Foundation for Basic Research, under Grant 98-02-16263.

N. E. Andreev, M. V. Chegotov, and A. A. Pogosova are with the High Energy Density Research Center, Associated Institute for High Temperatures, Russian Academy of Sciences, Moscow 127412, Russia (e-mail: andreev@laslab.ivtan.msk.su).

M. C. Downer, E. W. Gaul, N. H. Matlis, and A. R. Rundquist are with the Department of Physics, University of Texas at Austin, Austin, TX 78712 USA.

Publisher Item Identifier S 0093-3813(00)09721-6.

II. Model of Numerical Simulations

The dynamics of plasma formation due to tunneling ionization of a gas in the field of a short, intense laser pulse can be described by the equations of ionization kinetics for the densities N_k of ions with ionization multiplicity k ($k = 0, 1, \ldots, Z_n - 1$, where Z_n is the charge number of an atom nucleus) [9], [10]. The electron production rate

$$\Gamma = \frac{\partial N_e}{\partial t} \equiv \sum_{k=1}^{Z_n} k \frac{\partial N_k}{\partial t} = \sum_{k=0}^{Z_n - 1} W_k N_k \equiv \sum_{k=0}^{Z_n - 1} \Gamma^{(k)} \quad (1)$$

is governed by the probabilities W_k of tunneling ionization per unit time for ions with multiplicity k, which are determined by the well-known ADK formula [12]. In the processes of tunneling, ionization Γ oscillates in time (if the laser pulse is not circularly polarized) and includes the zeroth and higher even harmonics of the laser pulse frequency. These should be taken into account in studies of the laser pulse propagation in an ionizing gas and wakefield generation in a plasma produced by the laser pulse [15]–[18].

To describe the laser pulse evolution and fields that vary on the time and spatial scales ω_0^{-1} and k_0^{-1} of laser radiation in a plasma produced by the short laser pulse, we use the relativistic hydrodynamic equations for cold plasma electrons and Maxwell's equations along with the ionization kinetics (1) of immobile ions [18] described above. We apply harmonic analysis with the slow-varying envelope approximation and expansion with the parameter $|a| = |eE_0|/(m\omega_0 c)$, where the dimensionless, slowly varying envelope amplitude a of the laser pulse is related to the electric field E by the expression

$$eE/(m\omega_0 c) = \mathrm{Re}\{e_0 a \exp[-i\omega_0 t + ik_0 z]\}. \quad (2)$$

Here, e_0 is the unit vector of the polarization, which is assumed to be linear, $k_0 = \omega_0/c$, and the laser pulse propagates along the z-axis. In such harmonic analysis, the zeroth and second harmonics of the electron density N_e should be taken into account: $N_e = n_0 + \mathrm{Re}[n_2 \exp(-2i\omega t)]$. As a consequence, we allow for zeroth (Γ_0) and the second (Γ_2) harmonics of the electron source Γ (1). For a wide range of gases and laser pulse parameters $\Gamma_2 \approx 2 \cdot \mu \cdot \Gamma_0$, where $\mu = 0.7 - 1$ [18], [19]. The zeroth harmonic of the electron source Γ_0 should be calculated using the envelope amplitude of the laser pulse by averaging the ADK formula for $\overline{W}_k$ [12], [16] over a laser period.

We use the quasi-static approximation [20], which assumes that the temporal variations of slow quantities are negligible

0093–3813/00$10.00 © 2000 IEEE

within the laser pulse duration. In addition, we assume that the plasma is sufficiently rarefied to ignore the difference between the pulse group velocity and the speed of light. These assumptions allow us to consider all slow quantities as functions depending mainly on the variables $r_\perp = e_x x + e_y y$ and $\xi = z - ct$ (and slightly on $\tau = t$ through the quantity $|a|$).

In these variables comoving with the laser pulse, the equations of ionization kinetics for ion densities $\overline{N}_k$ averaged over a laser period can be written in the form

$$\frac{\partial D_0}{\partial \xi} = \frac{1}{c}\overline{W}_0 D_0$$
$$\frac{\partial D_k}{\partial \xi} = \frac{1}{c}\left[\overline{W}_k D_k - \overline{W}_{k-1} D_{k-1}\right]$$
$$k = 1, 2, \ldots, Z_n - 1 \qquad (3)$$

where $D_k = \overline{N}_k / n_a$ are the relative ion densities normalized to the time-independent inhomogeneous gas density, which in turn equals the total ion density (including neutrals) $n_a(r) = \sum_{k=0}^{Z_n} N_k$. The solution to (3) makes it possible to define the zeroth harmonic of the electron density N_e and the electron production rate Γ

$$n_0 = n_a \left\{ (1 - D_0) Z_n - \sum_{k=1}^{Z_n - 1} (Z_n + 1 - k) D_k \right\}$$
$$\Gamma_0 = n_a \sum_{k=0}^{Z_n - 1} \overline{W}_k D_k \equiv \sum_{k=0}^{Z_n - 1} \Gamma_0^{(k)}. \qquad (4)$$

To describe the laser pulse evolution, we use the following equation (compare [19]) for the pulse envelope a:

$$2i\omega_0 \frac{\partial a}{\partial \tau} + c^2 \Delta_\perp a - \omega_p^2 \left[\frac{n}{n_0} - \frac{1}{4}|a|^2 \right] a$$
$$= \frac{\omega_0}{n_c} \left[\frac{i}{4} \Gamma_2 a^* - \frac{2i}{a^*} \sum_{k=0}^{Z_n - 1} \Gamma_0^{(k)} \frac{U_k}{mc^2} \right] \qquad (5)$$

where $\Delta_\perp = (1/r)(\partial/\partial r)(r(\partial/\partial r))$ is the transverse part of the Laplace operator, $\omega_p^2 = 4\pi e^2 n_0 / m$, $n_c = m\omega_0^2 / 4\pi e^2$ is the critical density for the laser frequency ω_0, and U_k is the potential of ionization of ions with multiplicity k to ionization multiplicity $k+1$, $\Gamma_2 = \mu \Gamma_0$; n_0 and $\Gamma_0^{(k)}$ are determined by (3) and (4). The total (slowly varying) electron plasma density n describes the nonlinear plasma response to the ponderomotive action of the laser pulse with consideration for tunneling ionization processes, namely, the wakefield generation.

In deriving (5), the scale of the plasma inhomogeneity is assumed to be larger than the wavelength of the laser radiation and the higher order space and time derivatives responsible for the laser pulse dispersion and laser energy depletion due to the wakefield generation are omitted. These second-order derivatives as well as the terms on the right-hand side in (5), which describe the laser energy losses due to ionization processes, are small (see [18] and [19]) and can be neglected for the cases discussed below of rather low gas pressure, weakly relativistic laser pulse intensities, and atoms with few electrons.

With the same assumptions as were used to obtain (5), the low-frequency electric and magnetic fields in plasma can be expressed in terms of a single scalar function ϕ

$$\frac{eE_z}{mc^2} = \frac{\partial \phi}{\partial \xi}, \quad \frac{eE_r}{mc^2} - \frac{eB_\varphi}{mc^2} = \frac{\partial \phi}{\partial r} \qquad (6)$$

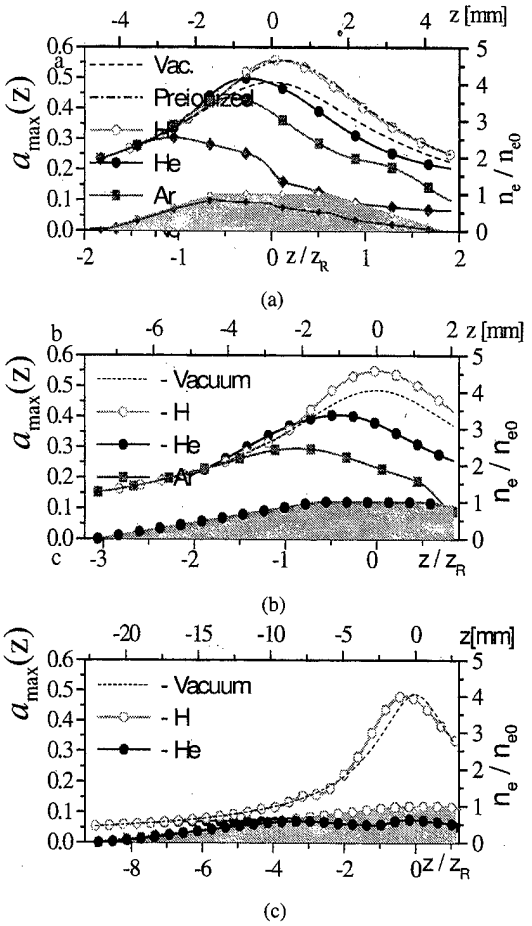


Fig. 1. (a) Axial normalized vector potential $a_{\max}(r = 0, z)$ at the peak of a 30-fs, 5-TW, 0.8-μ laser pulse focused at $\sim f/30$ into the inhomogeneous profile of neutral H, He, Ne, or Ar gas depicted by the shaded region at the bottom. A 3-mm long entrance and exit ramps with linear density gradients bound a 3-mm long plateau of uniform gas density $(2 \times 10^{18}\ \mathrm{cm}^{-3})/Z_{\max}$, where $Z_{\max} = 1$ (H), 2 (He), 8 (Ne), 8 (Ar) is the ionization level corresponding to removal of the outer electron shell. The axial vector potential for a focus into vacuum (dashed curve) and a fully preionized plasma of the same profile (dotted curve) are shown for comparison. Axial electron density profiles $n_e(z)$ resulting from propagation of the pulse through H and Ne profiles are plotted at the bottom. (b) Axial vector potentials for H, He, Ar as in (a), but with entrance and exit density ramps increased to 6-mm scale length. (c) Axial vector potentials for H, He as in (b), but with entrance and exit density ramps increased to 20.6-mm scale length.

which is determined by (compare [21])

$$\left(\Delta_\perp - k_p^2\right) \frac{\partial^2 \phi}{\partial \xi^2} + k_p^2 \left(\Delta_\perp - k_p^2\right) \phi - \frac{\partial \ln n_0}{\partial r} \frac{\partial^3 \phi}{\partial r \partial \xi^2}$$
$$= \frac{k_p^2}{4} \left(\Delta_\perp - k_p^2\right) |a|^2 - k_p^2$$
$$\times \int_{+\infty}^{\xi} \left(\phi + \frac{1}{4}|a|^2 - \mathrm{Re}\left[(a^*)^2 \frac{\Gamma_2}{16\Gamma_0} \right] \right) \frac{\partial k_p^2}{\partial \xi} d\xi \qquad (7)$$

where $k_p^2 \equiv k_p^2(r, \xi) = \omega_p^2 / c^2 = 4\pi e^2 n_0(r, \xi) / mc^2$ and the "background" electron density $n_0(r, \xi)$ is defined by the ionization kinetics (3), (4). The nonlinear plasma response (including the relativistic nonlinearity) can be also expressed via potential ϕ

$$k_p^2 \left(\frac{n}{n_0} - \frac{1}{4}|a|^2 \right)$$
$$= k_p^2 + \left(\Delta_\perp - k_p^2\right) \phi$$
$$+ \int_{+\infty}^{\xi} \left(\phi + \frac{1}{4}|a|^2 - \mathrm{Re}\left[(a^*)^2 \frac{\Gamma_2}{16\Gamma_0} \right] \right) \frac{\partial k_p^2}{\partial \xi} d\xi. \qquad (8)$$

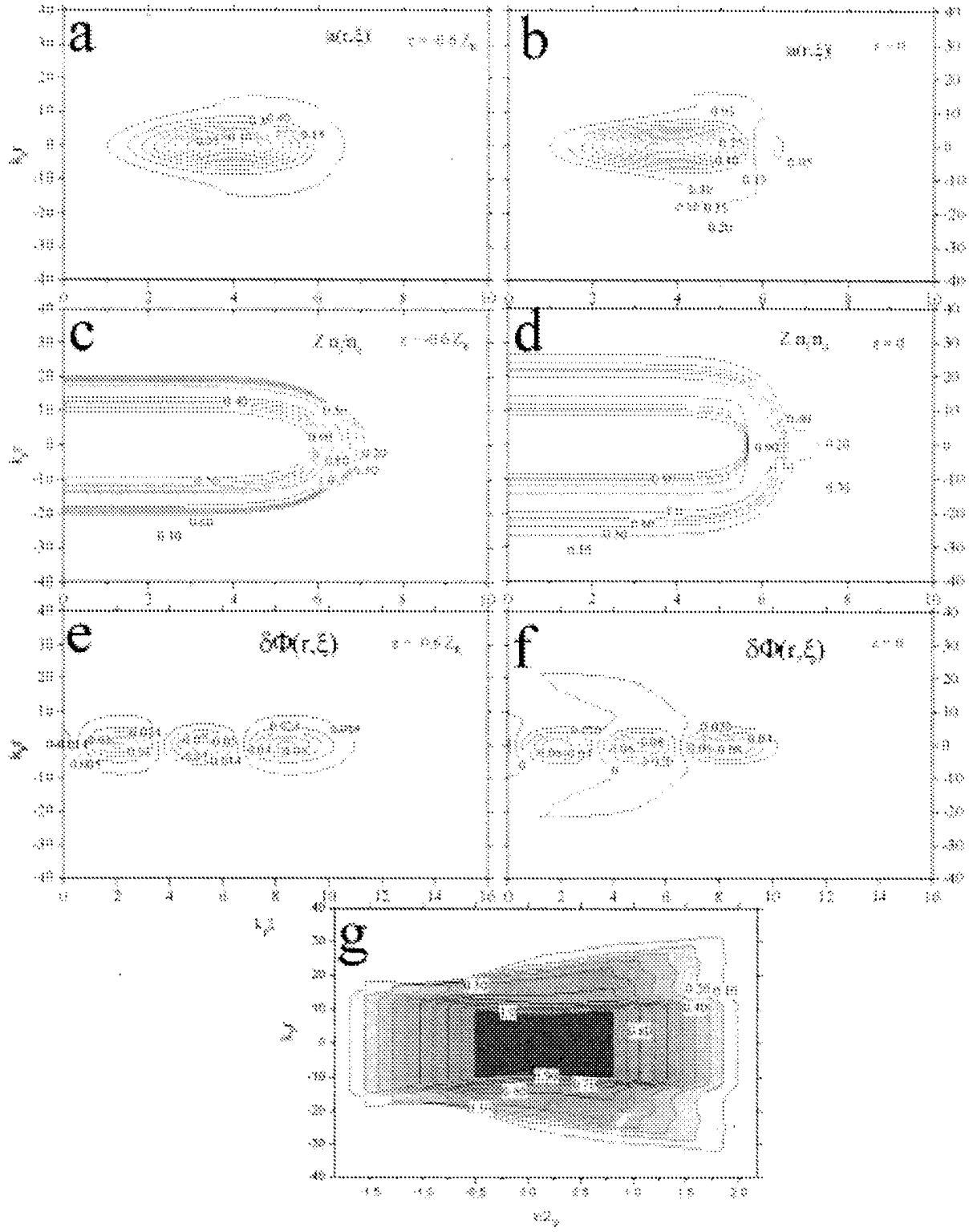


Fig. 2. Contour plots of normalized vector potential $a(r,\xi)$ of laser pulse at (a) $z = -0.6z_R$ and (b) $z = 0$ propagating into He profile with 3-mm entrance ramp; corresponding contour plots of normalized ion charge Zn_i/n_{e0} at (c) $z = -0.6z_R$ and (d) $z = 0$; corresponding laser wakefield potential! (r,ξ) for laser pulse at (e) $z = -0.6z_R$ and (f) $z = 0$. Panel (g) shows contour plots of Zn_i/n_{e0} after laser pulse has propagated through entire gas profile. Note that the intense core of the pulse propagates without distortion through the wide axial region of uniform, fully ionized plasma.

Equations (3)–(8) are the complete system of equations to describe the self-consistent dynamics of a short, intense laser pulse propagation and wakefield generation in an inhomogeneous ionizing gas.

The initial condition (with respect to τ) should be added to this system. In the laboratory frame, this condition corresponds to the boundary condition at the entrance of the gas slab $z = z_{in}$. We determined the initial distribution of the laser pulse electric

field as a Gaussian function of ξ and r

$$a(\xi, r, \tau = 0) = \frac{a_0}{\sqrt{1 + z_{in}^2/z_R^2}} \exp\left[-2\ln 2\,\frac{\xi^2}{c^2\tau_{imp}^2} - \frac{r^2}{r_0^2\,(1 + z_{in}^2/z_R^2)} + i\,\frac{r^2 k_0}{2R(z_{in})} - i\,\mathrm{arctg}\,\frac{z_{in}}{z_R}\right]$$

where r_0 is the minimum radius of the laser pulse at the best vacuum focus ($z = 0$), τ_{imp} is the full-width at half maximum (FWHM) pulse duration, $a_0 = eE_0/(m\omega_0 c)$, E_0 is the maximum laser electric field, $R(z_{in}) = z_{in}(1 + z_R^2/z_{in}^2)$ is the curvature radius of the laser pulse wave front, and $z_R = k_0 r_0^2/2$ is the Rayleigh length. The boundary conditions for the wakefield potential implies that $\phi = 0$ in the unperturbed plasma or gas in front of the pulse ($\xi \to \infty$) and at $r \to \infty$.

III. Results

The maximum of the normalized vector potential $a_{\max}(z)$ at the laser pulse axis of a 30-fs, 5-TW, 0.8-μm laser pulse focused at $\sim f/30$ into the inhomogeneous profile of neutral H, He, Ne, or Ar gas is shown in Fig. 1(a). The profile of a gas jet or of a differentially pumped gas cell is simulated by a 3-mm long entrance and exit ramps with linear density gradients bounding a 3-mm long plateau of uniform gas density $(2 \times 10^{18}\ \mathrm{cm}^{-3})/Z_{\max}$, where $Z_{\max} = 1$ (H), 2 (He), 8 (Ne), 8 (Ar) is the ionization level corresponding to removal of the outer electron shell. The peak of the vector potential for focusing into vacuum (dashed curve) and fully preionized plasma of the same profile (dotted curve) is shown for comparison. H, He, and a preionized gas show a peak vector potential greater than the one of a vacuum focus due to self-focusing. The laser pulse propagation in hydrogen is barely different from the one in preionized gas, because the only ionization step in hydrogen occurs far outside of the simulated gas profile. However, for Ar and even more for Ne, there are ionization steps inside the gas profile, which are nonuniform across the radial direction, thus, forming a negative lens in plasma and defocusing the laser pulse. The result is decreased peak intensity on-axis for those gases. The lower parts of Fig. 1(a)–(c) show the axial electron density profiles $n_e(z)$ resulting from propagation of the pulse through H and Ne [Fig. 1(a)] or He [(b) and (c)] profiles. To investigate the dependence on the gas profile, we used the same focusing geometry and laser parameters but increased the length of the ramp to 6 and 20.6 mm in Fig. 1(b) and (c), respectively. The increased length of the ramp decreases the laser intensity at the beginning of the gas; thus, there are additional ionization steps for argon within the gas profile and the laser pulse defocuses due to plasma lensing. For helium, the intensity is not high enough to doubly ionize the gas across the full beam, and we notice some decrease in peak axial vector potential [Fig. 1(b)]. If we increase the length of the ramp further [Fig. 1(c)], the laser pulse also defocuses in helium.

Fig. 2 shows contour plots of the normalized vector potential $a(r, \xi)$ [(a) and (b)] the normalized ion charge $\overline{Z} n_i/n_{e0} = n_0(r, \xi)/n_{e0}$ [(c) and (d)], and the corresponding laser wakefield potential $\phi(r, \xi)$ [(e) and (f)] for a laser pulse propagating into an He gas profile with a 3-mm entrance ramp at positions $z = -0.6 z_R$ and $z = 0$. Fig. 2(g) shows the contour plot of $\overline{Z} n_i/n_{e0} = n_0(r, z, t \to \infty)/n_{e0}$ after the laser pulse has propagated through the entire gas profile. Note that the intense core of the pulse propagates without distortion through the wide axial region of uniform, fully ionized plasma. The density step from first to second ionization can be recognized in the radial direction. There is a small defocusing on the radial edge of the pulse. If the focus is moved deeper into the gas, the peak of the normalized vector potential $a(r, \xi)$ and the corresponding wakefield amplitude $\delta n_{\max}/n_{0e}$ is decreased, as shown in Fig. 3. For contrast, the contour plots of $a(r, \xi)$ and $Z n_i(r, \xi)/n_{e0}$ for a laser pulse propagating into an He gas profile with a 20.6-mm entrance ramp at even earlier positions $z = -6.5 z_R$ and $z = -.28 z_R$ are shown in Fig. 4(a)–(d), and (e) shows the corresponding $\overline{Z} n_i/n_{e0} = n_0(r, z, t \to \infty)/n_{e0}$ after the laser pulse has propagated through the gas profile. The core of the pulse is strongly distorted because of strong radial electron density gradients near the axis. Note that Fig. 4 shows wider radial and slightly different axial dimensions than does Fig. 2. In addition to reduced peak intensity on-axis, the distorted pulse has random peaks off-axis and cannot drive a controlled wakefield.

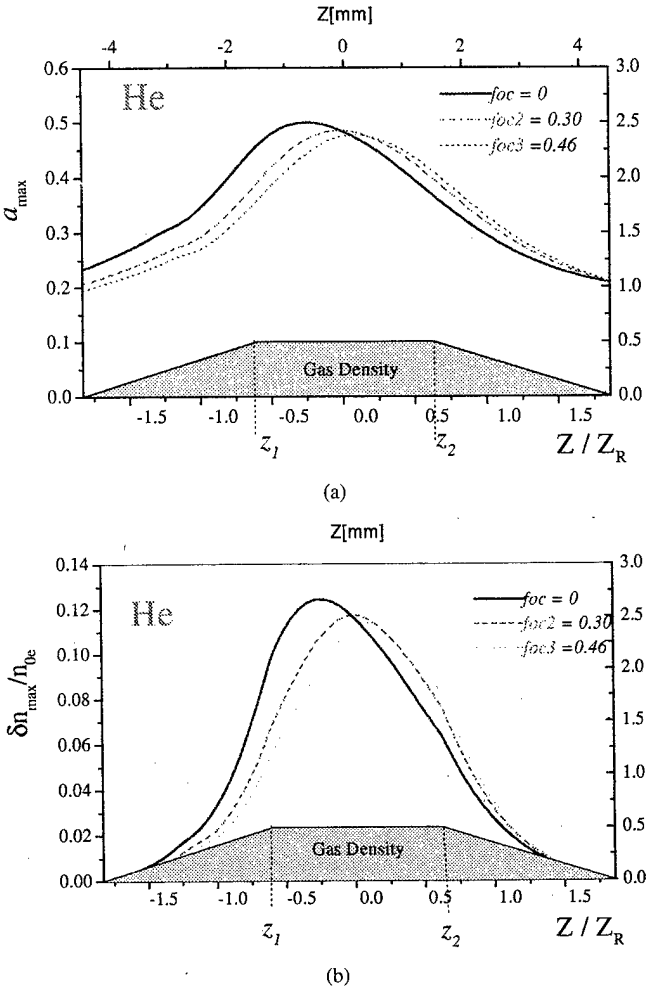


Fig. 3. Upper curves: axial normalized vector potential plots of the focused pulse for the 3-mm He density ramp as in Fig. 1(a), but for three different positions of the vacuum focus. Lower curves: corresponding amplitudes of laser wakefield.

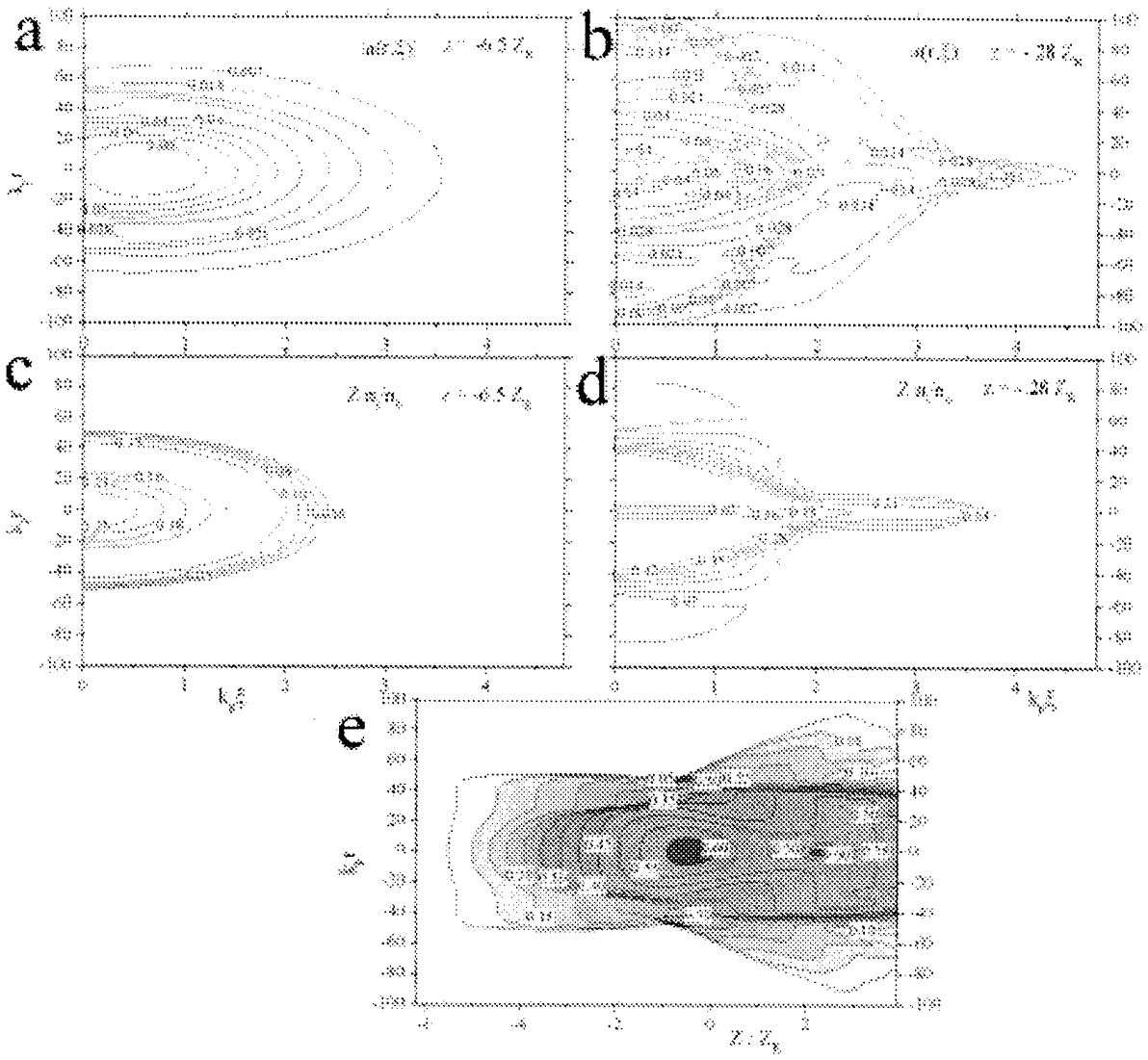


Fig. 4. Contour plots of normalized vector potential $a(r,\xi)$ of laser pulse at (a) $z = -6.5z_R$ and (b) $z = -0.28z_R$ propagating into the He profile with 20.6-mm entrance ramp; corresponding contour plots of normalized ion charge Zn_i/n_{e0} at (c) $z = -6.5z_R$ and (d) $z = -0.28z_R$ and (e) after propagation of pulse through entire profile. Note that intense core of the pulse is strongly distorted because of strong radial electron density gradients near the axis.

IV. Discussion

The rigorous, self-consistent results of the above sections can be understood intuitively by considering simple Gaussian focusing. The laser pulse can propagate stably to the vacuum focus provided that, at the entrance to the gas medium, the bulk of the energy in the pulse is inside the isointensity contour corresponding to the threshold for complete outershell ionization. For pure Gaussian focusing, the location of the corresponding threshold of the gas interface (from the vacuum focus) can be calculated so that the above criterion is met. If a fraction x of the beam energy is to be inside the given isointensity contour, the gas interface must be located no further from the focus than z_{th}, which is given by

$$z_{th} = z_R\sqrt{\frac{I_{\max}}{I_{th}}\exp\left[-2\sqrt{-\frac{1}{2}\ln(1-x)}\right] - 1} \quad (9)$$

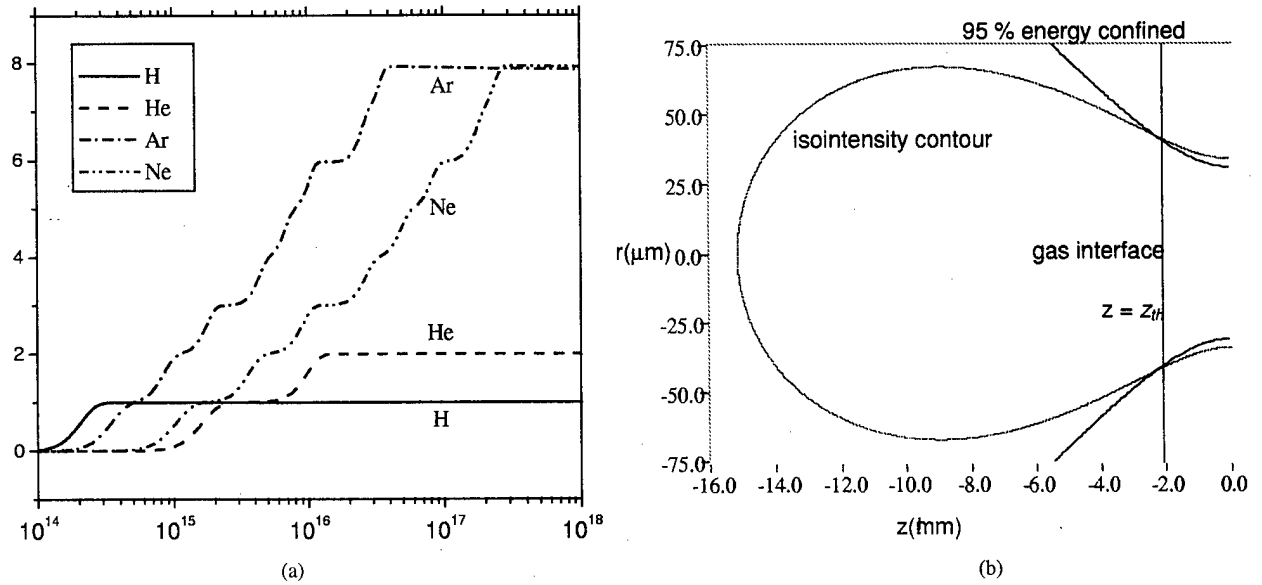
where

z_R Rayleigh length;
$I_{\max}$ peak intensity at the vacuum focus;
I_{th} intensity at the threshold for complete outer shell ionization.

The latter one can be extracted from Fig. 5(a). In Fig. 5(b), we show the geometry necessary to allow 95% of the beam to propagate undistorted to the focus for the focusing parameters of Fig. 1. This will occur as long as the gas interface is closer to the focus than is the vertical line at the intersection of the 95% ray and the outershell appearance isointensity contour. The inverse of this expression is

$$x = 1 - \exp\left[-\frac{1}{2}\left(\ln\left[\frac{I_{th}}{I_{\max}}\left(1+\left(\frac{z_{th}}{z_R}\right)^2\right)\right]\right)^2\right]. \quad (10)$$

Table I shows the percentage of the light that would interact with a flat plasma profile for the gases used in this work and for z_{th}



(a) (b)

Fig. 5. (a) Ionization stages versus intensity for H, He, Ne, Ar are shown in for 30-fs, 0.8-μm laser pulse. (b) The isointensity curve of the focused laser pulse (same geometry as before) is shown, where it ionizes helium the second time. The center of the focus is located at the right end of the figure. It also shows between 95% of the laser energy is confined, and a line connects the intersection of these curves.

TABLE I
PERCENTAGE OF THE BEAM WHICH REMAINS UNDISTORTED USING THE NONSELF-CONSISTENT CALCULATION OF SECTION IV FOR VARIOUS GASES AND TWO DIFFERENT GAS RAMP PROFILES

GAS	Appearance Intensity [W/cm^2]	End of outer shell isointensity contour [mm]	x (z_{th} = 4.5 mm) [%]	X (z_{th} = 7.5 mm) [%]
HYDROGEN	2.71 x 10^{14}	105	100	100
HELIUM	1.28 x 10^{16}	15	91	59
ARGON	3.43 x 10^{16}	9.0	52	6
NEON	2.31 x 10^{17}	2.7	0	0

set to 4.5 mm [3 mm for the length of the entrance ramp plus 1.5 mm for the distance to the vacuum focus in uniform gas density, as shown in Fig. 1(a)] and 7.5 mm [as shown in Fig. 1(b)].

Even for a 20.6-mm ramp, as is the case in Fig. 1(c), hydrogen still produces a value of 95%, although all the other gases have $x = 0$ for that case. It is interesting to note that although helium takes an order of magnitude of more intensity to be singly ionized as argon, argon distorts the beam more because the eighth electron is so much harder to ionize in argon than is the second in helium. Finally, it is clear that for all the geometries considered here, neon always presents a substantial plasma lens to the beam.

It should be stressed that the fraction of energy x, which is to be inside the given isointensity contour to provide stable pulse propagation, is dependent on the plasma density (i.e., the gas pressure) and the pulse power. For the parameters discussed above, this fraction has to be near 100%. It is evident that the necessary value of x for small pulse distortion will increase with gas pressure.

In practice, we cannot experimentally achieve a perfect gas/vacuum interface. We need to then calculate the defocusing effect of the background residual gas, which permeates the experimental chamber outside of the gas profile considered above because plasma begins for this gas at the isointensity surface of the lowest ionization level. A conservative upperbound to the tolerable background pressure can be calculated by finding the optical path length difference due to the plasma for the central ray. We can assume that the edge of the beam never experiences the plasma, and so its phase (due solely to the plasma) is zero. This is conservative because it is clear from Fig. 5(b) that even the 95% ray experiences the plasma and, thus, experiences some additional phase. This upperbound phase is given by

$$\Delta\psi = \frac{\omega_p^2 z_R}{2k_0 c}\left[\sum_{j=1}^{n}\sqrt{\frac{I_{\max}}{I_{th}^{(j)}} - 1} - n\frac{z_{th}}{z_R}\right] \tag{11}$$

where

- ω_p plasma frequency for the singly ionized gas;
- c speed of light;
- $I_{th}^{(j)}$ appearance intensity of the jth electron in the outer shell;
- n set equal to the number of electrons ionized at z_{th}.

As an example, for the focusing geometry of Fig. 1, the phase accumulated by the central ray due to the plasma leading up to z_{th} is 3.7 times the background pressure in torr if the gas is helium. In order to ensure that there is minimal distortion, this phase difference should be much less than pi, and thus, the background pressure for that geometry must be no higher than 10 mtorr. Recall, however, that this is a very conservative estimate, and hence, residual background pressures approaching 1 torr might still be reasonable. It should be noted also that in our analysis,

we did not take into account a nonlinear polarization of neutral gas that can contribute to a laser pulse focusing (see, e.g., [22]) when the fraction of ionized atoms is small, but cannot change substantially the discussed regimes when the laser pulse propagates mainly in ionized gases.

V. Conclusion

We have investigated the regime of focusing mildly relativistic, ultrashort laser pulses into a neutral gas medium. We have shown that in order to achieve the peak intensities possible in vacuum, the gas medium must be limited longitudinally so that the pulse is not severely distorted (either spatially or temporally) before the focus. The key issues are the intensity necessary to fully strip the outershell of the gas and the location of the vacuum–gas interface in relation to the focus. In order to have a smoothly varying spatial and temporal profile at the focus with sufficient intensities to drive a carefully controlled wakefield, we have found that using either preionized or low-Z gas is imperative. If a high-Z gas is used, the multiple steps in ionizing the outershell significantly distort the pulse as it travels from the vacuum–gas interface to the focus. We have presented and discussed both self-consistent numeric calculations and simple scaling rules based on Gaussian beam propagation, which show both the benefits of low-Z gas targets and the inherent distortions present with heavier gases.

References

[1] P. Mora and T. M. Antonsen, "Kinetic modeling of intense, short laser pulses propagating in tenuous plasmas," *Phys. Plasmas*, vol. 4, no. 1, pp. 217–229, Jan. 1997.

[2] T. M. Chiron, B. Lamouroux, R. Lange, J.-F. Ripoche, M. Franco, B. Prade, G. Bonnaud, G. Riazuelo, and A. Mysyrowicz, "Numerical simulations of the nonlinear propagation of femtosecond optical pulses in gases," *Eur. Phys. J. D*, vol. 6, no. 3, pp. 383–396, June 1999.

[3] P. Sprangle, B. Hafizi, and P. Serafim, "Dynamics of short laser pulses propagating in plasma channels," *Phys. Rev. Lett.*, vol. 82, pp. 1173–1176, Feb. 1999.

[4] E. Esarey and W. P. Leemans, "Nonparaxial propagation of ultrashort laser pulses in plasma channels," *Phys. Rev. E*, vol. 59, no. 1, pp. 1082–1095, Jan. 1999.

[5] P. Chessa, E. De Wispelaere, F. Dorchies, V. Malka, J. R. Marquès, G. Hamoniaux, P. Mora, and F. Amiranoff, "Temporal and angular resolution of ionization-induced refraction of a short laser pulse in helium gas," *Phys. Rev. Lett.*, vol. 82, no. 3, pp. 552–555, Jan. 1999.

[6] P. Monot, T. Ausguste, L. A. Lompre, G. Mainfray, and C. Manus, "Focusing limits of a terawatt laser pulse in an underdense plasa," *J. Opt. Soc. Am. B*, vol. 8, pp. 1579–1584, 1992.

[7] R. Rankin, C. E. Capjack, N. H. Burnett, and P. Corcum, "Refraction effects associated with multiphoton ionization and ultrashort-pulse laser propagation in plasma waveguides," *Opt. Lett.*, vol. 16, pp. 835–837, 1991.

[8] S. C. Rae, "Ionization induced defocusing of intense laser pulses in high pressure gases," *Opt. Commun.*, vol. 97, pp. 25–28, 1993.

[9] W. M. Wood, C. W. Siders, and M. C. Downer, "Measurement of femtosecond ionization dynamics of atmospheric density gases by spectral blueshifting," *Phys. Rev. Lett.*, vol. 67, no. 25, pp. 3523–3526, July 1979.

[10] S. P. Le Blanc, R. Sauerbrey, S. C. Rae, and K. Burnett, "Femtosecod vacuum-ultraviolet pulse propagation through a high pressure gas," *J. Opt. Soc. Am. B*, vol. 10, pp. 1801–1809, Oct. 1993.

[11] S. P. Nikitin, Y. L. Li, T. M. Antonsen, and H. M. Milchberg, "Ionization-induced pulse shortening and retardation of high intensity femtosecond laser pulses," *Opt. Commun.*, vol. 157, no. 1–6, pp. 139–144, Dec. 1998.

[12] M. V. Ammosov, N. B. Delone, and V. P. Krainov, "Tunnel ionization of complex atoms and of atomic ions in an alternating electric field," *Zh. Eksp. Teor. Fiz.*, vol. 91, p. 2008, 1986. [*Sov. Phys. JETP*, vol. 64, pp. 1191–1194, 1986].

[13] T. Tajima and J. M. Dawson, "Laser electron accelerator," *Phys. Rev. Lett.*, vol. 43, pp. 267–270, July 1979.

[14] E. Esarey, P. Sprangle, J. Krall, and A. Ting, "Overview of plasma-based accelerator concepts," *IEEE Trans. Plasma Sci.*, vol. 24, pp. 252–288, 1996.

[15] V. P. Kandidov, O. G. Kosareva, and S. A. Shlenov, "Influence of transient self-focusing on the propagation of high-power femtosecond laser pulses in gases under ionization conditions," *Quantum Electron.*, vol. 24, pp. 971–977, 1994.

[16] N. E. Andreev, M. V. Chegotov, M. E. Veisman, B. He, and J. T. Jhang, "Non-adiabatic energy deposition from the short intense laser pulse to the ionizing gas," in *Proc. ICONO'98: Ultrafast Phenomena and Interaction of Superstrong Laser Fields with Matter: Nonlinear Optics and High-Field Physics*, vol. 3735, M. V. Fedorov and V. M. Gordienko, Eds., 1999, pp. 234–241.

[17] N. E. Andreev, M. V. Chegotov, M. E. Veisman, T. Auguste, P. D'Oliveira, S. Hulin, P. Monot, A. Ya. Faenov, T. A. Pikuz, A. I. Magunov, I. Yu. Skobelev, F. B. Rosmej, and Myu. Romanovskii, "Nonadiabatic heating of a plasma produced by the ionization of a gas by a short intense laser pulse," *JETP Lett.*, vol. 68, pp. 592–598, 1998.

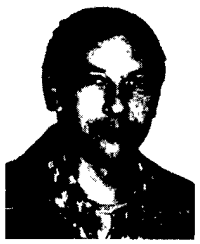
[18] N. E. Andreev, M. G. Cadjan, M. V. Chegotov, and M. E. Veisman, "Wake field generation in ionizing gases," *Plasma Phys. Rep.*, vol. 26, 2000.

[19] N. E. Andreev, M. V. Chegotov, and M. E. Veisman, "Wake field generation by elliptically polarized femtosecond laser pulse in ionizing gases," *IEEE Trans. Plsama Sci.*, vol. 28, pp. 1098–1105, Aug. 2000.

[20] P. Sprangle, E. Esarey, and A. Ting, "Nonlinear theory of intense laser-plasma interactions," *Phys. Rev. Lett.*, vol. 64, pp. 2011–2014, 1990.

[21] N. E. Andreev, E. V. Chizhonkov, A. A. Frolov, and L. M. Gorbunov, "On the laser wakefield acceleration in plasma channels," *Nucl. Instrum. Methods Phys. Res. A*, vol. 410, pp. 469–476, 1998.

[22] P. Sprangle, E. Esarey, and B. Hafizi, "Propagation and stability of intense laser pulses in partially-stripped plasmas," *Phys. Rev. E*, vol. 56, p. 5894, 1997.



Nikolai E. Andreev was born in Moscow, Russia, in 1945, and graduated from Moscow State University in 1967. He received the Ph.D. degree and Doctor of science degree in theoretical and mathematical physics from P.N. Lebedev Physical Institute of USSR Academy of Sciences, Moscow, in 1973 and 1985, respectively. Academic rank of Senior Scientist in 1986, and rank of Professor from Russian Ministry of Education in 1998.

Since 1970, he has been a Research Physicist in the Division of Plasma Phenomena Theory of P.N. Lebedev Physical Institute of Russian Academy of Sciences (RAS). He joined the High Energy Density Research Center of the Associated Institute for High Temperatures of RAS in 1987, where he is currently a Head of the Laser Plasma Laboratory and he is a Professor at the Moscow Institute of Physics and Technology. His current research includes laser light absorption, self-focusing and stimulated scattering, laser-driven particle accelerators, and nonlinear self-consistent structures in irradiated plasmas.



Mikhail V. Chegotov was born in Moscow, Russia, on February 20, 1962. He received the Ph.D. degree in 1988 in theoretical and mathematical physics from the Lebedev Physical Institute of the USSR Academy of Sciences, Moscow.

From 1988 to 1992, he was a Junior Research Fellow and from 1992 to 1994 a Research Fellow in the Division of Plasma Phenomena Theory of P.N. Lebedev Physical Institute of the Russian Academy of Sciences (RAS). From 1993 to 1994, he had a DAAD scholarship at Ruhr University, Bochum, Germany. Since 1995, he has been a Senior Research Fellow in the Laser Laboratory at the High Energy Density Research Center of the Associated Institute for High Temperatures of RAS. He has published over 40 technical articles and letters in refereed scientific journals. His research has concentrated on the areas of nonlinear laser–plasma interaction, ionization processes in ionized gases, transport phenomena in plasmas, and mathematical and physical aspects of ionized gases diagnostics.

Michael C. Downer, photograph and biography not avaiable at the time of publication.

Erhard W. Gaul, photograph and biography not avaiable at the time of publication.

Nicolas H. Matlis, photograph and biography not avaiable at the time of publication.

Alla A. Pogosova, photograph and biography not avaiable at the time of publication.

Andy R. Rundquist, photograph and biography not avaiable at the time of publication.

Wakefield Generation by Elliptically Polarized Femtosecond Laser Pulse in Ionizing Gases

Nikolai E. Andreev, Mikhail V. Chegotov, and M. E. Veisman

***Abstract*—Wakefield generation by a femtosecond laser pulse is described in the frame of the slowly varying amplitudes approximation. The amplitude of the wakefield A_p is studied as a function of laser pulse and background gas parameters, and is compared with well-known results for preformed, completely ionized plasma $A_{p,i}$. It is found that the ionization processes can increase A_p as compared to $A_{p,i}$ at comparatively high laser peak intensities. It is shown that the increase of the wakefield amplitude due to gas ionization is more pronounced for circularly polarized laser pulses than for linearly polarized laser pulses. The strongest enhancement of A_p in comparison with $A_{p,i}$ takes place for longer laser pulses with a duration in excess of the plasma wave period when the resonant conditions for ponderomotive excitation of the wakefield are not matched. Thus, ionization processes can expand the region of parameters for efficient generation of the laser wakefields.**

***Index Terms*—Ionization processes, laser wakefield, slowly varying amplitudes approximation.**

I. Introduction

THE USE of powerful short-pulse lasers for generation of a fast intense Langmuir wave in rarefied plasmas has opened new possibilities in elaboration of the compact ultra-high-gradient laser-plasma accelerators of charged particles (see, e.g., [1], [2] and references therein). The theory of a wake plasma wave generation by intense laser pulse in preionized plasmas was worked out intensively during the past decade and has checked out experimentally. At the present time, however, in the current and planed experiments on laser-plasma acceleration, it is assumed that the laser pulse will produce a plasma while propagating in a neutral gas. The theory of laser pulse propagation and plasma wakefield generation in an ionizing gas should include the adequate description of ionization kinetics in the intense laser field [3]–[6] and the influence of the ionization processes to the plasma waves' excitation in a laser-produced plasma [7]. Propagation of intense laser pulses through inhomogeneous ionizing gas profiles will be described elsewhere [8].

In the present paper, we have analyzed systematically the efficiency of wakefield generation depending on the gas and laser pulse parameters. Special attention has been concentrated on the dependence of wakefield amplitude on the polarization of the laser pulse in the conditions when ionization processes play an important role in the wakefield generation. It is shown that the increase of the wakefield amplitude due to the gas ionization is more pronounced for circularly polarized laser pulses as compared to the linear polarization of the laser. It is found, also, that ionization front (at the leading front of the laser pulse) provides the detectable wakefield amplitude (determined by the threshold for ionization laser intensity) independent of the relation between the laser pulse duration and plasma wave period. In particular, this "ionization wake" can fulfill the role of a seed for the intense wakefield generation by a self-modulation of the laser pulse [9]–[12] in ionizing gas.

The paper is organized as follows. In Section II, we introduce the basic equations that describe the slowly varying amplitude of the laser field and the plasma wave electric field in the presence of tunneling optical field ionization (OFI) processes. On the basis of the laser-field energy conservation, the conditions of smallness of the laser-energy losses due to gas ionization are discussed. In Section III, one-dimensional (1-D) analytical solutions for the wakefield generated by a given laser pulse in an ionizing gas are obtained and analyzed. The numerical results of wakefield generation in different gases are discussed in Section IV, depending on the laser-pulse parameters. A conclusion is presented in Section V.

II. Basic Equations

We describe the wakefield generation in terms of slowly varying amplitudes approximation, which implies that the laser pulse duration is in excess of a few optical cycles. The validity of such approximation is also a consequence of the fact that the ionization of comparatively light atoms occurs at nonrelativistic intensities [5], [6]. Besides, here we restrict our consideration to a 1-D approximation of the problem, which is justified if a wide laser pulse propagates over the distance smaller than its Rayleigh length, or diffraction effects are suppressed (see, e.g., [1]).

For transversal (laser) field $\mathbf{E}_l$, we take into account the only first harmonic of laser frequency ω_0

$$\mathbf{E}_l = \tfrac{1}{2}\left(E_x \mathbf{e}_x + E_y \mathbf{e}_y\right) \exp\left[-i\omega_0 \left(t - z/c\right)\right] + c.c.$$

Longitudinal (plasma) electric field E_z is described up to the second-order accuracy with respect to the relativistic parameter $e|\mathbf{E}_l|/(m\omega_0 c)$ and with regard to the zero and second harmonics of ω_0

$$E_z\left(z, t\right) = E_p\left(z, t\right) + \tfrac{1}{2}\left\{E_{p2}\left(z, t\right) \exp[-2i\omega_0(t - z/c)] + c.c.\right\}.$$

Manuscript received November 1, 1999; revised April 5, 2000. The work was partially supported by the Russian Foundation for Basic Research under Grant 98-02-16263 and by INTAS under Grant 97-10236.

The authors are with the High Energy Density Research Center, Associated Institute for High Temperatures, Russian Academy of Sciences, Moscow 127412, Russia (e-mail: andreev@laslab.ivtan.msk.su).

Publisher Item Identifier S 0093-3813(00)10497-7.

0093–3813/00$10.00 © 2000 IEEE

The source of free electrons Γ (total ionization rate) consists of ionization rates of ions with any ionization degree k from zero (neutral) to $Z-1$ (H—like atomic rest): $\Gamma = \sum_{k=0}^{Z-1} \Gamma^{\langle k \rangle}$ [5]–[7]. It is also expanded into the laser frequency harmonics series

$$\Gamma(z,t) = \Gamma_0(z,t) + \tfrac{1}{2}\{\Gamma_2(z,t)\exp[-2i\omega_0(t-z/c)] + c.c.\} + \ldots .$$

Harmonics of Γ originate from the strong nonlinear dependence of optic field tunneling ionization probability [3] of any ion (neutral) on the laser field $\mathbf{E}_l$.

With the help of hydrodynamic equations obtained in [5], [7] from kinetic description of plasma electrons in the presence of OFI processes, we derive the equation for slowly varying amplitude of transversal (laser) electric field

$$2\omega_0\frac{\partial \boldsymbol{a}}{\partial \tau} - 2ic\frac{\partial^2 \boldsymbol{a}}{\partial \xi \partial \tau} + i\left(\omega_0^2\frac{n_e}{n_c} - \omega_p^2\frac{|\boldsymbol{a}|^2}{4}\right)\boldsymbol{a} = -2\omega_0\frac{\boldsymbol{a}}{|\boldsymbol{a}|^2}\sum_{k=0}^{Z-1}\frac{\Gamma_0^{\langle k \rangle}}{n_c}\frac{U_k}{mc^2} + \frac{\Gamma_2\omega_0}{4n_c}\boldsymbol{a}^* \qquad (1)$$

and slowly varying plasma wave electric field

$$\frac{\partial^2 a_p}{\partial \xi^2} + {k_p}^2 a_p = \frac{{k_p}^2}{4}\left\{\frac{c}{\Omega_p}\frac{\partial |\boldsymbol{a}|^2}{\partial \xi} - 2|\boldsymbol{a}|^2\frac{\Gamma_0}{n_0\Omega_p} + 2\,\mathrm{Re}\left\{(\boldsymbol{a}^*)^2\frac{\Gamma_2}{4n_0\Omega_p}\right\}\right\} \qquad (2)$$

where

$\boldsymbol{a}$	$e(E_x\mathbf{e}_x + E_y\mathbf{e}_y)/(m\omega_0 c)$;
a_p	$eE_z/(m\Omega_p c)$;
ω_p^2	$4\pi e^2 n_0/m$;
n_0	$-(1/c)\int_{+\infty}^{\xi}\Gamma_0(\xi')\,d\xi'$;
Ω_p^2	$(4\pi e^2/mc)\int_{-\infty}^{+\infty}\Gamma_0(\xi)\,d\xi$;
k_p	ω_p/c;
n_c	${m\omega_0}^2/(4\pi e^2)$electron critical density;
$m(e)$	electron mass (charge);
$\xi = z - ct$ and $\tau = t$	coordinates in the comoving frame.

The electron density perturbation $n_e - n_0$ driven by the laser pulse can be expressed (in a 1-D approximation that is valid for laser spot sizes, and so for transverse scales of the wake, in excess of plasma wavelength $2\pi/k_p$) through the longitudinal electric field of the wake as follows: $(n_e - n_0)/n_c = ({\Omega_p c/\omega_0}^2)\cdot(\partial a_p/\partial\xi)$ (compare [8]). It might be wise to point out that in the present paper, (2) is derived on the basis of kinetic description of the gas ionization. This equation, completed by (1) for the laser-pulse envelope $\boldsymbol{a}$ and equations for n_0, Γ_0, and Γ_2 [4], [6], [7] describes the wakefield generation in the presence of OFI self-consistently, in contrast to phenomenological approaches [13], [14].

From (1), the following energy conservation relation is derived:

$$\frac{\partial}{\partial\tau}\int_{-\infty}^{\infty}d\xi\int d^2\mathbf{r}_\perp|\boldsymbol{a}|^2 = -\frac{c}{2}\int_{-\infty}^{\infty}d\xi\int d^2\mathbf{r}_\perp\frac{n_e-n_0}{n_c}\frac{\partial|\boldsymbol{a}|^2}{\partial\xi} + \frac{c}{2}\int_{-\infty}^{\infty}d\xi \cdot\int d^2\mathbf{r}_\perp\left\{|\boldsymbol{a}|^2\frac{\partial}{\partial\xi}\left(\frac{n_0}{n_c}\right) + \mathrm{Re}\left(\frac{\Gamma_2}{2cn_c}(\boldsymbol{a}^*)^2\right)\right\} - 2\sum_{k=0}^{Z-1}\frac{U_k}{mc^2}\frac{1}{n_c}\int_{-\infty}^{\infty}d\xi\int d^2\mathbf{r}_\perp\Gamma_0^{\langle k\rangle} \qquad (3)$$

where an integration is carried out over longitudinal coordinate ξ and also over cross section transversal to the laser-pulse propagation direction ($\mathbf{r}_\perp$). The first term in (3) describes laser-pulse energy losses due to plasma-wave generation [15], the second term originates from the losses to residual electron energy (REE) [16], and the third one is responsible for ionization energy losses that are proportional to the respective ionization potentials [4], [17]. In addition, the second term in the right-hand side of (1) changes polarization of the laser pulse if the latter one was not linearly polarized at the entrance of the gas. Relative influence of this term on the laser polarization is of the same order as the relative changes in the laser pulse energy originated from the REE losses. Note that relation (3) is valid also in the general case of 3-D laser-pulse propagation.

In accordance with [7] and [17], the nonadiabatic laser-pulse energy losses to REE [5], [6] and ionization are determined mostly by the gas density, laser-pulse path in the gas, and ionization potentials. For example, a 10-cm laser-pulse path in hydrogen with atomic density $N_{at} = 10^{18}$ cm^{-3} at Gaussian laser-pulse peak intensity $I_0 = 5\cdot 10^{17}$ W/cm^2, wavelength $\lambda = 0.8$ μm, and laser pulse duration $\tau_{imp} = 100$ fs leads to about 1% laser-pulse energy depletion because of the REE and ionization losses [7]. Besides, we neglect energy losses to the wakefield generation at comparatively low electron densities ($n_e \le 10^{18}$ cm^{-3}) and nonrelativistic laser intensities.

Neglecting such losses of the laser energy enables us to use stationary laser-pulse propagation approximation. We represent an electric field in elliptically polarized laser pulse in the following form:

$$\mathbf{E}_l = \frac{1}{2}\frac{E_l(\xi)}{\sqrt{1+\eta^2}}(\mathbf{e}_x + i\eta\,\mathbf{e}_y)\exp[i\omega_0\xi/c + i\varphi] + c.c.$$

where η is the degree of ellipticity and $\eta = 0(\eta = 1)$ corresponds to the linear (circular) polarization of the laser field. By a pertinent choice of a phase φ, we make an amplitude E_l a real function of ξ, which obeys the following relation with laser-irradiation intensity: $I_l = (c/8\pi){E_l}^2$.

It should be noted that the source Γ in the general case of an arbitrary ellipticity η contains an infinite number of laser-frequency harmonics, which decrease not so fast with their order. The reason is the above-mentioned strong nonlinear dependence of Γ on a modulus of the oscillating laser electric field. The only case of harmonic absence occurs at $\eta = 1$ (circular polarization). An example of ionization rate temporal behavior is

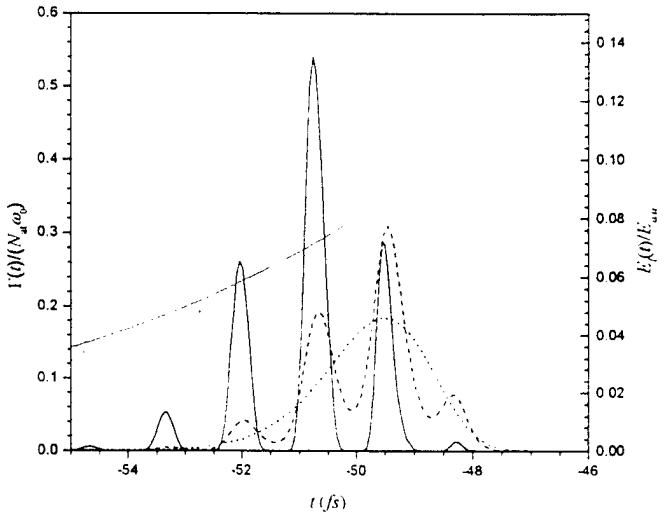


Fig. 1. Ionization rate $\Gamma(t)$ normalized on the product $\omega_0 N_{at}$ of the laser frequency ω_0 and initial atomic density N_{at} for hydrogen pumped by Gaussian laser pulse with $\tau_{imp} = 30$ fs, $\lambda = 0.8$ μm, $I_0 = 10^{18}$ W/cm^2, for different degree of ellipticity η: $\eta = 0$—solid curve, $\eta = 0.8$—dashed curve, $\eta = 1$—dotted curve. Fat curve is the corresponding temporal evolution of $E_l(t)/E_{a.u.}$ ($E_{at.u.} = 5.142 \cdot 10^9$ V/cm is the atomic field). Time is counted from the moment of laser peak intensity.

shown in Fig. 1 for different degrees of ellipticity η. Equation (2) contains the zero and second harmonics of Γ only as a result of expansion up to the second order of $a_l = eE_l/(m\omega_0 c)$. Apropos the strong localization of the ionization process on the laser-pulse temporal profile (see Fig. 1) enables to treat ionization as a threshold process with corresponding threshold intensity I_{th}.

Equation (2) differs from the equation for a_p in [7] by the ellipticity parameter η. This parameter strongly influences the relation between harmonics Γ_0 and Γ_2 of ionization rate. Further, it is convenient to express Γ_2 through the value $\mu \equiv \Gamma_2/(2\Gamma_0)$. It can be shown that if the polarization is close to linear one ($3\alpha_k/[1-\eta^2] \ll 1$), then

$$\mu(\xi) \approx \frac{\sum_{k=1}^{Z} N_{k-1}\left\{1+\frac{3}{2}\left[M_{k-1}-\frac{13}{8}-\frac{3}{2}\left(1-\eta^2\right)^{-1}\right]\alpha_k(\xi)\right\}}{\sum_{k=1}^{Z} N_{k-1}\left\{1+\frac{3}{2}\left[M_{k-1}-\frac{13}{8}+\frac{1}{2}\left(1-\eta^2\right)^{-1}\right]\alpha_k(\xi)\right\}} \qquad 1-\eta^2 \gg 3\alpha_k. \tag{4}$$

Here $E_{at.u.} = 5.142 \cdot 10^9$ V/cm, $M_k = (k+1)\sqrt{U_H/U_k}$, U_k is the ionization potential of ions of an ionization degree k, and N_k is the corresponding ion density ($U_H = 13.606$ eV is the ionization potential of hydrogen), $\alpha_k(\xi) \equiv [U_H/U_k]^{3/2}|E_l(\xi)|/E_{a.u.}$ is a small parameter ($\sim 10^{-1}$) in the region of ξ where substantial ionization takes place (see Fig. 1). As a result $\mu(\xi)$ is weakly dependent on ξ. In particular case of linear polarization the value of μ for different gases varies in the interval (0.7; 1); for hydrogen $\mu \approx 0.8$. In the opposite case of polarization, close to circular one

$$\mu(\xi) \approx \frac{\sum_{k=1}^{Z} N_{k-1}\left[\alpha_k^{-1}(\xi)+\frac{1}{2}-M_{k-1}\right]\left(1-\eta^2\right)}{\sum_{k=1}^{Z} N_{k-1}\left\{4-2\left[\alpha_k^{-1}(\xi)+\frac{1}{2}-M_{k-1}\right]\left(1-\eta^2\right)\right\}} \qquad 1-\eta^2 \ll 3\alpha_k. \tag{5}$$

In fact, the exact value of μ in this case is not important since $\mu \ll 1$ and second as well as other higher harmonics of ionization source Γ have no substantial influence on the plasma wakefield amplitude. As mentioned above, in the case of circular polarization ($\eta = 1$), all higher harmonics of the ionization source are absent and $\mu = 0$.

III. Analytic Solutions

The general solution to (2) behind the laser pulse has a form of harmonic oscillations

$$a_p(\xi) = A_p \cos(k_p \xi + \psi)$$

where $k_p = \Omega_p/c$ is the wave vector and ψ is the phase of the generated plasma wave. Further with the help of (2), we are going to obtain simple analytic formulas to analyze an influence of laser-field ellipticity and pulse duration on the wakefield amplitude A_p. The simple analytical solution to (2) can be easy obtained, if one takes into consideration the fact that ionization rate Γ is strongly localized in time with duration τ_{ion}, which is much less than both of the laser pulse duration τ_{imp} and the plasma wave period $2\pi/\Omega_p$ (see Fig. 1 and [5]–[7]). In view of this fact, we approximate the profile of an electron density $n_0(\xi)$ in the form $n_0(\xi) = N_{at}\sum_{k=1}^{Z_{\max}} \theta(\xi_k - \xi)$, where ξ_k is the coordinate of the kth ionization front and $Z_{\max}$ is the integer number equal to the largest possible number of ionized electron levels at given laser-radiation parameters. In the general case of multielectron atoms (when $Z_{\max}$ is large), the solution has a comparatively complicated form; therefore, we reproduce it for hydrogen ($Z_{\max} = 1$) only

$$a_p = -\tfrac{1}{2} a_l^2(\xi_1) G_\Gamma(\xi_1) \sin[k_p(\xi_1 - \xi)] + \tfrac{1}{4}\int_{\xi_1 - 0}^{\xi} a_l^2(\xi') \cdot \cos[k_p(\xi - \xi')] k_p \, d\xi' + \frac{B}{4} a_l^2(\xi_1 - 0) \cdot \sin[k_p(\xi_1 - \xi)], \qquad G_\Gamma(\xi) \equiv 1 - \frac{1-\eta^2}{1+\eta^2}\frac{\mu(\xi)}{2} \tag{6}$$

where $a_l = eE_l/(m\omega_0 c)$, ξ_1 is the point of a maximum of ionization rate Γ_0, $G_\Gamma(\xi)$ is the "ionization" source of the wakefield; the second and the third terms in a right-hand side of (4) represent the "ponderomotive" source of the wakefield. Coefficient $B = 0$ if the laser pulse propagates through the preionized plasma [with $\xi_1 = \infty$ and $a_l(\xi_1) = 0$]; $B = 1$ if the gas

is ionized by the laser pulse with smooth forward front and its spatial scale L_f considerably exceeds the ionization front width $L_{ion} = c\tau_{ion}$.

Equation (6) is convenient for analytical exploration of the influence of ionization processes at the forward front of a laser pulse on the wakefield generation in the ionizing gas. Let us first consider the approximation of a nearly rectangular pulse with envelope $E_l(\xi) = E_0$ for $|\xi| < L_{imp}/2$ assuming its duration L_{imp} to be much larger than the leading front ($L_{imp} \gg L_f$; but $L_f \gg L_{ion}$). For the rectangular pulse propagating through the homogeneous preionized plasma, the second term in (6) at $\xi < -L_{imp}/2$ yields a well-known result [15] $a_p = -(1/2)a_0^2 \cos[k_p\xi] \sin[k_pL_{imp}/2]$, where $a_0 = eE_0/(m\omega_0 c)$. In this case, the wakefield amplitude is maximum at $k_pL_{imp} = \pi(1+2n)$, where n is an integer and is equal to $(1/2)a_0^2$. In the case when a rectangular laser pulse ionizes gas during its propagation, (6) gives the following value of the wakefield at $\xi < -L_{imp}/2$:

$$a_p(\xi) = -\frac{a_0^2}{2} C \cos[k_p\xi + \psi] \tag{7}$$

where

C $[C_1^2 - C_1 \cos[k_pL_{imp}] + 1/4]^{1/2}$;
C_1 $(a_1/a_0)^2(G_\Gamma - 1/2) + 1/2$;
a_1 $a_l(\xi = \xi_1)$;
ψ $\arccos\{(C_1 + 1/2)\sin[k_pL_{imp}/2]/C\}$.

According to (7), the wakefield amplitude A_p is maximum under the same condition $k_pL_{imp} = \pi(1+2n)$ and equal to

$$A_{p,\max} = \left(a_0^2/2\right)\left[1 + (a_1/a_0)^2(G_\Gamma - 1/2)\right] \tag{8}$$

the phase $\psi = 0$ in this case.

It follows from (6), and (4) and (5) for $\mu(\xi)$ that G_Γ increases with η: $G_\Gamma \approx 0.6$ for linear polarization ($\eta = 0$); $G_\Gamma = 1$ for circular polarization ($\eta = 1$) of the laser pulse. Besides, the highest magnitude of the relative value $A_p/{a_0}^2$ will be achieved at laser pulse peak intensity I_0 close to ionization threshold intensity I_{th}. At such conditions, $a_1 \approx a_0$. In this case, (8) leads to $(A_p/a_0^2)_{\max} = 1/4 + G_\Gamma/2$, which is $\approx$0.55 for linear and $\approx$0.75 for circular polarization. Thus, the maximum relative wakefield amplitude exceeds $(A_p/a_0^2)_{\max}$ for preliminary totally ionized plasma by 10% for linear polarization and by 50% for circular polarization of laser radiation at $I_0 \approx I_{th}$. The minimum relative wakefield amplitude is attained at $k_pL_{imp} = 2\pi n$, $n = 1, 2, \ldots$ and, according to (7), equals $(A_p/a_0^2)_{\min} = (a_1^2/a_0^2)(G_\Gamma/2 + 1/4) - 1/2$. This value is not equal to zero in contrast to the case of preionized plasma, when $A_{p,\min} = 0$. Notice also, that according to (8), the contribution of ponderomotive force into the wakefield generation in the case $a_1 \approx a_0$ is half of that in the case of preionized gas.

If the peak intensity I_0 substantially exceeds the threshold intensity I_{th}, then the ionization rate Γ_0 reaches its maximum at an electric field strength much less than E_0; thus, $a_1 \ll a_0$. As a result, the wakefield amplitude and phase, in accordance with (8) and (7), will be close to the same as in the case of preionized plasma, if the laser pulse length $L_{imp} \neq 2\pi n/k_p$. If $L_{imp} = 2\pi n/k_p$, then the amplitude of the wakefield remains nonzero in ionizing gas in contrast to zero value in the case of preionized plasma.

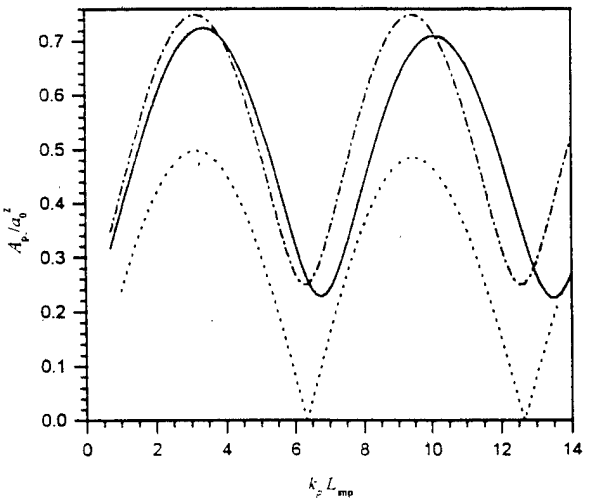


Fig. 2. Normalized amplitude of a plasma wakefield A_p/a_0^2 behind the laser pulse propagating in hydrogen as a function of the dimensionless full width at half of maximum intensity k_pL_{imp} for circularly polarized hyper-Gaussian laser pulse $I_l = I_0 \exp[-\ln 2(2\xi/L_{imp})^{24}]$ with $\lambda = 0.8$ μm, $\tau_{imp} = 100$ fs, $I_0 = 3 \cdot 10^{14}$ W/cm^2 (solid line). Dash-dotted line shows analytical results obtained by (7), dotted line shows the theoretical curve $A_p/a_0^2 = (1/2) \cdot |\sin(k_pL_{imp}/2)|$ for rectangular laser pulse in preionized plasma.

The example of the wakefield generation by a step-like hyper-Gaussian circularly polarized laser pulse with an envelope $I_l = I_0 \exp[-\ln 2(2\xi/L_{imp})^{24}]$ is shown in Fig. 2. In this figure, the solid line shows results obtained by means of (2), the dash-dotted line depicts calculations according to (7), and the dotted line shows $A_p/{a_0}^2 = 0.5|\sin[k_pL_{imp}/2]|$. One can see that the above analytical results are in reasonable agreement with more precise direct numerical solution of (2) [in fact, they differ mainly by some displacement along k_pL_{imp} axis].

The analogs' results can be obtained for Gaussian laser pulse with envelope $a_l(\xi) = a_0 \exp[-(\xi/\sigma_\xi)^2]$, $\sigma_\xi = L_{imp}/\sqrt{2\ln 2}$ (here, L_{imp} is the full width at half of maximum intensity). In this case, (6) can be transformed to

$$a_p(\xi) = -\frac{a_0^2}{2} e^{-2(\xi_1/\sigma_\xi)^2} \sin[k_p(\xi_1 - \xi)]\left(G_\Gamma - \frac{1}{2}\right) - \left\{\frac{a_0^2}{8} G_p e^{ik_p\xi}\left[\operatorname{erf}\left(\frac{-\sqrt{2}\xi}{\sigma_\xi} - i\frac{k_p\sigma_\xi}{2\sqrt{2}}\right) + \operatorname{erf}\left(\frac{\sqrt{2}\xi_1}{\sigma_\xi} + i\frac{k_p\sigma_\xi}{2\sqrt{2}}\right)\right] + c.c.\right\} \tag{9}$$

where $G_p \equiv (\sqrt{\pi}/2\sqrt{2})k_p\sigma_\xi \exp(-k_p^2\sigma_\xi^2/8)$.

Let's consider two limiting cases of this formula.

1) If $I_0 \gg I_{th}$, then the ionization occurs at the laser pulse leading front far from its peak intensity. In this case there are two possibilities:
   a) The laser pulse width is about the plasma wavelength (the near-resonant region), so as $k_p\sigma_\xi \approx 2$ and the inequality $k_p\sigma_\xi < 4\xi_1/\sigma_\xi$ holds. Setting $\xi_1 \to \infty$ for this case and omitting first two terms

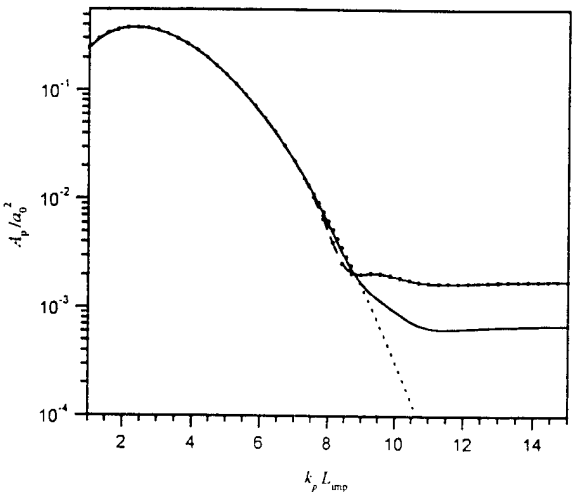


Fig. 3. A_p/a_0^2 calculated by (2) as a function of $k_p L_{imp}$ for Gaussian pulse $I_l = I_0 \exp[-\ln 2(2\xi/L_{imp})^2]$, $\lambda = 0.8$ μm, $I_0 = 10^{17}$ W/cm^2, $\tau_{imp} = 100$ fs, the gas is hydrogen. Solid curve is plotted for linear and —●— for circular polarization in the presence of ionization. Dotted curve is plotted for preionized gas.

in (9), we obtain the same wakefield as in the case of preliminary completely ionized plasma [15]

$$a_p(\xi) = -\frac{a_0^2}{4} G_p \left[\cos(k_p\xi) + \frac{1}{2} e^{ik_p\xi} \cdot \operatorname{erf}\left\{\frac{-\sqrt{2}\xi}{\sigma_\xi} - i\frac{k_p\sigma_\xi}{2\sqrt{2}}\right\} + k.c\right]$$

which amplitude A_p at $\xi \ll -\sigma_\xi$ is equal to $A_p = 0.5\, {a_0}^2 G_p$. This amplitude reaches its maximum at $k_p\sigma_\xi = 2$ (i.e., $k_p L_{imp} \approx 2.35$) and is equal to the conventional value $A_{p,i} = \sqrt{\pi/[8\exp(1)]}\, a_0^2 \approx 0.38\, a_0^2$ at resonance [15] (see Fig. 3).

b) The laser pulse width is far from resonant one ($k_p\sigma_\xi \gg 1$ that implies comparatively long laser pulse), so that the inverse inequality $\xi_1/\sigma_\xi \ll k_p\sigma_\xi/4$ holds. Notice that this is the region of the pulse duration where the self-modulation can take place [9]–[12]. In this case, the last term in (9) can be omitted in comparison with the first terms and one has

$$a_p(\xi) = -\frac{a_0^2}{2} e^{-2(\xi_1/\sigma_\xi)^2} [G_\Gamma - 0.5] \sin[k_p(\xi_1 - \xi)] = -\frac{a_1^2}{2} [G_\Gamma - 0.5] \sin[k_p(\xi_1 - \xi)]. \quad (10)$$

Though the value $A_p = 0.5(G_\Gamma - 0.5)a_1^2 = 0.5(G_\Gamma - 0.5)(I_{th}/I_0)a_0^2$ in this case is not large, as compared to $A_{p,i}$ in resonant conditions, the amplitude A_p can exceed the corresponding value in the preionized plasma $A_{p,i}$ by orders of magnitude for long enough pulses ($k_p\sigma_\xi \gg 1$)

$$\frac{A_p}{A_{p,i}} = 2\sqrt{\frac{2}{\pi}} \frac{G_\Gamma - 0.5}{k_p\sigma_\xi} \frac{I_{th}}{I_0} \exp\left\{\frac{k_p^2\sigma_\xi^2}{8}\right\} = 2\sqrt{\frac{2}{\pi}} \frac{G_\Gamma - 0.5}{k_p\sigma_\xi} \exp\left\{\frac{k_p^2\sigma_\xi^2}{8}\left[1 - \left(\frac{4\xi_1}{k_p\sigma_\xi^2}\right)^2\right]\right\} \gg 1.$$

This circumstance is demonstrated in Fig. 3 by the tail of A_p in the limit $k_p L_{imp} \gg 1$. In contrast to A_p, which remains practically constant, an amplitude of the wakefield in preionized plasma $A_{p,i}$ tends to zero exponentially fast with increase of the laser pulse duration (see Fig. 3). Just the value A_p can fulfill the role of a seed for the intense wakefield generation by self-modulation of the laser pulse [9]–[12] in ionizing gas.

2) In another limiting case, when $I_0 \approx I_{th}$, only half of the laser pulse after the peak intensity influences created plasma. Setting $\xi_1 \to 0$ and considering the wakefield behind the laser pulse (at $\xi \ll -\sigma_\xi$) we obtain in this case from (9), that

$$a_p(\xi \ll -\sigma_\xi) = -\frac{a_0^2}{4}\sqrt{G_p^2 + (2G_\Gamma - \tilde{G}_p)^2} \cdot \sin\left[\arcsin\left\{G_p\Big/\sqrt{G_p^2 + (2G_\Gamma - \tilde{G}_p)^2}\right\} - k_p\xi\right]$$

$$\tilde{G}_p = 1 - \sqrt{\pi}\frac{k_p\sigma_\xi}{2\sqrt{2}} \int_0^{(k_p\sigma_\xi)/(2\sqrt{2})} \cdot \exp\left(x^2 - \frac{k_p^2\sigma_\xi^2}{8}\right) dx. \quad (11)$$

Similar to the case of rectangular pulse, the contribution of ponderomotive force, according to the last formula, is half of that for preionized gas. The dependence of the wakefield amplitude calculated by (11) is shown in Fig. 4(a) by dashed line for linear polarization (with $G_\Gamma \approx 0.6$) and dash-dotted line for circular polarization ($G_\Gamma = 1$). Owing to the factor $\tilde{G}_p$, the curve $A_p(k_p L_{imp})$ is broadened and its maximum is displaced onto the right along the $k_p L_{imp}$ axis, as compared to the case of preionized plasma (from $k_p L_{imp} \approx 2.35$ to $k_p L_{imp} \approx 4$). In the case of linearly polarized laser pulse, the maximum value of the wakefield amplitude, calculated by (11), is ≈5% below, and is ≈45% above the maximum wake amplitude in preionized gas in the case of circularly polarized laser field. In the region that is far from resonance one, the contribution of ponderomotive forces is negligible but the "ionization term" G_Γ ensures considerable amplitude of the wakefield (≈$0.3a_0^2$ and $0.5a_0^2$ for linear and circular polarization respectively), comparable with that in the resonant region.

IV. Numerical Results

More precise calculations with the help of (2), completed by the equations of ionization kinetics [4], [6], [7], [solid and —●— curves on Fig. 4(a)] qualitatively agree with the above conclusions, but give rise to the faster decrease of $A_p(k_p L_{imp})$ at large $k_p L_{imp}$, if compared to that following from (11). This discrepancy is connected with θ-function approximation of the ionization front adopted in (6) [and, consequently, in (11)]: the width of ionization front increases when I_0 approaches the threshold intensity I_{th} and becomes comparable with the laser pulse width at $I_0 \sim I_{th}$.

The calculations according to (2) also have shown that the largest amplitude of the wakefield normalized on a_0^2 is reached

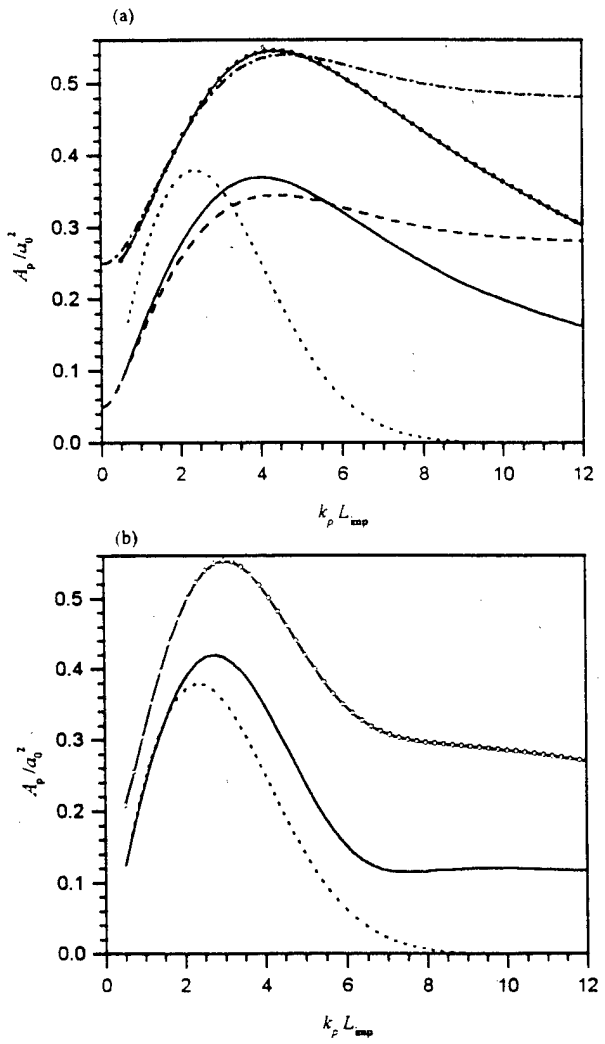


Fig. 4. A_p/a_0^2 as a function of k_pL_{imp} in hydrogen for Gaussian pulse $I_l = I_0 \exp[-\ln 2(2\xi/L_{imp})^2]$, $\lambda = 0.8$ μm. (a) $I_0 = 1.5 \cdot 10^{14}$ W/cm^2, $N_{at} = 2.5 \cdot 10^{-4} \cdot n_c \approx 2.8 \cdot 10^{17}$ cm^{-3}, ionization is not complete ($n_e/N_{at} \approx 0.4$): solid curve is plotted for linear and —●— for circular polarization by (2). Dashed (dash-dotted) curve is plotted for calculations according to (11) at linear (circular) polarization. Dotted curve on both (a) and (b) is plotted for preionized gas; (b) $I_0 = 5 \cdot 10^{14}$ W/cm^2, $N_{at} = 10^{-4} \cdot n_c \approx 1.12 \cdot 10^{17}$ cm^{-3}: solid curve is plotted for linear and —●— for circular polarization in the presence of ionization by (2).

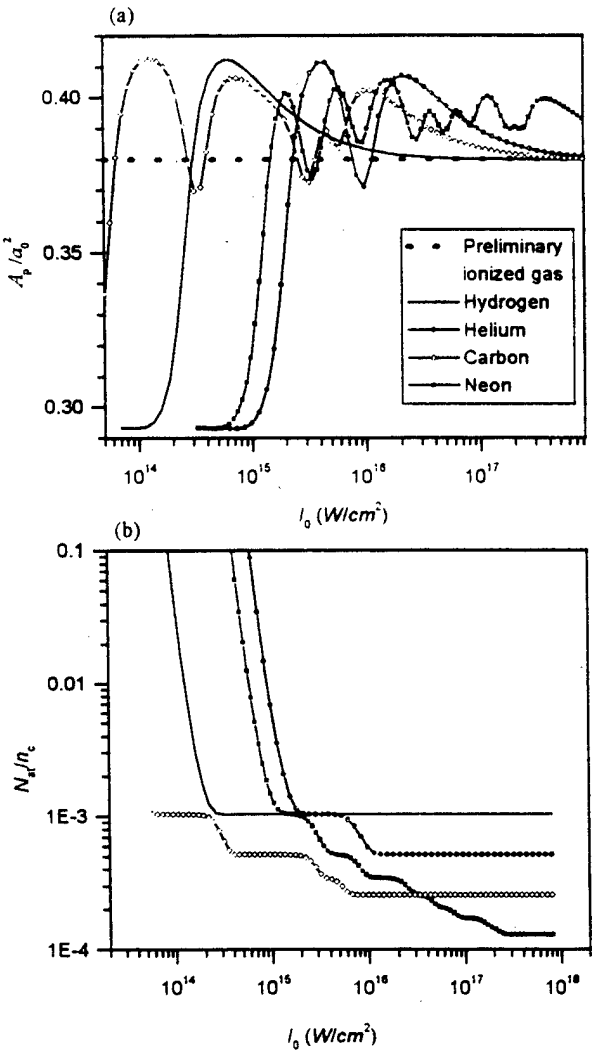


Fig. 5. (a) A_p/a_0^2 as a function of I_0 for various gases. The laser pulse has Gaussian envelope and linear polarization, $\lambda = 0.8$ μm, $\tau_{imp} = 32$ fs; $k_pL_{imp} = \text{const} = 2.4$ (which corresponds to $n_e/n_c = \text{const} = 10^{-3}$ behind the pulse). (b) N_{at}/n_c as a function of I_0 for various gases, which gives $n_e/n_c = \text{const} = 10^{-3}$ at chosen I_0.

at laser pulse peak intensities, which are 1.5 to three times higher than the threshold for ionization one [compare Fig. 4(a) and (b), see, also, Figs. 5–7]. Besides, at such intensities, the displacement of the maximum of the curve $A_p(k_pL_{imp})$ along the k_pL_{imp} axis is less pronounced, and the width of this curve is narrower, if compared to the case of $I_0 = I_{th}$.

In order to explore the A_p dependence on I_0 in more detail, the graphics of $A_p(I_0)$, calculated by means of (2), were plotted for various gases for linear [Fig. 5(a)] and circular [Fig. 6(a)] polarization of the laser pulse. The laser pulse width τ_{imp} was fixed and equal to $\tau_{imp} = 32$ fs, and the gas pressure was chosen so as to fulfill the resonant condition ($k_pL_{imp} = \text{const} = 2.4$, where $k_p = \Omega_p/c$, that corresponds to $n_e/n_c = \text{const} = 10^{-3}$ behind the pulse). The corresponding values of N_{at}/n_c are shown in Figs. 5(b) and 6(b). They illustrate the above conclusions about the dependence of A_p on I_0: A_p reaches the maximum at some peak intensity $I_0 > I_{th}$, then it decreases up to the value that is maximum in the case of preionized plasma (remember, k_pL_{imp} is in the resonant region). The peaks of the curve $A_p(I_0)$ are connected with successive ionization of the next electron levels. In accordance with the theory described above, the values of the first peaks are 10% larger for linear and 50% larger for circular polarization than the value $A_{p,i} \approx 0.38a_0^2$ for preionized plasma. The next peaks have smaller values than the first one, but they still exceed the value $A_{p,i}$ [see Figs. 5(a) and 6(a)].

In conclusion, we represent the example of dependence of A_p on both parameters I_0 and k_pL_{imp}. Fig. 7(a) shows the results of the calculation of $A_p(I_0, k_pL_{imp})$ carried out by means of (2) for neon; $\lambda = 0.8$ μm, $\tau_{imp} = 100$ fs. The gas densities were chosen so as to maintain the given values of k_pL_{imp} [see Fig. 7(b)]. One can conclude that the optical ionization processes in a gas can considerably enlarge the region of parameters, corresponding to effective generation of the plasma wakefield [compare solid and dashed lines of constant levels in Fig. 7(a)].

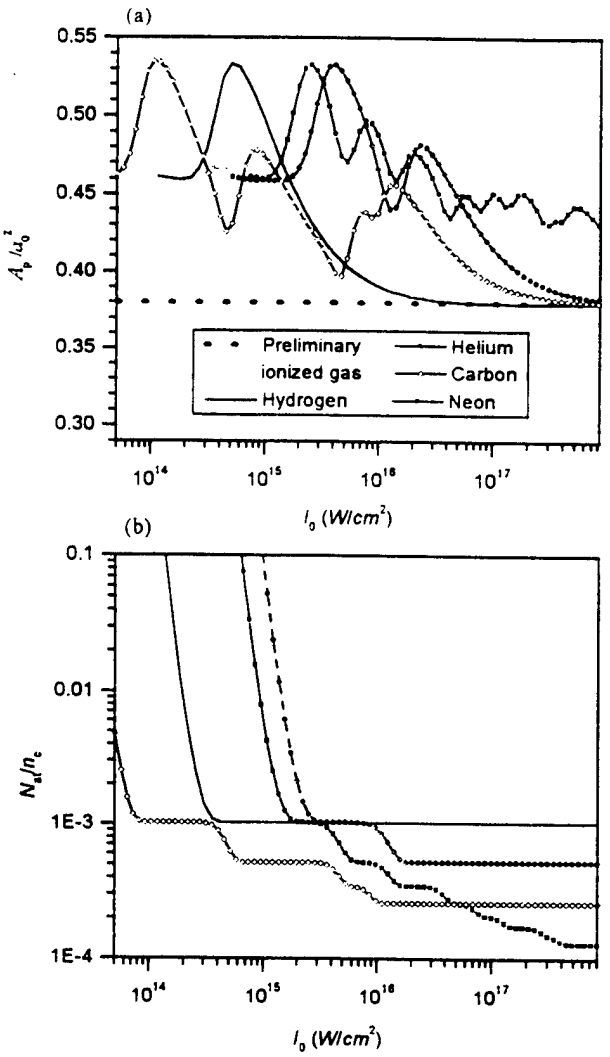


Fig. 6. The same data as in Fig. 5, but for circularly polarized laser pulse. All other parameters are the same as in Fig. 5.

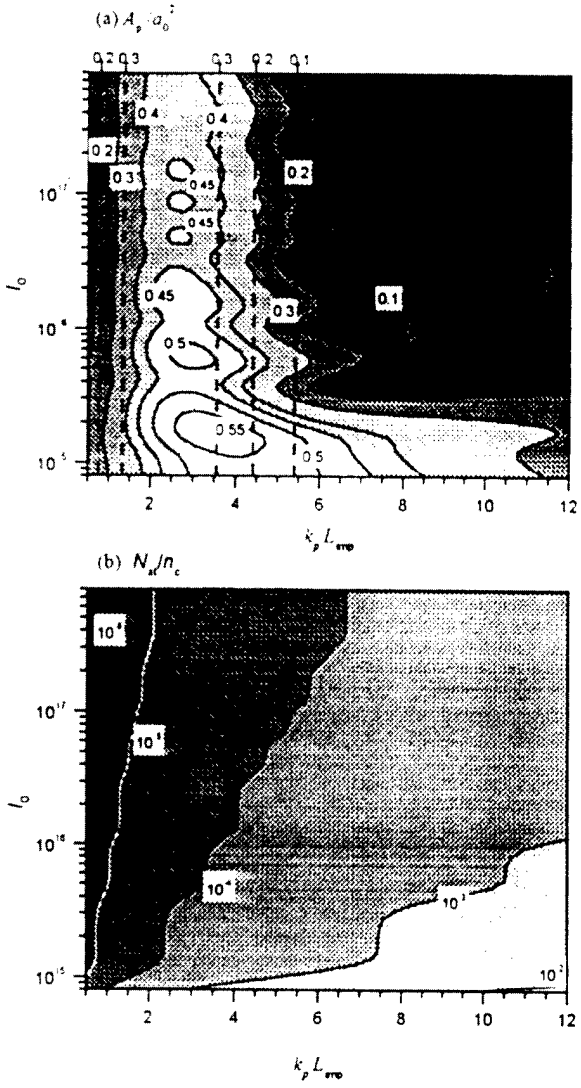


Fig. 7. (a) Dependence of A_p/a_0^2 on both k_pL_{imp} and I_0 for circularly polarized laser pulse with $\lambda = 0.8$ μm and $\tau_{imp} = 100$ fs. Gas is neon. Dashed straight lines show the contours of constant A_p/a_0^2 values for the case of preliminary completely ionized gas. (b) $N_{at}/n_c(k_pL_{imp}, I_0)$ corresponding to Fig. 7(a) to maintain the given values of k_pL_{imp}.

V. Conclusion

Wakefield generation by femtosecond laser pulse is described in the frame of slowly varying amplitudes approximation. Amplitude of the wakefield A_p is studied as a function of laser pulse and background gas parameters. We compare A_p with well-known results for preliminary created completely ionized plasma $A_{p,i}$ (see, e.g., [1], [2], [15]). It is found that ionization processes increase A_p in comparison with $A_{p,i}$ at relatively high laser peak intensities (when I_0 is of the order of ionization threshold intensity I_{th}). Besides, the enhancement of A_p due to gas ionization is more pronounced for circularly polarized laser pulses than for linear polarization of the laser radiation. This difference originates from the partial compensation of "ionization" source by higher harmonics of electron production rate for linear polarization [see (2), (4), (6)], which reflects the fact that electron density increase due to ionization in the linear polarized laser pulse takes place mainly at the moments when the laser field is maximum, and so the velocity of free electron oscillations is close to zero (in contrast to the circular polarization, when ionization rate does not depend on the phase of the laser pulse).

The strongest increase of A_p as compared to $A_{p,i}$ takes place if the resonant conditions for ponderomotive excitation of wakefield are not matched. The wakefield amplitude A_p determined by the ionization threshold intensity I_{th} [see (10) and Figs. 3, 4, and 7] remains practically constant independent on the laser pulse duration while $A_{p,i}$ decreases to zero exponentially fast for longer laser pulses with displacement from the resonance. From a practical point of view, it means that the ionization can essentially expand the region of parameters where the laser pulse generates the wakefield effectively.

Acknowledgment

N. E. Andreev acknowledges useful discussions with all the participants at the Kardamyli Workshop. In addition, particular thanks go to F. Amiranoff, G. Mourou, A. Ogata, M. Uesaka, and D. Umstadter.

REFERENCES

[1] E. Esarey, P. Sprangle, J. Krall, and A. Ting, "Overview of plasma-based accelerator concepts," *IEEE Trans. Plasma Sci.*, vol. 24, pp. 252–288, Apr. 1996.

[2] N. E. Andreev and L. M. Gorbunov, "Laser-plasma acceleration of electrons," *Phys.-Uspekhi*, vol. 42, no. 1, pp. 49–53, 1999.

[3] M. V. Ammosov, N. B. Delone, and V. P. Krainov, "Tunnel ionization of complex atoms and of atomic ions in an alternating electric field," *Zh. Eksp. Teor. Fiz.*, vol. 91, no. 4, p. 2008, 1986.

[4] V. P. Kandidov, O. G. Kosareva, and S. A. Shlenov, "Influence of transient self-focusing on the propagation of high-power femtosecond laser pulses in gases under ionization conditions," *Quantum Electron.*, vol. 24, no. 7, pp. 971–977, 1994.

[5] N. E. Andreev, M. V. Chegotov, M. E. Veisman, T. Auguste, P. d'Oliveira, S. Hulin, P. Monot, A. Ya.Faenov, T. A. Pikuz, A. I. Magunov, I. Yu.Skobelev, F. B. Rosmej, and M. Yu. Romanovsky, "Nonadiabatic heating of a plasma produced by the ionization of a gas by a short intense laser pulse," *JETP Lett.*, vol. 68, no. 7, pp. 592–598, 1998.

[6] N. E. Andreev, M. V. Chegotov, M. E. Veisman, B. He, and J. T. Zhang, "Non-adiabatic energy deposition from the short intense laser pulse to the ionizing gas," in *ICONO'98: Ultrafast Phenomena and Interaction of Superstrong Laser Fields with Matter: Nonlinear Optics and High-Field Physics*, M. V. Fedorov and V. M. Gordienko, Eds: Proc. SPIE, 1999, vol. 3735, pp. 234–241.

[7] N. E. Andreev, M. G. Cadjan, M. V. Chegotov, and M. E. Veisman, "Wake field generation in ionizing gases," *Plasma Phys. Rep.*, vol. 26, no. 11, pp. 132–150, 2000.

[8] N. E. Andreev, M. V. Chegotov, M. C. Downer, E. W. Gaul, N. H. Matlis, A. A. Pogosova, and A. R. Rundquist, "Propagation of intense laser pulses through inhomogeneous ionizing gas profiles," *IEEE Trans. Plasma Sci.*, vol. 28, pp. 1090–1097, Aug. 2000.

[9] N. E. Andreev, L. M. Gorbunov, V. I. Kirsanov, A. A. Pogosova, and R. R. Ramazashvili, "Resonant excitation of wakefields by a laser pulse in a plasma," *Pis'ma-v-Zhurnal-Eksperimental'noi-i-Teoreticheskoi-Fiziki*, vol. 55, pp. 551–555, May 25, 1992.

[10] T. M. Antonsen Jr. and P. Mora, "Self-focusing and Raman scattering of laser pulses in tenuous plasmas," *Phys. Rev. Lett.*, vol. 69, no. 15, pp. 2204–2207, 1992.

[11] J. Krall, A. Ting, E. Esarey, P. Sprangle, and G. Joyce, "Enhanced acceleration in a self-modulated laser wakefield accelerator," *Phys. Rev. E*, vol. 48, no. 3, pp. 2157–2161, 1993.

[12] N. E. Andreev, L. M. Gorbunov, and V. I. Kirsanov, "Stimulated processes and self modulation of short intense laser pulses in laser wake field accelerator," *Phys. Plasmas*, pt. 2, vol. 2, no. 6, pp. 2573–2582, 1995.

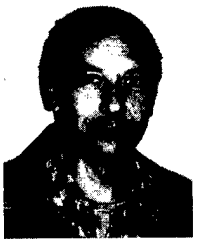
[13] D. L. Fisher and T. Tajima, "Enhanced Raman forward scattering," *Phys. Rev. E*, vol. 53, no. 2, pp. 1844–1851, 1996.

[14] W. B. Mori and T. Katsouleas, "Ponderomotive force of a uniform electromagnetic wave in a time varying dielectric medium," *Phys. Rev. Lett.*, vol. 69, no. 24, pp. 3495–3498, 1992.

[15] L. M. Gorbunov and V. I. Kirsanov, "Excitation of plasma waves by short electromagnetic wave packets," *Sov. Phys. JETP*, vol. 66, no. 2, p. 290, 1987.

[16] V. B. Gildenburg, V. I. Pozdnyakova, and I. A. Shereshevskii, "Frequency self-upshifting of focused electromagnetic pulse producing gas ionization," *Phys. Lett. A*, vol. 203, no. 3, p. 214, 1995.

[17] M. V. Chegotov, "A temporal structure of a short, powerful laser pulse under an operation of ionization processes," in *Proc. SPIE*, vol. 3683, 1999, p. 33.



Nikolai E. Andreev was born in Moscow, Russia, in 1945, and graduated from Moscow State University in 1967. He received the Ph.D. degree and Doctor of science degree in theoretical and mathematical physics from P.N. Lebedev Physical Institute of USSR Academy of Sciences, Moscow, in 1973 and 1985, respectively, Academic rank of Senior Scientist in 1986, and rank of Professor from Russian Ministry of Education in 1998.

Since 1970, he has been a Research Physicist in the Division of Plasma Phenomena Theory of P.N. Lebedev Physical Institute of Russian Academy of Sciences (RAS). He joined the High Energy Density Research Center of the Associated Institute for High Temperatures of RAS in 1987, where he is currently a Head of the Laser Plasma Laboratory and he is a Professor at the Moscow Institute of Physics and Technology. His current research includes laser light absorption, self-focusing and stimulated scattering, laser-driven particle accelerators, and nonlinear self-consistent structures in irradiated plasmas.



Mikhail V. Chegotov was born in Moscow, Russia, on February 20, 1962. He received the Ph.D. degree in 1988 in theoretical and mathematical physics from the Lebedev Physical Institute of the USSR Academy of Sciences, Moscow.

From 1988 to 1992, he was a Junior Research Fellow and from 1992 to 1994 a Research Fellow in the Division of Plasma Phenomena Theory of P.N. Lebedev Physical Institute of the Russian Academy of Sciences (RAS). From 1993 to 1994, he had a DAAD scholarship at Ruhr University, Bochum, Germany. Since 1995, he has been a Senior Research Fellow in the Laser Laboratory at the High Energy Density Research Center of the Associated Institute for High Temperatures of RAS. He has published over 40 technical articles and letters in refereed scientific journals. His research has concentrated on the areas of nonlinear laser–plasma interaction, ionization processes in ionized gases, transport phenomena in plasmas, and mathematical and physical aspects of ionized gases diagnostics.

M. E. Veisman, photograph and biography not provided at the time of publication.

On the Effect of Long-Wavelength Electron Plasma Waves on Large-Angle Stimulated Raman Scattering of Short Laser Pulse in Plasmas

Nikolai E. Andreev and Serguei Yu. Kalmykov

Abstract—**Spectral features of a large-angle stimulated Raman scattering (LA SRS) of a short electromagnetic pulse in an underdense plasma, which are caused by the presence in a plasma of a given linear long-wavelength electron plasma wave (LW EPW), are investigated. It is shown that the LW EPW, whose phase velocity coincides with a group velocity of a pulse and a density perturbation normalized to a background electron density $\delta n_{\rm LW}/n_0$ exceeds the ratio of the electron plasma frequency to the laser frequency ω_{pe}/ω_0, suppresses the well-known Stokes branch of the weakly coupled LA SRS. Under the same condition, the anti-Stokes band appears in the spectrum of the scattered radiation. Variation of a scattering angle and an electron temperature do not significantly modify qualitative features of the effect. In the case of strongly coupled LA SRS, the maximum of the increment is decreased by nearly one-half for $\delta n_{\rm LW}/n_0 \sim (a_0\omega_{pe}/\omega_0)^{2/3} \gg \omega_{pe}/\omega_0$, where a_0 is an amplitude of an electron quiver velocity in the laser field normalized to a speed of light c, and it decreases further with an increase in plasma density perturbation in LW EPW.**

I. Introduction

An intense laser radiation in a rarefied plasma [$\omega_0 \gg \omega_{pe}$, where ω_0 is a laser frequency and $\omega_{pe} = (4\pi e^2 n_0/m_e)^{1/2}$ is an electron plasma frequency corresponding to the background electron density n_0] is subject to parametric instabilities [1] in which both electrostatic and electromagnetic (EM) waves are excited [2]–[4], [31]. The incident EM wave (pump wave) can be scattered by spontaneous fluctuations of an electron density that, in turn, can be amplified by the ponderomotive force on beating of the pump and scattered EM waves. Provided that certain phase matching conditions are fulfilled, the feedback loop appears, and either temporal or spatial instability develops (see, for example, [4] and [31]). The scattering of the EM radiation off electron plasma modes is stimulated Raman scattering (SRS) [5], [32]–[35]. The ordinary (weakly coupled) SRS through large angles is the case when the normalized amplitude of the laser electric field $a_0 = eE_0/(m_e\omega_0 c)$ is much smaller than the ratio $(\omega_{pe}/\omega_0)^{1/2}$. This is a three-wave resonant process, in which a pump EM wave (ω_0, $\mathbf{k}_0$) decays into a scattered EM wave ($\omega_0 - \omega_{\rm BG}$, $\mathbf{k}_s$) and a plasma normal mode ($\omega_{\rm BG}$, $\mathbf{k}_e$), where $\mathbf{k}_e = \mathbf{k}_0 - \mathbf{k}_s$, and $\omega_{\rm BG} = [\omega_{pe}^2 + 3(k_e V_{T_e})^2]^{1/2} \approx \omega_{pe}$ is a Bohm–Gross frequency of the scattering electron plasma wave (EPW). The spectrum of the scattered radiation consists of the single Stokes band, which is narrow if compared with the electron plasma frequency (i.e., the temporal increment of the instability is much smaller than ω_{pe}). Under the condition of strong coupling [$a_0 \gg (\omega_{pe}/\omega_0)^{1/2}$], the scattering process becomes nonresonant [2], [4], [31], [6]. The electron plasma modes, which participate in this process, possess the spectrum wide in comparison with the electron plasma frequency (therefore, the increment of the instability has the maximum value larger than ω_{pe}). Temporal growth rates for SRS in different regimes were recently reviewed in [7]. The spatiotemporal behavior of the large-angle SRS (LA SRS) of a short laser pulse was considered in [7], [8], [36], [9], [37], [38].

Stimulated Raman side- and backscattering is known to have a significant effect on propagation of a short (<1 ps), intense laser pulse in a plasma and, hence, on operation of various schemes of laser–plasma particle accelerators [10]. For nonrelativistc pulse intensities, fluid [7], [11] and particle [12], [39], [13] simulations show that the LA SRS can erode the back of a lengthy pulse ($L_{\rm pulse} > \lambda_p = 2\pi c/\omega_{pe}$). So, in acceleration schemes that use such pulses, the detrimental pulse erosion caused by the LA SRS should be minimized. For relativistic pulse intensities, backward SRS (BSRS) usually saturates already in the head of the pulse and erodes mainly the pulse front portion, creating a sharp leading edge (as a consequence, a strong pulse depletion due to the generation of an intense plasma wakefield occurs) [12], [39], [13], [14], [40]. Trapping of electrons in a plasma wave generated by the BSRS [4], [31], [15], [41] produces fast electrons, which can be further accelerated in self-modulated laser wakefields [16], [42]. Saturation of the LA SRS caused by the electron trapping can lead to an enhanced plasma heating [17], [43], [44]. A problem of reducing the population of hot electrons generated by the SRS of a short ($\leq$1 ps), intense ($\leq 2 \times 10^{17}$ W/cm^2) laser pulse was considered in [18] for the purposes of optimization of the recombination X-ray schemes [19]. Summarizing, we conclude that establishing the conditions under which the growth of the stimulated Raman side- and backscattering can be reduced is vital for most applications of short, intense laser pulses in plasma physics.

We have already shown in previous works [20], [21], [45], [46] that certain processes of the nonlinear evolution of a short laser pulse in a rarefied plasma can suppress the weakly coupled backward and near-backward SRS of a laser pulse. Namely, when an amplitude modulation of the pulse occurs

Manuscript received November 1, 1999; revised April 3, 2000. This work was supported in part by the Russian Foundation for Basic Research, under Grant 98-02-16263.

The authors are with the High Energy Density Research Center, Associated Institute for High Temperatures, Russian Academy of Sciences, Moscow 127412, Russia (e-mail: andreev@iaslab.ivtan.msk.su).

Publisher Item Identifier S 0093-3813(00)10595-8.

0093–3813/00$10.00 © 2000 IEEE

with a spatial period close to λ_p (the resonant self-modulation [22], [47]–[49]), the LA SRS of higher frequency spectral components of the modulated pulse undergo resonant suppression [21], [45], [46] (see also [11]). The decline in the temporal increment of the weakly coupled LA SRS in a plasma was noted in [20] in the case that the plasma is perturbed by a long-wavelength electron plasma wave (LW EPW) whose density perturbation normalized to the background electron density achieves the value ω_{pe}/ω_0. The effects of suppression described in [20], [21], [45], and [46] are caused by the multiwave (not three-wave) nature of the scattering process, which manifests when the laser pulse consists of several spectral components or in the presence of an LW EPW. Note that different aspects of the effect of long-wavelength plasma density perturbations on parametric instabilities in plasmas have long been of interest. So, in [23], it was shown that the presence of long-wavelength plasma turbulence could turn a convective instability into an absolute instability. Suppression of stimulated Brillouin scattering by long-wavelength density perturbations was mentioned in [24].

The present work is aimed at studying the specific features of the LA SRS of a short laser pulse in a plasma perturbed by an LW EPW. We demonstrate that the maximum growth rate of the LA SRS in the regime of weak coupling can be greatly reduced in the presence of an LW EPW whose normalized density perturbation approaches, or exceeds, the value ω_{pe}/ω_0. Therefore, the laser pulse erosion due to the LA SRS, the condition of weak coupling being fulfilled, is less significant in the laser–plasma accelerators [10], where the laser-driven LW EPW may achieve a relatively large amplitude such that $\delta n_{\mathrm{LW}} > n_0(\omega_{pe}/\omega_0)$. Decline in the growth rate of the LA SRS in the presence of an LW EPW is also established under the condition of strong coupling; that is, the maximum of the increment is reduced by one-half for $\delta n_{\mathrm{LW}} \sim n_0(a_0\omega_{pe}/\omega_0)^{2/3} \gg n_0(\omega_{pe}/\omega_0)$ and nowhere drops to zero. We have considered an opportunity to suppress the strongly coupled LA SRS in the case that the LW EPW is excited by a laser pulse having a rectangular envelope. Then, $\delta n_{\mathrm{LW}} \sim n_0(a_0/2)^2 \gg n_0(a_0\omega_{pe}/\omega_0)^{2/3}$, and calculations show that the increment reduces by several times. In this paper, we address to the nonrelativistic laser intensities only ($a_0 < 1$), whereas analogous studies for relativistic pulses are reported elsewhere [25], [50].

The paper is organized as follows. In Section II, we introduce nonrelativistic equations that describe the LA SRS of a laser pulse in a rarefied plasma perturbed by a linear LW EPW. (The one-dimensional (1-D) version of the basic equations, which described the direct backscatter, was reported earlier [20].) The details of derivation of the basic equations are relegated to the Appendix, where the condition is also found under which the linear approximation of the LW EPW can be used in the theory of the LA SRS developed in the present paper.

In Section III, we consider the LA SRS of a short laser pulse in the presence of a linear LW EPW. We study the 1-D regime of spatial amplification of unstable modes in the frame of reference comoving with the pulse. Under the conditions of weak and strong coupling, we find the increments of spatial growth in the comoving frame of reference. These increments determine the maximum amplification, which can be achieved on a pulse length for the scattering angle that is large enough. For the maximum possible amplification, the ratio of the laser spot size $L_\perp$ to the pulse longitudinal size L_{pulse} must obey the condition $L_\perp/L_{\mathrm{pulse}} > \cot(\alpha/2)$ [9], [37], [38], where α denotes a scattering angle reckoned from the direction of the pulse motion. However, the total scattered energy is determined by the exact structure of the scattered EM field, which depends on the shape of the laser pulse. The question of how the shape of the pulse affects the energy losses due to the LA SRS will be answered in the other paper. We establish that the weakly coupled LA SRS in the presence of an LW EPW is an essentially multiwave process, which can be suppressed, provided $\delta n_{\mathrm{LW}} > n_0(\omega_{pe}/\omega_0)$. The suppression is the effect of a phase modulation of short-wavelength scattering plasma waves in the presence of an LW EPW. In a plasma perturbed by an LW EPW, the short-wavelength EPW, which are involved in the scattering process, possess a complex spectrum, which consists of a number of sidebands $(\omega_{\mathrm{BG}} + n\omega_{\mathrm{LW}}, \mathbf{k}_e + n\mathbf{k}_{\mathrm{LW}})$ shifted to integer multiples of a frequency $\omega_{\mathrm{LW}} \approx \omega_{pe}$ and wavenumber $k_{\mathrm{LW}} \ll k_e$ of an LW EPW with respect to the original normal mode $(\omega_{\mathrm{BG}}, \mathbf{k}_e)$ (we discuss this effect in the Appendix). These sidebands, which are not normal modes, can exist only at the expense of the original normal mode, whose energy can be completely exhausted, and amplitude tends to zero for $\delta n_{\mathrm{LW}} \sim n_0(\omega_{pe}/\omega_0)$ [26], [51]. Hence, in the presence of an LW EPW, the energy originally transmitted to the single normal mode of the plasma oscillations is expended in excitation of a great number of satellites, which are not normal modes, with the effect of dramatic decrease in the growth rate of the instability. We have found that for $\delta n_{\mathrm{LW}} > n_0(\omega_{pe}/\omega_0)$, the Stokes band in the spectrum of the scattered EM field is strongly suppressed, whereas the anti-Stokes band at $\omega_0 + \omega_{\mathrm{BG}}$ appears (however, with an increment of spatial growth small if compared with that of a Stokes band in an unperturbed plasma). Both finite electron temperature (such that $k_e V_{T_e} \ll \omega_{pe}$) and a deviation of a scattering angle from π were found to preserve the effect of suppression. As for the strongly coupled SRS in the presence of a given linear LW EPW, modulation of the wide spectrum of electron plasma modes, which participate in the scattering process, leads to the notable effect of suppression (i.e., halves the increment of the instability), when a larger amplitude LW EPW is taken, such that $\delta n_{\mathrm{LW}} \sim n_0(a_0\omega_{pe}/\omega_0)^{2/3}$. In Section IV, we summarize the results and make some conclusions.

II. Basic Equations

To describe the LA SRS of a laser radiation in rarefied plasmas, we represent a high-frequency (HF) electric field in a plasma as

$$\mathbf{a}(\mathbf{r}, t) = \tfrac{1}{2}\left\{\mathbf{a}_0(\mathbf{r}, t)e^{-i\omega_0 t + i(\mathbf{k}_0, \mathbf{r})} + \mathbf{a}_s(\mathbf{r}, t)e^{-i\omega_0 t + i(\mathbf{k}_s, \mathbf{r})}\right\} + \text{c.c.} \tag{1}$$

where the dimensionless amplitudes $\mathbf{a}_{0(s)} = e\mathbf{E}_{0(s)}/(m_e\omega_0 c)$ ($|\mathbf{a}_{0(s)}| \ll 1$, $|\mathbf{a}_s| \ll |\mathbf{a}_0|$) refer to the pump field and the scattered radiation, respectively (the fields have an arbitrary polarization). It is assumed that the laser pulse propagates along the OZ-axis so that $\mathbf{k}_0 = \mathbf{e}_z k_0$, and scattering occurs

through an angle $\alpha \leq \pi$ reckoned from the direction of a pulse motion. We presume that the wavenumbers $k_{0(s)} = |\mathbf{k}_{0(s)}|$ obey the same dispersion relation for EM waves in a plasma $(k_{0(s)}c/\omega_0)^2 = 1 - (\omega_{pe}/\omega_0)^2 \approx 1$; therefore, $k_s = k_0$, and $\mathbf{k}_s = (\mathbf{k}_{s\perp}, k_0 \cos\alpha)$, where $k_{s\perp} = |\mathbf{k}_{s\perp}| = k_0 \sin\alpha$. In a highly rarefied plasma ($\omega_{pe} \ll \omega_0$), the amplitudes a_0 and a_s are slowly varying with respect to time and space variables on scales ω_0^{-1} and k_0^{-1}, respectively; that is, $|\partial a_{0(s)}/\partial t| \ll \omega_0 |a_{0(s)}|$, $|\partial a_{0(s)}/\partial z| \ll k_{s_z}|a_{0(s)}|$, and $|\partial a_{0(s)}/\partial \mathbf{r}_\perp| \ll k_{s\perp}|a_{0(s)}|$.

The laser pulse in a plasma can perturb both ion and electron density. For sufficiently short pulses, we may neglect the perturbation of the ion density produced by the pulse and consider ions as an immobile, positive neutralizing background. A ponderomotive force due to beating of incident and scattered EM waves (1) excites a perturbation of the electron density

$$\delta\tilde{n}_s = \tfrac{1}{2}\,\delta n_s(\mathbf{r}, t)e^{i(\mathbf{k}_e, \mathbf{r})} + \text{c.c.} \tag{2}$$

whose wave vector obeys the resonant matching condition $\mathbf{k}_e = \mathbf{k}_0 - \mathbf{k}_s$ [hence, $|\mathbf{k}_e| = k_e = 2k_0 \sin(\alpha/2)$, $k_{ez} = 2k_0 \sin^2(\alpha/2)$, and $\mathbf{k}_{e\perp} = -\mathbf{k}_{s\perp}$]. When the scattering angle is not small [we suppose that $\sin(\alpha/2)$ is not close to zero, and, therefore, $k_e \sim k_0$], we treat the amplitude δn_s as a slowly varying function of the space variables ($|\partial \delta n_s/\partial \mathbf{r}| \ll k_e|\delta n_s|$). The short-wavelength EPW (2) is responsible for the stimulated Raman scattering of the laser radiation through large angles.

Stimulated Raman scattering through large angles, which produces relatively short-wavelength plasma waves (2), can occur in a plasma in the presence of long-wavelength electron plasma oscillations. These oscillations, which vary in space slowly if compared with k_0^{-1}, are responsible for such phenomena as the self-modulation of radiation and the wakefield excitation [22], [47]–[49]. In plasma-based accelerators [10], the laser-driven LW EPW can produce electron density perturbations of order of tens of percent of the background electron density.

We investigate the LA SRS in the presence of a linear LW EPW in terms of the coupled mode equations whose derivation is outlined in the Appendix. These equations are derived for the amplitudes of the scattered EM field and scattering EPW, and they include the quiver velocity $\tilde{\mathbf{v}}_{\text{LW}}(\mathbf{r}, t)$ of electrons in a linear LW EPW ($\tilde{\mathbf{v}}_{\text{LW}}$ known, the electron density perturbation $\delta\tilde{n}_{\text{LW}}(\mathbf{r}, t)$ in the LW EPW can be retrieved using the linear continuity equation). The basic equations read as

$$i\left(\frac{\partial}{\partial t} + (\mathbf{v}_g, \nabla)\right)\mathbf{a}_s = \frac{\omega_{pe}^2}{4\omega_0}\left[\mathbf{a}_0 - \frac{\mathbf{k}_{s\perp}}{k_0^2}(\mathbf{k}_{s\perp}, \mathbf{a}_0)\right]\frac{\delta n_s^*}{n_0} \tag{3}$$

$$\left(\left(\frac{\partial}{\partial t} - i(\mathbf{k}_e, \tilde{\mathbf{v}}_{\text{LW}})\right)^2 + \omega_{\text{BG}}^2\right)\frac{\delta n_s^*}{n_0} = -\frac{1}{2}(k_e c)^2(\mathbf{a}_0^*, \mathbf{a}_s). \tag{4}$$

In (3), $\mathbf{v}_g = c^2\mathbf{k}_s/\omega_0$ is a group velocity of the scattered EM wave (we consider below the strongly rarefied plasma and accept $|\mathbf{v}_g| = c$). The characteristic Bohm–Gross frequency of scattering plasma waves can be expressed through the electron temperature as

$$\omega_{\text{BG}} = \omega_{pe}\left(1 + \frac{12T_e}{m_e c^2}\,\frac{\omega_0^2}{\omega_{pe}^2}\,\sin^2(\alpha/2)\right)^{1/2} \approx \omega_{pe} \tag{5}$$

where $m_e c^2 = 0.512$ MeV. Note that (4) is nonlinear in the electron quiver velocity $\tilde{\mathbf{v}}_{\text{LW}}$, which must obey the condition $\tilde{v}_{\text{LW}}/c \sim \delta\tilde{n}_{\text{LW}}/n_0 \ll (\omega_{pe}/\omega_0)^{1/2}$ [see the Appendix, (43)]. In case the laser pulse and the LW EPW are both given, (3) and (4) form the basis of a linear theory of the LA SRS in plasmas.

III. Dispersion Analysis

A. General Dispersion Relation

Before proceeding to the dispersion analysis, we exclude the velocity $\tilde{\mathbf{v}}_{\text{LW}}$ from the second-order differential operator of (4) using a unitary replacement

$$\{\mathbf{a}_s, \delta n_s^*\} = \{\hat{\mathbf{a}}_s, \delta\hat{n}_s^*\}\exp[-i\tilde{\Psi}] \tag{6}$$

$$\tilde{\Psi} = -\int_0^t (\mathbf{k}_e, \tilde{\mathbf{v}}_{\text{LW}})\,d\tau \tag{7}$$

which accounts for the phase modulation of the decay waves. Because the transformation (6) preserves the absolute value, the instability onset may be studied in terms of the amplitudes $\{\hat{\mathbf{a}}_s, \delta\hat{n}_s^*\}$. Instead of z and t, it is convenient to use variables $\xi = z - ct$ and $\eta = t$ of the frame of reference comoving with the pulse ($\mathbf{r}_\perp$ remains the same in both frames). When the change of variables is made, the equations for the amplitudes of the modulated waves read as

$$i\left(\frac{\partial}{\partial\eta} + (\tilde{\mathbf{v}}_g, \tilde{\nabla})\right)\hat{\mathbf{a}}_s + \hat{\mathbf{a}}_s\left(\frac{\partial\tilde{\Psi}}{\partial\eta} + (\tilde{\mathbf{v}}_g, \tilde{\nabla})\tilde{\Psi}\right) = \frac{\omega_{pe}^2}{4\omega_0}\left[\mathbf{a}_0 - \frac{\mathbf{k}_{s\perp}}{k_0^2}(\mathbf{k}_{s\perp}, \mathbf{a}_0)\right]\frac{\delta\hat{n}_s^*}{n_0} \tag{8}$$

$$\left(\left(\frac{\partial}{\partial\eta} - c\frac{\partial}{\partial\xi}\right)^2 + \omega_{\text{BG}}^2\right)\frac{\delta\hat{n}_s^*}{n_0} = -\frac{1}{2}(k_e c)^2(\mathbf{a}_0^*, \hat{\mathbf{a}}_s). \tag{9}$$

Here, $\tilde{\mathbf{v}}_g = (c^2\mathbf{k}_{s\perp}/\omega_0, -2c\sin^2(\alpha/2))$ and $\tilde{\nabla} = (\partial/\partial\mathbf{r}_\perp, \partial/\partial\xi)$.

We consider below a given shape of both laser pulse and LW EPW, thus, neglecting their evolution on time scales of interest. It was shown [9], [37], [38] that the time interval $\tau_0 = \max\{L_{\text{pulse}}/c, L_{\text{pulse}}/[2c\sin^2(\alpha/2)]\}$ is required for the steady-state spatial amplification in the comoving frame to be established. It can be shown [9], [37], [38] that the purely 1-D regime of spatial amplification dominates in a plasma, if the transverse dimension $L_\perp$ of a pulse is large enough to satisfy the inequality $L_\perp/L_{\text{pulse}} \gg \cot(\alpha/2)$. Further, we treat this 1-D regime and determine the increments of the spatial growth in the comoving frame, thus, ignoring boundary conditions at $r_\perp = L_\perp$ and the spatial domain of two-dimensional (2-D) growth. In such a way, we determine the maximum possible amplification of the unstable waves in the comoving frame, rather than an exact structure of the scattered

EM field, which depends on both the shape of the laser pulse and boundary-value conditions at the pulse side boundaries.

To investigate the 1-D regime of the spatial amplification, we choose a 1-D rectangular longitudinal profile of the pulse

$$\mathbf{a}_0(\xi) = \mathbf{e}_0 a_0(\xi) \tag{10}$$

where $\mathbf{e}_0$ is a unit complex vector of the laser polarization and a_0 is a constant amplitude of the pump wave in the region $-L_{\text{pulse}} \le \xi \le 0$ and is zero outside this interval. In such a way, the pump wave is assumed to be a plane wave; that is, the spatial variation of the envelope transverse to the wave vector is neglected. The laser pulse, which propagates through an unperturbed plasma, encounters free thermal fluctuations of electron density. These fluctuations may be amplified inside the pulse, the unstable modes growing toward the pulse trailing edge. The steady-state amplification is described by the solution to the boundary-value problem for the set (8) and (9). The boundary-value conditions for this problem are formulated below.

In the absence of radiation in the unperturbed plasma ahead of the pulse, thermal fluctuations of an electron density with characteristic wave vector close to $\mathbf{k}_e$ may be approximated by the solution to the free (4), in which $\tilde{\mathbf{v}}_{\text{LW}} \equiv 0$

$$\frac{\delta n_f}{n_0} = \sum_{\sigma=\pm 1} A_f^{(\sigma)}(\mathbf{r}) e^{i\sigma\omega_{\text{BG}} t}. \tag{11}$$

We apply the Fourier transform with respect to the variable z to the expression (11), and we change the variables in the resulting expression. As a result, we get

$$\frac{\delta n_f}{n_0}(\xi, \mathbf{r}_\perp, \eta) = \sum_{\sigma=\pm 1} \int e^{-i\omega\eta} \left(e^{-iq_\sigma \xi} A_f^{(\sigma)}(q_\sigma, \mathbf{r}_\perp) \right) \frac{d\omega}{c} \tag{12}$$

where $q_\sigma = (\omega + \sigma\omega_{\text{BG}})/c$. Expression (12) is a Fourier transform with respect to the time variable η in the comoving frame of reference. The laser pulse occupies the region $-L_{\text{pulse}} \le \xi \le 0$, and the amplitude $\delta n_s(\xi, \mathbf{r}_\perp, \eta)$ and its derivative must be continuous at the leading edge of the pulse

$$\delta n_s(\xi = 0, \mathbf{r}_\perp, \eta) = \delta n_f(\xi = 0, \mathbf{r}_\perp, \eta) \tag{13}$$

$$\frac{\partial \delta n_s}{\partial \xi}(\xi = 0, \mathbf{r}_\perp, \eta) = \frac{\partial \delta n_f}{\partial \xi}(\xi = 0, \mathbf{r}_\perp, \eta). \tag{14}$$

Ahead of the pulse, the intensity of free thermal fluctuations of the EM field with a frequency close to ω_0 is assumed to be zero

$$\mathbf{a}_s(\xi = 0, \mathbf{r}_\perp, \eta) = 0. \tag{15}$$

We take the electron velocity $\tilde{\mathbf{v}}_{\text{LW}}$, which corresponds to the free, linear, 1-D LW EPW, in the form

$$\tilde{\mathbf{v}}_{\text{LW}} = \mathbf{e}_z \frac{\omega_{pe}}{k_{\text{LW}}} \frac{\delta n_{\text{LW}}}{n_0} \cos[k_{\text{LW}}\xi - (\omega_{pe} - ck_{\text{LW}})\eta]. \tag{16}$$

The constant amplitude of the long-wavelength density perturbation subject to the limitation $\delta n_{\text{LW}}/n_0 \ll (\omega_{pe}/\omega_0)^{1/2}$ [see the Appendix, (43)]. In general, k_{LW} may have an arbitrary value that is small compared with k_e. Then, in the comoving frame, the long-wavelength density perturbation oscillates at the frequency $\omega_{pe} - ck_{\text{LW}}$. We take below $k_{\text{LW}} = k_p = \omega_{pe}/c$, thus, choosing the linear LW EPW, which is stationary in the comoving frame of reference.

We substitute (10) and (16) into (8) and (9) and, according to the form of the boundary conditions (12), make the Fourier transform of the steady (in the comoving frame) solution to the boundary-value problem with respect to the variables η and $\mathbf{r}_\perp$ (passing to the variables ω and $\mathbf{k}_\perp$)

$$\hat{\mathbf{a}}_s(\xi, \mathbf{r}_\perp, \eta) = \int \left(\sum_{\sigma=\pm 1} \int e^{-i\omega\eta} \hat{\mathbf{a}}_s^{(\sigma)}(\xi, \mathbf{k}_\perp, \omega)\, d\omega \right) e^{i(\mathbf{k}_\perp, \mathbf{r}_\perp)}\, d\mathbf{k}_\perp \tag{17}$$

$$\delta\hat{n}_s^*(\xi, \mathbf{r}_\perp, \eta)/n_0 = \int \left(\sum_{\sigma=\pm 1} \int e^{-i\omega\eta} A^{(\sigma)}(\xi, \mathbf{k}_\perp, \omega)\, d\omega \right) e^{i(\mathbf{k}_\perp, \mathbf{r}_\perp)}\, d\mathbf{k}_\perp \tag{18}$$

with ω and $\mathbf{k}_\perp$ real. Then, we represent the Fourier transformants in the Floquet form

$$\left\{ \hat{\mathbf{a}}_s^{(\sigma)}, A^{(\sigma)} \right\}_{\xi, k_\perp, \omega} = \sum_j e^{ik_j\xi} \sum_{n=-\infty}^{+\infty} \left\{ \hat{\mathbf{a}}_j^{(\sigma, n)}, A_j^{(\sigma, n)} \right\}_{k_j, k_\perp, \omega} e^{ink_p\xi} \tag{19}$$

which provides the three-term recurrent relation for the amplitudes $\hat{a}_j^{(\sigma, n)} = |\hat{\mathbf{a}}_j^{(\sigma, n)}|$

$$-a_j^{(\sigma, n-1)}\mu_1 + a_j^{(\sigma, n)} X^{(n)} - a_j^{(\sigma, n+1)}\mu_1 = 0. \tag{20}$$

Here

$$X^{(n)} = D_1 + n\omega_{pe} + \frac{\omega_{pe}^3(\beta/2)}{(D_2^+ + n\omega_{pe})(D_2^- - n\omega_{pe})} \tag{21}$$

$$D_1 = \frac{(\omega/2)}{\sin^2(\alpha/2)} + c[k_j - k_\perp \cot(\alpha/2)] \tag{22}$$

$$D_2^\pm = \omega_{\text{BG}} \pm (\omega + ck_j) \tag{23}$$

where

$$\beta = \frac{a_0^2}{2} \frac{\omega_0}{\omega_{pe}} \left[1 - \frac{|(\mathbf{k}_{s\perp}, \mathbf{e}_0)|^2}{k_0^2} \right] \tag{24}$$

$$\mu_1 = \frac{\omega_0}{\omega_{pe}} \frac{\delta n_{\text{LW}}}{n_0} \sin^2\left(\frac{\alpha}{2}\right) = \mu \sin^2\left(\frac{\alpha}{2}\right). \tag{25}$$

In the representation (19), k_j is a complex number, which is the jth solution to the dispersion equation to the set (20)

$$X^{(n)} = \cfrac{\mu_1^2}{X^{(n+1)} - \cfrac{\mu_1^2}{X^{(n+2)} - \cdots} + \cfrac{\mu_1^2}{X^{(n-1)} - \cfrac{\mu_1^2}{X^{(n-2)} - \cdots}}}. \tag{26}$$

The positive imaginary part of k_j [$\text{Im}\, k_j = \kappa_j(\omega, k_\perp)$] is an increment of a spatial growth in the comoving frame as a function of a real frequency shift ω.

To describe the scattered EM field behind the pulse ($\xi < -L_{\rm pulse}$), we use the free (3), in which the change of variables is made. Using the continuity of the scattered radiation at the pulse trailing boundary (see also [6]), and returning to the variables of the laboratory frame in the obtained solution, we get

$$\begin{aligned}\mathbf{a}_s(z,\,k_\perp,\,t) &= \exp\{2i\mu_1\,\sin(k_pL_{\rm pulse})\}\int d\omega \\ &\times\sum_{\sigma=\pm1}\hat{\mathbf{a}}_s^{(\sigma)}(\xi=-L_{\rm pulse},\,k_\perp,\,\omega) \\ &\times\exp\left(i\left\{\frac{(\omega/2)\cos\alpha}{\sin^2(\alpha/2)}-ck_\perp\,\cot\left(\frac{\alpha}{2}\right)\right\}t\right. \\ &\left.-\,i\left\{\frac{(\omega/2c)}{\sin^2(\alpha/2)}-k_\perp\,\cot\left(\frac{\alpha}{2}\right)\right\}z\right). \qquad (27)\end{aligned}$$

Equation (27) associates the frequency shift ω with the frequency ω_d of the scattered light detected in the laboratory frame

$$\omega_d=\omega_0-\left[\frac{(\omega/2)\cos\alpha}{\sin^2(\alpha/2)}-ck_\perp\,\cot\left(\frac{\alpha}{2}\right)\right]. \qquad (28)$$

The spectrum of EM radiation in a rear plasma (27) includes the modes corresponding to the frequency domains of the spatial amplification [i.e., the frequency ranges in which the dispersion relation (26) has complex solutions]. It is clear from the expansion (19) that a large amount of daughter waves is involved in the process of scattering. Nevertheless, the EM field in a free plasma behind the pulse (27) does not possess such a complex modal structure because of a phase synchronism of the sidebands at the pulse trailing edge. Because the modulation of the solution inside the pulse occurs only with respect to the ξ-variable only (this is the case when the phase velocity of the LW EPW equals the pulse group velocity), the EM field at $\xi=-L_{\rm pulse}$ will be nonmodulated with respect to time in the comoving frame, and hence, the solution in a free plasma will be also nonmodulated. Note, however, that for the nonstationary LW EPW in the comoving frame, i.e., for $k_{\rm LW}\neq k_p$, the spectrum of the scattered radiation will include the sidebands shifted to integer multiples of $(\omega_{pe}/2)(1-k_{\rm LW}/k_p)$ [20]. The sidebands will be distinct when this frequency shift exceeds the width of the frequency domain of instability, and it will merge if $k_{\rm LW}\approx k_p$. The frequency domains of instability, which are very different under the conditions of weak ($\beta\ll1$) and strong coupling ($\beta\gg1$), will be determined, and the increments will be found in Sections III-B and III-C.

B. Weakly Coupled LA SRS

In the limit $\beta\ll1$, searching for the complex roots $k_j(\omega)$ of (26) will be performed in the domains of the parameters ω, k_j, and $k_\perp$, such that either the relations $D_1\approx0$ and $D_2^+\approx0$ or $D_1\approx0$ and $D_2^-\approx0$ are satisfied. It is clear [use (28)] that the frequency of the scattered light, which corresponds to the first of those regions, lies in the vicinity of the Stokes frequency $\omega_d=\omega_0-\omega_{\rm BG}$, and the other domain of parameters corresponds to the anti-Stokes domain near $\omega_d=\omega_0+\omega_{\rm BG}$. For $\mu_1\ll1$, we keep in (19) the fundamental terms ($n=0$) and the sidebands with $n=\pm1$. This means that four additional waves participate now in the scattering process. The electromagnetic sidebands have frequencies $\omega_0-\omega_{\rm BG}\pm\omega_{pe}$ and are still close to the normal modes. On the contrary, the low-frequency satellites with frequencies $\omega_{\rm BG}\pm\omega_{pe}$ are not normal modes, and they can be excited only at the expense of the original normal mode of plasma oscillations (having a resonant Bohm–Gross frequency $\omega_{\rm BG}$), which is resonantly involved in the scattering process. [The modal structure of short-wavelength plasma waves in the presence of a linear small-amplitude ($\mu\ll1$) LW EPW is shown in the Appendix, (45).] The six-wave scattering process is described now in terms of the reduced form of the dispersion equation (26)

$$X^{(0)}\approx\mu_1^2\left(\frac{1}{X^{(1)}}+\frac{1}{X^{(-1)}}\right). \qquad (29)$$

We can easily check that for $\mu_1\ll1$, the anti-Stokes branch is missing [(29) admits no complex solutions in that range of parameters], whereas in the Stokes domain, the unstable modes grow in the pulse frame with the following increment:

$$\kappa(\Delta\omega_d)\approx\frac{\Delta\omega_0}{2c}(1-\mu_1^2)\left[1-\frac{|(\mathbf{k}_{s\perp},\mathbf{e}_0)|^2}{k_0^2}-\left(\frac{\Delta\omega_d}{\Delta\omega_0}\right)^2\right]^{1/2} \qquad (30)$$

where $\Delta\omega_0^2=(a_0^2/2)\omega_0\omega_{pe}^2/\omega_{\rm BG}$, $\Delta\omega_d=\omega_d-(\omega_0-\omega_{\rm BG})$. The spatial increment (30) achieves the maximum value at the Stokes frequency $\omega_d=\omega_0-\omega_{\rm BG}$, other parameters given. In the cold plasma without LW EPW (then, $\mu_1=0$, and $\omega_{\rm BG}=\omega_{pe}$), the maximum possible value of a coefficient of amplification $G_0=\kappa_{\max}L_{\rm pulse}$, where $\kappa_{\max}=\sqrt{a_0^2k_pk_0/8}$, can be achieved. The coefficient of amplification G_0 corresponds to the direct backscattering and to the scattering through an arbitrary angle in the plane orthogonal to the direction of laser polarization [i.e., $(\mathbf{k}_{s\perp},\,\mathbf{e}_0)=0$]. For nonzero T_e, the thermal correction to the frequency (5) of the scattering plasma waves slightly reduces the increment by the factor $(\omega_{pe}/\omega_{\rm BG})^{1/2}$. It is clear from (30) that excitation of the pair of new low-frequency waves (not normal modes) reduces the increment by the factor $1-\mu_1^2$. The reduction is small until $\mu\ll1$, when we can account for the nearest sidebands. For larger μ_1, the amount of new waves—participants of the scattering process—grows, and their effect on the coefficient of amplification becomes more pronounced.

When $\mu_1\geq1$, we will find the solutions to the full dispersion equation (26). The complex solutions are searched for, as above, in both Stokes and anti-Stokes domains, and in this case, (26) may be simplified and reduced to the form of the finite algebraic equation

$$D_1+\frac{\beta/4}{1+2\mu_1^2f_1'(0)}\left[\frac{(1+\delta_T)^{-1/2}}{D_2^\pm}-\frac{[\mu_1^2f_1(0)f_2(0)]^2}{D_2^\pm-\delta_T}\right]=0 \qquad (31)$$

where $\delta_T=(\omega_{\rm BG}/\omega_{pe})^2-1$ and

$$f_n(x)=-\cfrac{1}{n+x-\cfrac{\mu_1^2}{n+1+x-\cdots}},\qquad f_1'=\frac{\partial f_1}{\partial x}.$$

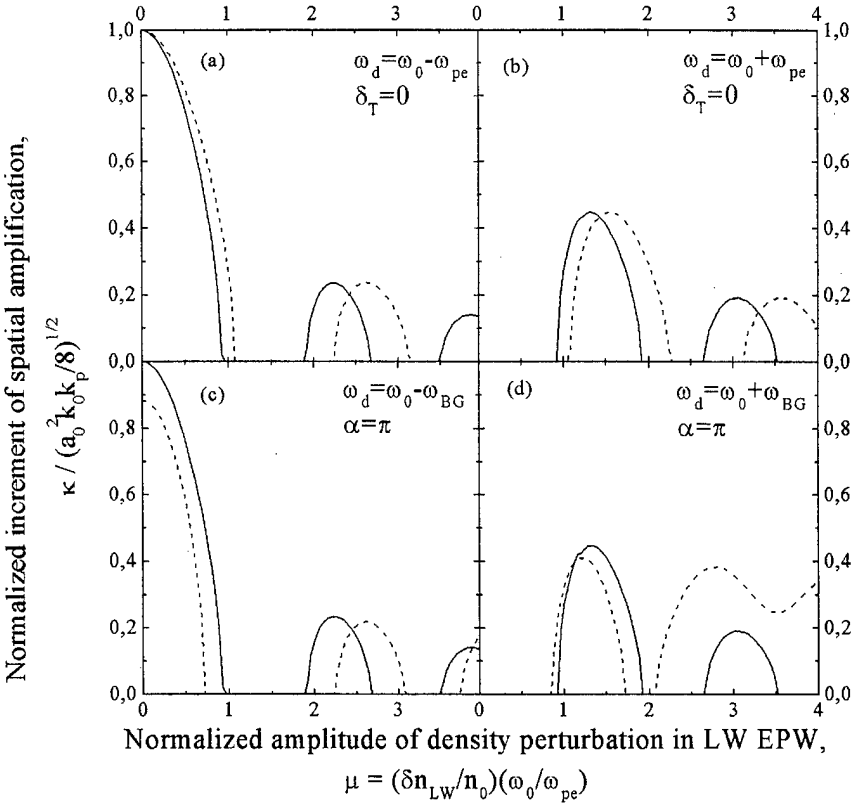


Fig. 1. Suppression of the LA SRS at the Stokes frequency $\omega_d = \omega_0 - \omega_{BG}$ is shown in the plots (a) and (c), and the onset of the instability at the anti-Stokes frequency $\omega_d = \omega_0 + \omega_{BG}$ is shown in the plots (b) and (d). (a) and (b) are obtained for $\delta_T = 0$: $\alpha = \pi$ (solid line), $\alpha = 3\pi/4$ (dotted line); (c) and (d) are obtained for $\alpha = \pi$ (direct backscattering): $\delta_T = 0$ (solid line), $\delta_T = \beta = 0.25$ (dotted line).

We consider below the scattering in the plane orthogonal to the direction of linear polarization of the laser, where the coupling coefficient β achieves the maximum value independent on the scattering angle. The increments of the spatial growth corresponding to the Stokes and anti-Stokes domains are found by solving (31) numerically. We plot in Fig. 1 the positive imaginary parts of the roots of (31), which correspond to both Stokes ($\omega_d = \omega_0 - \omega_{BG}$) and anti-Stokes ($\omega_d = \omega_0 + \omega_{BG}$) frequencies versus normalized amplitude μ of the long-wavelength density perturbation.

The primary effect of the LW EPW on the LA SRS is that the maximum increment in the Stokes domain reduces to zero when $\delta n_{LW} \sim n_0(\omega_{pe}/\omega_0)$. The effect of suppression is insensitive to the variation of the scattering angle near π [compare dependencies shown in Fig. 1(a) for $\alpha = \pi$ and $\alpha = 3\pi/4$]. Although the Stokes increment may be nonzero for some values δn_{LW} such that $\delta n_{LW} > n_0(\omega_{pe}/\omega_0)$, it is always less than the maximum possible value κ_{max} achieved in the cold plasma ($\delta_T = 0$) without LW EPW. When δn_{LW} exceeds $n_0(\omega_{pe}/\omega_0)$, the complex solutions of (31) appear in the anti-Stokes region. However, the increment given by this solution is less than κ_{max} [see Fig. 1(b) and (d)]. For nonzero plasma temperature [see Fig. 1(c) and (d)], both suppression of the Stokes and generation of the anti-Stokes branches of the instability do not subject to substantial changes.

An opportunity to create the wakefield intense enough to suppress the LA SRS occurs when the resonant self-modulation of the laser pulse develops (see [22], [47]–[49], and [10] and the references therein). Then, the amplitude of LW EPW can achieve tens of percent of the background electron density even for nonrelativistic laser intensity corresponding to the condition of weak coupling [29]. So, the suppression of the LA SRS, which is predicted above, admits an experimental verification.

C. Strongly Coupled LA SRS

In the limit $\beta \gg 1$, scattering plasma waves are not normal modes. In a plasma without LW EPW, the scattered radiation has a widespread spectrum extended to the blue side $-(3/2)\beta^{1/3}\omega_{pe} \le \omega_d - \omega_0 \le (\beta/2)\omega_{pe}$. The maximum value of the increment $\kappa_0 = (\sqrt{3}/2)k_p(\beta/2)^{1/3}[1 - 2^{-1/3}\beta^{-2/3}]$ corresponds to the frequency $\omega_d = \omega_0$ as follows from the dispersion equation $X^{(0)} = 0$. It is clear [see (24)] that for $\mathbf{k}_{s\perp} \perp \mathbf{e}_0$, the increment κ_0 is independent on angle.

When a plasma is perturbed by a small-amplitude LW EPW such that $\mu_1 \ll \beta^{1/6}$, we may describe the instability using (29). For $\omega_d = \omega_0$, the increment of the instability given by the solution to this dispersion equation reads as

$$\kappa = \kappa_0 - \mu_1^2 \frac{3\sqrt{3}}{8} k_p \left(\frac{\beta}{2}\right)^{-1/3}. \tag{32}$$

Equation (32) is useful for estimation of the effect of an LW EPW on the strongly coupled LA SRS even far beyond its strict validity region. So, (32) predicts a decrease in $\kappa(\omega_d = \omega_0)$ when μ becomes of order $\beta^{1/3}$, or $\delta n_{LW} \sim n_0(a_0\omega_{pe}/\omega_0)^{2/3}$. This prediction is confirmed by the results of numerical solution to

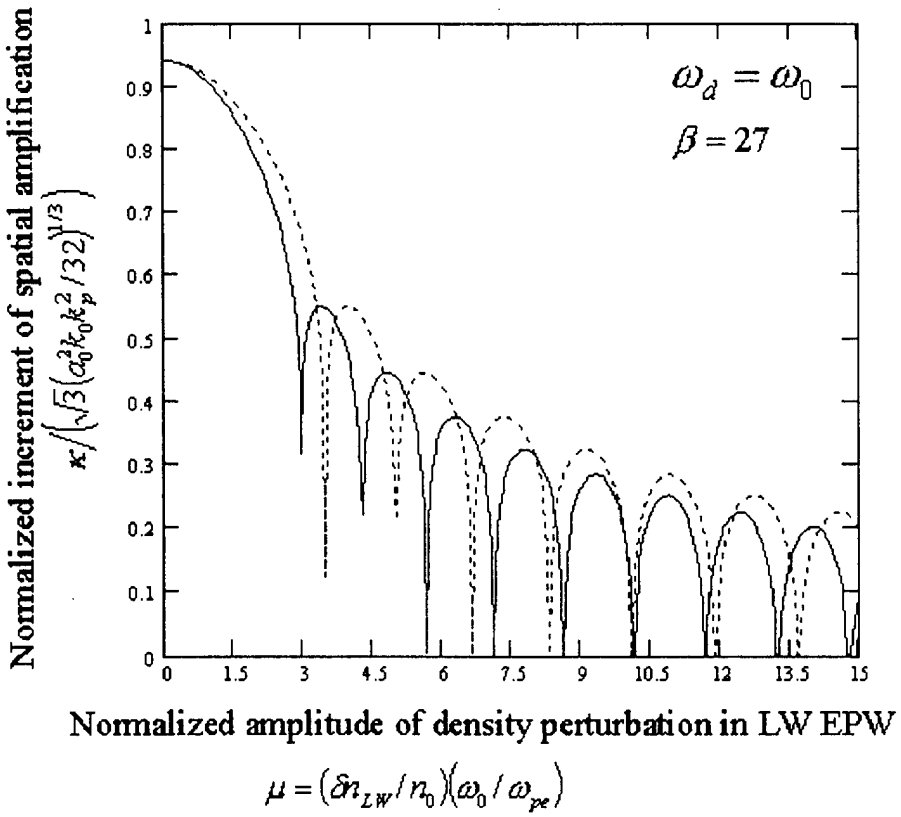


Fig. 2. Dependencies are shown of the maximum value of the increment of the strongly coupled LA SRS $\kappa(\omega_d = \omega_0)$ corresponding to $\beta = 27$ and $\delta_T = 0$ (cold plasma) versus normalized density perturbation in an LW EPW $\mu = (\delta n_{\rm LW}/n_0)(\omega_0/\omega_{pe})$ for the two values of the scattering angle: $\alpha = \pi$ (solid line), $\alpha = 3\pi/4$ (dotted line).

the general dispersion equation (26). We solved this equation for $\beta > 10$ and have established in that range the relation

$$\kappa(\mu \approx \beta^{1/3},\ \omega_d = \omega_0) \approx \tfrac{1}{2}\,\kappa(\mu = 0,\ \omega_d = \omega_0) \qquad (33)$$

i.e., the maximum of the increment proves to be reduced by nearly one-half when $\delta n_{\rm LW} \sim n_0(a_0\omega_{pe}/\omega_0)^{2/3}$. To demonstrate the effect of suppression, we show in Fig. 2 the dependencies $\kappa(\beta = 27,\ \omega_d = \omega_0)$ versus μ for two values $\alpha = \pi$ and $\alpha = 3\pi/4$ of the scattering angle (δ_T is taken to be zero and $\mathbf{k}_{s\perp} \perp \mathbf{e}_0$). We may check the ratio (33) against the dependence shown in Fig. 2. Note that decrease $\pi/4$ in the scattering angle just slightly modifies the suppression, making the effect less pronounced.

We can directly apply this result to the physical situation, when the LW EPW is excited by the leading front of a short laser pulse with a rectangular envelope [28], [52], [53]. Then, inside the pulse, the LW EPW amplitude is constant and equals $\delta n_{\rm LW} = n_0(a_0/2)^2$, so that $\mu = \beta/2$. Under the conditions of strong coupling, this value is significantly larger than that is necessary to halve the maximum increment [i.e., $\delta n_{\rm LW} \approx n_0(a_0\omega_{pe}/\omega_0)^{2/3}$], and we may expect the notable decline in the increment under such circumstances. Using the dependencies plotted in Fig. 2, it can be established that the maximum increment corresponding to $\mu = \beta/2 = 13.5$ equals approximately one-fifth of the increment in an unperturbed plasma. This means that complete suppression is not the case, but the increment reduction is dramatic. It should be remembered, though, that a limitation on an LW EPW amplitude $\delta n_{\rm LW} < n_0(\omega_{pe}/\omega_0)^{1/2}$, which arises from the requirement of the linearity of the LW EPW, necessitates for $\mu > 10$ the condition of strongly rarefied plasma, namely, $\omega_{pe}/\omega_0 < 10^{-2}$, or $n_0/n_c < 10^{-4}$. In a more dense plasma, the effect of harmonics of an LW EPW should be taken into account (see the Appendix), which can drastically modify the effect of LW EPW on the scattering process. This can be seen in the results of [25] and [50], where the BSRS of a short ($L_{\rm pulse} \sim \lambda_p$), relativistically strong ($a_0 \sim 1$) laser pulse generating a strongly nonlinear LW EPW was considered. In the regimes, corresponding to the parameter regions $\beta > 50$ (hence, $\mu > 25$), and $\omega_0/\omega_{pe} > 20$, significant variations of a spectral shape of BSRS depending on a pulse length and intensity were established instead of suppression of the instability.

IV. Conclusion

In the present paper, the analytical dispersion analysis of the LA SRS of a short laser pulse in an underdense plasma, which is perturbed by a linear long-wavelength electron plasma wave, was performed under the conditions of weak and strong coupling. The present work was aimed at calculation of the increments of spatial growth in the comoving frame of reference rather than at obtaining the exact structure of the scattered radiation and calculation of the SRS reflectivity, which need account for exact shape of the laser pulse. The increments of spatial growth in the frame of reference comoving with the pulse, which determine the maximum of the possible amplification of scattered radiation, were found. The obtained increments achieve

their maxima for scattering in the plane orthogonal to the direction of the linear polarization of the laser. In the absence of the LW EPW in the cold plasma, these maxima are independent on the scattering angle.

The presence of the LW EPW in a plasma causes the phase modulation of the waves, which participate in the scattering process, and it makes the LA SRS a substantially multiwave process, which can be strongly suppressed. The cause of suppression of the instability in the presence of an LW EPW is excitation in the spectrum of the scattering plasma waves of a number of sidebands, which are not normal modes. The energy loss of the resonantly excited normal mode due to the excitation of these sidebands can completely suppress the instability. We have considered the suppression of the instability in the presence of the linear LW EPW whose phase velocity coincides with the group velocity of a laser pulse.

When the normalized electron density perturbation in the LW EPW exceeds the ratio of the electron plasma frequency to the laser frequency, the spatial increment of weakly coupled LA SRS, which corresponds to the Stokes band of the scattered light, drops to zero, whereas an additional anti-Stokes band appears in the spectrum of scattered radiation. The maximum value of the increment of spatial growth, which corresponds to the anti-Stokes band, is always less than the maximum of the original increment of the instability in a plasma without LW EPW.

Under the condition of strong coupling, the LA SRS is a nonresonant process even in an unperturbed plasma and the instability subject to suppression for a significantly larger value of a density perturbation in an LW EPW; that is, $\delta n_{\mathrm{LW}} \sim n_0(a_0\omega_{pe}/\omega_0)^{2/3}$. When the linear LW EPW is generated by the rectangular laser pulse [$\delta n_{\mathrm{LW}} \sim n_0(a_0/2)^2 \gg n_0(a_0\omega_{pe}/\omega_0)^{2/3}$], the maximum increment of the instability can be reduced by several times. However, complete suppression of the instability under the conditions of strong coupling is not the case.

The phenomenon of suppression of the LA SRS by means of an LW EPW might play a positive role in the performance of the self-modulated laser wakefield accelerator [10], when a laser pulse amplitude satisfies the condition of the weakly coupled regime of the LA SRS [29]. The large-amplitude LW EPW excited in such an accelerator suppresses the LA SRS and, hence, reduces the laser pulse energy depletion and erosion of its form due to this instability.

Appendix
Derivation of Basic Coupled Mode Equations for LA SRS in the Presence of Large-Scale Electron Density Perturbations

We derive here the basic equations, which describe the LA SRS of a laser pulse in an underdense plasma under the assumption that a plasma is perturbed by an LW EPW whose characteristic wavelength strongly exceeds the laser wavelength.

The electron plasma in an HF electromagnetic field (1) performs both "fast" and "slow" motions, the characteristic time scale of these motions being $\tau_{\mathrm{fast}} \sim \omega_0^{-1}$ and $\tau_{\mathrm{slow}} \gg \omega_0^{-1}$, respectively. The nonrelativistic hydrodynamics of the electron plasma gives the following set of equations describing the "slow" motions of the electron fluid with a temperature T_e in a HF field:

$$\frac{\partial n}{\partial t} + \nabla(n\mathbf{v}) = 0 \tag{34}$$

$$\frac{\partial \mathbf{v}}{\partial t} + (\mathbf{v}, \nabla)\mathbf{v} = -\frac{e}{m}\nabla\varphi - \frac{c^2}{2}\nabla\langle \mathbf{a}^2\rangle - 3V_{T_e}^2 \nabla \ln n \tag{35}$$

$$-\Delta\varphi = 4\pi e\delta n \tag{36}$$

where $\mathbf{a}$ is a normalized HF electric field defined as (1), $\delta n = n - n_0$ is an electron density perturbation slow varying on scale ω_0^{-1}, and $V_{T_e} = \sqrt{T_e/m_e}$; $\langle\cdots\rangle$ means the average value over the laser period $2\pi\omega_0^{-1}$. According to the spatial dependence of the time-averaged ponderomotive potential, we represent the solution to (34)–(36) in the form

$$\{\delta n, \mathbf{v}, \varphi\} = \{\delta\tilde{n}_{\mathrm{LW}}, \tilde{\mathbf{v}}_{\mathrm{LW}}, \varphi_{\mathrm{LW}}\} + \tfrac{1}{2}\left(\{\delta n_s, \mathbf{v}_s, \varphi_s\}e^{i(\mathbf{k}_e, \mathbf{r})} + \text{c.c.}\right) \tag{37}$$

where $\mathbf{k}_e = \mathbf{k}_0 - \mathbf{k}_s$, $k_e = 2k_0\sin(\alpha/2)$. The terms in round brackets are responsible for the SRS of laser radiation. We presume that the beat period of laser and scattered radiation $2\pi k_e^{-1}$ is of order k_0^{-1}. Then, the spatial scales of variation of quantities labeled as "LW" ("long-wavelength") and "s" ("scatter") can be separated. Substituting (37) into (34)–(36) under the assumption that $k_e \gg |\nabla \ln\{\delta\tilde{n}_{\mathrm{LW}}, \tilde{\mathbf{v}}_{\mathrm{LW}}, \varphi_{\mathrm{LW}}\}|$, $\nabla(\delta n_s\tilde{\mathbf{v}}_{\mathrm{LW}}) \approx (\tilde{\mathbf{v}}_{\mathrm{LW}}, \nabla)\delta n_s$, and $|(\tilde{\mathbf{v}}_{\mathrm{LW}}, \nabla)\mathbf{v}_s| > |(\mathbf{v}_s, \nabla)\tilde{\mathbf{v}}_{\mathrm{LW}}|$, we obtain, in the linear approximation in δn_s, the single equation for the envelope of the scattering plasma waves

$$\left[\left(\frac{\partial}{\partial t} + (\tilde{\mathbf{v}}_{\mathrm{LW}}, \nabla) + i(\mathbf{k}_e, \tilde{\mathbf{v}}_{\mathrm{LW}})\right)^2 + \omega_{\mathrm{BG}}^2\right]\frac{\delta n_s}{n_0} = -\frac{1}{2}(k_e c)^2(\mathbf{a}_0, \mathbf{a}_s^*). \tag{38}$$

The quantities $\tilde{\mathbf{v}}_{\mathrm{LW}}(\mathbf{r}, t)$ and $\mathbf{a}_0(\mathbf{r}, t)$ may be either given or determined self-consistently. The equation (3) for the envelope of the scattered radiation follows from the Maxwell equations under the assumption that $|\delta\tilde{n}_{\mathrm{LW}}| \ll n_0$.

In the present paper, we consider the LA SRS in the presence of large-scale electron density perturbations produced by the given LW EPW. Note that (38) is nonlinear in the quiver velocity $\tilde{\mathbf{v}}_{\mathrm{LW}}$ of electrons in an LW EPW. In turn, the nonlinear relation between $\tilde{\mathbf{v}}_{\mathrm{LW}}$ and $\delta\tilde{n}_{\mathrm{LW}}$ exists even in a nonrelativistic limit $|\tilde{\mathbf{v}}_{\mathrm{LW}}| \ll c$. Below, we determine the validity condition for the linear approximation of the LW EPW in (38).

It is clear from (38) that the modification of the SRS in the presence of the LW EPW occurs due to the effect of the LW EPW on the scattering plasma waves. Let us consider the short-wavelength EPWs ($\mathbf{k} \approx \mathbf{k}_e$) in a plasma without radiation ($\mathbf{a} \equiv 0$) and examine the coupling of these waves to the given weakly nonlinear LW EPW having relativistic phase velocity. The highest nonlinearity of such an LW EPW, which can be treated in terms of fully nonrelativistic equations (34)–(36), is second order in $\delta\tilde{n}_{\mathrm{LW}}$ (description of the higher order nonlinearities needs account for the relativistic corrections

[30]). In the 1-D case, the electron quiver velocity in such a wave reads [30] as

$$\tilde{\mathbf{v}}_{\mathrm{LW}} \approx \mathbf{e}_z c \frac{\delta n_{\mathrm{LW}}}{n_0}\left(-\frac{\delta n_{\mathrm{LW}}}{2n_0} + \cos\phi + \frac{\delta n_{\mathrm{LW}}}{2n_0}\cos 2\phi\right) \tag{39}$$

where $\delta n_{\mathrm{LW}} \ll n_0$ is a constant amplitude of a density perturbation in the LW EPW, and $\phi = k_p z - \omega_{pe} t$, $k_p = \omega_{pe}/c$ (for the sake of simplicity, we presume the phase velocity of the linear wave equal to the speed of light in a vacuum). Solving the free equation (38) with an account of (39) and keeping the terms of order $(\delta n_{\mathrm{LW}}/n_0)^2$, we arrive at the expression for the short-wavelength free electron plasma modes

$$\begin{aligned}\frac{\delta\tilde{n}_s}{n_0} &= \frac{1}{2}\left(\sum_{\sigma=\pm 1} A^{(\sigma)}(\mathbf{r}) e^{i\sigma\omega_{\mathrm{BG}}t}\right)\exp[i(\mathbf{k}_c, \mathbf{r}) + i\tilde{\Psi}_l + i\tilde{\Psi}_{nl}] \\ &\quad + \text{c.c.} \\ &= \sum_{\sigma=\pm 1} |A^{(\sigma)}(\mathbf{r})|\cos[\Psi_\sigma + \sigma\tilde{\Psi}_l + \sigma\tilde{\Psi}_{nl}] \end{aligned} \tag{40}$$

where $A_\sigma(\mathbf{r}) \equiv |A_\sigma(\mathbf{r})|\exp(i\sigma\varphi_\sigma)$ are some arbitrary functions, $\Psi_\sigma = \omega_{\mathrm{BG}}t + \sigma(\mathbf{k}_c, \mathbf{r}) + \varphi_\sigma$, and

$$\tilde{\Psi}_l = -\int_0^t (\mathbf{k}_c, \tilde{\mathbf{v}}_{\mathrm{LW}})\, d\tau = 2\mu_1 \sin\phi \tag{41}$$

$$\begin{aligned}\tilde{\Psi}_{nl} &= \int_0^t \left[(\tilde{\mathbf{v}}_{\mathrm{LW}}, \nabla)\int_0^{t_1} (\mathbf{k}_c, \tilde{\mathbf{v}}_{\mathrm{LW}})\, d\tau\right] dt_1 \\ &= 2\mu_2 \sin 2\phi \end{aligned} \tag{42}$$

where

$$\mu_1 = (k_{cz}/2k_p)(\delta n_{\mathrm{LW}}/n_0)$$
$$\mu_2 = (\mu_1/2)(\delta n_{\mathrm{LW}}/n_0) \ll \mu_1.$$

The phase modulation produced by the second harmonic of the LW EPW (39) is negligible when $\mu_2 \ll 1$, which is the case for $\delta n_{\mathrm{LW}} \ll n_0(k_p/k_{cz})^{1/2}$ (note that $\mu_1 > 1$ is possible under this condition). The short-wavelength EPW, which participate in the LA SRS, possesses the characteristic wavenumber $k_c \approx 2(\omega_0/c)\sin(\alpha/2) \sim 2(\omega_0/c)$; hence, to neglect the effect of the LW EPW nonlinearity on the SRS process, the following condition must be fulfilled:

$$\frac{\delta n_{\mathrm{LW}}}{n_0} \ll \left(\frac{\omega_{pe}}{\omega_0}\right)^{1/2}. \tag{43}$$

When the inequality (43) holds, the terms $\sim(\mathbf{v}_{\mathrm{LW}}, \nabla)\delta n_s$ in (38), which produce the nonlinear phase component $\tilde{\Psi}_{nl}$, may be omitted, leading to the final form (4) of the equation for the scattering plasma waves.

To conclude with, let us examine the modal structure of the short-wavelength free plasma modes in the presence of the given weakly, nonlinear LW EPW. The modal structure of the short-wavelength modes, which follows from (40), reads as

$$\begin{aligned}\frac{\delta\tilde{n}_s}{n_0} &= \frac{1}{2}\left(\sum_{\sigma=\pm 1} A^{(\sigma)}(\mathbf{r}) e^{i\sigma\omega_{\mathrm{BG}}t}\right) e^{i(\mathbf{k}_c, \mathbf{r})} \sum_{n,m=-\infty}^{+\infty} J_n(2\mu_1) \\ &\quad \cdot J_m(2\mu_2) e^{-i(n+2m)\phi} + \text{c.c.} \end{aligned} \tag{44}$$

where J_n are ordinary Bessel's functions. From (44), it is clear that the spectrum of the short-wavelength EPW in the presence of the weakly nonlinear LW EPW (39) consists of a number of sidebands shifted to integer multiples of the frequency and wavenumber of the LW EPW with respect to the original normal modes $(n, m = 0)$. When $\mu_1 \geq 1$ [i.e., $\delta n_{\mathrm{LW}} \geq n_0(2k_p/k_{cz})$], the amplitude of the sidebands becomes of order of the amplitudes of the fundamental modes $(n, m = 0)$. This coincides with the conclusions of [26] and [51], where the coupling was considered between the electron plasma waves having almost the same frequency but strongly differing in wavenumbers. Finally, let us obtain the modal structure of the short-wavelength modes in the case of weak modulation; we set $\mu_1 \ll 1$ and $\mu_2 = 0$ in (44) and make a series expansion in powers of μ_1 keeping the terms up to the second order

$$\begin{aligned}\frac{\delta\tilde{n}_s}{n_0} &= \sum_{\sigma=\pm 1} |A^{(\sigma)}(\mathbf{r})|\left\{(1-\mu_1^2)\cos\Psi_\sigma\right. \\ &\quad - \sigma\mu_1[\cos(\Psi_\sigma - \phi) - \cos(\Psi_\sigma + \phi)] \\ &\quad \left. + \frac{\mu_1^2}{2}[\cos(\Psi_\sigma + 2\phi) + \cos(\Psi_\sigma - 2\phi)]\right\} \end{aligned} \tag{45}$$

which exactly coincides with the modal structure obtained in [26] and [51] from a Lagrangian theory.

REFERENCES

[1] V. P. Silin, *Parametric Effect of High Intensity Radiation on Plasmas* (in Russian) Nauka, Moscow, 1973.

[2] J. F. Drake, P. K. Kaw, Y. C. Lee, G. Schmidt, C. S. Liu, and M. N. Rosenbluth, "Parametric instabilities of electromagnetic waves in plasmas," *Phys. Fluids*, vol. 17, pp. 778–785, 1974.

[3] W. M. Manheimer and E. Ott, "Parametric instabilities induced by coupling of high- and low-frequency plasma modes," *Phys. Fluids*, vol. 17, pp. 1413–1421, 1974.

[4] D. W. Forslund, J. M. Kindel, and E. L. Lindman, "Theory of stimulated scattering processes in laser-irradiated plasmas," *Phys. Fluids*, vol. 18, pp. 1002–1016, 1975.

[5] G. G. Comisar, "Theory of the stimulated Raman effect in plasmas," *Phys. Rev.*, vol. 141, pp. 200–203, 1966.

[6] C. B. Darrow, C. Coverdale, M. D. Perry, W. B. Mori, C. Clayton, K. Marsh, and C. Joshi, "Strongly coupled stimulated Raman backscatter from subpicosecond laser-plasma interactions," *Phys. Rev. Lett.*, vol. 69, pp. 442–445, 1992.

[7] T. M. Antonsen, Jr. and P. Mora, "Self-focusing and Raman scattering of laser pulses in tenuous plasmas," *Phys. Fluids B*, vol. 5, pp. 1440–1452, 1993.

[8] P. Mounaix, D. Pesme, W. Rosmus, and M. Casanova, "Space and time behavior of parametric instabilities for a finite pump duration in a bounded plasma," *Phys. Fluids B*, vol. 5, pp. 3304–3318, 1993.

[9] C. J. McKinstrie, R. Betti, R. E. Giacone, T. Kolber, and E. J. Turano, "Two-dimensional stimulated Raman scattering of short laser pulses," *Phys. Rev. E*, vol. 51, pp. 3752–3755, 1995.

[10] E. Esarey, P. Sprangle, J. Krall, and A. Ting, "Overview of plasma-based accelerator concepts," *IEEE Trans. Plasma Sci.*, vol. 24, pp. 252–288, 1996.

[11] N. E. Andreev, V. I. Kirsanov, and L. M. Gorbunov, "Stimulated processes and self-modulation of a short intense laser pulse in the laser wake-field accelerator," *Phys. Plasmas*, vol. 2, pp. 2573–2582, 1995.

[12] C. D. Decker, W. B. Mori, K.-C. Tzeng, and T. Katsouleas, "Modeling single-frequency laser-plasma acceleration using particle-in-cell simulations: The physics of beam breakup," *IEEE Trans. Plasma Sci.*, vol. 24, pp. 279–292, 1996.

[13] S. V. Bulanov, F. Perogaro, and A. M. Pukhov, "Two-dimensional regimes of self-focusing, wake-field generation, and induced focusing of a short intense laser pulse in underdense plasma," *Phys. Rev. Lett.*, vol. 74, pp. 710–713, 1995.

[14] S. V. Bulanov, I. N. Inovenkov, V. I. Kirsanov, N. M. Naumova, and A. S. Sakharov, "Nonlinear depletion of ultrashort and relativistically strong laser pulses in an underdense plasma," *Phys. Fluids B*, vol. 4, pp. 1935–1942, 1992.

[15] H. H. Klein, E. Ott, and W. M. Manheimer, "Effect of trapping on the saturation of the Raman backscatter instability," *Phys. Fluids*, vol. 18, pp. 1031–1033, 1975.

[16] C. I. Moore, A. Ting, K. Krushelnick, E. Esarey, R. F. Hubbard, B. Hafizi, H. R. Burris, C. Manka, and P. Sprangle, "Electron trapping in self-modulated laser wakefields by Raman backscatter," *Phys. Rev. Lett.*, vol. 79, pp. 3909–3912, 1997.
[17] K. Estabrook, W. L. Kruer, and B. F. Lasinski, "Heating by Raman backscatter and forward scatter," *Phys. Rev. Lett.*, vol. 45, pp. 1399–1403, 1980.
[18] C. S. Wilks, W. L. Kruer, E. A. Williams, P. Amendt, and D. C. Eder, "Stimulated Raman backscatter in ultraintense, short pulse laser-plasma interactions," *Phys. Plasmas*, vol. 2, pp. 274–279, 1995.
[19] N. H. Burnett and G. D. Enright, "Population inversion in the recombination of optically-ionized plasmas," *IEEE J. Quantum Electron.*, vol. 26, pp. 1797–1808, 1990.
[20] N. E. Andreev and S. Yu.Kalmykov, "On the theory of SRS of short laser pulse in underdense plasma," in *Proc. SPIE Laser Optics'95 and ICONO'95: Superintense Laser Fields*, vol. 2770, A. A. Andreev and V. M. Gordienko, Eds., 1996, pp. 53–64.
[21] ——, "Backward stimulated Raman scattering of a modulated laser pulse in plasmas," *Phys. Lett.*, vol. 227A, pp. 110–116, 1997.
[22] N. E. Andreev, L. M. Gorbunov, V. I. Kirsanov, A. A. Pogosova, and R. R. Ramazashvili, "Resonant excitation of wakefields by a laser pulse in a plasma," *Pis'ma Zh. Eksp. Teor. Fiz.*, vol. 55, pp. 551–555, 1992.
[23] D. R. Nickolson and A. N. Kaufman, "Parametric instabilities in turbulent, inhomogeneous plasma," *Phys. Rev. Lett.*, vol. 33, pp. 1207–1210, 1974.
[24] A. V. Maximov, W. Rozmus, V. T. Tichonchuk, D. F. DuBois, H. A. Rose, and A. M. Rubenchik, "Effects of plasma long-wavelength hydrodynamic fluctuations on stimulated Brillouin scattering," *Phys. Plasmas*, vol. 3, pp. 1689–1699, 1996.
[25] A. S. Sakharov, N. M. Naumova, and S. V. Bulanov, "Spectra of backward stimulated Raman scattering of short relativistically strong laser pulses in an underdense plasma," *Fizika Plazmy*, vol. 24, pp. 880–887, 1998.
[26] M. J. Everett, A. Lal, C. E. Clayton, W. B. Mori, T. W. Johnston, and C. Joshi, "Coupling between high-frequency plasma waves in laser-plasma interactions," *Phys. Rev. Lett*, vol. 74, pp. 2236–2239, 1995.
[27] N. E. Andreev and L. M. Gorbunov, "Stimulated Raman backscatter from short laser pulses in plasmas," in *Proc. SPIE*, vol. 2097, 1994, pp. 437–447.
[28] L. M. Gorbunov and V. I. Kirsanov, "Excitation of plasma waves by an electromagnetic wave packet," *Zh. Eksp. Teor. Fiz.*, vol. 93, pp. 509–518, 1987.
[29] K. Nakajima, D. Fisher, T. Kawakubo, H. Nakanishi, A. Ogata, Y. Kato, Y. Kitagawa, R. Kodama, K. Mima, H. Shiraga, K. Suzuki, K. Yamakawa, T. Zhang, Y. Sakawa, T. Shoji, Y. Nishida, N. Yugami, M. Downer, and T. Tajima, "Observation of ultrahigh gradient electron acceleration by a self-modulated intense short laser pulse," *Phys. Rev. Lett.*, vol. 74, pp. 4428–4431, 1995.
[30] C. J. McKinstrie and D. W. Forslund, "The detuning of relativistic Langmuir waves in the beat-wave accelerator," *Phys. Fluids*, vol. 30, pp. 904–908, 1987.
[31] D. W. Forslund, J. M. Kindel, and E. L. Lindman, "Plasma simulation studies of stimulated scattering processes in laser-irradiated plasmas," *Phys. Fluids*, vol. 18, pp. 1016–1030, 1975.
[32] N. Bloembergen and Y. R. Chen, "Optical nonlinearities of a plasma," *Phys. Rev.*, vol. 141, pp. 298–305, 1966.
[33] M. V. Goldman and D. F. Du Bois, "Stimulated incoherent scattering of light from plasmas," *Phys. Fluids*, vol. 8, pp. 1404–1405, 1965.
[34] N. E. Andreev, "Excitation of the Langmuir oscillations in plasmas by the field of a transversal wave," *Zh. Eksp. Teor. Fiz.*, vol. 59, pp. 2105–2109, 1970.
[35] G. G. Comisar, "Theory of the stimulated Raman effect in plasmas," *Sov. Phys. JETP*, vol. 32, p. 1141, 1971.
[36] P. Mounaix and D. Pesme, "Space and time behavior of parametric instabilities in the modified decay regime," *Phys. Plasmas*, vol. 1, pp. 2579–2590, 1994.
[37] C. J. McKinstrie and E. J. Turano, "Spatiotemporal evolution of parametic instabilities driven by short laser pulses: One-dimensional analysis," *Phys. Plasmas*, vol. 3, pp. 4683–4696, 1996.
[38] ——, "Spatiotemporal evolution of parametric instabilities driven by short laser pulses: Two-dimensional analysis," *Phys. Plasmas*, vol. 4, pp. 3347–3357, 1997.
[39] C. D. Decker, W. B. Mori, K.-C. Tzeng, and T. Katsouleas, "The evolution of ultra-intense, short-pulse lasers in underdense plasmas," *Phys. Plasmas*, vol. 3, pp. 2047–2056, 1996.
[40] A. S. Sakharov and V. I. Kirsanov, "Theory of Raman scattering for a short ultrastrong laser pulse in a rarefied plasma," *Phys. Rev. E*, vol. 50, pp. 3274–3282, 1994.
[41] B. I. Cohen and A. N. Kaufman, "Effects of beat-wave electron trapping on stimulated Raman and Thompson scattering," *Phys. Fluids*, vol. 21, pp. 404–412, 1978.
[42] E. Esarey, B. Hafizi, R. Hubbard, and A. Ting, "Trapping and acceleration in self-modulated laser wakefields," *Phys. Rev. Lett.*, vol. 80, pp. 5552–5555, 1998.
[43] K. Estabrook and W. L. Kruer, "Theory and simulation of one-dimensional Raman backward and forward scatter," *Phys. Fluids*, vol. 26, pp. 1892–1903, 1983.
[44] D. W. Forslund, J. M. Kindel, W. B. Mori, C. Joshi, and J. M. Dawson, "Two-dimensional simulations of single-frequency and beat-wave plasma heating," *Phys. Rev. Lett.*, vol. 54, pp. 558–561, 1984.
[45] N. E. Andreev and S. Yu. Kalmykov, "Spectral features of the stimulated Raman backscattering of modulated laser pulses in a plasma," *Fizika Plasmy*, vol. 24, pp. 926–936, 1998.
[46] ——, "Spectral features of the stimulated Raman backscattering of modulated laser pulses in a plasma," *Plasma Phys. Rep.*, vol. 24, pp. 862–872, 1998.
[47] N. E. Andreev, L. M. Gorbunov, V. I. Kirsanov, A. A. Pogosova, and R. R. Ramazashvili, "Resonant excitation of wakefields by a laser pulse in a plasma," *JETP Lett.*, vol. 55, pp. 571–576, 1992.
[48] T. M. Antonsen, Jr. and P. Mora, "Self-focusing and Raman scattering of laser pulses in tenuous plasmas," *Phys. Rev. Lett.*, vol. 69, pp. 2204–2207, 1992.
[49] P. Sprangle, E. Esarey, J. Krall, and G. Joyce, "Propagation and guiding of intense laser pulses in plasmas," *Phys. Rev. Lett.*, vol. 69, pp. 2200–2203, 1992.
[50] A. S. Sakharov, N. M. Naumova, and S. V. Bulanov, "Spectra of backward stimulated Raman scattering of short relativistically strong laser pulses in an underdense plasma," *Plasma Phys. Rep.*, vol. 24, pp. 818–824, 1998.
[51] M. J. Everett, A. Lal, C. E. Clayton, W. B. Mori, T. W. Johnston, and C. Joshi, "Coupling between electron plasma waves in laser-plasma interactions," *Phys. Plasmas*, vol. 3, pp. 2041–2046, 1996.
[52] L. M. Gorbunov and V. I. Kirsanov, "Excitation of plasma waves by an electromagnetic wave packet," *Sov. Phys. JETP*, vol. 66, pp. 290–294, 1987.
[53] ——, "Excutation of plasma waves by electromagnetic pulses," in *Proc. Lebedev Physics Institute*, O. N. Krokhin, Ed. New York: Nova Science, 1993, vol. 213, pp. 1–86.



Nikolai E. Andreev was born in Moscow, Russia, in 1945 and graduated from Moscow State University in 1967. He received the Ph.D. degree and Doctor of science degree in theoretical and mathematical physics from P.N. Lebedev Physical Institute of USSR Academy of Sciences, Moscow, in 1973 and 1985, respectively, and the rank of Professor from Russian Ministry of Education in 1998.

Since 1970, he has been a Research Physicist in the Division of Plasma Phenomena Theory of P.N. Lebedev Physical Institute of the Russian Academy of Sciences (RAS). He joined the High Energy Density Research Center of the Associated Institute for High Temperatures of RAS in 1987, where he is currently Head of the Laser Plasma Laboratory; he is also a Professor at the Moscow Institute of Physics and Technology. His current research includes laser light absorption, self-focusing and stimulated scattering, laser-driven particle accelerators, and nonlinear self-consistent structures in irradiated plasmas.

Serguei Yu. Kalmykov was born in 1972. He graduated from the Moscow Institute of Physics and Technology, Moscow, Russia, in 1995.

He is currently a Junior Research Physicist in the Laser Plasma Laboratory, High Energy Density Research Center, Russian Academy of Sciences, Moscow. His main interest is in the theory of parametric processes in laser plasmas.

Proposed Beatwave Experiment at RAL with the Vulcan CPA Laser

D. Neely, J. L. Collier, R. Allott, C. N. Danson, S. Hawkes, Z. Najmudin, R. J. Kingham, K. Krushelnick, and A. E. Dangor

Abstract—**A chirped pulse amplification (CPA) laser configuration capable of driving a plasma beat wave into saturation before modulation instabilities can grow is reported. The proposal is based on generating a single sub-ps, broad bandwidth pulse (~16 nm) and stretching and filtering to select two wavelength components (separation ~7 nm). The two spectral components are temporally stretched (to >100 ps) and separated (by ~1 ns). The pulses are then amplified sequentially in a single Nd : glass chain to greater than 15 J per pulse. Using a single-pass reflective grating compressor, the pulses are compressed (from 2 to 5 ps) and automatically synchronized. The system is capable of introducing a chirp, such that the compressed pulses can compensate for relativistic detuning of the plasma wave. The optimum laser amplification and recombination configuration for generating a saturated laser-driven beatwave is presented, and options for future work are discussed.**

I. Introduction

BECAUSE the beatwave scheme was first proposed [1] as a possible electron accelerator, it has generated much interest [2]. The beatwave acceleration scheme is based on two laser beams of different frequencies resonantly driving a plasma wave at the difference frequency. Extremely large electric fields>GVcm^{-1} can be envisaged. Experiments have been conducted using microwaves [3], CO_2 lasers [4], [5], and glass lasers [6], [7] as the drive beams. In the experiments, the plasma wave was not driven to its limiting relativistic saturation level because of the growth of modulational instabilities, which have a growth rate determined by the ion plasma frequency. We here propose to generate chirped pulse amplified (CPA) laser pulses [8], [9] of sufficiently short duration and intensity to drive the plasma wave to saturation before modulation instabilities can grow. The proposed system generates two pulses, which are separated everywhere in time in the amplification system and temporally overlapped only in the interaction region. The system is inherently jitter free, which is an essential requirement to use short pulses. The system also avoids any nonlinear optical interaction between the pulses in the beam line, which can generate unwanted sidebands, complicating diagnostics.

Manuscript received November 17, 1999; revised February 17, 2000.

D. Neely, J. L. Collier, R. Allott, C. N. Danson, and S. Hawkes are with the Central Laser Facility, Rutherford Appleton Laboratory, Chilton, Didcot, OX11 OQX Oxon, U.K. (e-mail: D.Neely@rl.ac.uk).

Z. Najmudin, R. J. Kingham, K. Krushelnick, and A. E. Dangor are with the Imperial College, SW7 2BZ, London, U.K.

Publisher Item Identifier S 0093-3813(00)07240-4.

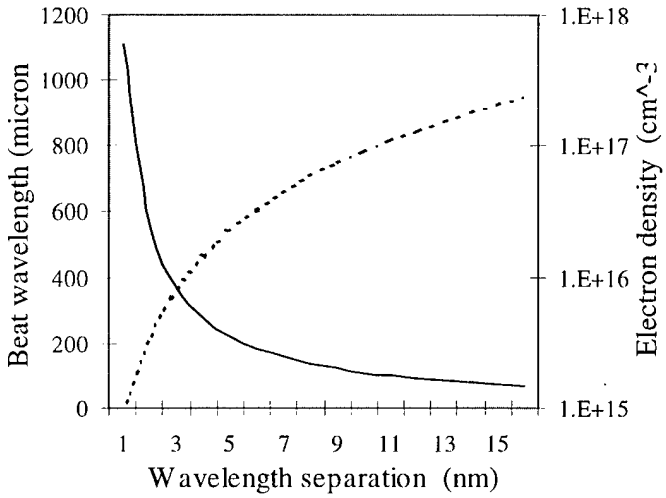


Fig. 1. Graph shows the beat wavelength (solid line) and the required electron density (dashed line) as a function of the wavelength separation of the two drive wavelengths centered on 1054 nm.

A requirement for a practical accelerator is that the radial gradients in the plasma wave should be smaller than the longitudinal field. To achieve this, a laser spot size comparable to or larger than the plasma wavelength λ_p is required. In Fig. 1, the plasma wavelength λ_p as a function of wavelength separation $\Delta\lambda = \lambda_0 - \lambda_1$ of the two laser components is plotted. This was calculated assuming that the beat frequency between the laser pulses is matched to the plasma frequency. The required electron density for resonant excitation of the plasma is also shown in Fig. 1. As λ_p is inversely proportional to $\Delta\lambda$, the required laser energy will scale as $\sim 1/\Delta\lambda^3$, favoring operation at the maximum possible drive laser wavelength separation. This is derived assuming a $1/\Delta\lambda^2$ energy dependence on focal spot size and an additional $1/\Delta\lambda$ dependence caused by the time required to reach saturation [10]. One-dimensional modeling [11] has shown that the modulational instability does not inhibit the plasma wave growth provided $I\lambda^2 > 10^{16}$ Wcm^{-2} μm^2. Thus, for $\Delta\lambda$ and pulse lengths of the order 10 nm and 5 ps, the required laser energy per pulse is of the order 10 J. This would give a relativistic saturated plasma wave amplitude $\delta n/n$ in the region of 10%.

Relativistic detuning of the plasma wave as it grows can be compensated by introducing a chirp [12] in the difference frequency between the two laser pulses as a function of time. This effectively changes the beat wavelength from the start to finish of the laser pulses to match the relativistic detuning in the plasma. Modeling has indicated that the effect of using a

0093–3813/00$10.00 © 2000 IEEE

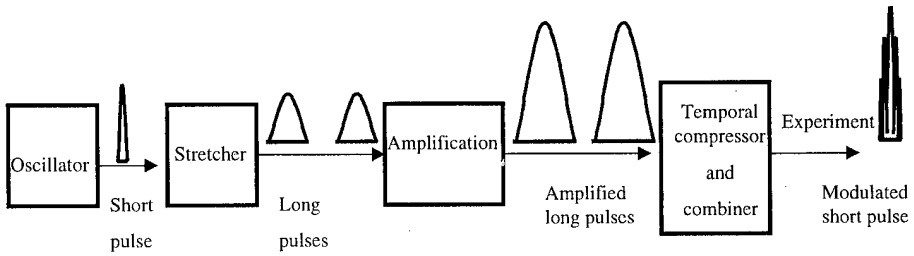


Fig. 2. Schematic diagram of the two-pulse CPA scheme.

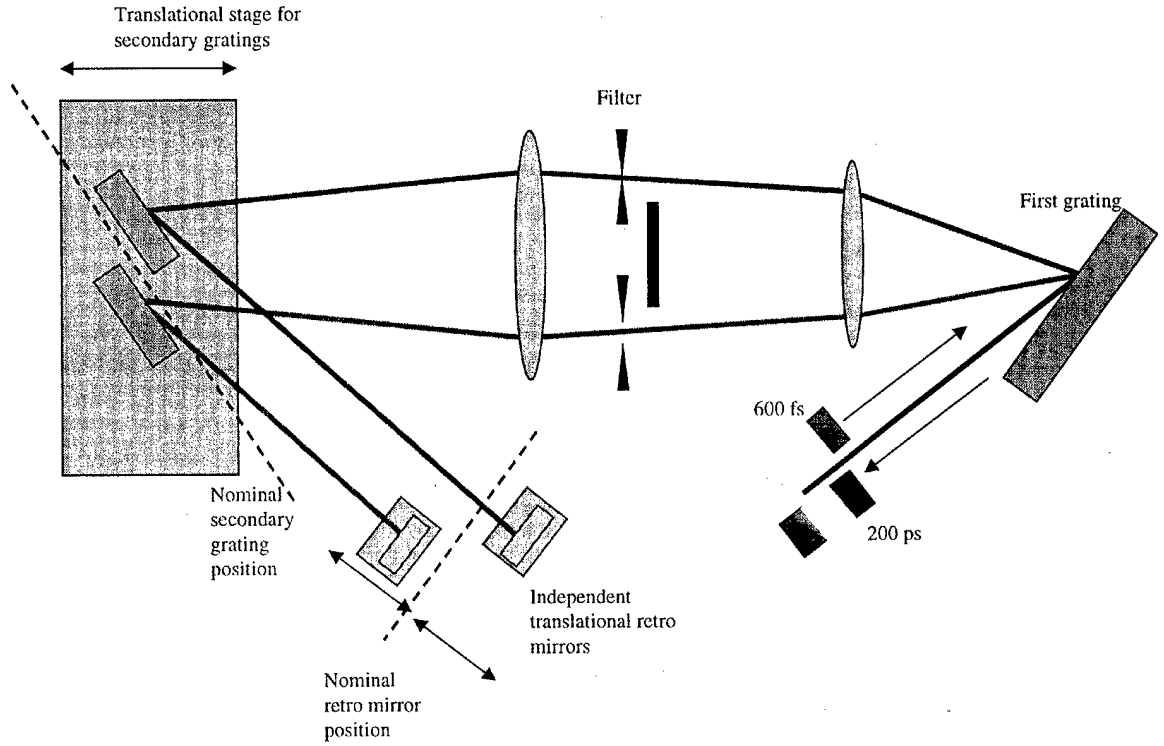


Fig. 3. Schematic diagram shows the stretcher. Independent motion of the secondary gratings and retro mirrors enables introduction of a controlled chirp of the beat frequency.

chirped difference frequency drive becomes more pronounced as the drive intensity is increased [13]. The CPA-based system we here propose is ideally suited for generating such a chirp.

There are considerable other advantages of using short laser pulses to drive the plasma wave, the most important of which is that a much larger density mismatch and inhomegenity can be tolerated, easing experimental requirements [14].

II. Laser Scheme

A layout of the Vulcan CPA system is shown schematically in Fig. 2. The initial oscillator pulse is generated by a commercial Kerr lens mode-locked oscillator using Ti : Sapphire as the active medium. It produces an 80-MHz pulse train of 5-nJ, 120-fs pulses of which one is used. The sech^2 pulse has a full-width at half maximum bandwidth of 16 nm centered at 1054 nm.

A. The Stretcher

The pulses are injected into a double-pass grating stretcher as shown in Fig. 3. An amplitude filter is used to select two narrow bandwidth portions of the input pulse. The bandwidth of each pulse is selected via the width of the slits, whereas the separation of the slits defines the wavelength difference and, hence, the beat frequency. The required amplitude filter is placed in the dispersed beam of the stretcher away from the Fourier plane. It is important to place the slits away from the Fourier plane because slits in this plane impose an extremely hard spectral clip on each pulse. Upon temporal compression, these hard clips would generate a pulse with a very poor temporal contrast after amplification, typically, no better than 100 : 1 many tens of pulse lengths away from the peak. By placing the slits away from this plane, the pulses are clipped in the near field and are thus selected with "softer" spectral edges and have better contrast ratios. This results in contrast ratio improvement of the amplified pulse of four to five orders of magnitude, as illustrated in Fig. 4.

An alternative scheme involving the use of an etalon placed inside an amplifier [15], which is regenerative, has been tested. However, this system is not as versatile as the stretcher described below, which can produce a changing beat frequency between the compressed pulses. This will be discussed below.

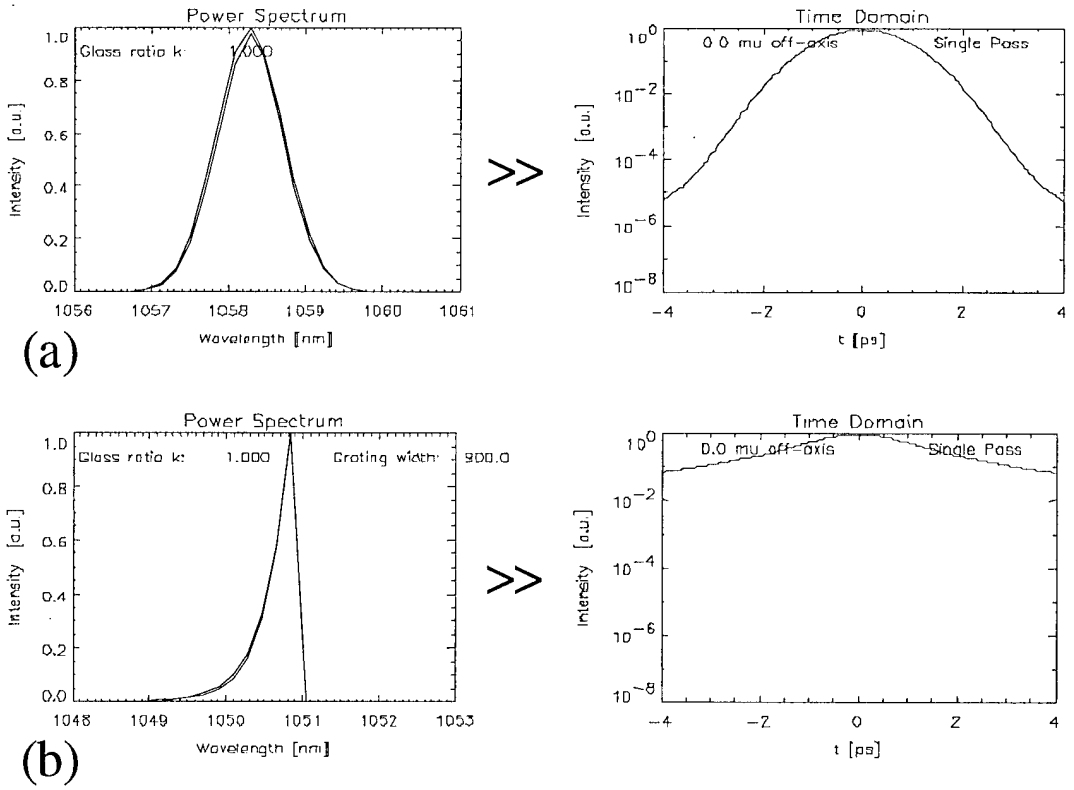


Fig. 4. Comparison of the power spectrum and pulse shape a soft- and hard-clipped pulse after amplification (a) filter away from the Fourier plane and (b) in the Fourier plane.

B. Introducing a Chirp on the Beat Frequency

A chirp in the wavelength difference between the compressed pulses beat can be realized in a straightforward manner, as indicated in Fig. 3. Two separate gratings, the locations of which are independently variable, replace the usual second grating in the stretcher. Also, two individual mirrors replace the retro mirror reflector, one for each grating. The two spectrally selected pulses can now be generated each with an arbitrary and different chirp. If the chirp parameter [16], $d\omega/dt$, for each pulse is β_1 and β_2, at the beat frequency $(\omega_2 - \omega_1)$, the frequency change after a time $\Delta\tau$ will be $\Delta\tau \cdot (\beta_1 - \beta_2)$. The chirp parameters β_1 and β_2 can be varied independently by changing the location of the gratings. For a few millimeter grating displacement, this frequency change can become comparable to the beat frequency.

The compressed pulse length of each pulse is determined by its bandwidth and chirp parameter. Thus, if two pulses are generated with different β's, they will have different pulse lengths if they possess the same bandwidth. This will limit the overlap time to the duration of the shorter pulse. Equal pulse lengths with different chirp parameters can be realized if each pulse has a bandwidth in proportion to its chirp. This is achieved by independently varying the slit widths and adjusting the grating positions to maintain the same pulse lengths. The intensity of the amplified compressed pulses can then be equalized by tuning the line center of the oscillator to effectively provide more energy for the narrower pulse.

For example, consider the case of two pulses centered at 1050 nm and 1056 nm, initially of equal bandwidth 1.0 nm. The unchirped bandwidth limited pulse duration will be ~1.5 ps. Assuming that $\beta_1 = 4.5 \times 10^{22}$ Hz/s (6 ps/nm) and $\beta_2 = 9 \times 10^{22}$ Hz/s (3 ps/nm), the nominal beat frequency of 1.6×10^{12} Hz will be chirped at 4.5×10^{10} Hz/ps. The pulse durations will be approximately 6.2 ps and 3.4 ps. Thus, the beat will only occur over 50% of the temporal overlap and the chirp will change the beat frequency by about 10% over this overlap time of 3.4 ps. However, either by reducing the bandwidth of the 1050-nm pulse to 0.5 nm (case 1) or increasing the bandwidth of the 1056 pulse to 2.0 nm (case 2), 100% overlap can be achieved with the same rate of change in beat frequency with a pulse duration of either 3.4 ps (case 1, 10% change in beat frequency) or 6.2 ps (case 2, 20% change in beat frequency). In selecting the pulse bandwidth, a compromise must be reached between maximizing the laser energy and maintaining a low B-integral.

C. Amplification

The two pulses produced by the stretcher are temporally separated. We propose to amplify the pulses in a single beam line. The propagation and amplification of these pulses by the Vulcan Nd:glass laser has been be modeled numerically. In the simulation, a fluorescence curve for the phosphate glass amplifier, centered at 1053.5 nm, is used as the gain curve. A top hat function simulates the spectral filter of the stretcher.

The amplifier chain gain bandwidth significantly reduces the amplification available for the spectrally separated pulses the further they are located from the center wavelength. Fig. 5 shows the gain required as a function of wavelength to maintain a

constant output of 20 J for a narrow bandwidth of 0.1 nm and a constant input energy from the oscillator of 1 nJ. However, such a narrow bandwidth cannot be amplified to the 20-J level through the Vulcan system. This is because if the bandwidth is too narrow, the stretched pulse length is short and the energy it can be amplified to is limited by damage thresholds and B-integral effects. Taking these factors into account, the wavelength separation as a function of bandwidth is presented in Fig. 6. This illustrates that larger separations necessarily need larger bandwidths. The gain available in the Vulcan amplifier chain is such that pulses at the 20-J level can be generated for $\Delta\lambda \sim 9$ nm with a bandwidth of $\sim$1.3 nm. The use of mixed phosphate and silicate glass amplifiers could in the future allow pulses of greater wavelength separation to be used in the system.

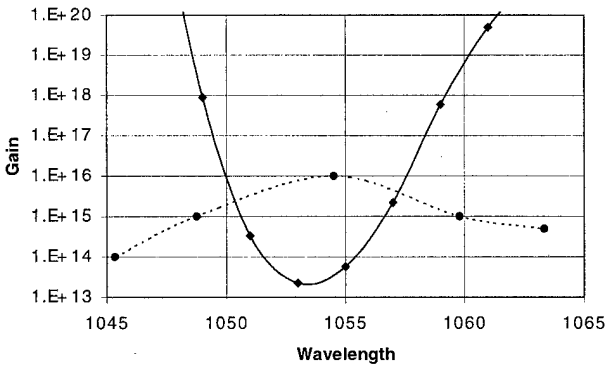


Fig. 5. Graph shows the required gain (solid line) in the Vulcan Nd : glass as a function of wavelength to maintain constant output energy of 20 J for 0.1-nm bandwidth pulse. The dashed line shows the system gain with an additional 9-mm diameter rod amplifier. The intersection represents the maximum wavelength difference the system can be used at.

III. Pulse Compression and Combining

A two-grating compressor is shown in Fig. 7. Both laser pulses are incident onto the first grating and overlap only partially on the second grating, as they diffract apart after leaving the first grating because of their different wavelengths. Thus, in the interaction region, not all of the initial energy in the pulses is used to drive the beat wave. D is the distance between the grating centers, L is the length of the gratings, p is the grooves density per meter, and N is the diffraction order at which we can define a cutoff wavelength λ_{cut}. For a single beam illuminating the first grating composed of two monochromatic components equally spaced about a central wavelength by $\sim\lambda_{\text{cut}}/2$, they will diffract out to such an extent that they both just miss the second grating and no energy is transmitted through the system. λ_{cut} is given by

$$\lambda_{\text{cut}} \approx \frac{2L\cos^2\phi_{\text{out}}}{NpD}. \tag{1}$$

Each wavelength component will fill a fraction $(1 - \Delta\lambda/\lambda_{\text{cut}})$ of the final grating resulting in an overlap fraction of $(1 - 2\Delta\lambda/\lambda_{\text{cut}})$. If we require the beams to overlap significantly (i.e., at least overlap over the central half of the final grating), we can define a maximum wavelength separation $\Delta\lambda \leq \lambda_{\text{cut}}/4$. The present Vulcan compressor uses two 1740 lines per millimeter CPA gratings that have a surface ruling across 390 × 190 mm and are used in first order with a grating separation of 3.5 m and at an input angle of 73.2°. This gives $\lambda_{\text{cut}} \sim 30$ nm. Therefore, to use the existing system would give a maximum wavelength separation of $\Delta\lambda \leq 7$ nm. This corresponds to a plasma wave $\lambda_p \geq 158$ μm.

The three-grating compressor shown in Fig. 8 does not suffer from the problem of limited beam overlap. In this scheme, the two input pulses must be on different beam lines that are incident onto two separate input gratings. In this scheme, the beams must diffract sufficiently that when the two input gratings are just touching, full beam overlap is obtained on the final grating. This condition can be expressed as $\Delta\lambda = \lambda_{\text{cut}}/2$. By appropriately increasing the separation between the input gratings, full overlap on the second grating can be achieved at $\Delta\lambda \geq \lambda_{\text{cut}}/2$. An additional degree of freedom is available in that it is possible to move the input gratings in opposite directions relative to the output grating and introduce temporally dependent opposite chirps on the two pulses. It should be noted that the three-grating compressor requires amplification of the pulses in separate chains or a suitable method of separating the pulses before the input gratings.

The maximum intensity $I_{\max}$ in the focal region that can be delivered using a two-grating compressor for a beat wave experiment is given to a first-order approximation by

$$I_{\max} = SD_T e_d^2 (1 - \Delta\lambda/\lambda_{\text{cut}}) \left(\tau\pi\lambda_p^2\right)^{-1} \tag{2}$$

where S is the surface area of the gratings, e_d is the diffraction efficiency, and D_t is the damage threshold energy density of the gratings. Experience [9] with the 1740 lines per millimeter, 1053-nm optimized, gold overcoated holographic gratings (supplied by J. Yvon) in the Vulcan CPA system has shown that sustainable long-term (hundreds of shots) average drive fluence is approximately 130 mJcm^{-2} for no detectable surface degradation. The diffraction efficiencies of the two wavelengths are equal to within a few percent. Setting the gratings at an input angle of 73.2° gives a measured first-order diffraction efficiency e_d of 89%. For $\Delta\lambda = 7$ nm, this gives $I_{\max} \sim 7/\tau$ (ps) × 10^{16} Wcm^{-2} with a Rayleigh length $\sim$ centimeter. In adapting the Vulcan system to support two narrow spectral components, self-phase modulation effects limit the maximum deliverable energy per pulse, reducing the above to $I_{\max} \sim 3/\tau$ (ps) × 10^{16} Wcm^{-2}. This estimate is approximate because it does not account for the fact that the beam has different sizes in the horizontal and vertical planes caused by the beam aperture being noncircular.

The two-grating compressor is much simpler to set up and is ideal in situations in which the spectral separation is small. In situations in which it is necessary to have a long duration stretched pulse in the amplifier to avoid nonlinear effects, the three-grating compressor is advantageous.

The Vulcan CPA system is currently being upgraded [17] to the PW level, and when completed in 2002, the system will be capable of delivering pulses suitable for a beat-wave drive. The system will use 1480 lines per millimeter gratings separated by 13.5 m, which gives $\lambda_{\text{cut}} \sim 31$ nm, very similar to the present configuration. However, with an increase in grating size to $\sim$0.9-m diameter, the system will be able to support energies

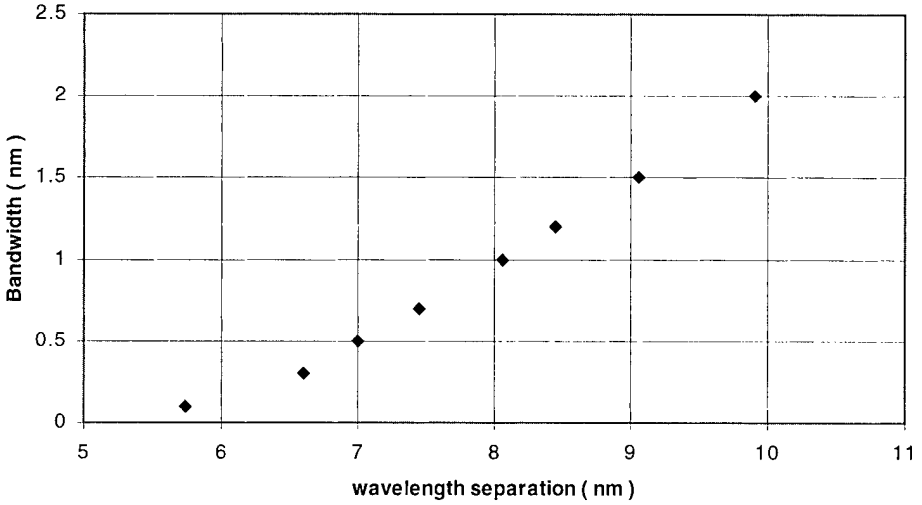


Fig. 6. Graph shows the minimum pulse bandwidth necessary to maintain ~20 J of energy per pulse as a function of the wavelength separation between the laser pulses on Vulcan. This limit is set to avoid damage thresholds in the amplifier chain and B-integral effects.

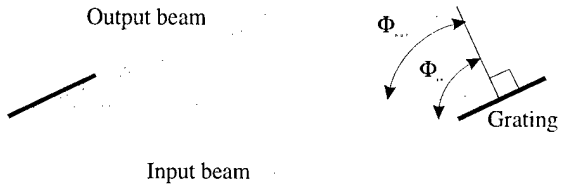


Fig. 7. Schematic layout shows a two-grating pulse compressor and combiner.

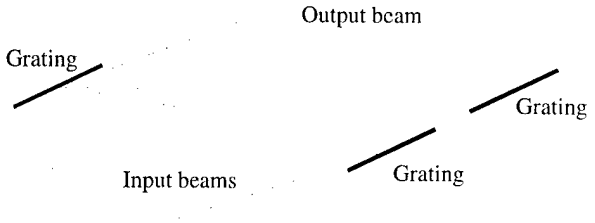


Fig. 8. Schematic layout shows a three-grating pulse compressor and combiner.

of ~100 J per pulse, enabling much longer interaction lengths to be achieved.

IV. Summary

A novel laser configuration capable of generating the necessary conditions to drive a plasma beat wave into saturation before modulation instabilities can grow to cause significant disruption is proposed. The scheme relies on generating a single sub-ps, broad bandwidth pulse and spectrally stretching and filtering to select two wavelength components that are inherently synchronous. A stretcher capable of introducing a chirp such that the compressed pulses have a changing beat frequency capable of compensating for relativistic detuning is proposed. The two laser pulses can also be amplified on the Vulcan CPA Nd:glass chain greater than 20 J per pulse and will be used early in 2000 for a beat-wave experimental investigation.

References

[1] T. Tajima and J. M. Dawson, *Phys. Rev. Lett.*, vol. 43, p. 267, 1979.
[2] E. Esarey, P. Sprangle, J. Krall, and A. Ting, *IEEE Trans. Plasma Sci.*, vol. 24, pp. 252–288, Apr. 1996.
[3] J. H. Rogers, D. Q. Hwang, J. C. Thomas, R. L. Horton, J. Killeen, and G. Dimonte, *Phys. Fluids B*, vol. 4, p. 1920, 1992.
[4] C. E. Clayton, C. Joshi, C. Darrow, and D. Umstadter, *Phys. Rev. Lett.*, vol. 54, p. 2343, 1985.
[5] C. E. Clayton, K. A. Marsh, A. Dyson, M. Everett, A. Lal, W. P. L eemans, R. Williams, and C. Joshi, *Phys. Rev. Lett.*, vol. 70, p. 37, 1993.
[6] F. Amiranoff, M. Laberge, J. R. Marques, F. Moulin, E. Fabre, B. Cros, G. Matthieussent, P. Benkheiri, F. Jacquet, J. Meyer, P. Mine, C. Stenz, and P. Mora, *Phys. Rev. Lett.*, vol. 68, p. 3710, 1992.
[7] A. Dyson, A. E. Dangor, A. K. L. Dymoke-Bradshaw, T. Ashfar-Rad, P. Gibbon, A. R. Bell, C. Danson, C. B. Edwards, F. Amiranoff, G. Matthieusent, S. Karttunen, and R. Salomaa, *Plasma Phys. Contr. Fusion*, vol. 38, p. 505, 1996.
[8] D. Strikland and G. Mourou, *Opt. Commun.*, vol. 56, pp. 219–221, 1985.
[9] C. Danson, J. Collier, D. Neely, L. J. Barzanti, A. Damerell, C. B. Edwards, M. H. R. Hutchinson, M. H. Key, P. A. Norreys, D. A. Pepler, I. N. Ross, P. F. Taday, W. T. Toner, M. Trentleman, F. N. Walsh, T. B. Winstone, and R. W. W. Wyatt, *J. Mod. Opt.*, vol. 45, pp. 1653–1669, 1998.
[10] M. N. Rosenbluth and C. S. Liu, *Phys. Rev. Lett.*, vol. 29, p. 701, 1972.
[11] P. Mora, D. Pesme, A. Heron, G. Laval, and N. Silvestre, *Phys. Rev. Lett.*, vol. 61, p. 14, 1988.
[12] A. Ghizzo, P. Bertrand, J. Lebas, T. W. Johnstonand, and M. Shoueri, *Phys.Plasmas*, vol. 5, no. 11, pp. 4041–4054, 1998.
[13] R. J. Kingham, private communication.
[14] C. Joshi, C. E. Clayton, W. B. Mori, J. M. Dawson, and T. Katsouleas, "Comments on plasma physics," *Controlled Fusion*, vol. 16, pp. 65–77, 1994.
[15] A. Hankla, A. B. Bullock, W. E. White, J. A. Squier, and C. P. J. Barty, *Opt. Lett.*, vol. 22, pp. 1713–1715, 1997.
[16] C. Fiorini, C. Sauteret, C. Rouyer, N. Blanchot, S. Seznec, and A. Migus, *IEEE J. Quantum Electron.*, vol. 30, pp. 1662–1670, 1994.
[17] C. N. Danson, R. Allott, J. Collier, R. Clark, C. B. Edwards, S. Hancock, P. Hatton, S. Hawkes, M. H. R. Hutchinson, C. Hernandez-Gomez, A. Kidd, W. Lester, D. Neely, P. Norreys, M. Notley, D. Pepler, M. Pitts, C. Reason, D. A. Rodkiss, T. B. Winstone, R. W. W. Wyatt, and B. Wyborn, Int. Fusion Sci. Applicat. Conf. Proc., Bordeaux, France, 1999, to be published.

D. Neely, photograph and biography not available at the time of publication.

J. L. Collier, photograph and biography not available at the time of publication.

R. Allott, photograph and biography not available at the time of publication.

C. N. Danson, photograph and biography not available at the time of publication.

S. Hawkes, photograph and biography not available at the time of publication.

Z. Najmudin, photograph and biography not available at the time of publication.

R. J. Kingham, photograph and biography not available at the time of publication.

K. Krushelnick, photograph and biography not available at the time of publication.

A. E. Dangor, photograph and biography not available at the time of publication.

Scaling of Accelerating Gradients and Dephasing Effects in Channel-Guided Laser Wakefield Accelerators

Richard F. Hubbard, *Member, IEEE*, Phillip Sprangle, *Fellow, IEEE*, and Bahman Hafizi, *Member, IEEE*

***Abstract*—Future wakefield accelerator (LWFA) experiments are expected to operate in the short pulse resonant regime and employ some form of laser guiding, such as a preformed plasma channel. Performance of an LWFA may be characterized by the maximum axial electric field E_m, the dephasing length L_d, and the corresponding dephasing limited energy gain W_d. Dephasing is characterized by the normalized phase slippage rate $\Delta\beta_p$ of the wakefield relative to a particle moving at the velocity of light. This paper presents analytical models for all of these quantities and compares them with results from simulations of channel-guided LWFAs. The simulations generally confirm the scaling predicted by the analytical models, agreeing within a few percent in most cases. The results show that with the proper choice of laser and channel parameters, the pulse will propagate at a nearly constant spot size r_M over many Rayleigh lengths and generate large accelerating electric fields. The spot size correction to the slippage rate is shown to be important in the LWFA regime, whereas $\Delta\beta_p$ is essentially independent of laser intensity. An example is presented of a 25-TW, 100-fs laser pulse that produces a dephasing limited energy gain in excess of 1 GeV.**

***Index Terms*—Intense lasers, laser-plasma interactions, laser wakefield accelerators, optical guiding, plasma channels.**

I. Introduction

PLASMA-BASED accelerators such as the laser wakefield accelerator (LWFA) offer the possibility of accelerating gradients far beyond those achievable by conventional means. In the LFWA [1]–[3], the laser produces a large amplitude plasma wave that moves with the laser pulse and traps and accelerates the electrons. The (full-width, at half-maximum) laser pulse length τ_L in the regime for a LWFA is less than 1 ps, the beam power exceeds 10^{12} W = 1 TW, and the spot size is typically tens of microns. The axial electric field and accelerating gradient can approach the nonrelativistic wavebreaking field given by [3]

$$E_0 = mc\omega_{p0}/e \tag{1}$$

where $\omega_{p0} = (4\pi n_0 e^2/m)^{1/2}$ is the electron plasma frequency based on the nominal on-axis plasma density n_0, and e and m are the electron charge and mass. The field E_0 thus depends only on the plasma density and can be expressed in volts/meter as E_0 [V/m] $= 96 n_0^{1/2}$ [cm^{-3}]. At a plasma density of 10^{18} cm^{-3}, $E_0 \approx 100$ GV/m, which is approximately three orders of magnitude above the highest accelerating gradients in conventional accelerators. The wavelength of the plasma wave in a LWFA is near the plasma wavelength $\lambda_p = 2\pi c/\omega_{p0}$. In the original resonant or "standard" LWFA concept [1]–[8], [49], the laser pulse length $c\tau_L$ is somewhat shorter than λ_p, and the laser wavelength λ is much shorter than λ_p.

The electron beam energy from an LWFA is determined by the average accelerating gradient $\langle E_z \rangle$ and the effective interaction length L_a over which acceleration can be maintained. Although $\langle E_z \rangle$ can be large, several factors may limit the interaction. Perhaps the most important of these is diffraction of the laser pulse. The characteristic distance for the beam to expand because of diffraction is the Rayleigh length Z_R, given by

$$Z_R = \pi r_0^2/\lambda \tag{2}$$

where r_0 is the radius or spot size of the laser pulse at the focus. We can show that the maximum energy gain in an unguided LWFA is less than 100 MeV for any reasonable laser parameters [6]. A recent unguided LWFA experiment produced an energy gain of 1.6 MeV [7].

Much higher energies may be achieved if the pulse can be optically guided over many Rayleigh lengths, thus, increasing L_a. One basic approach is to modify the index of refraction η of the plasma so that it peaks on axis [2], [3], [6], [8], [9]. A very intense laser pulse may generate the desired refractive index profile through relativistic corrections to the electron mass [1], [8]–[12]. However, this relativistic guiding mechanism can be shown to be ineffective in the resonant LWFA regime where $c\tau_L < \lambda_p$ [10]. It is believed to play an important role in the long pulse, self-modulated LWFA regime, where $c\tau_L \gg \lambda_p$, and the laser power exceeds the critical relativistic focusing power P_r [8]–[12]. (The critical power in terawatts is given by [9]–[12] P_r [TW] $= 0.017(\lambda_p/\lambda)^2$.) Several experiments operating in this regime [13]–[18] have reported detection of electrons at high energies, exceeding 100 MeV in some cases. However, propagation physics of the laser pulse is highly nonlinear, and the electron beam quality is generally poor, with a very large spread in electron energies. For this reason, the standard or resonant regime is generally considered more suitable for a practical accelerator.

Preformed plasma channels offer a promising method for providing such guiding for a resonant LWFA. Channels produced by one or more lower power axicon-focused lasers [19]–[24] or capillary discharge [25]–[34] have successfully guided laser

Manuscript received October 12, 1999; revised January 28, 2000. This work was supported by the Department of Energy and the Office of Naval Research.

R. F. Hubbard and P. Sprangle are with the Beam Physics Branch, Plasma Physics Division, Naval Research Laboratory, Washington, DC 20375-5346 USA (e-mail: hubb@ppd.nrl.navy.mil).

B. Hafizi is with the Icarus Research, Inc., Bethesda, MD 20824-0780 USA.

Publisher Item Identifier S 0093-3813(00)09158-X.

0093–3813/00$10.00 © 2000 IEEE

pulses over distances of several centimeters at relatively high intensities. In both cases, the channel has a density minimum on-axis in which the plasma temperature is somewhat higher. The axicon-focus method, which was originally developed by Milchberg *et al.* [19]–[22], uses a line focus to create the heated channel. The capillary discharge method, which was pioneered by Zigler *et al.* [25]–[33], is an electrically driven system that produces the plasma by ablating material from the wall of the capillary. Recent experiments have demonstrated guiding of terawatt pulses over 2 cm [29] and lower intensity pulses over 6.6 cm [27]. Hosokai *et al.* [34] have demonstrated guiding in gas-filled capillary discharges in which the pinch current in the capillary plays an important role. In most guiding experiments to date, the plasma density has exceeded 10^{18} cm^{-3}, which requires exceedingly short laser pulses to be in the standard LWFA regime. Although these methods are promising, laser wakefield acceleration and guiding in a preformed plasma channel has not yet been demonstrated experimentally.

A second major limitation on laser wakefield acceleration is caused by the mismatch between the accelerated electron velocity and the phase velocity of the wake potential or plasma wave that provides the acceleration [1], [3], [6], [8]. Acceleration will persist only as long as the particle remains in the accelerating and focusing portion of the wake potential. The wake phase velocity is approximately equal to the group velocity of the laser pulse and thus is smaller at the higher plasma densities that may produce larger amplitude accelerating fields. If optical guiding is successfully achieved, dephasing is likely to be the primary factor limiting the energy gain.

This paper treats laser pulse propagation, wakefield generation, and dephasing effects in a channel-guided LFWA. Section II reviews analytical models for the laser spot size r_M in the channel, the peak accelerating electric field E_m, and the dephasing effects. The approach here is similar to that taken by Hubbard *et al.* [32], except that the analysis is formulated by the laser strength parameter a_0 instead of the laser peak power P_0. Although the laser spot size in the channel is determined by the channel parameters, the range of these parameters is strongly constrained by the laser pulse length, because for a given τ_L, wakefield generation is optimized for a relatively narrow range of plasma densities. The model for the peak electric field is valid for the standard LWFA regime in which the pulse length is less than the plasma wavelength, and it includes an approximate amplitude and pulse length scaling based on previously published one-dimensional (1-D) numerical models [3], [35]. Dephasing is characterized by a normalized phase slippage rate $\Delta\beta_p$, leading to the usual estimates for the dephasing length L_d and dephasing-limited energy gain W_d. The dephasing model includes the finite spot size correction to the slippage rate and assumes that the wakefield is sinusoidal and that acceleration and focusing of the electron beam ends when the wakefield slips by a quarter of a plasma wavelength relative to a particle moving at c.

The analytical models are compared with results from a laser propagation simulation developed originally by Krall *et al.* [11], [36]. Simulations are restricted to the regime of interest for future channel-guided resonant LWFA experiments. The laser pulse is injected into the channel with a spot size near the matched radius r_M; so oscillations in the laser spot size are modest in amplitude. Section III describes changes in the pulse during propagation and the wakefield generation process. The simulation results generally agree well with the models described in Section II. The simulations also exhibit additional features such as pulse distortion and envelope damping of ultrashort pulses. These processes have been recently analyzed by Sprangle *et al.* [37]–[39] and Esarey and Leemans [40] and are caused in part by finite pulse length corrections to the wave equation [10], [11], [37]–[41]. Also, the scaling and evolution of the peak accelerating field E_{ms} exhibit behavior not contained in the analytical models. Section IV describes an analysis of dephasing effects in the simulations and compares the results with the analytical models. The agreement between the simulation and analytical phase slippage rates is excellent. There is a clear tradeoff in the choice of laser pulse length for a LWFA. Short pulse lengths and high plasma densities can generate very high accelerating gradients, but the dephasing effects may severely limit the energy gain. An example is presented of a channel-guided LWFA driven by a 25-TW, 100-fs long 0.8-μm wavelength laser that generates peak accelerating gradients of 10 GV/m and a dephasing-limited energy gain in excess of 1 GeV.

II. Theoretical Background

This section reviews analytical models for various laser and plasma quantities in a channel-guided, resonant LWFA. These predictions are later compared with LWFA simulations using a two-dimensional laser propagation code.

A. Equilibrium Spot Size and Intensity

For optical guiding in a LWFA, it is desirable to minimize any oscillations in the laser spot size r_L. A matched (constant spot-size) optical beam can occur if beam expansion caused by diffraction is exactly balanced by the refraction. An exact equilibrium exists for a beam with a Gaussian radial profile and a plasma channel with a parabolic radial profile. For a Gaussian laser beam, the laser electric field $\mathbf{E}_L$and vector potential $\mathbf{A}_L$ scale as $\exp(-r^2/r_L^2)$. The laser amplitude is expressed by the normalized vector potential $a = e|\mathbf{A}_L|/mc^2$. The parabolic density channel profile is given by $n(r) = n_0 + \Delta n r^2/r_{ch}^2$, where r_{ch} is the channel radius. With these assumptions, the equilibrium or matched beam radius is [3], [5], [8]

$$r_M = (r_{ch}^2/\pi r_e \Delta n)^{1/4} \tag{3}$$

where $r_e = e^2/mc^2$ is the classic electron radius. Equation (3) assumes the laser power is small compared with the critical powers for relativistic [3], [6], [8]–[12] or nonlinear atomic [6] focusing, an assumption that is generally valid in the resonant LWFA regime. The radial profiles for the normalized vector potential $a(r)$ and plasma density $n(r)$ are shown in Fig. 1 for an example with $\Delta n/n_0 = 2$ and $r_{ch}/r_M = 3$.

The choice of r_{ch} is somewhat arbitrary in practice because the behavior of the laser pulse is insensitive to $n(r)$ for $r \gg r_M$. In the simulation model used in this paper [11], [36], it is desirable to limit the plasma density far from the axis, so the plasma density is assumed to be constant for $r > r_{ch}$. This assumption is reflected in Fig. 1. If no limit is imposed on the

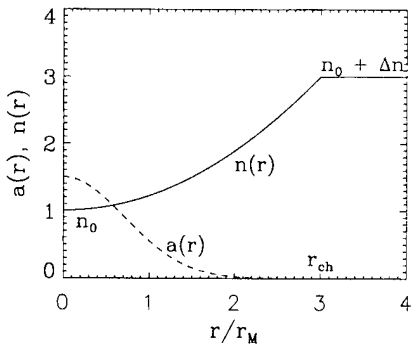


Fig. 1. The radial profiles for the normalized vector potential $a(r)$ and plasma density $n(r)$ for a Gaussian laser pulse (dashed line) propagating at the matched spot size r_M in a parabolic plasma density channel (solid line). The channel has on-axis density n_0, normalized channel depth $\Delta n/n_0 = 2$, and channel radius $r_{ch} = 3r_M$.

density, the number of free parameters defining the channel may be reduced from three to two by defining a single nominal channel radius r^*_{ch} in which the normalized channel depth $\Delta n/n_0 = 1$. The two definitions of the channel radius are thus related by $r^*_{ch} \equiv r_{ch}/(\Delta n/n_0)^{1/2}$; so $r^*_{ch}/r_M = 2.12$ in Fig. 1. A shallow or weak channel has $r^*_{ch} \gg r_M$, whereas a deep or strong channel has $r^*_{ch} \sim r_M$. Extremely deep channels with $r^*_{ch} \ll r_M$ are probably not practical and are not considered in this study.

The evolution of $r_L(z)$ may be described by an envelope equation [3], [8], [42] that may include other refractive contributions, such as relativistic guiding. If the focused radius r_0 is near the matched beam radius r_M, so that $|r_0 - r_M| \ll r_M$, the spot size $r_L(z)$undergoes envelope oscillations with a period

$$\lambda_c = \pi Z_M = \pi^2 r_M^2/\lambda. \tag{4}$$

Here, $Z_M = \pi r_M^2/\lambda$ is the Rayleigh length associated with the matched beam radius.

Although the equilibrium spot size is independent of the laser parameters in this model, the accelerating gradient in a resonant LFWA is a sensitive function of the ratio of the pulse length to the plasma wavelength. It is convenient to characterize the linkage between the pulse length and the plasma density by the resonance ratio, α_r, defined as the ratio of the pulse length to the plasma wavelength [32]

$$\alpha_r \equiv c\tau_L/\lambda_p. \tag{5}$$

Thus, the plasma wavelength $\lambda_p = c\tau_L/\alpha_r$, and the on-axis density is

$$n_0 = \left(\frac{\pi m}{e^2}\right)\frac{\alpha_r^2}{\tau_L^2}. \tag{6}$$

The linkage between the laser pulse length and the spot size may be illustrated by expressing r_M by r_{ch}, τ_L, α_r, and the normalized channel depth $\Delta n/n_0$. The (squared) matched spot size r_M^2 is given by

$$r_M^2 = \left(\frac{c}{\pi}\right)\frac{r_{ch}\tau_L}{\alpha_r(\Delta n/n_0)^{1/2}} = \left(\frac{c}{\pi}\right)\frac{r^*_{ch}\tau_L}{\alpha_r} \tag{7}$$

where the second form is in terms of the nominal channel radius $r^*_{ch} = r_{ch}/(\Delta n/n_0)^{1/2}$. From this scaling in (7), it is apparent that long pulse length tends to increase the spot size. Although the matched radius given in (3) is independent of the on-axis density n_0, there are practical limits on how large the normalized channel depth $\Delta n/n_0$ can be or, equivalently, how small r^*_{ch} can be.

The matched beam intensity for a Gaussian pulse is given by $I_0 = 2P_0/\pi r_M^2$. The peak intensity I_0 of the matched laser pulse in the channel will thus be determined by the channel parameters and the peak laser power P_0. The laser intensity is often expressed by the laser strength parameter a_0, which is defined as the maximum value of the normalized vector potential a within the laser pulse. The square of the laser strength parameter is related to the intensity by

$$a_0^2 = \frac{2e^2\lambda^2 I_0}{\pi m^2 c^5} = \frac{4e^2\lambda^2 P_0}{\pi^2 m^2 c^5 r_M^2}. \tag{8}$$

For a resonant LWFA accelerator, it is desirable to choose laser and channel parameters so that $a_0 \sim 1$.

B. Electric Field Models

The accelerating electric field in a LWFA scales with the characteristic field E_0 given in (1). This quantity is the usual 1-D nonrelativistic wavebreaking field. The peak accelerating field E_m in a LWFA depends primarily on E_0, a_0, and α_r. For a resonant LWFA, the peak field is generally located at a point that is approximately a plasma wavelength behind the head of the pulse. Analytical and numerical estimates of E_m have been reported by Sprangle *et al.* [35] and Esarey *et al.* [3] using the 1-D nonlinear Poisson equation. Their results suggest a general scaling for a linearly polarized laser pulse that can be expressed in the following form:

$$E_m/E_0 = \alpha_E \frac{a_0^2/2}{(1 + a_0^2/2)^{1/2}} S(\alpha_r). \tag{9}$$

Here, α_E is an overall scale factor, and the function $S(\alpha_r)$ depends on the pulse shape. The numerical results reported by Esarey *et al.* [3] suggest that $\alpha_E \approx 0.8$, and $S(\alpha_r)$ resembles a sine curve peaked near $c\tau_L = \lambda_p/2$. The validity of this choice for α_E and $S(\alpha_r) = \sin \pi\alpha_r$ is examined in Section III-B, using the two-dimensional (2-D) simulation code.

C. Dephasing and Energy Gain

Dephasing occurs because an electron moving at axial velocity $v_z \approx c$ will eventually slip out of the accelerating and focusing portion of the wakefield because of the difference between the particle velocity and the wake phase velocity. The phase velocity $\beta_p c$ of the wake is approximately equal to the group velocity $\beta_g c$ of the laser pulse in the plasma channel. If we include the finite spot-size correction to the group and phase velocities [6], [40] and neglect other contributions, the wake phase velocity is

$$\beta_p \approx 1 - \lambda^2/2\lambda_p^2 - \lambda^2/2\pi^2 r_M^2. \tag{10}$$

The last term in (10) is the spot-size correction to β_p. The normalized slippage rate relative to a particle moving at c is $\Delta\beta_p = 1 - \beta_p$. Dephasing is assumed to occur when the wake slips by a distance $\lambda_p/4$ relative to a particle moving at c. The factor of 4 develops because although one-half of the wake cycle has an accelerating electric field, electrons on the second half of the accelerating cycle experience a defocusing radial electric field

that expels them from the channel. The dephasing distance L_d is, therefore

$$L_d = \lambda_p/4\Delta\beta_p. \tag{11}$$

This analysis neglects contributions to the pulse group velocity from relativistic quiver motion and atomic focusing in the intense laser field and uses the on-axis value of the plasma density. Simulations that test the validity of this assumption are described in Section IV. The analysis also assumes that the relativistic factor γ_e associated with the particle, averaged over the acceleration cycle, is much greater than $\gamma_p = (1-\beta_p^2)^{-1/2}$.

Most analyzes of dephasing neglect the finite spot-size contribution. In this case, the uncorrected laser pulse group velocity (and wake phase velocity) is $\beta_{g0} \approx 1-\lambda^2/2\lambda_p^2$, the uncorrected dephasing length is $L_{d0} = \lambda_p^3/2\lambda^2$, and the phase velocity relativistic factor is $\gamma_p = \lambda_p/\lambda$.

However, the spot-size correction to the group velocity [6], [40] is frequently important in the regime for LWFAs. The effect is to increase the phase slippage rate by a factor $(1+\alpha_s)$, where

$$\alpha_s = \lambda_p^2/\pi^2 r_M^2. \tag{12}$$

This effect reduces the dephasing length and the dephasing-limited energy gain. Simulations that confirm the importance of retaining this correction are presented in Section IV-B.

The dephasing-limited energy W_d is obtained by averaging the electric field over the quarter-cycle dephasing distance. In the linear regime, the wakefield is sinusoidal; so the average accelerating field $\langle E_z \rangle = 2E_m/\pi$. If we neglect the spot-size correction, this leads to the usual dephasing limit on energy with the relativistic factor γ_{d0} given by

$$\gamma_{d0} = 2(E_m/E_0)(\lambda_p^2/\lambda^2). \tag{13}$$

Applying the finite spot-size correction [6], [40] to the dephasing length, and using (9) for E_m with $S(\alpha_r) = \sin \pi\alpha_r$ the dephasing limited energy relativistic factor γ_d becomes

$$\gamma_d = \frac{\alpha_E a_0^2 \lambda_p^2 \sin \pi\alpha_r}{(1+\alpha_s)(1+a_0^2/2)^{1/2}\lambda^2}. \tag{14}$$

In the limit $\gamma_d \gg 1$, the dephasing-limited energy is $W_d = mc^2\gamma_d$.

As an example, consider a Ti-sapphire laser-driven LWFA system with $\lambda = 0.8$ μm, $\tau_L = 100$ fs, and $a_0 = 0.5$, propagating in a density channel with $\alpha_r = 0.5$, $r_{ch} = 100$ μm, and $\Delta n/n_0 = 5$. The on-axis density for this case is 3.1×10^{17} cm^{-3}, the plasma wavelength $\lambda_p = 60$ μm, the nominal channel radius $r_{ch}^* = 44.7$ μm, the matched spot size $r_M = 29.2$ μm, the wavebreaking field $E_0 = 53.5$ GV/m, and the laser power $P_0 = 7.16$ TW. From (9), the model calculates the peak accelerating field $E_m/E_0 = 0.0943$, and thus $E_m = 5.04$ GV/m. The spot-size correction factor $1+\alpha_s = 1.427$. The dephasing length from (10) and (11) is therefore 11.8 cm, which leads to a dephasing-limited energy gain W_d of 380 MeV. W_d may be increased by increasing the laser power and lowering the plasma density while holding τ_L, λ, r_{ch}, and $\Delta n/n_0$ unchanged. For example, choosing $P_0 = 25$ TW and $n_0 = 2 \times 10^{17}$ cm^{-3}, gives $E_m = 10.2$ GV/m, $L_d = 21.4$ cm, and $W_d = 1400$ MeV. These parameters represent an attractive point design for a future gigaelectronvolt-class LFWA.

III. Simulation of Laser Guiding and Wakefield Generation

A. Description of Simulation Model

This section describes simulations of laser guiding in plasma channels in the regime appropriate for resonant LFWAs. The simulations employed the axisymmetric laser electromagnetic (LEM) code originally described by Sprangle *et al.* [10] and Krall *et al.* [11], [36]. The code has been used more recently to describe laser guiding in capillary discharge experiments [26], [27], [30], [32], [33] and LFWAs [30], [32], [33].

LEM calculates laser fields and plasma response in a frame moving with the pulse at the speed of light, with independent variables r, $\zeta = z - ct$, and $\tau = t$. The model uses the normalized potentials ϕ and $\mathbf{a}$, where $\phi = e\Phi/mc^2$, $\mathbf{a} = e\mathbf{A}/mc^2$, and Φ and $\mathbf{A}$ are the scalar and vector potentials. It is assumed that the laser wavelength λ satisfies $\lambda \ll \lambda_p$ and $\lambda \ll Z_R$. This allows the laser pulse evolution and plasma response to be calculated on a slow time scale. The laser evolution is described by a wave equation for $\hat{\mathbf{a}}_f$, the slowly varying amplitude of the normalized vector potential of the laser pulse. The fast laser oscillations are described by $\mathbf{a}_f = \hat{\mathbf{a}}_f \exp(ik_0\zeta)/2 + \text{c.c.}$ (where c.c. denotes the complex conjugate) and $k_0 = 2\pi/\lambda$.

The plasma is assumed to be a cold relativistic electron fluid with immobile ions. The pulse length $c\tau_L$ is assumed to be much shorter than the Rayleigh length. The short pulse length assumption is embodied in the quasistatic approximation [35]. This implies that the equations describing the plasma response neglect derivatives in τ and involve only r and ζ. As described in [11, Appendix], it is possible to reduce the plasma response to a single equation of the form $\partial^2\psi/\partial\zeta^2 = G(\psi, |\hat{\mathbf{a}}_f|^2)$, where the normalized wake potential $\psi = \phi - a_z$ and G is a complicated function of the normalized potentials.

LEM shares many features with the WAKE code developed by Mora and Antonsen [43]–[45] and has been used for similar applications. Both codes separate the fast-time scale optical frequency from the slow-scale plasma response and employ the short-pulse quasistatic approximation. Neither code provides a direct treatment of accelerated electrons that move with the laser pulse. The primary difference between the codes is that WAKE can treat the plasma response using simulation particles. The particle simulation version of WAKE can treat regions where the plasma exhibits strong instabilities or nearly complete electron expulsion (cavitation) near the axis where LEM may fail. However, the results presented in this paper are in a stable regime where the fluid model used in LEM should be valid.

A primary quantity of interest is the spot size $r_L(\zeta, \tau)$. LEM has the option of initiating the laser pulse in vacuum and focusing it onto the entrance of the plasma channel at a focused spot-size radius r_0 [26], [27]. However, in the simulation described below, the pulse is initiated in the plasma channel with $r_0 \approx r_M$. The simulation also calculates a single characteristic spot size $r_L(z)$. This quantity is calculated at a reference point $\zeta^*(z)$ that originates at the center of the pulse at $z = 0$ and moves back in the pulse frame at the nominal group velocity $\beta_{g0}c = (1-\lambda^2/2\lambda_p^2)c$ of the pulse. (This does not include the spot-size correction to the group velocity.) Because the spot size

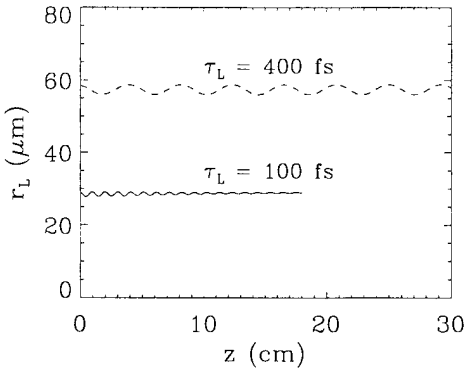


Fig. 2. Characteristic spot size $r_L(z)$ from two LEM simulations with pulse lengths for $\tau_L = 100$ fs (solid line) and 400 fs (dashed line). The laser has $\lambda = 0.8$ μm and $a_0 = 0.5$, the channel has $r_{ch} = 100$ μm and $\Delta n/n_0 = 5$, and the resonance ratio has $\alpha_r \equiv c\tau_L/\lambda_p = 0.5$. The on-axis plasma density is $n_0 = 3.1 \times 10^{17}$ cm^{-3} for the 100-fs pulse and is a factor of 16 lower for the longer pulse. The oscillations in $r_L(z)$ are centered near the expected matched radii of 29.2 μm (100-fs case) and 58.4 μm (400-fs case).

is close to its matched value, oscillations in $r_L(z)$ have modest amplitudes.

B. Evolution of Pulse Envelope and Intensity

The analytical model described in Section II-A predicts that a Gaussian beam injected into a parabolic density channel with $r_0 \approx r_M$ will propagate at a nearly constant spot size with small amplitude envelope oscillations at the period λ_e given by (4). Simulations in the high-density regime for capillary discharges experiments [30], [32] agree well with the analytical model for both spot-size and envelope oscillation periods. The agreement between simulation and theory is examined here for the lower density LWFA regime.

An example is shown in Fig. 2, which plots the characteristic spot size $r_L(z)$ for $\tau_L = 100$ and 400 fs from two LEM simulations. The laser had $\lambda = 0.8$ μm and $a_0 = 0.5$; the channel had $r_{ch} = 100$ μm, $r_{ch}^* = 44.7$ μm, and $\Delta n/n_0 = 5$; and the resonance ratio was $\alpha_r \equiv c\tau_L/\lambda_p = 0.5$. The on-axis plasma density was $n_0 = 3.1 \times 10^{17}$ cm^{-3} for the 100-fs pulse and was a factor of 16 lower for the longer pulse. The calculated values for the matched beam radius r_M for the two cases based on (3) or (7) are 29.2 μm and 58.4 μm, respectively. As expected, r_L in the simulations oscillates about an average near these matched values. The damping in the spot-size oscillations seen in the 100-fs simulation is caused by nonparaxial effects in the wave equation, resulting in envelope modulation and phase-mix damping. This phenomenon has been discussed in recent papers by Sprangle *et al.* [37]–[39] and Esarey and Leemans [40].

Fig. 3 provides surface plots of the normalized intensity $a^2(r, \zeta)$ at injection ($z = 0$) and at $z = 10.8$ cm for the $\tau_L = 100$-fs simulation shown in Fig. 2. At $z = 0$, the front of the pulse is at $\zeta = 0$, and at its point of maximum intensity ($r = 0$, $\zeta = -30$ μm), $a^2 = a_0^2 = 0.25$. At $z = 10.8$ cm, the changes in the pulse are modest even though it has propagated over 30 Rayleigh lengths. The peak intensity is slightly higher, and there is a modest increase in $r_L(\zeta)$ in the back of the pulse. The most obvious effect is the slippage of the pulse in the

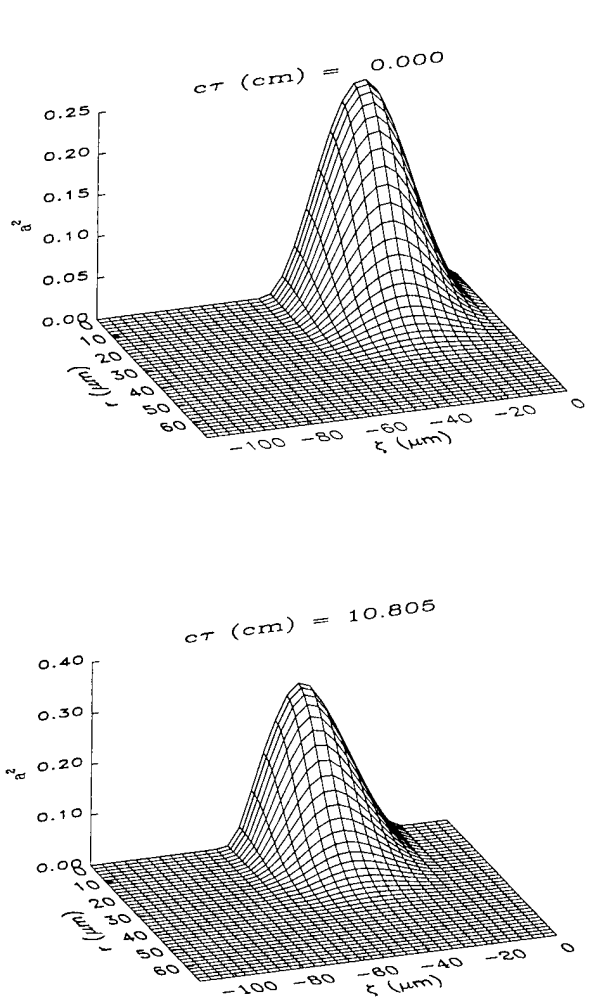


Fig. 3. Surface plots of the normalized intensity $a^2(r, \zeta)$ at injection ($z = 0$) and at $z = 10.8$ cm for the $\tau_L = 100$-fs simulation shown in Fig. 2. At $z = 0$ (a), the front of the pulse is at $\zeta = 0$, and at its point of maximum intensity ($r = 0$, $\zeta = -30$ μm), $a^2 = a_0^2 = 0.25$. At $z = 10.8$ cm (b), the changes in the pulse are modest even though it has propagated over 30 Rayleigh lengths. The pulse has slipped back, and there is a modest increase in the peak intensity.

speed-of-light frame, with the peak intensity moving from its initial location at $\zeta = -30$ μm to $\zeta \approx -45$ μm at $z = 10.8$ cm.

However, for very short pulse lengths and long propagation distances, relativistic and nonparaxial effects can distort the pulse substantially. Fig. 4 plots the $a^2(r, \zeta)$ at $z = 0$ [Fig. 4(a)] and 3.6 cm [Fig. 4(b)] for a pulse with $\tau_L = 50$ fs and $n_0 = 1.24 \times 10^{18}$ cm^{-3}. At $z = 3.6$ cm, the peak intensity has increased by almost a factor of two from its initial value, and $a^2(0, \zeta)$ rises more slowly in the front of the pulse and drops quickly after the peak is attained. However, as discussed in Section IV-A, the propagation distance (3.6 cm) is more than a factor of two beyond the dephasing length and, thus, is beyond the regime of interest for an LWFA.

A similar simulation with $a_0 = 0.1$ instead of 0.5 exhibits much less distortion and does not show the large increase in peak intensity. This suggests that relativistic effects are playing a major role in the propagation of the pulse shown in Fig. 4. One potential candidate for producing the observed pulse distortion is the relativistic modulational instability (RMI) [6], [46].

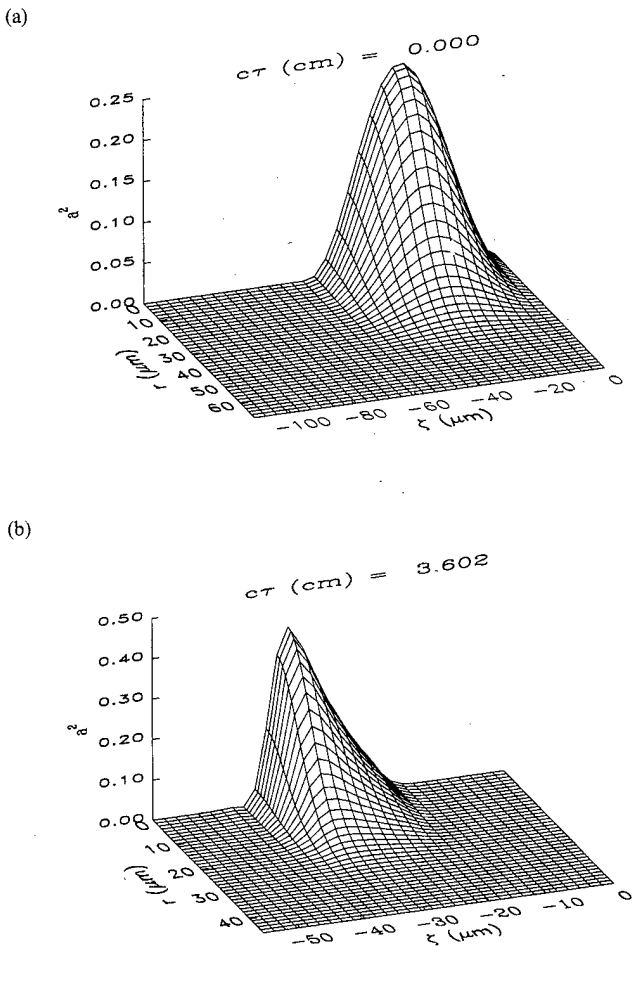


Fig. 4. Normalized intensity $a^2(r, \zeta)$ at $z = 0$ (a) and 3.6 cm (b) for a pulse with $\tau_L = 50$ fs and $n_0 = 1.24 \times 10^{18}$ cm^{-3}. In (b), the peak intensity has increased by almost a factor of two from its value at injection, and $a^2(0, \zeta)$ rises more slowly in the front of the pulse and drops quickly after the peak is attained.

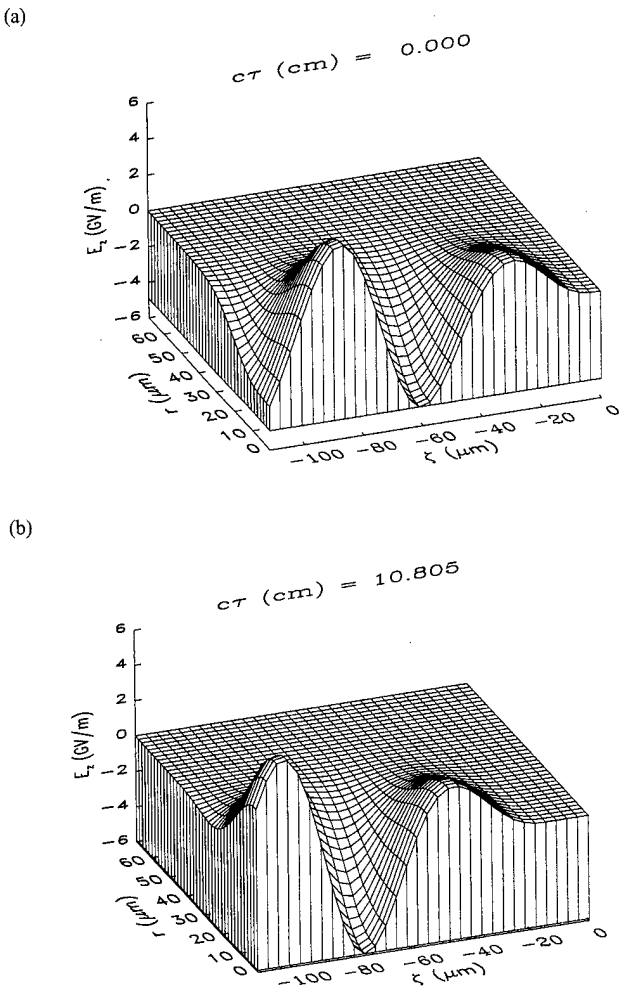


Fig. 5. Surface plots of the axial electric field $E_z(r, \zeta)$ from the simulation shown in Fig. 3. The top (a) is at $z = 0$; the bottom (b) is at $z = 10.8$ cm. The maximum accelerating gradient occurs at the first minimum of $E_z(r = 0, \zeta)$.

The RMI is caused by the interplay between self-phase modulation and group velocity dispersion. In one dimension, RMI leads to the growth of the laser pulse amplitude in the back of the pulse, consistent with that observed in Fig. 4(b). This is in contrast to the situation with a long laser pulse ($c\tau_L \gg \lambda_p$). In the long pulse case, the RMI is less important, and the propagation is dominated by the development of Raman instability on the trailing end of the pulse [43].

C. Wakefield Generation and Resonance Ratio

The simulation described in the previous section generates an axial wakefield capable of accelerating electrons to high energies. Fig. 5 gives surface plots of $E_z(r, \zeta)$ at the same two locations as in Fig. 3. The maximum accelerating gradient occurs at the first minimum of $E_z(r = 0, \zeta)$. For $z = 0$, this point occurs at $\zeta = -60$ μm, where the on-axis field is -5.04 GV/m. At $z = 10.8$ cm, the peak field has increased to 6.02 GV/m, and the location has slipped back approximately 15 μm. The increase in the field amplitude at this location is consistent with the modest increase in the peak in a^2 shown in Fig. 3(b).

From (1) and (9), the predicted peak axial electric field $E_m = 5.15$ GV/m. The simulation peak field $E_{ms}(z)$ varies as the pulse propagates. It undergoes oscillations that reflect the envelope oscillations shown in Fig. 2 and has a moderate long-term secular increase, as described in the next section. An average of $E_{ms}(z)$ over an envelope oscillation near injection gives $E_{ms} = 5.34$ GV/m, which is 3.7% above the analytical estimate.

Another aspect of the analytical model that can be tested numerically is the dependence of E_m in (9) on the resonance ratio $\alpha_r \equiv c\tau_L/\lambda_p$ and the choice of the electric field scale factor α_E. The value of E_m in the previous paragraph assumed $\alpha_E = 0.8$ and $S(\alpha_r) = \sin \pi\alpha_r$. Fig. 6 plots the normalized peak electric field E_m/E_0 from a series of simulations in a density channel with $n_0 = 2 \times 10^{17}$ cm^{-3}, $a_0 = 0.7$, $\Delta n/n_0 = 5$, and $r_{ch} = 100$ μm. These simulations use the initial Gaussian profile laser pulse at $z = 0$ and do not evolve self-consistently. Each simulation used a different value for the pulse length τ_L and thus a different α_r. The solid curve represents the theoretical result from (9) with the nominal scaling choice $\alpha_E = 0.8$, and the asterisks are the code results. The slight asymmetry seen

TABLE I
COMPARISON OF ANALYTICAL AND SIMULATION RESULTS FOR CHANNEL-GUIDED LASER WAKEFIELD ACCELERATORS WITH DIFFERENT PULSE LENGTHS

τ_L (fs)	n_0 (cm^{-3})	P_0 (TW)	r_M (μm)	r_{MS} (μm)	E_m (GV/m)	E_{ms} (GV/m)	$\Delta\beta_p$	$\Delta\beta_{ps}$
50	1.24×10^{18}	3.65	20.7	20.0	10.3	12.0	4.32×10^{-4}	4.73×10^{-4}
100	3.1×10^{17}	7.30	29.2	28.5	5.15	5.34	1.27×10^{-4}	1.31×10^{-4}
200	7.75×10^{16}	14.6	41.3	40.5	2.57	2.50	4.12×10^{-5}	3.95×10^{-5}
400	1.94×10^{16}	29.2	58.4	57.3	1.29	1.04	1.51×10^{-5}	1.43×10^{-5}

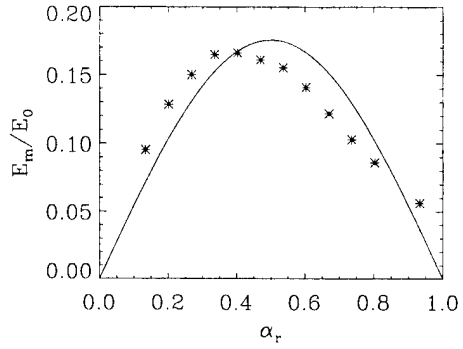


Fig. 6. The normalized peak electric field E_m/E_0 from a series of simulations in a density channel with $n_0 = 2 \times 10^{17}$ cm^{-3}, $a_0 = 0.7$, $\Delta n/n_0 = 5$, and $r_{ch} = 100$ μm. Each simulation used a different value for the pulse length τ_L and thus a different α_r. The simulations results are for the initial Gaussian profile laser pulse at $z = 0$. The solid curve represents the theoretical result from (9) with the nominal scaling choice $\alpha_E = 0.8$, and the asterisks are the code results.

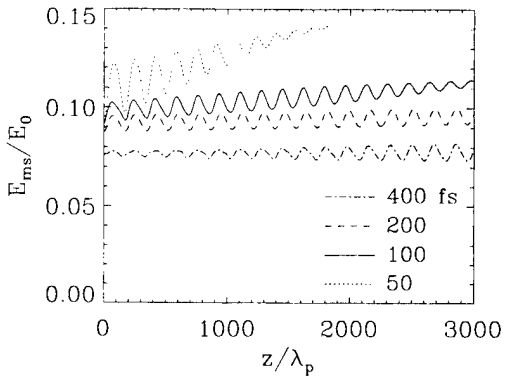


Fig. 7. Peak normalized accelerating electric field E_{ms}/E_0 versus normalized propagation distance z/λ_p for the four simulations described in Table I. The following parameters were held fixed: $\lambda = 0.8$ μm, $a_0 = 0.5$, $\alpha_r \equiv c\tau_L/\lambda_p = 0.5$, $r_{ch} = 100$ μm, and $\Delta n/n_0 = 5$. Because a_0 and α_r are held constant, the analytical model predicts $E_m/E_0 = 0.0943$, independent of τ_L and z. The modest systematic decrease in E_{ms} with increasing τ_L is not predicted by the analytical model.

in the numerical results resembles the 1-D numerical results reported by Esarey *et al.* [3]. The figure shows that the form for E_m postulated in (9), with $\alpha_E = 0.8$ and $S(\alpha_r) = \sin \pi\alpha_r$ provides a useful and reasonably accurate scaling for the peak accelerating gradient.

D. Scaling with Pulse Length and Channel Density

A series of simulations was carried out with the same resonance ratio α_r but different pulse lengths (and, thus, on-axis plasma densities). Parameters were similar to those on the example at the end of Section II-C. The following parameters were held fixed: $\lambda = 0.8$ μm, $a_0 = 0.5$, $\alpha_r \equiv c\tau_L/\lambda_p = 0.5$, $r_{ch} = 100$ μm, and $\Delta n/n_0 = 5$. Pulse length values of 50, 100, 200, and 400 fs were chosen. Table I shows the nominal plasma densities n_0 for the four values of τ_L and compares the analytical results for the spot size r_M, peak accelerating field E_m, and dephasing slippage rate $\Delta\beta_p$ with simulation results.

The matched spot size r_M as calculated from the analytical model in (3) or (7) is generally slightly larger than the simulation value r_{MS} for all four values of τ_L. The simulation values are from an average of r_L over an envelope oscillation. The increase in spot size with τ_L is caused by the smaller values of n_0 and Δn. Because a_0 is held fixed, the larger spot size associated with longer pulse lengths implies a larger laser power P_0. The values of P_0 in Table I were calculated from (8). Alternatively, we could hold P_0 constant and allow a_0 to vary. The scaling implications of this approach are examined in a related paper by Hubbard *et al.* [32].

The scaling of the peak electric field E_m is also listed in Table I, along with the corresponding simulation values E_{ms}. Although the simulation results are similar to the analytical calculations, E_{ms} is larger than E_m for the 50-fs pulse and is smaller for the 400-fs pulse. In addition, the shorter pulse simulations show a systematic increase with propagation distance z that can be attributed to the increase in the peak intensity discussed in Section III-B. These effects are exhibited in Fig. 7, which plots E_m/E_0 versus normalized propagation distance z/λ_p for the four simulations. Because a_0 and α_r are held constant, (9) predicts $E_m/E_0 = 0.0943$, independent of τ_L and z. The modest systematic decrease in E_{ms} with increasing τ_L is not predicted by the analytical model.

The phase slippage rates included in the table lead to the dephasing limitations on energy gain and are discussed in the next section.

IV. SIMULATION OF DEPHASING EFFECTS

A. Determination of Simulation Phase Slippage Rates

The relationship between the normalized wake phase velocity β_p and the dephasing limits on electron energy gain in an LWFA was discussed in Section II-C. The LEM simulation code can be

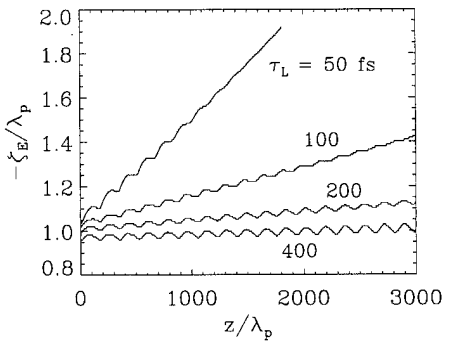


Fig. 8. Location $-\zeta_E$ of the peak accelerating gradient versus z for the four simulations listed in Table I, with fixed parameters the same as in Fig. 7. Both distances are normalized to the plasma wavelength. The oscillations in ζ_E correlate with envelope oscillations in the spot size such as those shown in Fig. 2. The slopes of the individual curves determine the simulation phase slippage rates $\Delta\beta_{ps}$. Values of $\Delta\beta_{ps}$ and the corresponding analytical slippage rate $\Delta\beta_p$ are listed in Table I.

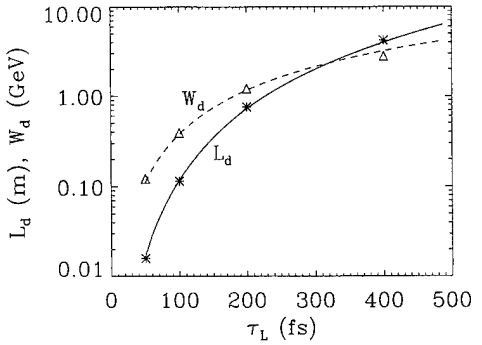


Fig. 9. The dephasing length and the dephasing limited energy gain as functions of pulse length for the parameters used in Fig. 7 and Table I. The solid curve gives L_d from (10) and (11), and the asterisks are the corresponding simulation values L_{ds} based on $\Delta\beta_{ps}$ in Table I. The dashed line is the model calculation of the dephasing-limited energy gain based on (14), and the triangles are the simulation values from (16).

used to calculate the wake phase velocity directly by monitoring the location ζ_E of the first and deepest minimum of $E_z(r = 0, \zeta)$ as a function of propagation distance z. The simulation phase slippage rate $\Delta\beta_{ps} = 1 - \beta_{ps}$ may be defined as

$$\Delta\beta_{ps} = -\left\langle \frac{d\zeta_E}{dz} \right\rangle \tag{15}$$

where the brackets represent an average over many envelope oscillations and may be determined by the slope of a straight line fit to a plot of ζ_E as a function of z. The simulation value may then be compared with the analytical phase slippage rate $\Delta\beta_p = 1 - \beta_p$ from (10).

Fig. 8 plots $-\zeta_E$ versus z for the four simulations listed in Table I. Both distances are normalized to the plasma wavelength. As expected, the slope and slippage rate is much higher for the short pulse cases. The oscillations in ζ_E are caused by envelope oscillations in the spot size, such as those shown in Fig. 2. The slopes of the individual curves determine the simulation phase slippage rates $\Delta\beta_{ps}$, which are listed in Table I. The analytical slippage rates $\Delta\beta_p$ based on (10) are also listed in the table. The agreement between simulation and theory is within 10% in all cases.

The dephasing length L_{ds} in the simulations is the distance at which ζ_E/λ_p has changed by 0.25. Using (11), it can also be calculated from the slippage rate, so that $L_{ds} = \lambda_p/4\Delta\beta_{ps}$. The dephasing-limited energy gain can be estimated from the simulation values for the peak accelerating field E_{ms} and the dephasing length L_{ds}

$$W_{ds} = (2/\pi)E_{ms}L_{ds}. \tag{16}$$

This estimate does not take into account a number of effects, including the apparent secular increase in E_{ms} with propagation distance exhibited in Fig. 7 for short pulse lengths. Test particle tracking calculations using the actual fields from the simulation could be used to predict the energy gain more accurately.

Fig. 9 plots both the dephasing length and the dephasing limited energy gain as functions of pulse length for the parameters listed in Fig. 7. The solid curve gives L_d from (10) and (11), and the asterisks are the corresponding simulation values L_{ds} based on $\Delta\beta_{ps}$ in Table I. The dashed line is the model calculation of the dephasing-limited energy gain based on (14), and the triangles are the simulation values from (16). The agreement between the analytical and simulation models for both quantities is within a few percent in all cases. There is a substantial increase in both the dephasing length and the dephasing-limited energy gain for longer pulse lengths. Because L_d exceeds 1 m for the longer pulse length cases, the effective acceleration length L_a and thus the final electron beam energy are likely to be limited by practical limitations on the channel length rather than by dephasing. In addition, because a_0 is fixed, and r_M increases with τ_L, the peak laser power is also larger.

B. Effect of the Spot Size and Normalized Intensity on the Phase Slippage Rate

The analytical slippage rate $\Delta\beta_p$ given by (10) may be expressed by the spot size correction factor α_s as

$$\Delta\beta_p = \frac{\lambda^2}{2\lambda_p^2}(1 + \alpha_s) \tag{17}$$

where α_s is given by (12). Although there is generally good agreement between the phase slippage rate $\Delta\beta_p$ from the analytical model and the corresponding simulation rate $\Delta\beta_{ps}$, the cases discussed so far do not isolate the spot-size contribution. A more exacting test is to hold all simulation parameters fixed except the channel radius r_{ch}. This causes r_M to vary according to (3) or (7), whereas λ_p remains fixed. The spot-size correction factor α_s, thus, varies according to (12).

A series of simulations was carried out with parameters similar to those in Table I, except that the pulse length was fixed at $\tau_L = 100$ fs and $a_0 = 0.3$ instead of 0.5 to reduce any relativistic effects on the slippage rate. The channel radius r_{ch} was chosen to be 50, 100, 200, and 400 μm, with $\Delta n/n_0 = 5$; so r_{ch}^* was 22.4, 44.7, 89.4, and 179 μm, respectively. The channel had $n_0 = 3.1\times10^{17}$ cm^{-3}; so $\lambda_p = 60$ μm and the laser wavelength $\lambda = 0.8$ μm. Results from these four simulations are given in Table II. The agreement between simulation and theory for the slippage rates is close, with the spot-size effect clearly apparent. The results are represented graphically in Fig. 10, which plots $\Delta\beta_p$ as a function of r_M from (17) for the nominal simulation parameters. The asterisks are the individual simulation values.

Table II also shows two cases in which the normalized intensity a_0 is raised to 0.6. This was done to test for the possible

TABLE II
COMPARISON OF ANALYTICAL AND SIMULATION RESULTS FOR CHANNEL-GUIDED LASER WAKEFIELD ACCELERATORS WITH DIFFERENT CHANNEL RADII AND LASER SPOT SIZES

Case	r_{ch} (μm)	a_0	P_0 (TW)	r_M (μm)	α_s	$\Delta\beta_p$	$\Delta\beta_{ps}$
1	50	0.3	1.31	20.7	0.856	1.65×10^{-4}	1.65×10^{-4}
2	100	0.3	2.63	29.2	0.427	1.27×10^{-4}	1.25×10^{-4}
3	200	0.3	5.25	41.3	0.214	1.08×10^{-4}	1.05×10^{-4}
4	400	0.3	10.5	58.4	0.107	0.98×10^{-4}	1.00×10^{-4}
5	50	0.6	5.26	20.7	0.856	1.65×10^{-4}	1.69×10^{-4}
6	400	0.6	42.0	58.4	0.107	0.98×10^{-4}	1.05×10^{-4}

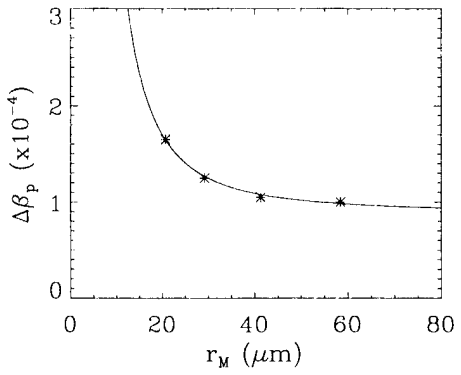


Fig. 10. Results from an analytical calculation and simulations that test the validity of the laser spot size correction to the slippage rate $\Delta\beta_p$ given in (17). The curve is the analytical result, and the asterisks are from individual simulations. The following parameters were fixed: $\tau_L = 100$ fs, $n_0 = 3.1 \times 10^{17}$ cm^{-3}, $\lambda_p = 60$ μm, $\Delta n/n_0 = 5$, $\lambda = 0.8$ μm and $a_0 = 0.3$. The spot size r_M was varied in the simulations by changing the channel radius r_{ch}, which was chosen to be 50, 100, 200, and 400 μm. Results are also given in Table II. The agreement between the theory and simulation is excellent.

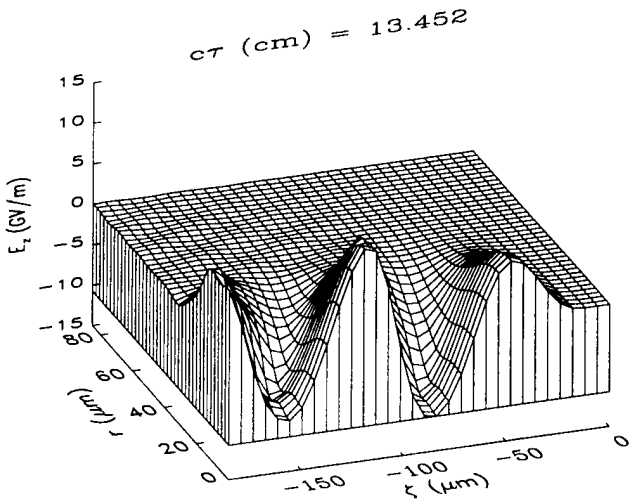


Fig. 11. Simulation plot of $E_z(r, \zeta)$ at $z = 13.5$ cm for a prototype gigaelectronvolt-class LWFA. Laser parameters are: $\lambda = 0.8$ μm, $\tau_L = 100$ fs, and $P_0 = 25$ TW, and channel parameters are: $n_0 = 2 \times 10^{17}$ cm^{-3}, ($\alpha_s = 0.4$), $r_{ch} = 100$ μm, and $\Delta n/n_0 = 5$. The peak axial electric field E_{ms} averaged over an envelope oscillation is 10.2 GV/m, the simulation dephasing length is $L_{ds} = 20.9$ cm, and the dephasing-limited energy is $W_{ds} = 1.36$ GeV.

role of relativistic effects on the slippage rate. Inclusion of relativistic corrections to the plasma wavelength would result in a modest increase in the pulse group velocity [3], [18], [47], [48], [50]. If we assume that the wake phase velocity equals the pulse group velocity, the normalized wake slippage rate $\Delta\beta_p$ would be lower at for the larger a_0 cases. However, comparing Case 5 with Case 1 and Case 6 with Case 4 in Table II, the higher intensity cases do not show a reduction in $\Delta\beta_{ps}$; its value is actually slightly higher for the higher intensity cases.

The modest increase in $\Delta\beta_{ps}$ with increasing a_0 observed in these simulations is consistent with the results of Decker and Mori [47], [50]. Their simulations showed an increase in the slippage rate of the peak electric field with a_0, even though the slippage rate $\Delta\beta_{g0}$ of the pump pulse itself decreased with a_0. This effect has also been seen in other LEM simulation reported by Hubbard *et al.* [32]. For simplicity, the analysis presented in Section II-C assumes that the wake phase velocity is independent of the intensity.

C. Example of a Gigaelectronvolt LWFA

The simulations in the previous sections were intended primarily to make comparisons with the analytical models. This section describes a simulation at slightly higher intensities that is intended to produce large energy gain and high accelerating gradients. This simulation has $\tau_L = 100$ fs, $P_0 = 25$ TW, $n_0 = 2 \times 10^{17}$ cm^{-3}, $\Delta n/n_0 = 5$, $r_{ch} = 100$ μm, and $r_0 = 30$ μm. Fig. 11 plots $E_z(r, \zeta)$ at $z = 13.5$ cm. The peak axial electric field E_{ms} averaged over an envelope oscillation is 10.2 GV/m, the simulation dephasing length $L_{ds} = 20.9$ cm, and the dephasing-limited energy $W_{ds} = 1.36$ GeV. The analytical model values for these performance quantities are $E_m = 10.2$ GV/m, $L_d = 21.4$ cm, and $W_d = 1.40$ GeV; so the agreement is excellent.

V. SUMMARY

Optical guiding is expected to play a crucial role in future experiments on LFWAs. Plasma channels provide the most obvious means for providing this guiding. For a given set of laser and channel parameters, a channel-guided LWFA may be characterized by the spot size r_M, the peak accelerating axial electric field E_m, and the dephasing-limited energy gain W_d. This paper has presented analytical models that estimate these quantities and compared the results from a laser propagation simulation code.

The pulses in the simulations propagate with an average spot size r_{MS} that is close to the matched value, and there is usually little change in the pulse shape over many Rayleigh lengths. An exception occurs for very short pulses, which can be distorted because of nonparaxial effects. The short pulse effects are consistent with recent analyzes by Sprangle *et al.* [37]–[39] and Esarey and Leemans [40]. The peak electric field E_{ms} in the simulations generally agrees well with the analytical value E_m, but exhibits additional features. For example, the ratio E_{ms}/E_m systematically decreases with increasing τ_L (and decreasing plasma density n_0). Also, shorter pulses ($\lesssim$100 fs) exhibit a slow increase in E_m as the pulse propagates. The variation in the simulation peak electric field E_{ms} with the resonance ratio $\alpha_r = c\tau_L/\lambda_p$ is similar to the $\sin \pi\alpha_r$ scaling postulated in Section II-B, but the peak occurs near $\alpha_r = 0.4$ instead of 0.5.

Analytical estimates of the dephasing length L_d in a LWFA are made based on standard models for the wake phase velocity β_p or phase slippage rate $\Delta\beta_p$. These are compared with simulation phase slippage rates $\Delta\beta_{ps}$ that are determined by monitoring the instantaneous location of the peak axial electric field in the pulse. The analytical estimates include a finite spot-size correction to β_p, and the simulations confirm the importance of retaining this correction. The dephasing-limited energy gain W_d is estimated in the analytical model from the peak field E_m and dephasing length L_d. The corresponding values from the simulation can be used to determine the simulation dephasing-limited energy gain W_{ds}. The simulations generally agree well with the analytical predictions and confirm the usefulness of these models in designing future experiments on LFWAs.

ACKNOWLEDGMENT

This work has been motivated in part by an ongoing experimental collaboration on laser guiding in capillary discharges with A. Zigler, D. Kaganovich, Y. Ehrlich, A. Ting, C. Moore, and T. Jones. Conversations with T. Antonsen, T. Hosokai, J. Krall, E. Esarey, and J. Peñano are also gratefully acknowledged.

REFERENCES

[1] T. Tajima and J. M. Dawson, "Laser electron accelerator," *Phys. Rev. Lett.*, vol. 43, pp. 267–270, 1979.

[2] P. Sprangle, E. Esarey, A. Ting, and G. Joyce, "Laser wakefield acceleration and relativistic optical guiding," *Appl. Phys. Lett.*, vol. 53, pp. 2146–2148, 1988.

[3] E. Esarey, P. Sprangle, J. Krall, and A. Ting, "Overview of plasma-based accelerator concepts," *IEEE Trans. Plasma Sci.*, vol. 24, pp. 252–288, 1996.

[4] L. M. Gorbunov and V. I. Kirsanov, "Excitation of plasma waves by an electromagnetic wave packet," *Zh. Eksp. Teor. Fiz.*, vol. 93, pp. 509–518, 1987.

[5] P. Sprangle and E. Esarey, "Interaction of ultrahigh laser fields with beams and plasmas," *Phys. Fluids B*, vol. 4, pp. 2241–2248, 1992.

[6] P. Sprangle and B. Hafizi, "Guiding and stability of short laser pulses in partially stripped ionizing plasmas," *Phys. Plasmas*, vol. 6, pp. 1683–1689, 1999.

[7] F. Amiranoff, S. Baton, D. Bernard, B. Cros, D. Descamps, F. Dorchies, F. Jacquet, V. Malka, J. R. Marquès, G. Matthieussent, P. Miné, A. Modena, P. Mora, J. Morillo, and Z. Najmudin, "Observation of laser wakefield acceleration of electrons," *Phys. Rev Lett.*, vol. 81, pp. 995–998, 1998.

[8] P. Sprangle, E. Esarey, and J. Krall, "Laser driven electron acceleration in vacuum, gases and plasmas," *Phys. Plasmas*, vol. 3, pp. 2183–2190, 1996.

[9] E. Esarey, P. Sprangle, J. Krall, and A. Ting, "Self-focusing and guiding of short laser pulses in ionizing gases and plasmas," *IEEE J. Quantum Electron.*, vol. 33, pp. 1879–1914, 1997.

[10] P. Sprangle, E. Esarey, J. Krall, and G. Joyce, "Propagation and guiding of intense laser pulses in plasmas," *Phys. Rev. Lett.*, vol. 69, pp. 2200–2203, 1992.

[11] J. Krall, E. Esarey, P. Sprangle, and G. Joyce, "Propagation of radius-tailored laser pulses over extended distances in a uniform plasma," *Phys. Plasmas*, vol. 1, pp. 1738–1743, 1994.

[12] N. E. Andreev, L. M. Gorbunov, V. I. Kirsanov, A. A. Pogosova, and R. R. Ramazashvili, "Resonant excitation of wakefields by a laser pulse in a plasma," *JETP Lett.*, vol. 55, pp. 571–576, 1992.

[13] K. Nakajima, D. Fisher, T. Kawakubo, H. Hashaniki, A. Ogata, Y. Kato, Y. Kitagawa, R. Kodama, K. Mima, H. Shiraga, K. Suzuki, K. Yamakawa, T. Zhang, Y. Sakawa, T. Shoji, Y. Nishida, N. Yagami, M. Downer, and T. Tajima, "Observation of ultrahigh gradient electron acceleration by a self-modulated intense short laser pulse," *Phys. Rev. Lett.*, vol. 74, pp. 4659–4662, 1995.

[14] A. Modena, Z. Najmudin, A. E. Dangor, C. E. Clayton, K. A. Marsh, C. Joshi, V. Malka, C. B. Darrow, and C. Danson, "Observation of Raman forward scattering and electron acceleration in the relativistic regime," *IEEE Trans. Plasma Sci.*, vol. 24, pp. 289–295, 1996.

[15] D. Umstadter, S. Y. Chen, A. Maksimchuk, G. Mourou, and R. Wagner, "Nonlinear optics in relativistic plasmas and laser wakefield acceleration of electrons," *Science*, vol. 273, pp. 472–475, 1996.

[16] A. Ting, C. I. Moore, K. Krushelnick, C. Manka, E. Esarey, P. Sprangle, R. Hubbard, H. R. Burris, and M. Baine, "Plasma wakefield generation and electron acceleration in a self-modulated laser wakefield experiment," *Phys. Plasmas*, vol. 4, pp. 1889–1899, 1997.

[17] C. I. Moore, A. Ting, K. Krushelnick, E. Esarey, R. F. Hubbard, B. Hafizi, H. R. Burris, C. Manka, and P. Sprangle, "Electron trapping in self-modulated laser wakefields by Raman backscatter," *Phys. Rev. Lett.*, vol. 79, pp. 3909–3912, 1997.

[18] D. Gordon, K. C. Tzeng, C. E. Clayton, A. E. Dangor, V. Malka, K. A. Marsh, A. Modena, W. B. Mori, P. Muggli, Z. Najmudin, D. Neely, C. Danson, and C. Joshi, "Observation of electron energies beyond the linear dephasing limit from a laser-excited relativistic plasma wave," *Phys. Rev. Lett.*, vol. 80, pp. 2133–2136, 1998.

[19] C. G. Durfee III and H. M. Milchberg, "Light pipe for high intensity laser pulses," *Phys. Rev. Lett.*, vol. 71, pp. 2409–2411, 1993.

[20] H. M. Milchberg, T. R. Clark, C. G. Durfee III, T. M. Antonsen, and P. Mora, "Development and applications of a plasma waveguide for intense laser pulses," *Phys. Plasmas*, vol. 3, pp. 2149–2155, 1996.

[21] T. R. Clark and H. M. Milchberg, "Time- and space-resolved density evolution of the plasma waveguide," *Phys. Rev. Lett.*, vol. 78, pp. 2773–2376, 1997.

[22] S. P. Nikitin, T. M. Antonsen, T. R. Clark, Y. L. Li, and H. M. Milchberg, "Guiding of intense femtosecond pulses in preformed plasma channels," *Opt. Lett.*, vol. 22, pp. 1787–1789, 1997.

[23] P. Volfbeyn, E. Esarey, and W. P. Leemans, "Guiding of laser pulses in plasma channels created by the ignitor-heater technique," *Phys. Plasmas*, vol. 6, pp. 2269–2277, 1999.

[24] W. P. Leemans, P. Volfbeyn, K. Z. Guo, S. Chattopadhyay, C. B. Schroeder, B. A. Shadwick, P. B. Lee, J. S. Wurtele, and E. Esarey, "Laser-driven plasma based accelerators: Wakefield excitation, channel guiding and laser triggered particle injection," *Phys. Plasmas*, vol. 5, pp. 1615–1623, 1998.

[25] A. Zigler, Y. Ehrlich, C. Cohen, J. Krall, and P. Sprangle, "Optical guiding of high intensity laser pulses in a long plasma channel formed by a slow capillary discharge," *J. Opt. Soc. Am. B*, vol. 13, pp. 68–71, 1996.

[26] Y. Ehrlich, C. Cohen, A. Zigler, J. Krall, P. Sprangle, and E. Esarey, "Guiding of high intensity laser pulses in straight and curved plasma channel experiments," *Phys. Rev. Lett.*, vol. 77, pp. 4186–4189, 1996.
[27] Y. Ehrlich, C. Cohen, D. Kaganovich, A. Zigler, R. F. Hubbard, P. Sprangle, and E. Esarey, "Guiding and damping of high-intensity laser pulses in long plasma channels," *J. Opt. Soc. Am. B.*, vol. 15, pp. 2416–2423, 1998.
[28] D. Kaganovich, P. V. Sasarov, Y. Ehrlich, C. Cohen, and A. Zigler, "Investigation of double capillary discharge scheme for production of wave guide in plasma," *Appl. Phys. Lett.*, vol. 71, pp. 2295–2297, 1997.
[29] D. Kaganovich, A. Ting, C. I. Moore, A. Zigler, H. R. Burris, Y. Ehrlich, R. Hubbard, and P. Sprangle, "High efficiency guiding of terawatt subpicosecond laser pulses in a capillary discharge plasma channel," *Phys. Rev. E*, vol. 59, pp. R4769–R4772, 1999.
[30] R. F. Hubbard, Y. Ehrlich, D. Kaganovich, C. Cohen, C. I. Moore, P. Sprangle, A. Ting, and A. Zigler, "Intense laser pulse propagation in capillary discharge plasma channels," in *Proc. Conf. Adv. Accelerator Concepts*, W. Lawson, Ed. Woodbury, NY: American Institute of Physics, 1999, vol. 472, pp. 394–403.
[31] D. Kaganovich, P. Sasorov, C. Cohen, and A. Zigler, "Variable profile capillary discharge for improved phase matching in a laser wakefields accelerator," *Appl. Phys. Lett.*, vol. 775, pp. 772–774, 1999.
[32] R. F. Hubbard, D. Kaganovich, B. Hafizi, C. I. Moore, P. Sprangle, A. Ting, and A. Zigler, "Simulation and design of channel-guided laser wakefield accelerators," Phys. Rev. E, submitted for publication.
[33] R. F. Hubbard, C. Moore, P. Sprangle, A. Ting, D. Kaganovich, A. Zigler, and B. Hafizi, "Simulation of density channel guiding in capillary discharge experiments and laser wakefield accelerators," in *Proc. 1999 Particle Accelerator Conf.*, A. Luccio and W. MacKay, Eds. New York: IEEE, 1999, pp. 3693–3695.
[34] T. Hosokai, M. Kando, H. Dewa, H. Kotaki, S. Kondo, N. Hasegawa, K. Horioka, M. Nakajima, and K. Nakajima, "Application of fast imploding capillary discharge for laser wakefield acceleration," in *Proc. 1999 Particle Accelerator Conf.*, A. Luccio and W. MacKay, Eds. New York: IEEE, 1999, pp. 3690–3692.
[35] P. Sprangle, E. Esarey, and A. Ting, "Nonlinear interaction of intense laser pulses in plasmas," *Phys. Rev. A*, vol. 41, pp. 4463–4469, 1990.
[36] J. Krall, A. Ting, E. Esarey, and P. Sprangle, "Enhanced acceleration in a self-modulated laser wakefield accelerator," *Phys. Rev. E*, vol. 48, pp. 2157–2161, 1993.
[37] P. Sprangle, B. Hafizi, and P. Serafim, "Dynamics of short laser pulses propagating in plasma channels," *Phys. Rev. Lett.*, vol. 82, pp. 1173–1176, 1999.
[38] ——, "Propagation of finite length laser pulses in plasma channels," *Phys. Rev. E*, vol. 59, pp. 3614–3623, 1999.
[39] P. Sprangle, B. Hafizi, and J. Peñano, "Laser pulse modulation instabilities in plasma channels," *Phys. Rev. E*, vol. 61, pp. 4381–4393, 2000.
[40] E. Esarey and W. P. Leemans, "Nonparaxial propagation of ultrashort laser pulses in plasma channels," *Phys. Rev. E*, vol. 59, pp. 1082–1095, 1999.
[41] E. Esarey, P. Sprangle, M. Pilloff, and J. Krall, "Theory and group velocity of ultrashort, tightly focused laser pulses," *J. Opt. Soc. Am. B*, vol. 12, pp. 1695–1703, 1995.
[42] P. Sprangle, A. Ting, and C. M. Tang, "Analysis of focusing and steering in the free electron laser by use of a source-dependent expansion technique," *Phys. Rev. A*, vol. 36, pp. 2773–2781, 1987.
[43] T. M. Antonsen and P. Mora, "Self-focusing and Raman scattering of laser pulses in tenuous plasmas," *Phys. Fluids B*, vol. 5, pp. 1440–1452, 1993.
[44] P. Mora and T. M. Antonsen, "Kinetic modeling of intense short laser pulses propagating in tenuous plasmas," *Phys. Plasmas*, vol. 4, pp. 217–229, 1997.
[45] ——, "Electron cavitation and acceleration in the wake of an ultraintense self-focused laser pulse," *Phys. Rev. E*, vol. 53, pp. R2068–R2071, 1996.
[46] C. J. McKinstrie and R. Bingham, "Stimulated Raman forward scattering and the relativistic modulational instability of light waves in rarefied plasmas," *Phys. Fluids B*, vol. 4, pp. 2626–2633, 1992.
[47] C. D. Decker and W. B. Mori, "Group velocity of large amplitude electromagnetic waves in a plasma," *Phys. Rev. Lett.*, vol. 72, pp. 490–493, 1994.
[48] E. Esarey, B. Hafizi, R. Hubbard, and A. Ting, "Trapping and acceleration in self-modulated laser wakefields," *Phys. Rev. Lett.*, vol. 80, pp. 5552–5555, 1998.
[49] L. M. Gorbunov and V. I. Kirsanov, "Excitation of plasma waves by an electromagnetic wave packet," *Sov. Phys. JETP*, vol. 66, pp. 290–294, 1987.
[50] C. D. Decker and W. B. Mori, "Group velocity of large amplitude electromagnetic waves in a plasma," *Phys. Rev. E*, vol. 51, pp. 1364–1375, 1995.



Richard F. Hubbard (M'98) received the B.A. degree in physics and mathematics from the University of Kansas in 1970. He received the M.A. degree in physics in 1972, and the M.A. degree in business administration and Ph.D. degree in physics in 1975 from the University of Iowa.

He is currently Head of the Radiation and Acceleration Physics Section in the Beam Physics Branch at the U. S. Naval Research Laboratory (NRL). His primary areas of expertise involve intense beams, including laser, electron, ion, and microwave beams, with emphasis on the stability and transport of beams in plasmas and initially-neutral gases. He is a theoretical and computational Physicist who has collaborated on major experimental programs at NRL and Lawrence Livermore and Sandia National Laboratories. His recent work has concentrated on ultra intense lasers, laser driven accelerators, and novel radiation sources. Prior to joining NRL in 1985, he was employed by JAYCOR in Alexandria, VA, and held postdoctoral positions at the University of Maryland and NASA's Goddard Space Flight Center. He holds two patents, is a member of five major professional societies, and is a four time winner of NRL's Alan Berman publication award.

Phillip Sprangle (M'90–SM'92–F'97) received the B.S. degree in electrical engineering from Polytechnic Institute of Brooklyn in 1968, the M.S. degree in chemistry from the University of Puerto Rico in 1969, and the Ph.D. degree in applied physics from Cornell University in 1972.

He is currently Chief Scientist for Radiation and Acceleration Physics and head of the Beam Physics Branch at the U.S. Naval Research Laboratory. He has served on the NRL staff since 1972. His primary areas of research in plasma physics include linear and nonlinear collective wave-particle processes, collective particle acceleration mechanisms, and radiation sources and processes based on relativistic electron beams. His research has concentrated on developing advanced concepts in accelerator physics and radiation source physics. His present theoretical research centers on laser driven accelerators, cyclotron masers, free electron lasers, and advanced high current accelerators. He has over 190 refereed journal publications and holds 11 U.S. patents. His theoretical accomplishments include the initial formulation and analysis of the nonlinear electron cyclotron maser instability, the modified betatron and laser wakefield accelerators, and efficiency enhancement and optical guiding in the free electron laser.

He was the winner of the 1986 E. O. Hulburt Award and the 1991 International Free Electron Laser Prize. He is a Fellow of the American Physical Society (APS), is an IEEE Fellow, was a member of the Executive Committee of the Division of Plasma Physics of the APS, and is a member of Sigma Xi. He was named one of Washington Technology's Top Ten Talents in 1989. In 1988, he received a Department of the Navy Senior Executive Service career appointment.

Bahman Hafizi (M'97) received the B.Sc. and Ph.D. degrees in physics from Imperial College, London, in 1974 and 1978, respectively.

He is currently President of ICARUS Research, Inc., Bethesda, MD. He previously worked as a Research Associate in the Department of Astro-Geophysics at the University of Colorado and as a Staff Scientist for Science Applications International Corporation. His current research areas of interest include propagation of ultra intense laser pulses, laser-driven electron accelerators, laser-plasma interactions, and nonlinear optics. He has also worked on advanced sources of electromagnetic radiation such as free electron lasers, laser synchrotron sources, and ultra broadband sources, with application to imaging, lithography, and remote sensing. Earlier research included studies of electromagnetic radiation from turbulent plasmas, Langmuir collapse, and nonlinear waves and dynamics. He is an associate of the Royal College of Science and a member of the American Physical Society, the European Physical Society, and IEEE.

Experimental Verification of Laser Photocathode RF Gun as an Injector for a Laser Plasma Accelerator

Mitsuru Uesaka, Kenichi Kinoshita, Takahiro Watanabe, Jun Sugahara, Toru Ueda, Koji Yoshii, Tetsuya Kobayashi, Nasr Hafz, Kazuhisa Nakajima, Fumio Sakai, Masaki Kando, Hideki Dewa, Hideyuki Kotaki, and Shuji Kondo

Abstract—**The feasibility of the laser photocathode RF gun, BNL/GUN-IV, as an injector for a laser plasma accelerator was investigated at the subpicosecond S-band twin linac system of the Nuclear Engineering Research Laboratory, University of Tokyo. Electron beam energy of 16 MeV, emittance of 6π mm·mrad, bunch length of 240 fs (FWHM), and charge per bunch of 350 pC were confirmed at 10 Hz. As for diagnosis of the femtosecond electron bunch, the quantitative comparison of performance of the femtosecond streak camera, the coherent transition radiation (CTR) Michelson interferometer, and the far-infrared polychromator was carried out. We concluded that the streak camera is the most reliable up to 200 fs and that the polychromator is the best for the shorter electron bunch. The 3.5-ps (rms) resolved synchronization between the YLF laser driver for the gun and the electron bunch was achieved. Based on the above experiences, we have designed and installed a much better laser-electron synchronization system using the Kerr-lens mode-locked Ti : Sapphire laser with the min harmonics synchrolocker and the stable 15-MW klystron. The timing jitter is expected to be surpressed down to 320 fs (rms).**

Index Terms—**Diagnosis, femtosecond electron bunch, injector for laser plasma accelerator, laser photocathode RF gun, linac-laser synchronization.**

I. Introduction

ACCORDING to recent remarkable development and progress of table-top terawatt femtosecond lasers, the possibility of a 1-GeV laser plasma accelerator has become promising. The candidates as an injector for it are the laser photocathode RF gun [1]–[5], the plasma cathode [6]–[8], the inverse free electron laser [9], the pulsed photodiode [10], and the W-band linac [11]. As for the RF gun, the BNL/GUN-IV was installed at the second linac of the subpicosecond S-band twin linac system, and its overall performance was investigated under the University of Tokyo/KEK/JAERI/Sumitomo Heavy Industries collaboration on laser wakefield acceleration [12]–[15]. On the other hand, a new idea of plasma cathode based on a terawatt femtosecond laser beam and wake wavebreaking has been proposed, and the particle in cell in two-dimensions (PIC-2D) simulations were first performed by Hafz *et al.* [16]. At present, the laser photocathode RF gun looks the most promising from the point of view of technical feasibility. It is also important to develop diagnostic methods to evaluate ultrashort electron bunches less than hundreds of femtoseconds with reliability. So far, the zero-phasing method [17], the strip-line monitor [18], the femtosecond streak camera [19], [20], the CTR interferometer [21]–[24], and the far-infrared polychromator [25] have been proposed and tested. Among them, we did careful and quantitative comparison among the streak camera, the CTR interferometer, and the polychromator using the subpicosecond electron linac.

Manuscript received October 7, 1999; revised February 1, 2000.

M. Uesaka, K. Kinoshita, T. Watanabe, J. Sugahara, T. Ueda, K. Yoshii, T. Kobayashi, and N. Hafz are with the Nuclear Engineering Research Laboratory, Graduate School of Engineering, The University of Tokyo, Tokai, Naka, Ibaraki, 319-1106 Japan (e-mail: uesaka@tokai.t.u-tokyo.ac.jp).

K. Nakajima is with the High Energy Accelerator Organization, Tsukuba, Ibaraki, 305-0032 Japan.

F. Sakai is with the Sumitomo Heavy Industries Co. Ltd., Yato, Tanashi, Tokyo, 188-8585 Japan.

M. Kando, H. Dewa, H. Kotaki, and S. Kondo are with the Japan Atomic Energy Research Institute, Kansai Research Establishment, Kizu, Kyoto, 619-0215 Japan.

Publisher Item Identifier S 0093-3813(00)08174-1.

II. Requirement of an Injector for a Laser Plasma Accelerator

At the working group of the international workshop on second-generation laser and plasma accelerators, the requirement of an injector for a laser plasma accelerator was discussed in details [26]. It was set as follows.

Electron energy $\gamma_{\text{inj}} = 10$–20.

$$\text{Change per bunch } N_e(100\%\text{b.l.}) = 5 \times 10^5 \sqrt{n_0}\,\frac{E}{E_0}\,\pi\,\frac{c^2}{\omega_p^2}. \tag{1}$$

$$\text{Emittance } \varepsilon_n = f^2\,\frac{\lambda_p\sqrt{2\gamma_{\text{ing}}E/E_0}}{2\pi}. \tag{2}$$

$$\text{Electron bunch length (rms)} = \frac{\lambda_p}{10 \times 2.35}. \tag{3}$$

$$\text{Phase-jitter (rms) } \Delta t = \frac{\lambda_p}{20}$$

where n_0 is the plasma density. The plasma frequency ω_p and the plasma wavelength λ_p are given as

$$\omega_p = \sqrt{\frac{4\pi e^2 n_0}{m_e}} \tag{4}$$

$$\lambda_p = \frac{C}{2\pi\omega\rho} \tag{5}$$

where m_e is the mass of an electron. In addition, the following conditions are fixed:

$$f = \frac{\sigma_{\text{inj}}}{R_p} = \frac{1}{3}, \quad \frac{E}{E_0} = \frac{1}{3}$$

0093–3813/00$10.00 © 2000 IEEE

TABLE I
SPECIFICATION AND ACHIEVED DATA FOR AN INJECTOR FOR A LASER PLASMA ACCELERATOR

	E (MeV)	Ne Q (pC)	ε_n (π mm.mrad)	σ_z (μm)	jitter (fs)	rep. rate (Hz)
Specs (1)	>5	$1.5\ 10^8$ 24.	10	15.	45.	10
Specs (2)	>5	$1.5\ 10^7$ 2.4	1	1.5	4.5	10
RF-Gun + booster +magn. Compressor	17	2.10^9 350pC	6	72	3.5ps 320 (design)	10

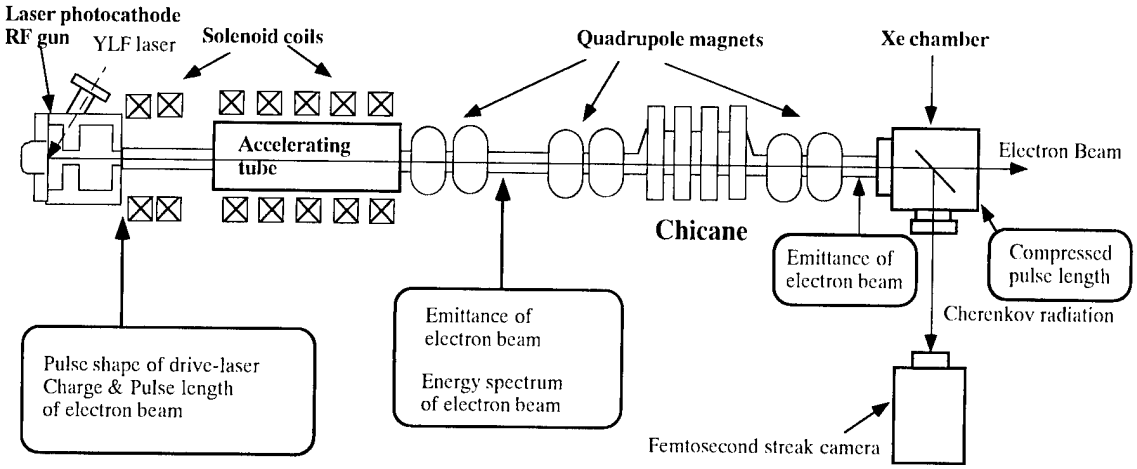


Fig. 1. S-band laser photocathode RF gun and 18L linac.

where

$\sigma_{\rm inj}$ elecrtron beam spot size;
R_p radius of the plasma channel;
E amplitude of the electric field in the plasma wave;
E_0 wavebreaking limit of the plasma wave.

Based on the requirement, we formed the following two sets of specifications:

1) $n_0 = 10^{16}$ cm^{-3}, $N_e = 1.5 \times 10^8$, $\sigma_z = 15$ μm, $\Delta t = 45$ fs, $\varepsilon_n = 10\pi$ mm.mrad;
2) $n_0 = 10^{18}$ cm^{-3}, $N_e = 1.5 \times 10^7$, $\sigma_z = 1.5$ μm, $\Delta t = 4.5$ fs, $\varepsilon_n = 1\pi$ mm.mrad.

The repetition rate of a driver laser is 10 Hz according to the state-of-art technical feasibility of laser amplifiers. The specification and achieved data from our system are summarized in Table I.

III. LASER PHOTOCATHODE RF GUN AND LINAC

Configuration of the S-band second linac with the laser photocathode RF gun, BNL/GUN-IV, is drawn in Fig. 1. It consists of the gun, one 2-m–long S-band accelerating tube, a chicane-type magnetic bunch compressor, and several diagnostic devices. The design of the beam transport and magnetic bunch compressor was performed by using SUPERFISH, POISSON, and PARMELA [14]. The pulsewidth of the YLF laser driver of 11 ps full-width at half maximum (FWHM), the charge per bunch of 1 nC, and the 7-MW RF fed into the gun were used so that 5.2-MeV, 8-ps (FWHM), 1-nC electron bunch was obtained. The cathode material is copper. After the accelerating tube with a maximum field gradient of 100 MV/m, the beam parameters are 16 MeV, 8 ps (FWHM), 1 nC and energy spread is 2%. The bunch compression yields 200 fs (FWHM) without electron loss.

Overall evaluation of the performance of the gun and linac was carried out by using the diagnostic devices, such as the quad-scan, energy analyzer, Faraday cup, and streak camera with 200-fs resolution at FWHM (Photonics Hamamatsu, Japan, FESCA-200). Measured beam energy, emittance, energy spread, pulsewidth, and charge per bunch as a function the RF gun phase are shown in Figs. 2–5. The emittance measurement was done after acceleration up to 16 MeV and without using the chicane. As shown in Figs. 2–5, the maximum energy of 3.33 MeV, the lowest emittance of 6π mm.mrad, the shortest pulsewidth of 10 ps, and the maximum charge of 2 nC were obtained at the different phases. Thus, we have to choose the phase according to what we want as a priority. Results of bunch shapes without and with the bunch compression are given in Fig. 6. The 13-ps bunch is compressed to 440 fs at FWHM. The best pulse compression was done around the phase of the best emittance. After this measurement, we performed the calibration of the streak camera using the 86-fs (FWHM) Ti : Sapphire laser (Spectra-Physics, Tsunami). The 86-fs laser pulse was elonged to 390 fs. Thus, according to the error propagation law, the error at the camera was estimated to be 370 fs (FWHM). We found that this error mainly attributed to the degradation of the microchannel plate (MCP) in the streak tube. If we assume the independent Gaussian distributions for both the electron bunch and the error, the error propagation law gives the bunch length

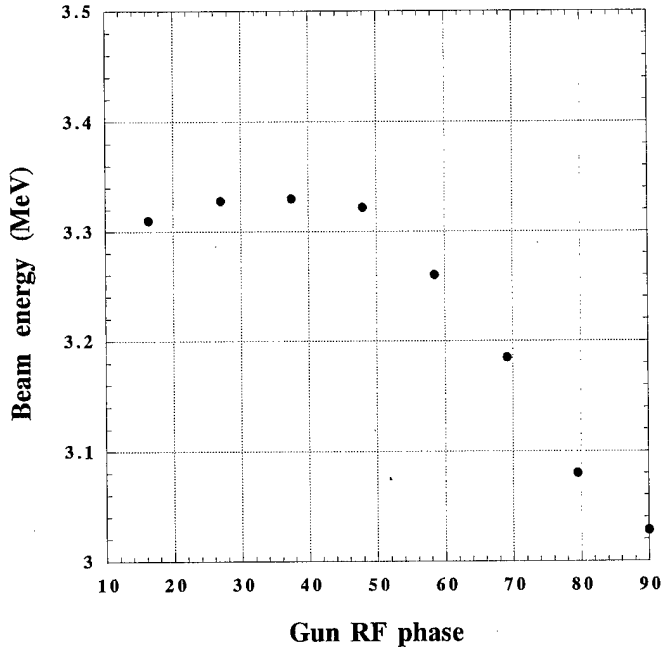


Fig. 2. Beam energy versus gun RF phase.

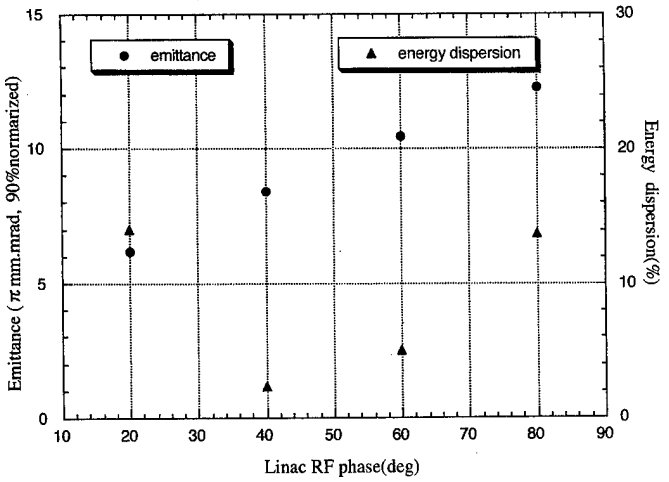


Fig. 3. Normalized emittance and energy dispersion versus linac RF phase.

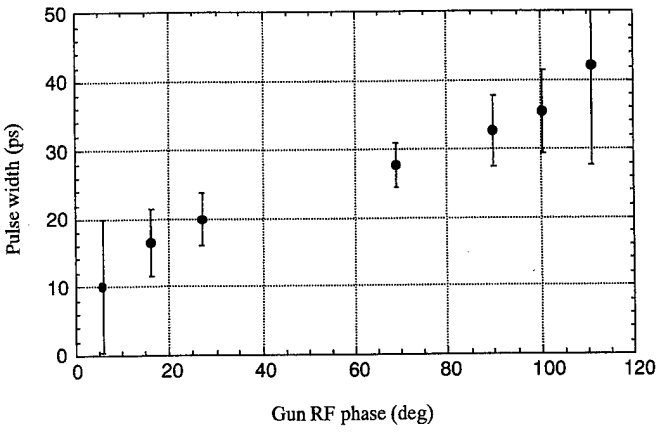


Fig. 4. Pulsewidth (FWHM) versus gun RF phase.

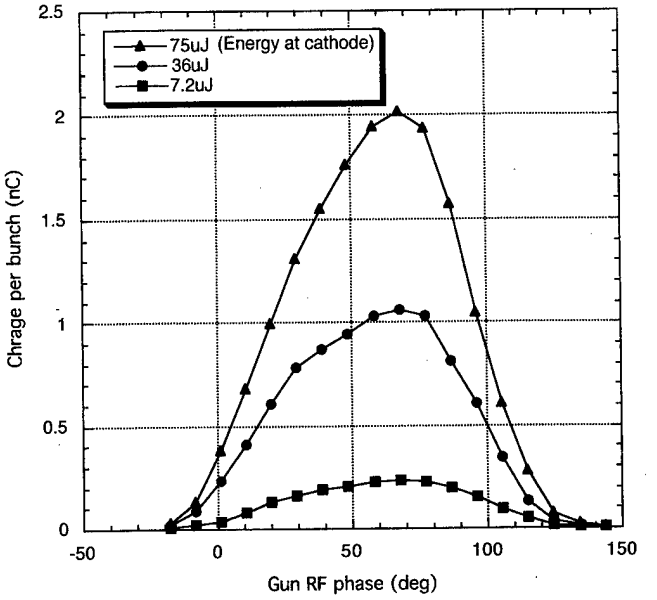


Fig. 5. Charge per bunch versus gun RF phase.

of 240 fs (FWHM) after the error reduction. When we do not assume the Gaussian and evaluate and use the error propagation function from all measured data, the bunch length becomes 290 fs (FWHM). After this experiment, we have replaced the degraded MCP with a new one, the error of which has been evaluated to be 240 fs by the same procedure.

Recently, the BNL/GUN-IV is operated at BNL, APS, SLAC-GTF, UCLA, and here. Updated measured results of electron microbunches from the gun are summarized in [27], and the other remarkable measured results are 200 fs and 0.5 mm.mrad with 40 pC. Further, the inverse free electron laser with CO_2 laser yielded 2.5-μm (8-fs) micromultibunches [9]. We are sure to reduce the charge, emittance, and bunch length by controlling the laser spot size at the cathode of the RF gun to fulfill the specification [28], [29]. Smaller values derived by simulation from one operating mode of Neptune photoinjector are 17 pC, 15.9 MeV, 0.2 μm.mrad, and 42 μm (σ_z; 140 fs) for reference.

Hajima *et al.* analyzed the effect of normal space-charge force, noninertial space-charge force, and coherent radiation force on the emittance, energy spread, and bunch shape by their computer code, and we carried out the measurement at this linac in 1998 [30]. They calculated the total emittance growth of 29π mm.mrad, an energy shift of 240 keV, and bunch broadening from 100 fs to 500 fs (FWHM), assuming 1 nC per bunch at the chicane. We measured the energy shift of 94 keV, but not the emittance growth and bunch broadening for 0.6 nC per bunch. The calculated energy shift of 105 keV for 0.6 nC agrees well with the measurement. Calculated emittance growth was 5π mm.mrad for 0.6 nC, but we could not measure it. Disagreement could be attributed to the change of the beam parameters during the measurement. We plan to measure it again later.

Other important aspects of the RF gun, to be precisely investigated and overcome, are dark current and degradation of the quantum efficiency (QE). We have been continuing the careful

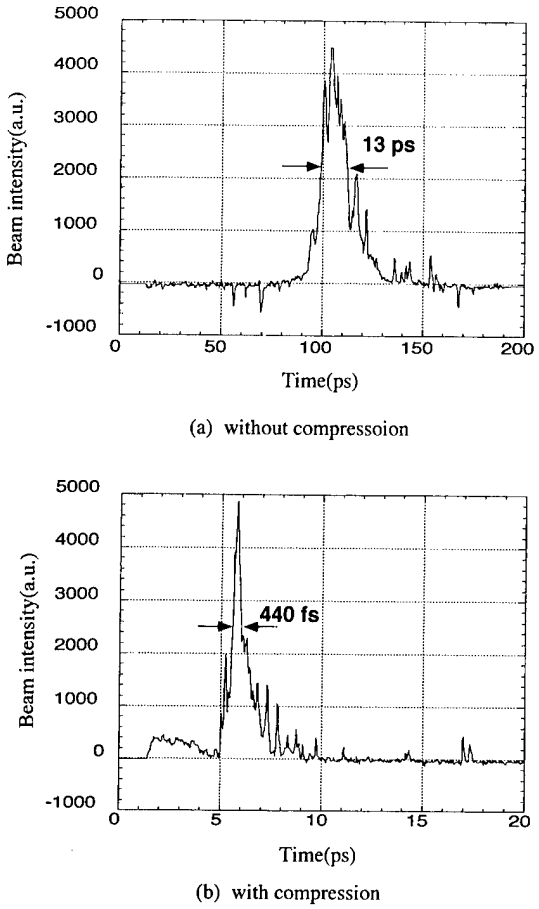


Fig. 6. Pulse shapes without and with compression measured by the femtosecond streak camera.

observation and treatment. Measured dark currents as a function of the RF field and feeding repetition rate at the gun for 5- and 8-μs RF pulses are shown in Fig. 7. The 100-MV/m corresponds to 7-MW RF power fed into the gun. It is clear that the longer 8-μs RF pulse yields more dark current by one order. We usually operate the gun at 4-μs RF pulse at 50 Hz, here the dark current is 35 nA, 0.7 nC per RF pulse, and 0.06 pC per bunch. This was reduced by a factor of 2 at the beam transport and chicane so that the value per RF pulse became about the same as 350 pC measured for a 440-fs photoemitted election bunch. However, the dark current within the main photoemitted bunch is about 0.03 pC, which is negligible. Instead, surrounding satellites of dark current would be serious as an injector to a plasma accelerator. The influence of RF aging, laser cleaning, and vacuum on QE was observed as shown in Fig. 8. QE is evaluated using

$$\mathrm{QE} = \frac{hcQ}{eW\lambda} \tag{6}$$

where

- Q charge per bunch from the gun measured by the Faraday cup;
- W UV laser energy;
- λ wavelength of the UV light (265 nm);
- h Planck constant;
- c speed of light;
- e charge of an electron.

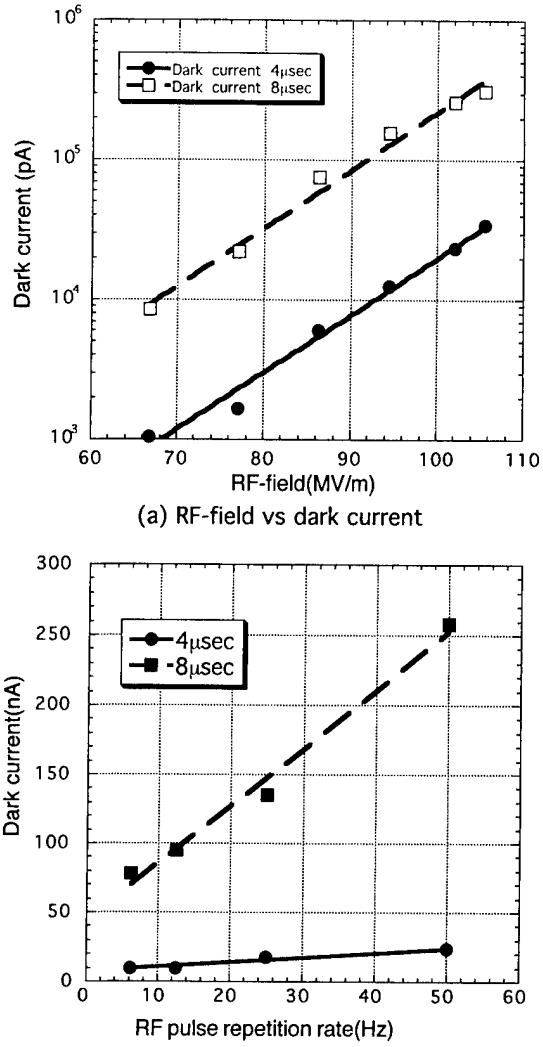


Fig. 7. Evaluation of dark current.

QE was degraded from 4.5×10^{-5} to 0.5×10^{-5} because of about 5 h $\times$ 10 days RF aging with 8-μs RF pulse and averaged power of 2.8 kW. Then, the laser cleaning operation of a few hours per day with a 4-μs RF pulse recovered QE gradually, as shown in the figure. Especially, it was remarkably recovered up to 1.4×10^{-4} by the installation of a new vacuum pump of NEQ, although we observed a temporary decrease because of a bad vacuum condition during the installation. The vacuum in the gun without RF feeding was improved from 3×10^{-9} torr to the region of 10^{-10} torr. Thus, as reported in [4], [31], and [32], the main sources of QE degradation are poor vacuum and surface contamination, and the proper laser cleaning is necessary.

IV. Electron Bunch Diagnosis

For the purpose of diagnosing ultrashort electron bunches, several methodologies, such as the zero-phasing method, the strip-line monitor, the femtosecond streak camera, and the CTR interferometer, have been developed and evaluated. We have been using the femtosecond streak camera since 1995 as a major diagnostic tool [20]. Because its limitation of resolution is 200 fs (FWHM), we introduced the CTR Michelson

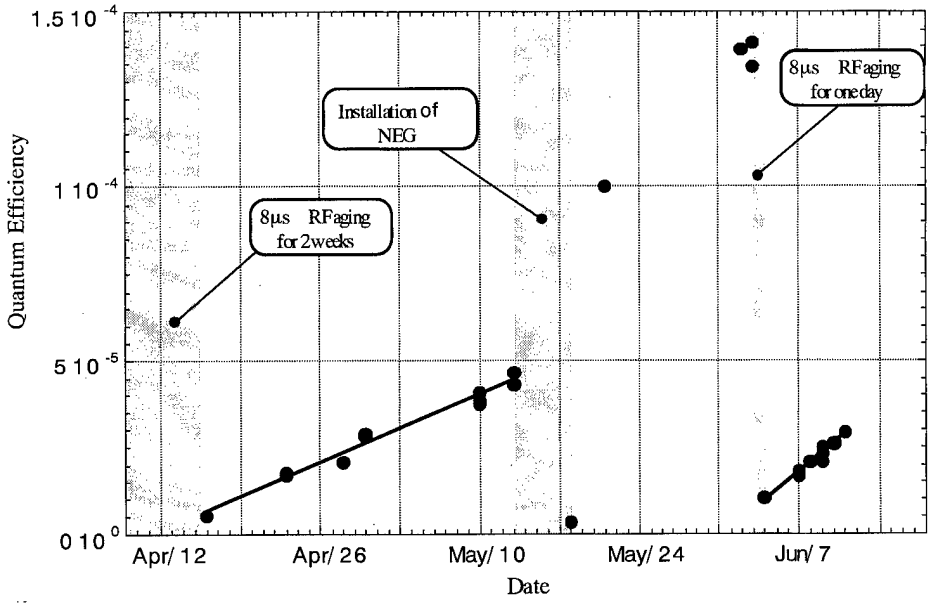


Fig. 8. Typical history of degradation and recovery of QE.

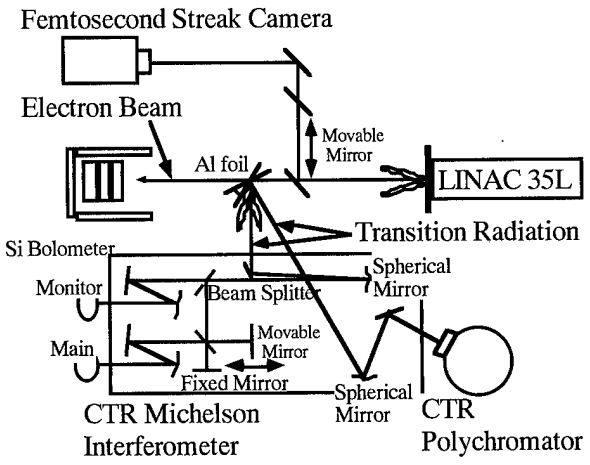


Fig. 9. Electron bunch diagnostic setup.

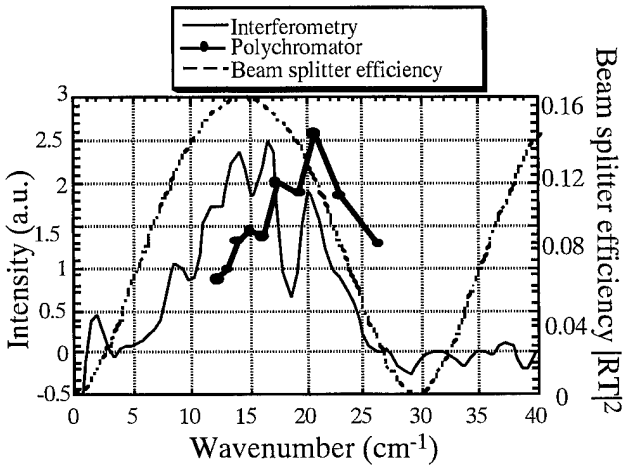


Fig. 10. Spectrum of CTR.

interferometer [24] after having tested the Martin–Pupplett interferometer [14]. Further, we have tried the far-infrared polychromator, which consists of one grating, 10-ch InSb bolometer array, and cryostat, for single-shot measurement [25]. The power spectrum of CTR can be obtained shot by shot by using it. The shot-by-shot diagnosis is useful and important for investigating the fluctuation and instability of RF linacs. Thus, we have prepared the diagnostic tools in both temporal and spectral regions. It is important to have more than two methodologies based on different physics to confirm the results.

We have simultaneously performed the comparison of measurement of subpicosecond electron pulses among the femtosecond streak camera, the Michelson interferometry, and the polychromator measurement, as shown in Fig. 9. The measurement was done using the first linac with the 90-keV thermionic gun. Because it can also generate a subpicosecond electron bunch [20], it is not a problem for checking their time resolutions. We measured the transition radiation in the far-infrared region emitted by an electron bunch at the Al-foil in the air after the 50-μm–thick Ti window at the end of the first linac with the thermionic gun. We used liquid He-cooled Si bolometers as a detector for the far-infrared radiation. The major beam parameters are as follows: the energy was 34 MeV, the pulse length is about 600 fs (FWHM), and the electron charge per bunch is controlled to be from 10 to 100 pC, avoiding the overscale of the detectors.

The longitudinal distribution is evaluated based on the theory of coherent transition radiation. The longitudinal bunch form factors obtained by the two methods were rather limited because of the nonuniform transparency of the 100-μm–thick Mylar beam splitter in the Michelson interferometer and measurement region that depends on the grating pitch (1.0 mm) installed in the polychromator. Therefore, we have to adopt theoretical extrapolation assuming the Gaussian or exponential distributions out of the range, referring to the pulse shape measured by the streak camera. The CTR spectrum calculated

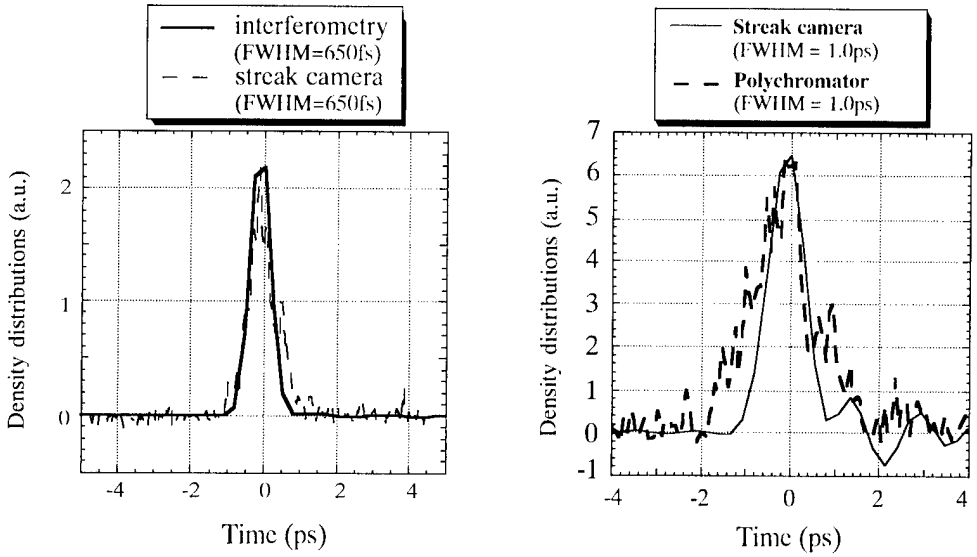


Fig. 11. Bunch distributions obtained by the femtosecond streak camera, CTR Michelson interferometer, and far-infrared polychrometer.

from the interferogram and by the polychromator are shown by the solid curves and the transparency of the beam splitter by the dashed curve in Fig. 10. From the figure, we decided to use the experimental data in the range of 9.5 to 18.0 cm^{-1} for the analysis in the interferometry, whereas the measurable range of the polychromator was already determined from 12.2 to 26.2 cm^{-1} discretely by the 1-mm grating pitch.

Finally, we reconstructed the longitudinal bunch distributions after using Kramers–Kronig relation to derive the phase information. The result of the subpicosecond pulse measurement by the interferometry and that by the polychromator were 650 fs ps at FWHM, as shown in Fig. 11. The typical result by the streak camera is also shown in the same figure. Here, we have reasonable agreement and confirm enough reliability of the diagnostics methods by the CTR measurement.

Up to 200 fs (FWHM), the streak camera is the best because direct bunch shape can be obtained shot by shot. However, we expect that the CTR methods are promising for the shorter electron beam than 200 fs with better resolution, because the coherent spectrum shifts from the far-infrared region to the infrared or visible region where the sensitivity of the detector becomes better. Especially, the polychromator can be expected to be the most powerful method because of the advantage of diagnostics by a single shot.

V. Electron-Laser Synchronization

In a future laser plasma accelerator with a laser photocathode RF injector, one laser driver is to supply, via a passive beam splitter, two laser pulses for both electron emission at the RF gun and wakefield generation in a plasma. Because the time period of the wake would be very short as 200 fs, the reduction of timing jitter between the electron bunch and original laser pulse is important. We previously evaluated the timing jitter between the 3-TW 100-fs laser and our first linac with the thermionic gun to be 3.7 ps (rms) [33]. Here, we synchronized them via the master RF of 119-MHz, RF synchronized trigger pulses and timing stabilizer at the fundamental RF frequency (Spectra-Physics, Lok-to-clock). The laser and electron pulses were simultaneously measured in the same streak image at 100 times. The histogram of the time difference gives the standard deviation of 3.7 ps, assuming that the distribution is Gaussian. Now, we have done the same measurement for the second linac and the YLF laser driver using the same streak camera. One typical streak image is shown in Fig. 12. The histogram in Fig. 13 indicates the timing jitter of 3.5 ps (rms) this time. It should be emphasized that almost the same jitter is observed, although only one laser driver is used here. This is because the timing jitter between the laser pulse and the accelerating RF phase still remains, and it is dominant to the total jitter. The improvement for this problem will be discussed in Section VI.

VI. Next Project at University of Tokyo

A new femtosecond, ultrafast quantum phenomena research facility has been installed at the laboratory in 1999. Here, the upgraded femtosecond S-band twin linac system mentioned in Section V, the 12-TW 50-fs laser, X-ray diffraction analysis devices, X-ray CCD camera system, X-ray photo-electron spectroscopy (XPS) device, and the Fourier transform infrared spectroscopy device (FTIR) have been installed as shown in Fig. 14.

In order to achieve subpicosecond linac-laser synchronization, we have designed and constructed a new system introducing the most advanced technologies, as shown in the left-hand-side of Fig. 14. The design is based on the achievement at FELIX of FOM, where the timing jitter between the electron and FEL pulse is 400 fs (rms) [34]. The technologies are a Kerr-lens mode-locked Ti : Sapphire laser with the timing stabilizer at the min harmonics RF (Coherent, Santa Clara, CA, Synchro-lock), the compact laser amplifiers, one stable 15-MW klystron RF power supplier (Mitsubishi, Hami, Japan, Modifed PV-3015), temperature-controlled (within 1 °C) laser clean room (CLASS 10 000), the vacuum laser transport line, and so on. Timing jitters between the electron and laser pulses in the previous and new systems are evaluated in Table II. Kobayashi *et al.* achieved 77-fs (rms) timing jitter at their mode-locked Ti : Sapphire laser

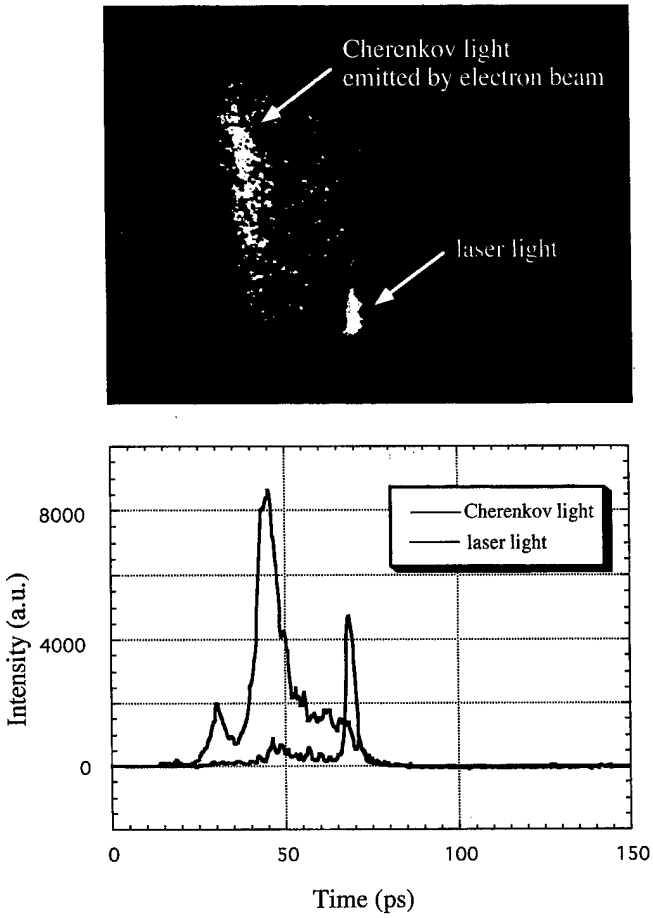


Fig. 12. Electron and laser pulses measured by the femtosecond streak camera.

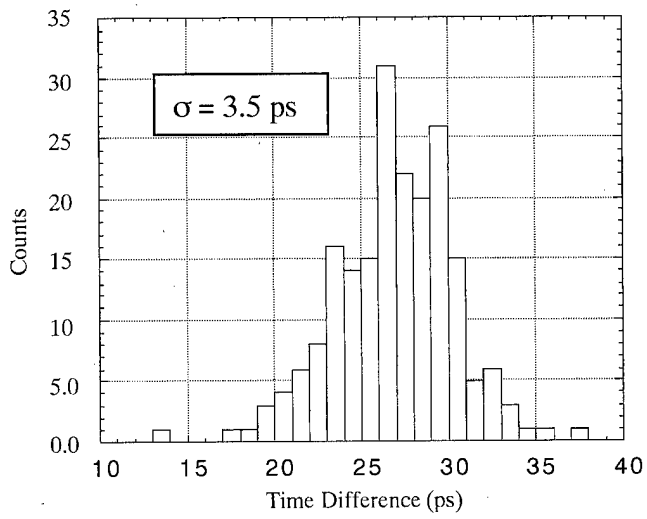


Fig. 13. Histogram of the time difference between the electron and laser pulses.

[35]. Concerning the timing jitter at a laser oscillator, recent passive Ti : Sapphire passive mode-locker using the Kerr-lens effect (for example, Coherent, Mira) is superior to conventional active Ti : Sapphire mode-lockers using an A/O crystal (for example, Spectra-Physics, Tsunami). The nonlinear Kerr-lens effect in the Ti : Sapphire crystal enables much faster feedback tuning of the resonance frequency of the laser pulses. The timing stabilizer operating at the min harmonics of the input RF of 79.3 MHz is also effective. This is because the spectral noise caused by the timing jitter is enhanced by the square of the harmonic number, whereas that caused by the power fluctuation is constant [36]. When we use two independent klystrons for the RF gun and accelerating tube, respectively, the electron bunch suffer from the mutual RF fluctuation between the two klystrons. In order to avoid this effect, we have chosen to use one klystron to feed RF into them. The electron beam jitter corresponds to the jitter of of the electron bunch behind the chicane because of fluctuations of RF power and phase, which are evaluated by the klystron performance data and PARMELA simulation. Here, we used the RF voltage fluctuation of 0.02 dB (rms) and phase fluctuation of 0.2°(rms) based on the measurement using another same type of the klystron. The jitter of the time-of-flight gives the timing jitter of 300 fs (rms) in the linac. The total timing jitter between the electron and laser pulses is expected to be ~320 fs (rms), according to (7), in the new system

$$\sigma_{\text{total}}^2 = \sigma_{rf}^2 + \sigma_{\text{laser}}^2. \tag{7}$$

We also plan to try the other plasma-cathode–like candidate by using the 12-TW 50-fs laser. When the 12-TW 50-fs laser is focused down to about 10 μm in diameter into a 1-mm ϕ gas jet in a vacuum chamber, laser plasma and electromagnetic wake wave are induced. If the laser vector potential proceeds the wake wavebreaking limit, the wake wave energy is transferred to the longitudinal energy of electrons in the plasma. Thus, preacceleration and injection of an electron bunch onto the wake wave is achieved. We call it as a laser plasma linac, in which only a single 12-TW 50-fs laser is used and the wake wavebreaking is sophisticatedly handled. PIC-2D simulations show that about 10 fs, a 20-MeV, 10-pC electron bunch is available [16]. The experiment started in early 2000. Electron beam parameters such as energy, charge, emittance, and bunch length are to be evaluated. Because the accelerated electron beam is bunched around the stable phase of the plasma wave, the timing jitter between the beam and the plasma wave in a main laser plasma accelerator could fulfill the specification of Table I. This is because both the plasma waves are excited by one multiterawatts laser and a passive beam splitter.

VII. Conclusion

The feasibility and reliability of the laser photocathode RF gun, BNL/GUN-IV, as an injector for a laser plasma accelerator were carefully investigated and evaluated. The 17-MeV, 6-π mm.mrad, 350-pC, 240-fs (72-μm) (FWHM) electron bunch was tested and evaluated. According to the simulation by Rosenzwig *et al.* [2], we can reduce the emittance and bunch length to fulfill the specification by tuning the laser intensity and reducing the change per bunch. Present timing jitter between the drive laser and electron bunch is 3.5 ps (rms). As for improving the timing jitter, a new linac-laser synchronization system to establish 320-fs (rms) resolution has been constructed and is going to be commissioned, as mentioned in Section VI. However, the large timing jitter caused by RF fluctuation is still serious. We may have to additionally introduce a kind of feedback control

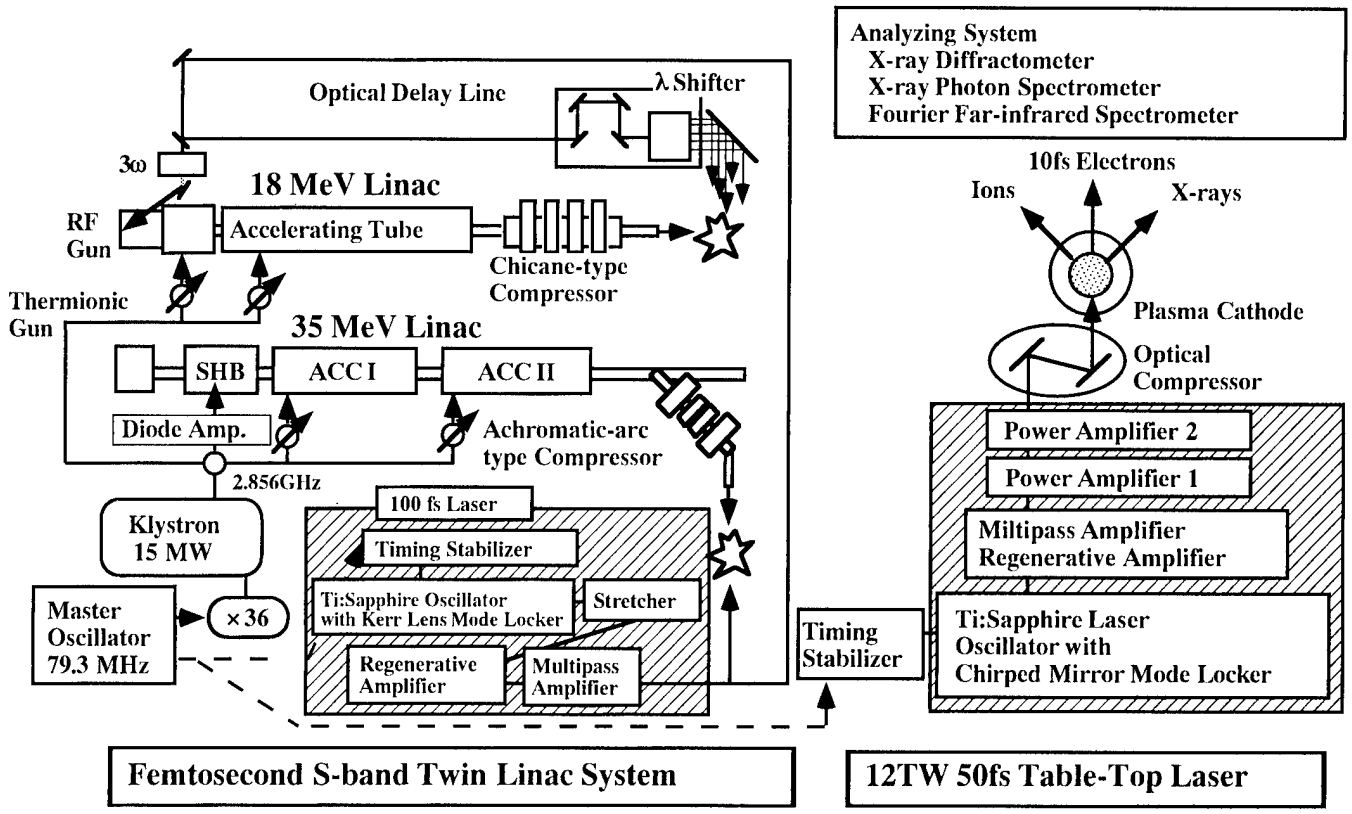


Fig. 14. Femtosecond ultrafast quantum phenomena research facility.

TABLE II
MEASURED AND DESIGNED TIMING JITTERS (RMS) IN THE PREVIOUS AND NEW SYSTEMS

	Previous system (measured)		New system (design)
	Thermionic	Photocathode	Photocathode
RF linac (σ_{rf})	a few ps	a few ps	300fs
Mutual jitter between two klystrons (σ_{rf2})	a few ps	a few ps	~0fs
Laser (σ_{laser})	< 3ps	< 3ps	100fs
Laser mode-locker	Active by A/O		Passive by Kerr lens
Timing stabilizer	at the fundamental (79.3MHz)		at 10th harmonics (793MHz)
Total	3.7ps	3.5ps	320fs

system in which the RF phase in the gun is detected and the laser pass length is tuned, for example, [37]. Other important aspects, such as dark current and performance of QE, are also under continuous observation and close to being overcome. Although other candidates, such as the inverse free electron laser, plasma cathode, pulsed photodiode, and W-band linac, have many advantages, enough experimental evidences have not yet been accumulated. Thus, in order to make the laser photocathode RF gun + booster + magnetic bunch compressor be more feasible for the injector, we have to continue making efforts to reduce the emittance, bunch length, and timing jitter.

ACKNOWLEDGMENT

The authors would like to thank Dr. X. Wang, Dr. I. Ben-Zvi of BNL, Prof. M. Washio of Waseda University, and Dr. A. Endo of Sumitomo Heavy Industries for their collaboration and discussion on the development of the RF gun. They would also like

to thank Dr. G. Knipples for his discussion on the linac-laser synchronization.

REFERENCES

[1] X. J. Wang, M. Babzien, K. Batchelor, I. Ben-Zvi, R. Malone, I. Pogorelsky, X. Qui, J. Sheehan, J. Sharitka, and T. Srinivasan-Rao, "Experimental characterization of the high-brightness electron photoinjector," *Nucl. Instrum. Methods A*, vol. 375, pp. 82–86, 1996.

[2] J. Rosenzweig, S. Anderson, K. Bishofberger, X. Ding, A. Murokh, C. Pellegrini, H. Suk, A. Tremaine, C. Clayton, C. Joshi, K. Marsh, and P. Muggli, "The neptune photoinjector," *Nucl. Instrum. Methods A*, vol. 410, no. 3, pp. 437–451, 1998.

[3] D. T. Palmer, X. J. Wang, R. H. Miller, M. Babzien, I. Ben-Zvi, C. Pellegrini, J. Sheehan, J. Skaritka, H. Winick, M. Woodle, and V. Yakimenko, "Emittance sudies of the BNL/SLAC/UCLA 1.6 cell photocathode RF gun," in *Proc. 1999 Particle Accelerator Conf.*, 1999, pp. 2687–2689.

[4] S. V. Milton *et al.*, "The FEL development at the advanced photon source," *SPIE*, vol. 3614, pp. 86–95, 1999.

[5] I. Ben-Zvi, "Recent progress in photoinjectors," in *Adv. Accelerator Concepts (1996), AIP Conf. Proc.*, 1997, pp. 40–54.

[6] D. Umstadter, J. K. Kim, and E. Dodd, "Laser injection of ultrashort electron pulses into wakefield plasma waves," *Phys. Rev. Lett.*, vol. 76, no. 12, pp. 2073–2076, 1996.

[7] E. Esarey, R. F. Hubbard, W. P. Leemans, A. Ting, and P. Sprangle, "Electron injection into plasma wake fields by colliding laser pulses," *Phys. Rev. Lett.*, vol. 79, no. 14, pp. 2682–2685, 1997.

[8] S. Bulanov, N. Naumova, F. Pegoraro, and J. Sakai, "Particle injection into the wave acceleration phase due to nonlinear wake wave breaking," *Phys. Rev. E*, vol. 58, no. 5, pp. R5257–R5260, 1998.

[9] Y. Liu, X. J. Wang, D. B. Cline, M. Babzien, J. M. Frang, J. Gallardo, K. Kusche, I. Pogorelsky, J. Skaritka, and A. van Steenbergen, "Experimental observation of femtosecond electron beam microbunching bya inverse free-electron-laser acceleration," *Phys. Rev. Lett.*, vol. 80, no. 70, pp. 4418–4421, 1998.

[10] C. Clayton, private communication, 1999.

[11] D. T. Palmer, M. J. Hogan, M. Ferrario, and L. Serafini, "A 90 GHZ photoinjector," in *Proc. 1999 Particle Accelerator Conf.*, 1999, pp. 1997–1999.

[12] H. Dewa, H. Ahn, H. Harano, M. Kando, K. Kinoshita, S. Kondoh, H. Kotaki, K. Nakajima, H. Nakanishi, A. Ogata, H. Sakai, M. Uesaka, T. Ueda, T. Watanabe, and K. Yoshii, "Experiments of high energy gain laser wakefield acceleration," *Nucl. Instrum. Methods A*, vol. 410, no. 3, pp. 357–363, 1998.

[13] M. Uesaka, K. Kinoshita, T. Watanabe, T. Ueda, K. Yoshii, H. Harano, J. Sugahara, K. Nakajima, A. Ogata, F. Sakai, H. Dewa, M. Kando, H. Kotaki, and S. Kondo, "Femtosecond electron beam generation by S-band laser photocathode RF gun and linac," in *Proc. Adv. Accelerator Concepts (1998), AIP Conf.*, 1999, pp. 908–917.

[14] M. Uesaka, K. Kinoshita, T. Watanabe, T. Ueda, K. Yoshii, H. Harano, K. Nakajima, A. Ogata, F. Sakai, H. Kotaki, M. Kando, H. Dewa, S. Kondo, Y. Shibata, K. Ishi, and M. Ikezawa, "Femtosecond electron beam generation and measurement for laser synchrotron radiation," *Nucl. Instrum. Methods A*, vol. 410, no. 3, pp. 424–430, 1998.

[15] K. Nakajima, "Laser accelerator developments for future high-energy accelerators," *Nucl. Instrum. Methods A*, vol. 410, no. 3, pp. 514–519, 1998.

[16] N. Hafz, M. Uesaka, J. Koga, K. Nakajima, and S. Bulanov, "Numerical analysis of tens relativistic electron beam generation using single 127 WSOFS laser pulse," *Nucl. Instrum. Methods A*, to be published.

[17] D. X. Wang, G. A. Krafft, and C. K. Sinclair, "Measurement of femtosecond electron bunches using a RF zero-phasing method," *Phys. Rev. E*, vol. 57, no. 2, pp. 2283–2286, 1998.

[18] K. T. McDonald and D. P. Russell, *Method of Emittance Measurement*. New York: Springer-Verlag, 1998, pp. 122–132. Lecture Note 343.

[19] A. H. Lumpkin, *FEL Challenges II* San Jose, CA, Jan. 1999.

[20] M. Uesaka, T. Ueda, T. Kozawa, and T. Kobayashi, "Precise measurement of a subpicosecond electron single bunch by the femtosecond streak camera," *Nucl. Instrum. Methods A*, vol. 406, pp. 371–379, 1998.

[21] Y. Shibata, T. Takahashi, T. Kanai, K. Ishi, and M. Ikezawa, "Diagnostics of an electron beam of a linear accelerator using coherent transition radiation," *Phys. Rev. E*, vol. 50, no. 2-B, pp. 1479–1484, 1994.

[22] R. Lai, U. Happek, and A. J. Sievers, "Measurement of the longitudinal asymmetry of a charged particle bunch from the coherent synchrotron or transition radiation spectrum," *Phys. Rev. E*, vol. 50, no. 6, pp. R4294–R4297, 1994.

[23] H. Lihn, P. Kung, C. Settakorn, H. Wiedemann, and D. Bocek, "Measurement of subpicosecond electron pulses," *Phys. Rev. E*, vol. 53, no. 6, pp. 6413–6418, 1996.

[24] T. Watanabe, M. Uesaka, J. Sugahara, T. Ueda, K. Yoshii, Y. Shibata, F. Sakai, S. Kondo, M. Kando, H. Kotaki, and K. Nakajima, "Subpicosecond electron single beam diagnostics by coherent transition radiation interferometer and streak camera," Nucl. Instrum. Methods A, to be published.

[25] J. Sugahara, T. Watanabe, K. Yoshii, T. Ueda, M. Uesaka, Y. Kondo, Y. Shibata, K. Ishi, and M. Ikezawa, "Comparison of femtosecond electron beam diagnostic methodologies," in *Proc. 1999 Particle Accelerator Conf.*, 1999, pp. 2187–2189.

[26] L. Serafini and D. Umstadter *et al.*, private communication, 1999.

[27] X. J. Wang, "Producing and measureing small electoron bunches," in *Proc. 1999 Particle Accelerator Conf.*, 1999, pp. 229–233.

[28] V. Yakimenko, M. Babzien, I. Ben-Zvi, R. Malone, and X. J. Wang, "Emittance control of a beam by shaping the transverse charge distribution, using a tomography diagnostic," in *Proc. 1998 Eur. Particle Accelerator Conf.*, 1998, pp. 1641–1643.

[29] M. Babzien, I. Ben-Zvi, R. Malone, X. J. Wang, and V. Yakimenko, "Recent progress in emittance control of the photoelectron beam using transverse laser shape modulation and tomography technique," in *Proc. 1999 Particle Accelerator Conf.*, 1999, pp. 2158–2160.

[30] R. Hajima, "Self-interaction of subpico-second electron bunch traveling through a Chicane-based bunch-compressor," *Nucl. Instrum. Methods A*, vol. 429, pp. 264–268, 1999.

[31] T. Srinivasan-Rao, J. Yu, and X. J. Wang, "Study on the sensitivity of quantum efficiency of copper photocathodes on sample preparation," BNL 62 626, 1996.

[32] T. Srinivasan-Rao, I. Ben-Zvi, J. Smedley, X. J. Wang, M. Woodle, D. T. Palmer, and R. H. Miller, "Performance of magnesium cathode in the S-band RF gun," in *Proc. 1997 Particle Accelerator Conf.*, 1997, pp. 2790–2792.

[33] M. Uesaka, T. Watanabe, T. Ueda, M. Kando, K. Nakajima, H. Ktaki, and A. Ogata, "Production and utilization of synchronized femtosecond electron and laser single pulses," *J. Nucl. Mater.*, vol. 248, pp. 380–385, 1997.

[34] G. M. H. Knippels, M. J. van de Pol, H. P. M. Pellemans, P. C. M. Planken, and A. F. G. van der Meer, "Two-color facility based on a broadly tunable infrared free-electron laser and a subpicosecond-synchronized 10-fs-Ti : Sapphire laser," *Opt. Lett.*, vol. 23, no. 22, pp. 1754–1756, 1998.

[35] K. Kobayashi, T. Miura, Z. Zhang, and K. Torizuka, "Sub 100 fs timing jitter of mode-locked laser," *SPIE*, vol. 3616, pp. 156–164, 1999.

[36] D. von der Linde, "Characterization of the noise in continuously operating mode-locked lasers," *Appl. Phys. B*, vol. 39, pp. 201–217, 1986.

[37] P. Muggli, private communication, 1999.

Mitsuru Uesaka, photograph and biography not available at the time of publication.

Kenichi Kinoshita, photograph and biography not available at the time of publication.

Takahiro Watanabe, photograph and biography not available at the time of publication.

Jun Sugahara, photograph and biography not available at the time of publication.

Toru Ueda, photograph and biography not available at the time of publication.

Koji Yoshii, photograph and biography not available at the time of publication.

Tetsuya Kobayashi, photograph and biography not available at the time of publication.

Nasr Hafz, photograph and biography not available at the time of publication.

Kazuhisa Nakajima, photograph and biography not available at the time of publication.

Fumio Sakai, photograph and biography not available at the time of publication.

Masaki Kando, photograph and biography not available at the time of publication.

Hideki Dewa, photograph and biography not available at the time of publication.

Hideyuki Kotaki, photograph and biography not available at the time of publication.

Shuji Kondo, photograph and biography not available at the time of publication.

Inverse Cerenkov Acceleration and Inverse Free-Electron Laser Experimental Results for Staged Electron Laser Acceleration

Lora P. Campbell, Christian E. Dilley, Stephen C. Gottschalk, Wayne D. Kimura, *Senior Member, IEEE*, David C. Quimby, Loren C. Steinhauer, Marcus Babzien, Ilan Ben-Zvi, Juan C. Gallardo, Karl P. Kusche, Jr., Igor V. Pogorelsky, John R. Skaritka, Arie van Steenbergen, *Senior Member, IEEE*, Vitlay E. Yakimenko, David B. Cline, Ping He, Yabo Liu, and Richard H. Pantell, *Life Fellow, IEEE*

***Abstract*—The goal of the staged electron laser acceleration (STELLA) experiment is to demonstrate staging of the laser acceleration process whereby an inverse free electron laser (IFEL) will be used to prebunch the electrons, which are then accelerated in an inverse Cerenkov accelerator (ICA). As preparation for this experiment, a new permanent magnet wiggler for the IFEL was constructed and the ICA system was modified. Both systems have been tested on a new beamline specifically built for STELLA. The improved electron beam (e-beam) with its very low emittance (0.8 mm-mrad normalized) enabled focusing the e-beam to an average radius (1σ) of 65 μm within the ICA interaction region. This small e-beam focus greatly enhanced the ICA process and resulted in electron energy spectra that have demonstrated the best agreement to date in both overall shape and magnitude with the model predictions. The electron energy spectrum using the new wiggler in the IFEL was also measured. These results will be described as well as future improvements to the STELLA experiment.**

***Index Terms*—Carbon dioxide lasers, electron accelerators, electron linear accelerators, inverse Cerenkov accelerators, inverse free electron laser, laser accelerators, linear accelerators, particle beam measurements.**

I. Introduction

EXCITING progress has been made in the last several years on laser accelerators, including energy gains of >100-MeV and GeV/m acceleration gradients [1]. At the Brookhaven National Laboratory (BNL) Accelerator Test Facility (ATF), Upton, NY, there are two laser acceleration experiments—an inverse Cerenkov accelerator (ICA) [2] and an inverse free electron laser (IFEL) [3] that uses an electromagnet wiggler. Both of these experiments have been routinely accelerating electrons. The next logical step in the evolution of laser accelerators is to address the issue of multiaccelerator module staging and reacceleration of the microbunches produced during the laser acceleration process.

Achieving a high net energy gain will undoubtedly require using multiple acceleration stages as is done in microwave linacs. To efficiently accelerate the electrons throughout these stages, it is necessary to prebunch the electrons into a microbunch whose longitudinal length is a small fraction of the accelerating wave. In laser accelerators, this accelerating wave can be an optical wave with wavelengths of order 10 μm, such as in an ICA or IFEL device, or a plasma wave with wavelengths of order 100 μm, such as in a plasma beatwave or wakefield device [4], [5].

Generating these optical microbunches is already occurring in these devices. In experiments, such as the ICA and IFEL, the electrons presently interact with the laser light over all phases of the lightwave. Consequently, some of the electrons are accelerated and some are decelerated. If allowed to drift, the fast electrons catch up with the slow electrons, resulting in a longitudinal density modulation whose spacing is the same as the wavelength of the laser light (e.g., 10.6 μm at the ATF).

Evidence of this microbunching has already been detected from the IFEL in a separate experiment [6] using a coherent transition radiation (CTR) diagnostic. In this diagnostic, the microbunches pass through a thin metal foil and generate enhanced transition radiation at the harmonics of the laser light [7]. This enhancement over the spontaneous (i.e., nonmicrobunched) radiation at the harmonics of the laser light is indicative of microbunches occurring at optical wavelengths.

Staging requires rephasing the microbunches with the accelerating lightwave. Efficient acceleration of the electrons contained within a microbunch also requires capturing the electrons within the acceleration potential well. This implies the need to limit the phase extent of the microbunch and to minimize effects that can lead to bunch smearing. The latter term refers to electrons that for whatever reason no longer stay within the main bunch distribution. These reasons may be because of trajectory differences of the electrons within the microbunch, gas scattering effects in the case of ICA, and space-charge spreading [8]. Although these effects are analogous to those encountered in microwave linacs, they can have a much greater impact in laser acceleration because of the orders of magnitude shorter wavelengths that are involved.

Manuscript received October 1, 1999; revised February 2, 2000. This work was supported by the U.S. Department of Energy, under Grants DE-FG03-98ER41061, DE-AC02-98CH10886, and DE-FG03-92ER40695.

L. P. Campbell, C. E. Dilley, S. C. Gottschalk, W. D. Kimura, D. C. Quimby, and L. C. Steinhauer are with STI Optronics, Inc., Bellevue, WA 98004-1495 USA (e-mail: wkimura@stioptronics.com).

M. Babzien, I. Ben-Zvi, J. C. Gallardo, K. P. Kusche, Jr., I. V. Pogorelsky, J. R. Skaritka, A. van Steenbergen, and V. E. Yakimenko are with the Brookhaven National Laboratory, Upton, NY 11973 USA.

D. B. Cline, P. He, and Y. Liu are with the University of California at Los Angeles, Los Angeles, CA 90095 USA.

R. H. Pantell is with Stanford University, Stanford, CA 94305 USA.

Publisher Item Identifier S 0093-3813(00)07244-1.

0093–3813/00$10.00 © 2000 IEEE

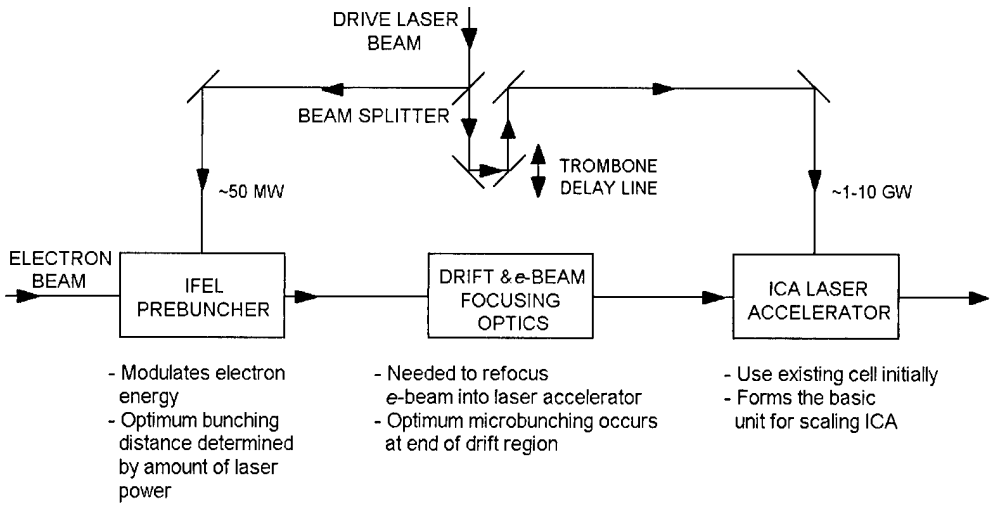


Fig. 1. Conceptual layout for the STELLA experiment.

Therefore, the primary goal of the staged electron laser acceleration (STELLA) experiment at the BNL ATF is to demonstrate effective acceleration by an ICA acceleration stage of microbunches generated by an IFEL. During the course of this experiment, other related issues, such as generation and preservation of the microbunch and effective control of the rephasing process, will be examined. These results will directly benefit laser acceleration research in general by demonstrating that efficient staging is possible. This accomplishment will open the door to the next step of adding multiple laser acceleration stages in series to achieve high net energy gain.

As part of preparations for STELLA, the IFEL was relocated upstream of the ICA system. As described below, a new permanent magnetic wiggler was constructed to replace the electromagnet used during the previous IFEL experiments, and the ICA system was slightly modified. In parallel to these preparations, the ATF electron beam (e-beam) and CO_2 laser were upgraded to improve their performance and reliability. Most noteworthy of these improvements is the very low emittance of the e-beam as a result of improvements to the photocathode RF gun system, including the drive laser [9]. This enabled the e-beam to be focused to a near-optimum radius ($1\sigma = 50$–100 μm) within the ICA interaction region. Hence, during the process of recommissioning the ICA system, new laser-modulated electron energy data were obtained, which exhibited significantly improved agreement with the model predictions compared with earlier ICA measurements. The primary subject of this paper is the new ICA results plus data from the IFEL with its new wiggler, and their comparisons with model predictions.

Section II describes the experiment. The experimental results are presented in Section III. Improvements to the ICA optical system are discussed in Section IV, and conclusions are given in Section V.

II. Description of Experiment

Details of the STELLA experiment can be found elsewhere [10], [11] and are briefly reviewed here. Fig. 1 is a schematic diagram of the basic STELLA layout. The e-beam from the ATF linac, which consists of a single ~6-ps, 45-MeV macropulse, enters the IFEL prebuncher from the left. A relatively small amount of laser power is sent using a beamsplitter to the IFEL for modulating the electron energy. The objective is to modulate the energy just enough so that maximum bunching occurs at the end of the drift region just before the entrance to the ICA laser acceleration stage. The rest of the laser power passes through a trombone delay line and to the ICA stage. This trombone delay line is used to adjust the relative phase of the laser light in the ICA cell with the microbunches created by the IFEL.

The electrons in the macropulse leave the IFEL with their energies modulated by the laser beam inside the wiggler. This energy modulation of the macropulse transforms into a longitudinal density modulation as the electrons drift between the IFEL and the ICA cell. This density modulation is characterized by the formation of a train of microbunches with each microbunch roughly 1 μm in length, separated by the laser wavelength, i.e., 10.6 μm, and contained within the 6-ps envelope of the single macropulse. The e-beam exiting the IFEL is refocused into the ICA gas cell using a quadrupole triplet located in the drift region.

One modification made to the ICA gas cell is shortening the interaction region length to 6.5 cm from its original 20-cm length. This helps reduce the effects of gas scattering, which tends to smear out the microbunches traveling through the cell.

After the electrons exit the gas cell, they enter the energy spectrometer at the end of the beamline. This spectrometer [12] was specially designed for the STELLA experiment and features a wide energy acceptance range of up to $\pm 20\%$, with a 2% or better energy resolution. This permits the entire laser-modulated energy spectrum to be measured during each shot, which eliminates a major source of error during previous ICA measurements when multiple shots were needed to construct the full spectrum [2].

Additional characterization of the microbunches is performed using a CTR diagnostic located just before the ICA interaction region. This diagnostic is based on the earlier version demonstrated at the ATF [6].

A key aspect of the experiment is rephasing of the microbunches with the laser light in the ICA stage. The

modulation imparted by the laser beam in the IFEL defines a specific microbunch longitudinal density distribution within the macropulse. To efficiently trap and accelerate the microbunches, the laser beam in the ICA cell must be properly synchronized in phase with the microbunches entering the cell. As mentioned, this is accomplished using the trombone optical delay line shown in Fig. 1.

Other than the shortened interaction region, the ICA system is essentially the same as during previous experiments. For example, it still features a radially polarized laser beam [13] and an axicon mirror for focusing the laser beam onto the e-beam [14]. The shortened interaction region, however, means the laser beam diameter entering the cell is smaller. (Outer radius = 1.6 mm instead of 5 mm.) This limits the amount of laser peak power that can be delivered to the cell to roughly <100 MW in order to avoid damaging the ZnSe input window. (Future improvements will be made to overcome this limitation.)

The electromagnet wiggler used in the previous IFEL experiments [3] features a 60-cm long sapphire tube with an inner diameter of 2.8 mm, through which both the e-beam and laser beam must propagate. This small-diameter tube made it difficult to maintain the necessary e-beam quality as the e-beam passed through the wiggler to the ICA gas cell. To overcome this difficulty, a new permanent magnetic wiggler was designed and constructed at STI Optronics, Inc., Bellevue, WA, to replace the electromagnet wiggler. With a fixed-gap spacing of 8.14 mm, it uses a conventional metal vacuum pipe (ID = 4.75 mm, length = 40.6 mm) for transmission of the e-beam and laser beam. Table I gives the other pertinent specifications for the new wiggler. Because it is a fixed-gap permanent magnet device, achieving proper resonance for energy exchange between the electrons and laser beam requires the e-beam energy to be tuned to 45.65 MeV.

Because the STELLA experiment is located on a beamline shared by other users of the ATF, the new wiggler was designed to be easily removed away from the beamline by lifting it vertically off its kinematic feet using a pair of manually driven translation stages. This allows the e-beam to propagate through the wiggler vacuum tube without being affected by the wiggler magnets. However, the wiggler was also designed to be essentially transparent to the e-beam as it enters and exits the wiggler. Hence, in practice, it has been unnecessary to lift the wiggler away for the other users.

The modified ICA system and the IFEL with its new wiggler were tested separately; i.e., the wiggler was not installed during the recommissioning of the ICA system, and the IFEL was tested without the ICA gas cell installed on the beamline. Tables II and III list the parameters during the ICA recommissioning and IFEL experiments, respectively.

III. Experimental Results

A. Inverse Cerenkov Accelerator

Fig. 2(a) shows the laser-off electron energy spectrum ($\sim$150 pC), i.e., the spectrum of the e-beam after passing through the gas cell diamond windows and the hydrogen gas used for phase matching during the ICA process, but without the laser beam present. Superimposed on the data curve is the histogram generated by the ICA model [15] for the conditions given in Table II. (In all of the plots presented in this paper, the data and the model are plotted normalized to the integral under their curves.)

The ICA model is a Monte Carlo simulation that incorporates all effects, including gas scattering by the diamond windows and gas. It does not include space-charge effects, which separate analysis indicates will not have an appreciable effect on the STELLA experiment [8] as long as the macropulse charge is $\leq$150 pC. (As explained below, space charge can have a much greater effect for the IFEL prebuncher.)

The ICA model also assumes an ideal radially polarized laser beam. This point is important because the actual laser beam used during the experiment is not perfectly radially polarized. Moreover, it also contains optical imperfections, such as interference fringes, that tend to reduce the amount of laser field available to accelerate the electrons. As will be shown, this means the amount of laser energy that is useful for accelerating the electrons is generally less than is the amount delivered to the gas cell.

The agreement between the data and model for the laser-off case is very good, with the data displaying a slightly larger energy spread. This may be caused by limitation of the spectrometer. In order to have a wide energy acceptance range, the spectrometer tends to partially map the e-beam transverse size at its input plane onto its output plane. This e-beam image on the output plane then appears like energy dispersion. Fortunately, the results of Fig. 2(a) seem to indicate that this does not appear to be a significant effect.

Fig. 2(b) gives the results with the laser on. Again, the data and model are plotted normalized to the areas under their curves; no other adjustments are made to their overall magnitudes. This permits comparing the shape and magnitude of the laser-on cases. This is the first time such an accurate comparison could be performed.

The data and model exhibit both accelerated and decelerated electrons because the electrons interact with the laser beam inside the ICA cell over all phases of the lightwave. (Recall the ATF linac produces a single $\sim$6-ps e-beam pulse, whereas the CO_2 laser pulse is 200–300 ps long.) During STELLA, the microbunches produced by the IFEL will interact over only a portion of the lightwave phase in the ICA cell. Hence, depending on this phase point, the microbunches can either be accelerated or decelerated.

For the laser-on case, the model simulation used the parameters listed in Table II, where an average e-beam focus radius (1σ) of 65 μm is assumed. Only the net effective laser power delivered to the interaction region is a parameter that must be chosen. As explained earlier, it is known that the laser beam driving the ICA is not perfect, and therefore, the peak power used in the model must be derated from the amount measured at the entrance to the cell. The simulation depicted in Fig. 2(b) assumes a laser power of 45 MW, which is 1.9 times smaller than what is being delivered to the cell. The very good fit with the data implies that this value for the peak power is probably close to the true effective value. However, the apparent two-time reduction in the laser power implies that not all of the laser field

TABLE I
MEASURED SPECIFICATIONS FOR THE STELLA PERMANENT-MAGNET WIGGLER

Quantity	Value	Comments
Period	3.30 cm	
Overall length	33.0 cm	
Pole material	Pure iron	
Magnet material	NdFeB	
Number of poles	20	
Number of full strength poles	16	First two magnets at start and end of wiggler at 84% and 41% of average field strength
Wiggler parameter, K	2.91	
Effective field	0.945 T	Corresponds to 45.65 MeV resonance energy
Peak field	0.986 T	
Magnetic gap (fixed)	8.14 mm	
First integral, B_x, B_y	B_x = -0.2 G-cm B_y = 19 G-cm	Ambient field subtracted out of final measured values. B_y is in direction of primary field component (horizontal).
Internal trajectory, B_x, B_y	B_x not measured $-860 \le B_y \le 790$ G-cm^2	Corresponds to $<\pm 60$ μm at 45 MeV for all z, wiggle averaged
Second integral, B_x, B_y	B_x not measured B_y = -900 G-cm^2	
Integrated quadrupole, normal and skew	Normal = 15 G Skew = 12 G	
RMS optical phase error	2.6 deg.	

is being effectively used. This issue is discussed later in Section IV.

We should emphasize that the data shown in Fig. 2(b) is the first comparison of a full laser-on spectrum without the uncertainties introduced by combining multiple shots from different sections of the spectrum. Hence, this represents a marked improvement over previous data obtained from the ICA experiment.

Additional measurements were obtained to confirm that the amount of energy modulation scales as the square-root of the laser power by varying the laser power from ≈20 MW to ≈500 MW (damage of optics began to occur at this higher power level).

B. Inverse Free Electron Laser

Fig. 3 shows the laser-on electron energy spectrum produced by the IFEL operating with the permanent magnet wiggler. [The laser-off spectrum is similar to Fig. 2(a).] The solid line is the data, and the histogram is the model prediction, assuming 50 MW of laser peak power is delivered to the wiggler.

A different model from the ICA one is used for the IFEL. It is a one-dimensional electron tracking code used to follow the electron dynamics in FEL phase space. The model uses a simplified single-frequency version of the code described in [16], and electron slippage is neglected. The gain or loss of optical power (and intensity) is computed self-consistently with the electron

TABLE II
EXPERIMENTAL PARAMETERS DURING ICA RECOMMISSIONING EXPERIMENTS

Parameter	Value
E-beam energy	45 MeV
E-beam intrinsic energy spread (1σ)	0.28%
E-beam charge	~150 pC
Normalized rms emittance ($\gamma r\theta$)	0.8 mm-mrad
E-beam size in center of gas cell (1σ)	58 μm × 72 μm
E-beam pulse length (1σ)	~6 ps
Laser beam peak power at entrance to gas cell	87 MW
Laser beam pulse length (≈FWHM)	200-300 ps
Average laser beam radius at entrance to gas cell	1.6 mm (OD), 0.55 mm (ID)
Cerenkov angle	20 mrad
Diamond window thickness	2.1 μm
Hydrogen gas pressure	1597 Torr
Temperature of gas cell	70.3° F (21.3° C)

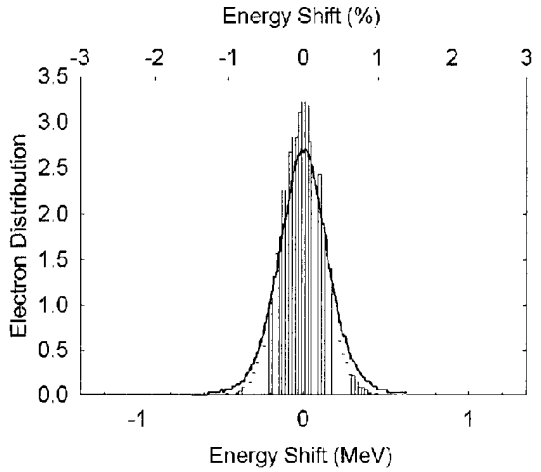
TABLE III
EXPERIMENTAL PARAMETERS DURING IFEL TESTS WITH PERMANENT-MAGNET WIGGLER

Parameter	Value
E-beam energy	45.65 MeV
E-beam intrinsic energy spread (1σ)	0.1%
E-beam charge	200 pC
Normalized rms emittance ($\gamma r\theta$)	~1 mm-mrad
E-beam pulse length (1σ)	~6 ps
Laser beam peak power delivered to wiggler	≈50 MW
Laser beam pulse length (≈FWHM)	200-300 ps

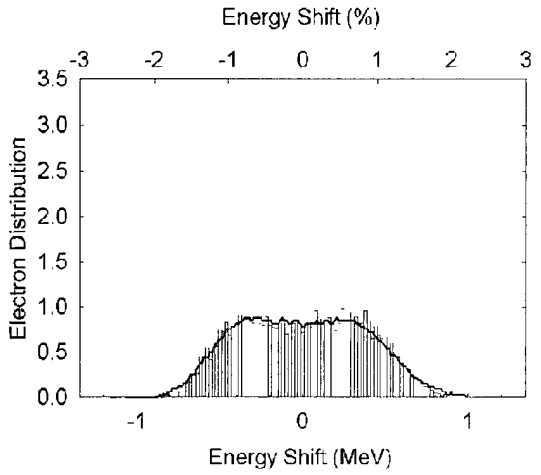
energy gain or loss. However, several simplifying assumptions are incorporated in this IFEL model. The transverse optical intensity and phase profiles are assumed to be spatially independent (i.e., the diffraction-free approximation). The intensity and phase profiles within the wiggler should be slowly varying with longitudinal position because the externally injected laser beam is focused as a Gaussian beam into the center of the wiggler vacuum pipe.

Variations seen in the maximum energy modulation of the laser-on data are indicated by the horizontal error bar on the right side of Fig. 3. These variations from shot-to-shot may be caused by changes in the laser peak power, changes in the *e*-beam overlap within the wiggler, or space-charge effects. This latter phenomenon could in fact be the dominant effect.

Our analysis [8] indicates that space-charge effects can affect the energy spectrum detected at the spectrometer location when the microbunches generated by the IFEL pass through a focus located at the optimum bunching point before being sent to the spectrometer. (This focus is nominally where the ICA gas cell is located.) This is because at this focus point, the charge density becomes appreciable in the longitudinal and the transverse dimensions. Space-charge forces acting on the electrons will alter the energy spread of the beam. Under certain conditions, it is possible for space charge to impart a greater energy spread than that induced by the laser in the IFEL. Consequently, the energy spread measured at the spectrometer would appear larger than that predicted for the laser-induced spread.



(a)



(b)

Fig. 2. Results for ICA tests. (a) Laser-off electron energy spectrum for the data (solid line) and model (histogram, 10 000 electrons). (b) Laser-on electron energy spectrum for the data (solid line) and model (histogram, 10 000 electrons). The data and model have been normalized to have equal integrals under their curves. The energy shift given in percentage at the top of the figure is for a 45-MeV e-beam. See text for discussion of the parameters used in the model.

Thus, the fact the energy spread of the data in Fig. 3 appears slightly larger than the spread predicted by the IFEL model may be because of space-charge effects. (Note, the e-beam charge was 0.2 nC during these measurements.) The disappearance in the data of the double peaks seen in the model simulation would also be consistent with space charge smearing the energy distribution. However, further studies and measurements are needed to verify and quantify this effect.

IV. Discussion

The improvement in the quality of this recent data over earlier ICA results can be attributed primarily to the higher quality of the e-beam and the subsequent ability to focus the e-beam into a small spot along the interaction region of the gas cell. In particular, the normalized rms emittance during these recent experiments was 0.8 mm-mrad, whereas during the first ICA experiments at the ATF [2], the normalized rms emittance was >60 mm-mrad. This large emittance meant the e-beam could

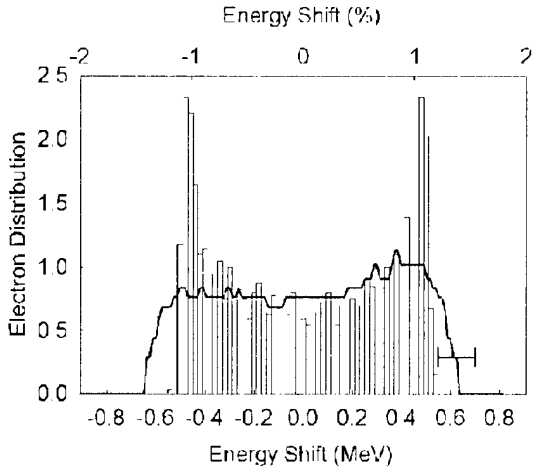


Fig. 3. Laser-on electron energy spectrum for the IFEL tests with permanent magnet wiggler. The data (solid line) and model (histogram, 2000 electrons) have been normalized to have equal integrals under their curves. The energy shift given in percentage at the top of the figure is for a 45.65-MeV e-beam. See text for discussion of the parameters used in the model.

not be focused to the optimum size within the ICA interaction region.

When the radially polarized laser beam is focused by the axicon, it creates a line focus along the e-beam trajectory and generates a longitudinal electric field that follows a $J_0(2\pi r\theta_c/\lambda)$ dependence, where J_0 is the Bessel function of the first kind of order zero, r is the radial position from the center of the electron trajectory, θ_c is the Cerenkov angle, and λ is the laser wavelength. For $\theta_c = 20$ mrad and $\lambda = 10.6$ μm, the width of the first lobe of the J_0 Bessel function is 200 μm [full-width at half maximum (FWHM)]. The e-beam during the earlier ICA experiments had a diameter of 500 μm. Consequently, the electrons within any transverse slice of the e-beam pulse would experience a wide range of laser electric field values. In other words, electrons intersecting the optical wave at, say, the optimum phase for acceleration are not all accelerated by the same amount. In fact, some of the electrons are decelerated because their large radial position takes them outside of the first lobe of the J_0 Bessel function and into its second lobe, where the sign of the field reverses.

As predicted by the model and confirmed by the earlier ICA measurements (see [2]), the laser-modulated energy spectrum under these nonoptimum focal conditions is more Gaussian in shape rather than having a flat-top distribution, as shown in Fig. 2(b). This is because most of the electrons are not being accelerated or decelerated effectively.

Contrast this with the recent ICA measurements where the 65-μm (1σ radius) e-beam focus fits well within the 200-μm wide J_0 Bessel function. Now, all of the electrons within any slice of the e-beam pulse experience nearly the same electric field. The net result is a more flat-top energy distribution.

The ATF CO_2 laser system is capable of delivering $\approx$1-GW peak power when operating with only its oscillator and preamplifier. Its new high-pressure CO_2 amplifier will allow delivering hundreds of gigawatts of peak power. Eventually $\sim$1 TW will be possible from the system.

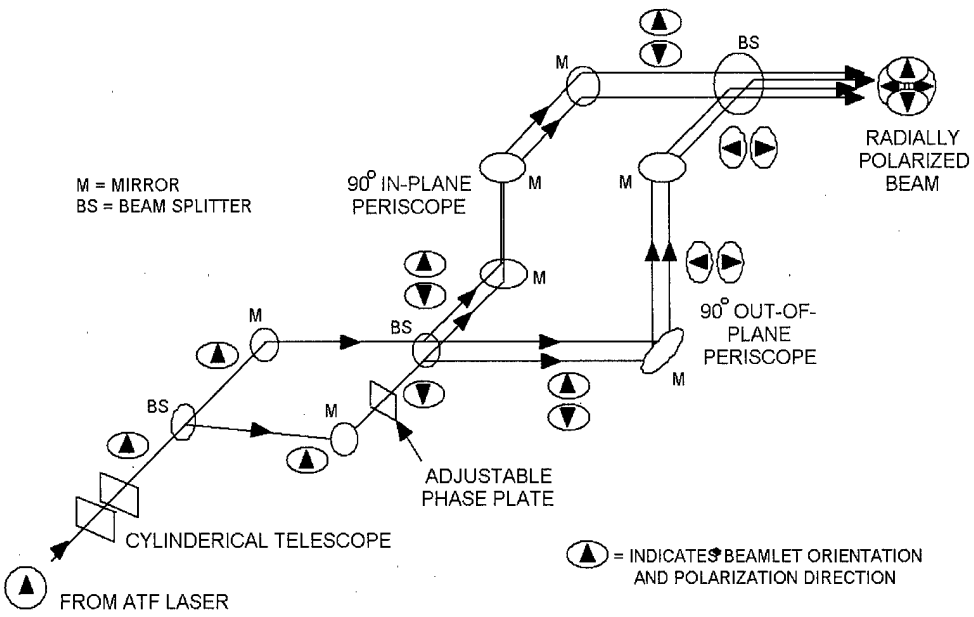


Fig. 4. Three-dimensional schematic of new radial polarization converter system.

In the near term, the first STELLA experiments will be conducted at low laser powers less than 1 GW to avoid optical damage problems. During this time, modifications will be made to the ICA optical system so that >100 MW can be delivered to the ICA interaction region. Although initial staging experiments will be conducted at the present 45-MW effective laser power level, the model simulations predict the capturing of the microbunch will not be as pronounced as when the laser power is ~1 GW. Hence, it is highly desirable to increase the laser power delivered to the interaction region.

Just as important as overcoming the optical damage limitations is improving the laser beam quality so that more of the delivered laser power is useful for accelerating the electrons. Results from an upgraded ICA model [17], which can simulate the effects of a nonideal laser beam, indicate that the laser beam quality does indeed affect the amount of acceleration and can make the net effective laser power appear to be much smaller than the amount sent into the gas cell.

This upgraded model also demonstrates that the resultant energy spectrum to first order appears the same, regardless of whether an ideal laser beam at a lower peak power level or a nonideal laser beam is used. We believe this is because the final energy of an electron passing through the gas cell is the integrated result of the net electric field it experiences in the longitudinal direction. Effects, such as gas scattering and laser beam imperfections that can affect this longitudinal field component, tend to yield an average field value that is less than the maximum possible. Hence, to the electron, this is equivalent to reducing the peak power of an ideal laser beam.

A number of different sources can degrade the laser beam quality. One drawback with the present radial polarization converter system is the creation of interference fringes within the laser beam entering the gas cell. These fringes imply the existence of phase reversals across the wavefront of the laser beam, which degrades the quality of the J_0 Bessel pattern. In addition, this converter system is only capable of creating at best 80–85% radial polarization. This plus other possible imperfections with the present laser beam may explain why only roughly 50% of the laser power appears to be useful for accelerating the electrons.

A new radial polarization converter system is being developed as a possible replacement to the present one. It features a method for creating the radially polarized beam without the need for specialized optics[1] that can cause diffraction effects. A three-dimensional schematic of the new radial polarization converter system is shown in Fig. 4.

The linearly polarized laser beam from the ATF CO_2 laser is directed first through a cylindrical telescope that makes the beam slightly elliptical in shape. (The ideal elliptical shape is in fact the same as one lobe of a TEM_{01} or TEM_{10} beam.) This elliptical beam enters the first of two end-to-end Mach–Zehnder interferometers, where the beam is split equally into four beamlets. The beamlets are aligned using slightly decentered positions on the mirrors so that a pair of beamlets propagate parallel to each other with a small gap between the beamlets. The first Mach–Zehnder interferometer ensures the beamlets within each of the pairs are in phase with each other and, through the use of a phase plate, that their polarization vectors point opposite to each other.

The second Mach–Zehnder interferometer serves two functions. It rotates one pair of beamlets orthogonal to the other pair and interferometrically recombines all beamlets into a single annular beam. Just as in the present radial polarization converter, the vectorial sum of the polarization vectors in these four beamlets yields a beam with radial polarization.

[1]As explained in [13], the present radial polarization converter system uses specialized optics referred to as spiral-phase-delay (SPD) plates. These plates impart one wave of phase delay in the azimuthal direction across the laser beam transverse profile. Because this one wave of phase delay must begin and end at some point in azimuthal angle, this introduces an abrupt discontinuity in the phase at this angle, which is a source of diffraction effects.

One pair of beamlets has already been tested during earlier ICA experiments. The complete system will be assembled and tested later during the STELLA program.

V. Conclusion

The data obtained with the recommissioned ICA system demonstrate the importance of low e-beam emittance and small e-beam focus within the ICA interaction region. Under these conditions, it is possible to obtain very good agreement with the model. From this, it has been determined that the effective laser power for accelerating the electrons appears to be reduced by approximately a factor of 2 from the laser power entering the interaction region. We believe this is caused by a radially polarized laser beam quality that is less than perfect.

The modulated electron energy spectrum generated by the new wiggler in the IFEL was measured. Indications exist that space-charge effects may be affecting the results. This needs to be further investigated. If it is true, this may limit the amount of charge that can be sent through the IFEL during the STELLA experiment.

Improvements to the ICA optical system are planned to permit delivering higher laser power and to improve the quality of the radially polarized laser, thereby improving the utilization of the delivered laser power.

Nevertheless, the high quality of the IFEL and ICA data collected with the STELLA hardware demonstrates that the STELLA experiment is ready to begin its first staging experiment in the near future.

Acknowledgment

The authors wish to acknowledge Dr. J. Fontana for his technical advice during the initial planning of this experiment and Dr. X. Wang for his on-going assistance and support.

References

[1] W. Lawson, C. Bellamy, and D. Brosius, Eds., *Advanced Accelerator Concepts*. New York: American Institute of Physics, 1999. Baltimore, MD, AIP Conference Proceedings 472.

[2] W. D. Kimura, G. H. Kim, R. D. Romea, L. C. Steinhauer, I. V. Pogorelsky, K. P. Kusche, R. C. Fernow, X. Wang, and Y. Liu, "Laser acceleration of relativistic electrons using the inverse Cerenkov effect," *Phys. Rev. Lett.*, vol. 74, pp. 546–549, 1995.

[3] A. van Steenbergen, J. Gallardo, J. Sandweiss, J.-M. Fang, M. Babzien, X. Qiu, J. Skaritka, and X. J. Wang, "Observation of energy gain at the BNL inverse free-electron-laser accelerator," *Phys. Rev. Lett.*, vol. 77, pp. 2690–2693, 1996.

[4] C. E. Clayton, K. A. Marsh, A. Dyson, M. Everett, A. Lai, W. P. Leemans, R. Williams, and C. Joshi, "Ultrafast-gradient acceleration of injected electrons by laser-excited relativistic electron plasma waves," *Phys. Rev. Lett.*, vol. 70, pp. 37–40, 1993.

[5] P. Sprangle, E. Esarey, A. Ting, and G. Joyce, "Laser wakefield acceleration and relativistic optical guiding," *Appl. Phys. Lett.*, vol. 53, pp. 2146–2148, 1988.

[6] Y. Liu, X.-J. Wang, D. B. Cline, M. Babzien, J.-M. Fang, J. Gallardo, K. Kusche, I. Pogorelsky, J. Skaritka, and A. van Steenbergen, "Experimental observation of femtosecond electron beam microbunching by inverse free-electron-laser acceleration," *Phys. Rev. Lett.*, vol. 80, pp. 4418–4421, 1998.

[7] J. Rosenzweig, G. Travish, and A. Tremaine, "Coherent transition radiation diagnosis of electron beam microbunching," *Nucl. Inst. Methods Phys. Res.*, vol. A 365, pp. 255–259, 1995.

[8] L. C. Steinhauer and W. D. Kimura, "Longitudinal space charge debunching and compensation in high frequency accelerators," *Phys. Rev. ST Accel. Beams*, vol. 2, p. 081301, 1999.

[9] D. T. Palmer, X. J. Wang, R. H. Miller, M. Babzien, I. Ben-Zvi, C. Pellegrini, J. Sheehan, J. Skaritka, H. Winick, M. Woodle, and V. Yakimenko, "Emittance studies of the BNL/UCLA 1.6 cell photocathode RF gun," in *1997 IEEE Part. Accel. Conf. Proc., IEEE 97CH36167*, vol. III, 1998, pp. 2687–2689.

[10] W. D. Kimura, M. Babzien, I. Ben-Zvi, L. P. Campbell, D. B. Cline, R. B. Fiorito, J. C. Gallardo, S. C. Gottschalk, P. He, K. P. Kusche, Y. Liu, R. H. Pantell, I. V. Pogorelsky, D. C. Quimby, K. E. Robinson, D. W. Rule, J. Sandweiss, J. Skaritka, A. van Steenbergen, L. C. Steinhauer, and V. Yakimenko, "STELLA experiment: Design and model predictions," in *Advanced Accelerator Concepts*, W. Lawson, C. Bellamy, and D. Brosius, Eds. Baltimore, New York, MD, NY: American Institute of Physics, 1999, AIP Conference Proceedings no. 472, pp. 563–572.

[11] K. P. Kusche, M. Babzien, I. Ben-Zvi, L. P. Campbell, D. B. Cline, R. B. Fiorito, J. C. Gallardo, S. C. Gottschalk, P. He, W. D. Kimura, Y. Liu, R. H. Pantell, I. V. Pogorelsky, D. C. Quimby, K. E. Robinson, D. W. Rule, J. Sandweiss, J. Skaritka, A. van Steenbergen, L.C. Steinhauer, and V. Yakimenko, "STELLA experiment: Hardware issues," in *Advanced Accelerator Concepts*, W. Lawson, C. Bellamy, and D. Brosius, Eds. Baltimore, New York, MD, NY: American Institute of Physics, 1999, AIP Conference Proceedings no. 472, pp. 573–580.

[12] V. Yakimenko. [Online]. Available: http://www.nsls.bnl.gov/AccTest/experiments/STELLA/STELLA.htm. see Section 8 on World Wide Web page

[13] S. C. Tidwell, G. H. Kim, and W. D. Kimura, "Efficient radially polarized laser beam generation using a double-interferometer," *Appl. Opt.*, vol. 32, pp. 5222–5229, 1993.

[14] J. R. Fontana and R. H. Pantell, "A high-energy, laser accelerator for electrons using the inverse Cerenkov effect," *J. Appl. Phys.*, vol. 54, pp. 4285–4288, 1983.

[15] R. D. Romea and W. D. Kimura, "Modeling of inverse Cerenkov laser acceleration with axicon laser beam focusing," *Phys. Rev.*, vol. D42, pp. 1807–1818, 1990.

[16] D.C. Quimby, J. M. Slater, and J. P. Wilcoxon, "Sideband suppression in free-electron lasers with multiple synchrotron periods," *IEEE J. Quantum Electron.*, vol. QE-21, pp. 979–987, 1985.

[17] L. P. Campbell, W. D. Kimura, S. C. Gottschalk, and V. Heyfitch, . unpublished data.

Lora P. Campbell, photograph and biography not available at the time of publication.

Christian E. Dilley, photograph and biography not available at the time of publication.

Stephen C. Gottschalk, photograph and biography not available at the time of publication.

Wayne D. Kimura (S'75–M'80–SM'91), photograph and biography not available at the time of publication.

David C. Quimby, photograph and biography not available at the time of publication.

Loren C. Steinhauer, photograph and biography not available at the time of publication.

Marcus Babzien, photograph and biography not available at the time of publication.

Ilan Ben-Zvi, photograph and biography not available at the time of publication.

Juan C. Gallardo, photograph and biography not available at the time of publication.

Karl P. Kusche, Jr., photograph and biography not available at the time of publication.

Igor V. Pogorelsky, photograph and biography not available at the time of publication.

John R. Skaritka, photograph and biography not available at the time of publication.

Arie van Steenbergen (SM'79), photograph and biography not available at the time of publication.

Vitaly E. Yakimenko, photograph and biography not available at the time of publication.

David B. Cline, photograph and biography not available at the time of publication.

Ping He, photograph and biography not available at the time of publication.

Yabo Liu, photograph and biography not available at the time of publication.

Richard H. Pantell (S'49–A'51–M'60–SM'73–F'77–LF'93), photograph and biography not available at the time of publication.

Adiabatic Plasma Buncher

M. Ferrario, T. C. Katsouleas, *Fellow, IEEE*, L. Serafini, and Ilan Ben Zvi

***Abstract*—In this paper, we present a new scheme of injection into a plasma accelerator, aimed at producing a high-quality beam while relaxing the demands on the bunch length of the injected beam. The beam dynamics in the injector, consisting of a high-voltage pulsed photodiode, is analyzed and optimized to produce a $\lambda_p/20$ long electron bunch at 2.5 MeV. This bunch is injected into a plasma wave in which it compresses down to $\lambda_p/100$, while accelerating up to 250 MeV. This simultaneous bunching and acceleration of a high-quality beam requires a proper combination of injection energy and injection phase. Preliminary results from simulations are shown to assess the potentials of the scheme.**

***Index Terms*—Bunching, injector, plasma accelerator, pulsed photodiode.**

I. Introduction

SECOND-GENERATION plasma accelerators are expected to be very demanding in terms of the required bunch length [1]. This is because the accelerated beam is required to be short with respect to the wavelength of the excited Langmuir plasma wave to maintain high beam quality and small energy spread. Because the anticipated wavelength ranges from 100 to 300 μm, 1.5- to 15-μm long bunches (rms) are required, with a bunch population of the order of 10^8 particles and a good emittance, namely, less than 10 mm·mrad rms normalized to achieve the correct beam matching into the plasma channel (about 100 μm wide).

Among the photocathode-based injectors [2], the pulsed photodiode [3] seems a good candidate to achieve very short bunches, mainly because of the high field gradient that can be applied on the photocathode surface, in excess of 1 GV/m. It is also attractive for its compactness and simplicity. The energy of the diode is typically low (e.g., 1–2 MeV) compared with RF guns. We will show how this low energy can be used to advantage because it allows for longitudinal bunch compression in the plasma that is not possible at higher energies.

The basic idea of the scheme described in this paper is for the bunch to undergo one-quarter of a synchrotron oscillation in the bucket of the plasma wave, with injection on the minimum of the bucket close to the separatrix (zero acceleration phase) and extraction at the resonant energy γ_r just at the median line of the bucket (maximum acceleration). This phase oscillation in the bucket performs a bunching while it increases the absolute energy spread. Later, the relative $\Delta\gamma/\gamma$ is damped away. It will be shown that the final beam is fully consistent with the requirements on bunch length for a second generation plasma accelerator [1], even though the injected beam is not (i.e., it is longer than the requirement). Such a compression mechanism can in principle be exploited even with a different injector, e.g., a radiofrequency gun. However, we should prove the ability of RF guns to produce 15-μm long bunches at 24 pC of charge at energies of a few MeV (<3), so as to exploit the compression up to its maximum efficiency. In this paper, we explore the use of a pulsed photodiode for the simplicity and compactness of the apparatus, which allows a very short drift in between the diode and the plasma channel, minimizing in this way the debunching effect caused by space charge.

It is worthwhile to mention that the idea to use a plasma wave to compress or modulate the density of an electron beam is not new: the plasma klystron concept, presented in [9] is actually based on this idea. While the plasma klystron induces a density modulation on a beam that is much longer than the plasma wavelength [9], producing in this way a train of bunchlets, the system presented in this paper is expected to produce a single bunch shorter than the plasma wavelength.

In the second section of this paper, we present a discussion of the beam dynamics in the diode and the drift to the plasma accelerator, with emphasis on how to transport the beam with minimum degradation of its quality (in particular, the rms bunch length and energy spread). The beam dynamics modeling is based on a time-dependent space-charge code, HOMDYN [4], recently developed in the framework of RF photoinjectors. The code allows us to scan quickly over the parameter space, taking into account at the same time the emittance behavior and the debunching effect casued by the longitudinal space-charge field of the electron bunch. The model underlying the code is summarized in Section III, which also presents the results from the simulations, with particular concern to the adiabatic compression effect occurring when the beam is injected at zero phase (no acceleration). Section IV describes a possible method to control the time jitter between the HV pulse in the diode and the laser driving the plasma wave.

II. The Pulsed Photodiode: A Compact Injector Suitable for Short Electron Bunch Generation

The pulsed photodiode is essentially an accelerating gap terminating a coaxial transmission line where a short (few nanoseconds) high-voltage pulse (1–2 MV) is applied. The system basically consists of three components: a low voltage pulse generator (with a DC source at 25 kV), a Tesla transformer, and a high-voltage transmission line with SF_6 switches to sharpen the rise and fall times of the HV pulse.

Because of the short time duration of the pulse and the short gap of the diode (1–2 mm), it has been experimentally demonstrated [3] that it is possible to hold such high-voltage pulses

Manuscript received February 14, 2000; revised March 28, 2000.

M. Ferrario is with INFN-LNF, 00044 Frascati, Italy.

T. C. Katsouleas is with the University of Southern California, Los Angeles, CA 90089-0484 USA.

L. Serafini is with INFN-Milano, 20133 Milano, Italy (e-mail: luca.serafini@mi.infn.it).

I. Ben Zvi is with Brookhaven National Laboratory, Upton, NY 11973 USA.

Publisher Item Identifier S 0093-3813(00)07236-2.

0093–3813/00$10.00 © 2000 IEEE

without breakdown phenomena: very high field gradients, in excess of 1 GV/m, have been successfully applied at the photocathode surface. The high-voltage pulse can be synchronized within 150 ps to an external laser (this will be later discussed in further details), so that the device can be operated as a DC photoinjector: a metallic photocathode hit by the laser emits photoelectrons during the laser pulse time duration. In this case, the high-voltage DC-pulsed electric field plays the role of RF high gradient fields in RF guns. The electron bunch extracted from the diode is easily split from the laser beam, illuminating the cathode in many ways: as an example, we can illuminate the photocathode at an angle (60°–70°) as usually done in S-band RF guns [2], with proper correction of the laser wave fronts to avoid a tilt between them and the cathode plane (this would bring us to an undesirable lengthening of the cathode emission time with respect to the laser pulse duration).

Because of such a strong field, we can generate electron bunches at the cathode and accelerate them rapidly up to relativistic velocities (1–2 MeV). This should be done quickly, to freeze the space-charge forces. Of particular concern is the longitudinal force that tends to introduce a bunch lengthening that would be detrimental to the quality of the beam. In view of the need for bunches no longer than 10 μm, and the fact that the cathode spot size is larger than 100 μm, we have to operate the beam in the surface-charge regime typical of high aspect ratio bunches that look like thin pancakes. In this regime [5], the longitudinal space-charge field scales like the inverse square of the bunch radius and is very weakly dependent on the bunch length.

Equation (1) shows a first-order formula [5], giving the final electron bunch length σ_z (rms value at the diode exit) as a function of the incident laser pulse length σ_{las}, the laser spot size at the cathode σ, the normalized field gradient $\gamma' \equiv eE_0/mc^2$ (where E_0 is the field gradient at the cathode), and the nominal beam peak current I_p

$$\frac{\sigma_z}{\sigma_{las}} = \frac{I_p}{I} = 1 + \Delta_{SC} \tag{1}$$

where

$$\Delta_{SC} = \frac{I_p}{I_A(\gamma'\sigma)^2} f(A_l, \gamma)$$

is the space-charge debunching factor ($I_A = 17$ kA). For high aspect ratios $A_l = \sigma/\sigma_l$, as typical of cases under discussion here, and final γ at the exit of the diode larger than 5, the factor $f(A_l, \gamma)$ can be well approximated by $f \cong A_l/3 - \sqrt{A_l}/80 - A_l^{1/4}/360$ [as far as $1 < A_l < 100$; the limit of $f(A_l, \gamma)$ for very large A is $\ln(2)$].

In the drift following the diode gap, we should expect a further debunching produced by the space-charge–induced energy spread, namely, $\Delta\gamma_{SC}/\gamma = I_p\sigma_z/I_A\gamma'\sigma^2$; this effect can be even larger than in the diode, because the bunch lengthening can be expressed, at first order, by $\Delta L = (L_{\text{drift}}/\gamma^2)(\Delta\gamma_{SC}/\gamma)$. According to these scaling laws, we should, for a given desired peak current I_p (or for a given bunch length and charge), try to maximize the field gradient γ' and the cathode spot size σ (which is limited anyway by the anode aperture). Minimizing the drift length is also crucial.

As a particular example, consider a laser pulse of length $\sigma_l = 12$ fs (4 μm), spot size $\sigma = 300$ μm, diode gap 2 mm, and field gradient at the photocathode 1.3 GV/m (so that $\gamma = 6$ at the diode exit), with a bunch charge of 24 pC ($1.5\ 10^8$ electrons, $I_p = 600$ A). This leads to a predicted space-charge debunching in the diode that is modest, $\Delta_{SC} = 4.2\%$. The induced energy spread $(\Delta\gamma_{SC}/\gamma) = 0.05\%$, gives a further debunching $\Delta L = 8$ μm at the end of the 26-cm long drift space to the plasma channel. It will be shown in the final section that the simulations agree remarkably well with these analytical predictions. This points out the need for short laser pulses and high field gradients to keep the bunch length within the demands of the plasma accelerator.

The transverse beam dynamics sets up some other constraints dealing with the matching of the beam into the plasma wave. The most important issue is the minimum drift length achievable compatibly with the need to apply some focusing to obtain the correct matching. In fact, the diode, having a flat cathode, is equivalent to having a defocusing lens. A curved cathode should be avoided because it leads to bunch lengthening caused by electron trajectories of varying lengths emerging from various points on the curved cathode [6]. The rms beam divergence at the exit is predicted to be

$$\sigma' = \frac{\sigma}{2d} F(\gamma' d) + \frac{\pi I_p}{12 I_A \sigma \gamma \gamma'}. \tag{2}$$

Here, d is the diode gap length, and the expression for the factor $F(\nu)$ is reported in the Appendix. $F(\nu)$ is very close to 1 for our case of interest, where $\gamma = \gamma' d \gg 1$.

According to (2), we conclude that the diode applies a serious defocusing kick to the beam. The source is the first term in the RHS of (2), which is from the radial field lines of the exit aperture close to the cathode. This term is much larger than the space-charge kick (second term in the RHS), in fact, for the parameters listed above, we obtain $\sigma' = 75$ mrad + 2 mrad. In order to overcome such a high beam divergence at the exit of the diode, we place a solenoid lens at 11 cm from the cathode, set at 2.5-kGauss peak field. The solenoid must focus down the beam into the plasma wave accelerator, which requires a beam spot size of about 50 μm. The simulation results are shown at the end of the next section.

III. The HOMDYN Model and Its Enhancement to Treat Acceleration in Plama Waves

Time-dependent space-charge effects play a crucial role in the beam dynamics of high brightness injectors. A fast running code (HOMDYN) has been developed to deal with the evolution of high-charge, not fully relativistic multibunch beams in RF fields of an accelerating cavity, taking into account the field induced by the beam in the fundamental and higher order modes, and the variation of bunch sizes caused by both the RF fields and space charge. Such a code is also suitable for the present application in which instead of an RF cavity, we have an accelerating gap followed by a plasma channel.

In modeling the plasma wave, we include the fields of an externally driven linear plasma wave, but neglect the self-generated wake fields from the beam loading of the plasma wake.

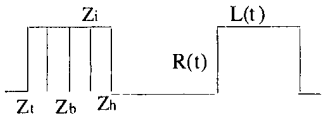


Fig. 1. Electron bunch as modeled by the code HOMDYN to calculate the space-charge field: uniform cylindrical distribution represented by N slices. See text for definitions of the slice coordinates z_s, bunch sizes $R(t)$, $L(t)$, and bunch coordinates z_t, z_b, z_h.

This is justified providing the beam load is not too large [7], namely, when the electron number N is such that

$$eN \ll (100\ \text{pC}) \quad E[\text{GeV/m}]\ \frac{\text{wave area}}{[100\ \mu\text{m}]^2}.$$

We review in this section the main features of the model, with some modifications added specifically for the case under study.

The basic approximation in the description of beam dynamics lays in the assumption that each bunch is described by a uniform charged cylinder, whose length and radius can vary under a self-similar time evolution while keeping a uniform charge distribution inside the bunch. By slicing the bunch in an array of cylinders (multislices approximation; see Fig. 1), each one subject to the local fields, we also obtain the energy spread and the emittance degradation caused by phase correlation of RF and space-charge effects.

The longitudinal space-charge fields on axis at a distance $\zeta_s = z_s - z_t$ of the sth slice from the bunch tail located at z_t, is given by [6]

$$E_r^{sc}(\zeta_s) = \frac{Q}{2\pi\varepsilon_o R_s^2} H(\zeta_s, A_{r,s})$$

where

$$H(\zeta_s, A_{r,s}) = \sqrt{(1-\zeta_s/L)^2 + A_{r,s}^2} - \sqrt{(\zeta_s/L)^2 + A_{r,s}^2} - (1 - 2\zeta_s/L)$$

and Q is the bunch charge, L is the bunch length, R_s is the slice radius, and $A_{r,s} \equiv R_s/(\gamma_s L)$ is the slice rest frame aspect ratio.

The radial space-charge fields (linear component) of the same slice, are given by

$$E_r^{sc}(\zeta_s) = \frac{Q}{4\pi\varepsilon_o R_s L} G(\zeta_s, A_{r,s})$$

where

$$G(\zeta_s, A_{r,s}) = \frac{1-\zeta_s/L}{\sqrt{(1-\zeta_s/L)^2 + A_{r,s}^2}} + \frac{\zeta_s/L}{\sqrt{(\zeta_s/L)^2 + A_{r,s}^2}}.$$

The plasma longitudinal and transverse (linear component) fields are

$$E_z^{pl}(z_s) = E_o \sin(\omega_{\text{pl}} t - k_{\text{pl}} z_s + \psi_o)\left(1 - \frac{R_S^2}{a^2}\right)$$

and

$$E_r^{pl}(z_s) = -\frac{2E_o R_s}{a^2 k_p} \cos(\omega_{\text{pl}} t - k_{\text{pl}} z_s + \psi_o).$$

The equations for the longitudinal motion for each slice are

$$\dot{z}_s = \beta_s c$$
$$\dot{\beta}_s = \frac{e}{m_o c \gamma_s^3}\left(E_z(z_s, t) + E_z^{sc}(\zeta_s, t) + E_z^{pl}(z_s, t)\right).$$

The evolution of each slice radius R_S is described in the time-domain according to an envelope equation, including damping caused by acceleration (second term), solenoid focusing (third), RF-focusing (fourth), plasma focusing (fifth), space-charge effects (sixth), image charges from the cathode surface (seventh), and thermal emittance pressure (eigth)

$$\ddot{R}_s + \beta_s \gamma_s^2 \dot{\beta}_s \dot{R}_s + \left(K_s^{sol} + K_s^{\text{rf}} + K_s^{pl}\right) R_s = \frac{2c^2 k_p}{R_s \beta_s}\left(\frac{G(\zeta_s, A_r)}{\gamma_s^3} - \left(1+\beta_s^2\right)\frac{G(\zeta_s, A_r)}{\gamma_s}\right) + \left(\frac{4\varepsilon_n^{th} c}{\gamma_s}\right)^2 \frac{1}{R_s^3}$$

where the dots indicate the derivation with respect to time,

$$K_s^{sol} = \left(\frac{eB_z(z_s)}{2m_o\gamma_s}\right)^2$$

is the solenoid focusing gradient,

$$K_s^{\text{rf}} = \frac{e}{2\gamma_s m_o}\left(\frac{\partial E_z}{\partial z} + \frac{\beta_s}{c}\frac{\partial E_z}{dt}\right)$$

is the RF focusing gradient expressed through the linear expansion off-axis of the accelerating field $E_z = E_z(0, z, t)$,

$$K_s^{pl} = \frac{2eE_o}{\gamma_s m_o a^2 k_p} \cos(\omega_{\text{pl}} t - k_{\text{pl}} z_s + \psi_o)$$

is the plasma focusing gradient,

$$k_p = \frac{I(\zeta_s)}{2I_o}$$

is the beam perveance, and ε_n^{th} is the rms normalized thermal beam emittance.

In order to evaluate the degradation of the rms emittance produced by longitudinal correlation in space-charge and transverse external forces, we use the following expression for the correlated emittance:

$$\varepsilon_n^{cor} = \frac{1}{4}\sqrt{\langle R_S^2\rangle\langle(\beta\gamma R_S')^2\rangle - \langle R_S \beta\gamma R_S'\rangle^2}$$

where $R_S' = (d/dz)R_S$ and the average $\langle\ \rangle = (1/N)\sum_{s=1}^{N}$ is performed over the N slices. The total rms emittance will be given by a quadratic summation of the thermal emittance and the correlated emittance

$$\varepsilon_n = \sqrt{(\varepsilon_n^{th})^2 + (\varepsilon_n^{cor})^2}.$$

The simulations of the system have been carried out choosing the following set of parameters: the diode is driven by a 1.3-MV HV pulse applied to a 2-mm gap, whereas the laser pulse hitting the photocathode is 40 fs long (assumed to be flat top in time; note that this is equvalent to a 12-fs rms laser pulse length) and is focused down to a 0.6-mm spot size (hard edge radius of a uniform radial intensity profile), extracting 24 pC of charge. In order to take under control the large defocusing kick received by crossing the anode hole (as discussed in Section II), we apply a focusing solenoid lens located 11 cm from the cathode with a field amplitude of 2.5 kGauss (peak field on axis). The plasma wave is assumed to have a plasma wavelength of 300 microns,

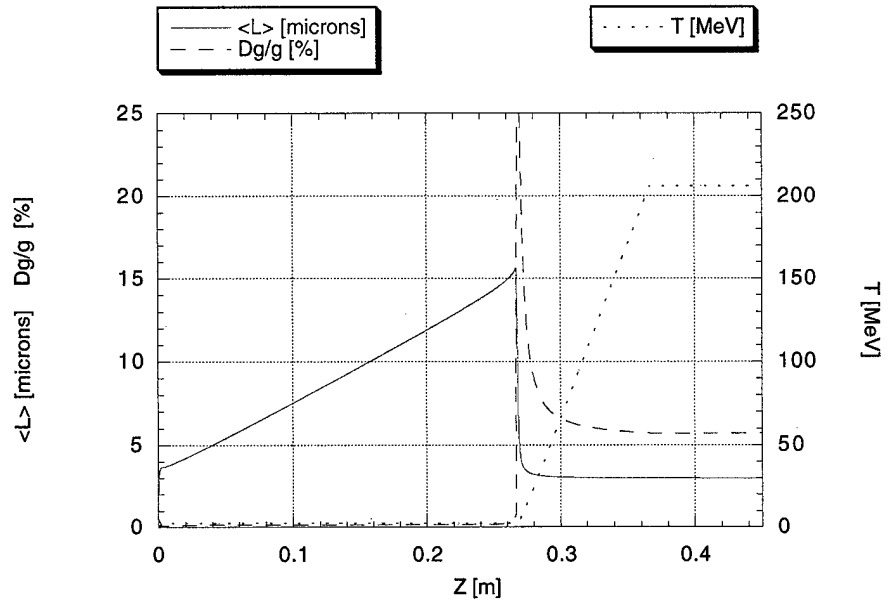


Fig. 2. Longitudinal dynamics at 0° injection phase (no acceleration). Solid line (left scale) represents the rms electron bunch length. Dotted line (right scale) represents the bunch average energy, and dashed line (left scale) represents the rms energy spread.

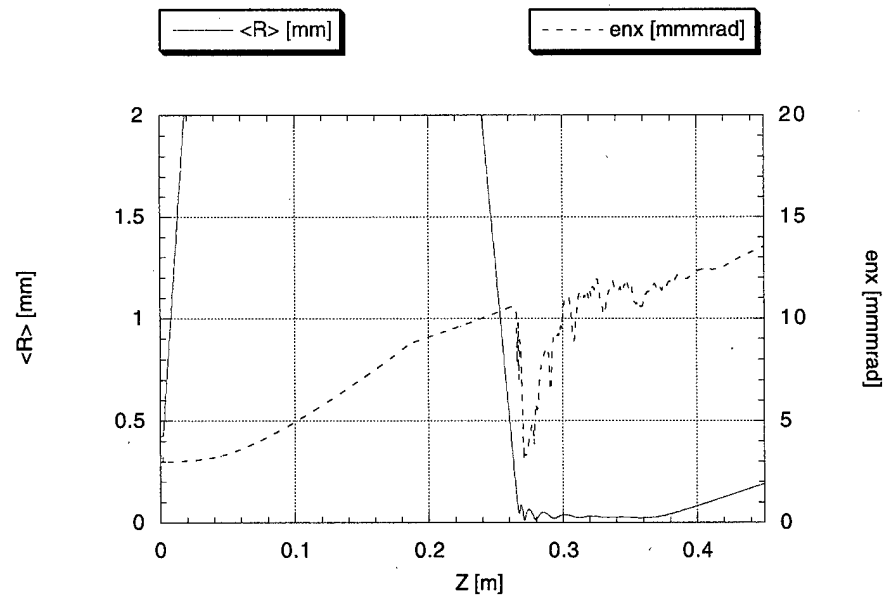


Fig. 3. Transverse dynamics at 0° injection phase (no acceleration). Solid line (left scale) represents the rms electron bunch radius: the scale is set to show the matching into the plasma wave at $z = 0.267$ (maximum rms radius is 8 mm at $z = 0.11$). Dashed line (right scale) represents the rms normalized transverse emittance.

radius $a = 100$ microns, starting 26.7 cm from the cathode and extending through 10 cm with an accelerating gradient of 3 GV/m. The resonant *gamma* of the wave is taken to be $\gamma_r = 400$.

The beam kinetic energy (dotted line), the rms energy spread (dashed line), and the rms bunch length (solid line) are shown in Fig. 2 for the case of injection at zero acceleration phase (i.e., $\psi_o = 0°$) into the plasma wave. The injection energy is 2.45 MeV, with a bunch length of 3.5 μm at the diode exit and 15.5 μm at the end of the drift to the plasma wave. Bunch lengthening is caused by the longitudinal space-charge field. The bunching action of the plasma wave, effective at a proper injection phase of 0° (no acceleration), causes a reduction of the bunch length in opposition to the space-charge effect, with a final equilibrium bunch length of 3 μm with an energy spread of 6%. Matching the beam into the strong focusing channel of the plasma wave is critical. An example is shown in Fig. 3, indicating the rms radius (solid line) and the rms normalized emittance (dashed line). The beam is blown up radially to 8-mm rms radius in the center of the solenoid (11 cm from the cathode) and focused down to 50 μm into the plasma wave.

It is interesting to notice that an injection at 60° assures maximum acceleration up to 292-MeV exit energy but no bunching effect, as shown in Fig. 4, where the final bunch length is 17 μm at an energy spread of 12%.

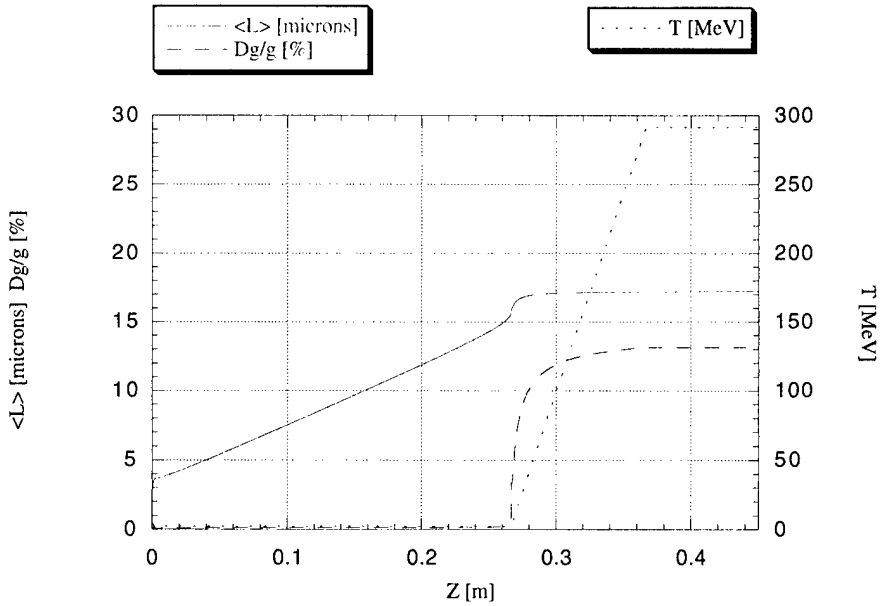


Fig. 4. Longitudinal dynamics at 60° injection phase (maximum acceleration). Solid line (left scale) represents the rms electron bunch length. Dashed line (left scale) represents the rms energy spread. Dotted line (right scale) represents the bunch average energy.

IV. Control of the Time Jitter Between the Plasma Wave and the HV Pulse

The acceleration in the plasma wave changes rapidly with the injection phase of the electron bunch. In order to get a consistent acceleration and small energy jitter (pulse-to-pulse), we must control the timing of the injection with unprecedented precision.

The attainment of such stability by synchronization of lasers is hopeless. Therefore, we assume that a single laser controls the timing of both photocathode illumination and plasma wake generation. This still requires attention to minute details in maintaining constant laser path lengths in the system. That includes highly stable optical component support, covered and temperature controlled light pathways, and similar, well-known optical-transport practices. This leaves us with the main challenge being the variation of the electron time-of-arrival.

The variation in the electron timing is caused by the shot-to-shot variation in the accelerating potential. The pulsed diode waveform is timed by spark gaps. The triggering of a spark gap is a statistical process of creating an avalanche. The use of special liquids in the spark gap, laser triggering, and advanced geometry can reduce the jitter to under 1 ns. Because the pulse cannot be made absolutely uniform over the entire waveform, which is approximately flat-top over 1 ns, we have to deal with pulse-to-pulse acceleration voltage jitter of a few percent. Thus, a timing jitter is generated by the time of flight dependence on the voltage.

The time jitter per a fraction of the accelerating voltage jitter is given as the sum of two terms, the jitter in the diode and the jitter in the drift space past the diode.

The first is given as $1/(c\gamma')$, and the other as $(L_{\mathrm{drift}}/c)(2\gamma' d/(2+\gamma' d))(2\gamma' d+\gamma'^2 d^2)^{-1/2}$. For typical values of $d = 0.002$ m and $\gamma' d = 2$, we see that the timing jitter in the diode is of the order of 30 fs per percent amplitude jitter. In a drift of 0.3 m past the diode, the jitter is about 3 ps per percent.

In other words, a pulse-to-pulse correction of the order of a few picoseconds is necessary to maintain the electron bunch and the plasma wave in synchronism.

We propose to correct this jitter by a feedforward scheme. The principle is simple: a pick-up electrode inserted in the high-voltage transmission line will measure the voltage of the diode. The voltage of the pulse is so high that even a weakly coupled probe will generate enough signal to eliminate the need for an amplifier.

The electric signal will change the path length of the laser propagating toward the photocathode. The magnitude of the change is adjusted so that a compensation of the jitter is accomplished.

To make this possible, it is necessary to design the path length of the high-voltage pulse from the measurement point to the cathode to allow enough delay to enable the feedforward adjustment. The laser pulse must arrive at the cathode at the same time that the part of the pulse that produced the path length change arrives.

The laser variable delay line will be composed of optically active material that changes the index of refraction on the application of an electrical field. The optical path length of a laser beam in a medium changes dramatically if the medium is highly dispersive at the laser wavelength and the molecular levels contributing to the dispersion are shifted. Such an energy level shift can be accomplished either by applying an electric field or by even using the electric field associated with the laser by invoking the Stark effect. The appropriate choice of the medium and the magnitude of the field may result in the required path length. The major drawback of this technique would be the corresponding change in the absorption coefficient. The transport loss of the laser will then be a function of the field, which needs to be corrected.

The photocathode laser starts as an IR laser, which is, usually, multiplied to the UV. The calculations that we will present

to establish the principle correspond to the effect in ammonia, at a wavelength of 10.6 μm, where data have been available. More research is necessary to identify a proper material and wavelength for UV operation.

Stark shifting of a vibrational–rotational line of ammonia has been done for spectroscopic applications [8]. The ammonia lines have been shifted in and out of resonance by applying moderate electric fields. The fields necessary to tune through resonance varied, depending on the line in question. A voltage as low as 30 V over 2-mm gap (field of 15 kV/m) is sufficient for some lines. This introduces a large change in the refractive index and, hence, the path length of the laser to correct for the jitter. Based on data taken from [8], the produced change in the refractive index Δn_r as the resonance is shifted between 9.503 μm and 9.443 μm is 2.928–0.419 = 2.509. Therefore, the length required to change the path length by 1 ps is $L = 1 \times 10^{-12}$ s $\times$ 3×10^{10} cm/s/2.509 = 120 μm.

The imaginary part of the refractive index that affects the absorption changes from 1.459 to 2 in this change of wavelength.

Incidentally, ammonia has also a resonance line in UV at 200 nm, where the change in the refractive index Δn_r is 0.3. If this resonance is used, the required length would be 1 mm. However, it is most likely that there are other material candidates.

Concerning the possible breakdown of the laser transported through the cell, it should be noted that the necessary power is not very high. With the high electric field on the cathode and using clean copper surfaces, a quantum efficiency of 0.05% was obtained at 100 MV/m, and at the diode's operating field of 1 GV/m, the expected quantum efficiency is 0.5%. At this quantum efficiency, the necessary laser energy is about 24 nJ, or a power of 1 MW. This is not expected to result in breakdown problems over a spot size of about 1 mm.

This example is given just as a demonstration of principle, and more work is necessary to produce a practical working device. Besides the identification of the optimal resonant Stark effect material, there are some other concerns to be addressed. These are listed below as pointers for further research.

The calculation above was made with solid ammonia, where the number density is ~4 orders of magnitude larger than the atmospheric gas. High-pressure ammonia gas may be used, but because the refractive index is directly proportional to the electron density, the length of the ammonia cell would have to be increased.

What would be the optical quality of this ammonia column, as solid or gas? Can the laser beam quality be maintained after passage through this cell?

Stark shift measurements have been done only in gaseous ammonia. Are the results valid in solid ammonia?

How does broadening from pressure and laser intensity affect the results?

Can the ammonia hold off the large background field of the pulse (besides the ripple used to affect the shift?)

The necessary response time is commensurate with the rate of change of the voltage on the pulsed diode, which is of the order of tens of one hundred picoseconds. Is the response time of the molecule to the applied field sufficiently fast?

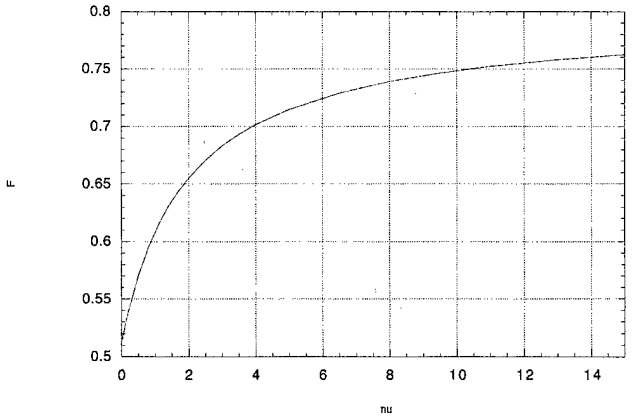


Fig. 5. Form factor $F(\nu)$ plotted as a function of ν for the case $f(x) = e^{-x^2/2}$, i.e., a Gaussian electric field distribution on axis through the diode gap.

Finally, the change in absorption needs to be calculated and corrected for.

V. Conclusion

We have shown by means of a preliminary analysis that a proper injection (by using a specific beam energy and phase) into a plasma wave can relax the demands for beam quality, in particular, the maximum bunch length and energy spread acceptable at injection, to meet the requirements of second generation plasma accelerators. We found great advantages in the use of pulsed photodiodes as injectors and beam sources, mainly because of their compactness and the very high gradient achievable at the photocathode surface.

Other issues have to be more carefully investigated besides what has been done for this analysis: wake fields effects in the plasma wave (i.e., beam loading), spatial variation of the plasma wave accelerating gradient from laser envelope, and multiparticle effects not addressable with the use of HOMDYN. These are topics for future investigations.

Appendix

We assume a first-order, linear, on-axis expansion for the static accelerating field

$$\begin{cases} E_z = E_0 f(x) \\ E_r = -\dfrac{E_0 r}{2d} f'(x); \end{cases} \qquad x = \frac{z}{d}, \quad f' = \frac{df}{dx}$$

where the field form factor on-axis is specified generically by the normalized function $f(x)$, such that $f(0) = 1$ and $f \underset{x\to\infty}{\longrightarrow} 0$. The beam normalized energy at the gap exit will be given by

$$\gamma = 1 + \nu \int_0^\infty f\, dx$$

where the dimensionless quantity $\nu = eE_0 d/mc^2$ represents an effective normalized gap voltage across the gap of length d. Recalling that the transverse momentum change through the gap is $\Delta p_r = \int_0^\infty eE_r\, dt$ and $d/dt = (d/\beta c)(d/dx)(\beta = \sqrt{1 - 1/\gamma^2})$, the beam rms divergence at the gap exit, defined

by $\sigma' = \Delta p_r(r=\sigma)/mc\beta\gamma$ under the assumptions of straight electron trajectories through the gap and laminar beam, will be given by

$$\sigma' = \frac{\sigma}{2d} F(\nu)$$

where:

$$F(\nu) = -\frac{\nu}{\sqrt{\left(1+\nu\int_0^\infty f(x)\,dx\right)^2 - 1}} \times \int_0^\infty \frac{f'(x)}{\sqrt{1-\left(1+\nu\int_0^x f(y)\,dy\right)^{-2}}}\,dx.$$

The form factor $F(\nu)$ has a relativistic limit, i.e., at $\nu \gg 1$, given by $F \underset{\nu\to\infty}{\longrightarrow} F_\infty = 1/\int_0^\infty f(x)\,dx$ [typically, $F_\infty = O(1)$ implying), $\sigma'(\nu \gg 1) = \sigma/2d$], whereas the limit at very small ν is $F \underset{\nu\to 0}{\longrightarrow} F_0 = (1/2)\int_0^\infty (f'(x)/\sqrt{\int_0^x f(y)\,dy})\,dx$, which is again a quantity typically of the order of 1 for a well-behaved function $f(x)$, as previously specified [implying $\sigma'(\nu \ll 1) = \sigma/4d$].

The behavior of the form factor $F(\nu)$ corresponding to a gaussian electric field distribution on-axis, i.e., for $f(x) = e^{-x^2/2}$, which is close to that of a flat cathode-flat anode geometry for the diode gap, is plotted in Fig. 5 versus γ.

ACKNOWLEDGMENT

The authors thank T. Srinivasan-Rao for stimulating discussions on optical feedback mechanisms.

REFERENCES

[1] C. Clayton and L. Serafini, "Generation and transport of ultrashort phase-locked electron bunches to a plasma beatwave accelerator," *IEEE Trans. Plasma Sci.*, vol. 24, pp. 400–408, Apr. 1996.
[2] C. Travier, "RF guns a review," *Part. Accel.*, vol. 36, pp. 33–75, 1991.
[3] T. Srinivasan-Rao *et al.*, "Table top, pulsed, relativistic electron gun with GV/m gradient," *AIP CP*, vol. 398, pp. 730–738, 1997.
[4] M. Ferrario *et al.*, "Multi-bunch energy spead.induced by beam-loading in a standing wave structure," *Part. Accel.*, vol. 52, pp. 1–30, 1996.
[5] L. Serafini, "The short bunch blow-out regime in RF photoinjectors," *AIP CP*, vol. 413, pp. 321–334, 1997.
[6] ——, "Micro-bunch production with radio frequency photoinjectors," *IEEE Trans. Plasma Sci.*, vol. 24, pp. 421–427, Apr. 1996.
[7] T. Katsouleas *et al.*, "Beam loading in plasma accelerators," *Part. Accel.*, vol. 21, pp. 81–99, 1987.
[8] J. V. Martonchik *et al.*, "Optical properties of NH3 ice from far infrared to the near ultraviolet," *Appl. Opt.*, vol. 24, pp. 541–547, 1984.
[9] T. Katsouleas *et al.*, "A plasma Klystron for generating ultra-short electron bunches," *IEEE Trans. Plasma Sci.*, vol. 24, pp. 443–447, 1996.

M. Ferrario, photograph and biography not available at the time of publication.

T. C. Katsouleas (M'88–SM'91–F'96), photograph and biography not available at the time of publication.

L. Serafini, photograph and biography not available at the time of publication.

Ilan Ben Zvi, photograph and biography not available at the time of publication.

Transverse Stability of the Electron Beam in the Wiggler Plasma Wave Accelerator

V. Petrillo and C. Maroli

Abstract—**We give an analysis at the single-particle level of description of the electron beam transverse motion and stability in a plasma accelerator, which uses an external magnetic field like that in the undulator of a free-electron laser. The numerical results show strong focusing of all electron trajectories when the electrons of the beam are accelerated to a few gigaelectronvolts.**

Index Terms—**Magnetized plasmas, plasma-based accelerators, transverse beam stability.**

I. Introduction

THE initial acceleration gradient and maximum theoretical energy gain at the dephasing limit in plasma- based accelerators could be considerably increased if the plasma were placed in a strong magnetic field transverse to the beam motion, like in the "surfatron" scheme [1], but periodic along the beam motion, like in the undulator of a free-electro laser.

As shown in [2] and [3], the increase in the efficiency of the process is due to the diamagnetic currents that tend to develop inside the plasma in equilibrium with the magnetic field of the undulator. If these currents are strong enough, they give rise to a relativistic increase in the electron mass and a general lowering of all wave frequencies ω, in some cases, well below the plasma frequency $\omega_p = (4\pi e^2 n_0/m)^{1/2}$. As a consequence, the axial electric field of the accelerating plasma waves increases by the factor ω_p/ω.

In addition, this strong acceleration takes place in plasmas that have a considerably lower density than in existing experiments and with carrier accelerating waves of much longer wavelengths. For instance, initial acceleration gradients of nearly 1 GeV/m could be obtained by using an undulator with period $\lambda_u = 5$ cm, which is loaded with a cold plasma of volume density n_0 between 10^{13} and 10^{14} cm^{-3}, and an accelerating carrier wavelength of a few centimeters. The volume density of the beam is $n_b \approx 10^{-3} n_0$, and the injection energy is of a few megaelectronvolts. The peak value of the undulator magnetic field must instead be very large, of the order of several Tesla.

These results, however, are based on the solution of a set of nonlinear, one-dimensional (1-D) equations; with the electron beam represented, as usual, by a number of uniformly charged planes moving along the z-axis, the undulator field has a simple form that is valid *exactly* on the axis and the transverse dimensions of the beam and of the accelerating wave pulse are considered to be infinite.

Manuscript received October 7, 1999; revised March 13, 2000.

The authors are with the Dipartimento di Fisica dell'Università di Milano, Istituto Nazionale di Fisica della Materia e Istituto Nazionale di Fisica Nucleare, I-20133 Milano, Italy.

Publisher Item Identifier S 0093-3813(00)10529-6.

The large undulator magnetic field with its periodicity along the beam motion gives rise, as must be expected, to appreciable changes in the dispersion properties of the (strongly) magnetized plasma. In particular, the accelerating wave pulse consists of waves that are only partially longitudinal and with a complicated structure of the transverse electric and magnetic fields components. The situation is different from that of plasma-based accelerators that do not use external magnetic fields, and it is, therefore, necessary to add to the 1-D treatment a description of the transverse motion and stability of the beam.

In this work, we carry out the analysis of the transverse effects at the single-particle level of description, namely, by supposing that the electrons of the beam move under the action of fixed external fields only. The effects due to the finite transverse size of the beam and of the accelerating wave pulse, to the radial components of the electric field of the wave that arise as a consequence of the Panofsky–Wenzel (PW) theorem, as well as to the full off-axis structure of the wiggler magnetic field are taken into consideration.

II. Nonlinear Reference Trajectory

We begin by singling out a "reference trajectory," which is that traced by the electron of the beam that starts at $t = 0$ from a set of "preferred" initial conditions, i.e., from the origin of the reference frame ($x = 0$, $y = 0$, $z = 0$) and with a (relativistic) momentum directed exactly along the z-axis ($p_x = 0$, $p_y = 0$, $p_z = p_0$) (that is assumed as the direction of motion of the beam as a whole). This trajectory is calculated by solving the complete nonlinear equations of motion and by taking all kinds of (external) forces into account. A list that comprises all forces is as follows.

A. Undulator Magnetic Field

A complete and relatively simple form of the undulator field is that given in [4]. The mathematical expression takes the full off-axis structure of the field into account. The undulator we consider is of the helical type, with the magnetic field $\mathbf{B}_U = -\nabla V$ derived from the scalar potential

$$V(x, y, z) = -2B_U \frac{I_1(k_u r)}{k_u r} [x \sin(k_u z) - y \cos(k_u z)] \quad (1)$$

where $r = \sqrt{x^2 + y^2}$, $I_1(k_u r)$ is a modified Bessel function and $\lambda_u = 2\pi/k_u$ is the period of the field along the z-axis.

We can see that the magnetic field $\mathbf{B}_U$ has only transverse components $B_{U,x}$ and $B_{U,y}$; $\mathbf{B}_U = B_U \sin(k_u z)\mathbf{e}_x - B_U \cos(k_u z)\mathbf{e}_y$, when considered exactly on the axis; i.e.,

0093–3813/00$10.00 © 2000 IEEE

when $x = 0$ and $y = 0$. In this case, it can also be written as $\mathbf{B}_U = e_z \times (\partial/\partial z)\mathbf{A}_U$, namely, in terms of the vector potential

$$\mathbf{A}_U = -i\frac{B_U}{\sqrt{2}k_u}\left(e^{-ik_u z}\hat{\mathbf{e}} - \text{cc}\right) \tag{2}$$

where $\hat{\mathbf{e}} = 1/\sqrt{2}(\mathbf{e}_x + i\mathbf{e}_y)$ and "cc" means complex conjugate. In the immediate vicinity of the axis, i.e., up to terms of second order in the radial distance r, we find a (small) longitudinal component and the field assumes the form

$$\begin{aligned}\mathbf{B}_U = {} & B_U \sin(k_u z)\mathbf{e}_x - B_U \cos(k_u z)\mathbf{e}_y \\ & - B_U k_u (x\cos(k_u z) + y\sin(k_u z))\mathbf{e}_z + O(r^2).\end{aligned} \tag{3}$$

B. Electric and Induction Fields of the Accelerating Wave Pulse

The wave pulse that accelerates the beam is assumed to be fairly intense, but still well described by the linear theory. The carrier of the pulse must be chosen by fixing both frequency ω and wavenumber k in such a way that the wave beta factor $\beta_W = \omega/ck$ is smaller but very near to 1. The wave belongs to the branch of the dispersion relation with $\omega < \omega_p$ and a quasi-longitudinal polarization (see, in particular, [2, Fig. 1] and [3, Fig. 1]). The accelerating wave is not purely electrostatic like in the usual nonmagnetized plasma-based accelerators, but the transverse (radiation) components of its electric $\delta\mathbf{E}_\perp$ and induction fields $\delta\mathbf{B}$ are, in general, smaller than the axial component δE_z, which is, in this case also, the main accelerating cause.

The axial electric field follows from the assumed explicit form of the relative density perturbation $\delta n/n_0$ and Poisson equation and is written as

$$\delta E_z = \frac{8\pi e n_0}{k}|A_0|\sin(kz - \omega(k)t + \varphi) \tag{4}$$

where φ is an arbitrary constant and $\omega(k)$ must satisfy the dispersion relation.

The transverse components of the fields $\delta\mathbf{E}_\perp$ and $\delta\mathbf{B}$ may be derived from a transverse vector potential $\delta\mathbf{A}$, which when written in the helical frame of the undulator, i.e., using the vector $\hat{\mathbf{e}}$ and its complex conjugate $\hat{\mathbf{e}}^*$, rather than $\mathbf{e}_x$ and $\mathbf{e}_y$, has the form

$$\begin{aligned}\delta\mathbf{A} = {} & -\frac{mc^2}{e}|A_0|\,Q(k)\left[e^{i((k-k_u)z-\omega t+\varphi)}\hat{\mathbf{e}} + \text{cc}\right] \\ & - \frac{mc^2}{e}|A_0|\,Q(-k)\left[e^{i((k+k_u)z-\omega t+\varphi)}\hat{\mathbf{e}}^* + \text{cc}\right]\end{aligned} \tag{5}$$

with the polarization ratio $Q(k)$ given by

$$Q(k) = \frac{\gamma_{p0}\theta(k)}{\sqrt{2}\beta_{p0}c^2k^2}\,\frac{\theta(k) - c^2(k+k_u)^2}{\theta(k) - c^2(k^2+k_u^2)} \tag{6}$$

and where $\theta(k) = \omega^2(k) - \omega_p^2/\gamma_{p0}$, $\gamma_{p0} = (1-\beta_{p0}^2)^{-1/2}$.

The two waves with wavenumbers $k \mp k_u$ originate from the splitting, due to the strong external magnetic field, of the twofold degenerate transverse branch in the dispersion relation of the cold and nonmagnetized plasma. The number β_{p0} measures the strength of the relativistic effects produced by the diamagnetic currents and is defined as $\beta_{p0} = |\mathbf{u}_{\perp 0}|/c$, where $|\mathbf{u}_{\perp 0}|$ is the intensity of the (ordered) mean velocity of the electrons of the plasma. It must be noted that the polarization factor $Q(k) = O(\beta_{p0})$, and therefore, all transverse components of the wave electric and induction fields disappear when the undulator magnetic field tends to zero. In this limit, the accelerating wave turns back to the usual longitudinal wave of the nonmagnetic plasma, as it should be. The transverse fields are, at this point, calculated from (5) by means of the usual definitions $\delta\mathbf{E}_\perp = -(1/c)(\partial/\partial t)\delta\mathbf{A}$ and $\delta\mathbf{B} = e_z \times (\partial/\partial z)\delta\mathbf{A}$, which give explicitly

$$\begin{aligned}\delta E_x &= \sqrt{2}\frac{mc\omega}{e}|A_0|\left\{Q(k)\sin(\psi_- + \varphi) + Q(-k)\sin(\psi_+ + \varphi)\right\} \\ \delta E_y &= \sqrt{2}\frac{mc\omega}{e}|A_0|\left\{Q(k)\cos(\psi_- + \varphi) - Q(-k)\cos(\psi_+ + \varphi)\right\} \\ \delta B_x &= -\sqrt{2}\frac{mc^2}{e}|A_0|\left\{(k-k_u)Q(k)\cos(\psi_- + \varphi) - (k+k_u)Q(-k)\cos(\psi_+ + \varphi)\right\} \\ \delta B_y &= \sqrt{2}\frac{mc^2}{e}|A_0|\left\{(k-k_u)Q(k)\sin(\psi_- + \varphi) + (k+k_u)Q(-k)\sin(\psi_+ + \varphi)\right\}\end{aligned} \tag{7}$$

with $\psi_\mp = (k \mp k_u)z - \omega(k)t$.

C. Radial Dependence of the Axial Electric Field

We assume that the amplitude of the axial electric field as given in (4) has a radial dependence; i.e., rewrite the equation in the new form

$$\delta E_z = \frac{8\pi e n_0}{k}|A_0|\,F(r)\sin(kz - \omega(k)t + \varphi) \tag{4'}$$

where $F(r)$ is a slowly varying function of the radial distance r from the axis. It is known, at least in the nonmagnetic case, that this radial dependence gives, for consistency, rise to a correspondingly small radial component of the wave electric field δE_r that is different from zero only inside the region around the beam axis where the amplitude of the main axial field $\delta E_z(r)$ decreases to zero [5]. In our case, as in all other cases in which the plasma is subjected to strong magnetic fields, these radial fields should be calculated through some kind of generalized PW theorem and added to the transverse fields like that written in (7).

However, when, for any reason, an appreciable fraction of the electrons of the beam are able to move off the beam axis and well inside the region where these PW fields have large values, the quality of the beam immediately deteriorates. As a consequence and to avoid a possible large increase in the beam overall emittance, the transverse size of the beam should always be fairly smaller than the size of the accelerating pulse.

For this reason, we did not consider it important to develop in detail the demanding calculations that are necessary to extend the PW theorem to the case of a magnetized plasma, and simply, although inconsistently, added to the transverse fields in

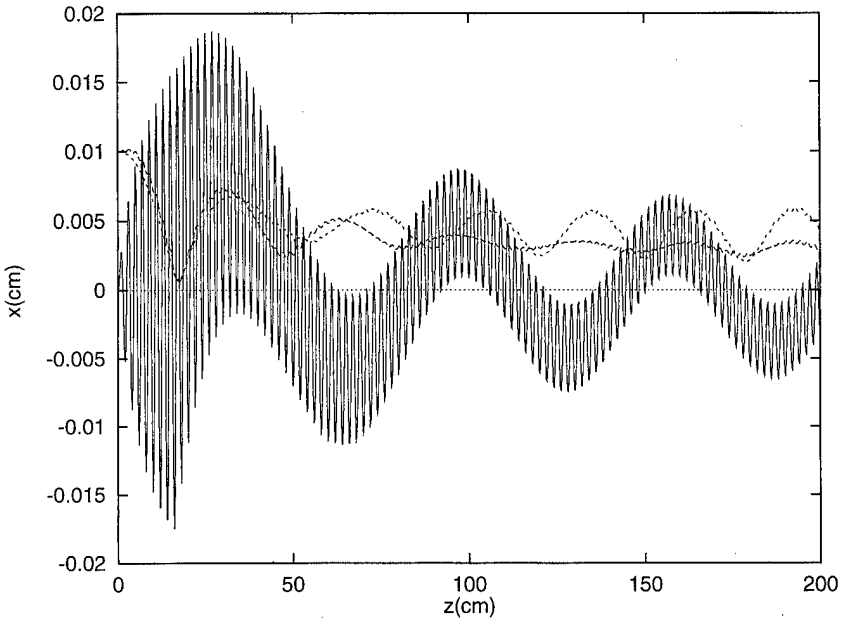


Fig. 1. The full line gives x versus z (both in centimeters) for the reference trajectory and the choice of parameters described in the text. The dashed and dotted lines give σ_x (cm) and σ_y (cm), respectively, versus z.

(7) the PW terms that arise in the more common case of nonmagnetic plasmas. Choosing for simplicity $F(r) = \exp[-2r^2/R^2]$, where R is a measure of the transverse radius of the accelerating wave pulse, we write the PW terms as [5]

$$(\delta E_x)_{\mathrm{PF}} = \frac{32\pi e n_0}{k^2 R^2} |A_0| e^{-2r^2/R^2} x \cos(kz - \omega t + \varphi)$$
$$(\delta E_y)_{\mathrm{PF}} = \frac{32\pi e n_0}{k^2 R^2} |A_0| e^{-2r^2/R^2} y \cos(kz - \omega t + \varphi). \quad (8)$$

III. Linear Analysis Around the Reference Trajectory

The reference trajectory is, in all cases, a solution of the nonlinear equations that describe the motion of a relativistic electron in (more or less) complicated electromagnetic fields; i.e.,

$$\frac{d}{dt}\mathbf{x}(t) = \mathbf{v}(t) = \frac{\mathbf{p}(t)}{m\gamma(t)}, \qquad \gamma(t) = (1 + p^2/m^2c^2)^{1/2}$$
$$\frac{d}{dt}\mathbf{p}(t) = -e\left[\delta\mathbf{E}(\mathbf{x}(t), t) + \frac{\mathbf{p}(t)}{mc\gamma(t)} \times \delta\mathbf{B}(\mathbf{x}(t), t)\right]. \quad (9)$$

Let us indicate the reference trajectory with $\mathbf{x}_o(t)$, $\mathbf{p}_o(t)$ and linearize the preceding equations by looking for solutions of the type $\mathbf{x}(t) = \mathbf{x}_o(t) + \delta\mathbf{x}(t)$, $\mathbf{p}(t) = \mathbf{p}_o(t) + \delta\mathbf{p}(t)$, where $\delta\mathbf{x}(t)$ and $\delta\mathbf{p}(t)$ are "small" disturbances. If we introduce the corresponding displacement in phase-space

$$\delta\mathbf{u}(t) = \begin{pmatrix} \delta\mathbf{x}(t) \\ \delta\mathbf{p}(t) \end{pmatrix} \quad (10)$$

it is easy to see that it satisfies the following (linear) system of equations:

$$\frac{d}{dt}\delta\mathbf{u}(t) = \overleftrightarrow{M} \cdot \delta\mathbf{u}(t) \quad (11)$$

where the 6×6 matrix $\overleftrightarrow{M}$ is made of the 3×3 matrices $\overleftrightarrow{0}$, $\overleftrightarrow{A}$, $\overleftrightarrow{B}$, and $\overleftrightarrow{C}$, like in the scheme

$$\overleftrightarrow{M} = \begin{pmatrix} \overleftrightarrow{0} & \overleftrightarrow{C} \\ \overleftrightarrow{A} & \overleftrightarrow{B} \end{pmatrix} \quad (12)$$

and $\overleftrightarrow{A}$, $\overleftrightarrow{B}$, and $\overleftrightarrow{C}$ are expressed as follows in terms of the external EM fields calculated on the reference trajectory exactly as

$$\overleftrightarrow{A} = -e(\nabla\mathbf{E})_o^T + \frac{e}{mc\gamma_o}\mathbf{p}_o \times (\nabla\mathbf{B})_o$$
$$\overleftrightarrow{B} = \frac{e}{mc\gamma_o}\left\{\overleftrightarrow{\Omega}_o + \frac{1}{m^2c^2\gamma_o^2}(\mathbf{p}_o \times \mathbf{B}_o)\mathbf{p}_o\right\}$$
$$\overleftrightarrow{C} = \frac{1}{m\gamma_o}\left\{1 - \frac{\mathbf{p}_o\mathbf{p}_o}{m^2c^2\gamma_o^2}\right\} \quad (13)$$

and

$$\overleftrightarrow{\Omega}_o = \begin{pmatrix} 0 & -B_{oz} & B_{oy} \\ B_{oz} & 0 & -B_{ox} \\ -B_{oy} & B_{ox} & 0 \end{pmatrix}. \quad (14)$$

It is also easy to find that within the validity of the linear hypothesis

$$\delta\mathbf{u}(t) = \overleftrightarrow{N}(t) \cdot \delta\mathbf{u}(0) \quad (15)$$

where the new 6×6 matrix $\overleftrightarrow{N}(t)$ is by definition equal to matrix $\overleftrightarrow{1}$ at $t = 0$. In addition, $\overleftrightarrow{N}$ is a solution of the equation

$$\frac{d}{dt}\overleftrightarrow{N}(t) = \overleftrightarrow{M} \cdot \overleftrightarrow{N} \quad (16)$$

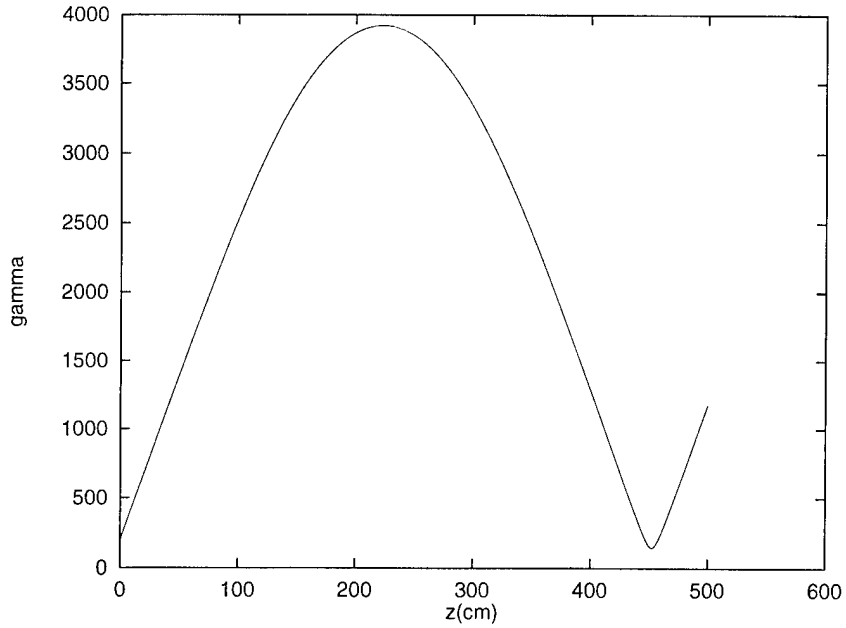


Fig. 2. Behavior of factor γ of the reference electron along the orbit, versus z (in centimeters). The initial value is $\gamma(0) = 200$.

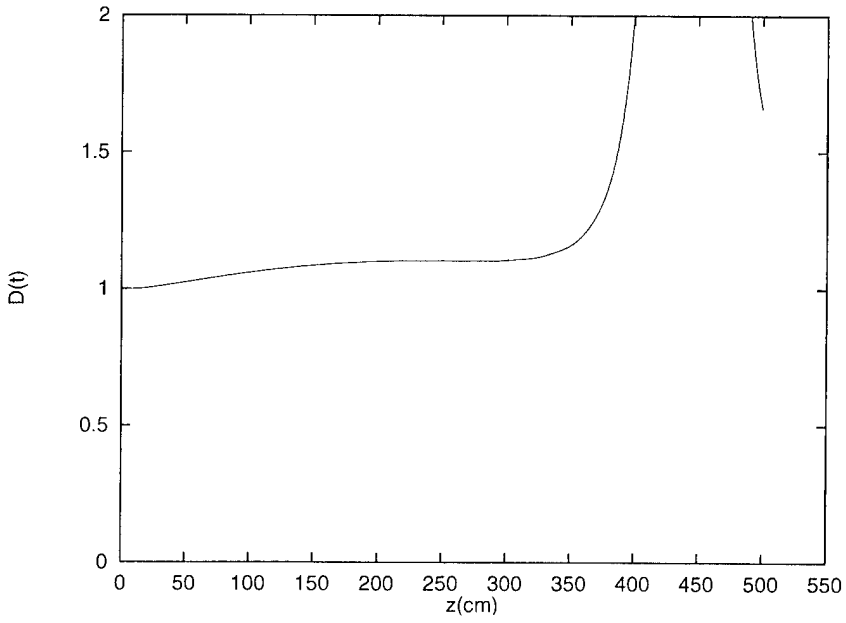


Fig. 3. Behavior of the determinant $D(t)$ of matrix $\overleftrightarrow{N}$, versus z.

and if we call $D(t)$ the determinant of $\overleftrightarrow{N}(t)$, we have

$$\begin{cases} \dfrac{d}{dt} D(t) = (\mathrm{Tr}\, \overleftrightarrow{M}) D(t) \\ D(0) = 1. \end{cases} \tag{17}$$

Because the trace of $\overleftrightarrow{M}$ is identically zero, as can be seen by direct inspection of (12) and (13), it follows that $D(t) = 1$ at all times.

Finally, introducing the phase-space dyadic $\delta\mathbf{u}\delta\mathbf{u}$, we have

$$\delta\mathbf{u}(t)\delta\mathbf{u}(t) = \overleftrightarrow{N}(t) \cdot \delta\mathbf{u}(0)\delta\mathbf{u}(0) \cdot \overleftrightarrow{N}^T(t) \tag{18}$$

where $\overleftrightarrow{N}^T$ is the transposed of $\overleftrightarrow{N}$. Averaging over the values of the dyadic $\delta\mathbf{u}(0)\delta\mathbf{u}(0)$, at the initial time, we get in the end

$$\langle \delta\mathbf{u}(t)\delta\mathbf{u}(t) \rangle = \overleftrightarrow{N}(t) \cdot \langle \delta\mathbf{u}(0)\delta\mathbf{u}(0) \rangle \cdot \overleftrightarrow{N}^T(t) \tag{19}$$

and from this expression we should be able to extract all (statistical) data of a macroscopic character that concern the aspect in the ordinary space and the stability of the electron beam along its motion.

In practice, however, the elements of $\overleftrightarrow{N}(t)$ are more conveniently calculated by using the operational definition (15) and the complete nonlinear equations of motion (9). The validity of the process of linearization around the reference trajectory can then be checked *a posteriori* by looking at the time evolution of

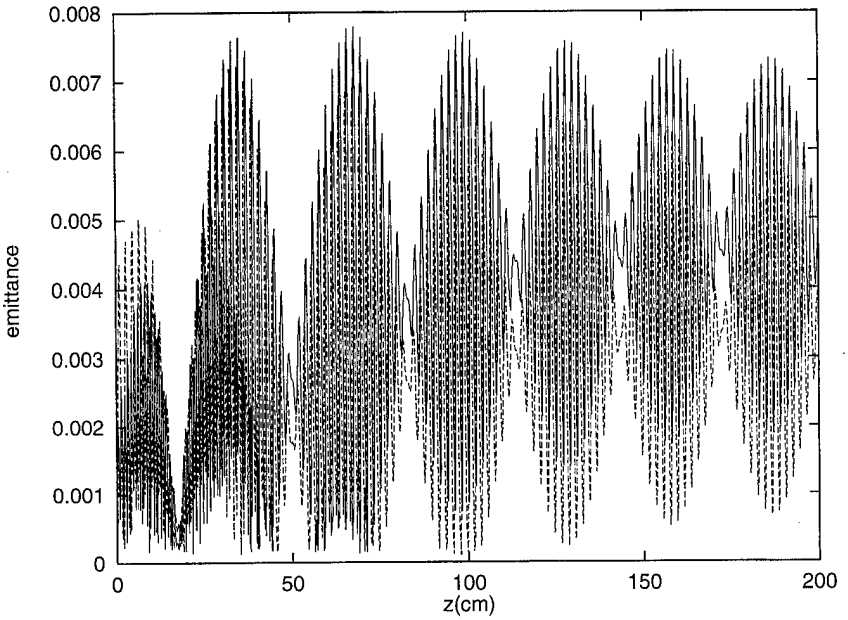


Fig. 4. Behavior of ε_x (solid line) and ε_y (dashed line), as defined in (20), versus z.

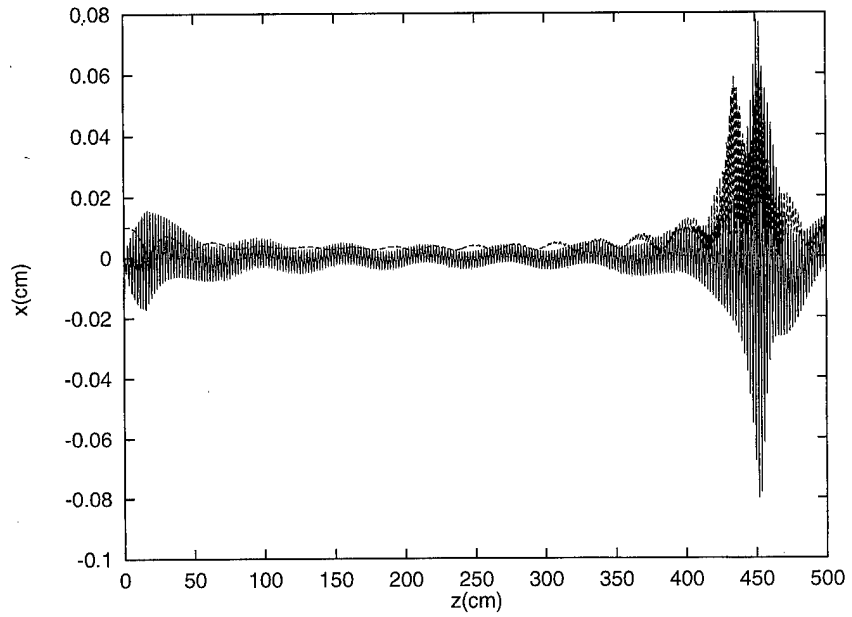


Fig. 5. Behavior of x versus z for the reference trajectory (solid line) and $\sigma_x(z)$ (dashed line). The quality of the motion deteriorates seriously for values of z between 4 and 5 m, where the electrons of the beam have lost by dephasing all of the energy gained in the acceleration phase.

the determinant $D(t)$, which should be a constant of the (linear) motion.

IV. Numerical Results and Conclusion

The figures show typical results that have been obtained with the following choice of parameters: unperturbed plasma density $n_0 \approx 10^{14}$ cm^{-3}, accelerating wave frequency $\omega \approx 0.46\,\omega_p = 2.6\,10^{11}$ rad/s^{-1}, $R = 0.5$ cm and wavelength $\lambda = 0.7$ cm and with $\beta_W = 0.999$ [$\gamma_W = (1 - \beta_W^2)^{-1/2} \approx 22$], an undulator with period $\lambda_u = 2$ cm and peak amplitude $B_u \approx 16$ T, and an injection energy of the electron beam of about 100 MeV.

Fig. 1 shows the behavior of x versus z (both in centimeters) for the reference trajectory and along an undulator length of 2 m. It also shows the two rms transverse dimensions of the beam $\sigma_x(z) = \sqrt{\langle \delta x^2 \rangle}$ and $\sigma_y(z) = \sqrt{\langle \delta y^2 \rangle}$, calculated with the matrix $\langle \delta \mathbf{u} \delta \mathbf{u} \rangle$ in (19), versus the distance z (always in centimters) and with the initial values $\sigma_x(0) = \sigma_y(0) = 0.01$ cm. The reference trajectory in this figure shows the characteristic "wiggling" motion of the electron over the undulator period of 2 cm and the superimposed much longer (secular) " betatron" oscillation.

Fig. 2 shows the increase in the relativistic energy of the reference electron versus z (centimeters). The electron has been followed, in this case, for a really long time, to show the saturation in energy gain due to dephasing with the accelerating wave and even the successive deceleration stage. The (theoret-

ical) maximum energy gained is of about 2 GeV, over a distance of 2–3 m.

Fig. 3 shows the behavior of the determinant $D(t)$ of the matrix $\overleftrightarrow{N}$ versus z (centimeters). Within the validity of the linear analysis, $D(t)$ should stay equal to one for all times. We can see, on the contrary, that there is a serious breakdown in the linear analysis for distances greater than about 3 m along the undulator.

Finally, Fig. 4 shows the behavior of the two transverse rms beam emittances

$$\varepsilon_x = \frac{1}{mc}\sqrt{\langle(\delta x\delta p_x - \langle\delta x\rangle\langle\delta p_x\rangle)^2\rangle}$$
$$\varepsilon_y = \frac{1}{mc}\sqrt{\langle(\delta y\delta p_y - \langle\delta y\rangle\langle\delta p_y\rangle)^2\rangle} \tag{20}$$

versus z (centimeters) and over a length that comprises the first 100 undulator periods.

These results show that the electron trajectories are strongly focused around the reference trajectory over lengths of about 100 undulator periods. Speaking more generally, however, we may say that when the electron Lorentz factors increase up to values of the order of a few thousands, as in this example, the focusing of all trajectories around the beam axis becomes a nearly obvious consequence of the relativistic increase in the electron mass. Fig. 5 has been added to emphasize this idea, because it follows the reference electron up to the point where the γ-factor decreases in the region from between 4 and 5 m inside the undulator. It shows that the quality of the motion deteriorates seriously at exactly this point along the beam axis.

We have found that the only condition that must be satisfied with accuracy to preserve the quality of the beam is that most electron trajectories develop well inside the region where the PW radial fields are negligible. This is verified if the beam radius is smaller than the wave pulse radius at $t = 0$ and if the beam is injected with a sufficiently high energy to ensure a small off-axis displacement at the first maximum of the "betatron" oscillation. In particular, this requires that the electron beam be injected with energy values moderately larger than those used in our preceding 1-D calculations [2], [3].

REFERENCES

[1] T. Katsouleas and J. M. Dawson, "Unlimited electron acceleration in laser-driven plasma waves," *Phys. Rev. Lett.*, vol. 51, pp. 392–395, 1983.

[2] C. Maroli, V. Petrillo, and R. Bonifacio, "Plasma-based inverse free-electron laser for high-gradient electron acceleration," *Phys. Rev. Lett.*, vol. 76, pp. 3578–3581, 1996.

[3] V. Petrillo and C. Maroli, "High-gradient electron acceleration in a plasma-loaded wiggler," *Eur. Phys. J. A. P.*, vol. 5, pp. 311–320, 1999.

[4] T. Scharlemann, "Selected topics in FELs," in *High-Gain, High-Power Free Electron Laser*, R. Bonifacio, L. De Salvo Souza, and C. Pellegrini, Eds. North-Holland: Elsevier Science, 1989, pp. 95–125.

[5] T. Katsouleas, C. E. Clayton, K. W. Wharton, R. Kinter, T. Peters, S. Heifets, and T. Raubenheimer, "Beam dynamics in plasma accelerators," in *AIP Conf. Proc.* Arcidosso, Italy, 1996, Nonlinear and collective phenomena in beam physics, pp. 75–86.

V. Petrillo, photograph and biography not available at the time of publication.

C. Maroli, photograph and biography not available at the time of publication.

Energy Spread in Plasma-Based Acceleration

Albert Reitsma, Raoul Trines, and Vladimir Goloviznin

Abstract—**Electron acceleration in a one-dimensional plasma wave has been simulated, with emphasis on minimizing the energy spread of an accelerated electron bunch, while keeping the mean energy gain at a reasonable level. Bunch length, beam loading, and the injection phase are tuned to reach this goal. The simulation results show that, in a wide range of initial bunch lengths and beam loading parameters, an optimum acceleration distance exists, which combines low energy spread and high energy gain. The energy spread at the optimum is found to be weakly dependent on bunch length and beam loading, while it is highly sensitive to deviations in the injection phase.**

Index Terms—**Electron bunch characteristics, plasma-based electron acceleration.**

I. Introduction

THE WORLDWIDE study of excitation of strong plasma waves by using high-intensity lasers is directed toward the developments of a compact laser-plasma accelerator [1], [2]. the design for such an accelerator had originally been proposed in [3]. Until now, the emphasis, both in experimental work and simulations, has been on the high acceleration gradients and energy gain provided by such an accelerator. The highest acceleration gradient so far (100 GeV/m) has been demonstrated in [4]. This is about 1000 times higher than the acceleration field in conventional linacs. However, no external bunch has been injected, but the accelerated electrons originated from the buld plasma as a result of self-trapping in the plasma wave. Recently, energy gain of several megaelectronvolts in a few millimeters has been demonstrated for a bunch of injected electrons [5]. Typically, the accelerated electrons come in a broad energy range from practically zero to some maximum value. Wilks *et al.* [6] showed that, in general, a low energy spread can be reached at the expense of energy gain. Van der Meer [7] proposed a special shaping of the electron bunch that reduces the energy spread considerably. Katsouleas *et al.* [8] developed a strategy for phasing and beam loading that minimizes energy spread without special shaping. The present work is an extension of the latter paper. In addition to the injection phase and beam loading, the bunch length as a tunable parameter has been included.

This paper is organized as follows: from the basic equations, the acceleration length at which a minimum in the energy spread of the accelerated electrons occurs is estimated. Subsequently we verify this estimate numerically, by simulating electron acceleration in a one-dimensional plasma wave.

Manuscript received October 7, 1999; revised February 2, 2000.

A. Reitsma and R. Trines are with the Technische Universiteit Eindhoven, 5600 MB Eindhoven, The Netherlands (e-mail: raoul@ktn.phys.tue.nl).

V. Goloviznin is with the FOM Instituut voor Plasmafysica Rijnhuizen, 3430 BE Nieuwegein, The Netherlands.

Publisher Item Identifier S 0093-3813(00)09156-6.

II. Basic Equations

A longitudinal electrostatic wave is assumed

$$E = E_0 \cos \psi. \tag{1}$$

Here, E denotes the electric field in the z direction, which is the direction of propagation for both the accelerated electrons and the plasma wave. The plasma wave has amplitude E_0 and phase $\psi \equiv kz - \omega t$, where z is the space coordinate, t the time, and ω the plasma frequency. The wave vector k is related to the frequency ω as $k = \omega/v_\phi$, with v_ϕ the phase velocity of the wave, which is close to c. The assumption of no (x, y) dependence is relevant for linear wake waves in plasma accelerator with a hollow channel as shown in [9]. For small beams in a hollow channel, transverse beam emittance is well preserved and the transverse beam dynamics have little effect on energy gain and energy spread [10], so that we may consider the acceleration as a purely one-dimensional process.

The equations of motion for a single electron with momentum P and phase ψ are

$$\frac{d\psi}{dt} = (v/v_\phi - 1) \tag{2}$$

$$\frac{dP}{dt} = -E_0 \cos \psi \tag{3}$$

where v is the velocity of the electron and $P = \gamma v/c$ its momentum. Here, we introduce the dimensionless quantities $t \rightarrow \omega t$, $P \rightarrow P/mc$, $E \rightarrow eE/m\omega c$, with e being the unit charge.

From Hamiltonian theory [11], a simple calculation for the energy gain $\mathcal{E}$ of a trapped electron injected at $\psi = \psi_{\text{in}}$ and extracted at $\psi = \psi_{ex}$ yields

$$\mathcal{E} = 2\gamma_\phi^2 E_0 mc^2(\sin \psi_{\text{in}} - \sin \psi_{ex}) \tag{4}$$

where γ_ϕ denotes the Lorentz factor corresponding to v_ϕ. The acceleration distance d can be estimated from the injection and extraction phases as

$$\frac{\pi d}{\lambda \gamma_\phi^2} = (\psi_{ex} - \psi_{\text{in}}) \tag{5}$$

where $\lambda = 2\pi/k$ is the plasma wavelength. Estimates (4) and (5) are derived under the condition that γ obeys $\gamma \gg \gamma_\phi$ for a sufficiently large part of the acceleration distance.

As stated in Section I, the goal of this paper is to find values for the beam length, beam loading, and injection phase such that the energy spread is minimized while the energy gain is kept at a reasonable level. The energy spread is, in fact, the sum of two contributions. The first one results from the bunch length L. In order to estimate this contribution, a simple two-particle model is used [8]. At $t = 0$, a bunch with uniform density and length

0093–3813/00$10.00 © 2000 IEEE

L is located between $\psi = \psi_{\rm in} \pm kL/2$. During the acceleration process, the distance between the electrons is assumed not to change significantly, so that, at extraction, the bunch is located between $\psi = \psi_{ex} \pm kL/2$. From (4), the difference in energy at extraction between a particle at the head of the bunch and a particle at the tail of the bunch reads

$$\Delta\mathcal{E}_1 = 4\gamma_\phi^2 E_0 mc^2 \sin(kL/2) \times (\cos\psi_{ex} - \cos\phi_{\rm in}). \quad (6)$$

From (6), it is obvious that the use of short bunches reduces this contribution to the energy spread.

The second contribution to the energy spread results from the wakefields of the electrons in the bunch: each electron is influenced by the wakefields of all electrons in front of it. These wakefields can be calculated by employing the charge density of the bunch as a source term in the wave equation for the electric field, under the condition that the field is unperturbed in front of the bunch. For a uniform bunch located between $\psi = \psi_{\rm in} \pm kL/2$, the bunch wakefield is, according to [8],

$$E = \eta E_0 \times \begin{cases} 0, & \psi - \psi_{\rm in} > kL/2 \\ -\dfrac{\sin(\psi - \psi_{\rm in} - kL/2)}{2\sin(kL/2)}, & -kL/2 < \psi - \psi_{\rm in} < kL/2 \\ \cos(\psi - \psi_{\rm in}), & \psi - \psi_{\rm in} < -kL/2. \end{cases} \quad (7)$$

Here, the bunch wakefield amplitude is introduced as a fraction of the laser wake amplitude E_0. This fraction η is commonly called the *beam loading fraction* . For example, a slab beam of width b and charge density n_b in a plasma with background density n_0 has a beam loading fraction [8]

$$\eta = 2kb \sin(kL/2)\frac{n_b}{n_0 E_0}. \quad (8)$$

At this point, an estimate for the beam loading effect can be derived using the constant retarding force on a tail electron due to the wakefield of the bunch. This induces an energy difference

$$\Delta\mathcal{E} = 2\eta\gamma_\phi^2 E_0 mc^2 \times \cos(kL/2)(\psi_{ex} - \psi_{\rm in}) \quad (9)$$

between the head and tail electron. Under certain circumstances, the contributions of (9) and (6) can cancel each other. The head and tail particles will then have approximately the same energy, resulting in a low relative energy spread. We denote the acceleration distance at which this minimum in energy spread occurs by $d_{\rm opt}$. Using (5) and taking $\psi_{\rm in}, \psi_{ex}$ close to π, one can estimate this distance as

$$\frac{\pi d}{\lambda\gamma_\phi^2} = \frac{\eta}{\tan(kL/2)} + 2(\pi - \psi_{\rm in}). \quad (10)$$

As we will see, (10) gives a correct scaling for $d_{\rm opt}$ in terms of L, η, and $\psi_{\rm in}$, apart from a constant offset.

III. Numerical Analysis

In our simulations, the electron bunch is represented by N macroparticles, having charge $-Q$, mass M, momentum P_n, and phase $\psi_n (n = 1 \cdots N)$. Mass and charge are chosen such that $Q/M = e/m$ (electron charge-to-mass ratio). One can think of these one-dimensional particles as charged sheets with uniform electron density in the transverse direction and a δ shape in the longitudinal direction (wide-beam limit). The wakefield of the nth macroparticle is

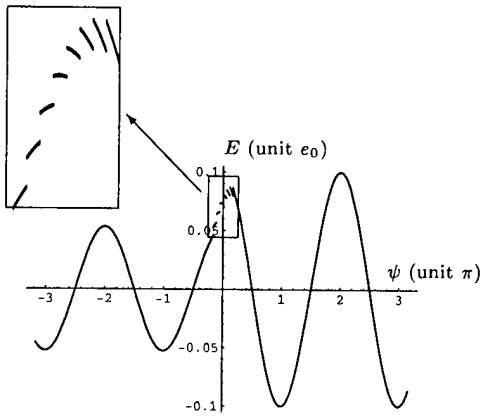


Fig. 1. Example of electric field as a function of phase with only 7 macroparticles in the bunch, visible in the inset dicontinuities in E. Beam loading fraction: $\eta = 0.5$.

$$E_n(\psi) = \begin{cases} -\dfrac{1}{N}\alpha E_0 \cos(\psi - \psi_n), & \psi < \psi_n \\ -\dfrac{1}{2N}\alpha E_0, & \psi = \psi_n \\ 0, & \psi > \psi_n. \end{cases} \quad (11)$$

The number α is a measure for the charge of a macroparticle, related to the beam loading fraction as

$$\eta = \frac{\sin(kL/2)}{kL/2}\alpha. \quad (12)$$

With this definition, taking the limit $N \to \infty$ in (11) correctly reproduces the wakefield of the continuous bunch, as given in (7). At the phase of the macroparticles, the electric field is non-continuous (see Fig. 1).

The equations of motion are $(n = 1, \ldots, N)$

$$\frac{d\psi_n}{dt} = (v_n/v_\phi - 1) \quad (13)$$

$$\frac{dP_n}{dt} = \left(E_0 \cos\psi_n + \sum_{m=1}^{N} E_m(\psi)\right). \quad (14)$$

In our simulations, a simple finite-difference scheme is used (leap-frog algorithm) to integrate (13) and (14). For the electric field, the analytic expressions (1) and (11), are used, in which at every time step all macroparticle phased are inserted. At the start of a simulation, all macroparticles have the same energy $\gamma_0 M_c^2$ and are uniformly distributed around injection phase $\psi_{\rm in}$

$$\begin{cases} \phi_n = \psi_{\rm in} + kL\left(\dfrac{n-1}{N-1} - \dfrac{1}{2}\right) \\ P_n = P_0 \equiv Mc\sqrt{\gamma_0^2 - 1}. \end{cases} \quad (15)$$

At every time step of the simulation, the mean energy $\langle\mathcal{E}\rangle$ and the energy spread $\Delta\mathcal{E}$ (standard deviation of particle energy) of the macroparticles are calculated. The initial energy spread is zero, because all macroparticles have the same initial energy.

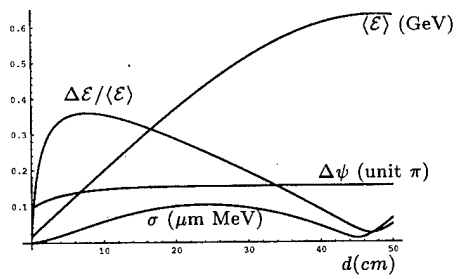


Fig. 2. Mean energy $\langle\mathcal{E}\rangle$, relative energy spread $\Delta\mathcal{E}/\langle\mathcal{E}\rangle$, phase spread $\Delta\psi$ and longitudinal rms emittance σ as functions of acceleration distance. Injection phase $\psi_{\rm in} = \pi$, bunch length $L = \lambda/6$, beam loading fraction $\eta = 0.8$.

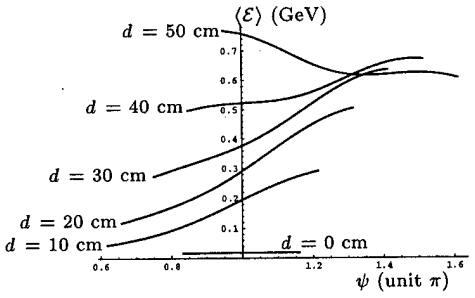


Fig. 3. Phase space snapshots for various acceleration distances for the run of Fig. 2.

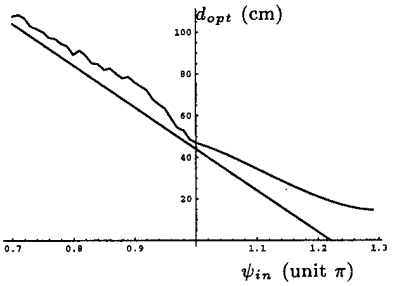


Fig. 4. Optimal distance $d_{\rm opt}$ as a function of injection phase $\psi_{\rm in}$. Upper curve: simulation result, lower curve: solution of (10).

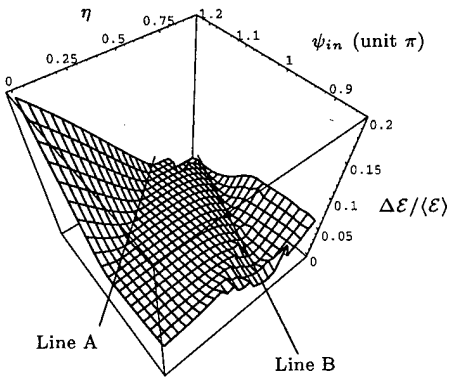


Fig. 5. Relative energy spread as a function of beam loading fraction and injection phase at $L = \lambda/6$.

The evolution of the bunch is calculated until the first local minimum in the relative energy spread $\Delta\mathcal{E}/\langle\mathcal{E}\rangle$ (see Fig. 2, for example) is encountered.

In the course of acceleration, some macroparticles may lose so much velocity that they become detrapped. These are mostly macroparticles in the tail of the bunch, if their phase is too close to $\pi/2$, the edge of the wave crest. In the calculations of the mean energy and energy spread, only macroparticles that are still trapped are taken into account. A particle is considered trapped if it is located within one wavelength from the wavecrest in which the bunch was injected at the start of the simulation. As soon as a particle violates this condition, it is discarded for the rest of the calculation. The fraction of detrapped (*i.e.*, lost) particles should not become too high, but a small fraction may be sacrificed in order to improve energy gain and/or spread. In our calculations, only a small fraction of the particles becomes detrapped.

The following set of parameters is fixed for all results shown in this article:

- $\gamma_\phi = 100$;
- $e_0 = 0.1$;
- $\gamma_0 = \gamma_\phi/3$;
- number of macroparticles, 100.

We chose the above set of parameters with a realistic case in mind; plasma electron density 10^{17} cm^{-3}, laser wavelength 1 μm, wake wavelength 100 μm, and electrons of initially 16.7 MeV.

IV. Simulation Results

Fig. 2 shows $\langle\mathcal{E}\rangle$ and $\Delta\mathcal{E}/\langle\mathcal{E}\rangle$ as functions of the acceleration distance d for a bunch with initial phase $\psi_{\rm in} = \pi$, length $L = \lambda/6$ and beam loading $\eta = 0.8$. The same figure shows phase spread $\Delta\psi$ (standard deviation of mean phase) and rms longitudinal emittance as functions of the acceleration distance.

A minimum in energy spread is seen to be reached at an acceleration distance of about 47 cm. At this point, the bunch has a mean energy of about 635 MeV with 2.6% spread. The bunch has increased its length by a factor of about 1.6 and the rms longitudinal emittance is rather small (about 0.02 μm MeV). This behavior is typical for most of our simulation runs.

Snapshots of the phase space distribution of accelerated macroparticles after propagation over various distances are given in Fig. 3. These curves show that during the first part of the acceleration, it is mostly the head of the bunch that gains energy. As the bunch slips against the wave, the other parts are accelerated as well. At the point of minimum energy spread (after 47 cm), the energy distribution is more or less balances.

A check of (10), our estimate of optimal distance is given in Fig. 4, in which $d_{\rm opt}$ is shown as a function of $\psi_{\rm in}$, both from our simulation results and from (10). Parameters are $\eta = 0.8$, $L = \lambda_p/6$. This plot shows a rough qualitative agreement with a general trend that the acceleration takes longer than expected from our estimate. This has to do with the first stage of the acceleration, during which the condition $\gamma \gg \gamma_\phi$ is violated. At $\psi_{\rm in} > 1.22\pi$, our estimate gives a negative acceleration distance, which is incorrect. Instead, the solution should be $d_{\rm opt} = 0$. Fig. 4 shows that for these cases $d_{\rm opt}$ is rather small. Consequently, the energy gain is very low and this region is not interesting for acceleration.

The next two figures illustrate the influence of beamloading and injection phase at *fixed* bunch length. In Figs. 5 and 6, we show relative energy spread and mean energy after accelerative

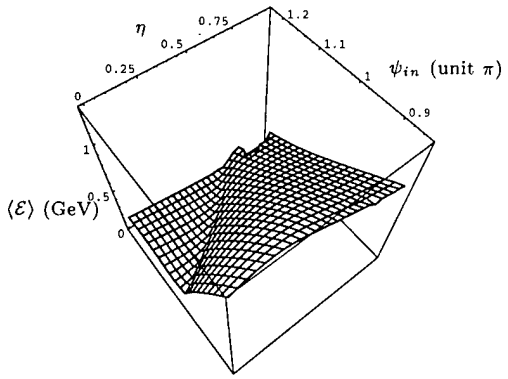


Fig. 6. Mean energy as a function of beam loading fraction, injection phase at $L = \lambda/6$.

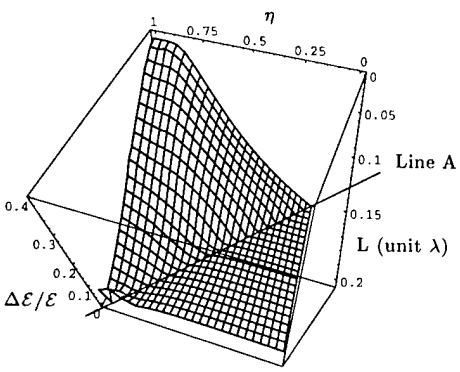


Fig. 9. Relative energy spread as a function of beam loading fraction, bunch length at $\psi_{\rm in} = \pi$.

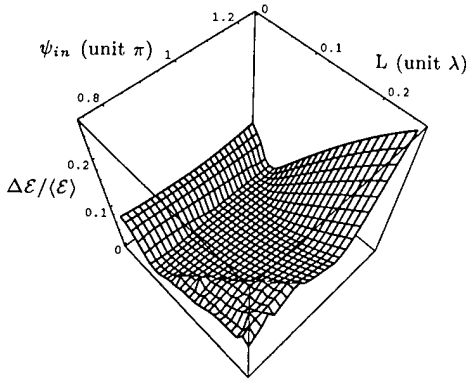


Fig. 7. Relative energy spread as a function of bunch length, injection phase at $\eta = 0.2$.

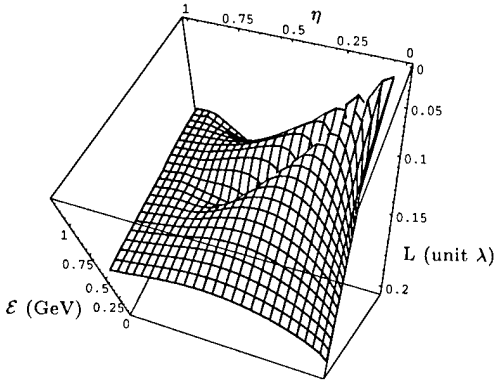


Fig. 10. Mean energy as a function of beam loading fraction, bunch length at $\psi_{\rm in} = \pi$.

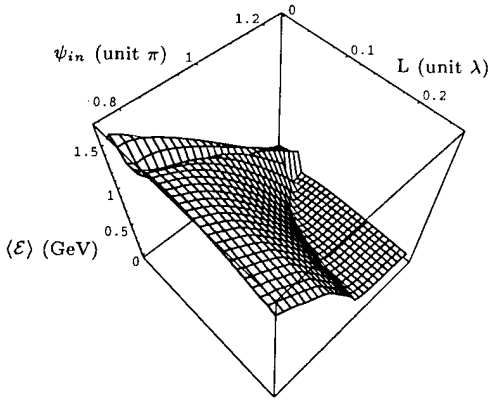


Fig. 8. Mean energy as a function of bunch length and injection phase at $\eta = 0.2$.

over $d_{\rm opt}$. In the region between the lines A and B, $d_{\rm opt}$ is in agreement with (10). To the left of line A, (10) gives a negative $d_{\rm opt}$ so this region is not suitable for acceleration, as confirmed by the low $\langle\mathcal{E}\rangle$-values of Fig. 6 in this region. The region near line B seems to be attractive for acceleration. Here, $d_{\rm opt}$ is close to the distance at which a maximum in energy gain occurs. In the region to the right of line B, it takes longer to reach a minimum in energy spread than to reach a maximum in energy gain.

In Figs. 7 and 8, we plot relative energy spread and mean energy as functions of bunch length and injection phase at a *fixed* beam loading fraction ($\eta = 0.2$). As before, we stop the runs at $d_{\rm opt}$. The region in Fig. 8 with low $\langle\mathcal{E}\rangle$-values corresponds to a negative d region, as discussed earlier. From Fig. 7, one can see that $L = 0.05\lambda$ gives and optimal result for $\eta = 0.2$. In practice, bunches are usually not that short (5 μm). Our results show that a low energy spread can be maintained up to $L = 0.2\lambda$, but with a smaller range of suitable $\psi_{\rm in}$. The decrease in relative energy spread at the front corner of the graph is due to particle loss.

We conclude our investigations by considering the effect of changing both bunch length and beam loading at a fixed injection phase $\psi_{\rm in} = \pi$. Figs. 9 and 10 show relative energy spread and mean energy as functions of beam loading fraction and bunch length. Again, the simulations were stopped at $d_{\rm opt}$. Fig. 9 demonstrates that a low energy spread can be reached for nearly every value of η between 0–1 by tuning the bunch length L. In the region below line A, $d_{\rm opt}$ is in agreement with (10). In the other region, where the energy spread is much higher, the value indicated by (10) is too large. Here, the minimum in energy spread is reached after a maximum in energy gain has occurred. This means that at some stage, a part of the bunch is decelerated and another part is still accelerated. Consequently, our assumption that the distance between particles does not change breaks down, and the relative energy spread increases dramatically. The above results suggest that an optimum in $\Delta\mathcal{E}/\langle\mathcal{E}\rangle$ can be reached by a proper tuning of the beam parameters η, L, and $\psi_{\rm in}$. In practical terms, the injection phase is the most difficult parameter to tune: it implies a femtosecond accuracy in injecting the bunch into the plasma wave. Solving this difficulty

is a major challenge for the future design of a plasma-based accelerator.

V. Summary and Conclusion

In summary, we have studied the dynamics of electron acceleration in a one-dimensional plasma wave, with particular attention for a minimization of energy spread. The two major mechanisms that contribute to the energy spread (finite bunch length L and beam loading η) have been shown to counterbalance each other at a certain acceleration distance $d_{\rm opt}$. We have obtained an approximate relation (10) that expresses $d_{\rm opt}$ in terms of η, L, and injection phase $\psi_{\rm in}$. Using a particle code, we have demonstrated that indeed, a low energy spread and high energy gain can be achieved if the parameters η, L, $\psi_{\rm in}$, and d are properly tuned. The corresponding parameter window is relatively wide, with the most crucial parameter being $\psi_{\rm in}$, which requires a femtosecond accuracy in bunch injection.

Acknowledgment

The authors would like to thank L. P. J. Kamp and T. J. Schep for valuable input.

References

[1] E. Esarey *et al.*, "Overview of plasma-based accelerator concepts," *IEEE Trans. Plasma Sci.*, vol. 24, p. 252, 1996.
[2] J. S. Wurtele, "The role of plasma in advanced accelerators," *Phys. Fluids B.*, vol. 5, p. 2363, 1993.
[3] T. Tajima and J. M. Dawson, "Laser electron accelerator," *Phys. Rev. Lett.*, vol. 43, p. 267, 1979.
[4] A. Modena *et al.*, "Electron acceleration from the breaking of relativistic plasma waves," *Nature*, vol. 377, p. 606, 1995.
[5] F. Dorchies *et al.*, "Acceleration of injected electrons in a laser wakefield experiment," *Phys. Plasmas*, vol. 6, p. 2903, 1999.
[6] S. Wilks *et al.*, "Beam loading in plasma waves," *IEEE Trans. Plasma Sci.*, vol. 15, p. 210, 1987.
[7] S. van der Meer, "Improving the power efficiency of the plasma wakefield accelerator,", Note 3 CERN/PS/(AA), 1985.
[8] T. C. Chiou and T. Katsouleas, "High beam quality and efficiency in plasma-based acceleration," *Phys. Rev. Lett.*, vol. 81, p. 3411, 1998.
[9] T. C. Chiou *et al.*, "Laser wakefield acceleration and optical guiding in a hollow plasma channel," *Phys. Plasmas*, vol. 2, p. 310, 1995.
[10] T. Katsouleas *et al.*, "Beam dynamics in plasmas accelerators," in *Proc. AIP Conf.*, S. Chattopadhyay *et al.*, Ed., 1996, vol. 395, p. 75.
[11] R. D. Ruth and A. W. Chao, "Plasma laser acceleration: Longitudinal dynamics, the plasma/laser interaction, and a qualitative design," in *Proc. AIP Conf.*, P. J. Channell, Ed., 1981, vol. 91, p. 94.
[12] C. B. Schroeder *et al.*, "Multimode analysis of the hollow plasma channel wakefield accelerator," *Phys. Rev. Lett.*, vol. 82, p. 1177, 1999.



Albert Reitsma received the M.Sc. degree in theoretical physics from Utrecht University, Utrecht, The Netherlands, in 1998. He is currently working toward the Ph.D. degree at Eindhoven University of Technology, Eindhoven, The Netherlands.

His fields of interest are plasma-based particle acceleration and laser-plasma interaction.



Raoul Trines received the M.Sc. degrees in mathematics and applied physics (both cum laude) in 1998 from Eindhoven University of Technology, Eindhoven, The Netherlands where he is currently working toward the Ph.D. degree. His fields of interest are plasma-based particle acceleration and laser-induced fast particle generation.



Vladimir Goloviznin was born in Kirov, Russia. He graduated from Moscow State University, Moscow, Russia, and received the Ph.D. degree in theoretical and mathematical physics from Kurchatov Institute of Atomic Energy, Moscow, Russia in 1977 and 1983, respectively.

From 1980 and 1997, he was with Kurchatov Institute of Atomic Energy, where he was involved in research projects on electron channeling in crystals and on free-electron lasers. In 1991–1992, he was also with the University of Bielefeld, Germany, as an Alexander von Humboldt Fellow. Since 1997, he has been with the FOM-Institute for Plasma Physics, Nieuwegrin, The Netherlands, and the University of Eindhoven, Eindhoven, The Netherlands. His current field of research interests includes analytical and numerical studies on plasma-based acceleration, generation of coherent X-ray radiation, and ultraintense laser-plasma interactions.

Laser Wakefield Acceleration of Short Electron Bunches

Nikolai E. Andreev and Sergey V. Kuznetsov

Abstract— **The theory of electron acceleration in a plasma wake wave is developed, and the dependence of the main characteristics of accelerated electron bunches on the wakefield parameters is investigated. It is shown that using a prebunching stage, under proper conditions, the final electron density of a compressed and accelerated bunch can exceed the initial electron beam density by orders of magnitude and that longitudinal bunch compression provides quasi-monoenergetic acceleration to high energies. It is demonstrated that, for an initial electron beam radius smaller than the optimal one for efficient beam trapping, the energy spread of the compressed and accelerated electron bunch and its length can be evaluated by using the simple analytical predictions of a one-dimensional (1-D) theory. The obtained analytical results are confirmed by three-dimensional (3-D) numerical modeling.**

I. Introduction

THE new methods of electron acceleration in a fast plasma wake wave excited by a short, intense laser pulse in rarefied plasma attract the attention of many investigators (see reviews [1] and [2] and references therein). Further progress in laser–plasma accelerators is dependent not only on the realization of ultrahigh accelerating gradients, but also on the possibility to provide extended quasi-monoenergetic acceleration for appreciably bulk electron charges. For many applications, the important characteristics are the duration and emittance of accelerated electron bunches [3]. The inhomogeneity of a comparatively short-wavelength plasma wakefield is responsible for the electron bunching in the energy distribution [4], [18], [5] and in space [6]–[8], which makes it possible to produce ultrashort relativistic electron bunches [9].

In the present paper, we develop the theory of electron acceleration in a plasma wake wave to investigate the dependence of the main characteristics of accelerated electron bunches on the wakefield parameters. Special attention is paid to the formation of short, compressed bunches from a lengthy electron beam. It is shown that using the prebunching stage, under proper conditions, the final electron density of the compressed and accelerated bunch can exceed the initial electron beam density in orders of magnitude. At the same time, the longitudinal compression of the electron bunch provides quasi-monoenergetic acceleration to high energies. The obtained analytical predictions are confirmed by the results of three-dimensional (3-D) numerical modeling.

Manuscript received November 1, 1999; revised April 3, 2000. This work was supported in part by the Russian Foundation for Basic Research under Grant 98-02-16263.

The authors are with the High Energy Density Research Center, Associated Institute for High Temperatures, Russian Academy of Sciences, Moscow 127412, Russia (e-mail: andreev@laslab.ivtan.msk.su).

Publisher Item Identifier S 0093-3813(00)09722-8.

The paper organized as follows. In Section II, we briefly review the main regularities of the finite-size electron bunch acceleration in the laser wakefield. Section III describes the effect of longitudinal compression of finite-size electron bunches and 3-D tree-dimensional bunching of lengthy electron beams. The main characteristics of preliminary compressed and accelerated electron bunch are discussed in Section IV. A conclusion is presented in Section V.

II. General Regularities of Electron Bunch Acceleation in the Plasma Wakefields

To investigate the acceleration of relativistic electrons in the wakefield generated by a laser pulse propagating along the axis OZ, we use the equations of motion in the form [10]

$$\frac{dp_z}{d\tau} = F_z(\xi, \rho) \tag{1}$$

$$\frac{d\boldsymbol{p}_r}{d\tau} = \boldsymbol{F}_r(\xi, \boldsymbol{\rho}) \tag{2}$$

$$\frac{d\xi}{d\tau} = \frac{p_z}{\sqrt{1+p_z^2+p_r^2}} - \beta \tag{3}$$

$$\frac{d\boldsymbol{\rho}}{d\tau} = \frac{\boldsymbol{p}_r}{\sqrt{1+p_z^2+p_r^2}} \tag{4}$$

where $p_z, \boldsymbol{p}_r = \{p_x, p_y\}$ are normalized to mc longitudinal and perpendicular to the axis OZ-components of momentum of an accelerating electron; $\xi = k_p(z - V_{ph}t), \boldsymbol{\rho} = k_p\boldsymbol{r} = k_p\{x, y\} = k_p r\{\cos\varphi, \sin\varphi\}, \varphi = \mathrm{arctg}(y/x)$ are its dimensionless coordinates; $\tau = \omega_p t$; electron plasma frequency $\omega_p = \sqrt{4\pi e^2 n_0/m}$ and wavenumber of the plasma wave $k_p = \omega_p/c$ are determined by the background plasma density n_0; and $\beta = V_{ph}/c$ is the dimensionless phase velocity of the wake. The axial and radial ($\boldsymbol{F}_r = \{F_x, F_y\} = F_r\{\cos\varphi, \sin\varphi\}$) components of the normalized force acting on the accelerating electron moving with the velocity of light c along the OZ-axis can be expressed by the wakefield potential ϕ as follows:

$$F_z \equiv \frac{eE_z}{mc\omega_p} = \frac{|e|}{mc^2}\frac{\partial\phi}{\partial\xi} \tag{5}$$

$$F_r \equiv \frac{eE_r}{mc\omega_p} - \frac{eB_\varphi}{mc\omega_p} = \frac{|e|}{mc^2}\frac{\partial\phi}{\partial\rho}. \tag{6}$$

We consider the axisymmetric geometry of the problem when the laser pulse intensity and, hence, the wakefield potential are independent on the azimuth angle. We suppose also that the wakefield potential depends only on comoving with the laser pulse variable ξ and ρ (and does not depend directly on time),

0093–3813/00$10.00 © 2000 IEEE

which assumes a stationary (channel-guided) laser pulse propagation [11]. Note that (6) for the radial force of allowing for wakefield magnetic field B_φ is valid (strictly speaking) for accelerating electrons with radial velocities smaller than the velocity of light c. But, in the cases of not very high nonlinearity of the wake wave ($|e\phi|/mc^2 \leq 1$) and characteristic transverse scale of the wake is in excess of plasma skin depth k_p^{-1}, the wakefield magnetic field is small in comparison with the electric field of the wake [12], [19], and both components of force (5), (6) are potential independently on radial velocities of accelerated electrons.

The stationarity of the wakefield in the frame of the wave (moving with the phase velocity V_{ph} along the OZ-axis) makes it possible to write the energy conservation of accelerated electron in the wave frame

$$E' - |e|\phi'(z', r') = E'_{\text{inj}} - |e|\phi'(z'_{\text{inj}}, r'_{\text{inj}}) \tag{7}$$

where

- E' kinetic energy of an electron (including the rest energy);
- ϕ' wakefield potential;
- $z'_{\text{inj}}, r'_{\text{inj}}$ initial coordinates of injection of electron to the wakefield; the primes denote that all quantities are recast to the wave frame by the relativistic transformation.

For the analysis of electron acceleration, we start in one-dimensional (1-D) approximation, neglecting radial motion when the wakefield potential depends mainly on the longitudinal variable ξ (that is the case of a small radius of electron bunch in comparison with the transverse scale of wakefield). We also suppose that the initial energy of injected electrons E_{inj} is no less than the resonant one defined by the phase velocity of the wake ($E_{\text{inj}} \geq \gamma mc^2$). The use of (1), (3), and (7) leads to the expression for the energy spread ΔE of an initially monoenergetic electron bunch of a comparatively small length $L_{b0} < k_p^{-1}$ [13]. The maximal relative energy spread in accordance with this result can be estimated by a rather simple formula (compare [14])

$$\Delta E/E \approx \frac{k_p L_{b0}}{\phi(\xi) - \phi(\xi_{\text{inj}})} \left\{ \frac{d\phi(\xi_{\text{inj}})}{d\xi} - \frac{d\phi(\xi)}{d\xi} \right\} \tag{8}$$

which shows that the energy spread increases linearly with the initial bunch length, and it is determined by the space dependence of the wakefield potential in the region used for acceleration. For example, in a linear harmonic wake wave with the potential

$$\phi(\xi, \rho) = -\phi_0 \cos(\xi) \exp(-\rho^2/(k_p R_p)^2) \tag{9}$$

the energy spread (8) does not depend on the wakefield amplitude ϕ_0 and increases with the length of acceleration up to the value

$$\Delta E/E = k_p L_{b0} \tag{10}$$

when the electron bunch injected in the maximum of accelerating field at $\xi_{\text{inj}} = \pi/2$ (that is beginning of the focusing phase) reaches the maximum of the potential at $\xi = \pi$.

Fig. 1 shows the energy spread of electron bunches of different sizes in relation to the length of acceleration L_{acc} normalized to the dephasing length $L_{ph} = \pi k_p^{-1}(1-\beta)^{-1} = \gamma^2 \lambda_p$, which is the distance an electron travels in the laboratory frame when, in the wave frame, it passes between the minimum and the maximum of the potential (from $\xi = 0$ to $\xi = \pi$). The wakefield potential was chosen in the form (9) with the amplitude $\phi_0 = 0.3$ and $k_p R_p = 3$. The phase of electron bunch injection for all examples was at the beginning of focusing phase ($\xi_{\text{inj}} = \pi/2$).

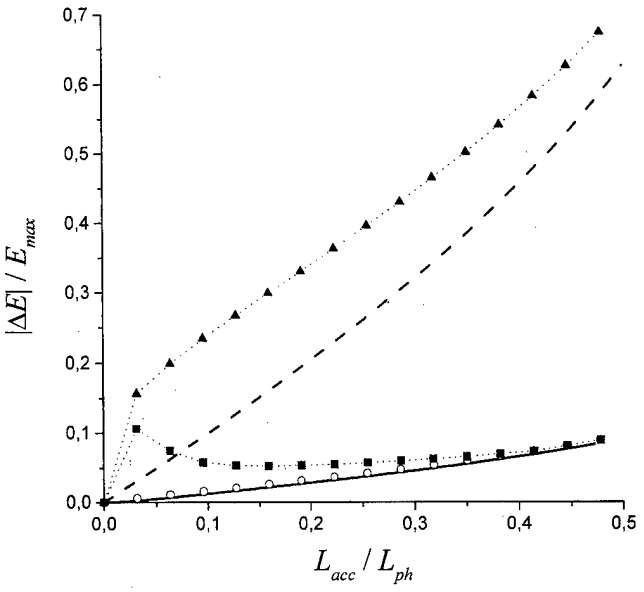


Fig. 1. Normalized energy spread as a function of accelerating length L_{acc} (in units of dephasing length $L_{ph} = \pi k_p^{-1}(1-\beta)^{-1} = \gamma^2 \lambda_p$) for electron bunches of different sizes: squares—$k_p L_{b0} = 0.1, k_p R_b = 1.0$; triangles—$k_p L_{b0} = k_p R_b = 0.628$; circles—$k_p L_{b0} = 0.1$, 1-D modeling; solid and dash lines are analytical predictions by (8) for $k_p L_{b0} = 0.1$ and 0.628, respectively. The wakefield potential was chosen in the form (9) with the amplitude $\phi_0 = 0.3$ and $k_p R_p = 3$.

As indicated by Fig. 1, the initial electron bunch radius R_b can influence substantially the energy spread at the beginning of acceleration. However, when the length of acceleration is comparable with the maximum one (i.e., L_{acc} is of order $L_{ph}/2$), the 1-D estimation (8) describes the results of 3-D numerical modeling accurately, even for rather long bunches [when $k_p L_{b0} \approx 1$, that is the boundary of applicability of analytical result (8)]. From this analysis, it is apparent that the initial bunch length is the main parameter defining the final energy spread when a gain in electron bunch energy approaches the maximum value $E_{\max} = 2mc^2\gamma^2\phi_0$ at $L_{\text{acc}} \approx L_{ph}/2$.

III. Longitudinal Compression of the Finite Size Electron Beam

The longitudinal bunch compression in the plasma wakefield before the main accelerating stage was analyzed [7], [9], [13], [15], [20] and proposed to minimize the energy spread [16], [21]. The strongest bunch compression will take place in the area of the highest negative gradient of the accelerating force (where $\partial^2\phi/\partial\xi^2 < 0$), i.e., near the wakefield potential maximum $\phi(\xi_m) = \phi_{\max}$. It was shown that the length (L_b) of the bunch, injected at $\xi_{\text{inj}} = \xi_m$ with the energy below the resonant one ($E_{\text{inj}} < \gamma mc^2, \gamma = 1/\sqrt{1-\beta^2}$), decreases with the bunch

slippage from ξ_m to the trapping point ξ_{tr} (turning point of the electron motion in the wave frame) as follows [9]:

$$\frac{L_b(\xi)}{L_{b0}} = \frac{E_{\rm inj}p'(\xi)}{E(\xi)p'_{\rm inj}} + \frac{|e|\gamma^2 p'(\xi)}{2mcE(\xi)} I(\xi) \left|\frac{\partial^2\phi(\xi_m)}{\partial\xi^2}\right| k_p L_{b0}$$
$$\equiv \alpha_1(\xi) + \alpha_2(\xi) k_p L_{b0}. \quad (11)$$

In deriving this equation, the injected bunch was assumed monoenergetic, homogeneous, and located in the interval $[\xi_m - k_p L_{b0}, \xi_m]$, $k_p L_{b0} < 1$. The minimal length of the bunch (without regard for the radial electron motion) is determined by its initial length L_{b0} and the wakefield potential at the points of injection and trapping

$$L_b(\xi_{tr}) = \alpha_2(\xi_{tr}) k_p L_{b0}^2 \equiv \frac{k_p L_{b0}^2}{2} \frac{|\partial^2\phi(\xi_m)/\partial\xi^2|}{\partial\phi(\xi_{tr})/\partial\xi}. \quad (12)$$

This equation shows that for effective compression, the initial bunch length should not exceed the plasma skin depth k_p^{-1} and that the compression factor L_{b0}/L_b increases with reduction of the initial bunch length and does not depend directly on the amplitude and phase velocity of the wake if the electron capture condition is fulfilled. The minimal bunch length will be obtained when at the trapping point, the accelerating force has a maximum. For example, in the linear harmonic wake wave (9) at $\xi_{\rm inj} = \xi_m = \pi$, the maximum bunch compression takes place when $\xi_{tr} = \pi/2$ (at the beginning of the focusing phase), and in accordance with (12), we have

$$L_b = k_p L_{b0}^2/2. \quad (13)$$

In order that electrons with the initial energy $E_{\rm inj}$ (injected in the vicinity of the maximum of potential $\phi_{\max}$) were trapped at the given point ξ_{tr}, the potential difference should satisfy the condition

$$|e|[\phi_{\max} - \phi(\xi_{tr})]$$
$$= E_{\rm inj} - \left[(1-\gamma^{-2})\left(E_{\rm inj}^2 - m^2c^4\right)\right]^{1/2} - mc^2/\gamma. \quad (14)$$

Fig. 2 illustrates the dependency (14) of the wakefield amplitude on the electron injection energy for $\xi_{tr} = \pi/2$ and $\gamma = 50$. It shows the substantial increase of the wave amplitude, necessary for the electron bunch trapping, with the decrease of the energy of an injected bunch. For small injection energy of order 1 MeV, the normalized wakefield amplitude should be high, of order of 10%, whereas for $E_{\rm inj} \approx 10$ MeV, the amplitude of the wakefield, sufficient for trapping of an injected bunch, appears to be rather small, $|e|\phi_0/mc^2 \geq 0.01$.

Consequently, the different schemes of prebunching should be used depending on the electron injection energy. For small enough energies of injection (of order 1 MeV), the bunch compression and acceleration can be achieved in the same high amplitude wake wave by a proper injection phase at the maximum of the wakefield potential [17]. Although for higher injection energies (of order of 10 MeV or more), the wakefield amplitude, necessary for the effective bunch compression, should be too small in order that the compressed electron bunch could be substantially accelerated in the same wakefield after its trapping. In this case, the acceleration of compressed bunch in high-amplitude wakefield has to be in the separate section after prebunching [9], [13], [15], [20]. Note again that the final minimal size of compressed bunch (13) does not depend on the wakefield amplitude and so on the injection electron energy.

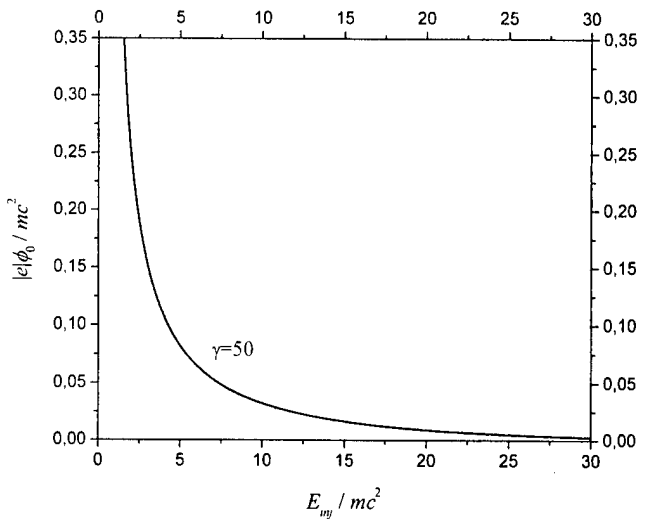


Fig. 2. Dependency (14) of the wakefield amplitude, necessary for the electron bunch trapping, on the electron injection energy $E_{\rm inj}$ for $\xi_{tr} = \pi/2$ and $\gamma = 50$.

The energy spread of an initially monoenergetic and comparatively short ($L_{b0} < k_p^{-1}$) electron bunch due to its compression can be estimated as follows [13]:

$$|\Delta E| = |e|\gamma \left\{ \frac{E_{\rm inj}}{|p'_{\rm inj}|c} \cdot \frac{d\phi(\xi)}{d\xi} \cdot k_p L_{b0} \right\} \quad (15)$$

where $p'_{\rm inj}$ is the impulse of injected electrons in the frame of wave. This expression shows that at the trapping point [in accordance with (14)], the spread is dependent only on the injection energy and initial bunch length

$$|\Delta E| = E_{\rm inj} k_p L_{b0} \sqrt{\frac{E'_{\rm inj} - mc^2}{E'_{\rm inj} + mc^2}}. \quad (16)$$

From (16), it is evident that for small enough energies of injection (of order of a few electronvolts), the energy spread increases practically linearly with the injection electron energy (as $E'_{\rm inj} \gg mc^2$ in this case). The results of 3-D numerical modeling confirm simple analytical predictions (12), (13) and (15), (16) for the cases of a small radius of electron bunch in comparison with the transverse scale of the wakefield [9], [13].

It should be reminded that for efficient compression, the initial bunch length should not exceed the plasma skin depth k_p^{-1} [see (12) and (13)] that imposes rather hard constraints on the initial bunch duration. For example, if the wakefield with $\gamma = 50$ is generated by a 1-μm laser, the electron bunch duration should not exceed 20 fs. Below, we describe the formation of short compressed bunches from a lengthy electron beam, which the duration is in excess of the plasma wave period.

Equation (12) can be used also to describe the local electron density distribution in the vicinity of the trapping point (in 1-D approximation) [9]

$$n(\xi) = n_0/\sqrt{\alpha_2(\xi_{tr})(\xi_{tr} - \xi)} \quad (17)$$

where n_0 is the initial density of injected lengthy electron beam (assumed to be homogeneous with the energy below the resonant one, $E_{\rm inj} < \gamma mc^2$), α_2 is determined by (12), and ξ_{tr} is the trapping coordinate of a beam electron located initially at the maximum of the potential. Note that at the instant, this electron is trapped, all surrounding electrons are behind it, at $\xi < \xi_{tr}$, in accord with (17). In the harmonic wakefield (9), $\alpha_2 \approx 0.5$ if $\xi_{tr} \approx \pi/2$. The singular (integrated) density distribution (17) shows that the initially homogeneous electron beam is strongly bunched near the trapping point. This bunching effect can be used to form short electron bunches due to the radial forces. If the trapping point [determined by the wakefield amplitude and injection energy; see (14)] will be in the vicinity of the beginning of the focusing phase $\xi_{\rm foc}$ [$\xi_{\rm foc} = \pi/2$ for the potential (9)], the bunched electrons within the small interval $[\xi_{\rm foc}, \xi_{tr}]$ will still be in the focusing phase, whereas the tail of the distribution (17) at $\xi < \xi_{\rm foc}$ will start to spread due to defocusing radial forces of the wakefield.

The averaged density (per unit length) of compressed electron bunch can be estimated with the help of distribution (17)

$$\langle n\rangle \equiv \frac{1}{k_p L_b(\xi_{tr})}\int_{\xi_{\rm foc}}^{\xi_{tr}} n(\xi)\,d\xi = 2n_0/\sqrt{\alpha_2(\xi_{tr})k_p L_b(\xi_{tr})} \tag{18}$$

where $k_p L_b(\xi_{tr}) = \xi_{tr} - \xi_{\rm foc}$ is the bunch length cut by the boundary of the focusing phase. This expression shows that when the trapping point approaches the boundary of the focusing phase ($k_p L_b(\xi_{tr}) \ll 1$), the averaged density of the compressed bunch exceeds substantially the initial density of the injected electron beam. Moreover, for the electron beams longer than the plasma wavelength, the discussed process will produce a sequence of short compressed bunches at the boundaries of each focusing phase [at $\xi = \pi/2 + 2\pi n, n = 0, 1, 2, \ldots$ for the wakefield potential (9)], and this train will be in phase with the wakefield that provides the effective acceleration to all compressed bunches in the wake with the same phase velocity. The estimation (18) was confirmed by 1-D numerical modeling (that is the case of small beam radius $R_b \ll R_p$) [9].

In the case of wide enough injected beams, the important parameter is the effective acceptance radius, which determines the transverse size of the beam that can be trapped, and so controls the averaged density (and the number of electrons) in the compressed bunch. For the wakefield potential (9), the boundary of area from which electrons will be trapped in the focusing phase can be found by (7)

$$R(\xi) = R_p\left\{\ln\left[\frac{-\cos(\xi)|e|\phi_0'}{E_{\rm inj}' - mc^2}\right]\right\}^{1/2} = R_p\left\{\ln\left[\frac{-\cos(\xi)|e|\phi_0}{E_{\rm inj} - \beta\sqrt{E_{\rm inj}^2 - m^2c^4} - mc^2/\gamma}\right]\right\}^{1/2}. \tag{19}$$

Fig. 3 illustrates the area of electron trapping from a homogeneous beam of initial radius $R_b = 1.6k_p^{-1}$, energy $E_{\rm inj}/mc^2 = 20$, injected in the wakefield (9) with the flowing parameters: $|e|\phi_0 mc^2 = 0.01, k_p R_p = 3.0, \gamma = 50$. The points depict the initial positions of electrons (in the plane cross section $(y_{\rm inj}, \xi_{\rm inj})$ obtained by 3-D numerical modeling), which are trapped in the focusing phase after acceleration in the wakefield over the distance $L_{\rm acc} = 0.234L_{ph}$ that corresponds to the trapping of an electron, located initially at the potential maximum $\xi_m = \pi$, at the point $\xi_{tr} = 1.67$. The solid curve represents the analytically obtained boundary (19) and demonstrates the close agreement of simple predictions, based on the energy conservation law (7), with 3-D numerical modeling.

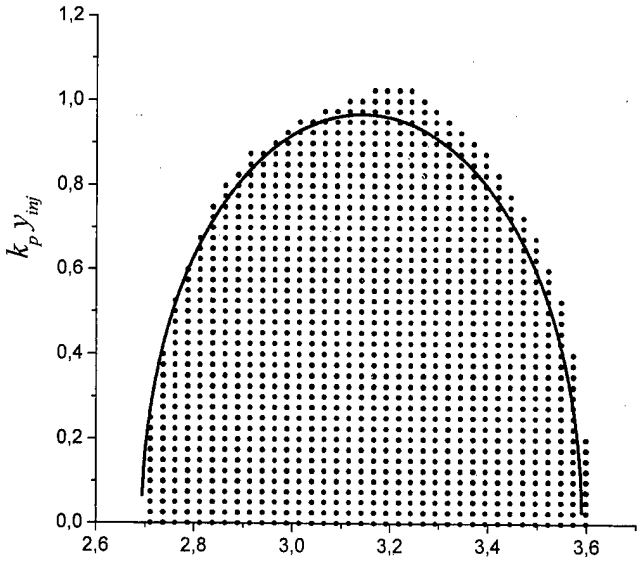


Fig. 3. Area of electron trapping from a homogeneous beam (with initial radius $R_b = 1.6k_p^{-1}$, energy $E_{\rm inj}/mc^2 = 20$), injected in the wakefield (9) with the flowing parameters: $|e|\phi_0 mc^2 = 0.01, k_p R_p = 3.0, \gamma = 50$. The points depict the initial positions of electrons (in the plane cross section $(y_{\rm inj}, \xi_{\rm inj})$ obtained by 3-D numerical modeling), which are trapped in the focusing phase after acceleration in the wakefield over the distance $L_{\rm acc} = 0.234L_{ph}$. The solid curve represents the analytically obtained boundary (19).

Equation (19) enables us to estimate the maximal radius of an injected electron beam, which can be trapped by the given wakefield depending on the injection electron energy:

$$R_{\max} = R_p\left\{\ln\left[\frac{|e|\phi_0}{E_{\rm inj} - \sqrt{(1-\gamma^{-2})(E_{\rm inj}^2 - m^2c^4)} - mc^2/\gamma}\right]\right\}^{1/2}. \tag{20}$$

For the parameters ($|e|\phi_0/mc^2 = 0.01, k_p R_p = 3.0, \gamma = 50, E_{\rm inj}/mc^2 = 20$) indicated above, this equation gives $R_{\max} = 0.97k_p^{-1}$ that limits the injected beam radius suitable for the bunch compression. If the beam having the initial radius $R_b \cong R_{\max} \cong k_p^{-1}$ is injected in the wakefield with the parameters discussed above, the trapping area (19) will contain an order of 10% of electrons falling into the plasma wavelength. The averaged electron density of the bunch trapped in the focusing phase will be approximately seven times larger than the initial beam density, whereas the 1-D estimate (18) gives a nine-fold increase of the initial electron density for the considered example. Note that for $R_b < R_{\max}$, the averaged bunch density can exceed the value (18) due to radial bunch

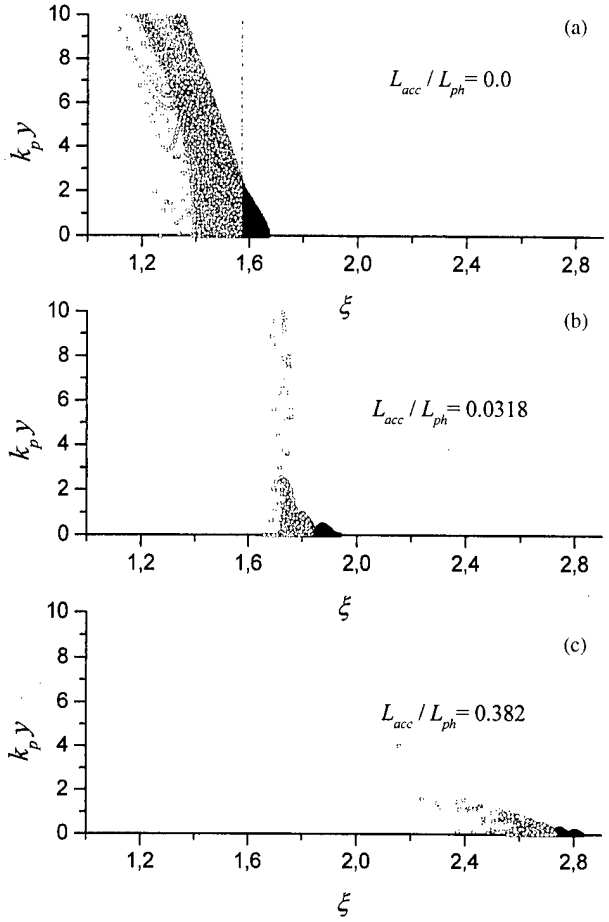


Fig. 4. Bunch separation and acceleration in the wakefield potential (9) with the amplitude $|e|\phi_0/mc^2 = 0.3, k_pR_p = 3.0$ and $\gamma = 50$. Snapshots at $L_{acc}/L_{ph} = 0.0; 0.0318$ and 0.382, respectively, demonstrate the bunch "cleanout" from the electrons located in the defocusing phase after the bunching stage. The initial parameters of the electron beam are the same as in Fig. 3 ($E_{inj}/mc^2 = 20, R_b = 1.6k_p^{-1}$).

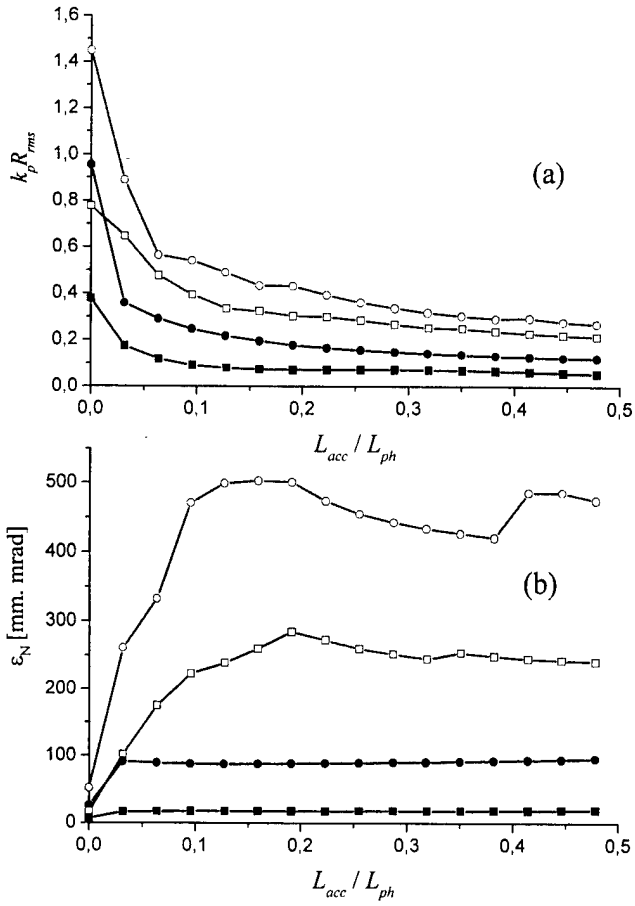


Fig. 5. Root-mean-square bunch radius R_{rms} (a) and normalized emittance ε_N (b) in relation to accelerating length for $R_b = 1.6k_p^{-1} > R_{max}$—circles and $R_b = 0.5k_p^{-1} < R_{max}$—squares. Solid circles and squares depict the electrons from focusing phase (compressed part of the bunch), and open figures depict all electrons with $r < R_p = 3k_p^{-1}$. The wakefield and initial beam parameters are the same as in Fig. 4.

compression by focusing forces (see below the example for $R_b = 0.5k_p^{-1}$).

IV. Wakefield Acceleration of Trapped Compressed Electron Bunches

After the trapping, the compressed electron bunch has a near-resonant energy $E \cong \gamma mc^2$ and can be effectively accelerated in a high amplitude plasma wave (in the next accelerating stage if a small amplitude wakefield was used at the bunching stage, or in the same wakefield for small enough energies of injected electrons; see previous section). Fig. 4 illustrates (in the plane cross section (y, ξ) obtained by 3-D numerical modeling) the bunch separation and acceleration in the wakefield potential (9) with the amplitude $|e|\phi_0/mc^2 = 0.3, k_pR_p = 3.0$, and $\gamma = 50$. The initial parameters of the electron beam were the same as in Fig. 3 ($E_{inj}/mc^2 = 20, R_b = 1.6k_p^{-1}$). The initial phase location of the bunch in Fig. 4(a) corresponds to that at the instant the bunch was trapped in the bunching stage (it means that the compressed bunch was injected into the accelerating stage just at the beginning of the focusing phase marked by the dashed line at $\xi = \xi_{foc} = \pi/2$). Fig. 4(b) and (c) at $L_{acc}/L_{ph} = 0.0318$ and $L_{acc}/L_{ph} = 0.382$, respectively, demonstrate the bunch "cleanout" from the electrons located in the defocusing phase just after the bunching stage.

For the initial beam radius smaller than the maximal trapping radius (20), the process of bunch separation and acceleration is much like the previous one described in Fig. 4. The main difference is reflected by the substantial reduction of the bunch emittance due to a decrease of the root-mean-square bunch radius (R_{rms}) during the processes of compression and acceleration, as is shown in Fig. 5 for $R_b = 1.6k_p^{-1} > R_{max}$ and $R_b = 0.5k_p^{-1} < R_{max}$. A decrease in the initial beam radius to $R_b = 0.5k_p^{-1}$ also leads to an enhancement of the averaged electron density of the compressed bunch up to 15 times, compared with the initial beam density, in the bunching stage and up to 7×10^2 times at the accelerating stage [see Fig. 5(a)].

Fig. 6 shows the maximum electron energy and the energy spread of compressed bunches of different initial radius in relation to the length of acceleration L_{acc} normalized to the dephasing length. The initial energy spread due to the prebunching stage [at $L_{acc} = 0$ in Fig. 6(b), solid circles and squares] can be closely approximated by (16) for electrons trapped in the focusing phase. Note that the initial length of the trapped beam

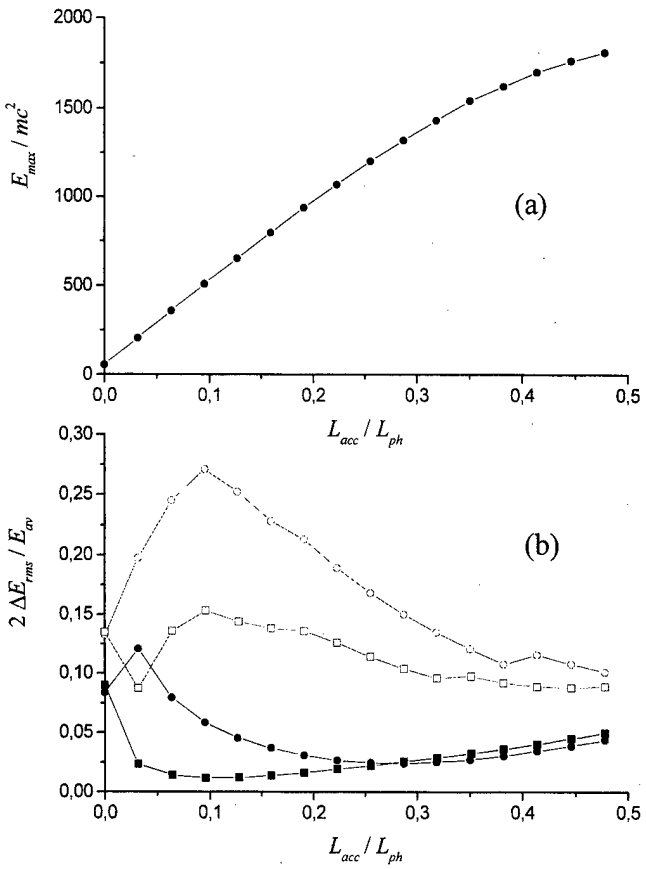


Fig. 6. Maximum electron energy and normalized energy spread of compressed bunches of different initial radius in relation to the length of acceleration $L_{\rm acc}$ normalized to the dephasing length. Notations and parameters are the same as in Fig. 5.

$L_{b0} \cong 0.9k_p^{-1}$ in accord with Fig. 3 and (19), and that the maximal energy spread, evaluated by (16), is equal to $2\sqrt{3}\Delta E_{\rm rms}$ for uniform energy distribution in the bunch. For the initial beam radius smaller than the maximal one (20), the increase in energy spread due to the bunch acceleration can be again closely approximated by 1-D theory using (8) and (10), as indicated by Fig. 6(b) [see solid-square line at $L_{\rm acc} > 0.1L_{ph}$ and take into account that the bunch length after compression, at the beginning of acceleration stage, $L_{b0} \cong 0.1k_p^{-1}$ in accord with Fig. 3 and (13)].

It is worth noting that fully 1-D numerical modeling of the beam compression and bunch acceleration (with the same parameters as in Figs. 3 and 4, except $R_b = 0$) has led to a practically identical dependence of energy spread on the accelerating length with Fig. 6(b) (solid-square line). It means that for initial electron beam radius smaller than $R_{\rm max}$ (20), the energy spread due to bunch compression and acceleration is determined mainly by the longitudinal electron motion in an inhomogeneous wakefield and that this spread (along with the bunch length) can be evaluated by using simple analytical predictions of 1-D theory presented above.

Note also that 1-D modeling of the bunch compression and acceleration with the injection electron energy $E_{\rm inj}/mc^2 \cong 2$ (and, consequently, with the wakefield amplitude $|e|\phi_0/mc^2 = 0.3$ for both bunching and acceleration stages) has led to the same energy spread as shown in Fig. 6(b) (solid-square line), except a small vicinity of $L_{\rm acc} = 0$. In this vicinity (at the beginning of acceleration stage, $L_{\rm acc} \ll L_{ph}$), the energy spread is determined by the spread due to the bunch compression and, in accordance with (16), falls with decreasing injection energy.

V. Conclusion

The dynamics of main characteristics of electron bunches accelerated in a wake plasma wave was investigated analytically and confirmed by 3-D numerical modeling. It is shown that using the prebunching stage, under proper conditions, the final electron density of the compressed and accelerated bunch can exceed the initial electron beam density in orders of magnitude. The simple estimation of the maximal radius $R_{\rm max}$ (20) of the electron beam that can be effectively trapped and compressed in the focusing phase of the wakefield is found. It is demonstrated that for initial electron beam radius smaller than $R_{\rm max}$, the energy spread of the compressed and accelerated electron bunch and its length can be evaluated by using simple analytical predictions of presented 1-D theory. The effect of longitudinal compression of finite-size electron bunches and 3-D bunching of lengthy electron beams provides quasi-monoenergetic acceleration to high energies.

Acknowledgment

The first author acknowledges useful discussions with all the participants at the Kardamyli Workshop. In addition, particular thanks go to T. Katsouleas, L. Serafini, and D. Umstadter.

References

[1] E. Esarey, P. Sprangle, J. Krall, and A. Ting, "Overview of plasma-based accelerator concepts," *IEEE Trans. Plasma Sci.*, vol. 24, pp. 252–288, 1996.

[2] N. E. Andreev and L. M. Gorbunov, "Laser-plasma acceleration of electrons," *Physics-Uspekhi*, vol. 42, pp. 49–53, 1999.

[3] A. Ogata, K. Nakajima, T. Kozawa, and Y. Yoshida, "Femtosecond single-bunched linac for pulse radiolysis based on laser wakefield acceleration," *IEEE Trans. Plasma Sci.*, vol. 24, pp. 453–459, 1996.

[4] N. E. Andreev, L. M. Gorbunov, and S. V. Kuznetsov, "Acceleration of a relativistic electron bunch in linear and nonlinear plasma waves," *Plasma Phys. Rep.*, vol. 21, pp. 1037–1041, 1995.

[5] N. E. Andreev and S. V. Kuznetsov, "Acceleration of electron beams in finite-amplitude wake waves," *Plasma Phys. Rep.*, vol. 25, pp. 746–752, 1999.

[6] T. Katsouleas, "Physical mechanism in the plasma wake-field accelerators," *Phys. Rev. A*, vol. 33, pp. 4412–4414, 1986.

[7] T. Katsouleas, C. E. Clayton, L. Serafini, C. Pelegrini, C. Joshi, J. Dawson, and P. Castellano, "A plasma klystron for generating ultra-short electron bunches," *IEEE Trans. Plasma Sci.*, vol. 24, pp. 443–447, 1996.

[8] A. Ogata, K. Nakajima, and N. Andreev, "Production of femtosecond single-bunched electrons by laser wakefield acceleration," *J. Nuclear Mater.*, vol. 248, pp. 392–399, 1997.

[9] N. E. Andreev and S. V. Kuznetsov, "Bunching effect by electron acceleration in a wake plasma wave," *Bull. Lebedev Phys. Inst. (RAS)*, no. 1, pp. 9–17, 1999. Translated from *Kratkie Soobshcheniya po Fizike*.

[10] N. E. Andreev, A. A. Frolov, S. V. Kuznetsov, E. V. Chizhonkov, and L. M. Gorbunov, "The laser wakefield electron acceleration in homogeneous plasma and plasma channels," in *Proc. Int. Conf. LASERS'97*, J. J. Carroll and T. A. Goldman, Eds. New Orleans, LA, Dec. 15–19, 1997, pp. 875–881. McLean, VA: STS Press, 1998.

[11] N. E. Andreev, L. M. Gorbunov, V. I. Kirsanov, K. Nakajima, and A. Ogata, "Structure of the wakefield in plasma channels," *Phys. Plasmas*, vol. 4, pp. 1145–1153, 1997.

[12] N. E. Andreev, E. V. Chizhonkov, A. A. Frolov, and L. M. Gorbunov, "On the laser wakefield acceleration in plasma channels," *Nucl. Instrum. Methods Phys. Res. A*, vol. 410, pp. 469–476, 1998.
[13] N. E. Andreev and S. V. Kuznetsov, "Dynamics of electron bunches accelerated in plasma wake waves," Plasma Phys. Rep., to be published.
[14] S. Vilks, T. Katsouleas, J. Dawson, P. Chen, and J. Su, "Beam loading in plasma waves," *IEEE Trans. Plasma Sci.*, vol. PS-15, pp. 210–217, 1987.
[15] N. E. Andreev, S. V. Kuznetsov, and I. V. Pogorelsky, "Monoenergetic laser wakefield acceleration," *Phys. Rev. Special Topics—Accelerators and Beams*, vol. 3, p. 21301, 2000.
[16] I. V. Pogorelsky, W. D. Kimura, D. C. Quimby, N. E. Andreev, and S. V. Kuznetsov, "Experimental approach to laser-driven monochromatic electron acceleration," in *Proc. SPIE ICONO'98: Ultrafast Phenomena and Interaction of Superstrong Laser Fields with Matter: Nonlinear Optics and High-Field Physics*, vol. 3735, M. V. Fedorov and V. M. Gordienko, Eds., 1999, pp. 175–186.
[17] T. Katsouleas and L. Serafini, "Working group summaries," in *Int. Workshop 2nd Generation Laser and Plasma Accelerators*, Kardamyli, Greece, June 27–July 2 1999.
[18] N. E. Andreev, L. M. Gorbunov, and S. V. Kuznetsov, "Energy spectra of electrons in plasma accelerators," *IEEE Trans. Plasma Sci.*, vol. 24, pp. 448–452, 1996.
[19] N. E. Andreev, E. V. Chizhonkov, A. A. Frolov, and L. M. Gorbunov, "On the laser wakefield acceleration in plasma channels," *Plasma Phys. Rep.*, vol. 24, pp. 825–831, 1998.
[20] I. V. Pogorelsky, N. E. Andreev, and S. V. Kuznetsov, "Monochromatic laser wakefield acceleration," in *Proc. Int. Conf. LASERS'98*, J. J. Carroll and T. A. Goldman, Eds. Tucson, AZ, Dec. 7–11, 1998, pp. 898–905. McLean VA: STS Press, 1999.
[21] I. V. Pogorelsky, N. E. Andreev, and S. V. Kuznetsov, "Practical approach to monochromatic LWFA," in *Proc. AIP Conf. 8th Workshop on Advanced Accelerator Concepts*, vol. 472, Baltimore, MD, July 6–10, 1998, 1999, p. 444.



Nikolai E. Andreev was born in Moscow, Russia, in 1945 and graduated from Moscow State University in 1967. He received the Ph.D. degree and Doctor of science degree in theoretical and mathematical physics from P.N. Lebedev Physical Institute of USSR Academy of Sciences, Moscow, in 1973 and 1985, respectively, and the rank of Professor from Russian Ministry of Education in 1998.

Since 1970, he has been a Research Physicist in the Division of Plasma Phenomena Theory of P.N. Lebedev Physical Institute of the Russian Academy of Sciences (RAS). He joined the High Energy Density Research Center of the Associated Institute for High Temperatures of RAS in 1987, where he is currently a Head of the Laser Plasma Laboratory; he is also a Professor at the Moscow Institute of Physics and Technology. His current research includes laser light absorption, self-focusing and stimulated scattering, laser-driven particle accelerators, and nonlinear self-consistent structures in irradiated plasmas.

Sergey V. Kuznetsov was born in Berlin, Germany, in 1948, and graduated from the Moscow Institute of Physics and Technology, Moscow, Russia, in 1972. He received the Ph.D. degree in theoretical and mathematical physics from P.N. Lebedev Physical Institute of USSR Academy of Sciences, Moscow, in 1987.

Since 1989, he has been a Staff Member of the Institute for High Temperatures. He joined the High Energy Density Research Center of the Associated Institute for High Temperatures of RAS in 1993. His main research includes interaction of strong electromagnetic waves with plasma, solitons, and nonlinear surface waves as well as laser-driven particle accelerators and nonlinear self-consistent structures in ionizing gases.

Ion Acceleration Regimes in Underdense Plasmas

Francesco Pegoraro, Sergei V. Bulanov, Francesco Califano, Timur Zh. Esirkepov, Tatiana V. Lisejkina, Natalia M. Naumova, Hartmut Ruhl, and Vitali A. Vshivkov

***Abstract*—Acceleration of large populations of ions up to high (relativistic) energies may represent one of the most important and interesting tools that can be provided by the interaction of petawatt laser pulses with matter. In this paper, the basic mechanisms of ion acceleration by short laser pulses are studied in underdense plasmas. The ion acceleration does not originate directly from the pulse fields, but it is mediated by the electrons in the form of electrostatic fields originating from channeling, double layer formation, and Coulomb explosion.**

***Index Terms*—Coulomb explosion, ion acceleration, particle-in-cell simulation, relativistic plasmas, ultraintense laser pulses.**

I. Introduction

PARTICLE acceleration by an ultraintense laser pulse interacting with a plasma is a fundamental theoretical subject with practical applications to inertial confinement fusion [1], nonlinear optics of relativistic plasmas [2], laser-induced nuclear reactions [3], [25], ion injection into conventional accelerators, hadrontherapy in medicine [4], and, for extreme accelerations, to the testing of Unruh radiation [5]. In addition, the presence of fast electrons and ions and their angular distribution can be used to identify various mechanisms occurring in the laser–plasma dynamics, such as wavebreak, self-focusing, filamentation and channel formation, magnetic field generation, soliton propagation, and so on.

The conversion of the laser energy into intense relativistic electron beams by ultrahigh electric fields can be achieved, for example, during the breaking of the wake plasma waves [6], [7]. The breaking and the particle acceleration can occur either in the direction of the laser pulse or in the transverse plane [8]. The formation of these electron beams and their dynamics depend on the complex nonlinear interplay of various additional plasma processes, such as relativistic pulse self-focusing [9]–[11], hosing [12], [26], self-modulation [13], [27], [28] channeling and magnetic field generation [14], [29]–[31]. For present day ultraintense laser pulses, typical electron energies are of the order of 100 Mev or more [15], [32], [33].

Manuscript received October 29, 1999; revised March 15, 2000.

F. Pegoraro is with the Dipartimento Fisica, Università di Pisa, Italy, and with the Istituto Nazionale Fisica della Materia, 56126 Pisa, Italy.

S. V. Bulanov and N. M. Naumova are with the General Physics Institute, RAS, Moscow, Russia.

F. Califano is with the Istituto Nazionale Fisica della Materia, 56126 Pisa, Italy.

T. Zh. Esirkepov is with the Moscow Institute of Physics and Technology, Dolgoprudnyi, Russia.

T. V. Lisejkina and V. A. Vshivkov are with the Institute of Computational Technologies of SD-RAS, Novosibirsk, Russia.

H. Ruhl is with the Theoretical Quantum Electronics, Darmstad, Germany.

Publisher Item Identifier S 0093-3813(00)09723-X.

Due to the strong difference between the ion and the electron mass, ion acceleration mechanisms are different from those effective on electrons and require more intense laser pulses. Indeed, when a laser pulse interacts with an underdense plasma, ions are usually assumed to be immovable, if the laser pulse is sufficiently short. When ion motion is important, as is the case of hole drilling in an overdense plasma, the ion energy is not considered to be relativistic. Plasma electrons become relativistic in the field of a laser pulse when the pulse dimensionless amplitude becomes of order one

$$a_e = \frac{eE}{m_e \omega c} \approx 1 \tag{1}$$

where E is the dimensional amplitude of the pulse electric field and ω is its carrier frequency. For the ions to become relativistic through the same mechanism, laser pulses would be required with a dimensionless amplitude calculated with the ion mass of order one, $a_i = eE/(m_i \omega c) \approx 1$. For a 1-$\mu$m laser pulse in a hydrogen plasma, such an amplitude would correspond to a pulse intensity $\approx 7 \times 10^{24}$ W/cm^2 that is well above the typical values of the most powerful present day (petawatt) lasers. However, in a plasma, the ion acceleration is mediated by the plasma electrons in such a way that ions become relativistic for values of the "hybrid" dimensionless amplitude

$$a_h \equiv \frac{eE}{\sqrt{m_e m_i}\omega c} \equiv \sqrt{\frac{m_e}{m_i}}\, a_e \tag{2}$$

of order one [16]–[19]. These values correspond to more moderate intensities $\approx 1.6 \times 10^{21}$ W/cm^2, i.e., to laser pulse powers in the petawatt range. The "hybrid" dimensionless amplitude in (2) is defined by the condition that an electron interacting with a plane electromagnetic wave of such intensity acquires an energy equal to the ion rest mass $\mathcal{E}_e = m_e c^2 a_e^2/2 = m_i c^2 a_h^2/2$ [20], [34] and can thus accelerate ions effectively.

When a laser pulse with a_e significantly larger than one interacts with an underdense plasma, the plasma dynamics is strongly nonlinear and the pulse self-focuses and filaments into channels that are partly evacuated by the electrons under the action of the ponderomotive force. Then, due to the electrostatic fields induced by the expelled electrons, the ions are accelerated in the radial direction. This mechanism is known as the "Coulomb explosion" [16], [21], [35]–[38] and can accelerate ions to large energies in the millielectronvolt range.

A similar mechanism also occurs in the direction of the pulse propagation. Under quasi-stationary conditions in the pulse frame, a short wide pulse (or a pulse with a steep leading edge) would produce a plasma wake wave with amplitude $\varphi = \mathcal{E}_e/e$, where φ is the electrostatic potential and $\mathcal{E}_e = m_e c^2 a_e^2/2$ is the electron energy. For $a_h \approx 2$, ions would become relativistic (ion energy $\approx m_i c^2$) during half a period of the wake wave.

0093–3813/00$10.00 © 2000 IEEE

Actually, for such large amplitudes, at the front of the pulse a double polarity region forms [16]–[18] with an electrostatic potential of the order of $m_i c^2$. This potential corresponds to an electrostatic double layer that propagates together with the laser pulse and accelerates both electrons and ions.

A very effective additional mechanism of ion acceleration in the pulse direction occurs when the laser pulse leaves the plasma. This mechanism is due to the fast expansion of electrons in vacuum and is observed in a plasma slab when the electrons can freely expand into the vacuum region [16] after the laser pulse has drilled a hole through the plasma slab.

In this paper, we present and discuss the results of large particle-in-cell (PIC) numerical simulations of laser–plasma interaction in the petawatt regime with planar slabs of (marginally) underdense plasma and focus our attention on the ion acceleration process. In this connection, it has been shown recently in [17] and [19] that ion acceleration and focusing can be improved by considering properly predeformed plasma slabs. This curved geometry case will not be addressed here. In addition, we will not discuss a related ion acceleration process that occurs in the Coulomb explosion of small material clusters, studied in [22] and [39], or in the explosion of a small region on the surface of an overdense plasma slab when the ponderomotive pressure of the laser pulse blows all of the electrons away from a finite diameter spot [16].

II. Numerical Results

In order to study the basic acceleration mechanisms in the petawatt regime, we have performed a number of two-dimensional (2-D) and and three-dimensional (3-D) fully relativistic PIC numerical simulations for (marginally) underdense plasma slabs. Here, we present three cases: a longer, 150λ, less-dense, $\omega/\omega_p = 0.45$, 2-D slab and two denser, $\omega/\omega_p = 1$, but shorter (30λ) 2-D and (15λ) 3-D slabs. Here, ω_p is the nonrelativistic unperturbed plasma frequency and the mass ratio corresponds to a hydrogen plasma. In all three cases, the pulse is circularly polarized and its amplitude is $a_e \simeq 50$, slightly larger than the square root of the mass ratio, the pulse length is 20λ, and its width is 10λ. In all of these runs, we use eight cells per λ in each direction. In the 2-D runs (Figs. 1 and 2), 16 particles per species per cell are used. This corresponds to a total number of particles per species of order $\sim$16 millions for the longer slab (Fig. 1) and $\sim$6 millions for the shorter slab (Fig. 2). In the 3-D run (Fig. 5), eight particles per species per cell are used (the total number per species is $\sim$18.5 millions).

Both in 2-D and in 3-D a few basic processes can be identified in the numerical simulations, as follows:

1) Formation of a partly evacuated channel along the pulse path and the corresponding transverse ion acceleration;
2) Formation of lateral channels where the dimensionless amplitude of the electromagnetic fields is still relativistic, even if much smaller than the square root of the mass ratio;
3) Formation of density filaments in the plasma channel due to "return" particles from the walls and from the front of the plasma channel;
4) Ion acceleration inside the partly evacuated channel to quasi-relativistic energies;

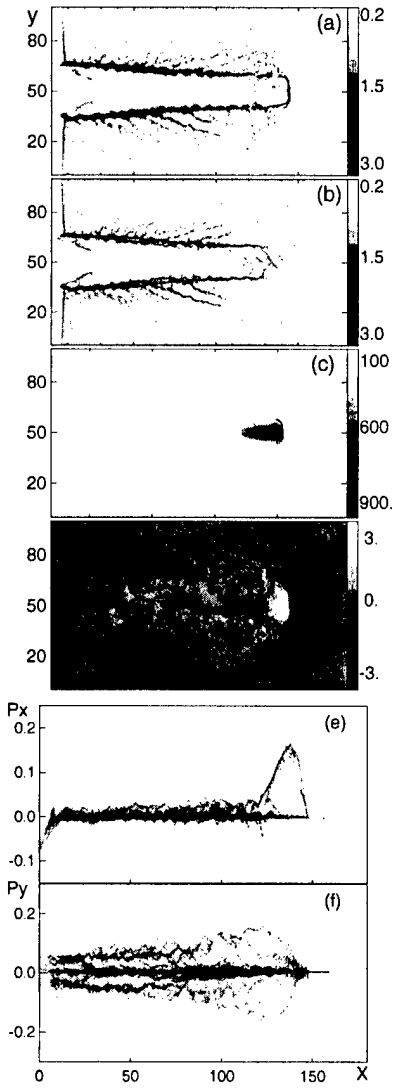


Fig. 1. The x–y-distribution of the (a) electron and (b) ion densities, the (c) electromagnetic energy density, the (d) x-component of the electric field, and the (e) ion phase spaces (P_x, x) and (f) (P_y, x) at $t = 170\ (2\pi/\omega)$ in the case of the pulse propagating in the longer 2-D plasma slab. The momentum of the ions is normalized on $m_i c$.

5) Electron expansion at the end of the slab and the resulting, very effective ion acceleration up to relativistic energies outside of the plasma slab;
6) Formation of strong quasi-static magnetic fields inside the channel and in the region where the electrons expand;
7) Formation of localized electromagnetic energy concentrations that correspond to the sub-cycle solitons recently identified in 2-D simulations in underdense plasmas [23], [40].

All of these features are in good qualitative and quantitative agreement (after appropriate rescaling of the pulse amplitude) with the results presented in [16], where a reduced value of the ion electron mass ratio was used.

A. Channel Formation and Transverse Ion Acceleration

The density channel in the longer plasma slab is shown in Fig. 1 at $t = 170\ (2\pi/\omega)$, just as the pulse is boring its way

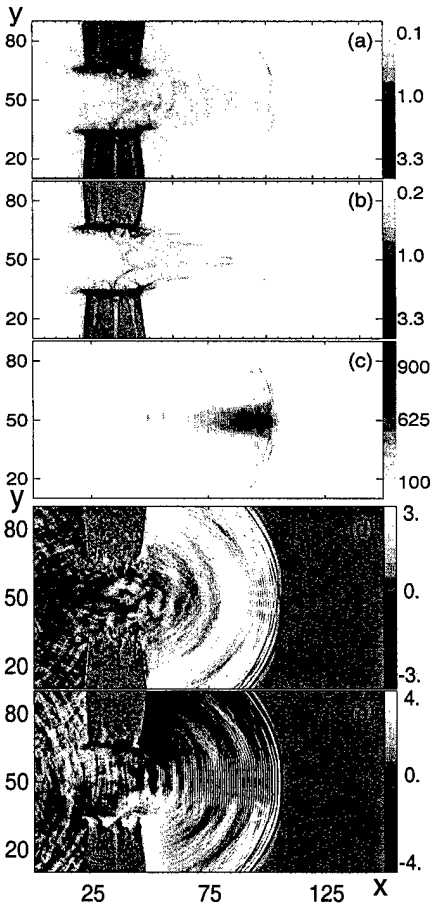


Fig. 2. The x–y-distribution of the (a) electron and (b) ion densities, the (c) electromagnetic energy density, the (d) x-component of the electric field, and the (e) z-component of the magnetic field in the case of the pulse propagating in the shorter denser 2-D plasma slab.

out of the plasma. Fig. 1(a) gives the electron density distribution in the x–y-plane, and (b) gives the ion distribution. Fig. 1(c) gives the electromagnetic energy distribution. The channel has been formed due to relativistic self-focusing of the laser pulse. Electrons are expelled first, by the pulse ponderomotive force of the front part of the pulse, both in the transverse direction and toward the front. Then, ions follow and are displaced mainly in the transverse direction. The transverse displacement of ions and electrons maintains approximate quasi-neutrality. The electron density channel is less sharp than is the ion channel due to electron vacuum heating at the walls. The walls of both the ion and the electron density channel are modulated with a periodicity length that is longer than is the laser wavelength and shorter than is the wavelength $\lambda_w = \sqrt{2}\mu/a_e$ of the longitudinal wake electric field in a one-dimensional (1-D) configuration [18] for $a_e > \sqrt{m_i/m_e}$. In the front of the channel, these modulations are well correlated with a (skew-symmetric) filamentary blob structure inside the channel that is evident mainly in the ion density. Further back in the channel, strong lateral spikes appear both in the electron and in the ion density distributions with a characteristic spatial scale close to that of the wall modulation. This change in the structure of the channel is parallelled by a change in the structure in the ion phase space in the transverse direction. In Fig. 1(f), the transverse momentum distribution of the ions (normalized on $m_i c$) integrated over y is plotted versus x. In the region where the lateral density spikes occur, strong modulations of the transverse ion momentum distribution are seen, well correlated to the modulation of the channel walls. The electromagnetic fields inside the lateral density spikes are strongly inhomogeneous with amplitudes comparable to the amplitudes of the fields inside the main channel after the laser pulse has passed. These amplitudes are much smaller than is the laser–pulse amplitude ($a_e \approx 2$ inside the well-recognizable spike located in the lower part of Fig. 1(a) and (b) for $60\lambda < x < 100\lambda$). The "older" density spikes on the left of the frames have produced isolated blobs of electromagnetic energy, correlated to holes in the density. These blobs have very low propagation velocity. The electromagnetic fields inside the cavities in Fig. 1 are relatively small $a_e \approx 0.1$. They oscillate with frequency smaller than the plasma frequency of the surrounding plasma. These electromagnetic structures can be identified as subcycle solitons, of the type described in [23] and [40], and they originate from the depletion of the electromagnetic energy channeled inside the lateral spikes. Both the wall modulations and the spikes form at an early stage of the pulse propagation inside the slab. They are expected to result from an instability occurring as the channel walls expand laterally. The phase space of the ions shows a strong localized acceleration along x, Fig. 1(e), occurring in the front region of the pulse. This acceleration is caused by the electrostatic double layer structure originating from the charge separation produced by the faster response of the electrons to the ponderomotive force of the pulse in the x-direction. The electric field component along x corresponding to this double layer is shown in Fig. 1(d). It has a characteristic scale-length consistent with the estimate $\lambda_w = \sqrt{2}\mu/a_e$ given above for the wavelength of the wake wave and can accelerate both ions (in the region where it is positive) and electrons in the region where it is negative [black region in Fig. 1(d) behind the white, positive, region]. The ion momentum along x is large, $P_x \approx 0.15$, at the position of the positive part of the double layer (which, at the time shown in Fig. 1, is at the point of leaving the plasma slab) and is much smaller at the back (the negative part of the double layer slows the ions). The electron momentum distribution along x (not shown here, but essentially analogous to the case reported in [16] in the case of a reduced mass ratio) is more evenly distributed along x, as there is no effective field that can decelerate the electrons at the back of the double layer. The ion momentum distribution along y has a structure that is not correlated to the position of the double layer and exhibits a two-mode distribution. The one at the back corresponds to the wall modulation and to the lateral density spikes discussed above. The second, at the front, corresponds to a more regular lateral expansion of the front part of the channel under the action of the laser pulse and of the lateral electric field opposing charge separation. In the front part of the pulse, filaments are formed close to the channel axis both in the electron and in the ion density. The formation of such filaments has been discussed in [17] and attributed to an "inverted corona" mechanism [24] in which particles are extracted from the walls and from the front of the pulse and are focalized at the center of the channel by the quasi-static magnetic field that is generated by the plasma currents inside the channel. These filaments, and the electric current associated

to them are also important for the self-consistent sustainment of the magnetic field that, in turn, contributes to the localization of the filaments.

B. Ion Acceleration in the Electron Cloud

From the simulation results in the long plasma slab, we have obtained high ion energies that are however smaller than the ion rest mass and correspond to regimes where ions are not yet fully relativistic. Higher ion energies are obtained in the later phase of the laser–plasma interaction, when the pulse leaves the plasma slab and a population of electrons starts expanding in vacuum from the hole drilled in the plasma. As these electrons expand, they drag the preaccelerated ions into the vacuum region and accelerate them further to relativistic energies (anisotropic Coulomb explosion).

In order to analyze this later phase of the laser–plasma interaction better in 2-D configurations, we have considered a shorter (30λ) but denser plasma slab to be able to follow numerically the ion acceleration in vacuum for a longer time interval.

The formation of the density channel in the shorter 2-D plasma slab is shown in Fig. 2 at $t = 100\ (2\pi/\omega)$ after the pulse has gone through the plasma slab and the electrons have expanded in vacuum. The plasma dynamics in the shorter, denser slab is analogous to (although faster) that of the longer slab. A channel is drilled both in the electron and in the ion density distributions [Fig. 1(a) and (b)]. Lateral spikes are also formed, although in this denser, faster evolving case they are formed at an angle almost perpendicular to the direction of propagation of the laser pulse, similarly to the first spikes at the left of Fig. 1(a) and (b) in the case of the longer slab. The plasma slab is compressed both at its front, by the laser pulse, and at its back by the pressure exerted by the magnetic force on the induction surface currents that are exited as the electrons start expanding in vacuum. In Fig. 3, (a) and (c) give the ion phase spaces (P_x, x) and (P_y, x) and (b) and (d) give the corresponding electron phase spaces. The ion energies inside the channel are nonrelativistic, whereas electrons (as in the long slab case) are ultrarelativistic.

The electron expansion in vacuum is shown in Fig. 2(a). A few electrons are still propagating with the laser pulse [see (c), where the electromagnetic energy density is shown] and have been accelerated to energies approaching 3×10^3 times their rest mass. These energy values [Fig. 3(a)] are larger than is the quiver energy $m_e c^2 a^2/2$ of an electron in vacuum in the field of the laser pulse (not including, however, the increase of the laser pulse amplitude due to self-focusing) and corresponds to electrons "heavier" than ions. The main part of the expanding electron cloud lags behind the pulse and has smaller energy values, of the order of 10^3 times their rest mass. The spatial distribution of this cloud roughly coincides with that of the ions dragged by the electrostatic force due to charge separation. The characteristic values of the electron and ion densities in this cloud are $n_e \approx n_i \approx 0.3 \div 0.2$. The ions are accelerated to relativistic energies and are very collimated in velocity space in the x-direction, as shown in Fig. 3(b). The faster linear increase of the longitudinal momentum P_x of the ions as a function of x can be accounted for by assuming that the electric field in vacuum decreases with time as more ions are extracted from the channel,

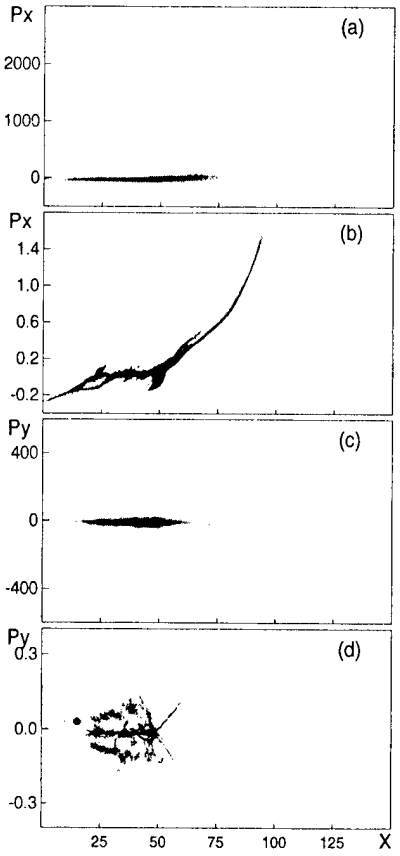


Fig. 3. The (a) electron and (b) ion phase space (P_x, x) and the (c) electron and (d) ion phase space (P_y, x) at $t = 100\ (2\pi/\omega)$ in the case of the pulse propagating in the shorter denser 2-D plasma slab. The momentum of the electrons (ions) is normalized on $m_e c$ $(m_i c)$.

leading to a reduced charge separation. Thus, the first ions to escape from the channel see a stronger electric field along their trajectories and are accelerated more efficiently than are the ions behind. Both electrons and ions have a fan-like distribution of the transverse momentum in the region where the expansion in vacuum occurs, as shown in Fig. 3(c) and (d). The electron fan is wider, as is consistent with the density distributions that show a stronger lateral spreading of electrons with respect to ions. The dependence of P_y of the ions on x, as determined by the sides of the fan, is approximately linear. This dependence, combined with the behavior of P_x, means that faster ions are better collimated in the forward direction (anisotropic Coulomb expansion). Magnetic pinching can contribute to the ion focalization [17]. Indeed, at the front of the ion cloud, a very well-collimated narrow beam can be seen. Its density, $n_i \approx 0.6$, is higher than the surrounding cloud density, and it originates from the filaments that were initially formed at the channel axis before the pulse drilled through the slab, as discussed in the case of the longer plasma slab.

The accelerating electric field along x is shown in Fig. 2(d). The white regions are the regions where ions are accelerated. The z-component of the magnetic field is shown in Fig. 2(e). Aside from the oscillating field related to the (circularly polarized) pulse, we see two almost isotropic regions with opposite polarity. These regions are well correlated to the E_x-distribution and to the spatial region that has been reached by the electron

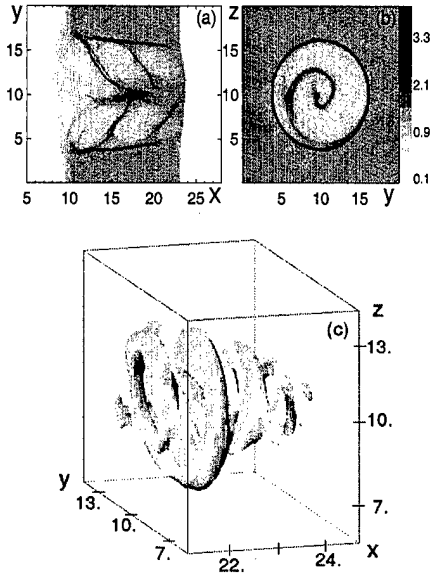


Fig. 4. The (a) x–y-distribution at $z = 0$, the (b) y–z-distribution of the ion density at $x = 15\lambda$, and the (c) isosurface $\sqrt{(E^2 + B^2)/2} = 40$ of the electromagnetic energy density in the case of the pulse propagating in the 3-D plasma slab.

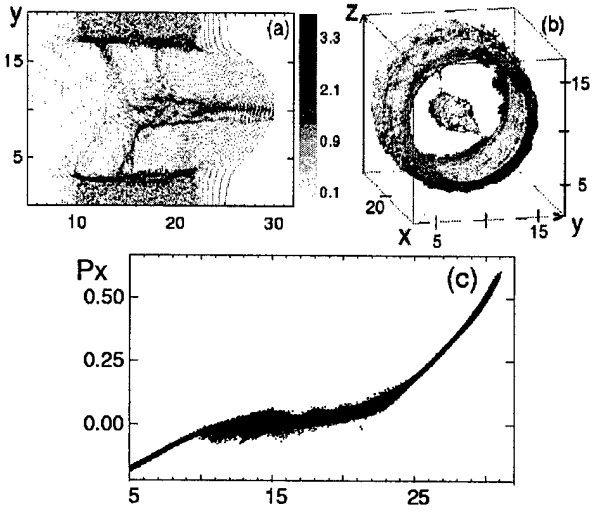


Fig. 5. The (a) x–y-distribution at $z = 0$, the (b) isosurface $n_i = 1.8$ of the ion density at $t = 48\ (2\pi/\omega)$, and the (c) ion phase space (P_x, x) in the case of the pulse propagating in the 3-D plasma slab.

cloud. Close to the mouth of the channel, this magnetic field is very intense, $|B| \approx 4$ in dimensionless units. The polarity in the vacuum region corresponds to a current distribution where electron are pushed outward along the x-axis (negative current), with a return (positive) current along the slab walls. As the magnetic field is expanding and, therefore, decreasing in time at a fixed position inside the plasma cloud, an inductive electric field is produced that contributes to the ion acceleration. This mechanism has been discussed in [17] and shown to give a contribution of the order of the electrostatic field.

C. 3-D Ion Acceleration

The electron expansion in a 2-D configuration can lead to an overestimate of the ion acceleration outside of the channel. This is due to the slower decrease with distance of the accelerating electrostatic field in two dimensions in comparison with the real 3-D case. Explicit estimates can be found in [17].

In order to evaluate the accelerated ion energy, we have run 3-D simulations using the same parameters of Figs. 2 and 3, but with a plasma slab 15λ long.

The formation of the channel in the ion density in the 3-D plasma slab is shown in Fig. 4 at $t = 30\ (2\pi/\omega)$ projected on the horizontal x–y-plane at $z = 0$ [Fig. 4(a)] and on the transverse y–z-plane at $x = 15\lambda$ [Fig. 4(b)]. The circularly polarized pulse has carved a staircase structure that resembles the helical chamber inside a shell. This structure is the 3-D counterpart of the skew-symmetric filamentary structure of Fig. 1(b). A similar helix, although less sharp, is also seen in the electron density (not shown here) and in Fig. 4(c), where the isosurface of the electromagnetic energy density corresponding to the amplitude value $\sqrt{(E^2 + B^2)/2} = 40$ is shown. The expansion and acceleration of the ions in the vacuum region, following the electron expansion when the pulse has drilled a hole through the slab, is shown in Fig. 5 at $t = 48\ (2\pi/\omega)$. The x–y-section at $z = 0$ of the ion density distribution shows a strongly collimated beam along the x-axis [Fig. 5(a)]. This beam collimation is also seen in the 3-D plot [Fig. 5(b)], where the isosurface corresponding to $n_i = 1.8$ is shown. We see that the beam collimation is stronger than in the corresponding 2-D simulations. As expected, the ion acceleration is smaller in 3-D (maximum value of the ion longitudinal momentum at $t = 48\ (2\pi/\omega)$ is $P_x = 0.61$, to be compared with $P_x = 0.85$ in 2-D for the same time and for the same length of the plasma slab). The longitudinal ion momentum distribution at $t = 48\ (2\pi/\omega)$ is shown in Fig. 5(c). The decrease of the perpendicular momentum of the ions is more marked (from 0.3 in 2-D to 0.15 in 3-D) in agreement with the strong beam collimation noted above. There is also a similar reduction in the energy of the electrons expanding in vacuum: the maximum value of the longitudinal electron momentum is $\approx$1390 (to be compared with $\approx$1800 in the same conditions in 2-D), and the perpendicular momentum is $\approx$310 ($\approx$380 in 2-D).

III. Conclusion

We show that a laser pulse with dimensionless amplitude of the order of the square root of the mass ratio accelerates ions effectively even in an underdense plasma. Such high amplitudes correspond to petawatt laser pulses. The laser–plasma interaction is accompanied by a broad range of physical processes that include the formation of filaments inside the channel drilled by the pulse in the plasma slab and the creation of relativistic collimated ion beams in the expanding plasma cloud.

Three-dimensional simulations of the ion acceleration process are also presented. Due to memory limitations in these runs, we have adopted a shorter plasma slab and a shorter integration time. By comparison with the equivalent 2-D runs, the 3-D simulations have indicated a stronger focalization of the ion beam expanding in the vacuum region under the pull of the electron cloud. However, as expected from geometrical considerations, the increase of the ion momentum with the distance from the plasma slab is slower in 3-D than in 2-D and the maximum value of P_x is correspondingly smaller.

ACKNOWLEDGMENT

The authors are pleased to acknowledge the Cineca supercomputing center of Bologna and the Scuola Normale Superiore of Pisa for the use of their Cray T3E and Origin 2000, respectively. Part of the calculation were performed under an INFM research project at Cineca.

REFERENCES

[1] M. Tabak, J. Hammer, M. E. Glinsky, W. L. Kruer, S. C. Wilks, J. Woodworth, E. M. Campbell, M. D. Perry, and R. J. Mason, "Ignition and high gain with ultrapowerful lasers," *Phys. Plasmas*, vol. 1, pp. 1626–1634, 1994.

[2] W. B. Mori, "Physics of the nonlinear optics of plasmas at relativistic intensities for short-pulse lasers," *IEEE J. Quantum Electron.*, vol. 33, pp. 1942–1953, 1997.

[3] T. Ditmire *et al.*, "High energy ions produced in explosion of superheated atomic clusters," *Nature*, vol. 386, pp. 54–56, 1997.

[4] G. Arduini, R. Cambria, C. Canzi, F. Gerardi, B. Gottschalk, R. Leone, L. Sangaletti, and M. Silari, "Physical specifications of clinical proton beams from a synchrotron," *Med. Phys.*, vol. 23, pp. 939–951, 1996.

[5] P. Chen and T. Tajima, "Testing Unruh radiation with ultraintense lasers," *Phys. Rev. Lett.*, vol. 83, pp. 256–259, 1999.

[6] S. V. Bulanov, V. I. Kirsanov, and A. S. Sakharov, "Limiting electric field of the wakefield plasma wave," *JETP Lett.*, vol. 53, pp. 565–569, 1991.

[7] C. D. Decker, W. B. Mori, and T. Katsouleas, "Particle-in-cell simulations of Raman forward scattering from short-pulse high-intensity lasers," *Phys. Rev. E*, vol. 50, pp. R3338–R3341, 1994.

[8] S. V. Bulanov, F. Pegoraro, A. M. Pukhov, and A. S. Sakharov, "Transverse-wake wave breaking," *Phys. Rev. Lett.*, vol. 78, pp. 4205–4208, 1997.

[9] P. Sprangle, C.-M. Tang, and E. Esarey, "Relativistic self-focusing of short-pulse radiation beams in plasmas," *IEEE Trans. Plasma Sci.*, vol. PS-15, pp. 145–153, 1987.

[10] S. V. Bulanov, F. Pegoraro, and A. M. Pukhov, "Two-dimensional regimes of self-focusing, wake field generation, and induced focusing of a short intense laser pulse in an underdense plasma," *Phys. Rev. Lett.*, vol. 74, pp. 710–713, 1995.

[11] T. V. Liseikina, F. Califano, V. A. Vshivkov, F. Pegoraro, and S. V. Bulanov, "Small-scale electron density and magnetic-field structures in the wake of an ultraintense laser pulse," *Phys. Rev. E*, vol. 60, pp. 5991–5997, 1999.

[12] G. Shvets and J. S. Wurtele, "Instabilities of short-pulse laser propagation through plasma channels," *Phys. Rev. Lett.*, vol. 73, pp. 3540–3543, 1994.

[13] T. M. Antonsen and P. Mora, "Self-focusing and Raman scattering of laser pulses in tenuous plasmas," *Phys. Rev. Lett.*, vol. 69, pp. 2204–2207, 1992.

[14] D. W. Forslund, J. M. Kindel, W. B. Mori, C. Joshi, and J. M. Dawson, "Two-dimensional simulations of single-frequency and beat-wave laser–plasma heating," *Phys. Rev. Lett.*, vol. 54, pp. 558–561, 1985.

[15] M. Key *et al.*, "Hot electron production and heating by hot electrons in fast ignitor research," *Phys. Plasmas*, vol. 5, pp. 1966–1972, 1998.

[16] T. Zh. Esirkepov, Y. Sentoku, K. Mima, K. Nishihara, F. Califano, F. Pegoraro, N. M. Naumova, S. V. Bulanov, Y. Ueshima, T. V. Liseikina, V. A. Vshivkov, and Y. Kato, "Ion acceleration by superintense laser pulses in plasmas," *JETP Lett.*, vol. 70, pp. 82–89, 1999.

[17] Y. Sentoku, T. V. Liseikina, T. Zh. Esirkepov, F. Califano, N. M. Naumova, Y. Ueshima, V. A. Vshivkov, Y. Kato, K. Mima, K. Nishihara, F. Pegoraro, and S. V. Bulanov, "Fast ion acceleration by petawatt laser pulses in plasmas," *Phys. Rev. E*, vol. 62, Nov. 2000.

[18] S. V. Bulanov, F. Califano, G. I. Dudnikova, T. Zh. Esirkepov, F. F. Kamenets, T. V. Liseikina, N. M. Naumova, F. Pegoraro, and V. A. Vshivkov, "Interaction of petawatt laser pulses with underdense plasmas," *Plasma Phys. Rep.*, vol. 25, pp. 701–714, 1999.

[19] S. V. Bulanov, T. Zh. Esirkepov, F. Califano, Y. Kato, T. V. Lisefkina, K. Mima, N. M. Naumova, K. Nishihara, F. Pegoraro, H. Ruhl, Y. Sentoku, and Y. Ueshima, "Generation of collimated beams of relativistic ions in laser-plasma interactions," *JETP Lett.*, vol. 71, pp. 407–411, 2000.

[20] H. M. Lai, "Particle acceleration by an intense solitary electromagletic pulse," *Phys. Fluids*, vol. 23, pp. 2373–2375, 1980.

[21] N. H. Burnett and G. D. Enright, "Population inversion in the recombination of optically-ionized plasmas," *IEEE J. Quantum Electron.*, vol. 26, pp. 1797–1808, 1990.

[22] T. Ditmire, J. W. G. Tisch, E. Springate, M. B. Mason, N. Hay, J. P. Marangos, and M. H. R. Hutchinson, "High energy ion explosion of atomic clusters: Transition from molecular to plasma behavior," *Phys. Rev. Lett.*, vol. 78, pp. 2732–2735, 1997.

[23] S. V. Bulanov, T. Zh. Esirkepov, N. M. Naumova, F. Pegoraro, and V. A. Vshivkov, "Solitonlike electromagnetic waves behind a superintense laser pulse in a plasma," *Phys. Rev. Lett.*, vol. 82, pp. 3440–3443, 1999.

[24] G. A. Askar'yan, S. V. Bulanov, and I. V. Sokolov, "Production of a hot dense plasma by the focusing of plasma flows on the symmetry axis," *Plasma Phys. Rep.*, vol. 25, pp. 549–555, 1999.

[25] V. Yu. Bychenkov, V. T. Tikhonchuk, and S. V. Tolokonnikov, "Nuclear reactions triggered by laser-accelerated high-energy ions," *JETP*, vol. 88, pp. 1137–1142, 1999.

[26] P. Sprangle, J. Krall, and E. Esarey, "Hose-modulation instability of laser pulses in plasmas," *Phys. Rev. Lett.*, vol. 73, pp. 3544–3547, 1994.

[27] N. E. Andreev *et al.*, "Resonant excitation of wakefields by a laser pulse in a plasma," *JETP Lett.*, vol. 55, pp. 571–576, 1992.

[28] E. Esarey, J. Krall, and P. Sprangle, "Envelope analysis of intense laser pulse self-modulation in plasmas," *Phys. Rev. Lett.*, vol. 72, pp. 2887–2890, 1994.

[29] G. A. Askar'yan, S. V. Bulanov, F. Pegoraro, and A. M. Pukhov, "Magnetic interaction od self-focusing channels and fluxes of electromagnetic radiation: Their coalescense, the accumulation of energy and the effect of external magnetic field on them," *JETP Lett.*, vol. 60, pp. 251–257, 1994.

[30] A. M. Pukhov and J. Meyer-Ter-Vehn, "Relativistic magnetic self-channeling of light in near-critical plasma: Three-dimensional particle-in-cell simulation," *Phys. Rev. Lett.*, vol. 76, pp. 3975–3978, 1996.

[31] R. J. Mason and M. Tabak, "Magnetic field generation in high-intensity-laser-matter interactions," *Phys. Rev. Lett.*, vol. 80, pp. 524–527, 1998.

[32] K. C. Tzeng, W. B. Mori, and T. Katsouleas, "Self-trapped electron acceleration from the nonlinear interplay between raman forward scattering, self-focusing, and hosing," *Phys. Plasmas*, vol. 6, pp. 2105–2116, 1999.

[33] E. Esarey, C. B. Schroeder, W. P. Leemans, and B. Hafizi, "Laser-induced electron trapping in plasma-based accelerators," *Phys. Plasmas*, vol. 6, pp. 2262–2268, 1999.

[34] B. Rau, T. Tajima, and H. Hojo, "Coherent electron acceleration by subcycle laser pulses," *Phys. Rev. Lett.*, vol. 78, pp. 3310–3313, 1997.

[35] P. E. Young, G. Guethlein, S. C. Wilks, J. H. Hammer, and K. G. Esabrook, "Fast ion production by laser filamentation in laser-produced plasmas," *Phys. Rev. Lett.*, vol. 76, pp. 3128–3131, 1996.

[36] G. S. Sarkisov, V. Yu. Bychenkov, V. T. Tikhonchuk, A. Maksimchuk, S. Y. Chen, R. Wagner, G. Mourou, and D. Umstadter, "Observation of the plasma channel dynamics and coulomb explosion in the interaction of a high-intensity laser pulse with a He gas jet," *JETP Lett.*, vol. 66, pp. 828–834, 1997.

[37] G. S. Sarkisov, V. Yu. Bychenkov, V. N. Novikov, V. T. Tikhonchuk, A. Maksimchuk, S. Y. Chen, R. Wagner, G. Mourou, and D. Umstadter, "Self-focusing, channel formation, and high-energy ion generation in interaction of an intense short laser pulse with a He jet," *Phys. Rev. E*, vol. 59, pp. 7042–7054, 1999.

[38] K. Krushelnick, E. L. Clark, Z. Najmudin, M. Salvati, M. Santala, M. Tatarakis, A. E. Dangor, V. Malka, D. Neely, R. Allot, and C. Danson, "Multi-MeV ion production from high-intensity laser interactions with underdense plasmas," *Phys. Rev. Lett.*, vol. 83, pp. 737–740, 1999.

[39] M. Lezius, S. Dobosz, D. Normand, and M. Schmidt, "Explosion dynamics of rare gas clusters in strong laser fields," *Phys. Rev. Lett.*, vol. 80, pp. 261–264, 1998.

[40] Y. Sentoku, T. Zh. Esirkepov, K. Mima, K. Nishihara, F. Califano, F. Pegoraro, H. Sakagami, Y. Kitagawa, N. M. Naumova, and S. V. Bulanov, "Bursts of superreflected laser light from inhomogeneous plasmas due to the generation of relativistic solitary waves," *Phys. Rev. Lett.*, vol. 83, pp. 3434–3437, 1999.

Francesco Pegoraro was born in 1947. He received the bachelor's degree in physics from the University of Pisa, Pisa, Italy, and Scuola Normale Superiore, Pisa, in 1970, and the Ph.D. degree in physics from the Scuola Normale Superiore in 1974.

He is currently a Professor of plasma physics at the University of Pisa. His research interests include theoretical plasma physics, studies of magnetic reconnection in laboratory and astrophysical plasmas, magnetically confined controlled thermonuclear fusion, nonlinear plasma dynamics, and laser–plasma interaction.

Sergei V. Bulanov was born in 1947. He graduated from the Moscow Institute for Physics and Technology, Moscow, Russia, in 1971, received the Ph.D. degree in 1974, and the Dr.Sci. degree in 1990.

Currently, he is the Head of the Laboratory of the Nonlinear Process, Plasma Physics Department, General Physics Institute, The Russian Academy of Sciences, Moscow, and a Professor at the Moscow Institute for Physics and Technology. His main research interests include the theory of nonlinear processes in laboratory and space plasmas.

Francesco Califano was born in 1963. He presently works on plasma physics and astrophysics with a long experience on cmoputational physics. His main interests concern basic processes, nonlinear effects, and kinetic effects.

Mr. Califano is presently affilidated with the Istituto Nazionale Fisica della Materia (INFM) (Research Unit of Pisa, Italy).

Timur Zh. Esirkepov was born in 1970. He graduated from Moscow Institute for Physics and Technology in 1993, Moscow, Russia, and received the Ph.D. degree in 1996.

Currently, he is an Assistant Professor in the Physics Department, Moscow Institute for Physics and Technology. His main research interests include theory and computer simulation of nonlinear processes in plasmas.

Tatiana V. Lisejkina was born in 1973. She gradudated from Novosibirsk State University, Novosibirsk, Russia, in 1995 and received the Ph.D. degree in 1998.

Currently, she is a Junior Researcher in the Laboratory of Plasma Physics, Institute of Computational Technologies SD RAS, Novosibirsk, and at the moment, she has a postdoctoral fellowship in Astrophysics at the Scuola Normale Superiore, Pisa, Italy. Her main research interests include theory and computer simulation of nonlinear processes in plasmas and astrophysics.

Natalia M. Naumova works in the Laboratory of Nonlinear Processes, Plasma Physics Departmet, General Physics Institute, The Russian Academy of Sciences, Moscow, Russia. Her main research interests include theory and computer simulation of nonlinear processes in plasmas.

Hartmut Ruhl was born in 1963. He received the master's degree in high energy physics from the University of Darmstadt, Darmstadt, Germany, in 1990 and received the Ph.D. degree in plasma physics from the University of Darmstadt in 1994.

Curerntly, he is a Coordinator of theoretical laser–plasma research at Max-Born Institute, Berlin, Germany. His main research interests include theory and computer simulations of nonlinear processes in laser–plasma physics and astrophysics.

Vitali A. Vshivkov was born in 1947. He graduated from Tomsk State University in 1971, received the Ph.D. degree in 1981, and the Dr.Sci. degree in 1997.

Currently, he is a main Researcher in the Laboratory of Plasma Physics, Institute of Computational Technologies SDRAS, Novosibirsk, Russia. His main research interests include computational mathematics, computational physics, mathematical modeling, and plasma physics.

Ultrahigh-Intensity Laser-Produced Plasmas as a Compact Heavy Ion Injection Source

K. Krushelnick, E. L. Clark, R. Allott, F. N. Beg, C. N. Danson, A. Machacek, V. Malka, Z. Najmudin, D. Neely, P. A. Norreys, M. R. Salvati, M. I. K. Santala, M. Tatarakis, I. Watts, M. Zepf, and A. E. Dangor

***Abstract*—The possibility of using high-intensity laser-produced plasmas as a source of energetic ions for heavy ion accelerators is addressed. Experiments have shown that neon ions greater than 6 MeV can be produced from gas jet plasmas, and well-collimated proton beams greater than 20 MeV have been produced from high-intensity laser solid interactions. The proton beams from the back of thin targets appear to be more collimated and reproducible than are high-energy ions generated in the ablated plasma at the front of the target and may be more suitable for ion injection applications. Lead ions have been produced at energies up to 430 MeV.**

***Index Terms*—Heavy ion accelerators, ion accelerators, ion source, laser-plasma interactions.**

I. Introduction

OVER the past several years, there have been significant advances in the use of high-power, short pulse lasers [1]. In particular, the potential of such lasers for applications in particle acceleration [2], X-ray generation [3], and inertial confinement fusion [4] seems promising. The complex interactions between matter and high-intensity laser light can produce electrons at energies greater than 100 MeV and gamma rays up to tens of MeV. However, it may also be possible to use such laser systems to produce plasmas that can be used as a source of energetic heavy ions for injection into ion storage rings and colliders.

In this paper, we will discuss some recent experiments that address the feasibility and advantages of this approach for producing a source of energetic ions. There has been considerable previous work on the use of laser-produced plasmas as such a source of highly ionized heavy ions [5]–[7], [18], where it was found that laser ion sources have several advantages over other methods, such as electron–cyclotron sources, electron beam ion sources, and metal vapor vacuum arcs. Heavy ions (of a few MeV) have been generated by the ablated plasma created by low-intensity solid target interactions, after which they were accelerated by an RF quadrupole to energies of a few hundred MeV before injection into an ion storage ring. Our research indicates that through the use of "table top" chirped pulse amplification (CPA) laser systems, it may be possible to produce heavy highly ionized ions at energies approaching a GeV in sufficient quantities to directly inject into ion storage rings. Such heavy ions can be generated in a gas jet plasma (which allows high repetition rates) or through solid target interactions (which may provide a more collimated and energetic source of such heavy ions). We present angular emission data and ion energy spectra as well as a possible source geometry.

Manuscript received October 2, 1999; revised February 24, 2000.

K. Krushelnick, F. N. Beg, Z. Najmudin, M. R. Salvati, M. I. K. Santala, M. Tatarakis, I. Watts, M. Zepf, and A. E. Dangor are with the Imperial College, SW7 2BZ, London, U.K.

E. L. Clark is with the Radiation Physics Department, AWE plc, RG7 4PR, Aldermaston, U.K., and the Imperial College, SW7 2BZ, London, U.K.

R. Allott, C. N. Danson, D. Neely, and P. A. Norreys are with the Rutherford Appleton Laboratory, Chilton, Didcot, OX11 OQX Oxon, U.K.

A. Machacek is with the Department of Physics, University of Oxford, OX1 3PU Oxford, U.K.

V. Malka is with LULI, CNRS-CEA, École Polytechnique-Université Pierre et Marie Curie, 91128 Palaiseau Cedex, France.

Publisher Item Identifier S 0093-3813(00)07243-X.

II. Interactions with Underdense Plasmas

Accelerated ions can be produced in underdense "gas jet" interactions via the "Coulomb explosion" of a high-intensity laser-produced plasma [8]. In this situation, ions are accelerated by electrostatic forces caused by charge separation induced by the laser ponderomotive pressure. In these experiments, we have measured peak ion energies of 1.0 MeV for deuterium gas interactions, 3.6 MeV for helium interactions, and greater than 6 MeV for interactions with neon.

As a high-intensity laser pulse propagates through an underdense plasma, the strong ponderomotive force of the laser forces electrons from the region of highest intensity. Ions are less affected by this ponderomotive force because of their larger mass; however, during the laser pulse, these ions will be given a impulse perpendicular to the axis of laser propagation that is produced by the large space-charge forces caused by charge separation. After the pulse passes, the plasma electrons will return to their original positions on a timescale of about $1/\omega_{pe}$, (where $\omega_{pe} = 4\pi n_e e^2/m_e$ is the electron plasma frequency); however, the lateral momentum given to the ions will be retained and they will continue moving out of the plasma, carrying low-energy electrons with them. The energy of these ions is thus directly related to the intensity of the focused laser pulse. The maximum energy that can be gained by an ion during these interactions is simply given as the relativistic ponderomotive energy, $U = Zm_e c^2(\gamma - 1)$, where Z is the ion charge and γ is the relativistic factor of the electron quiver motion in the laser field.

Our experiments were performed using the CPA arm of the VULCAN laser system at the Rutherford Appleton Laboratory. This system produces laser pulses having an energy of up to 50 J and a duration of 0.9–1.2 ps at a wavelength of 1.054 μm (Nd : Glass). The laser pulse was focused into a gas jet target (4-mm nozzle diameter) using an $f/4$ off-axis parabolic mirror. When helium was used as the target gas, the plasma had an electron density up to about 5×10^{19} cm^{-3}. Deuterium and neon were also used as target gases.

0093–3813/00$10.00 © 2000 IEEE

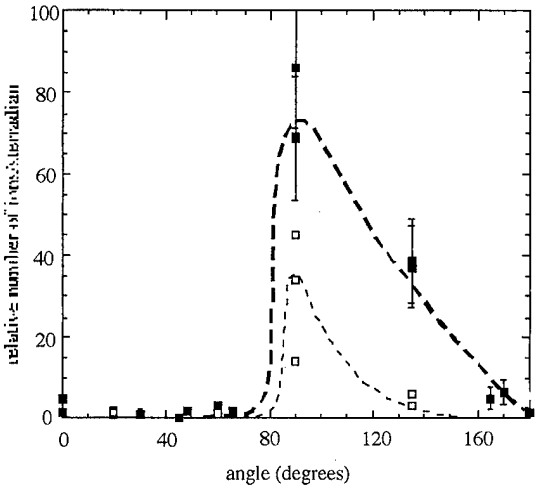


Fig. 1. Angular emission of energetic ions, where 0° is along the direction of laser propagation. Dark line: distribution of helium ions with energy greater than 400 keV; Light line: distribution of helium energy greater than 2 MeV (shown ×10. Note that lines are drawn as visual aid only.)

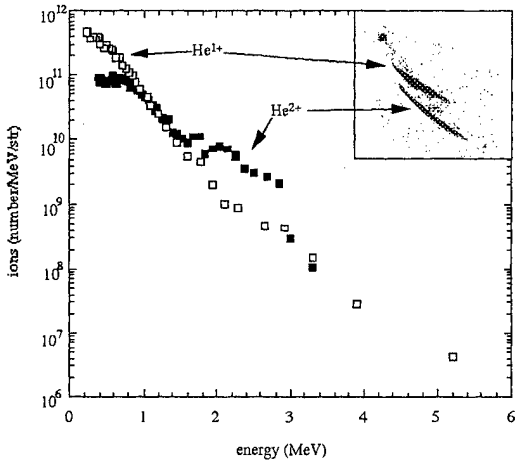


Fig. 2. Typical ion spectrum from helium interaction (90°) (Thomson parabola data are shown inset).

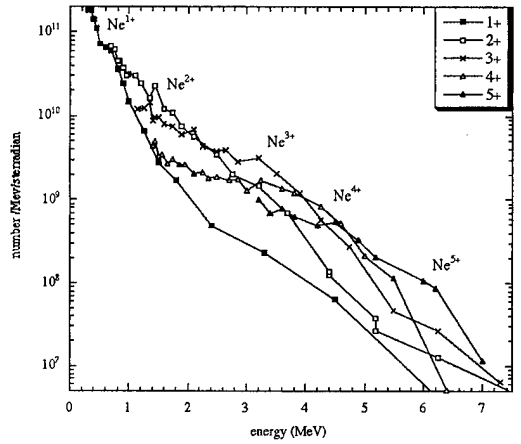


Fig. 3. Typical ion spectrum from neon interaction (90°).

The angular distribution of ions emitted during such high-intensity laser plasma interactions was recorded using CR-39 track detectors placed at various places surrounding the interaction region and that are sensitive to energetic ions greater than about 100 keV/nucleon [9]. As an energetic ion collides with the detector, it causes structural damage in the material so that an observable track can be recorded for each ion. In this way, the total number of ions can be counted.

It was found in these experiments that there was no significant variation in ion emission in the azimuthal direction (i.e., changing the laser polarization had little effect). However, a distinct peak was observed in the emission of ions with energies greater than 300 keV at 90° to the axis of propagation. Measurements of the ion emission at higher energies were also obtained by using CR-39 track detectors covered with thin aluminum filters (2 μm). Such filters block all signal from helium ions below about 2 MeV in energy.

Averaged measurements over four shots are shown in Fig. 1. Clearly, the majority of ion emission occurs in the 90° direction, although the emission lobe also extends in the backward direction somewhat. Emission at energies greater than 2 MeV shows a narrower lobe in the 90° direction. The spectrum of the energetic ions was also measured using a Thomson parabola ion spectrometer that spatially separates ion species having different charge to mass ratios through the use of parallel electric and magnetic fields. CR-39 was used as the detector. Typical experimentally measured spectra are shown in Fig. 2 for helium interactions and Fig. 3 for neon interactions.

For the helium interactions, it was found that approximately 0.25% of the incident laser energy is transferred to ions having greater than 300 keV of energy. It is interesting to note that in helium plasmas, both He^{1+} and He^{2+} ions were observed with very high energy. In the interaction region, helium ions are completely ionized because the intensity required to directly field ionize He^{1+} is about 10^{16} W/cm^2. This implies that the He^{1+} is generated by charge–exchange/recombination of ions as they travel out of the gas jet to the detector. In neon interactions, the atoms can be stripped up to the Ne^{8+} stage from direct field ionization; however, only neon species up to Ne^{5+} were observed in our experiment (see Fig. 3), also indicating significant charge exchange/recombination.

The maximum ion energy, such that there were more than 10^8 ions/MeV/sterradian, was found to be 3.6 MeV for helium, 1.0 MeV for deuterium, and greater than 6 MeV for neon. It should be noted that ionization-induced defocusing of the laser pulse in the neon plasma appeared to reduce the peak energy of neon ions obtainable from these interactions.

III. Solid Target Interactions

Major advances in understanding the mechanisms of energetic ion emission were made during early inertial confinement fusion experiments using high-power CO_2 lasers [10] and results from those experiments (at irradiances of about 10^{18} Wcm$^{-2}\mu$m^2) [11] indicated that ions with energies greater than 2 MeV/nucleon could be produced from interactions with solid density plasmas. The principal diagnostics employed in those measurements were Faraday cups and charge collection cups. Using such time of flight methods only, information concerning the ion velocity (energy/nucleon) can be obtained.

We have also performed experiments to examine the generation of high-energy ions from interactions with solid density plasmas at the Rutherford Appleton Laboratory. In these experiments, the VULCAN beam was focused using an $f/4$ off-axis parabolic mirror onto a thin (125-μm) aluminum target positioned at 45° to the axis of laser propagation. The intensity on target was up to 5×10^{19} W/cm^2. Both behind the target (25-mm distance) and at the front of the target (70 mm), we placed "sandwich detectors" aligned with the normal to the target. These detectors consist of several pieces of radiochromic film (RCF) and CR39 plastic track detectors placed back to back. The principal ions detected were energetic protons or carbon ions that were either from hydrocarbon contamination of the front or rear target surfaces (which has been observed in previous experiments [12]).

RCF is a transparent material (typically nylon) that is coated with an organic dye. Upon exposure to ionizing radiation, the film undergoes a color change. The optical density of the film is subsequently measured at a particular wavelength and is calibrated against dose (Gy) using a known ^{60}Co source. The equivalent dose from protons at a particular energy is calculated, and hence, the total number of protons passing through the film at each point can be determined.

In this experiment, the CR39 detectors only recorded signals caused by protons because the first piece of RCF (110 μm thick) in the "sandwich" will transmit protons having energies greater than 2.8 MeV, but will stop all but the highest energy aluminum and carbon ions. The stopping range of protons in CR39 and radiochromic film is easily calculated, and consequently, this allows a direct determination of the energy range for those protons that produce a particular series of pits. CR39/RCF "sandwich" detectors can therefore provide both spatial and spectral information of protons emitted during the interaction.

Fig. 4(a) shows a scanned image from the front piece of RCF in the "sandwich" detector from a typical shot at $I \sim 5 \times 10^{19}$ W/cm^2 from the rear of a target. The film contains signal only within a well-defined radius from the central hot-spot. The angle subtended by the perimeter of this circle covers a cone half angle of 30°, and the mark at the center of the film indicates a region where the film has been saturated. Fig. 4(b)–(e) shows the emission pattern observed on the CR39 from this shot for various energy ranges of ions (i.e., different pieces in the "sandwich"). RCF is also sensitive to both electrons and X-rays, which are generated during the interaction [13], [19]; however, it is clear from the images shown in Fig. 4(b)–(e) that the signal on the RCF coincides with that on the CR39, which is sensitive only to ions. Therefore, it is likely that the signal on the front piece of film is predominantly caused by energetic ion emission. Using this assumption, the total number of protons emitted with energies greater than 2 MeV can be estimated and was found to be approximately 10^{12} per shot.

The ion signal on the CR39 exhibits a ring pattern with decreasing diameter for increasing ion energy up to a maximum energy of 17.6 MeV. The central position of each ring is coincident with the direction of the target normal. The "ion ring" structure on the CR39 was observed consistently from shots at an intensity of $\sim 5 \times 10^{19}$ W/cm^2. The central hot spot on the RCF is correlated with the position of the highest energy ions on



(a) (b) (c) (d)

Fig. 4. Ring structure observed on back RCF/CR39 "sandwich" track detectors: (a) radiochromic film (front surface), (b) tracks on CR39 from 3-MeV, (c) 8.9-MeV, (d) 11.6-MeV, and (e) 17.6-MeV protons (track detectors were 5 cm × 5 cm × 0.75 mm thick).

the CR39, which exhibit collimated propagation, and the outer extreme of the RCF displays an abrupt decrease in signal level, which corresponds to a sharp low energy cutoff, below which no protons are observed.

It is possible that this relationship between the energy of the emitted protons and the angle at which they are emitted is caused by large azimuthal magnetic fields within the solid target material that develop and persist during the first few picoseconds after the laser pulse. The protons are consequently deflected like charged particles in a magnetic spectrometer. It is clear that such magnetic fields must be generated by an electron current, which would tend to focus a beam of electrons, but defocus or scatter ions. Such large fields have been predicted [14], and have been shown to contribute to the focusing of electrons at the rear of such targets resulting in plasma formation [15].

Simultaneously, measurements of the gamma-ray spectrum using a gamma-ray spectrometer (scintillators/photo-multipliers) as well as through the use of nuclear activation techniques [20], [21], implied that the hot electron temperature was in the range of 1 to 2 MeV. The spectrum of high-energy electrons propagating through the 125-μm targets was also measured, and it was found to extend to energies greater than 20 MeV. It is likely that part of the return current required for propagation of the hot electrons through the target material is provided by protons from the front surface plasma that are pulled along with these electrons as they propagate into the plasma. From these measurements, we have been able to infer the structure and magnitude of the magnetic field generated within a solid target during an ultrahigh-intensity laser interaction [16].

These results are in contrast to measurements of the heavy ion and proton spectra in the forward direction (i.e., in the plume of ablated plasma), which were similarly recorded with high spatial and spectral resolution. In this direction, we have observed the formation of a lower energy ring structure composed of protons (~4 MeV) and heavy ions that is probably created by magnetic fields that exist in the expanding plasma and a higher energy population that exhibits a less well-defined structure.

To measure both the heavy ion and proton spectra, a Thomson parabola ion spectrometer using CR39 plastic nuclear track detectors was situated at an angle of 20° from the target normal. In addition, the spectral and spatial distribution of the protons emitted from the interaction was determined by placing a "sandwich" of several pieces of radiochromic film and CR39 detectors in front of the target—similar to that which was used at the back.

The CR39/radiochromic film pack was covered with a 20-μm thick piece of aluminum and was aligned with the target at a distance of 70 mm from the surface, the center of which coincided with the target normal. The target was again a 125-μm thick piece of aluminum. Almost no heavy ions penetrate the first layer of radiochromic film and the signal on the subsequent pieces of CR39 is largely from energetic protons originating from hydrocarbon contaminants on the front surface of the target.

In this "sandwich" target, the first piece of radiochromic film shows a ring structure that is consistent with a ring of low energy ($\leq$4-MeV) protons recorded on the following piece of CR39. The center of the ring does not coincide with the target normal, but is shifted by about 10° back toward the direction of the incident laser, and down slightly. Overall, the low-energy ion emission occurs within a 20° cone (the plasma plume) and is characterized by a fine-scale filamentary structure. The surface of the CR39 records some of the proton signal from the ring, but little additional signal is seen.

Higher energy protons were measured by the subsequent pieces of CR39 in the "sandwich," which are separated by a single piece of radiochromic film. The energies at these surfaces are 11 MeV and 13 MeV, respectively. Here, no ring structure is observed and the protons cover an emission area that gets smaller as the energy of the protons increases, but has no apparent correlation with the lower energy component. Measurements of protons of energies up to 18 MeV and 20 MeV were made using a similar technique; however, they were observed to be much less collimated than were those measured at the back of the target. Similar data (which also showed the same low-energy ring structure) was consistently measured over a series of shots. Simultaneous measurements at the front and the rear of the target indicate that the maximum proton energies are almost the same in both directions (see below).

It is likely that the lower energy component of the proton emission is produced during the expansion phase of the plasma. During this period, temperature gradients along the target surface combined with nonparallel density gradients from the expanding plasma produce self-generated magnetic fields [17]. These fields may affect the plasma [15] as it expands, thus, forming the "ion ring," as discussed earlier. These ions, which include protons of up to 4 MeV, have energies that are consistent with plasma expansion velocities as measured by optical probing [15]. The magnetic pressure along the target normal collimates the expanding plasma at the laser spot to produce a plasma jet containing low-energy ions and electrons that can be seen as a bright central feature. This plasma jet is likely formed before the toroidal plasma formation and in the direction away from the target along the normal to the surface. The ring of plasma is formed as the magnetic field is generated in the ablating plume and is recorded as low-energy protons and ions on the radiochromic film. Such plasma formation has been observed in MHD simulations and in previous experiments [15]. A fine-scale filamentary structure can be seen on the radiochromic film at the edge of the ring, which is unlike the images recorded on radiochromic film at the rear of the target.

The higher energy component of the ion emission appears to be qualitatively different from the lower energy component and

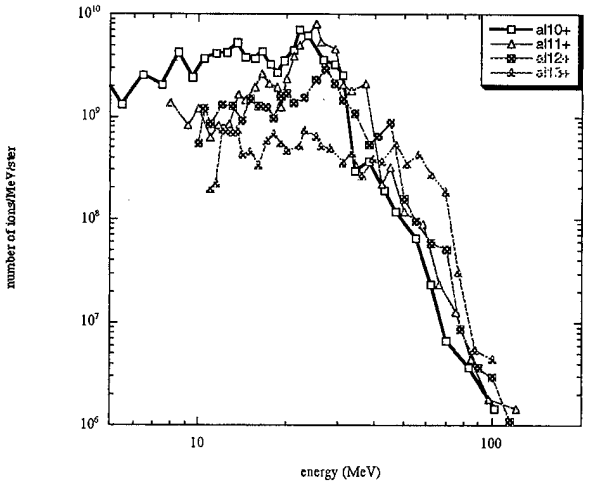


Fig. 5. Typical aluminum ion spectrum from front surface plasma during interactions at $\sim 3 \times 10^{19}$ W/cm^2.

does not exhibit a ring structure. It is possible that these ions are produced near the critical surface where large electrostatic fields can be generated via plasma wave generation (via a mechanism such as resonance absorption). The interaction process is therefore capable of producing equivalent maximum proton energies in both directions at the front target surface. The number of protons above 1 MeV is about the same as that measured at the rear of the target. The fact that the very highest energy ions in the plasma plume have a similar energy to those recorded at the back of the target suggests that they are not produced in the ablated plume, but they are generated by large electrostatic fields near the critical density surface, which may accelerate ions in both directions.

The detailed energy spectra of ions emitted during these interactions were obtained using the Thomson parabola ion spectrometer. Previous measurements suggest that the dominant component of the ion emission is protons, however, it is clear that a substantial contribution is from other ion species. Measurements of ion emission from lead targets indicate Pd-like Pb^{36+} ions up to 220 MeV and Xe-like Pb^{46+} ions up to 430 MeV. Fully stripped aluminum (Fig. 5) and carbon ions up to 150 MeV and 90 MeV were also measured. The total number of Al ions greater than 10 MeV was estimated to be $\sim 10^{11}$ ions/sterradian.

These experiments suggest that there are two components to proton and ion production. The lower energy part is formed many picoseconds after the laser pulse as the heated plasma ablates and is strongly influenced by the magnetic field generation to be in the plasma. In contrast, the higher energy component is likely generated during the laser interaction period.

IV. Ion Sources

The requirements for an ion source are that it be able to operate at repetition rates of at least 1 Hz, that it have short pulse length, high luminosity, and that it be flexible to make available a wide variety of ionized species. It is likely that an ion source using high-intensity laser-produced plasmas could meet these requirements easily. The pulse length of ions must be less than the revolution time for ions in a synchrotron.

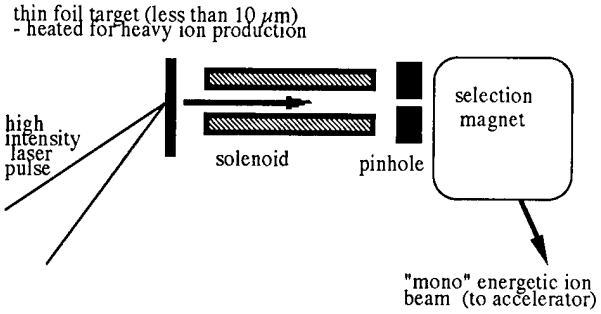


Fig. 6. Schematic of possible high intensity laser-plasma ion injector geometry.

From the above discussion, it is clear that there are distinct advantages to the use of high-intensity lasers for ion acceleration. If gas jets are used as the target, it seems likely that high repetition sources of highly ionized noble gases having energies of up to 10 MeV can be produced. The disadvantage of this approach is that the ion energies are typically low and that the ions are emitted with a broad angular distribution so that a complicated collection scheme may be necessary. There are also fewer energetic ions emitted from underdense interactions for similar focused laser intensities.

For solid target interactions, it appears that nonlinear acceleration mechanisms in the interaction region can produce high-energy ions. However, it is not clear how the peak ion energy scales with incident laser intensity. In the past, laser-produced ion sources have used ions produced in the ablated plasma plume, and while this seems to be possible using very intense laser pulses, a better design for a high-intensity ion source would involve the use of the forward-propagating beam of ions. Such ions are almost as energetic as the ions emitted in the plume, and it also appears that magnetic fields generated inside thin targets tend to focus and collimate the highest energy ions after they are emitted. A possible design for a high-intensity laser/dense plasma ion source is shown in Fig. 6. The energies of the emitted ions and the observed angular emission of these sources suggest that perhaps the linac pre-acceleration stage can be avoided with the use of high-intensity laser ion sources, although clearly further work is required to determine the reproducibility of the angular emission pattern and of the energy spectrum of emitted ions.

The authors would like to acknowledge the technical assistance of the VULCAN operations team in these experiments.

REFERENCES

[1] M. Perry and G. Mourou, "Terawatt to petawatt subpicosecond lasers," *Science*, vol. 264, pp. 917–924, 1994.

[2] E. Esarey, P. Sprangle, J. Krall, and A. Ting, "Overview of plasma-based accelerator concepts," *IEEE Trans. Plasma Sci.*, vol. 24, p. 252, 1996.

[3] N. H. Burnett and G. D. Enright, "Population inversin in the recombination of optically-ionized plasmas," *IEEE J. Quant. Electron.*, vol. 26, pp. 1797–1808, 1990.

[4] M. Tabak, J. Hammer, M. E. Glinsky, W. L. Kruer, S. C. Wilks, J. Woodworth, E. M. Campbell, M. D. Perry, and R. J. Mason, "Ignition and high gain with ultrapowerful lasers," *Phys. Plasmas*, vol. 1, pp. 1626–1634, 1994.

[5] M. Lezius, S. Dobosz, D. Normand, and M. Scmidt, "Explosion dynamics of rare gas clusters in strong laser fields," *Phys. Rev. Lett.*, vol. 80, pp. 261–264, 1998.

[6] J. Collier, G. Hall, H. Haseroth, H. Kugler, A. Kuttenberger, K. Langbein, R. Scrivens, T. Sherwood, J. Tambini, B. Sharkov, A. Shumshurov, and K. Masek, "The CERN laser-ion source," *Lasers Particle Beams*, vol. 14, pp. 283–292, 1996.

[7] P. Fournier, G. Gregoire, H. Kugler, H. Haseroth, N. Lisi, C. Meyer, P. Ostroumov, J. C. Schnuriger, R. Scrivens, F. V. Rodriguez, B. H. Wolf, S. Homenko, K. Makarov, Y. Satov, A. Stepanov, S. Kondrashev, B. Sharkov, and A. Shumshurov, "Status of the CO_2 laser ion source at CERN," *Rev. Sci. Instrum.*, vol. 71, pp. 924–926, 2000.

[8] K. Krushelnick, E. Clark, Z. Najmudin, M. Salvati, M. I. K. Santala, M. Tatarakis, A. E. Dangor, V. Malka, D. Neely, R. Allott, and C. Danson, "Multi-MeV ion production from high intensity laser interactions with underdense plasmas," *Phys. Rev. Lett.*, vol. 83, pp. 737–740, 1999.

[9] A. P. Fews, "Flexible analysis of etched nuclear-particle tracks," *Nucl. Instrum. Methods Phys. Res., Sect.*, vol. 72, pp. 91–103, 1992.

[10] R. L. Carlson, J. P. Carpenter, D. E. Casperson, R. B. Gibson, R. P. Godwin, R. F. Haglund, J. A. Hanlon, E. L. Jolly, and T. F. Stratton, "HELIOS—A 15 TW carbon dioxide laser fusion facility," *IEEE J. Quantum Electron.*, vol. QE-17, pp. 1662–1678, 1981.

[11] S. J. Gitomer, R. D. Jones, F. Begay, A. W. Ehler, J. F. Kephart, and R. Kristal, "Fast ions and hot electrons in the laser plasma interaction," *Phys. Fluids*, vol. 29, pp. 2679–2688, 1986.

[12] A. P. Fews, P. A. Norreys, F. N. Beg, A. R. Bell, A. E. Dangor, C. N. Danson, P. Lee, and S. J. Rose, "Plasma ion emission from high intensity intensity picosecond laser pulse interactions with solid targets," *Phys. Rev. Lett.*, vol. 73, pp. 1801–1804, 1994.

[13] P. A. Norreys, M. I. K. Santala, E. Clark, M. Zepf, I. Watts, F. N. Beg, K. Krushelnick, M. Tatarakis, A. E. Dangor, X. Fang, P. Graham, T. McCanny, R. P. Singhal, K. W. D. Ledingham, A. Creswell, D. C. W. Sanderson, J. Magill, A. Machacek, J. S. Wark, R. Allott, B. Kennedy, and D. Neely, "Observation of a highly directional gamma-ray beam from ultra-short, ultra-intense laser pulse interactions with solids," *Phys. Plasmas*, vol. 6, p. 2150, 1999.

[14] J. R. Davies, A. R. Bell, M. G. Haines, and S. M. Guerin, "Short-pulse high-intensity laser-generated fast electron transport into thick solid targets," *Phys. Rev. E*, vol. 56, pp. 7193–7203, 1997.

[15] M. Tatarakis, J. R. Davies, P. Lee, P. A. Norreys, N. G. Kassapakis, F. N. Beg, A. R. Bell, M. G. Haines, and A. E. Dangor, "Plasma formation on the front and rear of plastic targets due to high-intensity laser-generated fast electrons," *Phys. Rev. Lett.*, vol. 81, no. 5, pp. 999–1002, 1998.

[16] E. L. Clark, K. Krushelnick, J. R. Davies, F. N. Beg, M. I. K. Santala, M. Tatarakis, I. Watts, M. Zepf, A. E. Dangor, P. A. Norreys, and A. Machacek, "Measurements of energetic proton transport through magnetized plasma from intense laser interactions with solids," *Phys. Rev. Lett.*, vol. 84, pp. 670–673, 2000.

[17] J. A. Stamper, "Review on sponteneous magnetic fields in laser-produced plasma-phenomena and measurements," *Laser Particle Beams*, vol. 9, pp. 841–862, 1991.

[18] T. Ditmire, J. W. G. Tisch, E. Springate, M. B. Mason, N. Hay, J. P. Marangos, and M. H. R. Hutchinson, "High energy ion explosion of atomic clusters: Transition from molecular to plasma behavior," *Phys. Rev. Lett.*, vol. 78, pp. 2732–2735, 1997.

[19] F. N. Beg, A. R. Bell, A. E. Dangor, C. N. Danson, A. P. Fews, M. E. Glinsky, B. A. Hammel, P. Lee, P. A. Norreys, and M. Tatarakis, "A study of picosecond laser-solid interactions up to 10^{19} W cm^{-2}," *Phys. Plasmas*, vol. 4, pp. 447–457, 1997.

[20] M. I. K. Santala, E. Clark, I. Watts, F. N. Beg, M. Tatarakis, M. Zepf, K. Krushelnick, A. E. Dangor, T. McCanny, I. Spencer, R. P. Singhal, K. W. D. Ledingham, S. C. Wilks, A. C. Machacek, J. S. Wark, R. Allott, R. J. Clarke, and P. A. Norreys, "The effect of the plasma density scale length on the direction of fast electrons in relativistic laser-solid interactions," *Phys. Rev. Lett.*, vol. 84, pp. 1459–1462, 200.

[21] K. W. D. Ledingham, I. Spencer, T. McCanny, R. P. Singhal, M. I. K. Santala, E. Clark, I. Watts, F. N. Beg, M. Zepf, K. Krushelnick, M. Tatarakis, A. E. Dangor, P. A. Norreys, R. Allott, D. Neely, R. J. Clarke, A. Machacek, J. S. Wark, A. J. Cresswell, D. C. W. Sanderson, and J. Magill, "Photo-nuclear physics when a multiterawatt laser pulse interacts with solid targets," *Phys. Rev. Lett.*, vol. 84, pp. 899–902, 2000.

K. Krushelnick, photograph and biography not available at the time of publication.

E. L. Clark, photograph and biography not available at the time of publication.

R. Allott, photograph and biography not available at the time of publication.

F. N. Beg, photograph and biography not available at the time of publication.

C. N. Danson, photograph and biography not available at the time of publication.

A. Machacek, photograph and biography not available at the time of publication.

V. Malka, photograph and biography not available at the time of publication.

Z. Najmudin, photograph and biography not available at the time of publication.

D. Neely, photograph and biography not available at the time of publication.

P. A. Norreys, photograph and biography not available at the time of publication.

M. R. Salvati, photograph and biography not available at the time of publication.

M. I. K. Santala, photograph and biography not available at the time of publication.

M. Tatarakis, photograph and biography not available at the time of publication.

I. Watts, photograph and biography not available at the time of publication.

M. Zepf, photograph and biography not available at the time of publication.

A. E. Dangor, photograph and biography not available at the time of publication.

Optical Guiding of a Radially Polarized Laser Beam for Inverse Cherenkov Acceleration in a Plasma Channel

P. Serafim, *Senior Member, IEEE*, Phillip Sprangle, *Fellow, IEEE*, and Bahman Hafizi, *Member, IEEE*

***Abstract*—In a conventional inverse Cherenkov accelerator (ICA), the background neutral gas provides the necessary dispersion to maintain the synchronism between the drive laser and the accelerated electrons. A laser-driven ICA is susceptible to diffraction, and the acceleration length is limited to approximately a Rayleigh range (for a Gaussian beam). In this paper, an ICA configuration is proposed that avoids the laser diffraction limitation by employing a preformed plasma channel. It is shown that a radially polarized laser beam can be optically guided if the plasma density increases with radius-like r^2. Expressions for the guided axial and radial components of the laser field are derived, and a numerical example is discussed.**

I. Introduction

THERE are a number of fundamental issues associated with laser-driven acceleration [1], [2]. The drive laser must be optically guided over distances of many diffraction lengths, and the phase velocity of the accelerating field should be equal to or less than the speed of light to avoid phase velocity slippage. In addition, the drive laser or accelerated electrons should avoid ionizing the accelerating medium. Intense laser pulses have been optically guided in preformed plasma channels for distances greater than tens of Rayleigh lengths, corresponding to a few centimeters. These plasma channels have been produced by capillary discharges [3], axicon-focused laser beams [4], or intense self-guided laser pulses [5]. In general, achieving refractive guiding in plasma channels requires an index of refraction that has its peak along the propagation axis and decreases with radius. In order to maximize the refractive index along the axis, the plasma channel consists of a plasma column with minimum density on axis. For optical guiding of a laser beam with a Gaussian transverse profile, the plasma density must increase in the radial direction as r^2.

The inverse Cherenkov effect has been considered as a high-energy electron acceleration mechanism [6]–[10]. Experiments at Brookhaven National Laboratory [7] on the inverse Cherenkov accelerator (ICA), in which the drive laser was not optically guided, observed a 3.7-MV electron energy gain with an accelerating gradient of 31 MV/m. In these experiments, the energy of the injected electron beam was 40 MV, and a 580-MW, CO_2 laser in 2.2 atmosphere of H_2 gas was used.

Under appropriate conditions, a laser beam with a large axial electric field component and phase velocity equal to the speed of light can be optically guided along a plasma channel containing neutral gas. The combination of a plasma channel and neutral gas can provide the basis for an optically guided ICA. The neutral gas density must be sufficient to modify the refractive index of the channel in a way that will result in the phase velocity of the laser radiation to be equal to or less than the speed of light.

Electron acceleration in vacuum is limited by both laser diffraction and electron slippage [2], [11]–[13]. In ICAs in which the drive laser is not optically guided, the acceleration is limited by diffraction and not electron slippage. Ionization processes are also detrimental to the operation of ICAs for several reasons [14], [17]. Optical ionization of the gas can lead to significant modification of the dispersive properties of the medium, thus, altering the phase velocity of the accelerating field and causing slippage between the field and the accelerated electrons. Ionization can modify the refractive properties of the plasma channel used for the guidance of the laser beam and limit the acceleration distance. In addition, ionization processes limit the accelerating gradient and place an upper limit on the laser pulse duration in the accelerator. Use of ultrashort laser pulses to avoid ionization may result in group velocity slippage or lethargy in which the short laser pulse slips behind the accelerated electrons. Both phase and group velocity slippage can impose severe limitations on the acceleration level and the energy gain in the ICA.

The ICA configuration proposed here employs a preformed plasma channel and, hence, overcomes the diffraction limitation, allowing the interaction and acceleration to take place over long distances compared with the diffraction (Rayleigh) length. In this configuration, shown in Fig. 1, a hollow laser beam, which is predominantly polarized in the radial direction, is optically guided in a plasma channel containing neutral gas. Even though such a laser beam does not have a Gaussian transverse profile, it can be optically guided in a channel in which the plasma density increases as r^2. We formulate and solve the paraxial wave equation for the proposed configuration and derive the appropriate conditions for acceleration. Finally, we illustrate these results with a numerical example.

Manuscript received October 7, 1999; revised March 15, 2000. This work was supported by the Department of Energy and the Office of Naval Research.

P. Serafim is with the Electrical Engineering Department, Northeastern University, Boston, MA 02115 USA.

P. Sprangle is with the Beam Physics Branch, Plasma Physics Division, Naval Research Laboratory, Washington, DC 20375-5346 USA.

B. Hafizi is with Icarus Research, Inc., Bethesda, MD 20824-0780 USA.

Publisher Item Identifier S 0093-3813(00)09157-8.

0093–3813/00$10.00 © 2000 IEEE

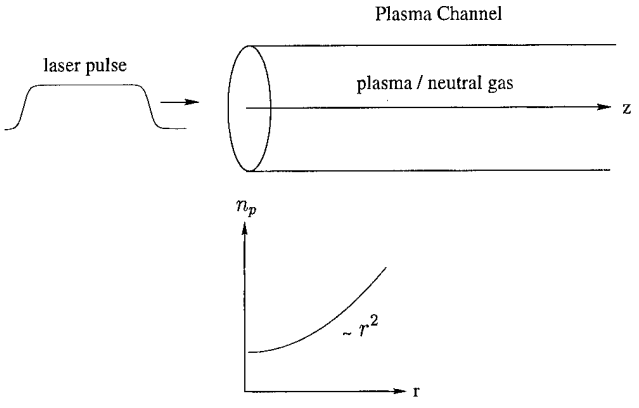


Fig. 1. Schematic of inverse Cherenkov accelerator configuration employing a plasma channel. The plasma density n_p is minimum on axis, rising as r^2, to provide guiding of the laser beam.

II. Paraxial Wave Equation

We consider a radially polarized laser pulse propagating in an inhomogeneous plasma channel containing neutral gas. The electric field $\mathbf{E}(r, z, t)$ of the hollow laser beam must satisfy the vector wave equation

$$\left(\nabla^2 - \frac{n_o^2}{c^2}\frac{\partial^2}{\partial t^2} - \frac{\omega_p^2(r)}{c^2}\right)\mathbf{E}(r, z, t) = 0 \tag{1}$$

where

∇^2 Laplacian for the vector radial field;
n_o refractive index of the neutral gas;
$\omega_p(r)$ plasma frequency of the plasma channel.

The plasma frequency varies with the radius r and is given by

$$\omega_p(r) = \omega_{po}\left(1 + \frac{\Delta n}{n_{po}}\frac{r^2}{r_c^2}\right)^{1/2} \tag{2}$$

where $\omega_{po} = \omega_p(0) = (4\pi q^2 n_{po}/m)$ is the plasma frequency on axis, Δn is the maximum variation of the plasma electron density across the plasma channel, and r_c is the radius of the channel.

We separate the slow- and fast-varying parts of the radial laser field, and we write it as follows:

$$\mathbf{E}(r, z, t) = (1/2)(E_r(r, z, t)\exp(i(k_o z - \omega_o t)) + \text{c.c.})\hat{\mathbf{e}}_r \tag{3}$$

where

E_r slowly varying complex part;
k_o longitudinal wavenumber;
ω_0 frequency;
$\hat{\mathbf{e}}_r$ unit radial vector.

Substituting (3) into (1) and neglecting the $\partial^2/\partial z^2$ and $\partial^2/\partial t^2$ operating on E_r yields the paraxial wave equation for the complex amplitude E_r

$$\left(\nabla_\perp^2 + k_\perp^2 - \frac{\omega_{po}^2}{c^2}\frac{\Delta n}{n_{po}}\frac{r^2}{r_c^2} + 2ik_o\frac{\partial}{\partial z} + 2i\frac{n_o^2}{c^2}\omega_o\frac{\partial}{\partial t}\right) \cdot E_r(r, z, t) = 0 \tag{4}$$

where $\nabla_\perp^2 = r^{-1}\partial(r\partial/\partial r)/\partial r - r^{-2}$ is the transverse Laplacian of the radial electric field component and $k_\perp$ is the transverse wavenumber, which has been introduced in anticipation of the finite spot size of the laser pulse. The transverse wavenumber $k_\perp$ is inversely proportional to the laser spot size. The particular value of $k_\perp$ is determined by the specific transverse modal structure of the laser pulse. The transverse wavenumber $k_\perp$ must satisfy the dispersion relation for a medium containing neutral gas and plasma with finite spot size effects

$$k_\perp^2 + k_o^2 - \frac{n_o^2}{c^2}\omega_o^2 + \frac{\omega_{po}^2}{c^2} = 0. \tag{5}$$

In order to simplify (4), it is expedient to perform a change of variables from (z, t) to (z, ξ), where $\xi = z - v_g t$. Then, $\partial/\partial z \rightarrow \partial/\partial z + \partial/\partial\xi$ and $\partial/\partial t \rightarrow -v_g\partial/\partial\xi$. Using these variables, (4) becomes

$$\left(\nabla_\perp^2 + k_\perp^2 - \frac{\omega_{po}^2}{c^2}\frac{\Delta n}{n_{po}}\frac{r^2}{r_c^2} + 2ik_o\frac{\partial}{\partial z}\right)E_r(r, z, \xi) = 0 \tag{6}$$

where the transformation velocity has been set equal to

$$v_g = \frac{c^2 k_o}{n_o^2\omega_o} = \frac{c}{n_0}\left(1 - \frac{\omega_{po}^2}{n_o^2\omega_o^2}\right)^{1/2}. \tag{7}$$

III. Matched Laser Beam Solution and Radial Electric Field

We now assume that the hollow laser pulse, which propagates along the plasma channel with the neutral gas, is matched to the channel. That is, both the amplitude and the spot size are independent of the propagation distance z. The phase of the matched complex amplitude may, in general, be proportional to z. The complex amplitude E_r for the hollow matched beam may be written as

$$E_{ro}(r, z) = \left(\sqrt{2}r/r_o\right)E_o\exp(i\Delta k z)\exp(-(1 + i\theta_o)r^2/r_o^2) \tag{8}$$

where r_o, Δk, and θ_o are constants to be determined by the conditions for matching the beam to the channel. The coefficient E_o is related to the peak intensity of the laser beam. The radial field is zero on axis and has a peak value of $E_{o,\,\text{peak}} = E_o/\sqrt{e}$ at $r = r_o/\sqrt{2}$, where $e \approx 2.72$. The peak value should be below the permitted upper limit for the electric field.

We introduce the expression (8) into (6), and we find that

$$\left(-\frac{8}{r_o^2}(1 + i\theta_o)\left(1 - (1 + i\theta_o)\frac{r^2}{2r_o^2}\right) + k_\perp^2 - \frac{\omega_{po}^2}{c^2}\frac{\Delta n}{n_{po}}\frac{r^2}{r_c^2} - 2\Delta k k_o\right)E_{ro}(r, z) = 0. \tag{9}$$

In (9), we equate the real and the imaginary parts for the terms with like powers of r and we obtain the following conditions for the matched laser beam:

$$\theta_o = 0 \tag{10a}$$

$$\Delta k = \frac{k_\perp^2 - 8/r_o^2}{2k_o} \tag{10b}$$

$$r_o = \left(4r_c^2\frac{c^2}{\omega_{po}^2}\frac{n_{po}}{\Delta n}\right)^{1/4}. \tag{10c}$$

Setting the transverse wavenumber of the radially polarized hollow mode equal to $k_\perp = 2\sqrt{2}/r_o$, we find that $\Delta k = 0$. Then, the dispersion relation in (5) becomes

$$k_o^2 - \frac{n_o^2}{c^2}\omega_o^2 + \frac{\omega_{po}^2}{c^2} + \frac{8}{r_o^2} = 0. \tag{10d}$$

For comparison, note that for a matched laser beam having a Gaussian transverse profile, $k_\perp = 2/r_o$. A more proper approach for solving (6) is to make use of the source dependent expansion method (SDE) [15], [18]. The use of the SDE method results in small numerical differences with the expressions in (10a)–(10d) and for $k_\perp$.

We introduce (10) into (8) and (3), and we obtain the amplitude for the radial electric field of the hollow matched laser pulse

$$E_{ro}(r, z) = \left(\sqrt{2}r/r_o\right) E_o \exp(-r^2/r_o^2)\cos(k_o z - \omega_o t). \tag{11}$$

In order to obtain the phase velocity v_{ph} of the laser pulse, we solve the dispersion relation (10d) for k_o

$$v_{ph} = \frac{\omega_o}{k_o} = c(n_o^2 - \omega_{po}^2/\omega_o^2 - 8c^2/(\omega_o^2 r_o^2))^{-1/2}. \tag{12}$$

Equating the phase velocity to the speed of light yields the refractive index associated with the neutral gas

$$\begin{aligned} n_o &= (1 + \omega_{po}^2/\omega_o^2 + 8c^2/(\omega_o^2 r_o^2))^{1/2} \\ &\cong 1 + (1/2)\omega_{po}^2/\omega_o^2 + 4c^2/(\omega_o^2 r_o^2). \end{aligned} \tag{13}$$

The approximate form for n_o is based on the assumptions $\omega_o \gg \omega_{po}$ and $2\sqrt{2}c/r_o$.

IV. Accelerating Electric Field and Power

The accelerating electric field is the axial component associated with the radial component calculated above. The longitudinal component of the electric field is determined from the radial component by use of Gauss's law for the full electric field of the laser pulse. Neglecting the polarization charge, because $n_o \approx 1$, we may write the consistency equation as $\nabla \cdot \mathbf{E} \cong 0$. Then, the axial electric field associated with the matched hollow laser pulse may be calculated by use of the equation

$$\begin{aligned} \partial E_z/\partial z &\cong -(1/r)\partial(rE_r)/\partial r : \\ E_z(r, z, t) &\cong -E_{z,\max}\left(1 - \frac{r^2}{r_o^2}\right)\exp(-r^2/r_o^2) \\ &\quad \cdot \sin(k_o z - \omega_o t). \end{aligned} \tag{14}$$

The peak axial electric field occurs along the axis ($r = 0$), that is, where it is needed for the acceleration

$$E_{z,\text{peak}} = \frac{\sqrt{2}}{\pi}\frac{\lambda_o}{r_o}E_o. \tag{15}$$

The radial variation of E_r and E_z is shown in Fig. 2.

The laser power intensity in the predominately radially polarized hollow laser pulse is given by the following expression, when the assumption $n_o \approx 1$ is made:

$$I = \frac{c}{4\pi}\langle|\mathbf{E}\times\mathbf{B}|\rangle_t \cong \frac{c}{4\pi}E_o^2\frac{r^2}{r_o^2}\exp(-2r^2/r_o^2) \tag{16}$$

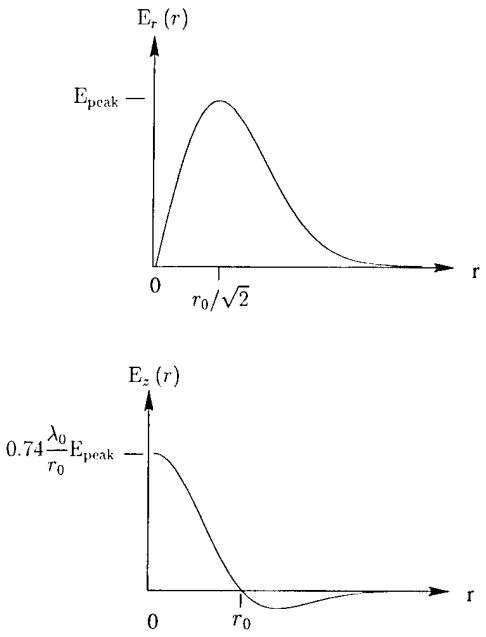


Fig. 2. Plots of the radial variation of the radial (E_r) and axial (E_z) components of the laser electric field. The axial field on axis is responsible for acceleration.

where $\langle\cdots\rangle_t$ denotes the time average operator. The power is then calculated easily as

$$P = \frac{c}{4\pi}\int_{\text{area}}\langle\mathbf{E}\times\mathbf{B}\rangle_t\, d\sigma \cong \frac{c}{16}r_o^2 E_o^2 \tag{17}$$

where the integral over the cross section of the laser beam is $\int_{\text{area}} d\sigma = 2\pi\int_0^\infty r\, dr$. Using (16) and (17), we find the peak value of the intensity in terms of the power and the spot size of the laser beam under the assumption $n_o \approx 1$

$$I_{\text{peak}} = \frac{c}{8\pi}E_o^2/e = \frac{2}{\pi e}P/r_o^2 \tag{18}$$

at $r = r_o/\sqrt{2}$, where $e \approx 2.72$. The spot size is related to the parameters of the problem through (10c).

It has been shown [16], [19] that for an ICA, it is advantageous to employ a laser having a Bessel beam profile as opposed to one having a Gaussian profile. That is, for equal laser beam powers, a Bessel beam results in a larger increase in electron energy. The advantage of a guided laser beam, as proposed here, is that in principle the interaction length can be much longer than that of a Bessel beam.

V. Numerical Illustration

As a numerical illustration, consider a radially polarized hollow laser pulse with wavelength $\lambda_o = 1$ μm, spot size $r_o = 20$ μm, and peak intensity $I_{\text{peak}} = 10^{12}$ W/cm^2 at $r = r_o/\sqrt{2} = 14.14$ μm. Using these values, we calculate peak radial electric field $E_o/\sqrt{e} = 2.75$ GV/m at $r = r_o/\sqrt{2} = 14.14$ μm, peak axial field $E_{z,\text{peak}} = 101.9$ MV/m on the axis, and total laser power $P = 17.1$ MW.

The refractive index of the neutral gas is specified by (13), i.e., $n_o \cong 1 + (1/2)\omega_{po}^2/\omega_o^2 + 4c^2/(\omega_o^2 r_o^2)$, which is the condition for the phase velocity to be synchronized with the speed of light. For $\lambda_o = 1$ μm and $n_o \approx 1$, the angular frequency

is $\omega_o \approx 1.885 \times 10^{15}$ rad/s. Taking the plasma density on the axis to be $n_{po} = 10^{16}$ cm^{-3}, we find $\omega_{po} = 5.64 \times 10^4 n_{po}^{1/2}$ rad/s $= 5.64 \times 10^{12}$ rad/s. Then, the first contribution to n_o is $(1/2)\omega_{po}^2/\omega_o^2 \approx 4.48 \times 10^{-6}$, and the second contribution is $4c^2/(\omega_o^2 r_o^2) \approx 2.53 \times 10^{-4}$. To achieve a refractive index of $n_o \approx 1 + 2.5 \times 10^{-4}$, we need a neutral gas with pressure $\sim$2 atm.

VI. Conclusion

A novel approach to inverse Cherenkov acceleration of electrons, employing a preformed plasma channel, is proposed. The plasma channel, having a density minimum on axis, fulfills the function of an optical guide, guiding the laser beam over many Rayleigh ranges. This, in principle, eliminates diffraction of the laser beam. Because the inverse Cherenkov acceleration process is inherently synchronous, this configuration is in principle capable of high-energy gains by extending the interaction length.

Acknowledgment

The authors acknowledge useful discussions with R. Hubbard, A. Ting, and C. Moore, and acknowledge the assistance of J. Penano.

References

[1] E. Esarey, P. Sprangle, J. Krall, and A. Ting, "Overview of plasma-based accelerator concepts," *IEEE Trans. Plasma Sci.*, vol. 24, pp. 252–288, 1996.

[2] P. Sprangle, E. Esarey, and J. Krall, "Laser driven electron acceleration in vacuum, gases and plasmas," *Phys. Plasmas*, vol. 3, pp. 2183–2190, 1996.

[3] Y. Ehrlich, C. Cohen, D. Kaganovich, A. Zigler, R. F. Hubbard, P. Sprangle, and E. Esarey, "Guiding and damping of high-intensity laser pulses in long plasma channels," *J. Opt. Soc. Am. B.*, vol. 15, pp. 2416–2423, 1998.

[4] H. M. Milchberg, T. R. Clark, C. G. Durfee, T. M. Antonsen, and P. Mora, "Development and applications of a plasma waveguide for intense laser pulses," *Phys. Plasmas*, vol. 3, pp. 2149–2155, 1996.

[5] K. Krushelnick, A. Ting, C. I. Moore, H. R. Burris, E. Esarey, P. Sprangle, and M. Baine, "Plasma channel formation and guiding during high intensity short pulse laser plasma experiments," *Phys. Rev. Lett.*, vol. 78, pp. 4047–4050, 1997.

[6] J. R. Fontana and R. H. Pantell, "A high-energy, laser accelerator for electrons using the inverse Cherenkov effect," *J. Appl. Phys.*, vol. 54, pp. 4285–4288, 1983.

[7] W. D. Kimura, G. H. Kim, R. D. Romea, L. C. Steinhauer, I. V. Pogorelsky, K. P. Kusche, R. C. Fernow, X. Wang, and Y. Liu, "Laser acceleration of relativistic electrons using the inverse Cherenkov effect," *Phys. Rev. Lett.*, vol. 74, pp. 546–549, 1995.

[8] W. D. Kimura *et al.*, "Advanced accelerator concepts," in *AIP Conf. Proc. 335*, P. Schoessow, Ed. New York: American Institute of Physics, 1995, pp. 563–580.

[9] T. B. Zhang, T. C. Marshall, M. A. LaPointe, J. L. Hirshfield, and A. Ron, "Microwave inverse Cherenkov accelerator," *Phys., Rev. E*, vol. 54, pp. 1918–1929, 1996.

[10] L. C. Steinhauer, R. D. Romea, W. D. Kimura, and J. R. Fontana, "Particle acceleration by laser fields in a dielectric disk-loaded waveguide," *J. Appl. Phys.*, vol. 83, pp. 5636–5643, 1998.

[11] P. Sprangle, E. Esarey, L. Krall, and A. Ting, "Vacuum laser acceleration," *Opt. Commun.*, vol. 124, pp. 69–73, 1996.

[12] E. Esarey, P. Sprangle, and J. Krall, "Laser acceleration of electrons in vacuum," *Phys. Rev. E*, vol. 52, pp. 5443–5453, 1995.

[13] B. Hafizi, A. Ting, E. Esarey, P. Sprangle, and J. Krall, "Vacuum beat wave acceleration," *Phys. Rev. E*, vol. 55, pp. 5924–5933, 1997.

[14] P. Sprangle, B. Hafizi, and R. F. Hubbard, "Ionization and pulse lethargy effects in inverse Cherenkov accelerators," *Phy. Rev. E*, vol. 55, pp. 5964–5975, 1997.

[15] P. Sprangle, A. Ting, and C. M. Tang, "Radiation focusing and guiding with application to the free electron laser," *Phys. Rev. Lett. 59*, pp. 202–205, 1987.

[16] B. Hafizi, E. Esarey, and P. Sprangle, "Laser driven acceleration with Bessel beams," *Phys. Rev. E*, vol. 55, pp. 3539–3545, 1997.

[17] P. Sprangle, B. Hafizi, and R. F. Hubbard, "Ionization and pulse lethargy effects in inverse Cherenkov accelerators," *Appl. Phys. Lett.*, vol. 70, pp. 2198–2200, 1997.

[18] P. Sprangle, A. Ting, and C. M. Tang, "Analysis of radiation focusing and steering in the free electron laser by use of the source dependent expansion technique," *Phys. Rev. A*, vol. 36, pp. 2773–2781, 1987.

[19] B. Hafizi, A. K. Ganguly, A. Ting, C. I. Moore, and P. Sprangle, "Analysis of Gaussian beam and Bessel beam driven laser accelerators," *Phys. Rev. E*, vol. 60, pp. 4779–4792, 1999.

P. Serafim (M'66–SM'77), photograph and biography not available at the time of publication.

Phillip Sprangle (M'90–SM'92–F'97) received the B.S. degree in electrical engineering from Polytechnic Institute of Brooklyn in 1968, the M.S. degree in chemistry from the University of Puerto Rico in 1969, and the Ph.D. degree in applied physics from Cornell University in 1972.

He is currently Chief Scientist for Radiation and Acceleration Physics and head of the Beam Physics Branch at the U.S. Naval Research Laboratory. He has served on the NRL staff since 1972. His primary areas of research in plasma physics include linear and nonlinear collective wave-particle processes, collective particle acceleration mechanisms, and radiation sources and processes based on relativistic electron beams. His research has concentrated on developing advanced concepts in accelerator physics and radiation source physics. His present theoretical research centers on laser driven accelerators, cyclotron masers, free electron lasers, and advanced high current accelerators. He has over 190 refereed journal publications and holds 11 U.S. patents. His theoretical accomplishments include the initial formulation and analysis of the nonlinear electron cyclotron maser instability, the modified betatron and laser wakefield accelerators, and efficiency enhancement and optical guiding in the free electron laser.

He was the winner of the 1986 E. O. Hulburt Award and the 1991 International Free Electron Laser Prize. He is a Fellow of the American Physical Society (APS), is an IEEE Fellow, was a member of the Executive Committee of the Division of Plasma Physics of the APS, and is a member of Sigma Xi. He was named one of Washington Technology's Top Ten Talents in 1989. In 1988, he received a Department of the Navy Senior Executive Service career appointment.

Bahman Hafizi (M'97) received the B.Sc. and Ph.D. degrees in physics from Imperial College, London, in 1974 and 1978, respectively.

He is currently President of ICARUS Research, Inc., Bethesda, MD. He previously worked as a Research Associate in the Department of Astro-Geophysics at the University of Colorado and as a Staff Scientist for Science Applications International Corporation. His current research areas of interest include propagation of ultra intense laser pulses, laser-driven electron accelerators, laser-plasma interactions, and nonlinear optics. He has also worked on advanced sources of electromagnetic radiation such as free electron lasers, laser synchrotron sources, and ultra broadband sources, with application to imaging, lithography, and remote sensing. Earlier research included studies of electromagnetic radiation from turbulent plasmas, Langmuir collapse, and nonlinear waves and dynamics. He is an associate of the Royal College of Science and a member of the American Physical Society, the European Physical Society, and IEEE.

Acceleration and Compression of Charged Particle Bunches Using Counterpropagating Laser Beams

Gennady Shvets, Nathaniel J. Fisch, and Alexander Pukhov

Abstract—**The nonlinear interaction between counterpropagating laser beams in a plasma results in the generation of large (enhanced) plasma wakes. The two beams need to be slightly detuned in frequency, and one of them has to be ultrashort (shorter than a plasma period). Thus produced wakes have a phase velocity close to the speed of light and can be used for acceleration and compression of charged bunches. The physical mechanism responsible for the enhanced wake generation is qualitatively described and compared with the conventional laser wakefield mechanism. We also demonstrate that depending on the sign of the frequency difference between the lasers, the enhanced wake can be used as a "snow-plow" to accelerate and compress either positively or negatively charged bunches. This ability can be used in an electron–positron injector.**

Index Terms—**Injectors, laser–plasma interactions, plasma accelerators.**

I. Introduction

PLASMA was suggested as an attractive medium for particle acceleration [1] because of the high electric field it can sustain. In a plasma-based accelerator [2], particles gain energy from a longitudinal plasma wave whose phase velocity is close to the speed of light. Excitation of such plasma wakes requires a relativistic driver, such as an electron beam in a plasma wakefield accelerator (PWA) [3] or a short laser pulse in laser wakefield accelerators (LWFA) [1]. The magnitude of the plasma wake in LWFA, measured in units of $E_{\rm wb} = mc\omega_p/e$, where $\omega_p = (4\pi e^2 n_0/m)^{1/2}$ is the plasma frequency, is approximately equal to $a_0^2/2$, where $a_0 = eA_0/mc^2$ is the normalized vector potential of the laser pulse. Here, n_0, $-e$, and m are the plasma electron density, electron charge, and mass, respectively. Because $a_0 = 1$ corresponds to the laser intensity $I_0 = 2.7 \times 10^{18}$ W/cm$^2/\lambda_0^2$ [μm], where $\lambda_0 = 2\pi c/\omega_0$ is the laser wavelength, a relatively high intensity is needed to produce an electric field comparable to $E_{\rm wb}$.

Recently, a novel approach to generating plasma wakes was suggested [4]. It employs two counterpropagating laser pulses: a short timing beam (TB) with frequency ω_0 and a long pumping beam (PB) with frequency ω_1. To produce a plasma wake of order $eE_z/mc\omega_p \sim \omega_p/\omega_0$, the TB has to be shorter than ω_p^{-1} and detuned from the PB by $|\Delta\omega = \omega_0 - \omega_1| \sim \omega_p$. Because this approach requires two colliding laser beams, it is referred to as a colliding beam accelerator (CBA). CBA has two important features: 1) the required intensities of the colliding laser pulses are much smaller than 10^{18} W/cm^2, and 2) the phase of the wake depends on the frequency detuning $\Delta\omega$. Feature 1) can be restated as follows: plasma wake due to the low-intensity short laser pulse alone is much smaller than the plasma wake due to the interference of the same short pulse with a long counterpropagating pulse. Therefore, the former wake is referred to as the "regular wake," and the latter wake is referred to as the "enhanced wake."

In this paper, we further elucidate the basic differences between the regular and enhanced wakes by exploring the analogy between the plasma wave excitation and the excitation of a pendulum. There are two ways to excite a pendulum: by displacing it and letting go, or by imparting it with momentum through an impulsive kick. It turns out that the excitation of the regular wake is analogous to the former, whereas the excitation of the enhanced wake is analogous to the latter. In addition, we demonstrate how CBA can be used as a compressor/injector of charged particle bunches. Because the phase (or, equivalently, the sign) of the enhanced wake can be controlled by the laser detuning $\Delta\omega$, such an injector can accelerate and compress either electron or positron bunches.

The basic idea of using a laser pulse as a "snow-plow" for direct ponderomotive acceleration in a plasma was recently suggested by McKinstrie and Startsev [5]. They found that if the group velocity of the laser pulse $v_g < c$, an intensity threshold, exists, past which an electron that initially moves with $v_0 < v_g$ can be accelerated to the velocity larger than the laser group velocity. The intensity threshold becomes infinite for a laser pulse moving with the speed of light. For the subthreshold intensities, the electron is eventually overtaken by the laser pulse without net energy gain. Du and Xu [6] later extended this idea by consistently taking into account the longitudinal electric field of the plasma (although assuming that the laser pulse is longer than the plasma period). They concluded that under these assumptions, electrons cannot be accelerated by the combined fields of the laser and plasma. Positrons, however, could be accelerated by the leading edge of the electrostatic potential produced in the plasma. Importantly, the intensity threshold does not diverge in the limit of $v_g \to c$. Unfortunately, the transverse electric field would sidescatter positrons unless some external focusing is applied.

Accelerators described in [5] and [6], where an injected particle is pushed by the leading edge of either the ponderomotive or the induced electrostatic potentials, can be referred to

Manuscript received November 1, 1999; revised April 3, 2000. This work was supported by the Department of Energy Division of High Energy Physics under Contract DE-FG030-98DP00210, and the Deutsche Forschungsgemeinschaft.

G. Shvets and N. J. Fisch are with the Princeton Plasma Physics Laboratory, Princeton University, Princeton, NJ 08543 USA.

A. Pukhov is with the Max-Planck-Institut für Quantenoptik, D-85748 Garching, Germany.

Publisher Item Identifier S 0093-3813(00)09725-3.

0093–3813/00$10.00 © 2000 IEEE

as the snow-plow accelerators. They differ from the conventional laser–plasma accelerators in that the final particle energy does not depend on the particle phase with respect to the plasma wake. As long as the intensity threshold is exceeded, the final energy of the particle, which is originally ahead of the pulse, is determined by the pure kinematics of the collision between a particle and a moving wall. From similar kinematic considerations, we conclude that an initially long bunch is compressed in the process of injection.

Although neither [5] and [6] suggested that a particle injector can be based on their ideas, such practical application is logical if two major drawbacks of the snow-plow acceleration can be overcome: 1) the mechanism only works for positrons, and 2) transverse electric field defocuses the accelerated particles. In this paper, we demonstrate how, in principle, the ideas of snow-plow acceleration and enhanced wake generation can be combined to construct such an injector. To do this, we develop a three-dimensional (3-D) theory of the CBA. The one-dimensional (1-D) theory was described in [4]. Other laser injection schemes, not based on the snow-plow acceleration, were recently suggested by Umstadter *et al.* [7] and Esarey *et al.* [8].

The remainder of the paper is organized as follows. In Section II, we present a qualitative 1-D analysis and numerical simulation of the CBA. The emphasis is on two properties of the enhanced plasma wake produced in a CBA: 1) large accelerating gradients (>1 GeV/m) can be obtained using laser pulses of subrelativistic ($\ll 10^{18}$ W/cm^2) intensities, and 2) the phase of the enhanced wake can be changed by $\Delta\phi = \pi$ by simply changing the sign of the frequency detuning between the timing and pumping beams. In Section III, we review the basics of the snow-plow acceleration in one dimension. The 3-D theory of the colliding beam accelerator in an almost-homogeneous plasma is derived in Section IV. Section V concludes.

II. One-Dimensional Theory of Colliding Beam Accelerator

To illustrate the concept of the CBA, the following physical problem was simulated using a 1-D particle-in-cell (PIC) code Virtual Laser Plasma Laboratory (VLPL) [9]. An ultrashort circularly polarized Gaussian laser pulse with duration $\tau_L = 1.5\omega_p^{-1}$ and normalized vector potential $a_0 = 0.12$, propagating in the positive z-direction, collides in a plasma with a long counterpropagating pulse with $a_1 = 0.05$. Plasma density was chosen such that $\omega_p/\omega_0 = 0.05$. The snapshot of the pulse intensity normalized to 2.7×10^{18} W/cm^2 is shown in Fig. 1(a). Two cases, corresponding to the different frequencies of the PB, $\omega_1 = 1.1\omega_0$ and $\omega_1 = 0.9\omega_0$, were simulated. The resulting plasma wakes are shown in Fig. 1(c) and (d), respectively. For comparison, we also plot the wake produced by a single TB in absence of the counterpropagating pulse in Fig. 1(b).

Because the intensity of the short pulse is chosen nonrelativistic, the magnitude of the plasma wake left behind the pulse is much smaller than the limiting (wavebreaking) field according to $E/E_{\rm wb} \sim a_0^2/2$. The situation changes dramatically when a counterpropagating beam is added. As Fig. 1(c) and (d) indicate, the addition of the pumping beam increases the electric field of the plasma wake by an order of magnitude. To

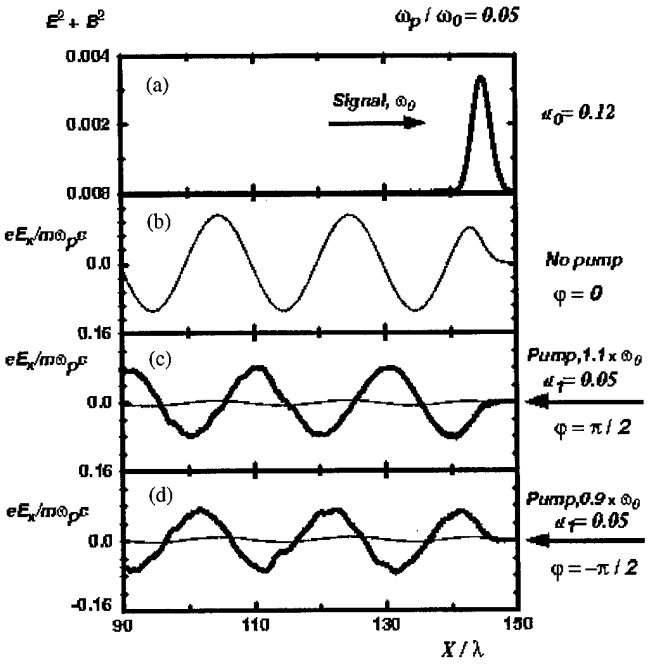


Fig. 1. Top to bottom: (a) single short laser pulse with $a_0 = 0.12$ and frequency ω_0 propagates from left to right; (b) short pulse generates a weak plasma wake E_x; (c) in the presence of counterpropagating pump with $a_1 = 0.05$ and frequency $\omega_1 = 1.1\omega_0$, the wake is enhanced, and its phase is shifted by $\pi/2$ with respect to the "regular" wake of (b), which is also shown for comparison; (d) same as (c), only a downshifted pump with $\omega_1 = 0.9\omega_0$ is used, and the phase shift is $-\pi/2$.

further illustrate this point, we plotted the regular wake [same as shown in Fig. 1(a)] in Fig. 1(c) and (d) for comparison. Note that the vertical scales of the Fig. 1(b)–(d) differ by a factor 20. Plasma wakes produced as a result of the collision between the counterpropagating beams is referred to as the enhanced wake because it can be much larger than the regular wake.

The origin of the enhanced wake can be qualitatively understood by comparing its phase with that of the regular wake. As the comparison of Fig. 1(b) and (c) indicates, the phase of the enhanced wake differs by $\Delta\phi = \pi/2$ from that of the regular wake. Recall that when a laser pulse of the duration $\tau_L < \omega_p^{-1}$ interacts with a plasma electron, an electron is displaced by $\xi_0 = c\int d\zeta |a_0|^2/2$ [10], where $\zeta = t - z/v_g$. The momentum gained by the electron from the laser pulse is small because the plasma response can be neglected for short pulse durations. Here, and elsewhere, we assume nonrelativistic laser intensities $a_{0,1} \ll 1$ for both the short and long pulses. Plasma is assumed tenuous, $\omega_p \ll \omega_0$, so that $\zeta \approx t - z/c$.

The above reasoning applies not only to a single plasma electron, but also to any small fluid element of the plasma. Fluid description is appropriate here because the electron displacement $|k_p\xi| \ll 1$ for a short laser pulse of nonrelativistic intensity. Therefore, electron trajectories do not cross, and the Lagrangian displacement of the fluid element at $z = z_0$ satisfies the harmonic oscillator equation $\ddot{\xi} + \omega_p^2\xi = 0$. The initial condition $\xi(z_0, t = z_0/c) = \xi_0$ and $\dot{\xi}(z_0, t = z_0/c) = 0$ is given along the world line of the short laser pulse that sets up the initial displacement ξ_0. The solution of the harmonic oscillator equation that satisfies this initial condition is $\xi = \xi_0 \cos\omega_p(t - z_0/c)$.

The electric field of the resulting plasma wake is found from $E_z = 4\pi e n_0 \xi$

$$\frac{eE_z}{mc\omega_p} = \frac{\omega_p \xi_0}{c}\cos\omega_p\zeta = \left(\frac{\sqrt{\pi}|a_0|^2}{2}\right)\cos\omega_p\zeta \qquad (1)$$

where we assumed that $a_0^2 \propto \exp[-\zeta^2/\tau_L^2]$.

Enhanced wake is shifted in phase by $\pi/2$ with respect to the regular wake because the initial conditions for every fluid element along the path of the short pulse are set up differently. Assume, for example, that every plasma fluid element is imparted with an initial velocity $\dot{\xi}_0$ instead of being initially displaced. With such an initial condition, the solution of the harmonic oscillator equation, $\xi = (\dot{\xi}_0/\omega_p)\sin\omega_p(t - z_0/c)$, exhibits the observed from the simulations phase shift. The initial velocity is imparted to the plasma via the backscattering of the long pulse into the short one (or vice versa, depending on the frequency detuning $\Delta\omega$), as explained below. Note that the backscattering takes place off the driven (nonresonant) plasma density perturbation, which is excited over a very short period of time $\tau_L \sim \omega_p^{-1}$. The frequency difference $\delta\omega$ need not (and is not in the example illustrated by Fig. 1) be equal to ω_p, distinguishing the mechanism of the enhanced wakefield generation from the usual Raman backscattering. By analogy to the plasma beatwave accelerator, an ultrashort TB could, in principle, be substituted by two longer beams separated in frequency by ω_p.

When two counterpropagating laser pulses interfere, an almost-standing intensity wave is produced. Its spatial and temporal periods are $2\pi/(k_0 + k_1) \approx \pi/k_0$ and $2\pi/\Delta\omega$, respectively. This intensity grating is slowly moving with the speed $v_{\rm ph} = \Delta\omega/(2k_0) \ll c$ and in the limit of the monochromatic beams becomes a standing wave. Plasma electrons are affected by the ponderomotive force $\vec{F} = -\nabla\Phi_p$, which is proportional to the gradient of the ponderomotive potential $\Phi_p = mc^2|a^2|/2$, created by the interference of the two lasers. This ponderomotive force, directed along the z-axis, is given by $F_p = 2k_0 a_0 a_1 \cos(2k_0 z - \Delta\omega t)$.

It is convenient to introduce an electron ponderomotive phase $\psi_j = 2k_0 z_j - \Delta\omega t$ of the jth particle inside a given ponderomotive period. Using this definition and the expression for the ponderomotive force, a useful quantity $\omega_B^2 = 4\omega_0^2 a_0 a_1$ can be constructed that has the dimension of the frequency squared, and it characterizes the strength of the ponderomotive force. If $\omega_B^2 > \omega_p^2$, the Coulomb interactions between the plasma electrons can be neglected in comparison with the ponderomotive force. Equation of motion for the j's electron in this case is particularly simple

$$\ddot{\psi}_j + \omega_B^2(\zeta)\sin\psi_j = 0 \qquad (2)$$

where, as before, a dot denotes a derivative with respect to time t or the comoving coordinate $\zeta = t - z/c$. The functional dependence of ω_B on ζ is determined by the longitudinal profile of the short pulse; the bounce frequency vanishes before and after the timing beam.

Plasma electrons, initially stationary in the laboratory frame, enter the time-dependent ponderomotive bucket with the initial "speed" $\dot{\psi} = -\Delta\omega$. If this speed is smaller than the bucket height $\dot{\psi}_{\max} = 2\omega_B$, some electrons (with the appropriate initial ponderomotive phase) become trapped and execute a synchrotron oscillation in the bucket. It turns out that by appropriately choosing the pulse duration and frequency detuning, a substantial average momentum P_z can be imparted to plasma electrons. Clearly, depending on their initial phase ψ_j, some electrons will gain positive or negative momentum. The emphasis, however, is on the average momentum transferred to a fluid element of size $\lambda_0/2$. The sign and magnitude of P_z varies on a scale of the short pulse duration, which is assumed much larger than $\lambda_0/2$. This constitutes the major difference between the generation mechanisms of the regular and enhanced wakes. In the case of a regular wake, the fluid description on all spatial scales is completely adequate. In the case of an enhanced wake, fluid description is sufficient on a long spatial scale (of order $c\tau_L$ or c/ω_p). Fully kinetic treatment may be necessary on a short scale of the ponderomotive period.

To model the electron dynamics on a scale of one ponderomotive period, we assume that the TB has a Gaussian temporal profile, $\omega_B^2(\zeta) \equiv \omega_B^2 \exp(-\zeta^2/2\tau_L^2)$, and solve the nonlinear pendulum equation (2) for an ensemble of test electrons. Before the arrival of the TB (at $\zeta = -\infty$), the electrons are uniformly distributed in phase $0 < \psi_j < 2\pi$ and have identical $\dot{\psi}_j = -\Delta\omega$. The average momentum P_z, gained by the electrons after the interaction, is calculated as $P_z = (m/2k_0)\sum_j \Delta\dot{\psi}_j$, where $\Delta\dot{\psi}_j = \dot{\psi}_j(\zeta = +\infty) - \dot{\psi}_j(\zeta = -\infty)$. In the color plot of Fig. 2, P_z is shown as the function of the normalized pulse duration $\omega_B\tau_L$ and frequency detuning $\Delta\omega/\omega_B$. From Fig. 2, the average momentum, gained by the electrons, has the same sign as the frequency detuning.

The largest average momentum gain $P_z \approx mc\Delta\omega/\omega_0$ is realized for $\Delta\omega \approx \omega_B$ and $\tau_L \approx 2/\omega_B$. For these parameters, most of the electrons execute half of a bounce in the ponderomotive bucket. Other bright color streaks in Fig. 2 correspond to the electrons executing 3/2, 5/2, etc., bounces. For those higher order resonances, P_z is maximized for longer pulse durations τ_L. If the pulse duration is longer than ω_p^{-1}, the neglected space-charge terms are likely to wash out these higher order resonances and to reduce P_z. The nonzero momentum transfer to the plasma electrons is due entirely to the short duration of the TB. Although it was long recognized [11], [18] that the interaction between laser beams in the plasma results in the momentum transfer to plasma electrons and ions, most calculations assumed long laser beams, in which case, most of the momentum was transferred to the ions.

The kinetic modeling presented above provides the averaged value of the transferred momentum as an input for a long-scale fluid calculation. Namely, with an initial condition for the fluid element velocity $\dot{\xi}_0 = P_z/m$, we calculate the electric field of the enhanced wake as

$$\frac{eE_z}{mc\omega_p} = \frac{\langle P_z\rangle}{mc}\sin\omega_p\zeta \approx \left(\frac{\Delta\omega}{\omega_0}\right)\sin\omega_p\zeta. \qquad (3)$$

In deriving (3), we assumed that the initial displacement of the fluid element $\xi_0 = 0$. This is because, as we observe from (2), plasma electrons k and j are "clamped" at the opposite sides of the ponderomotive period, $\psi_k = 0$ and $\psi_j = 2\pi$. Comparison between (1) and (3) indicates that the phase shift between the

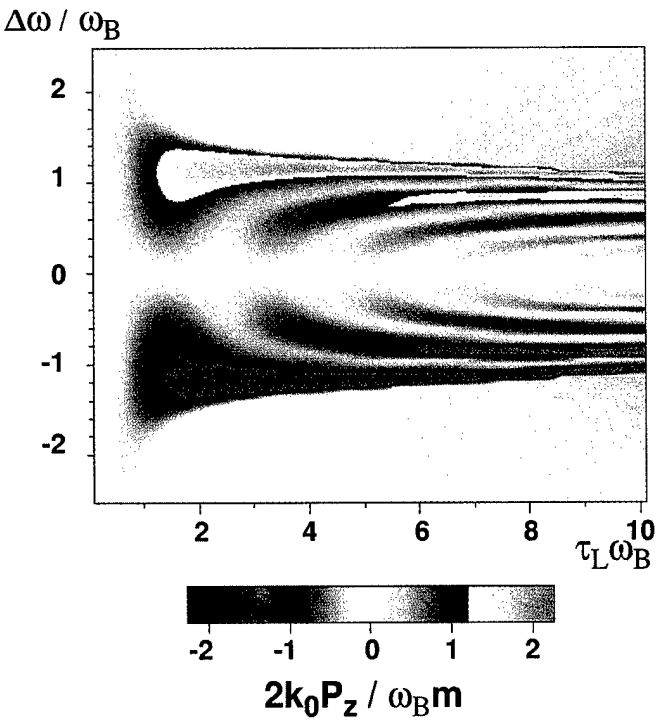


Fig. 2. Average momentum P_z gained by plasma electrons in the ponderomotive bucket as a function of the normalized TB duration $\omega_B \tau_L$ (horizontal axis) and the frequency detuning $\Delta\omega/\omega_B$ (vertical axis).

regular and the enhanced wakes is $\pi/2$, just as observed from Fig. 1(b) and (c). Moreover, changing the sign of the frequency detuning $\Delta\omega$ shifts the phase of the enhanced wake by π, in agreement with the simulations results from Fig. 1(c) and (d).

To conclude this section, we present an alternative derivation of the enhanced wake in one dimension that will be extended to three dimensions in Section IV. The electric field of the enhanced wake can be interpreted as a displacement current. As the photons are exchanged between the counterpropagating beams, electrons, on average, acquire the recoil momentum P_z and produce a nonlinear current $J_{\rm NL} = -en_0 P_z/m$. In 1-D, any current flowing through the plasma must be balanced by the displacement current [11], [18]. Therefore, an electric field E_z is produced, satisfying Ampeze's law $\partial E_z/\partial t = -4\pi J_z$, where J_z is the combined current in the plasma. Two flows contribute to J_z: the linear plasma flow in the field of the enhanced wake $J_f = -en_0 v_f$, and the nonlinear (space-averaged) flow $J_{\rm NL}$. Taking the time derivative of Ampeze's law (with $\nabla \times \vec{B} = 0$), we obtain

$$\left(\frac{\partial^2}{\partial \zeta^2} + \omega_p^2\right) E_z = -4\pi \frac{\partial J_{\rm NL}}{\partial \zeta}. \tag{4}$$

Equation (3) for the enhanced wake can be recovered from (4) by assuming that $J_{\rm NL}(\zeta) = -en_0 P_z/mH(\zeta)$. This assumption is justified when the TB duration is shorter than ω_p^{-1}.

III. Snow-Plow Acceleration: One-Dimensional Calculation

In this section, we explain how a combination of the ponderomotive force of a short laser pulse and plasma wake can be used to accelerate charged particles to the velocity exceeding the group velocity of a laser pulse in the plasma. The original idea of using ponderomotive force of the leading edge of a laser pulse to accelerate a charged particle (electron or positron) was suggested by McKinstrie and Startsev [5]. They found that if the particle is initially ahead (to the right) of the laser pulse moving with the group velocity $v_g = \beta_g c$, and its initial velocity $v_0 = \beta_0 c < v_g$, if the intensity of the laser pulse is sufficiently high, the particle can bounce off the laser pulse, gaining energy as the result. This calculation can be extended to the case of the laser pulse moving through the plasma.

In the reference frame moving with v_g, the initial energy-momentum of the particle are $\gamma' = \gamma_g\gamma_0(1 - \beta_g\beta_0)$ and $p' = \gamma_g\gamma_0(\beta_0 - \beta_g)$. Primed variables are calculated in the reference frame moving with the pulse. In the pulse frame, the particle velocity is negative if in the laboratory frame, $\beta_0 < \beta_g$. However, if the pulse is sufficiently intense, the particle can reflect off the pulse, reversing the sign of its momentum in the pulse frame. Transforming back to the laboratory frame, we find that, after reflection, the final particle energy is

$$\gamma_f = \gamma_0\gamma_g^2\left(1 + \beta_g^2 - 2\beta_g\beta_0\right). \tag{5}$$

The final energy does not depend on the exact details of the force experienced by the particle: in one dimension, energy and momentum can be expressed as functions of the interaction potential, which vanishes before and after the interaction. Therefore, (5) is simply a consequence of the conservation of energy and momentum.

For a laser pulse in vacuum, McKinstrie and Startsev found that a threshold laser intensity needed for reflecting an electron (or positron) is given by $a_0^2 = \gamma_g^2\gamma_0^2(1 - \beta_g\beta_0)^2 - 1$. This estimate also holds for a tenuous plasma, provided that the pulse is shorter than ω_p^{-1}. Note that for a pulse moving with a speed of light, the threshold intensity diverges.

In the presence of a dense plasma, the threshold for electrons is further increased because the ponderomotive pressure of the laser pulse on the ambient electron plasma leads to charge separation. The resulting electrostatic potential effectively decreases the ponderomotive potential of the laser pulse experienced by the electrons injected for acceleration. The situation is, however, reversed for positrons, as was pointed out by Du and Xu [6]. Moreover, because in the case of positrons injected into electron, plasma acceleration is done directly by the electric field, not by the ponderomotive force, the laser intensity threshold for snowplowing positrons remains finite. To see why this is the case, consider the 1-D equations of motion for a particle with charge $q = \pm e$ and mass m.

By conservation of the transverse canonical momentum, $\vec{v}_\perp = -(q/e)\vec{a}/\gamma$, where $\gamma = (1 + a^2 + u_z^2)^{1/2}$ and $u_z = \gamma\beta_z$. The corresponding equations for u_z and γ become

$$\frac{du_z}{dt} = -c\frac{\partial\tilde{\Phi}}{\partial z} - \frac{c}{2\gamma}\frac{\partial|a|^2}{\partial z} \tag{6}$$

$$\frac{d\gamma}{dt} = -\frac{cu_z}{\gamma}\frac{\partial\tilde{\Phi}}{\partial z} + \frac{1}{2\gamma}\frac{\partial|a|^2}{\partial t} \tag{7}$$

where the electric field is proportional to the derivative of $\tilde{\Phi}$: $E_z = -(mc^2/q)\partial\tilde{\Phi}/\partial z$. In a 1-D plasma wake, all fields are

functions of ζ alone; so the normalized potential $\tilde{\Phi}$ can always be introduced as an integral of E_z over ζ.

The first terms in the RHS of (6) and (7), which describe the electric field of the wake, dominate over the second (ponderomotive) terms for large γ. Therefore, in the remainder of the paper, we neglect the direct ponderomotive force. The opposite limit of $\gamma_g\tilde{\Phi} < |a^2|$ was taken in [5], where the vacuum threshold intensity was obtained. The complete system of (6) and (7), along with the Poisson's equation for $\tilde{\Phi}$, was earlier considered by Sprangle *et al.* [12].

From the invariant of the equations of motion $\gamma+\tilde{\Phi}-\beta_g u_z = \gamma_0(1-\beta_0\beta_g)$ and $\gamma^2 \approx 1+u_z^2$ (we dropped the $|a^2|$ term), particle momentum can be expressed as a function of $\tilde{\Phi}$

$$u_z = \gamma_g\left[\beta_g\gamma_g(C_0-\tilde{\Phi}) \pm \sqrt{\gamma_g^2(C_0-\tilde{\Phi})^2-1}\right] \quad (8)$$

$$\gamma = \gamma_g\left[\gamma_g(C_0-\tilde{\Phi}) \pm \beta_g\sqrt{\gamma_g^2(C_0-\tilde{\Phi})^2-1}\right] \quad (9)$$

where $C_0=\gamma_0(1-\beta_g\beta_0)$. The plus (minus) sign corresponds to a particle that is moving faster (slower) than the laser pulse. The switching from minus to plus signs takes place when the expression under the square root vanishes. This happens at ζ_r, which corresponds to $\tilde{\Phi}(\zeta_r) = C_0-\gamma_g^{-1}$. The accelerating potential has to be larger than this threshold value to ensure the snow-plow acceleration. It can be shown that $C_0-\gamma_g^{-1}>0$, so that a positive (negative) potential is required for accelerating positrons (electrons).

The most interesting case is $\gamma_0 \ll \gamma_g$. The final energy of the accelerated particle is then approximately given by $\gamma_f = \gamma_g^2/\gamma_0$. The threshold condition for snow-plow acceleration also simplifies to $\tilde{\Phi} > (2\gamma_0)^{-1}$. Therefore, the initially fast particles with $1 \ll \gamma_0 \ll \gamma_g$ are easier to trap than are the stationary ones. The relative energy boost γ_f/γ_0 is, however, decreased in the same proportion.

The relative energy boost is related to the bunch compression ratio. By conservation of the longitudinal phase space, $l_f\delta\gamma_f = l_0\delta\gamma_0$, where l_f and l_0 are the final and initial bunch lengths, and $\delta\gamma_f$ and $\delta\gamma_0$ are the final and initial energy spreads, respectively. Because the final energy scales as γ_0^{-1}, the final and initial energy spreads are related through $|\delta\gamma_f/\delta\gamma_0| = \gamma_f/\gamma_0$. Therefore, both the energy can be boosted and the bunch length decreased by a large factor γ_g^2/γ_0^2 if $\gamma_0 \ll \gamma_g$.

We arrive at the same result by requiring that the beam density remains unchanged in the reference frame of the laser pulse, where a particle bunch is scattered by a stationary potential. Using Lorenz transformation, the particle density n' in the pulse frame can be expressed in terms of the initial and final densities n_0 and n_f, respectively

$$\gamma_g n_0(1-\beta_0\beta_g) = n' = \gamma_g n_f(1-\beta_f\beta_g). \quad (10)$$

Therefore, $n_f/n_0 = (1-\beta_0\beta_g)/(1-\beta_f\beta_g)$. This ratio is equal to γ_f/γ_0 because the particle energy in the primed frame remains the same before and after the reflection: $\gamma_g(\gamma_0-\beta_g u_0) = \gamma_g(\gamma_f-\beta_g u_f)$. The bunch compression ratio l_f/l_0 is then given by $l_f/l_0 = n_0/n_f = \gamma_0/\gamma_f$.

One possible application of the snow-plow acceleration is an injector capable of accelerating and compressing initially low-energy long particle bunches. Because the ability to inject both electrons and positrons is crucial, such an injector should be able to produce positive as well as negative potential wells. Colliding beam accelerator can accomplish just that by adjusting the frequency detuning $\Delta\omega$ between lasers. The examples of the electron and positron injectors are shown in Fig. 1(c) and (d), respectively. Note an important difference in the dynamics of the cold ambient plasma electrons and the initially relativistic electrons injected into the plasma just ahead of the laser pulse. Although the slow plasma electrons experience the beatwave of the counterpropagating laser pulses, the fast electrons are barely affected by the beatwave ponderomotive force because the phase velocity of the beatwave is much smaller than the speed of light.

Let us calculate the maximum normalized potential $\tilde{\Phi}$ produced in a CBA using Fig. 1(c) as a blueprint for an electron injector. Assuming $\Delta\omega \approx -\omega_p$ and using (3), obtain, for injected electrons, $\tilde{\Phi} \approx \omega_p/\omega_0(1-\cos\omega_p\zeta)$. Therefore, the condition for the snow-plow acceleration becomes $2\omega_p/\omega_0 > (2\gamma_0)^{-1}$, or $\gamma_0 > \omega_0/4\omega_p$. The presence of the plasma naturally reduces the group velocity of the laser pulse: $\gamma_g = \omega_0/\omega_p$. Therefore, if the initial energy of the electron bunch is inside the interval $\omega_0/4\omega_p < \gamma_0 < \omega_0/\omega_p$, CBA can be used for snow-plow acceleration/bunch compression.

To calculate the interaction distance required to accomplish the snow-plow acceleration, approximate the normalized potential by a linear function, assuming for simplicity that $C_0-\tilde{\Phi} \equiv X = C_0(1-\zeta/\tau_g)+\gamma_g^{-2}$, where $\tau_g = \pi/\omega_p$ is a typical gradient scale, approximately set equal to ω_p^{-1}. The reflection point $\zeta_r = \tau_g$ and the starting (and final) point is $\zeta \approx 0$. Expanding (8) and (9) in the limit of $\beta_g \approx 1$ and using $\dot{\zeta} = 1-u_z/(\beta_g\gamma)$, we obtain the following equation of particle motion relative to the moving potential:

$$\frac{d\zeta}{dt} = \frac{\sqrt{X^2-\gamma_g^{-2}}\left(X+\sqrt{X^2-\gamma_g^{-2}}\right)}{1+X^2} \quad (11)$$

which is solved with initial condition $\zeta(t=0)=0$ (or $X=C_0$). The time it takes a particle to reach $\zeta=\tau_g$ and return back to $\zeta=0$ is given by

$$t_{ac} = \left(\frac{2\tau_g\gamma_g^2}{C_0}\right)\int_{\gamma_g^{-1}}^{C_0}\frac{dX\,X}{\sqrt{X^2-\gamma_g^{-2}}} = 2\tau_g\gamma_g^2\sqrt{1-C_0^{-2}\gamma_g^{-2}}. \quad (12)$$

In the limit of $\gamma_g C_0 \gg 1$, we find that $t_{ac} \approx 2\tau_g\gamma_g^2$. To gain more physical insight into this result, note that average acceleration gradient is equal to the $\langle W\rangle = mc^2\gamma_f/(ct_{ac}) = mc^2C_0/(c\tau_g)$, which is precisely the magnitude of the electric field.

Consider the following numerical example: plasma with density $n_0 = 2.5\cdot 10^{18}$ cm^{-3} (corresponding to $\omega_0/\omega_p = 20$) is used as a medium for compressing a 3.2-MeV electron bunch of 1-ps duration. Because $\gamma_g^2/\gamma_0^2 = 10$ for this example, the output of such an injector is a 100-fs, 32-MeV electron bunch. The required plasma length is estimated $ct_{ac} = 2.6$ mm by assuming that $\tau_g = \omega_p^{-1}$.

One-dimensional treatment of a snow-plow injector is sufficient only to determine its accelerating properties. A full 3-D description of the transverse electric and magnetic fields of the injector is needed to study the transverse particle dynamics. It is essential that the accelerated particles are focused to (or, at least, not defocused from) the laser axis. As McKinstrie and Startsev point out in [5], one of the limitations of the direct laser acceleration by the leading edge of the pulse is that the particles are scattered off-axis, and a very wide laser beam is needed to prevent particles from scattering out of the beam. The same drawback is found in the positron injector scheme of Du and Xu [6], where a long ($\gg\omega_p^{-1}$) laser pulse is used to adiabatically produce an electrostatic potential $\tilde{\Phi}$. Because the shape of this potential follows the shape of the laser intensity, it is peaked on axis, causing positrons to scatter out of the beam.

Although in this section we used the potential description of the longitudinal (accelerating) electric field, this was only done for notational convenience: an integral $\tilde{\Phi} = (q/mc)\int d\zeta\, E_z$ can always be introduced whether the electric field is curl-free (electrostatic). In one dimension, the E-field is always curl-free, so there is no need to introduce the distinction between the actual scalar potential and the quantity $\tilde{\Phi}$ defined above—both are the same. If the electric field is electrostatic in 3-D, and the accessible region for positrons (electrons) is $\tilde{\Phi} > 0$ ($\tilde{\Phi} < 0$), particles are going to be defocused from the axis if $|\tilde{\Phi}|$ peaks on-axis. In three dimensions, the enhanced wakefield is not curl-free. The full 3-D theory of CBA is developed in the next section.

IV. Three-Dimensional Theory of CBA

At the end of Section II, we presented an alternative derivation of the equation for the electric field in a CBA. This derivation was based on splitting the total current $\vec{J}$ flowing through the plasma into two components: the linear plasma flow in the field of the enhanced wake $\vec{J}_f = -en_0\vec{v}_f$ and nonlinearly generated recoil current $\vec{J}_{\rm NL} = -\hat{z}en_0P_z/m$, which is produced via the photon exchange between the counterpropagating laser beams. Plasma flow velocity $\vec{v}_f$ satisfies the linearized equation of motion $\partial\vec{v}_f/\partial t = -e\vec{E}/m$, where $\vec{E}$ is the enhanced wake field. In Section II, we assumed that $\vec{B} = 0$, as appropriate for a 1-D calculation. In this section, we keep the magnetic field, which is crucial for determining the focusing/defocusing properties of the enhanced wake. Almost-homogeneous plasma is assumed to avoid the subtleties associated with the wake excitation in plasma channels [13].

Taking the curl of the Lenz's law, substituting into the resulting formula the time derivative of the Ampere's law, and the using the equation of motion for the linear plasma flow, we obtain

$$\left(\frac{\partial^2}{\partial t^2} + \omega_{p0}^2\right)\vec{E} + c^2\nabla\times\nabla\times\vec{E} = -4\pi\frac{\partial\vec{J}_{\rm NL}}{\partial t}. \tag{13}$$

The density perturbation, related to $\vec{E}$ through the Poisson's equation, can be found by taking the divergence of (13) and assuming that $\vec{J}_{\rm NL} = \vec{e}_z J_{\rm NL}(\zeta, \vec{x}_\perp)$

$$\rho = \frac{J_{\rm NL}}{c} - \frac{\omega_p}{c}\int_{-\infty}^{\zeta} d\zeta' \sin\omega_p(\zeta-\zeta')J_{\rm NL}. \tag{14}$$

Electric field can now be solved component by component. First, the accelerating field is obtained by substituting ρ into (13)

$$\left(-\nabla_\perp^2 + k_{p0}^2\right)E_z = -4\pi k_{p0}^2\int_{-\infty}^{\zeta} d\zeta' \cos\omega_p(\zeta-\zeta')J_{\rm NL}. \tag{15}$$

For a wide beam, $\nabla_\perp^2 \ll k_{p0}^2$, and (15) yields the same expression for E_z as (4). Equation (15) is identical to the one derived by Keinigs and Jones [14] for a beam-driven PWA in the limit of $\beta_g = 1$. The key difference is that in a CBA, the current $J_{\rm NL}$, which drives the enhanced wake, is generated through the interaction between the counterpropagating laser pulses and not by an external electron beam. An important advantage of such "virtual beam" is that it can carry positive as well as negative current while propagating in the positive z-direction. By changing the sign of the frequency detuning between lasers in a CBA, we achieve the same effect as switching from electron to positron driver in a PWA.

The transverse component of the electric field $\vec{E}_\perp$ can be similarly calculated from (13) and (14). Using (15), it can be, moreover, shown that $\vec{E}_\perp$ is related to E_z through

$$\vec{E}_\perp = \frac{c}{\omega_{p0}^2}\vec{\nabla}_\perp\left(\frac{\partial E_z}{\partial\zeta}\right). \tag{16}$$

Let us consider the case of $E_z > 0$, which is peaked on axis, i.e., a positron injector. This corresponds to $\Delta\omega > 0$, when the short pulse photons scatter into the pump and deposit positive momentum into plasma electrons. This generates an increase in electron density on-axis, pulling positrons toward the axis. Equation (16) leads to the same conclusion: $E_{x,y} < 0$. However, $\vec{E}_\perp$ is not the only field that affects the transverse particle dynamics. Magnetic field generated by the "virtual beam" defocuses relativistic positrons. The equation for the transverse wakefield $\vec{W} = \vec{E}_\perp + \hat{z}\times\vec{B}$ that determines the transverse dynamics of ultrarelativistic particles is derived from the Lenz's law by assuming that both the electric and magnetic fields depend on the $\zeta \approx t - z/c$

$$\vec{W} = -c\int_{-\infty}^{\zeta}\vec{\nabla}_\perp E_z. \tag{17}$$

Equation (17), which is the Panowski–Wenzel theorem, indicates that whenever $|E_z|$ is peaked on-axis, the transverse wake defocuses the particles. Note that this conclusion can only be drawn for snow-plow acceleration, which takes place inside the leading portion of the enhanced wake where the sign of E_z does not change. If we were to use the wakefield shown in Fig. 1(c) for accelerating positrons in the second half-period of the wake (counting from the head of the laser pulse), the integral of the gradient of the accelerating field E_z in the RHS of (17) is positive, so that $W < 0$ in that region. If, however, we were to use the same wake for snow-plow acceleration of electrons in the leading portion of the wake, the transverse wake W is still negative, and electrons are defocused.

It appears that to ensure focusing during snow-plow acceleration, it is essential to generate a somewhat unusual accelerating

field profile, which has a local minimum of $|E_z|$ on-axis. Assuming that the laser spotsize is much larger than k_p^{-1}, we find that the transverse profile of E_z follows the transverse profile of $J_{\rm NL}$ according to (4). Therefore, producing a local minimum of $|E_z|$ requires generating $J_{\rm NL}$ with a local minimum on axis. Such a current profile would be challenging to produce using a finite emittance external beam driver. It appears that it can be produced in a CBA if plasma density has a minimum on-axis (plasma channel).

To see this, consider (3) for E_z, which indicates that for a fixed $\Delta\omega$, the magnitude of E_z at a given ζ is proportional to ω_p. Frequency detuning $\Delta\omega$ is yet another knob that can be tuned to maximize current deposition off-axis. We conjecture that by the proper choice of the plasma channel width, frequency detuning, and laser intensity, the desired profile of E_z can be produced to ensure particle focusing during snow-plow acceleration. Plasma channels, which have been produced in the laboratory [15], [16], [19], [20] play another beneficial role of guiding the laser pulse over extended distances much larger than the Rayleigh length. Three-dimensional particle simulations will be used in the future to demonstrate the focusing properties of the CBA injector.

Another way of avoiding particle defocusing is to use a hollow plasma channel. As was demonstrated in earlier publications [17], [21], evacuated channels with plasma outside have attractive accelerating properties, including a homogeneous accelerating field inside the channel. According to (17), the transverse wake vanishes inside the hollow channel. Closely following the calculations of [17] for a flat plasma channel of width b, we find two major differences in the wake excitation from that in a homogeneous plasma: 1) the wavelength of the plasma wake is $2\pi c\sqrt{1+k_{p0}b}/\omega_{p0}$, and 2) the amplitude of the wake is reduced by a factor $\sqrt{1+k_{p0}b}$ from its value given by (3).

V. Conclusion

In this paper, we presented a qualitative description of the CBA in one dimension, followed by the fully 3-D calculation of the plasma wakes generated by two counterpropagating laser beams. We reviewed the earlier ideas of snow-plow acceleration by the leading edge of the laser pulse and demonstrated how the concepts of CBA and snow-plow acceleration can be combined for particle injection and pulse compression. Some of the limitations of the earlier considered snow-plow accelerators are the large threshold intensity of the laser pulse, the inability to accelerate both electrons and positrons, and the strong sidescatter of the accelerated particles.

The suggested approach based on a CBA concept gets around these drawbacks. Laser intensity needed for snowplowing is reduced due to the strong nonlinear interaction among counterpropagating laser beams. The sign of the accelerating potential can be readily reversed by changing the frequency detuning among the lasers, enabling acceleration of either positive or negative charges. An example of bunch compression/acceleration is presented. We also conjecture that particle defocusing can be avoided by employing a plasma channel. This idea needs further investigation using 3-D particle simulations. Using a hollow plasma channel is yet another possibility to avoid particle defocusing.

References

[1] T. Tajima and J. M. Dawson, "Laser electron accelerator," *Phys. Rev. Lett.*, vol. 43, p. 267, 1979.

[2] E. Esarey, P. Sprangle, J. Krall, and A. Ting, "Overview of plasma-based accelerator concepts," *IEEE Trans. Plasma Sci.*, vol. 24, p. 252, 1996.

[3] P. Chen, J. M. Dawson, R. W. Huff, and T. Katsouleas, "Acceleration of electrons by the interaction of a bunched electron beam with a plasma," *Phys. Rev. Lett.*, vol. 54, p. 693, 1985.

[4] G. Shvets, N. J. Fisch, A. Pukhov, and J. Meyer-ter-Vehn, "Generation of periodic accelerating structures in plasma by colliding laser pulses," *Phys. Rev. E*, vol. 60, p. 2218, 1999.

[5] C. M. McKinstrie and E. A. Startsev, "Electron acceleration by a laser pulse in a plasma," *Phys. Rev. E*, vol. 54, p. 1070, 1996.

[6] C. Du and Z. Xu, "Particle acceleration by a leading edge of a laser pulse in a plasma," Europh. Lett., to be published.

[7] D. Umstadter, J. K. Kim, and E. Dodd, "Laser injection of ultrashort electron pulses into wakefield plasma waves," *Phys. Rev. Lett.*, vol. 78, p. 2073, 1996.

[8] E. Esarey, R. F. Hubbard, W. P. Leemans, A. Ting, and P. Sprangle, "Electron injection into plasma wakefields by colliding laser pulses," *Phys. Rev. Lett.*, vol. 79, p. 2682, 1997.

[9] A. Pukhov, "Three-dimensional electromagnetic relativistic particle-in-cell code VLPL (Virtual Laser Plasma Lab)," *APS Bull.*, vol. 41, p. 1502, 1996.

[10] J.-M. Rax and N. J. Fisch, "Ultrahigh intensity laser–plasma interaction: A Lagrangian approach," *Phys. Fluids B*, vol. 5, p. 2578, 1993.

[11] J. Dawson, *From Particles to Plasmas*. Reading, MA: Addison-Wesley, 1988.

[12] P. Sprangle, E. Esarey, and A. Ting, "Nonlinear interaction of intense laser pulses in plasmas," *Phys. Rev. A*, vol. 41, p. 4463, 1990.

[13] G. Shvets and X. Li, "Theory of laser wakes in plasma channels," *Phys. Plasmas*, vol. 6, p. 591, 1999.

[14] R. Keinigs and M. Jones, "Two-dimensional dynamics of the plasma wakefield accelerator," *Phys. Fluids*, vol. 30, p. 252, 1987.

[15] C. G. Durfee III and H. M. Milchberg, "Light pipe for high-intensity laser pulses," *Phys. Rev. Lett.*, vol. 71, p. 2409, 1993.

[16] Y. Ehrlich, C. Cohen, A. Zigler, J. Krall, P. Sprangle, and E. Esarey, "Guiding of high intensity laser pulses in straight and curved plasma channel experiments," *Phys. Rev. Lett.*, vol. 77, p. 4186, 1996.

[17] T. C. Chiou, T. Katsouleas, C. Decker, W. B. Mori, J. S. Wurtele, G. Shvets, and J. J. Su, "Laser wake field acceleration and optical guiding in a hollow plasma channel," *Phys. Plasmas*, vol. 2, p. 310, 1995.

[18] C. J. McKinstrie and M. Yu, "The role of ion momentum in stimulated Raman scattering," *Phys. Fluids B*, vol. 3, p. 3041, 1991.

[19] C. G. Durfee III, J. Lynch, and H. M. Milchberg, "Development of a plasma waveguide for high-intensity laser pulses," *Phys. Rev. E*, vol. 51, p. 2368, 1995.

[20] A. Zigler, Y. Ehrlich, C. Cohen, J. Krall, and P. Sprangle, "Optical guiding of high intensity laser pulses in a long plasma channel formed by a slow capillary discharge," *J. Opt. Soc. Am. B*, vol. 13, p. 68, 1996.

[21] G. Shvets, J. S. Wurtele, T. C. Chiou, and T. Katsouleas, "Excitation of accelerating wakes in inhomogeneous plasmas," *IEEE Trans. Plasma Sci.*, vol. 24, p. 351, 1996.



Gennady Shvets was born in Kiev, Ukraine, on September 7, 1969. He received the Ph.D. degree in physics in 1995 from the Massachusetts Institute of Technology, Cambridge.

He has been with the Princeton Plasma Physics Laboratory since 1995, where he is curretly a Research Physicist. His research interests include laser–matter interaction, plasma-based particle accelerators, novel technique of laser pulse compression, laser propagation in plasmas and plasma waveguides, and novel radiation sources.

Dr. Shvets was a Department of Energy Postdoctoral Fellow in 1995–1996, and he received a Presidential Early Career Award for Scientists and Engineers (PECASE) in 2000.

Nathaniel J. Fisch received undergraduate and graduate studies in the Department of Electrical Engineering and Compuer Science at the Massachusetts Institute of Technology, Cambridge.

He is a Professor of Astrophysical Sciences and Director of the Program in Plasma Physics at Princeton University. His current research is focused on various plasma devices and effects associated with the intense illumination of plasma by lasers.

Dr. Fisch is a Fellow of the American Physical Society, a former Gugenheim Fellow, and a former Chair of the APS Division of Plasma Physics. He was the recipient of the 1992 American Physical Society Award for Excellence in Plasma Physics, conferred in recognition for fundamental theoretical investigations of noninductive current generation.



Alexander Pukhov was born in Moscow, Russia, on December 27, 1964. He received the M.S. degree in 1988 and the Ph.D. degree in theoretical physics from Moscow Institute (University) for Physics and Technology (MIPT) in 1991.

From 1991 to 1994, he was employed as an Assistant Professor at MIPT. Since 1994, he is a Research Scientist at the Max-Planck-Institute for Quantum Optics, Garching, Germany. His research is concentrated on the areas of large-scale computer simulations of relativistic laser–plasma interactions, plasma sources of high energy particles, fast ignition concept in inertial confinement fusion, novel concepts for laser pulse amplification (compression) in plasma, free electron lasers. He developed the three-dimensional particle-in-cell code Virtual Laser Plasma Laboratory (VLPL) based on the first principles and able to simulate actual laser–plasma experiments.

Dr. Pukhov was the recipient of the Heinz-Billing-Prize for Scientific Computing, 1999.

Photon Kinetics for Laser–Plasma Interactions

L. O. Silva, W. B. Mori, R. Bingham, J. M. Dawson, Thomas M. Antonsen, Jr, *Member, IEEE*, and P. Mora

***Abstract*—A photon kinetic formalism is employed to describe the propagation of short laser pulses in tenuous plasmas. The photon kinetic theory contains all of the ingredients necessary to describe the relativistic nonlinear optics of short laser pulses in plasmas, and the shortest time scale is determined by the local evolution of the index of refraction. We use this feature to implement a photon in cell code, in which the typical time step is much bigger than is the laser field time scale. Additional information provided by the photon kinetic framework is illustrated by one-dimensional (1-D) and two-dimensional (2-D) simulations.**

***Index Terms*—Intense laser-plasma interactions, numerical simulation, photon kinetics.**

I. Introduction

IN THE early days of quantum mechanics, the intrinsically wave-like nature of quantum mechanics raised some resistance, and several authors attempted to bridge the gap between the classic picture and the wave formalism. They did this not only to build a more *comfortable* theory, but also to tackle the problems originating from the statistical nature of quantum mechanics. The most fruitful of these attempts is based on the ideas pioneered by Wigner [1]. Wigner showed that starting from the quantum wave function ψ, it is possible to build a phase-space distribution function for the canonical variables position and momentum, whose marginals give the correct description for the physically relevant quantity $\psi \cdot \psi^*$, either in configuration or in momentum space. Later, Moyal [2] derived the transport equation for the Wigner distribution function, and Leaf [3] extended the transport equation for Klein–Gordon, and Dirac quantum fields. From the statistical quantum field theory perspective, the Wigner–Moyal formalism is a mature subject [4], [5], with applications ranging from solid-state physics to quantum tomography.

Recent advances in the measurement of ultrashort laser pulses [6], [7] triggered the resurgence of the interest in the phase-space representation of classic fields. Tappert and Besieris [8], [29], [30] first identified the power of the Wigner–Moyal formalism to study classic wave equations, using phase space distribution functions. The field is represented by a Wigner distribution of quasi-particles, and in the limit of short wavelengths, the transport equation is formally equivalent to the Vlasov equation. An analogy between particle dynamics and field dynamics can then be easily established, leading to new, and revealing, physical pictures. A similar formalism has been employed as an extension of the geometrical optics approximation [9] (for electromagnetic wave propagation in random media), or as a generalization of weak turbulence theory for photons [10], [11].

In this paper, we employ the formalism introduced by Tappert to laser propagation in underdense plasmas, and we show that a photon kinetic theory provides all of the ingredients necessary to describe the different stimulated forward scattering instabilities. Based on the collisionless structure of the photon kinetic equation, the natural way to tackle the numerical simulation of photons is a particle-in-cell (PIC) model [12], [13]. In this paper, we describe how such a photon-in-cell code works and present results from a simple one-dimensional (1-D) photon kinetic code that includes dispersion and the relativistic mass correction, but does not include the plasma WAKE response. This code provides illustrative evidence for the formation of envelope solitons as well as informative phase space pictures that characterize this nonlinear structure.

Photon kinetics can be generalized to higher dimensions, and this is illustrated by analogy between the Wigner representation of a Gaussian beam and the distribution function of a particle beam. The quasi-static code WAKE [14] provides the ideal setting to test the principles of photon kinetics in a plasma in higher dimensions, because it is a two-dimensional (2-D) code in which the fast time scale (associated with the high-frequency laser field) is separated for the slow time scale (determined by the plasma dynamics, evolving in the plasma frequency time scale, and the ponderomotive force caused by gradients in the slowly varying laser pulse envelope). We have written a code, called QWAKE, in which the laser field evolution of WAKE (obtained by solving an extended paraxial wave equation for the laser envelope) is replaced by the equivalent photon kinetics. We find excellent agreement between the two approaches. Furthermore, the photon distribution function contains additional information, providing a clear physical picture for laser–plasma interactions. These features will be illustrated with 2-D slab results from QWAKE, the quasi-particle version of WAKE. Finally, the potential and future directions for photon kinetic theory and simulations will also be discussed.

II. Photon Kinetic Theory

In order to build a kinetic theory for fields in terms of quasi-particles, it is necessary to address two separate issues. First, a representation of the field in terms of a quasi-particle distribution function in phase space has to be built. Second, it is fun-

Manuscript received December 23, 1999; revised January 20, 2000. This work was supported in part by the National Science Foundation, under Grant AST-9713234 and Grant DMS 9722121, and by the U.S. Department of Energy, under Grant DE-FG03-98DP00211. The work of L. O. Silva was supported by PRAXIS XXI (Portugal). The work of R. Bingham was supported by PPARC (U.K.) and the University of California at Los Angeles.

L. O. Silva, W. B. Mori, and J. M. Dawson are with the Department of Physics and Astronomy, University of California at Los Angeles, Los Angeles, CA 90095 USA (e-mail: silva@physics.ucla.edu).

R. Bingham is with the Rutherford Appleton Laboratory, Chilton, Didcot, OX11 OQX Oxon, U.K.

T. M. Antonsen, Jr. is with the Institute for Plasma Research, University of Maryland, College Park, MD 20742 USA.

P. Mora is with the Centre de Physique Théorique, École Polytechnique, 91128 Palaiseau Cedex, France.

Publisher Item Identifier S 0093-3813(00)07239-8.

0093–3813/00$10.00 © 2000 IEEE

damental to understand how this distribution function is transported. These questions have been answered in a general way in a series of papers by Tappert *et al.* [8], [29], [30].

The wave equation for the laser field vector potential $\mathbf{A}$ in a plasma can be written as

$$\left(\partial_t^2 + \Omega^2\right)\mathbf{A} = 0 \tag{1}$$

where the positive self-adjoint Hermitian operator Ω^2 is defined as

$$\Omega^2 = -c^2\partial_x^2 + \omega_{pe0}^2\frac{\delta n}{\gamma} \tag{2}$$

where $\omega_{pe0} = (4\pi e^2 n_0/m_e)^{1/2}$ is the plasma frequency, n_{e0} is the background electron density, $\delta n = n_e/n_{e0}$ is the normalized electron density, and γ is the relativistic gamma factor of the plasma electrons. It is also assumed that all of the fractional powers of Ω^2 are defined, as well as the positive self-adjoint operators. A good discussion about the definition of fractional powers for operators is given in [15]. In general, the fractional powers of operators have to be interpreted as an integral operator.

We define the complex analytic signal as [8], [29]

$$\psi(\mathbf{x},t) = \frac{\Omega^{1/2}}{\sqrt{8\pi c}}\left(\mathbf{A} + \frac{i}{\Omega}\partial_t\mathbf{A}\right). \tag{3}$$

The operator Ω^{-1} is defined such that $\Omega\Omega^{-1} = \overline{\overline{1}}$. For instance, in vacuum $\Omega = ic\partial_x$, and $\Omega^{-1} = -i/c\int dx$. The wave energy density ϵ_γ, and the wave action density a_γ associated with $\mathbf{A}$, can then be written as

$$\epsilon_\gamma = \psi^t\cdot\Omega\psi \tag{4}$$

$$a_\gamma = \psi^t\cdot\psi. \tag{5}$$

The phase space distribution of the photons $\mathcal{N}$ is the Wigner function of ψ

$$\mathcal{N}(\mathbf{k},\mathbf{x},t) = \int d\mathbf{s}\exp(i\mathbf{k}\cdot\mathbf{s})\psi\left(\mathbf{x}-\frac{\mathbf{s}}{2},t\right)\cdot\psi^*\left(\mathbf{x}+\frac{\mathbf{s}}{2},t\right). \tag{6}$$

The distribution $\mathcal{N}$ has the good properties of a photon distribution function; i.e., momenta of the distribution function describe observable quantities with the appropriate physical meaning. It is a real-valued function, but not necessarily positive everywhere. The photon number density n_γ, or, equivalently, the classic wave action, which is equivalent to (5), is determined from

$$n_\gamma(\mathbf{x},t) = \int\frac{d\mathbf{k}}{(2\pi)^3}\mathcal{N} = \frac{1}{8\pi c^2}\left(\mathbf{A}\cdot\Omega\mathbf{A} + \partial_t\mathbf{A}\cdot\Omega^{-1}\partial_t\mathbf{A}\right). \tag{7}$$

The classic wave action is the classic analog of the quantum occupation number, thus, the designation photon number density. It is also possible to define a photon current density j_γ

$$j_\gamma(\mathbf{x},t) = \int\frac{d\mathbf{k}}{(2\pi)^3}\frac{c\mathbf{k}}{\Omega}\mathcal{N} \tag{8}$$

and the photon energy density ϵ_γ [also determined by (4)]

$$\epsilon_\gamma(\mathbf{x},t) = \int\frac{d\mathbf{k}}{(2\pi)^3}\Omega_W\mathcal{N} = \frac{1}{8\pi c^2}\left(\mathbf{A}\cdot\Omega^2\mathbf{A} + |\partial_t\mathbf{A}|^2\right) \tag{9}$$

where $\Omega_W(\mathbf{k},\mathbf{x},t)$ is the Weyl transform of the operator Ω [3], [5], [8]. For a given operator $\hat{A}$, the Weyl transform is defined as [3], [5]

$$A_W(\mathbf{k},\mathbf{x}) = \int d\mathbf{s}\left\langle\mathbf{x}+\tfrac{1}{2}\mathbf{s}|\hat{A}|\mathbf{x}-\tfrac{1}{2}\right\rangle\exp(-2\pi i\mathbf{s}\cdot\mathbf{k}) \tag{10}$$

where $|\mathbf{x}\rangle$ are the eigenkets of the position operator $\hat{x}$; i.e., $\hat{x}|\mathbf{x}\rangle = \mathbf{x}|\mathbf{x}\rangle$. The detailed properties of the Weyl transform are summarized in [5].

The laser field is completely characterized by the distribution $\mathcal{N}$, which can be calculated for different electromagnetic field configurations [16], [17]. Furthermore, there is a one-to-one correspondence between the distribution $\mathcal{N}$, and the analytic signal ψ, apart from a constant phase shift ϕ_0. Defining the inverse Fourier transform of $\mathcal{N}$, as

$$\mathcal{F}(\mathbf{x},\mathbf{x}',t) = \int\frac{d\mathbf{k}}{(2\pi)^3}\exp(-i\mathbf{k}\cdot\mathbf{x}')\mathcal{N}(\mathbf{x},\mathbf{k},t) \tag{11}$$

ψ is determined by

$$\psi(\mathbf{x},t) = \frac{\mathcal{F}(\mathbf{x}/2,\mathbf{x},t)}{\sqrt{\mathcal{F}(0,0,t)}}e^{i\phi_0}. \tag{12}$$

The phase shift ϕ_0 is determined from the initial value conditions, i.e., $e^{i\phi 0} = \psi(\mathbf{x}=0,t=0)/\sqrt{\mathcal{F}(0,0,0)}$, where we have assumed $\mathcal{F}(0,0,0)\neq 0$. Other properties of the Wigner function are compiled in [7].

By providing an alternative picture of the laser field [7], [16], $\mathcal{N}$ already gives additional physical information. However, the full impact of Wigner's formalism can only be achieved if the laser field is replaced by the photon distribution function, and if the wave equation for the laser field is replaced by a transport equation for $\mathcal{N}$. In the underdense limit $\epsilon = \omega_{pe0}/\omega \ll 1$, Tappert and Besieris [8], [29], [30] showed that the transport equation for $\mathcal{N}$ is

$$\frac{\partial\mathcal{N}}{\partial t} + \mathbf{v}_\gamma\cdot\frac{\partial\mathcal{N}}{\partial\mathbf{x}} + \mathbf{F}_\gamma\cdot\frac{\partial\mathcal{N}}{\partial\mathbf{k}} = O(\epsilon^2) \tag{13}$$

where

$$\mathbf{v}_\gamma = \frac{\partial\Omega_W}{\partial\mathbf{k}} = \frac{\mathbf{k}c^2}{\omega} \tag{14}$$

$$\mathbf{F}_\gamma = -\frac{\partial\Omega_W}{\partial\mathbf{x}} = -\frac{\omega_{pe0}^2}{2\omega}\nabla\frac{\delta n}{\gamma}. \tag{15}$$

We have used the fact that in the underdense limit, Ω_W reduces to

$$\Omega_W = \left(k^2c^2 + \omega_{pe0}^2 \frac{\delta n}{\gamma}\right)^{1/2} + O(\epsilon^2). \qquad (16)$$

Neglecting the correction terms of order $\epsilon^{n\geq 2}$, (13) states photon number conservation in the phase space $(\mathbf{k}, \mathbf{x})$, and it is formally equivalent to the Vlasov equation. Furthermore, the second (third) term on the LHS of (13) describes dispersion (photon acceleration/transverse focusing), as clearly pictured by (14) and (15). Coupling with the plasma occurs through the photon ponderomotive force, which can be expressed in terms of the distribution $\mathcal{N}$ [17]. The basic ingredients to describe the nonlinear optics of plasmas for short laser pulses at relativistic intensities [18] are all contained in this formalism, and it is possible to rederive all of the relevant temporal growth rates for Raman forward scattering, relativistic self-focusing, envelope self-modulation, and relativistic self-phase modulation for arbitrary laser intensities from the photon kinetic theory [19]. The analogy with particle beams is also evident: using the photon kinetic theory, we are able to describe the laser field evolution as an ensemble of quasi-particles, or a photon beam [20].

III. Photon Kinetic Simulations

The Vlasov-like structure of the photon kinetic equation provides the ideal setting to examine photon dynamics under the PIC framework [12], [13]. The basic ideas behind an implementation of a photon kinetic code are straightforward. First of all, it is necessary to specify the initial distribution of photons from the initial laser field, using (3) and (6). The distribution of photons $\mathcal{N}$ is deposited on the grid to calculate quantities relevant to the photon dynamics (such as $\mathbf{A}^2$), or the plasma dynamics (the photons' ponderomotive potential). If the background plasma is allowed to evolve, the plasma particles are pushed (under the Lorentz force from the self-consistent fields, and the ponderomotive force of the photons), and the self-consistent fields are updated. The quantities necessary to move the photons are now present (namely, the updated index of refraction), and the photons are pushed according to their equations of motion (14), (15). Details of the numerical implementation of a *photon-in-cell* code will be presented elsewhere [21]. Here, we will concentrate our discussion on some of the qualitative features of the numerical results, and the advantages that photon in cell simulations may provide.

A. One-Dimensional Relativistic Photon Dynamics Without Plasma Response

The most simple, and nontrivial, scenario that is possible to examine under the photon kinetic formalism is the propagation of an ultraintense laser beam, including the relativistic mass correction nonlinearity, but neglecting the underdense plasma response. This is equivalent to setting $\delta n = 1$ in (14)–(16); with $\gamma = \sqrt{1+\mathbf{a}^2}$, $(\mathbf{a} = e\mathbf{A}/m_e c^2)$, (1) is the nonlinear Klein–Gordon equation, with the potential $V(\mathbf{a}) = (1+\mathbf{a}^2)^{1/2}$. Furthermore, when $|\mathbf{a}| \ll 1$, and dispersion effects are neglected, the nonlinear Schroedinger equation is obtained. It is then expected that the time evolution of the photon beam first shows relativistic self-phase modulation [18], [22], and then evolves to envelope solitons [23], [24]. Under this scenario, we can demonstrate the key features of photon dynamics in phase space.

We first examine relativistic self-phase modulation (RSPM). Loading a uniform monochromatic photon beam, such that $\mathcal{N} = n_{\gamma 0}\delta(\mathbf{k} - \mathbf{k}_0)$, where $n_{\gamma 0} = \omega_0 \mathbf{a}^2$, with $\omega_0 = (k_0^2c^2 + \omega_{pe0}^2/\sqrt{1+\mathbf{a}^2})^{1/2}$, we expect the maximum growth rate for RSPM to occur for $k = |\mathbf{a}|\omega_0/\sqrt{2}c$ [18], [22]. The phase space evolution of the photon distribution is shown in Fig. 1, for $\mathbf{a}^2 = 0.4$, and $\omega_0/\omega_p = 10$. We first observe the effect of photon acceleration at $\tau = 150/\omega_p$, leading to a significant, and symmetric, spread in $\mathbf{k}$: photon acceleration generates phase-space shear along the $\mathbf{k}$ direction. At this point, dispersion is not playing any role, which means that the fastest growing mode corresponds to the shortest wavenumber allowed in the system. As the wavenumber spread increases, dispersion becomes important (Fig. 1 @ $\tau = 210/\omega_p$: photons with higher k move faster: dispersion generates phase-space shear along the $\mathbf{x}$ direction). Fast photons start to overtake the slow photons, leading to photon bunching, which in turn increases the relativistic nonlinearity, thus, closing the feedback loop. However, dispersion is not symmetric in $\mathbf{k}$ [see (14)], thus, leading to detuning between the sidebands, and giving rise to an instability cutoff at $k_{\max} = \omega_0|\mathbf{a}|/c$ [18], [22]. Large-scale nonlinear structures are formed, characterized by photon vortices in phase space, as illustrated in Fig. 1 @ $\tau = 600/\omega_p$, corresponding to six e-foldings for the maximum growth rate. As the photon beam evolves, we observe that the big beam breaks apart in a train of pulses, i.e., solitons, with energy cascading to lower wavenumbers. A typical situation after a long propagation distance is shown in Fig. 2. The usefulness of the photon kinetic description becomes apparent. For long propagation distances, the pulse shape of the individual photon pulses in real space remains almost unaltered, but the phase space evolution is rather complex. The photon bunches form vortices in phase space that clearly shows that dispersion has been compensated by the nonlinearity. The internal phase space structure of one pulse is characteristic of a photon shock. The pulses that have not attained a stationary envelope are still undergoing relativistic self-phase modulation (but now seeded by the pulse envelope gradient). This is clear for the last pulse in Fig. 2. The time evolution also shows that some pulses split in two. This is occurring for pulse 3, in which the second pulse is "radiating" outward from it.

As expected, the different bunches have different peak $\mathbf{a}^2$; this indicates the pulses move with slightly different average velocities (bigger $\mathbf{a}^2$ implies faster pulse velocities). Ideally, the long time evolution could result in the formation of a train of identical photon pulses.

B. QWAKE: A Two-Dimensional Quasi-Static Photon Kinetic Code

WAKE [14] is a 2-D quasi-static PIC code, which evolves the laser field in the plasma dynamical time scale. The obvious advantage of such an approach is the possibility to model ultrashort intense laser pulse propagation in underdense plasmas for

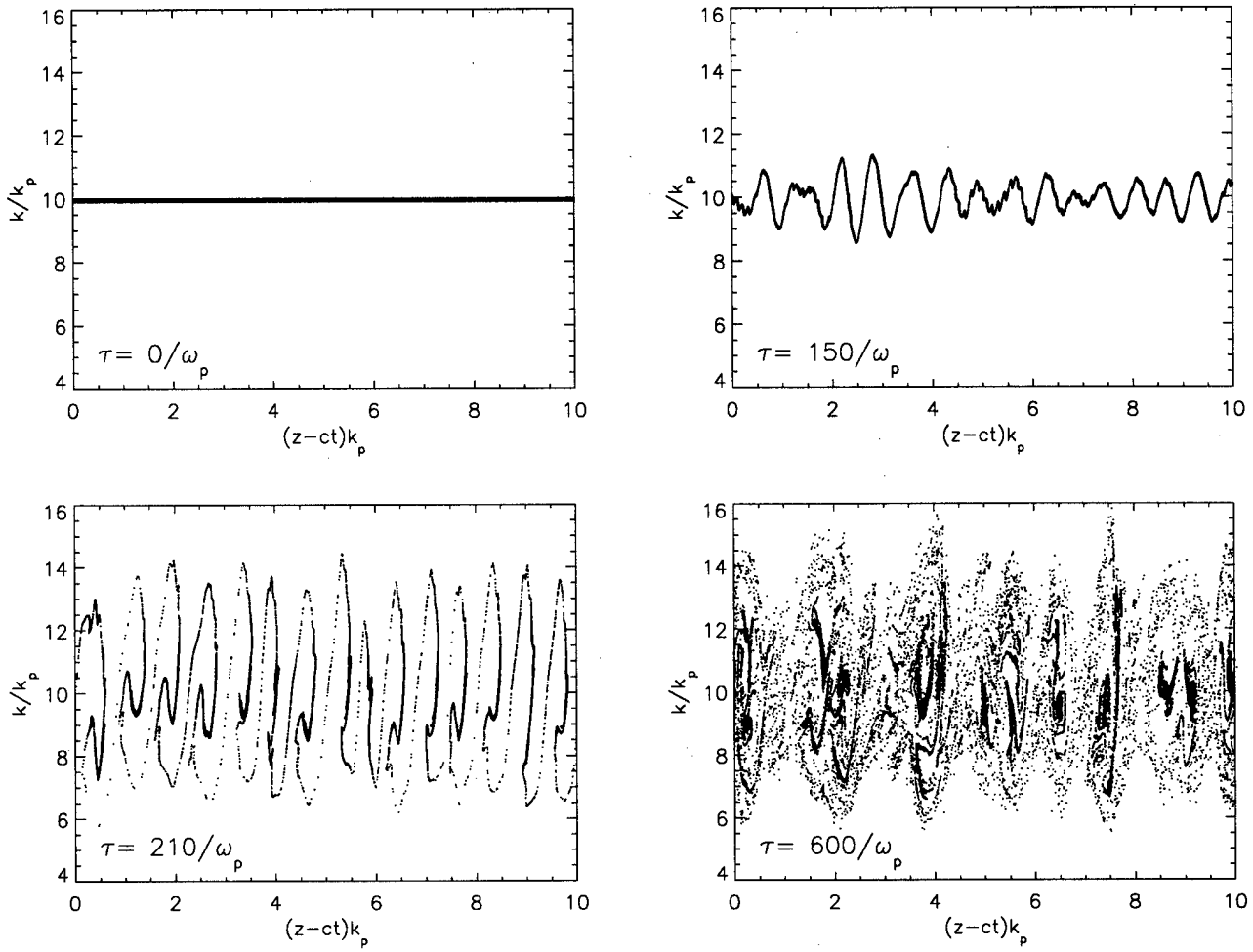


Fig. 1. Phase space evolution of a photon beam, exhibiting relativistic self-phase modulation. Simulation box is three times larger than displayed region, with 300 cells, and 2×10^4 photons, and periodic boundary conditions.

distances comparable to typical laboratory experiments length scales, even with modest computational resources. This is a critical issue to the design of plasma-based accelerators [25], [26]. In WAKE [14], the laser field evolution is decoupled from the plasma self-consistent fields, and because coupling with the plasma is through the laser ponderomotive force, this code provides the ideal framework to test the photon kinetic approach. In WAKE, the laser field envelope is described by an extended paraxial wave equation coupled with the plasma through the changes in the index of refraction of the laser field. In QWAKE, the laser field envelope is a moment of the photon distribution function, and the photon distribution function evolves according to the transport equation (13). The plasma dynamics is treated in the same way in both codes: the plasma particles are under the action of the laser ponderomotive force and the plasma self-consistent fields.

The generalization from 1-D photon kinetics to 2-D slab (or 3-D cartesian) is straightforward, only involving standard numerical techniques related with the generalization of the photon pusher, and the photon density deposition scheme. The key issue here is the determination of the initial photon distribution, which can be calculated numerically from (6). However, for some laser field configurations, it is possible to determine $\mathcal{N}$, and establish a close analogy with particle beams. For a monochromatic plane wave, the photon distribution is trivially calculated, corresponding to a monoenergetic photon beam [16]. It is also possible to calculate the photon distribution for the fundamental mode of a Gaussian beam propagating along z (z plays here the role of time, and k_z, the canonical conjugate variable of z, plays the role of ω), given by $\mathbf{A} \propto \exp[ik_z \mathbf{x}_\perp^2/2R(z)] \exp[-\mathbf{x}_\perp^2/W(z)^2]$ [20]

$$\mathcal{N}(\mathbf{x}_\perp, \mathbf{k}_\perp, z) \propto \exp - \left[2 \frac{\mathbf{x}_\perp^2}{W(z)^2} \left(1 + \alpha^2\right) - 2\alpha \mathbf{x}_\perp \cdot \mathbf{k}_\perp + \mathbf{k}_\perp^2 \frac{W(z)^2}{2} \right] \tag{17}$$

where $W(z) = W_0 \sqrt{1 + z^2/z_R^2}$ is the beam waist, $\alpha = k_z W(z)^2/2R(z)$ is the Twiss parameter, with $R(z) = z + z_R^2/z$ the Gaussian beam radius of curvature, z_R is the Rayleigh length, and W_0 is the minimum spot size. We note that (17) is similar to a Gaussian distribution of free-streaming electrons [20]. k_z does not appear explicitly in the photon distribution because for a Gaussian beam with frequency ω_0, k_z, and $\mathbf{k}_\perp$ satisfy the dispersion relation $k_z = \omega_0/c - (\omega_{pe0}^2 + \mathbf{k}_\perp^2 c^2)/2\omega_0 c$. This means that additional

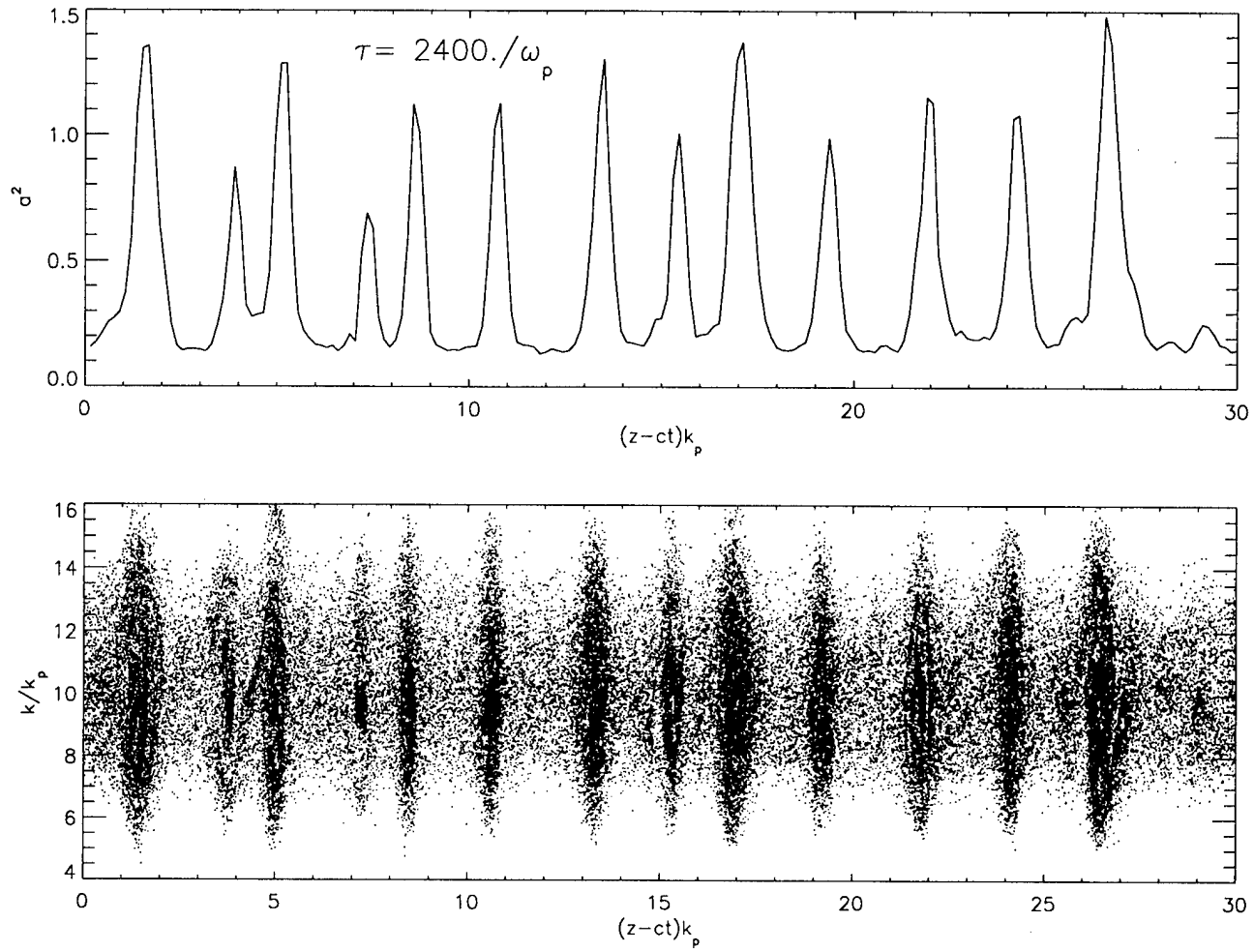


Fig. 2. Quasisatured state of a photon beam: $\mathbf{a}^2$ and photons' phase space distribution (peaks referenced in the text from left to right).

dependence on k_z is already included in (17) through the connection between k_z and $\mathbf{k}_\perp$.

We have performed several runs to benchmark the quasi-particle photon kinetic version of WAKE, QWAKE, in 2-D slab geometry. Comparable performances were observed with the two versions, leading to similar quantitative results. In Fig. 3, we present a typical result from QWAKE, portraying the evolution of $\mathbf{a}^2$ for a pulse duration $\tau = 20/\omega_p$, and a spot size $W_0 = 56.5c/\omega_{pe0}$, propagating in a underdense plasma such that $k_0/k_{pe0} = 11$, with $\mathbf{a}^2_{\max}(\tau = 0) = 0.25$. The result from WAKE for the same parameters (but with a finer transverse grid) is presented in Fig. 3(c). The results from QWAKE and WAKE show good qualitative agreement. In particular, the longitudinal profile along the laser pulse propagation axis comparing QWAKE and WAKE (Fig. 4) shows equivalent qualitative features, but small quantitative differences. However, we observe that the QWAKE results are almost independent of the transverse resolution, and the WAKE results were obtained for a very high transverse resolution run. Furthermore, QWAKE is not yet optimized for the photon dynamics, and the five-passage binomial smoother [13] along the z-direction prevents the observation of the finer details shown by the WAKE run. Detailed comparisons between the two approaches will be presented in a future publication [21].

For the conditions in Fig. 4, relativistic self-focusing leads to intensity enhancement and eventually to pulse splitting and pulse compression of the front part of the laser pulse [27]. This physical interpretation becomes more clear if additional diagnostics over the photon distribution $\mathcal{N}$ are calculated. It is possible to define averages over $\mathcal{N}$, for a given observable quantity f, as

$$\langle f\rangle(\mathbf{x},t) = \frac{\int d\mathbf{k}\, f\mathcal{N}}{\int d\mathbf{k}\,\mathcal{N}} \tag{18}$$

in configuration space, whereas in momentum space

$$\langle f\rangle(\mathbf{k},t) = \frac{\int d\mathbf{x}\, f\mathcal{N}}{\int d\mathbf{x}\,\mathcal{N}}. \tag{19}$$

Physical quantities with significant relevance are, for instance, the local average of the photons' frequency $\langle\omega\rangle$, and the local average of the photons' perpendicular momentum $\langle k_\perp\rangle$. The first quantity gives a measure of the laser field chirp and the effect of photon acceleration. The second quantity

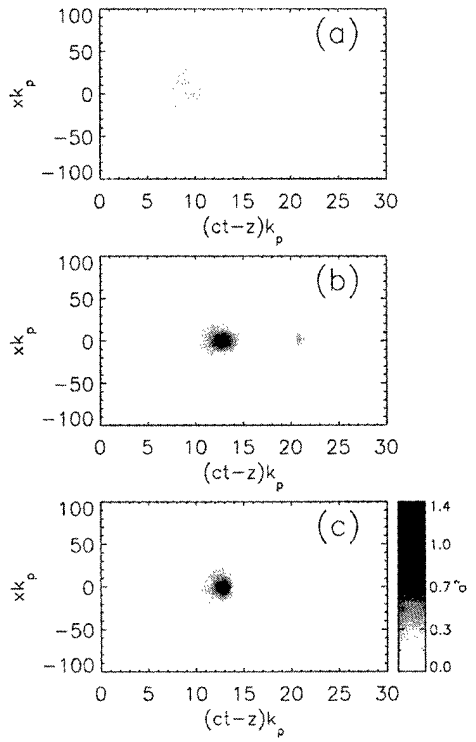


Fig. 3. $\mathbf{a}^2$ from QWAKE and WAKE: (a) Initial $\mathbf{a}^2$; (b) $\mathbf{a}^2$ obtained from propagating the photon distribution function after 0.04 Rayleigh lengths; (c) same conditions as in (b), but using WAKE i.e., solving directly for the laser field wave equation. For QWAKE, the simulation box is 100 cells wide (and 200 cells long), with 2×10^5 photons, and a moving window, whereas for WAKE the simulation box is 300 cells wide (and 200 cells long).

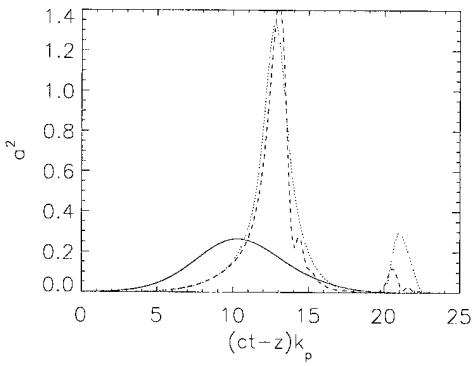


Fig. 4. $\mathbf{a}^2$ along the laser propagation axis $(ct - z)k_p$ for the conditions of Fig. 3(a)—solid line, Fig. 3(c)—short dashed line, and Fig. 3(c)—long dashed line.

indicates which regions of the laser field are focusing or defocusing, depending on if $\langle k_\perp \rangle$ is pointing inward, to the laser beam propagation axis, or outward. This is the relevant quantity to examine relativistic self-focusing, as illustrated in Fig. 5. We observe that the enhanced front part of the pulse is self-focusing, whereas pulse splitting is occurring in the defocusing (or diffracting) region, and pulse splitting should occur in this region. These zones are correlated with the appropriate region of the index of refraction profile leading to focusing/defocusing.

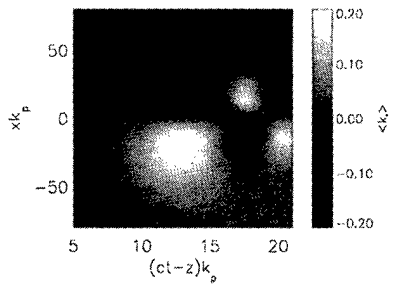


Fig. 5. Local k_x determined from the laser field photon distribution for the conditions of Fig. 3(b).

IV. Summary and Conclusion

Photon kinetic theory provides a novel framework for the study of intense electromagnetic fields interacting with underdense plasmas, in particular, when forward scattering instabilities dominate the plasma dynamics. The most powerful features are its simplicity, the strong connection with particle beam dynamics, and the natural way in which broadband and angular spread effects can be included in the formalism: under this new light, intense laser–plasma interactions are a combination of very well-defined physical processes [18]. The perfect setting for photon kinetic theory is high brightness, broadband, radiation-driven plasma instabilities, relevant for inertial confinement fusion and astrophysics [19].

The strong analogy of photon dynamics with particle dynamics leads to an obvious path toward the numerical realization of a photon kinetic code. Furthermore, the generalization to higher dimensions is easy, only relying on standard techniques. Thus, it might circumvent numerical difficulties associated with the solution of the wave equation in three dimensions, in reduced PIC codes [28].

With a 1-D photon kinetic code, we have analyzed some of the qualitative features of RSFM and the formation of envelope solitons. The photon phase space provides signatures for these nonlinear structures. By modifying WAKE to evolve a photon distribution coupled with the plasma, we were able to benchmark photon kinetics against a well-tested code. Excellent qualitative agreement was found between the two versions of the code, and the similar quantitative results show that photon kinetics is a promising representation for short laser pulse propagation in underdense plasmas. The additional diagnostics associated with photon kinetics established clear physical pictures for previous analytical, and numerical results [18], [27]. We have demonstrated that photon kinetic PIC codes include all of the fundamental physics, open the way to new photon diagnostics, and are computationally competitive with other reduced algorithms for short-pulse laser–plasma interactions.

Acknowledgment

The authors would like to thank B. Afeyan for useful discussions.

References

[1] E. Wigner, "On the quantum correction for thermodynamic equilibrium," *Phys. Rev.*, vol. 40, pp. 749–759, 1932.

[2] J. E. Moyal, "Quantum mechanics as a statistical theory," in *Proc. Cambridge Phil. Soc.*, vol. 45, 1949, p. 99.
[3] B. Leaf, "Weyl transformation and the classical limit of quantum mechanics," *J. Math. Phys.*, vol. 9, p. 65, 1968.
[4] R. P. Feynman, *Statistical Mechanics: A Set of Lectures*. Redwood City, CA: Addison-Wesley, 1972.
[5] R. L. Liboff, *Kinetic Theory*. New York: Wiley, 1998.
[6] D. J. Kane and R. Trebino, "Single-shot measurement of the intensity and phase of an arbitrary ultrashort pulse by using frequency-resolved optical gating," *Opt. Lett.*, vol. 18, pp. 823–825, 1993.
[7] J. Paye, "The chronocyclic representation of ultrashort light pulses," *IEEE J. Quantum Electron.*, vol. 28, pp. 2262–2273, 1992.
[8] F. D. Tappert, "Derivation of the collisionless wave kinetic equation," *SIAM Rev. (Chronicle)*, vol. 13, p. 281, 1971.
[9] S. W. McDonald, "Phase-space representation of wave equations with applications to the eikonal approximation for short-wavelength waves," *Phys. Rep.*, vol. 159, p. 337, 1988.
[10] R. Bingham, J. T. Mendonça, and J. M. Dawson, "Photon Landau damping," *Phys. Rev. Lett.*, vol. 78, pp. 247–249, 1997.
[11] N. L. Tsintsadze and J. T. Mendonça, "Kinetic theory of photons in a plasma," *Phys. Plasmas*, vol. 5, pp. 3609–3614, 1998.
[12] J. M. Dawson, "Particle simulation of plasmas," *Rev. Mod. Phys.*, vol. 55, p. 403, 1983.
[13] C. K. Birdsall and A. B. Langdon, *Plasma Physics Via Computer Simulation*. New York: McGraw-Hill, 1985.
[14] P. Mora and T. M. Antonsen, Jr., "Kinetic modeling of intense, short laser pulses propagating in tenuous plasmas," *Phys. Plasmas*, vol. 1, pp. 217–229, 1997.
[15] L. Fishman and J. J. McCoy, "Derivation and application of extended parabolic wave theories. I. The factorized Helmholtz equation," *J. Math. Phys.*, vol. 25, pp. 285–296, 1984.
[16] L. O. Silva and J. T. Mendonça, "Kinetic theory of photon acceleration: Time-dependent spectral evolution of ultrashort laser pulses," *Phys. Rev. E*, vol. 57, pp. 3423–3431, 1998.
[17] L. O. Silva, R. Bingham, J. M. Dawson, and W. B. Mori, "Ponderomotive force of quasiparticles in a plasma," *Phys. Rev. E*, vol. 59, pp. 2273–2280, 1999.
[18] W. B. Mori, "The physics of the nonlinear optics of plasmas at relativistic intensities for short-pulse lasers," *IEEE J. Quantum Electron.*, vol. 33, pp. 1942–1953, 1997.
[19] L. O. Silva *et al.*, Raman forward scattering by high brightness broadband radiation sources. to be published.
[20] ——, Quasi-particle representation of photon beams. to be published.
[21] ——, A photon in cell code for intense radiation-plasma interactions, . submitted for publication.
[22] C. Max, J. Arons, and A. B. Langdon, "Self-modulation and self-focusing of electromagnetic waves in plasmas," *Phys. Rev. Lett.*, vol. 33, pp. 209–212, 1974.
[23] V. I. Karpman and E. M. Kruskal, "Modulated waves in nonlinear dispersive media," *Sov. Phys. JETP*, vol. 28, p. 277, 1969.
[24] P. K. Kaw, A. Sen, and T. Katsouleas, "Nonlinear 1D laser pulse solitons in a plasma," *Phys. Rev. Lett.*, vol. 68, pp. 3172–3175, 1992.
[25] T. Tajima and J. M. Dawson, "Laser electron accelerator," *Phys. Rev. Lett.*, vol. 43, pp. 267–270, 1979.
[26] E. Esarey, P. Sprangle, J. Krall, and A. Ting, "Overview of plasma-based accelerator concepts," *IEEE Trans. Plasma Sci.*, vol. 24, pp. 252–288, 1996.
[27] C. Ren *et al.*, Compressing and focusing a short laser pulse by a thin plasma lens. to be published.
[28] D. Gordon, W. B. Mori, and T. M. Antonsen, "A ponderomotive guiding center particle-in-cell code for efficient modeling of laser–plasma interactions," *IEEE Trans. Plasma Sci.*, vol. 4, pp. 1224–1232, Aug. 2000.
[29] I. M. Besieris and F. D. Tappert, "Propagation of frequency modulated pulses in a randomly stratified plasma," *J. Math. Phys.*, vol. 14, pp. 704–707, 1973.
[30] ——, "Stochastic wave-kinetic theory in the Liouville approximation," *J. Math. Phys.*, vol. 17, pp. 734–743, 1976.
[31] F. S. Tsung *et al.*, Generation of single cycle pulses by photon deceleration. to be published.

L. O. Silva, photograph and biography not available at the time of publication.

W. B. Mori, photograph and biography not available at the time of publication.

R. Bingham, photograph and biography not available at the time of publication.

J. M. Dawson, photograph and biography not available at the time of publication.



Thomas M. Antonsen, Jr. (M'87) was born in Hackensack, NJ, in 1950. He received the B.S. degree in electrical engineering in 1973, and the M.S. and Ph.D. degrees in 1976 and 1977, all from Cornell University, Ithaca, NY.

He was a National Research Council Post Doctoral Fellow at the Naval Research Laboratory in 1976–1977, and a Research Scientist in the Research Laboratory of Electronics at MIT from 1977 to 1980. In 1980, he moved to the University of Maryland where he joined the faculty of the Departments of Electrical Engineering and Physics in 1984. He is currently a Professor of physics and electrical engineering. He has held visiting appointments at the Institute for Theoretical Physics (UCSB), the Ecole Polytechnique Federale de Lausanne, Switzerland, and the Institute de Physique Theorique, Ecole Polytechnique, Palaiseau, France. His research interests include the theory of magnetically confined plasmas, the theory and design of high power sources of coherent radiation, nonlinear dynamics in fluids, and the theory of the interaction of intense laser pulses and plasmas. He is the author and coauthor of more than 180 journal articles and coauthor of the book *Principles of Free-electron Lasers*. He has served on the editorial board of *Physical Review Letters*, *The Physics of Fluids*, and *Comments on Plasma Physics*.

Prof. Antonsen was selected as a Fellow of the Division of Plasma Physics of the American Physical Society in 1986.

P. Mora, photograph and biography not available at the time of publication.

Study of Propagation of Ultraintense Electromagnetic Wave Through Plasma Using Semi-Lagrangian Vlasov Codes

Fabien Huot, Alain Ghizzo, Pierre Bertrand, Eric Sonnendrücker, and O. Coulaud

***Abstract*—Interaction of relativistically strong laser pulses with underdense and overdense plasmas is investigated by a semi-Lagrangian Vlasov code. These Vlasov simulations revealed a rich variety of phenomena associated with the fast particle dynamics induced by the electromagnetic wave as electron trapping, particle acceleration, and electron plasma wavebreaking. To describe the distribution of accelerated particle momenta and energy will require a very detailed analysis of the kinetic and time history of the plasma wave evolution. The semi-Lagrangian Vlasov code allows us to handle the interaction of ultrashort electromagnetic pulse with plasma at strongly relativistic intensities with a great deal of resolution in phase space.**

***Index Terms*—Self-induced transparency, semi-Lagrangian Vlasov simulations.**

I. Introduction

THE excitation of large plasmas waves, which presents one of the traditional problems of basic plasma physics, continues to attract much attention, particularly because of the possibility of employing theses waves for high-gradient particle acceleration. As with recently developed pulsed lasers, intensities above 10^{19} W/cm^2 can be reached and relativistic plasma wavebreaking in laser–plasma interactions can be now experimentally investigated. Particularly, one of the most interesting problems in this domain is the laser propagation through overdense plasma, in which the propagation is classically forbidden (i.e., plasmas having densities above $n_c = 1.1 \times 10^{21} \lambda_o^2$ cm^{-3}, where λ_o is the laser wavelength in microns). However, at very high intensities, two penetration mechanisms have been considered: relativistic self-induced transparency and conventional hole boring or forward motion of the critical surface caused by the ponderomotive pressure. It is also convenient to define the Lorentz factor of an oscillatoring electron in the laser field by $\gamma_o = \sqrt{1 + a_{\rm osc}^2}$, with $a_{\rm osc}^2 = (p_{\rm osc}/{\rm mc})^2 = I\lambda_o^2/(1.368 \times 10^{18})$, where I is the laser intensity in Wcm^{-2}. Obviously, from this expression, increasing intensities lead to the relativistic increase of the electron inertia and the associated decrease of the effective plasma frequency. Therefore, wave propagation in homogeneous plasma with densities up to $n_e = \gamma n_c$ is allowed. It occurs only above an intensity such that $a_{\rm osc} \approx n_e/n_c$.

Manuscript received October 29, 1999; revised March 30, 2000.

F. Huot, A. Ghizzo, and P. Bertrand are with L.P.M.I.A., Université Henri-Poincaré, 54506 Vandoeuvre les Nancy Cedex, France.

E. Sonnendrücker and O. Coulaud are with the Institut Elie Cartan deNancy, Université Henri-Poincaré, 54506 Vandoeuvre les Nancy Cedex, France.

Publisher Item Identifier S 0093-3813(00)09159-1.

Plasma codes now have a long history since the first calculations were performed in the late 1950s. The history provides an interesting illustration of the subtle influences and connections between the state of the theory, the "fashionable" problems, and the power of the available computers. Two main classes of plasma simulation algorithms exist. "Particle" models represent the plasma by a large number of computational particles, which move according to classic mechanics in the self-consistent electromagnetic fields. "Vlasov" codes begin with the kinetic equation governing the distribution function $f(\mathbf{r}, \mathbf{v}, t)$. The question can be raised of the possible use between these two complementary methods. A simple calculation delineates clearly the problem. An electrostatic plasma of length L allows $(L/\lambda_D)^3$ collective modes (λ_D being the Debye length), whereas the importance of the individual effects is given by $n\lambda_D^3$ (n being the particle density). The number of particles $N_{\rm part} = nL^3 = n\lambda_D^3(L/\lambda_D)^3 = g^{-1}(L/\lambda_D)^3$, where $g^{-1} = n\lambda_D^d$ is the graininess parameter (with the dimension $d = 3$ here). In fusion and space plasma, $n\lambda_D^3$ is of order of $10^6 - 10^9$, whereas $L/\lambda_D \approx 10^3 - 10^4$. Obviously, we cannot treat 10^{18} particles because $N_{\rm part} = n\lambda_D^3(L/\lambda_D)^3$ (this number corresponds to $L/\lambda_D = 10^3$ and $n\lambda_D^3 = 10^9$). It was consequently realized quickly that a numerical solution of the Vlasov equation, which is based on the limit $g^{-1} \to +\infty$ (if $d = 3$), was a more appropriate approach. Indeed, the Vlasov approach allows the correct treatment of the purely collective plasma by introducing a phase space, i.e., a product of the configuration space by the velocity space. A sampling of this phase space for a plasma of dimension d ($d = 1, 2, 3$) and length L requires $(L/\lambda_D)^d N_v^d$ points, in which N_v is the number of points needed in each velocity component for a precise description of the density distribution $f(\mathbf{r}, \mathbf{v}, t)$. By considering that the numerical effort to treat one particle or one mesh point is similar, the ratio of the numerical efforts of a Vlasov code to a Particle-In-Cell (PIC) code is then $N_{\rm Vlasov}/N_{\rm part} = gN_v^d$. Typically, N_v is close to 100. Consequently, the effort is

	$d = 1$	$d = 2$	$d = 3$
$g = 10^{-2}$	1	10^2	10^4
$g = 10^{-4}$	10^{-2}	1	10^2
$g = 10^{-6}$	10^{-4}	10^{-2}	1

Although these numbers must be considered with caution, they give the general ideas for deciding the use of particle or

0093–3813/00$10.00 © 2000 IEEE

Vlasov–Eulerian (or semi-Lagrangian) code. In some cases, we can take $g = 10^{-2}$ to study basic phenomena. For one-dimensional (1-D) plasma, the efforts are equivalent, and in this case, the Vlasov code must be preferred because of the high accuracy of the distribution function in phase space afforded by the model. In two-dimensional (2-D) and three-dimensional (3-D) cases, the Vlasov code is too expensive. However, cases exist in which kinetic effects in phase space are important, in particular, in the interaction wave-particle that requires a smaller value of the graininess parameter; today, the power of the parallel computer allows us to begin to treat 2-D plasma using the Vlasov code. In the 3-D case, the treatment of kinetic effects could be investigated by both methods but only for $g = 10^{-6}$ and $L/\lambda_D = 1000$, i.e., using 10^{15} particles or grid points, which is not available today. Thus, fully 3-D plasma will for a long time be described by PIC codes.

Several numerical simulations on the laser–plasma interaction have been performed to investigate the details of the plasma wave-trapping dynamics responsible for the acceleration of electrons. However, these simulations [1]–[3], employing as they do the well-known (macro-) PIC technique, have difficulty in supplying a usefully precise description of the electron acceleration process. If three space dimension is involved, only PIC code is practicable so far. However, when one dimension will do (or two dimensions with the recent occurring of parallel computers), the semi-Lagrangian Vlasov codes (referred as SLV codes; see [4]–[7]) (where we calculate the Vlasov fluid density in phase space without the use of simulation macroparticles) have been found to be a powerful tool for studying in detail the particle acceleration dynamics both in a conveniently short but idealized periodic plasma and in the more realistic long, open system with external sources, which we characterize as "causal". The two methods of simulation are complementary. Roughly speaking, PIC codes are relatively efficient and readily scalable to three dimensions, but theses codes are noisy and lack detail in low-density regions of phase space because of the "graininess" of the simulation macroparticles. In one or two degrees of freedom, the semi-Lagrangian method is usually comparable in computer loading, is noiseless, and is much easier to realize in massively parallel computers because of the Eulerian character of the distribution function . We present here some examples of the use of a semi-Lagrangian Vlasov code.

An outline of the paper is as follows. Numerical simulations are first presented in Section II, for simplicity, in the case of a 1-D plasma using periodic boundary conditions in the case of the interaction of a circularly polarized electromagnetic wave. We use this SLV phase space resolution to describe in detail the wave–particle interaction, and we make a comparison with the analytical value of the growth rate of the instability in the relativistic regime. Features of trapping dynamics are considered in detail in Section III, including phase space density structures and separatrices. Then, this work on the spatially periodic case is intended as preparation for the application of similar analysis techniques to the simulations of the more realistic causal case (of an inhomogeneous plasma), in which spatial periodicity no longer applies. In this latter case, propagation of a relativistically strong laser pulse in a moderately overdense plasma is studied using 1-D and 1-D 1/2 SLV codes, and the results are presented in Section IV. Finally, in Section V, we present the major conclusion.

II. Numerical 1-D Periodic SLV Simulation of the Relativistic Plasma Instability Induced by an Ultraintense Laser Pulse

In the fully relativistic regime, perturbation theory cannot be used to take into account nonlinearities of the primary wave (thus, the case of an electromagnetic wave with linear polarization is more complicated with periodic boundary conditions). In order to overcome this difficulty, the nonlinear electromagnetic wave is assumed to be circularly polarized. It is well known that for such a polarization, the amplitudes of the electric field and the electron quiver velocity remain constant. We start from the 1-D relativistic Vlasov model

$$\frac{\partial f}{\partial t} + \frac{p_x}{m\gamma}\frac{\partial f}{\partial x} + e\left(E_x - \frac{mc^2}{2\gamma}\frac{\partial}{\partial x}(a^2)\right)\frac{\partial f}{\partial p_x} = 0 \tag{1}$$

where $\gamma = (1 + (p_x^2/m^2c^2) + a^2)^{1/2}$ is the Lorentz factor and $a(x, t) = (eA(x, t)/mc)$ is the normalized amplitude of the potential vector $\mathbf{A} = (0, A_y, A_z)$. The Vlasov equation is coupled with Maxwell's equations

$$\frac{\partial E_y}{\partial t} = -c^2\frac{\partial B_z}{\partial x} + \omega_p^2 A_y \rho(x, t) \tag{2}$$

$$\frac{\partial E_z}{\partial t} = c^2\frac{\partial B_y}{\partial x} + \omega_p^2 A_z \rho(x, t) \tag{3}$$

$$\frac{\partial B_y}{\partial t} = \frac{\partial E_z}{\partial x} \tag{4}$$

$$\frac{\partial B_z}{\partial t} = -\frac{\partial E_y}{\partial x} \tag{5}$$

where

$$\rho(x, t) = \int \frac{f}{m\gamma}\, dp_x. \tag{6}$$

The components of the potential vector are then computed using

$$\frac{\partial A_y}{\partial t} = -E_y \tag{7}$$

$$\frac{\partial A_z}{\partial t} = -E_z. \tag{8}$$

The longitudinal component of the electric field is obtained by solving Poisson's equation

$$\frac{\partial E_x}{\partial x} = \frac{e}{\varepsilon_o}(n_e(x, t) - n_i). \tag{9}$$

Equations (1), (7), and (8), together with the usual 1-D (x) Maxwell equations, make up the systems of equations used here and correspond to an exact class of solutions of the Vlasov equation by considering Dirac distribution in the transverse directions p_y and p_z. The details of the way in which the equations are advanced and the boundary conditions are imposed have been extensively described elsewhere (see [5] and [8]), but nonetheless, we find it useful here to recapitulate some of the discussion of boundary conditions for the initial-value space periodic case.

Although the demanding causal simulations are necessary to understanding realistic cases, theses simulations are also difficult to analyze in detail, sufficient to gain even qualitative physical understanding. One of the difficulties is that even the simplest cases of a plasma wave (say, with the generation of a plasma wave with a given wavenumber) involve the growth of the harmonic modes, involving several plasma waves in the system, loading to a more complicated structure in phase space. To assist in the development and testing new computational models, the much more limited and less-demanding spatially periodic simulations of evolution from an initial state can be very useful, because now we need to consider the behavior in time only of the discrete spatial Fourier modes, allowing direct comparison with the theoretical estimates of growth rates of the instability in the strong relativistic regime. Clearly, a periodic simulation will be significantly less demanding than a fully causal simulation only if the spatial period (the largest spatial wavelength) is much less than the size of the calculation length in a fully spatiotemporally causal calculation of useful size. This smaller spatial period necessarily means a coarsening of the allowed wave-vector spectrum.

We start with an initial homogeneous Maxwellian distribution function with a temperature $T_e = 3$ keV, without perturbation term. The initial large amplitude pump wave (ω_o, k_o) is taken as $\mathbf{E} = (0, E_o \cos k_o x, E_o \sin k_o x)$. (ω_o, k_o) satisfy the relativistic dispersion relation of circularly polarized waves $\omega_o^2 = \omega_p^2/\gamma_o + k_o^2 c^2$ with the Lorentz factor given by $\gamma_o^2 = 1 + a_{\rm osc}^2$. Choosing $k_o c/\omega_p = 1/\sqrt{2}$ and $a_{\rm osc} = \sqrt{3}$ (which corresponds to an irradiation of $I = 8, 20\ 10^{18}$ Wcm^{-2} for an electromagnetic wavelengh of 1 μm), we obtain $\omega_o = \omega_p$ (i.e., a ratio of the electron plasma density to the critical density of $n_e/n_c = 1$ or $n_e/\gamma_o n_c = 0.50$). By solving the dispersion relation in the case of a cold plasma, the growth rate of the relativistic parametric instability, induced by a high-intensity pump wave, can be evaluated as a function of the wavenumber; the result is shown in Fig. 1. We see clearly that the most unstable mode is located at $kc/\omega_p = 1.40$ and corresponds to a growth rate of $\gamma/\omega_p \approx 0.409$. The choice of $k_o (= \Delta k = 2\pi/L = 1/\sqrt{2})$ in effect determines the box length L in terms of c/ω_p. The corresponding plasma wave is then $k_e c/\omega_p = 2\Delta k$. In Fig. 2, we have plotted the time evolution of the most unstable plasma mode (mode 2) on a logarithmic scale: the curve indicates a growth rate around of $\gamma_{\rm num}/\omega_p \approx 0.406$ in good agreement with the expected value predicted by the linear theory.

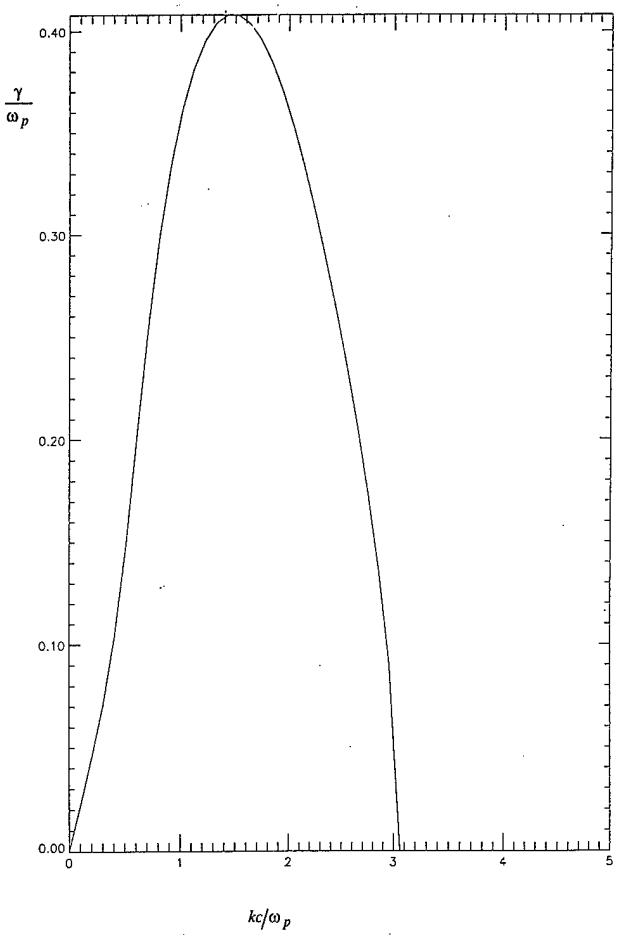


Fig. 1. Growth rate of the relativistic parametric instability γ/ω_p induced by an ultra intense circularly polarized electromagnetic wave versus the wavenumber kc/ω_p. The parameters are $a_{\rm osc} = \sqrt{3}$ and $n_e/n_c = 1$. We see clearly that the most unstable mode is located at $kc/\omega_p = 1.40$ and corresponds to a growth rate of $\gamma/\omega_p = 0.409$.

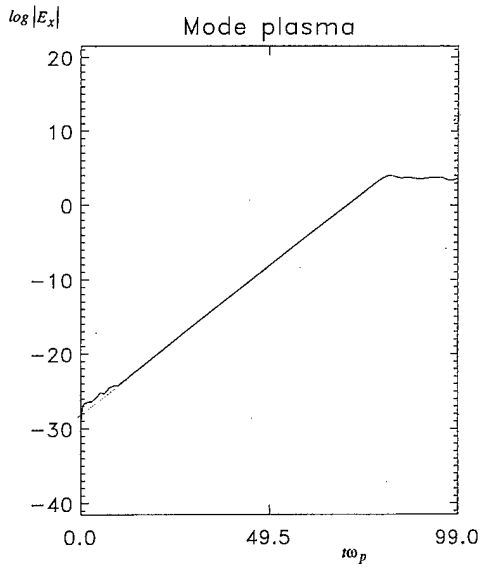


Fig. 2. Time evolution of the most unstable plasma mode (mode $2\Delta k$) on a logarithmic scale: The curve indicates a numerical growth rate $\gamma_{\rm num}/\omega_p \approx 0.406$ in good agreement with the expected theoretical value.

III. Accelerated Particles Dynamics

In an earlier paper dealing with an open "causal" system [4] (see also [5]), we have shown that the SLV code is able to give strikingly clear pictures of the phase space dynamics, showing impressive correlation with simple orbit theory for steady waves. In this section, the model is extended to take into account the ponderomotive term in the calculus of the trapped orbit trajectory, i.e., the separatrix of particles (as computed from the potential Φ and the vector potential $\mathbf{A}$ given by the code). We write the potential energy and the vector potential as a function of the new variable $x' = \gamma_\varphi(x - v_\varphi t)$, v_φ being the

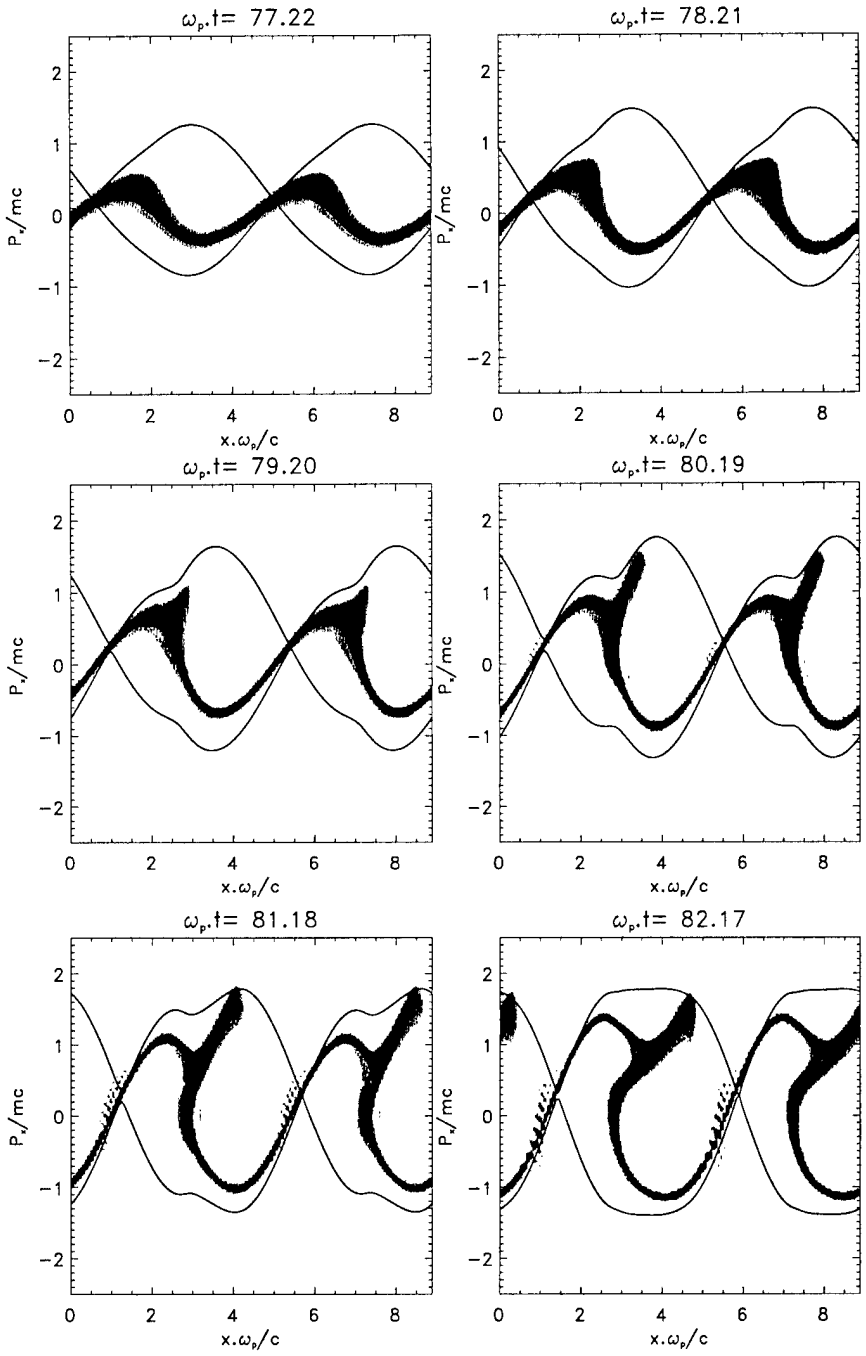


Fig. 3. Phase space representation of the electron distribution function in the case of the relativistic electron parametric instability with $a_{osc} = \sqrt{3}$ and $n_e/n_c = 1$. We have superimposed the separatices calculated through the electromagnetic fields given by the SLV code. We can see a very striking agreement between the separatrix and the particle orbits. A particle trapping/detrapping process gives rise to a more complicated structure in phase space at the end of the simulation.

plasma wave phase velocity and $\gamma_\varphi = (1 + p_\varphi^2/m^2c^2 + a_o^2)^{1/2}$ being the Lorentz factor evaluated at point $x' = x'_o$ and $a_o = eA(x'_o)/mc$. The motion of a test particle is obtained from the Hamiltonian in the laboratory frame

$$H = e\Phi(x') + mc^2\gamma \tag{10}$$

with

$$\gamma = \sqrt{1 + \frac{p_x^2}{m^2c^2} + a^2}. \tag{11}$$

In the moving frame $x' = \gamma_\varphi(x - v_\varphi t)$, we can write a new Hamiltonian H', which is now a constant of the motion. We have

$$H'/\gamma_\varphi = e\Phi(x') + mc^2\left(1 + a^2 + \frac{p_x^2}{m^2c^2}\right)^{1/2} - v_\varphi p_x. \tag{12}$$

In the following, we use dimensionless quantities $\xi = x\omega_p/c$, $\xi' = \gamma_\varphi(\xi - \beta_\varphi\tau)$, $u = p_x/mc$, $\tau = t\omega_p$, $\phi = e\Phi/mc^2$, $\beta_\varphi = v_\varphi/c$, and $h = H/mc^2$. We have

$$\frac{h'}{\gamma_\varphi} = \phi(x') + \sqrt{1 + a^2 + u^2} - \beta_\varphi u. \tag{13}$$

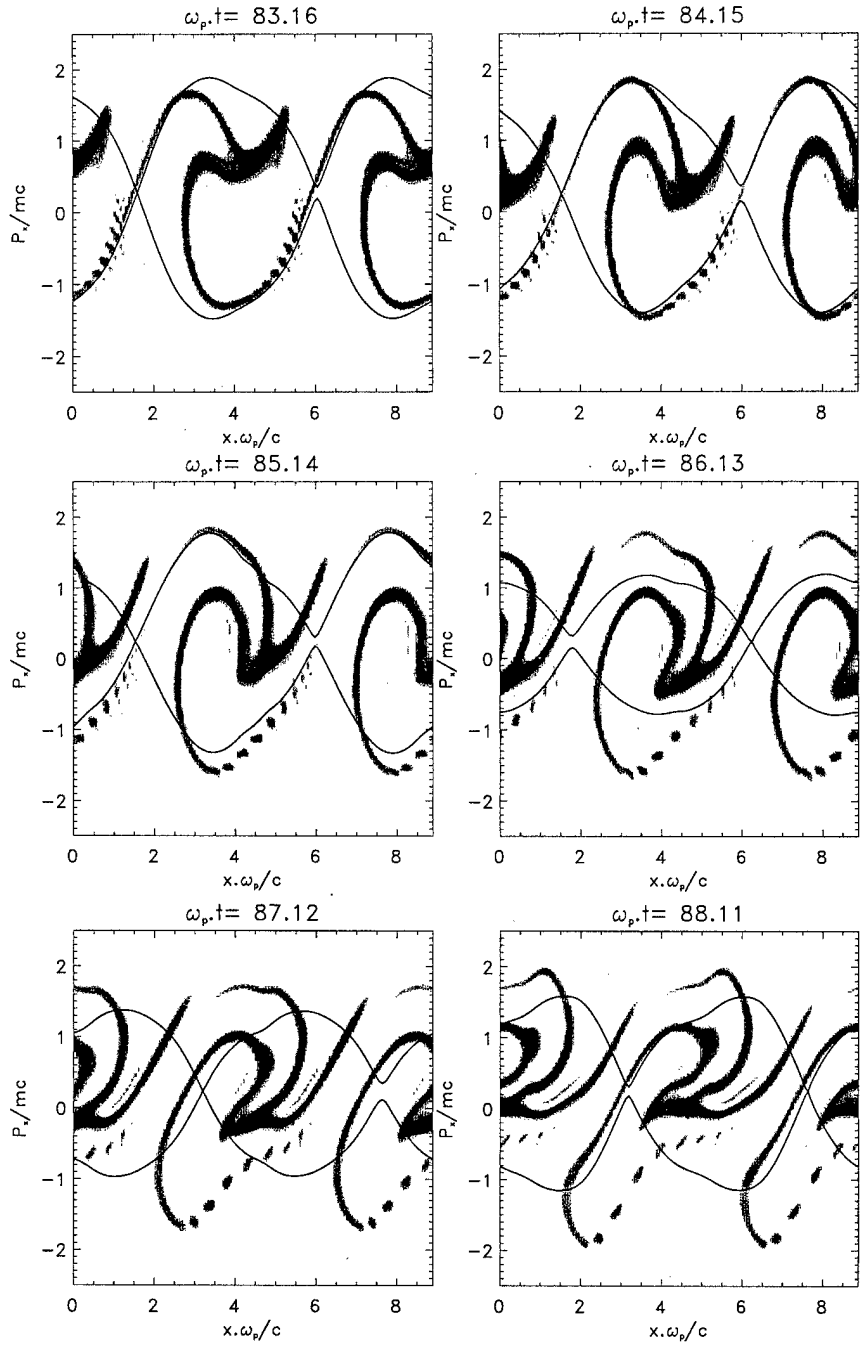


Fig. 3. *(Continued.)* Phase space representation of the electron distribution function in the case of the relativistic electron parametric instability with $a_{\rm osc} = \sqrt{3}$ and $n_e/n_c = 1$. We have superimposed the separatices calculated through the electromagnetic fields given by the SLV code. We can see a very striking agreement between the separatrix and the particle orbits. A particle trapping/detrapping process gives rise to a more complicated structure in phase space at the end of the simulation.

To find the values h'_s on the marginally trapped orbits ("the separatrix"), we notice that the fixed points of h' lie at $\xi = \xi_o$ and $u = u_\varphi = \gamma_\varphi \beta \varphi$ together with $\phi = \phi_o$ and $\gamma = \gamma_\varphi$. At these fixed points, h' takes on the separatrix value h'_s. We have

$$\phi(\xi') + \sqrt{1+u^2+a^2} - \beta_\varphi u = h'_s/\gamma_\varphi = \phi_o + \sqrt{1+u_\varphi^2+a_o^2} - \beta_\varphi u_\varphi. \quad (14)$$

If $h' < h'_s$, the particle is trapped; if $h' > h'_s$, it is not trapped. Combining (13) and (14), the equation for the marginally trapped orbit can be written in the following form:

$$\frac{1+a_o^2}{\gamma_\varphi^2}u^2 - 2\beta_\varphi u\left(\phi_o - \phi + \frac{1+a_o^2}{\gamma_\varphi}\right) + 1 + a^2 - \left(\phi_o - \phi + \frac{1+a_o^2}{\gamma_\varphi}\right)^2 = 0 \quad (15)$$

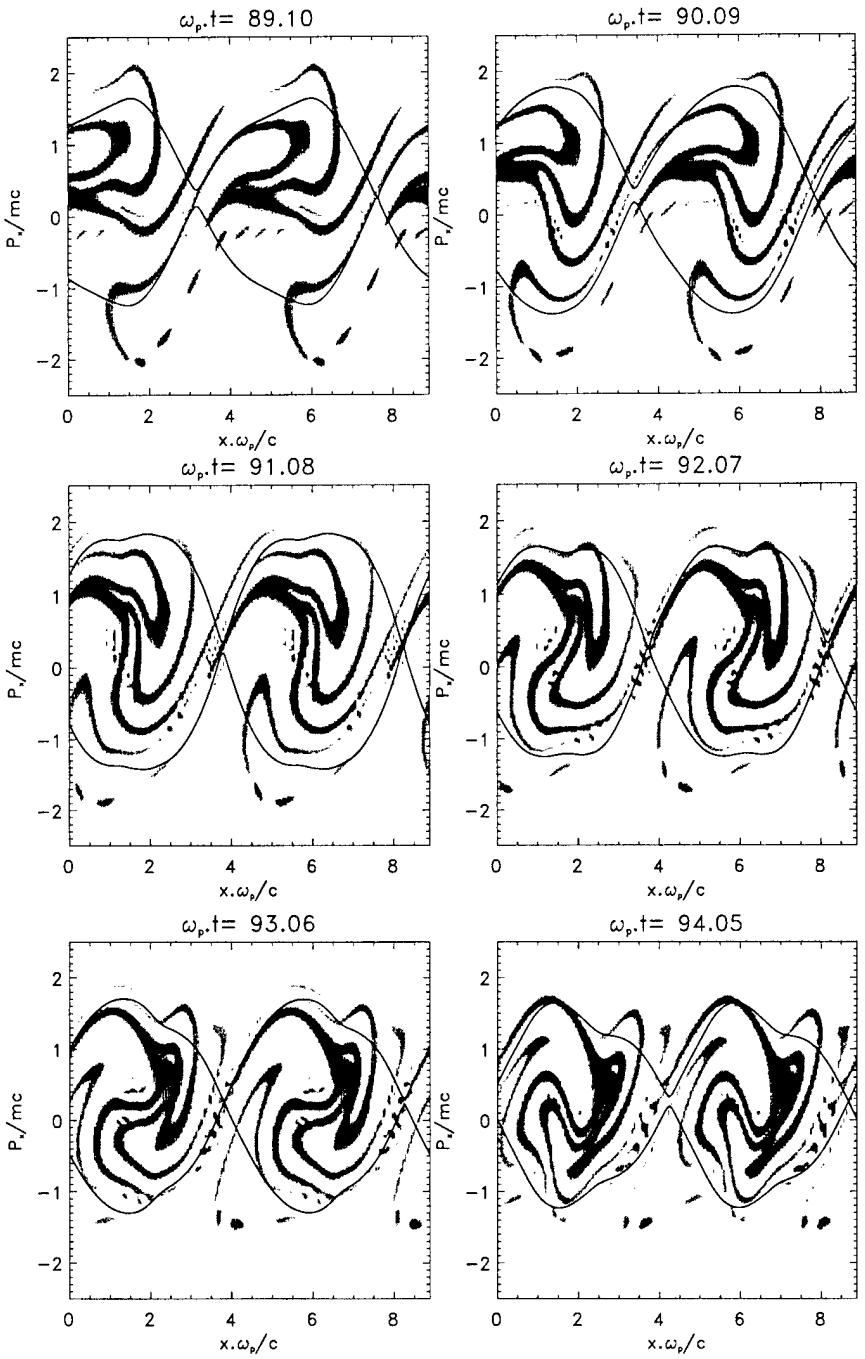


Fig. 3. *(Continued.)* Phase space representation of the electron distribution function in the case of the relativistic electron parametric instability with $a_{osc} = \sqrt{3}$ and $n_c/n_e = 1$. We have superimposed the separatices calculated through the electromagnetic fields given by the SLV code. We can see a very striking agreement between the separatrix and the particle orbits. A particle trapping/detrapping process gives rise to a more complicated structure in phase space at the end of the simulation.

which allows the determination of the separatrix from code values ϕ and a. The variable ξ_o is determined by considering the maxima of the function

$$G(\xi') = \phi + \frac{\sqrt{1+a_o^2}}{\gamma_\varphi}\sqrt{1+a^2}.$$

In Fig. 3, we present the separatrices calculated in this way from the simulation electromagnetic field superimposed on the accurate phase space representation afforded by the SLV code. Here, gray shading has been used to indicate the relative values of the normalized phase space density between 0.001 and 0.3. We can see a good agreement between the separatrix and the electron distribution function, although the dependence of the function on the coordinate $x-v_\varphi t$ is more complex at the plasma wavebreaking. Although this comparison must be considered with caution, it gives the general view of the trapped particle dynamics. The use of separatrices calculated directly by the data of the electromagnetic fields seen by particles gives new insight into the accelerated particle behavior. The separatrix amplitude oscillates rapidly in time, showing that the trapping process is

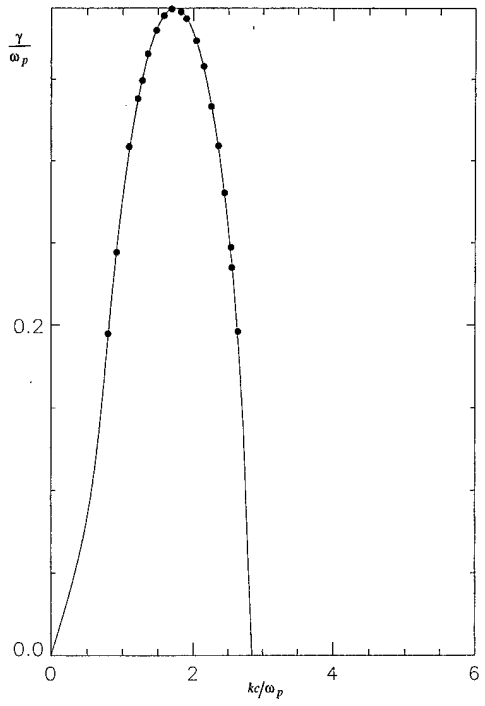


Fig. 4. Display of the growth rate of the electron relativistic instability for $n_e/n_c = 0.58$ and $a_{\rm osc} = 1$ as a function of the wavenumber kc/ω_p. We have superimposed on the curve the numerical values given by the SLV model.

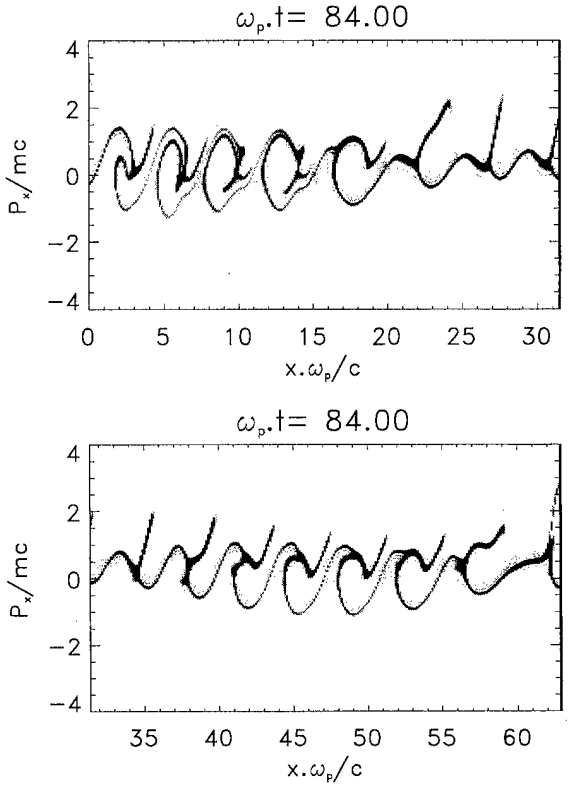


Fig. 5. Phase space representation of the electron distribution function at the beginning of the instability. The curve corresponds at time $t\omega_p = 84$ and gives more insight into the particle acceleration process. A local plasma wavebreaking scenario can be seen at $x\omega_p/c \approx 25$.

not adiabatic and the particle trapping–detrapping cycles seen in the electron distribution function behavior can be well explained using this representation.

The complex structures (arms and spirals) inside the separatrices implicitly reflect the history of the particles trapped as the wave built up. The simple spiral structure inside the trapping limit in the early frames clearly reflects the rapid increase followed by the decrease in wave energy. At the frame $t\omega_p \approx 83$, the amplitude of the field (including plasma wave and ponderomotive effect) is near its maximum, with a maximum separatrix momentum (near $x\omega_p/c$ value of 3) of 1.90 times mc. After the longitudinal force maximum is reached, the marginally trapped particles now begin to detrap, as evidenced by the fact they are now outside the upper wave separatrix boundaries (i.e., on the far side for each separatrix from the wave momentum value). This detrapping, which can be easily foreseen becomes manifest as the particles approach the separatrix X points, located at $x\omega_p/c = 2$. These electrons (forming the spiral structure) are now free to ride on the top of the waves. At time $t\omega_p \approx 86$, the field is at its minimum level and the spirals of the vortices are clearly outside the separatrix boundaries. This fast folding/detrapping evolution continues in frames $t\omega_p \approx 94$, leading to more complexity in phase space but little change in momentum.

To show the importance of the choice of the plasma box, we did a second simulation, but for a longer plasma, which exhibits at the beginning of the evolution ($t\omega_p \approx 84$), 16 vortices (with a phase space sampling of $N_x \times N_{p_x} = 2048 \times 256$ grid points, i.e., 524 288 "particles." The following parameters are used: pump wave frequency $\omega_o = 1.306\,\omega_p$, (corresponding to a ratio of the electron density to the critical density of $n_e/n_c = 0.58$), $a_{\rm osc} = 1$, and $k_o c/\omega_p = 1$. The fundamental wavenumber is $\Delta kc/\omega_p = 2\pi c/L\omega_p = 0.1$, which determines the plasma length $L\omega_p/c = 20\pi$. The most unstable plasma mode can be obtained by determining the growth rate of the relativistic parametric instability, as can be seen in Fig. 4, which gives a wavenumber $kc/\omega_p \approx 1.6$ (i.e., a plasma Fourier mode number of 16). We have then superimposed on the theoretical curve obtained directly by solving the dispersion relation the numerical values obtained by the SLV code. The agreement is particularly good, which validates our numerical model. The corresponding phase space representation of the electron distribution function is shown in Figs. 5–7 at the corresponding times $t\omega_p \approx 84$, 90, and 108. In the strongly nonlinear regime of the instability, the wave–particle interactions are important, which make the simple orbit theory approach difficult because of the presence of several plasma modes in the plasma. Fig. 5 gives more insight into the particle acceleration process at the beginning of the instability. It is interesting to mention that the fast electron dynamics in phase space is the result of a more complex mixing of several plasma modes (from mode 8–24). The electron phase space is strongly modulated and shows another region containing fast electrons located at $x\omega_p/c = 25$–30, corroborating a local plasma wavebreaking scenario. Figs. 6 and 7 display the phase space representation at two different times $t\omega_p = 90$ and 108 during the plasma evolution. It is clear that to understand the instability mechanism induced by the electromagnetic wave will require a very detailed analysis of the

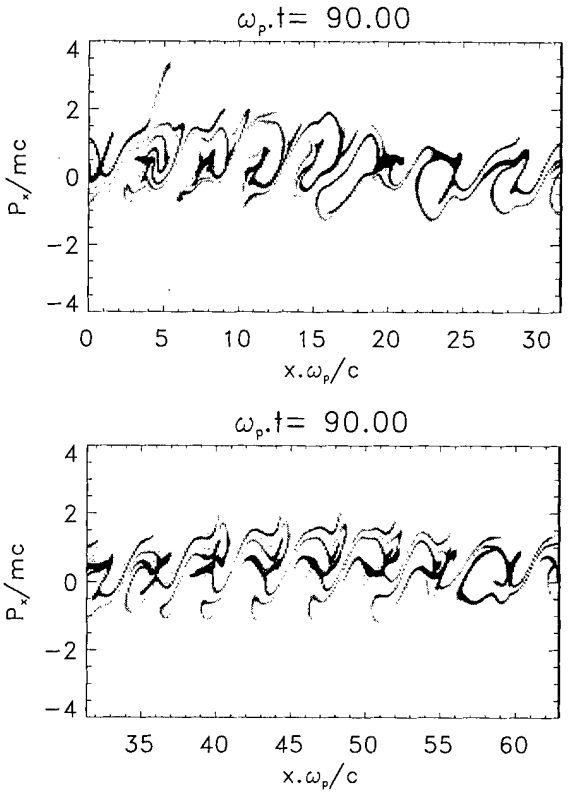


Fig. 6. Corresponding phase space behavior at time $t\omega_p = 90$. The phase space vortices became more and more complex because of the presence of several plasma modes.

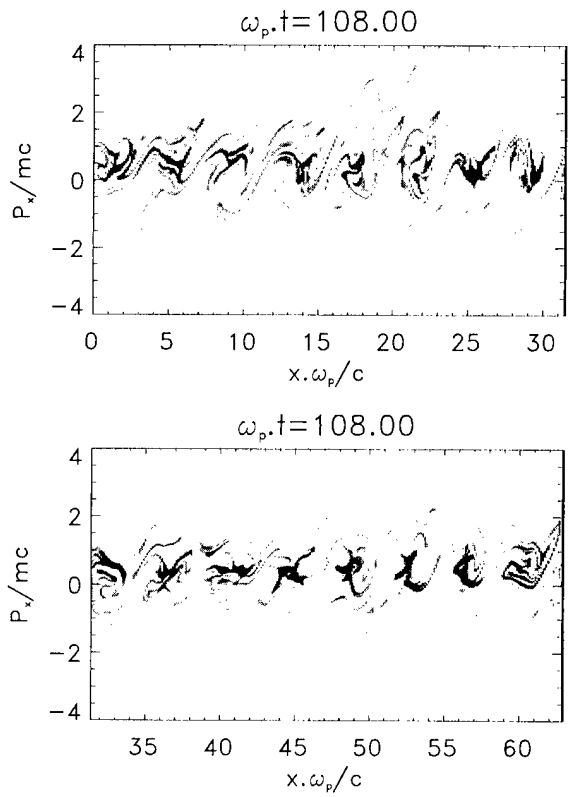


Fig. 7. Corresponding phase space representation at later time $t\omega_p = 108$. A multiple "trapping/detrapping" process leads to the heating of the plasma.

kinetics and time history of the accelerated particles. The SLV code allows us to follow exactly the evolution of these accelerated particles, and the use of separatrices (in a simplest case) allows us to analyze in detail the wave–particle interaction. We see indeed that the phase space structures (at time $t\omega_p = 108$) that characterize the plasma response caused by the injection of the electromagnetic wave become more and more complex. In the region of an intense plasma field, the potential (and then the separatrices orbit) is rapidly varying in space and time, leading to multiple reorganizations of the accelerated particle population (trapping/untrapping processes), leading to a "heating" process of the particles in the bulk of the plasma. Finally, obtaining these insights into this detailed behavior was only possible with the SLV code, which can provide a great deal of resolution in phase space. This work on a spatially periodic case is intended as preparation for the application of similar analysis techniques of the simulations of the more realistic causal case in which spatial periodicity no longer applies.

IV. Study of Laser Penetration in Overdense Plasma at Relativistic Intensities

It is known that a high-frequency electromagnetic wave with frequency less than the electron plasma wave ($\omega_o < \omega_p$) cannot propagate in a plasma. But if the intensity of the electromagnetic field is sufficiently high, to make electrons relativistic, the cutoff frequency ω_p is modified because of relativistic effects. The initial condition previously studied in Section III, which corresponds to an electromagnetic wave occupying uniformly the whole plasma, is rather unrealistic in that case because, in a practical experiment, the laser light is incident on a performed plasma or on a solid target (however, we can note that the periodic case allows us to characterize the nature of the solution for overdense plasmas in the case of the relativistic parametric instability). In the following, we suppose that the plasma is inhomogeneous, and we take into account the propagation of the electromagnetic wave. A comparison between a 1-D model (with two phase space variables $x - p_x$ plus a cold description in the perpendicular momentum direction) and a full 1-D 1/2 model (using now x, p_x and the kinetic momentum component p_y) has been investigated in the case of a linearly polarized electromagnetic wave to analyze the influence of the perpendicular temperature.

A. Numerical Results Using a 1-D SLV Code

First, let us recall briefly the main features of the 1-D electromagnetic Vlasov–Maxwell code. The plasma can be described by the usual Vlasov equation for the electron distribution function $f(x, p_x, t)$

$$\frac{\partial f}{\partial t} + \frac{p_x}{m\gamma}\frac{\partial f}{\partial x} + e\left(E_x + \frac{P_y(x,t)B_z}{m\gamma}\right)\frac{\partial f}{\partial p_x} = 0 \qquad (16)$$

with the Lorentz factor given by

$$\gamma = \sqrt{1 + \frac{p_x^2}{m^2c^2} + \frac{P_y^2(x,t)}{m^2c^2}}.$$

In the transverse p_y, we have assumed a fluid description. Defining P_y as the fluid transverse momentum, we have then

$$\frac{\partial P_y}{\partial t} = eE_y. \qquad (17)$$

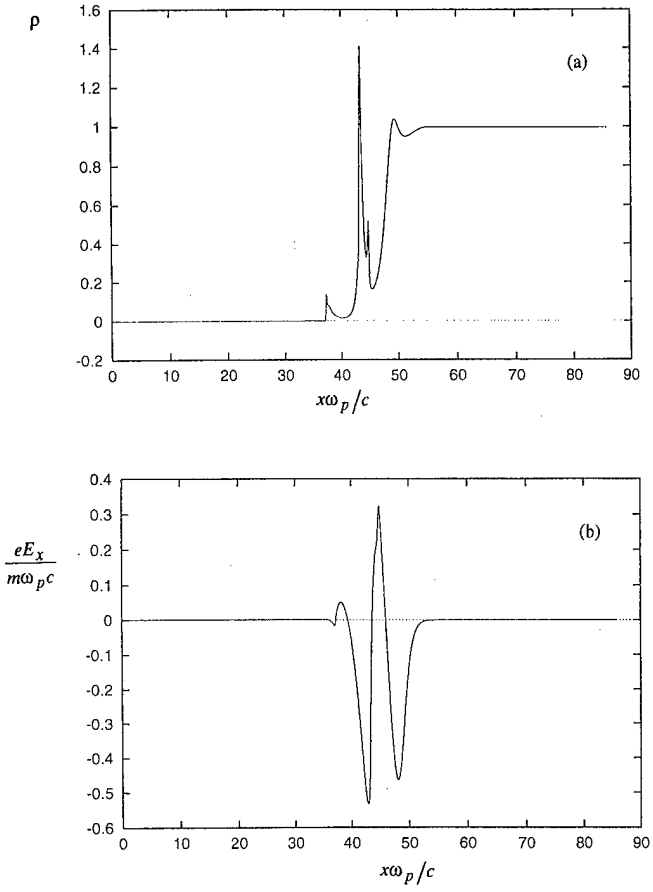


Fig. 8. (a) Display of the relativistic density $\rho = \int dp_x f/\gamma$ obtained from the SLV code versus the space at time $t\omega_p = 80$. The curve exhibits a strong peak in the profile as a result of a plasma wavebreaking scenario. (b) Corresponding longitudinal electric field behavior at the same time.

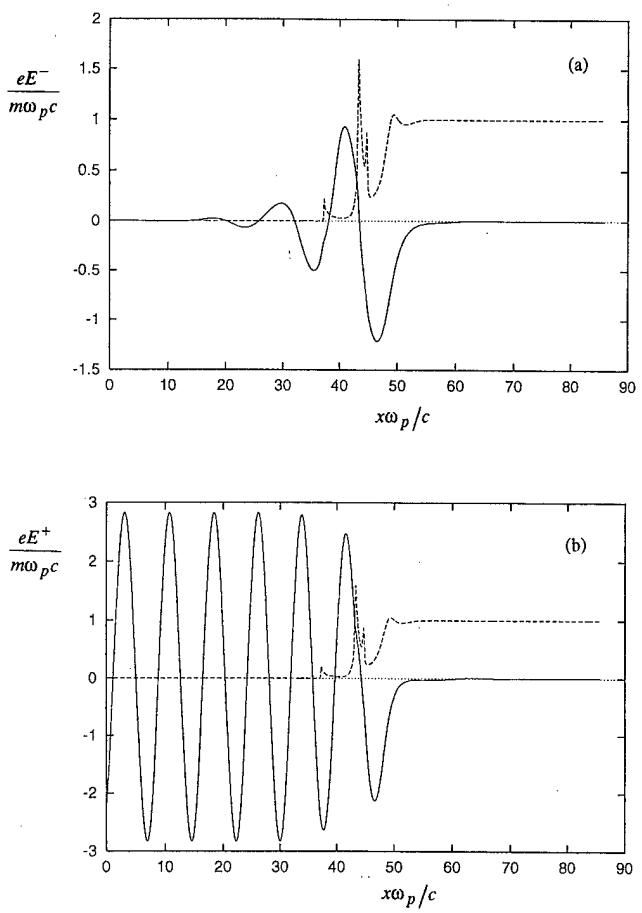


Fig. 9. (a) Electromagnetic wave part $E^- = E_y - cB_z$ propagating in the backward direction at the same time $t\omega_p = 80$. (b) Corresponding electromagnetic field $E^+ = E_y + cB_z$ propagating in the forward direction. We have superimposed on the curves the relativistic density profile ρ. We see clearly the reflection of the electromagnetic wave in the plasma and the strong absorption of the pump energy to plasma.

In our simulations, a laser pulse propagating in the x-direction and polarized in the y-direction is normally incident on an inhomogeneous density profile of 2.60 μm thick, followed by a uniform plasma of length 4 μm ($4\lambda_o$, with a pump wavelength of $\lambda_o = 1$ μm). For the simulations presented here, the ions form initially an immobile background with steep gradient in density, and the electron density is $n_e = 1.5n_c$. The irradiation is $I = 4.10 \times 10^{18}$ Wcm^{-2}, which corresponds to a normalized quiver momentum of $a_{\rm osc} = \sqrt{3}$, and the relativistic factor in vacuum is then $\gamma_o = \sqrt{1 + a_{\rm osc}^2} = 2$, leading to $n_e/\gamma_o n_c = 0.75$. The phase space sampling is $N_x \times N_{p_x} = 4096 \times 385$, i.e., 1.576.960 "particles" or grid points. We use in the calculation a time step $\Delta t\omega_p = 0.041$, and the plasma length is $L\omega_p/c \approx 86$.

The aim of the present section is to investigate the interaction of a relativistically strong laser pulse with an overdense plasma. The interest of this work stems from the fact, although the interaction between a laser pulse and a plasma has been widely studied using Eulerian–Vlasov codes for moderate intensities [4] and [9], and for high-frequency electromagnetic waves [6], [10]–[12], new physical phenomena involving the pulse absorption and the penetration of the electromagnetic energy in the plasma are found in the case of relativistically strong laser pulses. These phenomena include wavebreaking and the resulting acceleration of electrons previously observed in numerical simulations using PIC codes (see, for instance, [3] and [14]).

Fig. 8(a) displays the relativistic density $\rho(x, t) = \int dp_x f(x, p_x, t)/\gamma$ obtained from the SLV code as a function of the space at time $t\omega_p = 80$. The curve exhibits the appearance of a strong peak as the result of the laser–matter interaction. This agrees with the longitudinal plasma wavebreaking scenario. Fig. 8(b) shows at the same time the corresponding longitudinal electric field E_x. The strong oscillatory electric field (plus the ponderomotive field) that is excited at the plasma boundary (because of the strong nonuniformity) gives rise to a strong particle acceleration process. The maximum of the electric field is $eE_x/m\omega_p c \approx 0.50$. At the front wave, there is a strong discontinuity in the density profile (located at $x\omega_p/c \approx 45$) caused by the relativistic nature of the wave. The discontinuity acts as a mirror for the incoming laser light, which is reflected (with a Doppler shift). Fig. 9(a) shows the quantity $E^-(x, t) = E_y - cB_z$ (which describes the electromagnetic wave part propagating in the backward direction), as a function of space $x\omega_p/c$ at the same time. We have superimposed the electron density profile of Fig. 8(a) onto the same curve. Fig. 9(b) shows the electromagnetic value

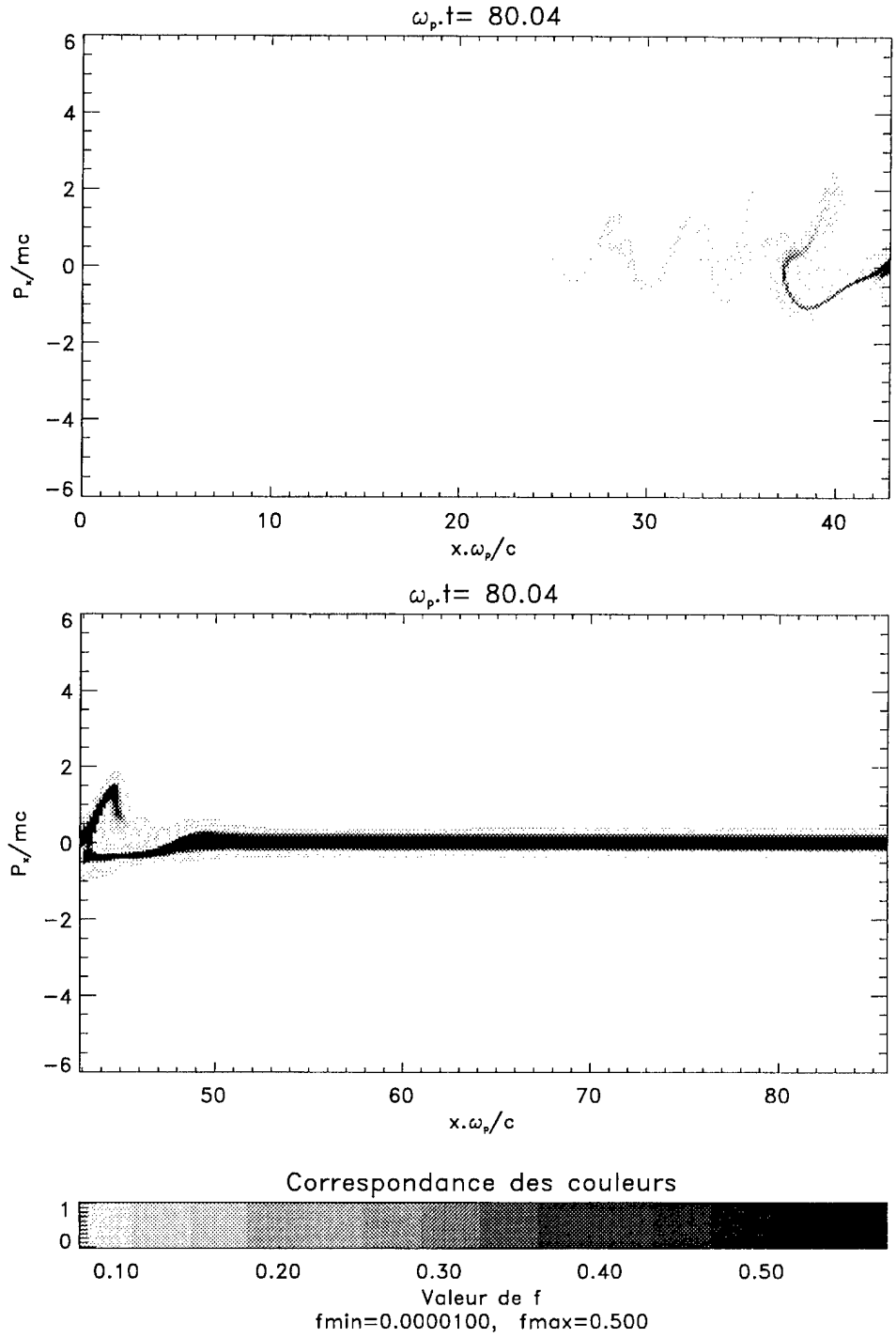


Fig. 10. Phase space representation of the electron distribution function at time $t\omega_p = 80$ in the case of the electron relativistic parametric instability in an overdense plasma with $n_e/n_c = 1.50$ and $a_{osc} = \sqrt{3}$. The plot exhibits clearly a strong particle trapping at $x\omega_p/c \approx 45$ as a result of a plasma wavebreaking scenario.

$E^+ = E_y + cB_z$ that propagates in the forward direction $+x$. We see clearly the reflection of the electromagnetic wave in plasma. We interpret it because of the Doppler effect produced by a reflecting charge sheet, formed in a narrow region at the plasma boundary, oscillating under the action of the laser pulse. The ratio of the reflected wavenumber k_r to the incident wavenumber k_i is found numerically close to $k_r/k_i \approx 0.68$. These curves also exhibit a strong absorption of the incident pump wave energy to plasma. The behavior of the electron distribution in phase space at the beginning of the parametric instability is presented in Fig. 10 at time $t\omega_p = 80$. The figure shows clearly the mechanism of plasma wavebreaking located at $x\omega_p/c \approx 45$, giving rise to a strong particle trapping process of the whole distribution function. This acceleration mechanism corresponds exactly to the electron density peak observed in Fig. 8(a). Fig. 11 shows the behavior of the plasma at later time $t\omega_p \approx 130$. The interaction of the laser pulse with a sharp-boundary plasma leads to the "vacuum heating" of the

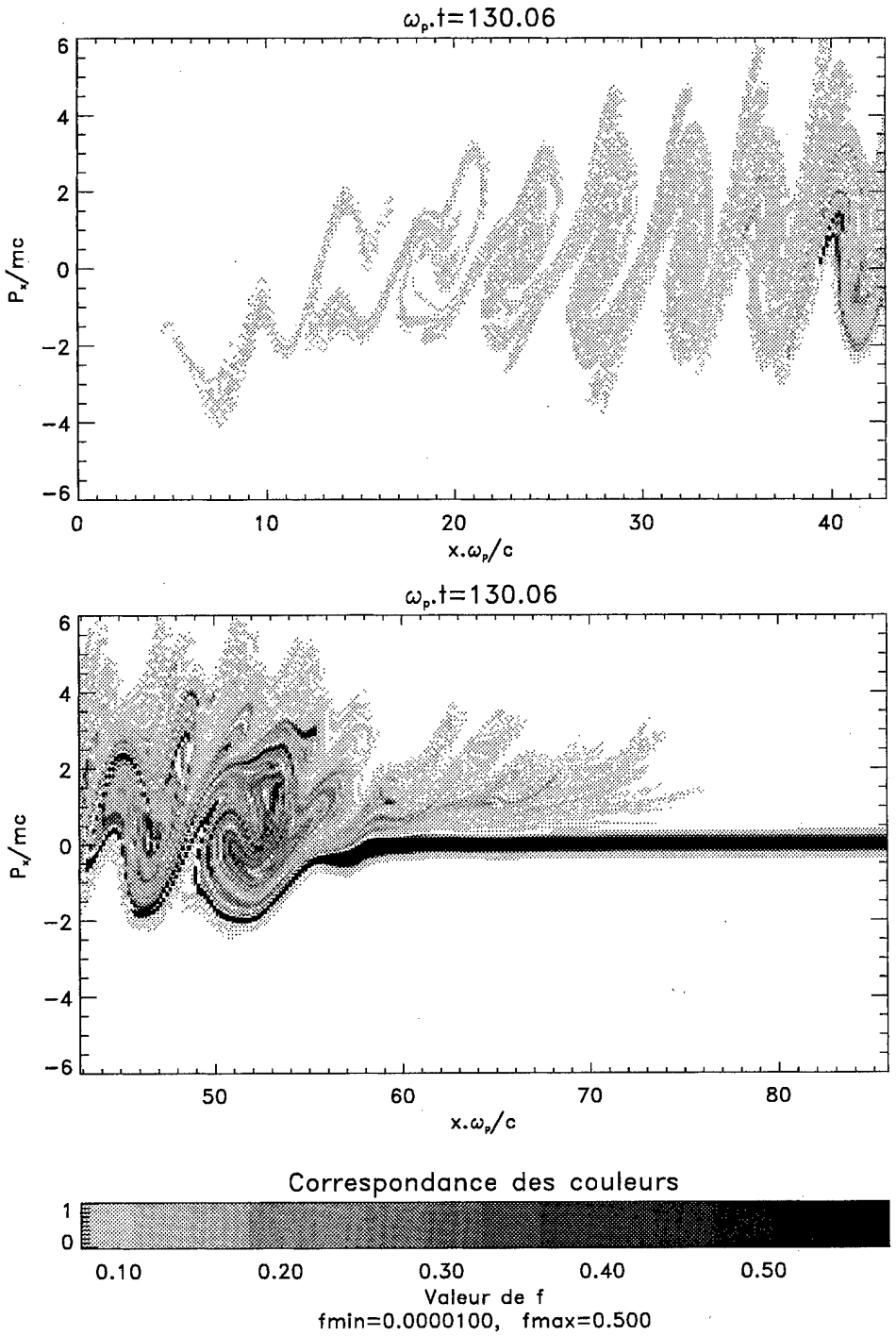


Fig. 11. Corresponding electron phase space at later time $t\omega_p = 130$. The laser–plasma interaction gives rise to the expulsion into the vacuum region of part of fast electrons leading to strong absorption of the electromagnetic wave.

electrons proposed by Brunel [15], i.e., to the expulsion from the plasma into the vacuum region of part of fast electrons, which leads to strong absorption of the electromagnetic radiation. We see also the propagation of a fast particle inside the plasma.

A second numerical simulation has been performed in the case of a quiver momentum $a_{\rm osc} = \sqrt{8}$ (corresponding to an irradiation of 1.09×10^{19} Wcm^{-2} and to a relativistic factor in vacuum of $\gamma_o = 3$, i.e., to a ratio $n_e/\gamma_o n_c = 0.50$) to analyze the penetration of the ultra intense laser pulse in the overdense plasma. Fig. 12 shows that the wave propagation in inhomogeneous plasma with density up to $n_e = \gamma n_c$ is allowed. Fig. 12(a) displays the electron density profile at time $t\omega_p \approx 130$ (we have also plotted the initial profile density in dashed lines), and Fig. 12(b) corresponds to the longitudinal electric field $eE_x/m\omega_p c$ plotted at the same time. The numerical simulation shows the penetration process in which the wave is penetrating by induced transparency inside the overdense plasma, leading to the growth of the longitudinal electric field with a maximum amplitude of $eE_x/m\omega_p c \approx 0.90$. Fig. 13 displays

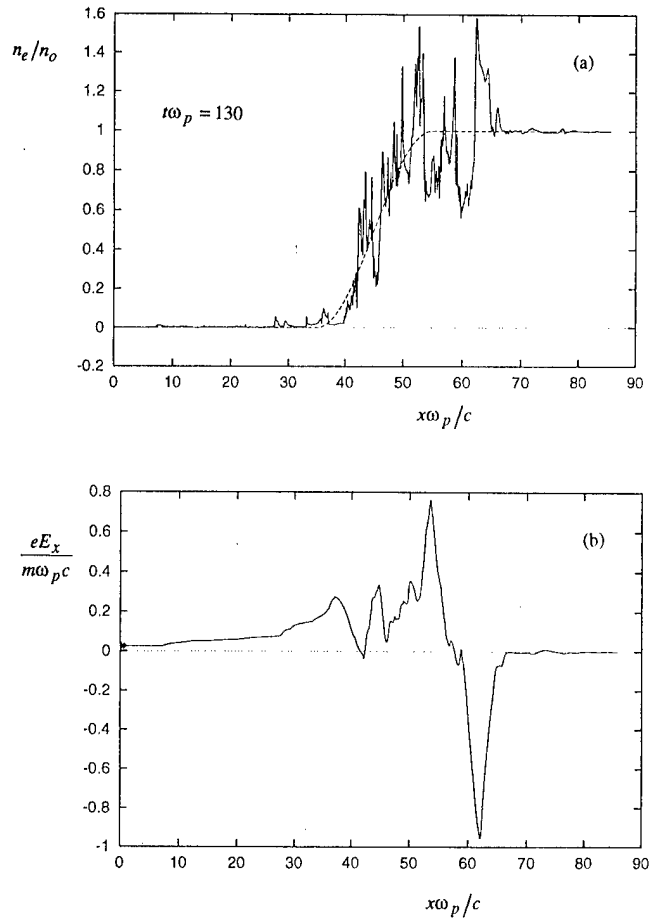


Fig. 12. (a) Electron density profile versus position $x\omega_p/c$ at time $t\omega_p = 130$ for parameters $n_e/n_c = 1.50$ and $a_{osc} = \sqrt{8}$. The dashed lines indicate the initial density profile. (b) Corresponding longitudinal electric field $eE_x/m\omega_p c$ versus the position.

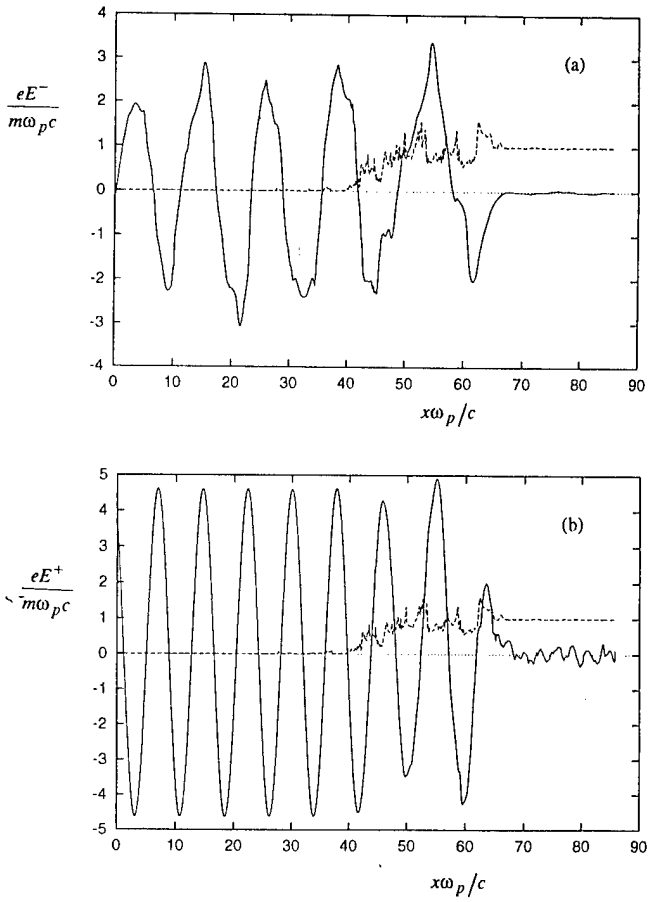


Fig. 13. Electromagnetic field contribution: backward-propagating part E^- is shown in (a), whereas the forward-propagating part E^+ is shown in (b). The curves exhibit the compression of the plasma critical density interface, pushed by the relativistic laser pulse and the total reflection of the wave at the interface.

the electromagnetic fields $E^-(x, t)$ in Fig. 13(a) and the corresponding field E^+ in Fig. 13(b) at the same time $t\omega_p \approx 130$. The dashed lines indicate the corresponding electron density profile at this step of the evolution. The transverse electric field first propagates through the overdense plasma. In this mechanism, the plasma critical-density interface is pushed forward by the ultra intense laser light and propagates inside the target. Fresh particles at the interface with the laser pulse are then pushed and accelerated. We see clearly the absorption of the forward-propagating wave at the wavefront and the total reflection of the electromagnetic wave on the interface. In the penetration zone, a large longitudinal electric field is generated [Fig. 12(b)] and a strong particle trapping takes place near the critical interface, as illustrated in Fig. 14, which shows the electron distribution function in phase space. In this context, in which a variety of physical effects can possibly be involved in the overdense penetration process, it is particularly important to study carefully the propagation through a moderately overdense system, with particular attention given to the electron dynamics in phase space.

B. Numerical Comparison Using a 1-D 1/2 SLV Code.

In the precedent section, the transverse kinetic treatment of the distribution function (in the p_y direction) was replaced by the cold fluid description using a Dirac $\delta(p_y - P_y(x, t))$ distribution. This has been greatly facilitated by the Eulerian character of the SLV model (because we treat a distribution function), which allows us to use an exact solution in the form of a Dirac distribution (which corresponds to taking one particle in the p_y-direction). In the 1-D 1/2 SLV model, we integrate numerically the Vlasov equation, including now the p_y kinetic variable, i.e.,

$$\frac{\partial f}{\partial t} + \frac{p_x}{m\gamma}\frac{\partial f}{\partial x} + e\left(E_x + \frac{p_y B_z}{m\gamma}\right)\frac{\partial f}{\partial p_x} + e\left(E_y - \frac{p_x B_z}{m\gamma}\right)\frac{\partial f}{\partial p_y} = 0 \tag{18}$$

with the corresponding Lorentz factor now given by

$$\gamma = \sqrt{1 + \frac{p_x^2}{m^2c^2} + \frac{p_y^2}{m^2c^2}}. \tag{19}$$

The sampling of the phase space used here is $N_x \times N_{p_x} \times N_{p_y} = 1024 \times 128 \times 64$, i.e., 8.388.608. "particles" or grid points, and we keep the same parameters previously used in Section IV-A, i.e., $n_e/n_c = 1.50$ and $a_o = \sqrt{3}$. The numerical integration of

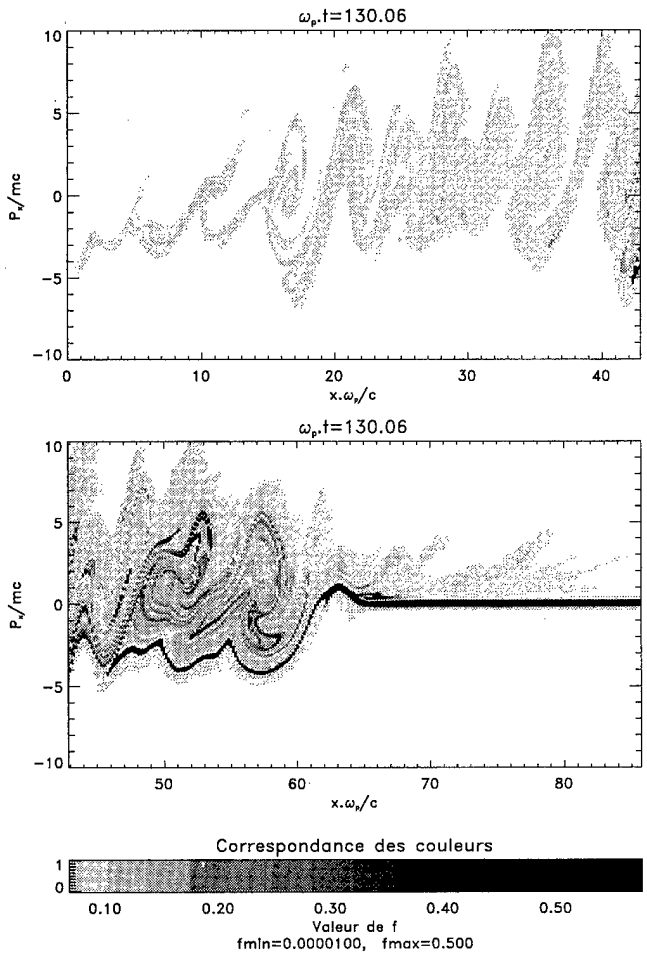


Fig. 14. Typical electron distribution function in phase space for the same parameters as in Fig. 12. The curves exhibit a strong particle trapping located near the plasma critical-density interface and the "vacuum heating," i.e., the emission of plasma electrons in vacuum.

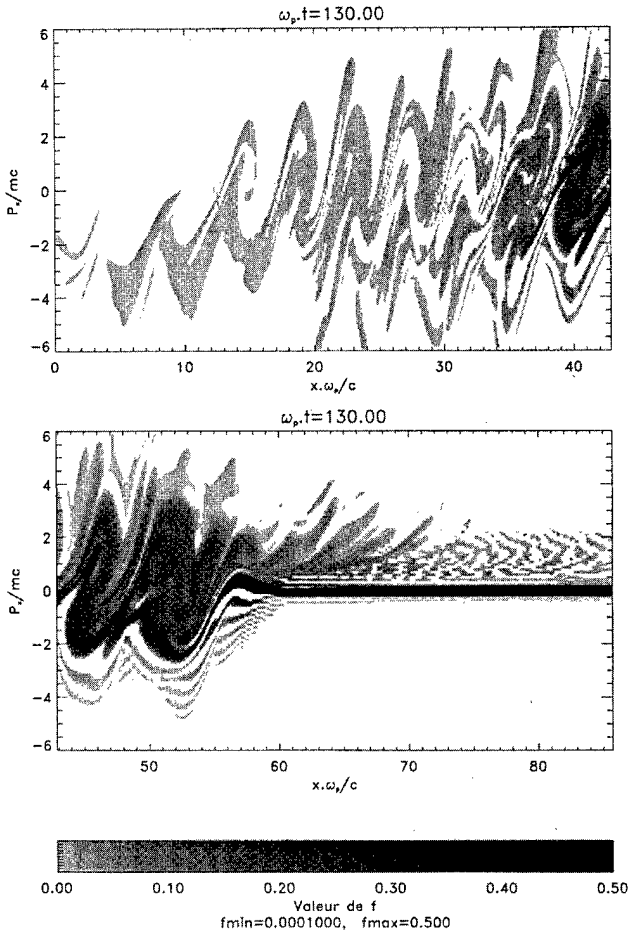


Fig. 15. $x-p_x$ phase space plot of the distribution function at time $t\omega_p = 130$ using a 1-D 1/2 SLV model with kinetic treatment along the p_y-direction. The numerical result seems to account rather well with the complex behavior met in Fig. 11 in the 1-D SLV model.

(18) is obtained by using a well-known fractional step or splitting scheme. The Vlasov equation is then split into parts. First, we solve

$$\frac{\partial f}{\partial t} + \frac{p_x}{m\gamma}\frac{\partial f}{\partial x} = 0 \tag{20}$$

corresponding to an advection in the real space x, and second:

$$\frac{\partial f}{\partial t} + e\left(E_x + \frac{p_y B_z}{m\gamma}\right)\frac{\partial f}{\partial p_x} + e\left(E_y - \frac{p_x B_z}{m\gamma}\right)\frac{\partial f}{\partial p_y} = 0 \tag{21}$$

i.e., a 2-D advection in momentum space. The main drawback of Lagrangian schemes is that a regular mesh rapidly distorts, losing discretization accuracy. Semi-Lagrangian schemes combine the regular mesh of an Eulerian scheme with the unconditional stability of a Lagrangian scheme. They build value of a regular mesh points x at time t by running a Lagrangian trajectory backward from (x, t) to some new point in phase space using the characteristic of the Vlasov equation. For example, in the treatment of (20), the exact solution is then given by $f(x, p_x, t_{n+1} = (n+1)\Delta t) = f(x - (p_x/m\gamma)\Delta t, p_x, t_n)$. The regular aspect of the distribution function is achieved by using a different set of "particles" at each time step, the set of particles being chosen such that they arrive exactly at the points of a regular Cartesian mesh at the end of the time step. The characteristics of the Vlasov equation are then needed to compute the trajectories of particles and the shifts in the x-direction. Thus, this semi-Lagrangian scheme needs only to transport the f-evaluation from x to $x - p_x\Delta t/m\gamma$ either by advection or interpolation from grid values. Cubic spline interpolation appears to be a good compromise between accuracy and cost (linear interpolation is too dissipative to be used). A similar method based on integration along characteristic in momentum space and 2-D B-spline interpolation is used for the numerical integration of (21). In Figs. 15–17, the results of the computer simulation are shown for the linearly polarized wave. Fig. 15 displays the $x - p_x$ phase space representation at time $t\omega_p = 130$, whereas Figs. 16 and 17 show, respectively, the corresponding $x - p_y$ and $p_x - p_y$ representation of the distribution function at the same time. We have added the time $t\omega_p = 125$ in Fig. 17. The particle dynamics in phase space calculated by using the 1-D 1/2 SLV model, which takes into account a kinetic transverse description for the p_y variable seems to account rather well with the complex behavior seen in the 1-D version previously shown in Fig. 11. Fig. 16 exhibits a strong modulation of the electron distribution function in the $x - p_y$ phase

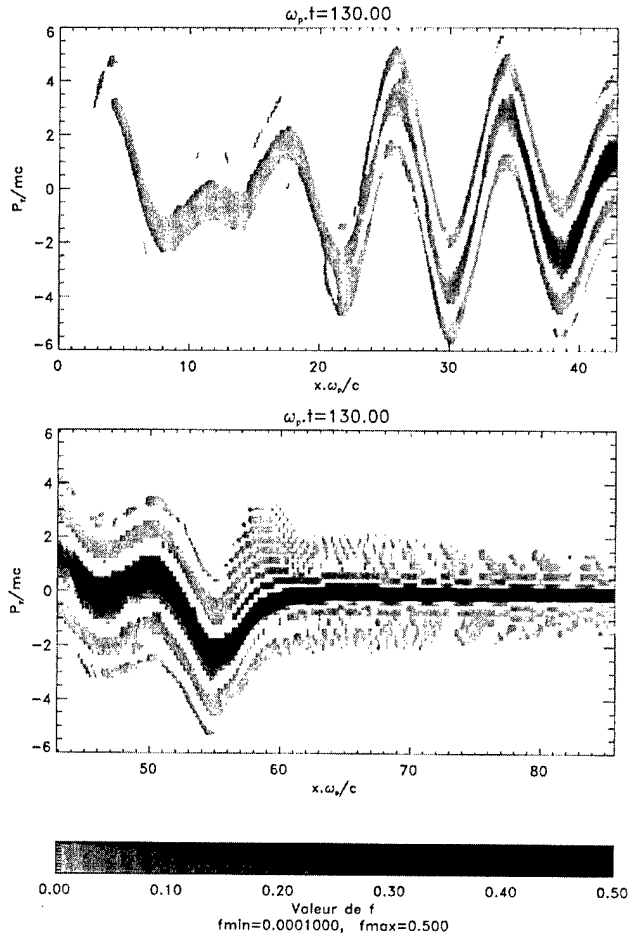


Fig. 16. $x-p_y$ phase space representation afforded by the 1-D 1/2 SLV model at time $t\omega_p = 130$, which characterizes the transverse motion of particles in the electromagnetic field of the laser pulse. Note that the distribution remains "cold" during the time evolution.

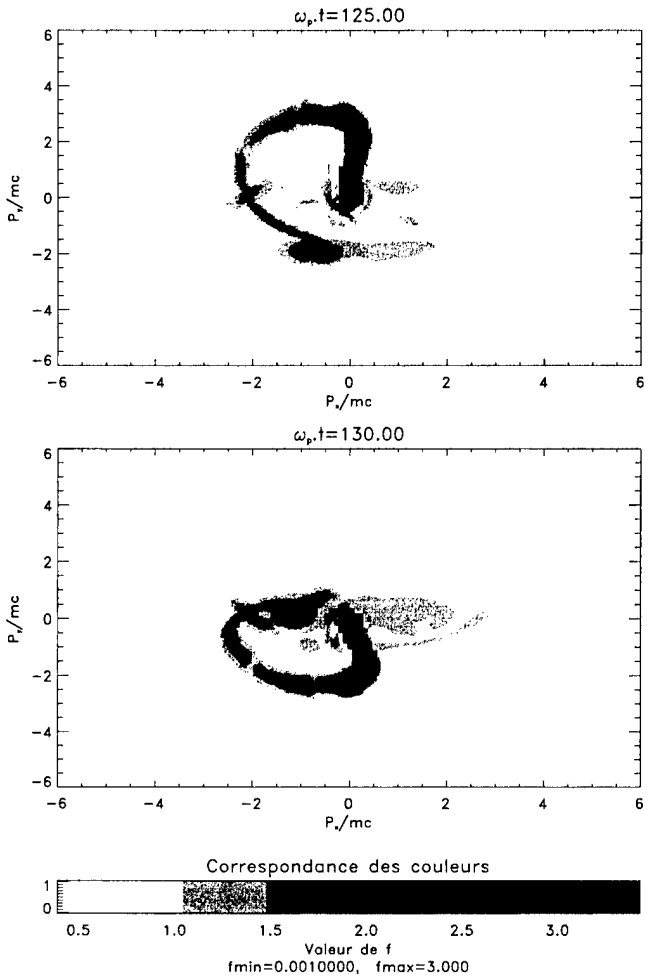


Fig. 17. $p_x - p_y$ momentum representation of the electron distribution function at two times $t\omega_p = 125$ and $t\omega_p = 130$. The parameters of the simulation are $n_e/n_c = 1.50$ and $a_{osc} = \sqrt{3}$.

space plane, induced by the strongly relativistic quiver velocity of particles. As shown in Figs. 16 and 17, a trapping mechanism of fast particles accompanies the penetration front as it moves inward. Finally, Fig. 17 displays the distribution function in the $p_x - p_y$ momentum space. Owing to the very good resolution in phase space afforded by the SLV model, we can begin to understand much of the details of the interaction. In keeping with the discussion of Fig. 15, showing at $x\omega_p/c \approx 50$ a strong particle trapping followed by particle acceleration of the whole electron distribution (a sign of plasma wavebreaking process), we see a strong modulation of the distribution function near the critical plasma-density interface caused by the strongly transverse electric field (induced by the relativistic quiver velocity of particle). In spite of the strong modulation of the distribution function (induced by the ultra intense laser pulse), the distribution remains cold during the instability process. The $x - p_y$ phase space representation characterizes the transverse motion of electrons in the electromagnetic field of the laser pulse. Further details of the plasma particle dynamics are illustrated by the plotting the $p_x - p_y$ momentum space (by integrating the distribution function over the x-coordinate). We see that the behavior of the whole distribution function is not symmetric in the p_x-coordinate space, which seems to indicate that the mechanism induced by the relativistic parametric instability does not lead to the usual heating of plasma, but to a final state as the result of trapping processes, with modification of the electron distribution function only in the positive momentum space.

V. Conclusion

A new semi-Lagrangian scheme has been assembled to simulate the interaction of an ultraintense electromagnetic wave with a plasma. We have begun to investigate the relativistic parametric instability induced by a strongly relativistic pump wave in a periodic plasma. The numerical results, in particular, the growth rates estimated by our SLV model, are found in good agreement with the theoretical values predicted by the model of Guérin *et al.* [1]. The interaction of intense laser radiation with underdense as well as overdense plasmas is well understood for fairly long pulses and of moderate intensities. However, the investigation of the interaction of an ultrashort and ultraintense pulse highlights new physical processes. The SLV code may be a good candidate to explore and understand these processes induced by the laser–plasma interaction in a strongly relativistic regime. It is clear that describing the population of trapped and accelerated particles will require a very detailed analysis of the

kinetics and time history of the plasma wave evolution. This work on a causal and 1-D system is intended as preparation for the application of similar analysis techniques to the simulations of the more realistic 2-D causal case in which filamentation takes place. In the latter case, we cannot use a 1-D plasma, but we must consider transverse spatial effects. This work is now in hand, and the results should be reported in due course.

ACKNOWLEDGMENT

The authors are indebted to the IDRIS Computational Center, Orsay, France, for computer time allocation on the Cray T3E and Cray YMP C98-C94 computers. The authors are grateful to J. Adam, A. Héron, T. Johnston, and B. Afeyan for helpful discussions.

REFERENCES

[1] S. Guérin, P. Mora, J. C. Adam, A. Héron, and G. Laval, "Propagation of ultra intense laser pulses through overdense plasma layers," *Phys. Plasmas*, vol. 3, pp. 2693–2701, 1996.

[2] A. Pukhov and J. Meyer-ter-Vehn, "Relativistic laser-plasma interaction by multi-dimensional particle-in-cell simulations," *Phys. Plasmas*, vol. 5, pp. 1880–1885, 1998.

[3] S. V. Bulanov, N. M. Naumova, and F. Pegoraro, "Interaction of an ultrashort relativiscally strong laser pulse with an overdense plasma," *Phys. Plasmas*, vol. 1, pp. 745–757, 1994.

[4] P. Bertrand, A. Ghizzo, T. W. Johnston, E. Fijalkow, and M. R. Feix, "A non periodic Euler–Vlasov code for the numerical simulation of laser plasma beat wave acceleration and Raman scattering," *Phys. Fluids*, vol. B2, pp. 1028–1037, 1990.

[5] T. W. Johnston, P. Bertrand, A. Ghizzo, M. Shoucri, E. Fijalkow, and M. R. Feix, "Stimulated Raman scattering: Action evolution and particle trapping via Euler–Vlasov fluid simulation," *Phys. Fluids*, vol. B4, pp. 2523–2537, 1992.

[6] A. Ghizzo, T. Reveille, P. Bertrand, T. W. Johnston, J. Lebas, and M. Shoucri, "An Eulerian Vlasov–Hilbert code for the numerical simulation of the interaction of high frequency electromagnetic waves with plasmas," *J. Comput. Phys.*, vol. 8, pp. 356–365, 1995.

[7] O. Coulaud, E. Sonnendrücker, E. Dillon, P. Bertrand, and A. Ghizzo, "Parallelization of semi-Lagrangian Vlasov codes," *J. Plasma Phys.*, vol. 61, pp. 435–448, 1999.

[8] A. Ghizzo, P. Bertrand, M. Shoucri, T. W. Johnston, E. Fijalkow, and M. R. Feix, "A Vlasov code for the numerical simulation of stimulated Raman scattering," *J. Comput. Phys.*, vol. 90, pp. 431–457, 1990.

[9] P. Bertrand, A. Ghizzo, S. J. Karttunen, T. J. H. Pättikangas, R. R. E. Salomma, and M. Shoucri, "Two stage electron acceleration stimulated Raman backward and forward scattering," *Phys. Plasmas*, vol. 2, pp. 3115–3129, 1995.

[10] A. Ghizzo, P. Bertrand, J. Lebas, T. W. Johnston, and M. Shoucri, "Study of high-frequency beatwave experiment and Manley–Rowe evolution in a finite causal system," *Phys. Plasmas*, vol. 3, pp. 650–667, 1996.

[11] ——, "A hybrid semi-Lagrangian Vlasov code, II numerical simulation of chirped beatwave experiment," *Phys. Plasmas*, vol. 5, pp. 4041–4054, 1998.

[12] A. Ghizzo, P. Bertrand, M. L. Begue, T. W. Johnston, and M. Shoucri, "A Hilbert–Vlasov code for the study of high-frequency plasma beatwave accelerator," *IEEE Trans. Plasma Sci.*, vol. 24, pp. 370–378, 1996.

[13] M. L. Begue, A. Ghizzo, P. Bertrand, E. Sonnendrücker, and O. Coulaud, "Two-dimensional semi-Lagrangian Vlasov simulation of laser-plasma interaction in the relativistic regime," *J. Plasma. Phys.*, vol. 62, pp. 367–388, 1999.

[14] J. Fuchs, J. C. Adam, F. Amiranoff, S. D. Baton, N. Blanchet, P. Gallant, L. Gremillet, A. Héron, J. C. Kieffer, G. Laval, G. Malka, J. Miquel, P. Mora, H. Pépin, and C. Rousseaux, "Experimental study of laser penetration in overdense plasmas at relativistic intensities, II Explosion of thin foils by laser driven fast electrons," *Phys. Plasmas*, vol. 6, pp. 2569–2578, 1999.

[15] F. Brunel, "Anomalous absorption of high intensity subpicosecond laser pulses," *Phys. Fluids*, vol. 31, pp. 2714–2719, 1988.



Fabien Huot was born in France on August 29, 1971. He is currently pursuing the Ph.D. degree at the laboratory LPMI at the University Henri Poincare, Nancy, France.

Alain Ghizzo was born in France in 1960. He received the Ph.D. degree in numerical simulation in plasma physics in 1987 and in 1988 he joined the Canadian Center of Magnetic Fusion (CCFM) at Varennes, Montrdal, Canada for a postdoctoral position. He is currently a Professor at the University Henri-Poincare, Nancy, France. His research interests include laser-plasma interaction, and the development of new methods of computer simulation in plasma physics.



Pierre Bertrand was born in France in 1946. He received the Ph.D. degree in physics in 1972. He is currently a Full Professor at the University Henri-Poincare, Nancy, France. He has been performing research in the field of computer experiments in plasma physics. His recent research includes laser-plasma interaction and gyrokinetic models for plasma edge physics in tokamaks.

Eric Sonnendriicker was born in 1967 in Strasbourg, France. He did undergraduate studies in mathematics at the Ecole Normale Superieure de Cachan, France, and received the Ph.D. degree in applied mathematics from the Ecole Normale Superieure de Cachan in 1995 while at the Lawrence Livermore National Laboratory (USA) and CEA Limed-Valenton (France). He was Post-Doc at Forschungszentrum Karlsruhe, Germany (1996) and Lawrence Berkeley National Laboratory USA (1998–1999), an Associate researcher at CNRS in Nancy, France (1996–2000), and a Professor in applied mathematics at the University of Strasbourg, France starting September 2000.

O. Coulaud was born in 1961 in Paris, France. He received the Ph.D. degree in spectral methods for porous media in 1990.

He was a researcher at INRIA (Institut National de Recherche en Informatique et en Automatique) in NUMATH project in INRIA-Lorraine. From 1996, he was the vice Director of the computational Charles Hermite Center. From 1997 to 2000, he has been the head of the NUMATH project. Since 1999, he has been the Research Director at INRIA. His research interests are high performance algorithms and distributed computing, and numerical methods for molecular simulation.

A Ponderomotive Guiding Center Particle-in-Cell Code for Efficient Modeling of Laser–Plasma Interactions

Daniel F. Gordon, W. B. Mori, and Thomas M. Antonsen, Jr., *Member, IEEE*

***Abstract*—A novel particle simulation code is described that self-consistently models certain classes of laser–plasma interactions without resolving the optical cycles of the laser. This is accomplished by separating the electromagnetic field into a laser component and a wake component. Although the wake component is treated as in a fully explicit particle-in-cell (PIC) code, the laser component is treated in the high-frequency limit, which allows the optical cycles to be averaged out. This leads to enormous reductions in computer time when the laser frequency is much greater than all other frequencies of interest.**

This work is an extension of the work of Mora and Antonsen, Jr. [1], [2], who derived the time-averaged equations coupling the laser with the particles and developed a code to solve these equations in the quasi-static limit. The code presented here is distinguished by the fact that it is useful when the plasma length is much less than the laser pulse length. Also, it is already parallelized and should be straightforward to extend to three dimensions.

***Index Terms*—Particle code, plasma simulation.**

I. Introduction

THE physics of nonlinear laser–plasma interactions is directly relevant to a number of applications, including laser fusion [3]–[5], plasma based accelerators [6], and advanced radiation sources [7], [8]. The complexity of these systems has led many researchers to make heavy use of computer modeling to predict their behavior. The most accurate of such models is probably the particle-in-cell, or "PIC" code. A PIC code self-consistently calculates the motions of a large number of charged particles and the fields they produce. The drawback of such a code is that it requires enormous computing resources to run. This problem becomes particularly acute with regard to laser–plasma interactions because resolving the high-frequency laser field requires a large number of simulation cycles.

Various attempts to overcome this difficulty have been made. The simplest was to prescribe a nonevolving laser field and superimpose its ponderomotive force over the self-consistent force on a particle [9]. Because the ponderomotive force varies slowly on the timescale of the laser frequency (ω_0), only the plasma frequency (ω_p) had to be resolved and an $(\omega_0/\omega_p)^2$-fold increase in the speed of the simulation was obtained. The problem with this approach is that the laser radiation is not allowed to evolve. Processes such as self-focusing and stimulated Raman scattering (SRS) are therefore excluded from the model.

A more sophisticated solution, from Mora and Antonsen, Jr. [2], was to derive a self-consistent description of the interaction between the particles and the laser field in terms of only the slowly varying laser envelope and the associated ponderomotive force. In this way, a factor $(\omega_0/\omega_p)^2$ performance increase was obtained while still allowing the laser pulse to evolve. The code, called WAKE, has been successfully used to model the self-modulation and self-focusing of an intense laser pulse in a plasma. Some of the limitations of WAKE are as follows. First, it uses the quasi-static approximation [10] to solve for the particle motions and the plasma fields. This implies that high-energy particles may not be modeled accurately. Second, because the model equations were expressed in terms of laser coordinates ($\xi = t - x/c, \tau = t$), the code automatically does all of its calculations in a window moving with the laser pulse. Although this is exactly what is desired in some cases, it is not desirable in others. Finally, because of the structure of the code, it is difficult to parallelize.

In this paper, we describe a new parallel code called turboWAVE that solves Maxwell's equations for the plasma fields and the Mora and Antonsen, Jr. equations for the laser fields. The turboWAVE algorithm is based largely on the Los Alamos code WAVE [11], which has been well tested over the years. Although turboWAVE and WAVE are close algorithmically, programatically turboWAVE is an entirely new object-oriented C++ code.

The distinction between turboWAVE and WAKE can be understood as follows. In both codes, the cell size must be small enough to resolve the nonlinear wake. In turboWAVE, this implies that the timestep must be small enough to resolve a plasma period in order to satisfy the Courant condition. In WAKE, on the other hand, the quasi-static assumption is made and only the laser evolution time needs to be resolved. However, the box size has to be larger than the laser pulse length because the calculation is done in the laser frame. By contrast, turboWAVE allows a laser to be injected into a stationary box that is much shorter than the laser. This is advantageous, for example, when modeling beatwave acceleration experiments. In addition, the removal of the quasi-static approximation allows turboWAVE to model the acceleration of charged particles to high energies,

Manuscript received January 20, 2000; revised February 9, 2000. This work was supported by NSF, under Grant DMS-9722121, and DOE, under Grant DE-FG03–92–ER40727.

D. F. Gordon is with the Naval Research Laboratory, Washington, DC 20375 USA.

W. B. Mori is with the Department of Electrical Engineering and the Department of Physics and Astronomy, University of California at Los Angeles, Los Angeles, CA 90095 USA.

T. M. Antonsen, Jr., is with the Institute for Plasma Research, University of Maryland, College Park, MD 20742 USA.

Publisher Item Identifier S 0093-3813(00)07238-6.

0093–3813/00$10.00 © 2000 IEEE

provided the accelerated particles are not affected too strongly by the laser fields.

At present, turboWAVE has the following features and limitations.

1) It solves for high-frequency fields and their effects on particles using a time-averaged model that can lead to much shorter simulation times than those obtained using an ordinary PIC code.
2) In terms of push time per particle per timestep, it runs roughly a factor of two slower than other PIC codes because of the complexity of the algorithm.
3) It functions as a fully explicit two-dimensional (2-D) PIC code when the laser fields are zero.
4) It operates on a 2-D cartesian grid only.
5) It is parallelized via the message passing interface (MPI) and one-dimensional (1-D) domain decomposition.
6) It offers a moving window option.
7) It models tunneling ionization.

In what follows, we outline the algorithms used to realize these features and present preliminary results from the code. Further details will be presented in another paper.

II. Mathematical Description of the Algorithm

TurboWAVE is based on the proposition that the electromagnetic field can be divided into two parts: a "laser" field and a "wake" field. The laser field is characterized by two requirements. First, a typical charged particle should move through a large amount of optical phase before the field strength changes. Second, the laser energy should be confined to a small region of k-space far from the origin. The whole electromagnetic field, expressed using the normalized units typical of simulation codes, is determined by the wave equation

$$(\Delta - \partial_{tt})(\mathbf{A} + \tilde{\mathbf{a}}) = -\mathbf{J} - \tilde{\mathbf{j}} + \nabla\partial_t\phi$$

where $\tilde{\mathbf{a}}$ represents the laser component of the field and $\mathbf{A}$ represents the wake component. Correspondingly, the current density is decomposed into a rapidly varying component associated with the laser, $\tilde{\mathbf{j}}$, and a slowly varying component associated with the wake, $\mathbf{J}$. The rapidly varying current is defined as that which would be driven by the laser if the spot size was infinite

$$\tilde{\mathbf{j}} = -\tilde{\mathbf{a}}\sum_i \frac{q_i\rho_i}{m_i}.$$

Here, the sum is over the particles, ρ_i is the distribution of charge density for the ith particle, q_i is the charge, and m_i is the relativistic mass. The laser field is then defined by some initial condition, along with

$$(\Delta - \partial_{tt})\tilde{\mathbf{a}} = -\tilde{\mathbf{j}}. \tag{1}$$

Now, consider a particular component of the laser field expressed in the form

$$\tilde{a} = \frac{a(x,y,t)}{2}\, e^{i\psi} + cc$$

where $\psi = \omega(t - x)$ and ω is the laser frequency. Mora and Antonsen, Jr., showed [2] that if the radiation is dominantly forward propagating, the evolution of the laser envelope a is approximated by

$$(\Delta_T - 2i\omega\partial_\tau + 2\partial_{\tau\xi})a = -\chi a \tag{2}$$

where $\xi = x - t$, $\tau = t$, Δ_T is the transverse Laplacian, and

$$\chi = -\sum_i \frac{q_i\rho_i}{\langle m_i\rangle}$$

$$\langle m\rangle = \sqrt{m_0^2 + P^2 + \frac{q^2|a|^2}{2}}.$$

Here, m_0 is the rest mass and P is the momentum induced by the wake. Thus, the particles couple to the laser through the parameter χ, which depends on the charge density ρ and the average relativistic mass $\langle m\rangle$.

TurboWAVE models the wake fields using the same algorithm as WAVE. In particular, the potentials are updated according to

$$(\Delta - \partial_{tt})\mathbf{A} = -\mathbf{J} + \nabla\hat{G}(\nabla\cdot\mathbf{J})$$
$$\phi = -\hat{G}\rho,$$

where $\hat{G}$ represents a Poisson solver. The use of $\partial_t\phi = \hat{G}(\nabla\cdot\mathbf{J})$ ensures charge conservation. The electric field $\mathbf{E}$ and magnetic field $\mathbf{B}$ are found from $\mathbf{E} = -\partial_t\mathbf{A} - \nabla\phi$ and $\mathbf{B} = \nabla\times\mathbf{A}$. The exact differencing scheme involves various subtle smoothing operations, which we will not discuss here.

The coupling between the laser and the wake takes place through the intermediary of the particles. This is expressed by the momentum equation [2]

$$\partial_t\mathbf{P} = q\left(\mathbf{E} + \mathbf{v}\times\mathbf{B} - \frac{1}{4}\frac{q}{\langle m\rangle}\nabla|a|^2\right).$$

Here, $\mathbf{E}$ and $\mathbf{B}$ are the fields associated with the wake potentials $\mathbf{A}$ and ϕ. The term involving a represents the ponderomotive force due to the laser. This expression is accurate, provided the particles move through a large number of optical cycles before the laser intensity changes significantly. Once the particle states are updated, the source terms ρ, $\mathbf{J}$, and χ can be updated. These are then used to update $\mathbf{E}$, $\mathbf{B}$, and a, so that the process can start over. Taking $a = 0$, this reduces to the usual cycle of a PIC code.

III. The Laser Field Solver

In solving numerically for the laser fields, we approximate (2), which can be written as

$$\left(1 - \frac{\partial_\xi}{i\omega}\right)\partial_\tau a = \frac{1}{2i\omega}(\chi a + \Delta_T a).$$

Multiplying both sides by $1 + \partial_\xi/i\omega$, and transforming to ordinary coordinates using $\partial_\tau = \partial_t + \partial_x$ and $\partial_\xi = \partial_x$, we obtain

$$(\partial_x + \partial_t)a = \frac{1}{2i\omega}\left(1 + \frac{\partial_x}{i\omega}\right)(\chi a + \Delta_T a) \tag{3}$$

where a term of order $1/\omega^2$ has been dropped from the left-hand side. The effect of this term is to reduce the axial group velocity of waves propagating at an angle to the axis. It can be neglected in the case of forward or near-forward Raman scattering, but could be important for Raman sidescatter.

We use Crank–Nicholson to solve (3) stably. In particular, the terms $\partial_t a$ and $\Delta_T a/2i\omega$ are evaluated using data from timesteps $n-1$ and $n+1$, whereas all other terms are evaluated at timestep n.

IV. The Pusher

TurboWAVE uses a modified version of the Boris pusher [12]. At timestep n, we regard as known r^n, $P^{n-1/2}$, ϕ^n, $A^{n-1/2}$, $A^{n+1/2}$, $a^{n-1/2}$, and $a^{n+1/2}$. This gives E^n, B^n, and $F^n = \nabla|a^n|^2$ in straightforward way. However, to advance P in a manner accurate to second order in the timestep requires knowledge of m^n. An implicit equation for m^n is

$$m^n \approx m^{n-1/2} + q\left(\mathbf{E}^n - \frac{q}{4m^n}\mathbf{F}^n\right)\cdot\frac{\mathbf{P}^{n-1/2}}{m^{n-1/2}}\frac{\Delta t}{2}$$

which can be solved using the quadratic formula. The momentum is then updated using

$$\mathbf{P}^{n+1/2} = \hat{R}\left(\mathbf{P}^{n-1/2} + \frac{\mathbf{I}}{2}\right) + \frac{\mathbf{I}}{2}$$

where

$$\mathbf{I} = \left(q\mathbf{E}^n - \frac{1}{4}\frac{q^2}{m^n}\mathbf{F}^n\right)\Delta t$$

and $\hat{R}$ is an operator that rotates a vector about the magnetic field by an angle

$$\theta = -\frac{qB^n}{m^n}\Delta t.$$

The update of the particle position is also subtle because knowledge of $m^{n+1/2}$ is required. This quantity depends implicitly on $r^{n+1/2}$ through its dependence on a. An implicit equation for $m^{n+1/2}$ is obtained by Taylor expanding $a^{n+1/2}$ about r^n

$$(m^{n+1/2})^2 = m_0^2 + (P^{n+1/2})^2 + \frac{q^2a^2}{2}$$

where

$$a^2 = [a^{n+1/2}(r^n)]^2 + \nabla[a^{n+1/2}(r^n)]^2\cdot\frac{\mathbf{P}^{n+1/2}}{m^{n+1/2}}\frac{\Delta t}{2}.$$

Again, this can be solved using the quadratic formula.

V. The Wake Field Solver

As mentioned above, the field solver for the wake is nearly identical to that of WAVE. The only difference is in the Poisson solver, where we have added the option of using open-ended boundary conditions [13]. This allows for the possibility of a nonneutral simulation box. Use of open boundary conditions is also necessary in cases in which the plasma does not fill the box transversely, such as when it is created by tunneling ionization. In such cases, neither axial boundary can be taken to be an equipotential because electron diffusion will lead to a restoring space-charge field.

VI. Moving Window

We have implemented a moving window option using a technique similar to that of PEGASUS [14]. However, in turboWAVE, boundary conditions are difficult because in the Coulomb gauge, neither $\mathbf{A}$ nor ϕ are causal quantities. A temporary solution has been to use the open boundary conditions for the Poisson solver, and to obtain a boundary condition for A_y by requiring

$$E_y = -\partial_t A_y - \partial_y\phi = 0$$

at the front of the window. The boundary condition for A_x is then found from the gauge condition

$$\partial_x A_x + \partial_y A_y = 0.$$

This technique assumes that all charges are neutralized by the time they pass through the rear boundary of the window. It is desirable, therefore, to leave a large space between the rear of the laser pulse and the rear of the window.

Although we have not yet implemented it, there is a way of rigorously computing the potentials in the moving window even for $\nabla\cdot\mathbf{A} = 0$. The method is an interesting study in causality. It accounts for sources behind the window without any knowledge of their motions. In the Appendices, we show that the effects of these sources can be expressed entirely in terms of a scalar potential ϕ_1 determined from

$$\partial_t\phi_1(\xi,k,t) = \begin{cases} -\rho_0(t)\xi/2, & k=0 \\ -k\phi_1 + \rho_0(t)e^{-k\xi}/2k, & k\neq 0. \end{cases} \quad (4)$$

Here, a Fourier transform has been performed in the y-direction, k is the Fourier wavenumber, $\xi = x - t$ is a coordinate moving with the window, and ρ_0 is the charge density at the rear boundary of the window ($\xi = 0$). The total scalar potential is then $\phi_1 + \phi$, where ϕ is computed assuming $\rho = 0$ outside the window.

An alternative solution is to rewrite the field solver to operate in the Lorentz gauge. In particular, we could solve

$$(\Delta - \partial_{tt})\mathbf{A} = -\mathbf{J} + \nabla\hat{G}(\partial_t\rho + \nabla\cdot\mathbf{J})$$
$$(\Delta - \partial_{tt})\phi = -\rho.$$

Here, again, the Poisson solver $\hat{G}$ is used to ensure charge conservation. Although $\hat{G}$ is not a causal operator, the vector potential will be very nearly causal nevertheless. This is because for a linearly weighted $\mathbf{J}$, the contribution of a particle to $(\partial_t\rho+\nabla\cdot\mathbf{J})$ takes the form of a quadrupole. The resulting "correction field" is therefore highly localized to the region of the particle [13]. With both potentials causal, the moving window boundary conditions can be done as in PEGASUS.

VII. Ionization

In many laser–plasma interaction experiments, the plasma is created by the laser via tunneling ionization. It is desirable therefore to include this process in any laser–plasma simulation code. Tunneling ionization is modeled in turboWAVE by computing an ionization rate based on the Keldysh model [15]. This rate is computed in each grid cell to determine the number of new particles to create in that cell. The particles are given a thermal

velocity selected by the user and can be positioned either uniformly or randomly throughout the cell.

VIII. Parallelization

Parallelization of turboWAVE is accomplished using the (MPI). One-dimensional domain decomposition is done in the x-direction. This is largely straightforward, except for the Poisson solver. The WAVE Poisson solver works by transforming to frequency space in the y-direction and finite differencing in the x-direction. The operation in the y-direction parallelizes immediately because it is independent of x. After this transformation, the scalar potential at each y is determined from a second-order difference equation in x. Because the domain decomposition is performed in the x-direction, solution of this equation requires a parallel tridiagonal solver. We have devised and implemented such an algorithm. It is presented in the Appendices.

IX. Benchmarking

We have tested turboWAVE by modeling phenomena that can be described analytically, and by comparing it with fully explicit calculations done using WAVE and PEGASUS. We treat these benchmarks in order of increasing complexity.

A. Vacuum Propagation

The simplest test is to verify that the laser field solver correctly propagates a Gaussian beam in vacuum. In slab geometry, a Gaussian beam is described by

$$a(x,y,t) = a_0 \frac{w_0}{\sqrt{w_0 w}} e^{-y^2/w^2} e^{-i\psi}$$

where

$$w = w_0\sqrt{1+\frac{x^2}{x_R^2}}$$
$$\psi = \frac{1}{2}\tan^{-1}\frac{x}{x_R} - \frac{wy^2}{2R}$$
$$R = x\left(1+\frac{x_R^2}{x^2}\right)$$

and the Rayleigh length is

$$x_R = \tfrac{1}{2}\omega w_0^2.$$

As a test, we focus a laser pulse to the center of a simulation box $2.67x_R$ long. This is done simply by setting the amplitude and phase of a in the left ghost cell according to $a(-1.33x_R, y, t)$. Fig. 1(a) shows the resulting transverse amplitude profile in the center of the box. The vertical dotted lines show the locations of $\pm w_0$, and the horizontal dotted line shows the location of a_0/e. The curve passes through the intersections of these lines just as expected.

Fig. 1(b) shows the relative phase of a on axis. A "Guoy phase shift" of $\pi/4$ radians is expected as the laser propagates through $2x_R$. This is exactly what is observed.

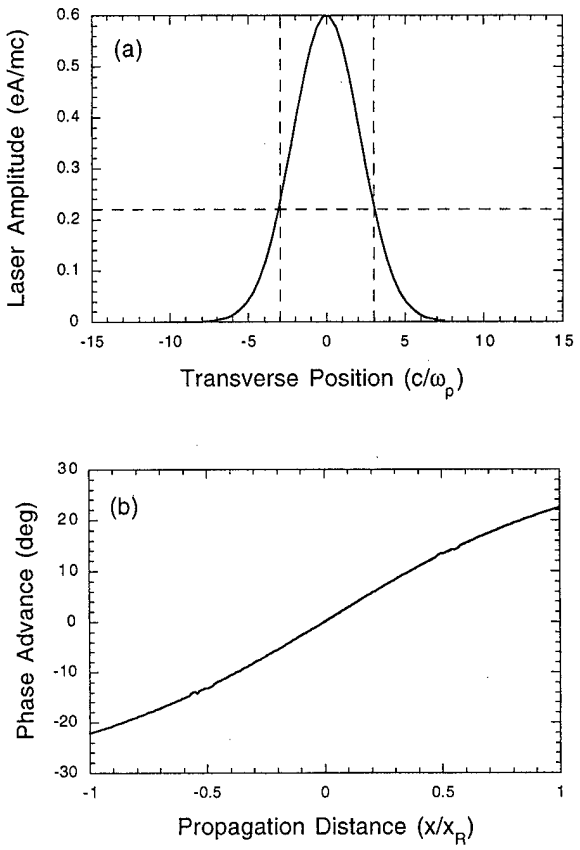


Fig. 1. Test of propagation in vacuum (a) amplitude profile at best focus. The curve is expected to pass through the intersections of the dotted lines (b) Guoy phase shift. The phase shift through one Rayleigh length is expected to be 22.5°.

B. Linear Propagation in Plasma

For the next test, we propagate a small amplitude wave through a uniform plasma in one dimension. Let

$$\tilde{a} = e^{i\omega(t-x)}e^{i\phi(x)} = e^{i(\omega t - kx)}$$

where ϕ is the phase change due to plasma. It follows that $k = \omega - \phi/x$. Assuming the plasma is homogeneous, it further follows that $\phi = mx$, where m is constant. Using the well-known dispersion relation for electromagnetic waves in a plasma, we obtain

$$m = \omega - \sqrt{\omega^2 - \omega_p^2}.$$

In Fig. 2, we plot $\phi(x)$ for an electromagnetic wave with $\omega = 10$ propagating through a box with a vacuum region and a plasma region. The slope of the curve corresponds to m. As expected, the slope is zero in the vacuum region and ≈ 0.05 in the plasma region.

C. Beat Excitation of a Plasma Wave

It was shown by Rosenbluth and Liu [16] that a two-frequency laser will drive a plasma wave such that the electrostatic field grows according to

$$\frac{E_x(t)}{E_0} = \frac{a_1 a_2}{4}\omega_p t$$

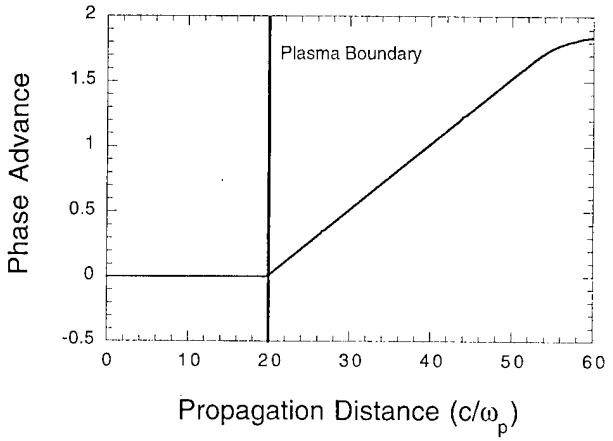


Fig. 2. Linear propagation in a plasma for $\omega = 10\omega_p$. The slope of the curve corresponds to $c(k_{vac} - k)/\omega_p$. The expected slope in the plasma region is 0.05, just as is observed in the plot.

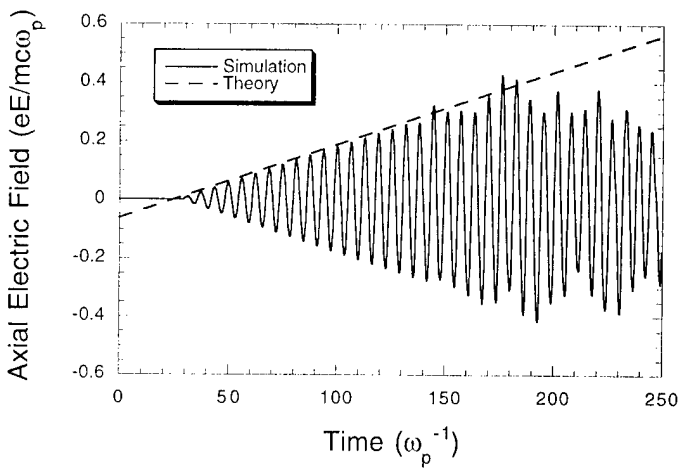


Fig. 3. Beat excitation of a plasma wave with $a_1 = a_2 = 0.1$, $\omega_1 = 9.5$, and $\omega_2 = 10.5$. The electric field grows secularly at the expected rate until relativistic detuning occurs.

where E_0 is the cold wavebreaking field, a_1 and a_2 are the normalized amplitudes of the two lasers, and the frequencies of the two lasers are chosen such that $\omega_1 - \omega_2 = \omega_p$. Fig. 3 shows the results of a 1-D simulation in which $a_1 = a_2 = 0.1$ and $(\omega_1 + \omega_2)/2 = 10\omega_p$. A particular point in the simulation box was chosen, and $E_x(t)$ was plotted. The field grows linearly at the expected rate until relativistic detuning saturates it.

D. Wakefield Excitation

In the (1-D) nonrelativistic limit, the amplitude of the wake excited by a short pulse laser is [6]

$$\phi = \frac{1}{4}\int_0^{\zeta} |a(\zeta')|^2 \sin(\zeta - \zeta')\, d\zeta' \tag{5}$$

where $\zeta = x - t$. We test the accuracy of this in both one and two dimensions, using both the moving and stationary windows. The temporal profiles of the pulses used are of the form

$$f(t) = \begin{cases} 10\tau^3 - 15\tau^4 + 6\tau^5, & 0 < t < t_w \\ 10\xi^3 - 15\xi^4 + 6\xi^5, & t_w < t < 2t_w \end{cases}$$

where $\tau = t/t_w$, $\xi = 2 - t/t_w$, and t_w is the full-width at half-maximum (FWHM) of the pulse. The function f has the following properties: $f(0) = f(2t_w) = 0$, $f(t_w) = 1$, $f(t_w/2) = f(3t_w/2) = 1/2$, $f'(0) = f'(t_w) = f'(2t_w) = 0$, and $f''(0) = f''(t_w/2) = f''(t_w) = f''(3t_w/2) = f''(2t_w) = 0$.

Fig. 4(a) shows the results of both 1-D and 2-D simulations in which the wake amplitude ϕ was measured as a function of the driver amplitude a. The 2-D simulations used the moving window. The laser parameters were $\omega = 20$ and $t_w = 3.0$. For the 2-D runs, the spot size was $w_0 = 3.0$. The theoretical curve was obtained by numerically integrating (5). The agreement between theory and simulation is excellent for small a. For large a, relativistic effects are expected to reduce the wake amplitude from the theoretical value, as is indeed observed in the figure.

Fig. 4(b) shows the results of 1-D simulations in which the wake amplitude ϕ was measured as a function of the pulse length t_w. The laser amplitude was $a = 0.4$, and the frequency was

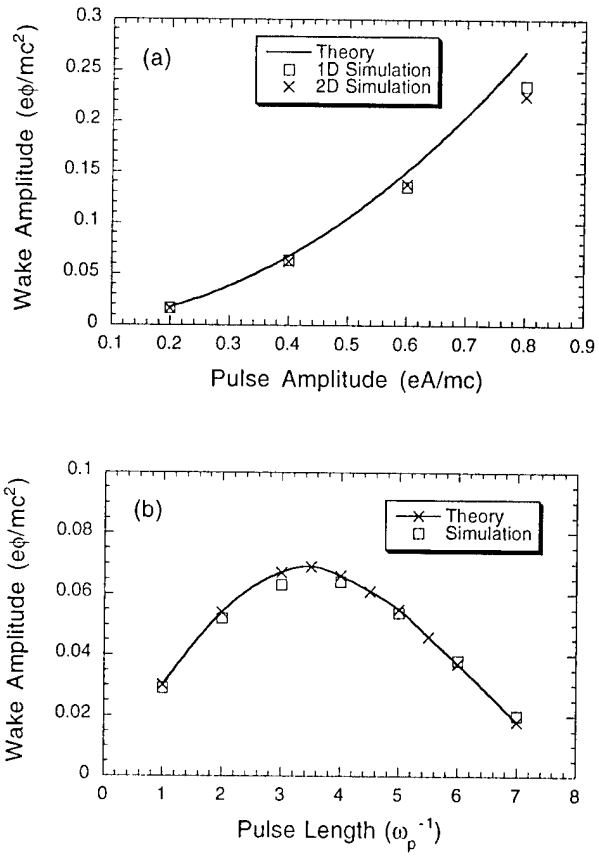


Fig. 4. Excitation of wakes by a short-pulse (a) scaling with driver amplitude and (b) scaling with pulse length near the resonance.

$\omega = 20$. The theoretical curve was again obtained by numerically integrating (5). Again, the agreement between theory and simulation is excellent.

E. Nonlinear Beat Excitation

In [17], a fully explicit 2-D simulation of beat excitation was done using WAVE, in which $a_1 = a_2 = 0.56$, $\omega_1 = 4\omega_p$, and $\omega_2 = 5\omega_p$. The laser risetime was $\omega_p t = 300$. Late during this risetime, the wave amplitudes become large enough so that no

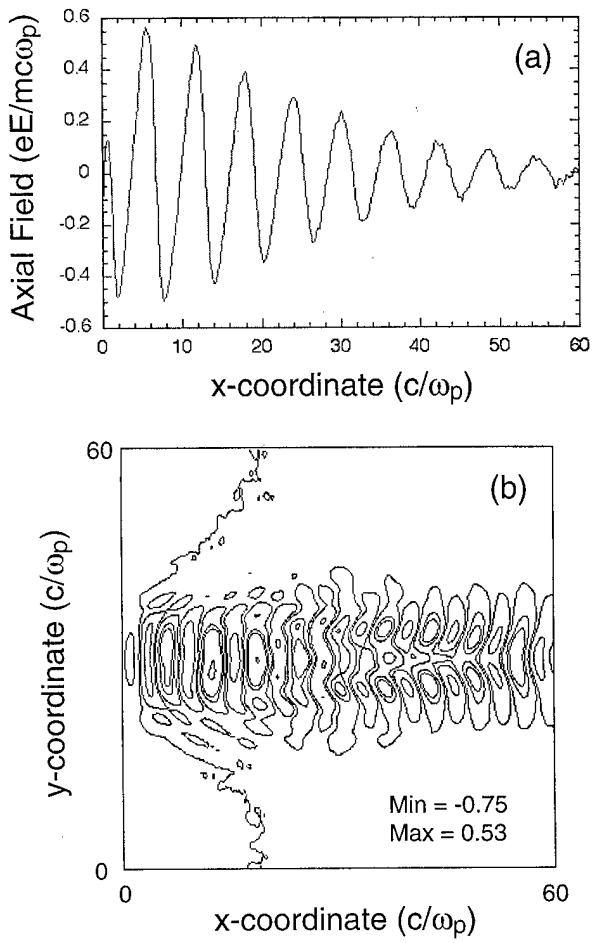


Fig. 5. Nonlinear beat excitation (a) axial electric field at $\omega_p t = 150$ and (b) scalar potential at $\omega_p t = 210$.

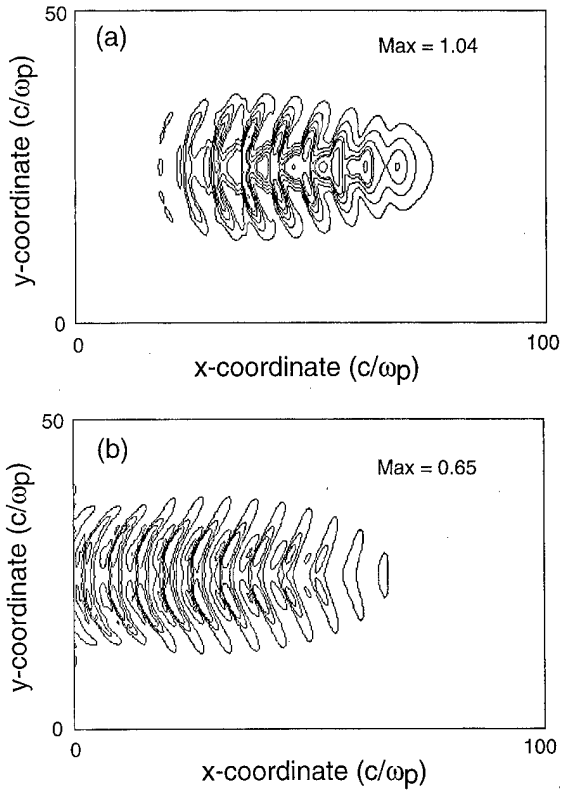


Fig. 6. Self modulation of a short-pulse (a) laser amplitude at $\omega_p t = 150$, including seed pulse and (b) accelerating electric field at $\omega_p t = 150$.

analytical treatment is available. To test how well turboWAVE works under such conditions, we repeat the simulation described in [17] using the ponderomotive guiding center algorithm.

Fig. 5(a) shows the on-axis axial electric field at at a time shortly before the waves become highly nonlinear. This corresponds to [17, Fig. 12(b)]. The agreement is excellent. Fig. 5(b) shows a contour plot of the scalar potential after a high degree of nonlinearity has set in. This corresponds to [17, Fig. 15(c)]. The similarity between the two sets of contours is striking.

F. Self Modulation

Finally, we consider the case of the self-modulation of a short pulse propagating through a plasma. This is a difficult problem to model using a ponderomotive guiding center code for two reasons. First, it has been shown [18], [14] that backscatter can strongly affect the outcome of such an interaction. This is because the Raman backscatter instability grows very quickly and acts as a seed for the forward Raman instability and self-modulation. In regimes in which this seeding mechanism dominates, its absence from the model causes the forward Raman to develop much more slowly than it should and the entire interaction can end up looking very different. The second difficulty is that the forward Raman leads to wavebreaking and the generation of large numbers of very high-energy electrons. These electrons may move too slowly through the optical phase fronts to be modeled accurately by the ponderomotive description.

Despite the difficulties described above, we have found that it is possible to obtain reasonable results in the self-modulated regime using turboWAVE. At sufficiently early times, the incorrect interaction between the high-energy electrons and the laser fields is not expected to strongly affect the evolution of the laser or the wake because the number of high-energy electrons is small. The backscatter problem is not serious, provided the wake driven by the rising edge of the laser pulse is sufficiently strong. In particular, if the wake is strong enough to seed the forward Raman as strongly and as quickly as backscatter, backscatter will not have a serious impact on the interaction. This is because once the forward instabilities are underway, they dominate over all other processes.

As an example that illustrates these difficulties, and how to overcome them, we attempt to reproduce the 2-D PEGASUS simulation described in [18]. Unfortunately, [18] describes the pulse shape in terms of a parameter $l_0 = 50c/\omega_p$ which is not precisely defined. We choose to interpret this parameter in the sense that makes the problem as challenging as possible—that is, we take the pulse shape to be as described in Section IX-D with $t_w = l_0$. Other parameters were $a_0 = 0.75$, $\omega = 5$, and $w_0 = 9$. In this case, the wake excited by the rising edge of the pulse takes much longer to excite the forward Raman than does backscatter. However, we find that the effects of backscatter can be simulated by superimposing a small short pulse ($t_w = \pi$) over the longer main pulse. This takes the place of the "notch" that backscatter would have created in the laser pulse via pump

depletion. Using this technique along with the moving window, we generated Fig. 6. The contours of laser amplitude at $\omega_p t = 150$ are shown in Fig. 6(a), whereas the contours of the axial electric field at the same time are shown in Fig. 6(b). These are to be compared respectively with [18, Figs. 3(c) and (d)]. The two sets of results are qualitatively similar. Better quantitative agreement might be obtained by adjusting the seed pulse. It should also be noted that the need for a seed pulse might be eliminated given a more favorable interpretation of l_0. We indeed ran a case with a different pulse shape (equal risetime, fall-time, and flat-top regions of $30\omega_p^{-1}$) and found that contours similar to those shown in Fig. 6 could be generated without a seed pulse.

X. Conclusion

The code turboWAVE provides an effective method of modeling laser–plasma interactions, in which the laser radiation is dominantly forward propagating and the laser–particle interaction is adequately modeled by the ponderomotive force. Plans for the future include implementation of cylindrical geometry and three dimensions, as well as the improved moving window algorithm discussed above. In addition, a method of handling high-energy particles whose interaction with the laser is not adequately modeled by the ponderomotive force is being contemplated.

Appendix A
Moving Window Poisson Solver

To solve for $\mathbf{A}$ and ϕ in a computational region, or "window," moving at the speed of light, requires a Poisson solver that accounts for sources behind the window without knowing what those sources are. The key to solving this problem lies in understanding the implications of causality. By causality, the fields in the window are independent of the sources behind the window. This means particles behind the window can undergo any motion whatsoever without affecting the solution for the fields in the window. The problem then is to choose some motion that makes it easy to solve for the potentials. The obvious choice is to immediately "freeze" the particles the moment they cross the rear boundary of the window. The particles then recede from the window at the speed of light while maintaining their transverse position.

The equations for the potentials can be written as follows:

$$(\Delta - \partial_{tt})\mathbf{A} = -\mathbf{J} + \nabla G * (\nabla \cdot \mathbf{J})$$
$$\phi = -G * \rho.$$

Here, G is a Green's function and $*$ represents convolution in space. If we choose to freeze the particles the moment they cross the rear boundary of the window, the current behind the window is zero and the sources behind the window do not contribute to the vector potential. To solve for the scalar potential due to sources behind the window, we Fourier transform in the transverse direction. This gives

$$\phi(x,k,t) = -\int_{-\infty}^{t} G(x-x',k)\rho(x',k,t)\,dx'$$

where for $k \neq 0$

$$G(x,k) = -\frac{1}{2k}\,e^{-k|x|}.$$

The upper limit in the integral $x = t$ is the location of the rear boundary of the window. Because the sources behind the window do not move, we have for $x < t$

$$\rho(x,t) = \rho(x,x) = \rho_0(x)$$

where $\rho_0(x)$ is the charge density on the boundary evaluated at the time $t = x$. This allows the convolution integral to be written as

$$\phi = \frac{e^{-kx}}{2k}\int_{-\infty}^{t} e^{kt'}\rho_0(t')\,dt'$$

where we renamed the integration variable to emphasize that the integration is effectively over time. In terms of a coordinate $\xi = x - t$ moving with the window, this becomes

$$\phi(\xi,k,t) = \frac{e^{-k(\xi+t)}}{2k}\int_{-\infty}^{t} e^{kt'}\rho_0(t')\,dt'$$

Differentiating both sides with respect to time gives (4). The solution for the $k = 0$ mode is found similarly, using for the Green's function

$$G(x,k=0) = \frac{|x|}{2}.$$

Appendix B
Parallel Tridiagonal Solver

We seek a parallelizable solution to the equation

$$A_{ji}\phi_i = -\rho_j$$

where A is a tridiagonal matrix. Consider $L+1$ diagonal submatrices of size $N \times N$ defined by

$$A^n_{ji} = A_{j+nN,i+nN}$$

where n varies from 0 to L and i, j vary from 1 to N. From the original matrix equation, it follows that

$$A^n\phi^n = -\rho^n - \theta^n\phi^{n-1}_N\mathbf{b}_1 - \eta^n\phi^{n+1}_1\mathbf{b}_N$$

where $\mathbf{b}_i$ are the standard basis vectors and

$$\theta^n = A_{nN+1,nN}$$
$$\eta^n = A_{nN+N,nN+N+1}.$$

Inverting this equation gives

$$\phi^n = \psi^n - \alpha^n\mathbf{v}^n - \beta^n\mathbf{w}^n \tag{6}$$

where

$$\alpha^n = \phi^{n-1}_N = \phi^n_0$$
$$\beta^n = \phi^{n+1}_1 = \phi^n_{N+1}$$
$$\psi^n = -(A^n)^{-1}\rho^n$$
$$\mathbf{v}^n = \theta^n(A^n)^{-1}\mathbf{b}_1$$
$$\mathbf{w}^n = \eta^n(A^n)^{-1}\mathbf{b}_N.$$

Let us now regard n as indicating one of the nodes on a parallel computer. The quantities ψ, $\mathbf{v}$, and $\mathbf{w}$ can be solved for inde-

pendently on each node via the usual tridiagonal algorithm. To obtain the full solution ϕ, it only remains to solve for α^n and β^n.

The quantities α^n and β^n can be viewed as the dirichlet boundary conditions to the left and right of node n, respectively. Equation (6) can, therefore, be viewed as expressing the solution on a single node in terms of the solution ψ using null boundary conditions, plus a correction taking into account the actual boundary conditions imposed by the presence of the other nodes. These boundary conditions are determined implicitly by combining the definitions of α^n and β^n with (6). In particular, we have $2L$ equations

$$\alpha^n = \psi_N^{n-1} - k_1^{n-1}\alpha^{n-1} - k_2^{n-1}\beta^{n-1}$$
$$\beta^n = \psi_1^{n+1} - k_3^{n+1}\alpha^{n+1} - k_4^{n+1}\beta^{n+1}$$

for the $2L$ unknowns $\alpha^1 \cdots \alpha^L$ and $\beta^0 \cdots \beta^{L-1}$. Here

$$k_1^n = v_N^n$$
$$k_2^n = w_N^n$$
$$k_3^n = v_1^n$$
$$k_4^n = w_1^n.$$

The system is closed by taking α^0 and β^L as given. These can be viewed as the dirichlet boundary conditions for the whole system. Alternatively, if the global boundary conditions are accounted for by the original equation $A\phi = -\rho$, then $\alpha^0 = \beta^L = 0$.

The above system of equations can be reexpressed in terms of two independent tridiagonal systems: one for α^n and one for β^n. In particular

$$a^n\alpha^{n-1} + b^n\alpha^n + c^n\alpha^{n+1} = s^n, \qquad n = \{1 \cdots L\}$$
$$x^n\beta^{n-1} + y^n\beta^n + z^n\beta^{n+1} = r^n, \qquad n = \{0 \cdots L-1\}$$

where for the α system, we have

$$s^n = \psi_N^{n-1} - k_2^{n-1}\psi_1^n + \left(k_2^{n-1}/k_2^n\right) k_4^n\psi_N^n$$
$$a^n = k_1^{n-1}$$
$$b^n = 1 - k_2^{n-1}k_3^n + \left(k_2^{n-1}/k_2^n\right) k_1^n k_4^n$$
$$c^n = \frac{k_2^{n-1}}{k_2^n}\, k_4^n$$
$$\alpha^{L+1} = \psi_N^L - k_1^L\alpha^L - k_2^L\beta^L$$

and for the β system, we have

$$r^n = \psi_1^{n+1} - k_3^{n+1}\psi_N^n + \left(k_3^{n+1}/k_3^n\right) k_1^n\psi_1^n$$
$$x^n = \frac{k_3^{n+1}}{k_3^n}\, k_1^n$$
$$y^n = 1 - k_2^n k_3^{n+1} + \left(k_3^{n+1}/k_3^n\right) k_1^n k_4^n$$
$$z^n = k_4^{n+1}$$
$$\beta^{-1} = \psi_1^0 - k_3^0\alpha^0 - k_4^0\beta^0.$$

The α^n factors can be computed on one node—the "alpha node"—whereas the β^n factors are computed on another—the "beta node." Once this is done, the alpha node transmits α^n to node n while the beta node transmits β^n to node n. Node n can then compute ϕ^n, and the problem is solved.

In many cases, the system $A\phi = -\rho$ has to be solved repeatedly under conditions in which ρ changes but A does not. In this case, certain quantities can be computed on the first pass through the program's main loop,whereas subsequent iterations reuse the results of that calculation. These quantities are $\mathbf{v}$, $\mathbf{w}$, k_1 through k_4, a, b, c, x, y, and z.

The message passing requirements for the algorithm just described are as follows. For each tridiagonal system to be solved, six numbers must be passed from every node to the alpha node. The same six numbers must be passed from every node to the beta node. These numbers are ψ_1, ψ_N, and k_1 through k_4. The alpha and beta nodes then operate on these parameters to produce L correction factors each. Finally, the alpha node sends one number to each node ($\alpha^n \rightarrow$ node n), while the beta node does likewise.

One way to improve the efficiency of the message passing is to write the routine in such a way that it handles multiple tridiagonal systems at a time. For example, one might have a 2-D grid on which a tridiagonal solution is required over each horizontal strip. In this case, it would be best to pass the ψ and k factors for every strip in one message. This alleviates the problem of latency.

REFERENCES

[1] P. Mora and T. M. Antonsen, "Electron cavitation and acceleration in the wake of an ultra-intense, self focused laser pulse," *Phys. Rev. E*, vol. 53, p. 2068, 1996.

[2] ——, "Kinetic modeling of intense, short laser pulses propagating in tenuous plasmas," *Phys. Plasmas*, vol. 4, p. 217, 1997.

[3] D. W. Forslund, J. M. Kindel, and E. L. Lindman, "Theory of stimulated scattering processes in laser-irradiated plasmas," *Phys. Fluids*, vol. 18, no. 8, pp. 1002–1016, Aug. 1975.

[4] K. Estabrook and W. L. Kruer, "Theory and simulation of one-dimensional Raman backward and forward scattering," *Phys. Fluids*, vol. 26, no. 7, pp. 1892–1903, July 1983.

[5] M. Tabak, J. Hammer, M. E. Glinsky, W. L. Kruer, S. C. Wilks, J. Woodworth, E. M. Campbell, M. D. Perry, and R. J. Mason, "Ignition and high gain with ultrapowerful lasers," *Phys. Plasmas*, vol. 1, p. 1626, 1994.

[6] E. Esaray, P. Sprangle, J. Krall, and A. Ting, "Overview of plasma-based accelerator concepts," *IEEE Trans. Plasma Sci.*, vol. 24, p. 252, 1996.

[7] W. B. Mori, "Special issue on generation of coherent radiation using plasmas," *IEEE Trans. Plasma Sci.*, vol. 21, 1993.

[8] N. H. Burnett and G. D. Enright, "Population inversion in the recombination of optically-ionized plasmas," *IEEE J. Quantum Electron.*, vol. 26, p. 1797, 1990.

[9] A. Lal, D. Gordon, K. Wharton, C. E. Clayton, K. A. Marsh, W. B. Mori, C. Joshi, M. J. Everett, and T. W. Johnston, "Spatio-temporal dynamics of the resonantly excited relativistic plasma wave driven by a CO_2 laser," *Phys. Plasmas*, vol. 4, p. 1434, 1997.

[10] P. Sprangle, E. Esarey, and A. Ting, "Nonlinear theory of intense laser-plasma interactions," *Phys. Rev. Lett.*, vol. 64, p. 2011, 1990.

[11] R. L. Morse and C. W. Nielson, "Numerical simulation of the Weibel instability in one and two dimensions," *Phys. Fluids*, vol. 14, no. 4, p. 830, Apr. 1971.

[12] J. P. Boris, "Relativistic plasma simulation-optimization of a hybrid code," presented at the Proc. 4th Conf. Numer. Simul. Plasmas, 1970.

[13] C. K. Birdsall and A. B. Langdon, *Plasma Physics via Computer Simulation*, Bristol, U.K.: IOP, 1991.

[14] K. C. Tzeng, W. B. Mori, and C. D. Decker, "Anomalous absorption and scattering of short-pulse high-intensity lasers in underdense plasmas," *Phys. Rev. Lett.*, vol. 76, p. 3332, 1996.

[15] L. V. Keldysh, "Ionization in the field of a strong electromagnetic wave," *Soviet Phys. JETP*, vol. 20, no. 5, pp. 1307–1314, May 1965.

[16] M. N. Rosenbluth and C. S. Liu, "Excitation of plasma waves by two laser beams," *Phys. Rev. Lett.*, vol. 29, pp. 701–705, Sept. 1972.

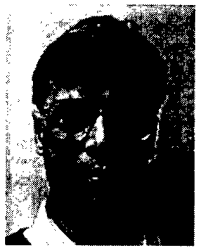
[17] W. B. Mori, "Theory and simulations on beat wave excitation of relativistic plasma waves," Ph.D. dissertation, University of California, Los Angeles, CA, 1987.

[18] C. Decker, W. B. Mori, and T. Katsouleas, "Particle-in-cell simulations of Raman forward scattering from short-pulse high-intensity lasers," *Phys. Rev. E*, vol. 50, p. 3338, 1994.

Daniel F. Gordon, received the B.S., M.S., and Ph.D. degrees in electrical engineering from the University of California, Los Angeles, in 1991, 1995, and 1999, respectively.

He is currently a National Research Council research associate at the Naval Research Laboratory, Washington, DC. His research interests are in high intensity, short pulse, laser-plasma interactions, plasma based accelerators, and computer modeling.

W. B. Mori, photograph and biography not available at the time of publication.



Thomas M. Antonsen, Jr. (M'87) was born in Hackensack, NJ, in 1950. He received the B.S. degree in electrical engineering in 1973, and the M.S. and Ph.D. degrees in 1976 and 1977, all from Cornell University, Ithaca, NY.

He was a National Research Council Post Doctoral Fellow at the Naval Research Laboratory in 1976–1977, and a Research Scientist in the Research Laboratory of Electronics at MIT from 1977 to 1980. In 1980, he moved to the University of Maryland where he joined the faculty of the Departments of Electrical Engineering and Physics in 1984. He is currently a Professor of physics and electrical engineering. He has held visiting appointments at the Institute for Theoretical Physics (UCSB), the Ecole Polytechnique Federale de Lausanne, Switzerland, and the Institute de Physique Theorique, Ecole Polytechnique, Palaiseau, France. His research interests include the theory of magnetically confined plasmas, the theory and design of high power sources of coherent radiation, nonlinear dynamics in fluids, and the theory of the interaction of intense laser pulses and plasmas. He is the author and coauthor of more than 180 journal articles and coauthor of the book *Principles of Free-electron Lasers*. He has served on the editorial board of *Physical Review Letters*, *The Physics of Fluids*, and *Comments on Plasma Physics*.

Prof. Antonsen was selected as a Fellow of the Division of Plasma Physics of the American Physical Society in 1986.

Fluid-Like Transport Variables in a Kinetic, Collisionless Plasma Near a Surface with Ion and Electron Reflection

Peng-Sheng Wei, *Member, IEEE,* and Feng-Bin Yeh

***Abstract*—Transport variables of the positive ions and electrons in the presheath and sheath of a plasma near a wall that partially reflects ions and electrons are determined from a kinetic analysis. Because velocity distributions of the ions and electrons near the wall are highly non-Maxwell–Boltzmann distributions, accurate predictions of transport variables, such as density, fluid velocity, mean pressure, fluid-like viscous stress, and conduction, require kinetic analysis. The results find that dimensionless transport variables of ions and electrons in the presheath and sheath can be exactly expressed in terms of transcendental functions determined by dimensionless independent parameters of ion and electron reflectivities of the wall, ion-to-electron mass ratio, charge number, and electron-to-ion temperature ratio at the presheath edge. The effects of the parameters on transport variables at the wall are also obtained. The computed transport variables in the presheath and sheath show agreement with available theoretical data for a completely absorbing wall.**

***Index Terms*—Plasma materials processing, plasma–wall interactions, space charge, transport processes of plasma.**

NOMENCLATURE

c	Particle thermal speed, $c^* = c/(k_B T_{e0}/m_i)^{1/2}$.
c_0	$(-2Z_i e\phi/m_i)^{1/2}$.
c_0'	$[2Z_i e(\phi_b - \phi)/m_i]^{1/2}$.
D	Dawson function, as defined in (9).
e	Electron charge.
f, F, g	Distribution function, $F^* = F(k_B T_{e0}/m_i)^{1/2}/n_{e0}$.
H	Heaviside function.
K	Function.
k_B	Boltzmann constant.
m	Particle mass.
M	m_i/m_e.
n	Particle density, $n^* = n/n_{e0}$.
N_1, N_2	Functions defined in (35).
p	Mean pressure, $p^* = p/n_{e0}k_B T_{e0}$.
q	Fluid-like conduction heat, $q^* = q/n_{e0}k_B T_{e0}(k_B T_{e0}/m_i)^{1/2}$.
T	Temperature.
u	Fluid velocity, $u^* = u/(k_B T_{e0}/m_i)^{1/2}$.
x, y, z	Cartesian coordinate.
Z	Charge number.

Greek Letters

γ	Incomplete gamma function defined in (20).
ε	Total energy $= m_i c_x^2/2 + Z_i e\phi$.
θ	$\sin^{-1}\sqrt{\chi_b/\chi}$.
Ξ	Function.
κ	T_{e0}/T_{i0}.
ρ	Reflectivity.
σ	$c_x/\lvert c_x\rvert$.
τ	Fluid-like viscous stress, $\tau^* = \tau/n_{e0}k_B T_{e0}$.
ϕ, χ	Dimensional and dimensionless potential, $\chi = -e\phi/k_B T_{e0}$.
$\chi_t =$	$-\varepsilon/(Z_i k_B T_{e0}) = -m_i c_x^2/(2Z_i k_B T_{e0}) + \chi$.
Ω	Function.
ε_t	$Z_i e\phi$.

Superscript

$*$	Dimensionless quantity.

Subscript

b	Boundary between sheath and presheath.
e, i	Electron and ion.
t	Turning point.
w	Wall.
0	Coordinate origin at $\phi = 0$ as shown in Fig. 1.

I. INTRODUCTION

THE plasma induced in metals processing is usually accompanied by strong momentum and energy transport near the workpiece surface. In view of the high thermal speed associated with rapid loss of the electrons to the wall, the plasma exhibits net positive charges. A thin layer called the sheath or space-charge region in a thickness of around several Debye lengths ($\sim 10^{-6}$ m), thus, exists on the cold wall [1]. The potential barrier adjusts so that the flux of electrons that have enough energy to go over the barrier to the wall is equal to the flux of ions reaching the wall. The presheath ($\sim 10^{-4}$ m), which lies between the bulk plasma and the sheath, is characterized by ionization to supply the ions lost to the wall. Regardless of the Debye shielding, small electrostatic potential in the presheath still accelerates the ions up to and beyond sonic speed before entering the sheath, as first explicitly pointed out by Bohm [2].

The use of a traditional fluid model (i.e., Navier–Stokes equations) obtained from the velocity moment equations of the Boltzmann's kinetic equation [3] to predict transport processes of the plasma near a surface is convenient but inaccurate.

Manuscript received April 16, 1999; revised May 25, 2000.

The authors are with the Department of Mechanical Engineering, National Sun Yat-Sen University, Kaohsiung, Taiwan 80424, R.O.C. (e-mail: pswei@mail.nsysu.edu.tw).

Publisher Item Identifier S 0093-3813(00)07249-0.

0093–3813/00$10.00 © 2000 IEEE

The traditional fluid model of the ions is only accurate for a small ion Knudsen number defined by the ratio between ion mean-free path and the characteristic length of the macroscopic system. The advantage is that the complicated collision terms, therefore, can be ignored in the zeroth approximation. Besides, if Debye length and Larmor radius are large in comparison with the length of the macroscopic system, the ion distribution function deviates slightly from the Maxwell–Boltzmann distribution. Transport coefficients such as viscosity, thermal and electrical conductivities, and diffusivities, thus, can be introduced to evaluate diffusion terms by applying the Enskog–Chapman perturbation method to the first order [3], [4]. Unfortunately, the ion Knudsen number in the presheath (and sheath) is marginally the order of unity, and velocities of the ions are of a highly non-Maxwell–Boltzmann distribution resulting from an electric field. Fluid equations, including shear stresses, conduction, and diffusion velocities, therefore, are not closed but involve higher order moments of kinetic distribution functions [5]. Truncating higher order moments inherently leads to an approximation or elimination of certain features of plasma behavior and constrains the regime of validity of the resultant fluid equation set.

A comparison between fluid and kinetic models in an unmagnetized presheath was provided by Bissell *et al.* [6]. The effects of collisions were included in fluid equations by introducing an adiabatic closure condition. Because experimental measurements rarely have accuracy levels as fine as $\pm 20\%$, the maximum deviation of $\pm 10\%$ for particle and heat fluxes to the wall among different models was acceptable. From a practical viewpoint, it was suggested that an isothermal fluid model is simple and adequate. Scheuer and Emmert [7] also made a similar comparison between fluid and kinetic models. In one-dimensional fluid models, either a constant temperature and cold plasma or approximate closure conditions was assumed. The effects of neutral gas–plasma interactions were simulated by source terms in fluid equations. Ion–ion collisional effects were included through the closure conditions. Ion density, flow velocity, parallel temperature, and total and conduction heat fluxes predicted by fluid equations compared well with kinetic results in the collisionless case. Ion–ion collisions exhibited negligible effects on ion particle and total and conduction heat fluxes to the wall.

A simplified kinetic analysis can be accurately enough used to evaluate transport variables of the plasma near the wall. Chodura [8] assumed approximately that velocities of the cold ions at the sheath edge were Maxwell–Boltzmann distribution shifted by sound speed, whereas the electrons were truncated Maxwell–Boltzmann distribution. The reemitted electrons started with zero velocity at the wall, which completely and partially absorbed the cold ions and electrons, respectively. Simple analytical solutions for densities, fluid speeds, mass fluxes, and energy fluxes of the ions and electrons to the wall, therefore, were obtained. Schwager and Birdsall [9] considered the presheath as a Maxwellian plane-source injecting equal fluxes of ions and electrons, based on that the width of the presheath does not affect potential drop [10], [11]. The ions and electrons exhibited truncated Maxwell–Boltzmann distributions in a region without collisions and ionization. Analytical expressions for density, fluid velocity, temperature, kinetic energy, and energy flux in the sheath on a completely absorbing wall were therefore obtained. The results agreed with those from a numerical particle-in-cell computation. Ordonez [12] extended the model of Schwager and Birdsall [9] to account for three-dimensional translation, reflection, and emission of electrons from a cold surface. Electron emission, however, can distort Maxwell–Boltzmann distribution in the presheath.

This study is to determine transport variables in a collisionless presheath and sheath on a wall partially reflecting ions and electrons from the highly non-Maxwell–Boltzmann velocity distributions of ions and electrons obtained by Wei *et al.* [13]. Reflections of ions and electrons are commonly encountered in sputter etching and deposition, ion implantation, and an analytical technique known as ion scattering spectroscopy [14]. It should be noted that hydrodynamic and thermal transport variables of the viscous stress and conduction heat take place for a distribution slightly deviated from a Maxwell–Boltzmann distribution resulting from collisions. Because ions and electrons of highly non-Maxwell–Boltzmann distributions result from electrostatic field, the transport variables in this work are termed as fluid-like transport variables [7], [15].

II. Kinetic Model and Analysis

The bulk plasma, presheath, and sheath between two electrically floating plates partially reflecting ions and electrons are illustrated in Fig. 1. In view of symmetry, the origin of the coordinate is conveniently set at the center of bulk plasma, where electrostatic potential is zero. Because potential decreases, the ions in the positive x-direction are accelerated. On the other hand, the electrons in the forward direction need to overcome potential. The major assumptions made are the same as the work provided by Wei *et al.* [13]. They are 1) steady state, 2) collisionless presheath and sheath, 3) unmagnetized electrostatic plasma, 4) neglect of secondary electron emission, thermal and field emissions of ions and electrons, and 5) Maxwell–Boltzmann distributions of the ions moving in the y- and z-directions.

A. Transport Variables of Ions

Transport variables in the presheath and sheath can be evaluated from different moments of distribution functions. Derivations are described as follows.

1) Presheath: Density, fluid velocity, mean pressure, fluid-like shear stress, and conduction heat of the ions yield

$$n_i = \int_{-\infty}^{\infty} F_i \, dc_x \tag{1}$$

$$u_i = \frac{1}{n_i} \int_{-\infty}^{\infty} F_i c_x \, dc_x \tag{2}$$

$$p_i \equiv \frac{1}{3} \int_{-\infty}^{\infty} f_i m_i \left[(c_x - u_i)^2 + c_y^2 + c_z^2 \right] dc_x \, dc_y \, dc_z \tag{3}$$

$$\tau_i \equiv p_i - \int_{-\infty}^{\infty} F_i m_i (c_x - u_i)^2 \, dc_x \tag{4}$$

$$q_i \equiv \int_{-\infty}^{\infty} f_i \frac{1}{2} m_i \left[(c_x - u_i)^2 + c_y^2 + c_z^2 \right] \times (c_x - u_i) \, dc_x \, dc_y \, dc_z \tag{5}$$

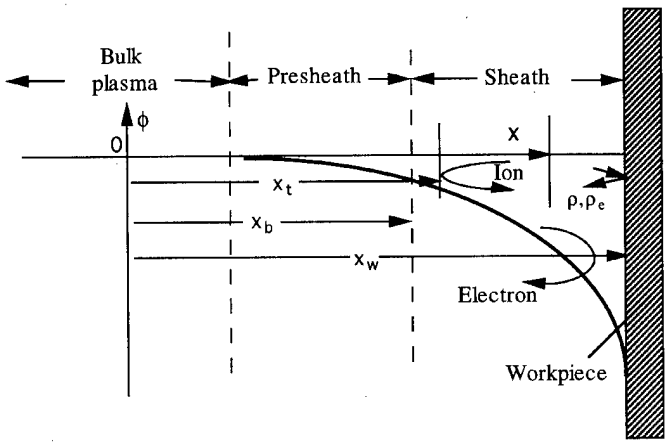


Fig. 1. System sketch for the model and coordinates.

where the ion distribution function is

$$f_i = F_i(x, c_x)\frac{m_i}{2\pi k_B T_{i0}}\exp\left[-\frac{m_i\left(c_y^2+c_z^2\right)}{2k_BT_{i0}}\right]. \quad (6)$$

The ion distribution function integrated over velocity components c_y and c_z is [13]

$$\begin{aligned}F_i(x,c_x) = {} & \frac{n_{e0}}{(1+\rho)Z_i}\sqrt{\frac{m_i}{2\pi k_BT_{i0}}}\exp\left(-\frac{\varepsilon}{k_BT_{i0}}\right)\\ & \cdot\{H(c_x-c_0)\{K(\chi_b)+K(\chi)+\rho[K(\chi_b)\\ & -K(\chi)]\}+H(c_x)H(c_0-c_x)\{K(\chi_b)\\ & -2K(\chi_t)+K(\chi)+\rho[K(\chi_b)-K(\chi)]\}\\ & +H(-c_x)H(c_0+c_x)\{K(\chi_b)-K(\chi)\\ & +\rho[K(\chi_b)-2K(\chi_t)+K(\chi)]\}\\ & +H(-c_x)H(-c_0-c_x)\{K(\chi_b)\\ & -K(\chi)+\rho[K(\chi_b)+K(\chi)]\}\}\end{aligned} \quad (7)$$

where function K introduced by Emmert *et al.* [10] yields

$$\begin{aligned}K(\chi)e^{Z_i\kappa\chi} = {} & K(\chi_b)e^{Z_i\kappa\chi}\operatorname{erf}\left(\sqrt{Z_i\kappa\chi}\right)\\ & +\frac{2}{\sqrt{\pi Z_i\kappa}}D(\sqrt{\chi}).\end{aligned} \quad (8)$$

The Dawson and error or complementary error functions in (8) are, respectively, defined as [16]

$$D(x) \equiv e^{-x^2}\int_0^x e^{t^2}\,dt \quad (9)$$

$$\operatorname{erf}(x) = 1-\operatorname{erfc}(x) \equiv \frac{2}{\sqrt{\pi}}\int_0^x e^{-t^2}\,dt. \quad (10)$$

Sheath edge potential in (8) is satisfied by

$$\frac{2}{\sqrt{\pi Z_i\kappa}}D(\sqrt{\chi_b}) = e^{Z_i\kappa\chi_b}\operatorname{erfc}\left(\sqrt{Z_i\kappa\chi_b}\right). \quad (11)$$

Aside from $K(0) = 0$, (8) by substituting (11) leads to $K(\chi_b) = 1$. Emmert *et al.* [10] obtained (8) and (11) for a completely absorbing wall. Substituting (6)–(10) into (1)–(5) and conducting lengthy integrations with the aid of integration formulas listed in the Appendix, dimensionless transport variables in the presheath lead to

$$n_i^* = \frac{1}{Z_i}e^{-\chi} \quad (12)$$

$$u_i^* = \Omega_1 \quad (13)$$

$$p_i^* = \frac{1}{3Z_i\kappa}e^{-\chi}\Omega_2 - \frac{1}{3}n_i^*u_i^{*2} + \frac{2}{3\kappa}n_i^* \quad (14)$$

$$\tau_i^* = n_i^*u_i^{*2} + p_i^* - \frac{1}{\kappa}n_i^*\Omega_2 \quad (15)$$

$$q_i^* = -\frac{1}{2}n_i^*u_i^{*3} - \frac{5}{2}u_i^*p_i^* + u_i^*\tau_i^* + \frac{1}{\kappa}n_i^*\Omega_3 \quad (16)$$

where the functions

$$\Omega_1 \equiv \frac{2(1-\rho)}{1+\rho}\sqrt{\frac{2}{Z_i}}\frac{1+Z_i\kappa}{\pi\kappa}e^{\chi}D(\sqrt{\chi}) \quad (17)$$

$$\Omega_2 \equiv Z_i\kappa[(1-\chi)e^{\chi}-1] + e^{\chi}e^{Z_i\kappa\chi}[1-\gamma(2, Z_i\kappa\chi)] \quad (18)$$

$$\Omega_3 \equiv \Omega_1\left[2-Z_i\kappa+\frac{Z_i\kappa}{D(\sqrt{\chi})}\sqrt{\chi}\right] \quad (19)$$

and the incomplete gamma function [17], [18] are defined as

$$\gamma(\nu, a) = \int_0^a \xi^{\nu-1}e^{-\xi}\,d\xi, \quad \nu > 0. \quad (20)$$

For a completely absorbing wall without emission, ion mass flux obtained from a product of (12) and (13) reduces to (49) and (50) in Emmert *et al.* [10].

2) Sheath: Conservation equations of mass, momentum, and energy fluxes are [19]

$$\int_{-\infty}^{\infty}F_i(x,c_x)m_ic_x\,dc_x = m_in_{ib}u_{ib} \quad (21)$$

$$\begin{aligned}&\int_{-\infty}^{\infty}F_i(x,c_x)m_ic_x^2\,dc_x - Z_ik_BT_{e0}\int_{\chi_b}^{\chi}n_i\,d\chi'\\ &\quad = m_in_{ib}u_{ib}^2 + p_b - \tau_{xb}\end{aligned} \quad (22)$$

$$\begin{aligned}&\int_{-\infty}^{\infty}f_i(x,\mathbf{c})\tfrac{1}{2}m_i\left(c_x^2+c_y^2+c_z^2\right)c_x\,dc_x\,dc_y\,dc_z\\ &\quad - Z_in_{ib}k_BT_{e0}u_{ib}(\chi-\chi_b)\\ &\quad = \tfrac{1}{2}m_in_{ib}u_{ib}^3 + \tfrac{5}{2}u_{ib}p_b + q_{xb} - u_{ib}\tau_{xb}.\end{aligned} \quad (23)$$

The ion distribution function in the sheath is [13]

$$\begin{aligned}\frac{F_i(x,c_x)}{m_i} = {} & H(c_x-c_0')|c_{xb}|g_b(\varepsilon,+1)\\ & +H(-c_0'-c_x)\rho|c_{xb}|g_b(\varepsilon,+1)\end{aligned} \quad (24)$$

where the first term on the right-hand side represents the distribution of the ions moving in the forward direction, whereas the last term is the distribution function for the ions in the negative direction after hitting the wall. The distribution function of the forward-moving ions at the sheath edge in (24) yields

$$\begin{aligned}|c_{xb}|g_b(\varepsilon,+1) = {} & \frac{2n_{e0}}{m_i(1+\rho)Z_i}\sqrt{\frac{m_i}{2\pi k_BT_{i0}}}\exp\left(-\frac{\varepsilon}{k_BT_{i0}}\right)\\ & \times\{H(c_{xb}-c_0)K(\chi_b)+H(c_{xb})\\ & \times H(c_0-c_{xb})[K(\chi_b)-K(\chi_t)]\}\end{aligned} \quad (25)$$

where the first term on the right-hand side refers to high-energy ions ($\varepsilon > 0$) coming from the presheath edge and ionized with positive velocities in the presheath, and the last term represents low-energy ions ($Z_i e\phi_b < \varepsilon < 0$) generated with positive velocities and negative velocities experiencing turning in the presheath. Substituting (24) and (25) into (1), (2), and (21)–(23) and integrating, transport variables in the sheath lead to

$$n_i^* = \frac{1}{Z_i}\left\{e^{Z_i\kappa\chi}\,\mathrm{erfc}[\sqrt{Z_i\kappa(\chi-\chi_b)}] - \Xi_1 + \Xi_2\right\} \tag{26}$$

$$n_i^* u_i^* = n_{ib}^* u_{ib}^* = n_{iw}^* u_{iw}^* \tag{27}$$

$$p_i^* = \frac{1}{3}\left(\Xi_3 - n_i^* u_i^{*2} + \frac{2}{\kappa}\,n_i^*\right) \tag{28}$$

$$\tau_i^* = n_i^* u_i^{*2} + p_i^* - Z_i E_i^* - n_{ib}^* u_{ib}^{*2} - p_{ib}^* + \tau_{ib}^* \tag{29}$$

$$q_i^* = u_i^*\tau_i^* + Z_i u_i^* n_i^*\chi - \frac{5}{2}\,p_i^* u_i^* - \frac{1}{2}\,n_i^* u_i^{*3} + \frac{5}{2}\,p_{ib}^* u_{ib}^* + \frac{1}{2}\,n_{ib}^* u_{ib}^{*3} + q_{ib}^* - u_{ib}^*\tau_{ib}^* - Z_i u_{ib}^* n_{ib}^*\chi_b \tag{30}$$

where dimensionless electrostatic field

$$E_i^* \equiv \int_{\chi_b}^{\chi} n_i^*\,d\chi' = \frac{1}{Z_i}\left[-\Xi_2 + e^{-\chi_b} + \frac{4}{\pi}\,D(\sqrt{\chi_b}) \times \sqrt{\chi-\chi_b} + \frac{Z_i\kappa+1}{Z_i\kappa}\left(\frac{2\theta}{\pi}-1\right) - \frac{1}{Z_i\kappa}\,\Xi_1 + \frac{1}{Z_i\kappa}\,e^{Z_i\kappa\chi}\,\mathrm{erfc}\left(\sqrt{Z_i\kappa(\chi-\chi_b)}\right) + \frac{2}{Z_i\kappa\sqrt{\pi}}\,e^{Z_i\kappa\chi_b} \times \mathrm{erfc}\left(\sqrt{Z_i\kappa\chi_b}\right)\sqrt{Z_i\kappa(\chi-\chi_b)}\right] \tag{31}$$

and the functions

$$\Xi_1 \equiv e^{Z_i\kappa\chi}\left\{1 - \mathrm{erf}\left(\sqrt{Z_i\kappa\chi_b}\right)\mathrm{erf}\left[\sqrt{Z_i\kappa(\chi-\chi_b)}\right] - \frac{2}{\pi}\,N_1(Z_i\kappa\chi_b,\theta)\right\} \tag{32}$$

$$\Xi_2 \equiv e^{-\chi}\left[1 + \frac{4}{\pi}\,e^{\chi}D\left(\sqrt{\chi-\chi_b}\right)D(\sqrt{\chi_b}) - \frac{2}{\pi}\,N_2(\chi_b,\theta)\right] \tag{33}$$

$$\Xi_3 \equiv \left(1+\frac{1}{Z_i\kappa}\right)\frac{2\theta}{\pi} + \frac{2N_1(Z_i\kappa\chi_b,\theta)}{\pi Z_i\kappa}\,e^{Z_i\kappa\chi} + \frac{4}{\pi}\sqrt{\chi-\chi_b}D(\sqrt{\chi_b}) - \Xi_2 - \frac{2}{\sqrt{\pi}Z_i\kappa} \times \mathrm{erfc}\left(\sqrt{Z_i\kappa\chi_b}\right)e^{Z_i\kappa\chi}\gamma\left[\frac{3}{2}, Z_i\kappa(\chi-\chi_b)\right] \tag{34}$$

$$N_1(a,\theta) \equiv \int_{\theta}^{\pi/2}\exp\left(-\frac{a}{\sin^2\varphi}\right)d\varphi$$

$$N_2(a,\theta) \equiv \int_{\theta}^{\pi/2}\exp\left(\frac{a}{\sin^2\varphi}\right)d\varphi. \tag{35}$$

Balance of currents for a floating wall is also required to determine wall potential

$$Z_i n_{iw}^* u_{iw}^* = n_{ew}^* u_{ew}^* \tag{36}$$

An electrically biased wall can be readily obtained by imposing an external electric current.

B. Transport Variables of Electrons in Sheath

The electron distribution function without wall emission in the sheath is [13]

$$F_e(x,c_x) = H(c_x + c'_{e0})m_e\,|c_{x_b}|\,g_{eb}(\varepsilon,+1) + H(-c_x - c'_{e0})\rho_e m_e\,|c_{x_b}|\,g_{eb}(\varepsilon,+1) \tag{37}$$

where the distribution function at the sheath edge

$$m_e\,|c_{x_b}|\,g_{eb}(\varepsilon,+1) = n_{eb}\sqrt{\frac{m_e}{2\pi k_B T_{e0}}}\exp\left(-\frac{\varepsilon+e\phi_b}{k_B T_{e0}}\right). \tag{38}$$

Substituting (37) into equations similar to (1)–(5) and integrating, dimensionless density, fluid velocity, mean pressure, fluid-like viscous stress and conduction heat of electrons are found to be

$$n_e^* = e^{-\chi}\left[1 + \frac{\rho_e - 1}{2}\,\mathrm{erfc}\left(\sqrt{\chi_w-\chi}\right)\right] \tag{39}$$

$$u_e^* = \frac{1-\rho_e}{n_e^*}\sqrt{\frac{M}{2\pi}}\,e^{-\chi_w} \tag{40}$$

$$p_e^* = \frac{1}{3}\left(\Xi_4 - \frac{1}{M}\,n_e^* u_e^{*2} + 2n_e^*\right) \tag{41}$$

$$\tau_e^* = 2(n_e^* - p_e^*) \tag{42}$$

$$q_e^* = n_e^* u_e^*(\chi_w - \chi + 1) - \frac{3}{2}\,u_e^*\Xi_4 + \frac{1}{M}\,n_e^* u_e^{*3} \tag{43}$$

where the function

$$\Xi_4 \equiv e^{-\chi} + \frac{\rho_e - 1}{2}\left[e^{-\chi}\,\mathrm{erfc}\left(\sqrt{\chi_w-\chi}\right) + 2\sqrt{\frac{\chi_w-\chi}{\pi}}\,e^{-x_w}\right]. \tag{44}$$

Equation (39) is a generalized formula of electron density for a wall partially reflecting ions and electrons. For zero electron reflectivity, (39) reduces to (A1) in Emmert *et al.* [10]. The last term on the right-hand side of (39) is small for a large potential drop across the sheath. For a typical dimensionless potential drop of 2, the complementary error function yields 0.0047. Electron density in the presheath, therefore, can be represented by a Maxwell–Boltzmann distribution, even though wall reflection (or low emission) takes place. On the other hand, the last term must be retained in the sheath if the difference in potentials between the wall and location considered is not large.

C. Wall Conditions

Dimensionless density, fluid velocity, mean pressure, fluid-like viscous stress, and heat flux of the ions at the wall

are obtained by evaluating (26)–(30) at the wall

$$n^*_{iw} = \frac{1}{Z_i}\left\{\Xi_{2w} + e^{Z_i\kappa\chi_w}\,\mathrm{erfc}[\sqrt{Z_i\kappa(\chi_w - \chi_b)}] - \Xi_{1w}\right\} \tag{45}$$

$$u^*_{iw} = \frac{1}{n^*_{iw}Z_i}\,e^{-\chi_b}\Omega_{1b} \tag{46}$$

$$p^*_{iw} = \frac{1}{3}\left(\Xi_{3w} - n^*_{iw}u^{*2}_{iw} + \frac{2}{\kappa}\,n^*_{iw}\right) \tag{47}$$

$$\tau^*_{iw} = p^*_{iw} + n^*_{iw}u^{*2}_{iw} - Z_iE^*_{iw} - n^*_{ib}u^{*2}_{ib} - p^*_{ib} + \tau^*_{ib} \tag{48}$$

$$\begin{aligned} q^*_{iw} = {} & u^*_{iw}\tau^*_{iw} + Z_iu^*_{iw}n^*_{iw}\chi_w - \frac{5}{2}\,p^*_{iw}u^*_{iw} \\ & - \frac{1}{2}\,n^*_{iw}u^{*3}_{iw} + \frac{5}{2}\,p^*_{ib}u^*_{ib} + \frac{1}{2}\,n^*_{ib}u^{*3}_{ib} \\ & + q^*_{ib} - u^*_{ib}\tau^*_{ib} - Z_iu^*_{ib}n^*_{ib}\chi_b. \end{aligned} \tag{49}$$

Dimensionless potentials χ_b and χ_w are, respectively, determined by (11) and (36). Dimensionless density, fluid velocity, mean pressure, fluid-like viscous stress, and conduction of the electrons at the wall evaluated from (39)–(43) at the wall are, respectively

$$n^*_{ew} = \frac{\rho_e + 1}{2}\,e^{-\chi_w} \tag{50}$$

$$u^*_{ew} = \frac{2(1-\rho_e)}{\rho_e + 1}\sqrt{\frac{M}{2\pi}} \tag{51}$$

$$p^*_{ew} = n^*_{ew}\left(1 - \frac{1}{3M}\,u^{*2}_{ew}\right) \tag{52}$$

$$\tau^*_{ew} = \frac{2}{3M}\,n^*_{ew}u^{*2}_{ew} \tag{53}$$

$$q^*_{ew} = n^*_{ew}u^*_{ew}\left(\frac{1}{M}\,u^{*2}_{ew} - \frac{1}{2}\right). \tag{54}$$

The error, Dawson, and incomplete gamma functions were numerically integrated by a Simpson's rule. Errors were less than 10^{-6} by comparing grids of 1000 and 500.

III. Results and Discussion

In this study, independent parameters controlling transport processes in a presheath and sheath are ion reflectivity (ρ) and electron reflectivity (ρ_e) of the wall, ion-to-electron mass ratio (M), charge number (Z_i), and electron-to-ion temperature ratio at the presheath edge (κ). Dimensionless sheath edge potential versus the product of charge number with electron-to-ion temperature ratio at the presheath edge is shown in Fig. 2. An increase in the product of a charge number with an electron-to-ion temperature ratio at the presheath edge increases dimensionless sheath edge potential. The same result was also provided by Emmert *et al.* [10]. It should be noted that dimensionless sheath edge potential is independent of ion and electron reflectivities and ion-to-electron mass ratio (11).

The effects of ion and electron reflectivities, ion-to-electron mass ratio, charge number, and electron-to-ion temperature ratio at the presheath edge on dimensionless wall potential are shown in Fig. 3. Dimensionless wall potential decreases with increasing electron reflectivity and charge number and decreasing ion reflectivity, ion-to-electron mass ratio, and

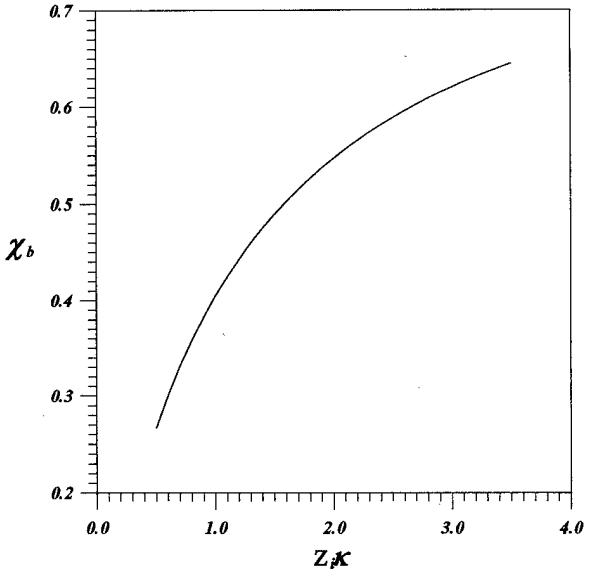


Fig. 2. Dimensionless sheath edge potential (χ_b) versus product of charge number with electron-to-ion temperature ratio at presheath edge ($Z_i\kappa$).

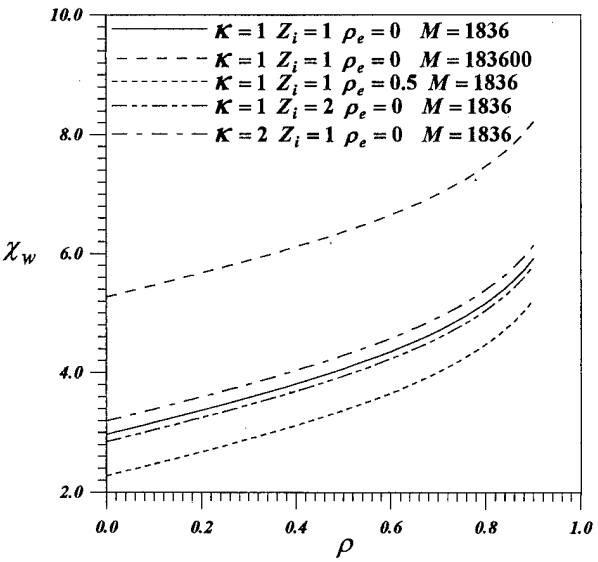


Fig. 3. Dimensionless wall potential (χ_w) versus ion reflectivity (ρ) for different electron reflectivities (ρ_e), ion-to-electron mass ratios (M), charge numbers (Z_i), and electron-to-ion temperature ratios at presheath edge (κ).

electron-to-ion temperature ratio at the presheath edge, respectively. An increase in charge number and decreases in ion reflectivity, ion-to-electron mass ratio, and electron-to-ion temperature ratio at the presheath edge increase ion current. In view of the floating wall, the corresponding increase of electron current is achieved by reducing dimensionless wall potential. An increase in electron reflectivity reduces electron current. This leads to a decrease of dimensionless wall potential to reduce ion current. Dimensionless wall potential is found to increase rapidly for a large ion reflectivity. It is noted that the effect of charge number on wall potential is contradictory to the simple estimation presented by Emmert *et al.* [10] and the computation from Procassini *et al.* [20], but it is consistent to the analytical derivation from Emmert *et al.* [10]. For a

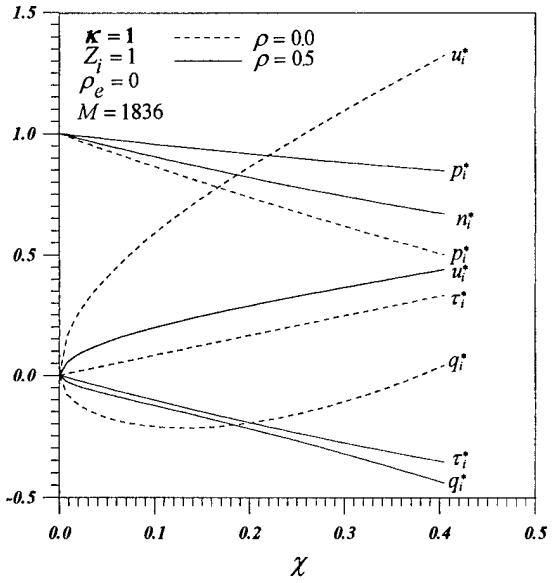


Fig. 4. Spatial variations of dimensionless ion density (n_i^*), fluid velocity (u_i^*), mean pressure (p_i^*), and fluid-like viscous stress (τ_i^*) and conduction (q_i^*) in presheath for different ion reflectivities (ρ).

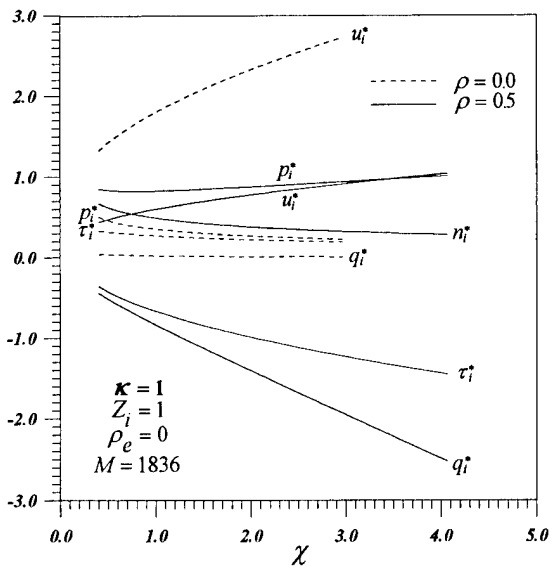


Fig. 5. Spatial variations of dimensionless ion density (n_i^*), fluid speed (u_i^*), mean pressure (p_i^*), and fluid-like viscous stress (τ_i^*) and conduction (q_i^*) in sheath for different ion reflectivities (ρ).

completely absorbing wall, dimensionless wall potential yields 2.965, which is identical to that obtained by Emmert *et al.* [10] and Scheuer and Emmert [21].

Spatial variations of dimensionless ion transport variables in the presheath for different ion reflectivities are shown in Fig. 4. The abscissa is dimensionless potential to represent the x-coordinate. Dimensionless potentials of 0 and 0.404 are referred to the presheath and sheath edges, respectively. It can be seen that dimensionless ion density decreases and fluid speed increases in the forward direction. Interestingly, ion density as a function of potential is independent of ion reflectivity (12). A decrease in ion reflectivity increases fluid speed because of an increase in the first moment of the ion distribution function [13]. For zero ion reflectivity, dimensionless fluid speed at the sheath edge is 1.32, which is identical to the collisionless kinetic result and is approximately equal to 1.36 for a collisionless fluid model and 1.38 for collisional fluid model, as proposed by Scheuer and Emmert [7]. From a kinetic viewpoint, mean pressure or kinetic temperature is an indication of the averaged kinetic energy relative to local velocity of fluid (3). In other words, mean pressure is the second moment of the distribution function. An increase in fluid velocity in the forward direction reduces mean pressure because of a decrease in the second moment of the distribution function. From a fluid mechanics viewpoint, fluid velocity is increased by decreasing mean pressure in the forward direction. Mean pressure is reduced by decreasing ion reflectivity as a result of an increase in fluid velocity. In order to induce high fluid velocity, fluid-like viscous stress acting as a driving force increases monotonically in the forward direction for zero ion reflectivity. On the other hand, fluid-like viscous stress retards fluid flow for ion reflectivity of 0.5. Fluid speed can be decreased by increasing either mean pressure or magnitude of negative viscous stress in the forward direction. Hence, for ion reflectivity of 0.5, the increase of fluid speed reduces when mean pressure and viscous stress become retarding forces.

Fluid-like conduction representing kinetic energy flux observed from a local fluid element is the third moment of a distribution function (5). Regardless of ion reflectivity, fluid-like conduction near the presheath edge is negative because of a rapid increase in fluid speed from zero. For ion reflectivity of 0.5, the magnitude of negative conduction increases monotonically in the forward direction. Hence, fluid-like conduction directs toward bulk plasma in high temperature. The same result was found and discussed by Scheuer and Emmert [7]. For zero ion reflectivity, negative fluid-like conduction has a minimum value and reaches small positive values near the sheath edge. Because most forward-moving ions reach high speeds, the third moment increases.

Similar variations of dimensionless transport variables of the ions in the sheath for different ion reflectivities are presented in Fig. 5. It should be noted that for zero ion reflectivity, dimensionless fluid speed increases from the sound speed 1.32 satisfying the Bohm criterion to hypersonic value of around 2.8 at the wall. Considering a hydrogen plasma at 5000 K, fluid speed hitting the wall is at a surprisingly high value of around 1.8×10^4 m/s. In the case of zero ion reflectivity, instead of the monotonic decrease, mean pressure near the wall becomes increasing for ion reflectivity of 0.5. Fluid-like conduction directs from the wall to the presheath for ion reflectivity of 0.5, even though temperature of plasma is higher than that of wall [7]. Referring to Figs. 4 and 5, dimensionless ion density, fluid speed, and potentials at the sheath edge and wall are, respectively, $n_{ib}^* = 0.667$, $u_{ib}^* = 1.320$, $\chi_b = 0.404$, and $\chi_w = 2.965$, which are, respectively, identical to those obtained by Emmert *et al.* [10], Scheuer and Emmert [21], and Bissell *et al.* [6].

The variations in dimensionless transport variables of the ions at the wall with ion reflectivity for different charge numbers are shown in Fig. 6. It can be seen that in view of a decrease in dimensionless wall potential, an increase in charge number results in a decrease of dimensionless ion density

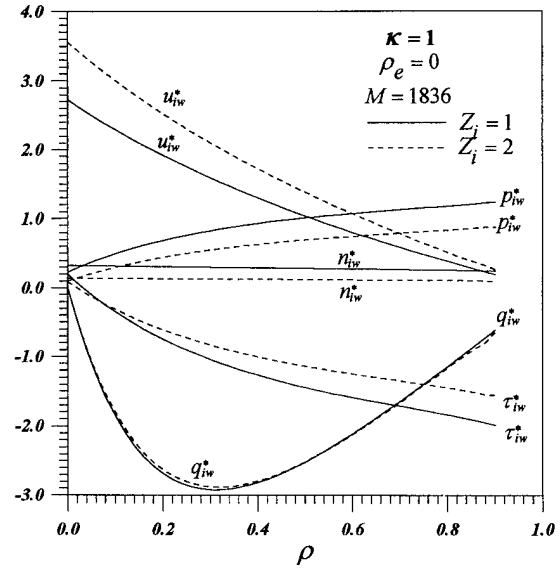


Fig. 6. Dimensionless ion density (n^*_{iw}), fluid speed (u^*_{iw}), mean pressure (p^*_{iw}), and fluid-like viscous stress (τ^*_{iw}) and conduction (q^*_{iw}) at wall versus ion reflectivity (ρ) for different charge numbers (Z_i).

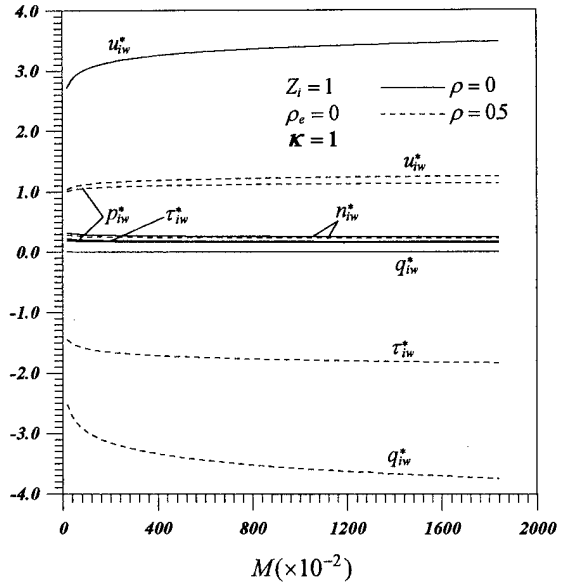


Fig. 7. Dimensionless ion density (n^*_{iw}), fluid speed (u^*_{iw}), mean pressure (p^*_{iw}), and fluid-like viscous stress (τ^*_{iw}) and conduction (q^*_{iw}) at wall versus ion-to-electron mass ratio (M) for different ion reflectivities (ρ).

at the wall. To balance electric current, fluid speed of ions increases with charge number. Because fluid speed increases, dimensionless mean pressure and negative fluid-like viscous stress decrease magnitudes with increasing charge number. Small ion reflectivity and charge number, however, result in positive fluid-like viscous stress. Except for the case of small ion reflectivity, fluid-like conduction on the wall is toward the plasma. Interestingly, magnitude of dimensionless fluid-like conduction reaches the maximum near ion reflectivity of 0.3. Fluid-like conduction is insignificant to the variations of charge number.

The effects of ion-to-electron mass ratio on dimensionless transport variables of the ions at the wall are shown in Fig. 7. The variations of transport variables are reduced by increasing ion-to-electron mass ratio. In most cases, the effects of ion-to-electron mass ratio on transport variables can be ignored (45)–(49). An increase in ion-to-electron mass ratio increases fluid speed as a result of an increase in dimensionless wall potential (see Fig. 3). Ion density, therefore, reduces to balance electric current. Mean pressure and fluid-like viscous stress decrease slightly by increasing ion-to-electron mass ratio for zero ion reflectivity. On the other hand, for ion reflectivity of 0.5, mean pressure and negative fluid-like conduction increase their magnitudes with ion-to-electron mass ratio. The effects of electron-to-ion temperature ratio at the presheath edge on transport variables of the ions at the wall for different ion reflectivities are shown in Fig. 8. All transport variables gradually decrease their magnitudes as electron-to-ion temperature ratio at the presheath edge increases.

Dimensionless transport variables of the electrons versus potential across the sheath for different ion reflectivities are shown in Fig. 9. Regardless of ion reflectivity, dimensionless electron density decreases in the forward direction because of increased dimensionless potential. To maintain electron current, fluid speed increases. Fluid speed is high for zero ion reflectivity. Even though electric field retards forward-moving

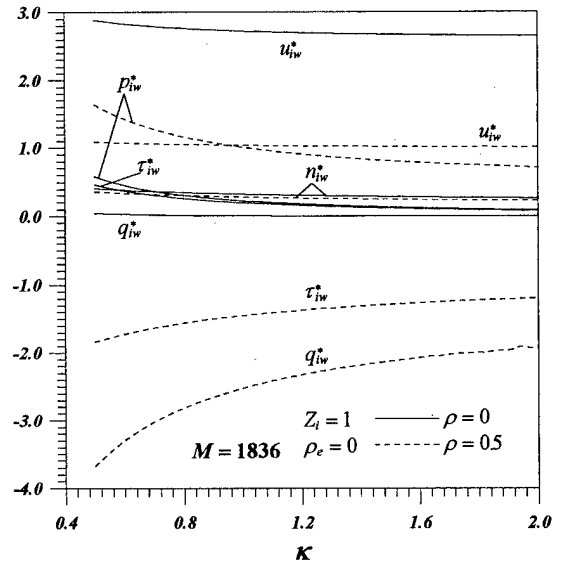


Fig. 8. Dimensionless ion density (n^*_{iw}), fluid speed (u^*_{iw}), mean pressure (p^*_{iw}), and fluid-like viscous stress (τ^*_{iw}) and conduction (q^*_{iw}) at wall versus electron-to-ion temperature ratio at presheath edge (κ) for different ion reflectivities (ρ).

electrons, fluid speed of electrons is much higher than that of ions. Kinetically speaking, decreases in density, mean pressure, and fluid-like viscous stress are attributed to decreases in the moments of the electron distribution function. In contrast to ions, fluid-like conduction of electrons directs to the wall.

The effects of electron reflectivity and charge number on dimensionless transport variables of the electrons at the wall are shown in Fig. 10. An increase in electron reflectivity increases density and mean pressure, and it decreases fluid speed and fluid-like viscous stress. Fluid-like conduction is changed from slightly positive to negative by increasing electron reflectivity. Fig. 11 shows the variations in transport variables

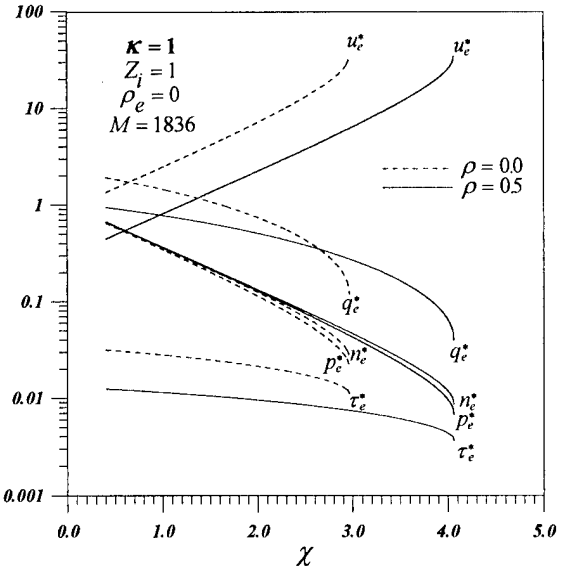


Fig. 9. Spatial variations of dimensionless electron density (n_e^*), fluid speed (u_e^*), mean pressure (p_e^*), and fluid-like viscous stress (τ_e^*) and conduction (q_e^*) in sheath for different ion reflectivities (ρ).

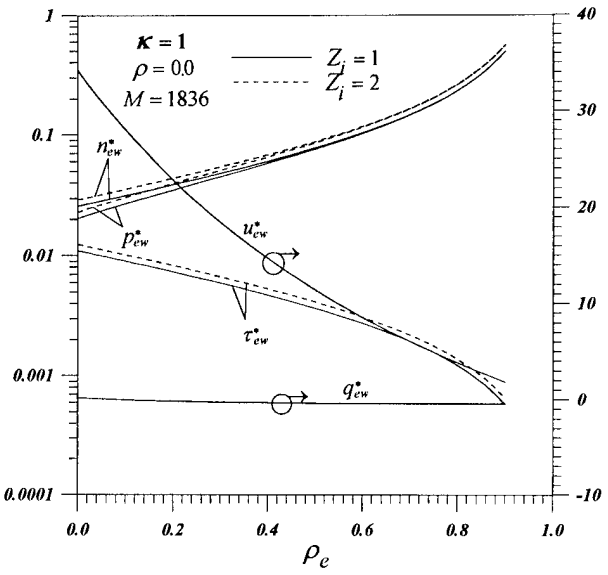


Fig. 10. Dimensionless electron density (n_{ew}^*), fluid speed (u_{ew}^*), mean pressure (p_{ew}^*), and fluid-like viscous stress (τ_{ew}^*) and conduction (q_{ew}^*) at wall versus electron reflectivity (ρ_e) for different charge numbers (Z_i).

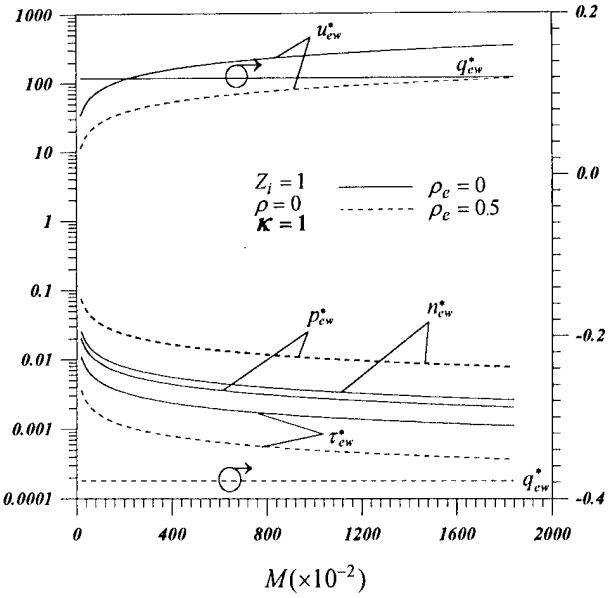


Fig. 11. Dimensionless electron density (n_{ew}^*), fluid speed (u_{ew}^*), mean pressure (p_{ew}^*), and fluid-like viscous stress (τ_{ew}^*) and conduction (q_{ew}^*) at wall versus ion-to-electron mass ratio (M) for different electron reflectivities (ρ_e).

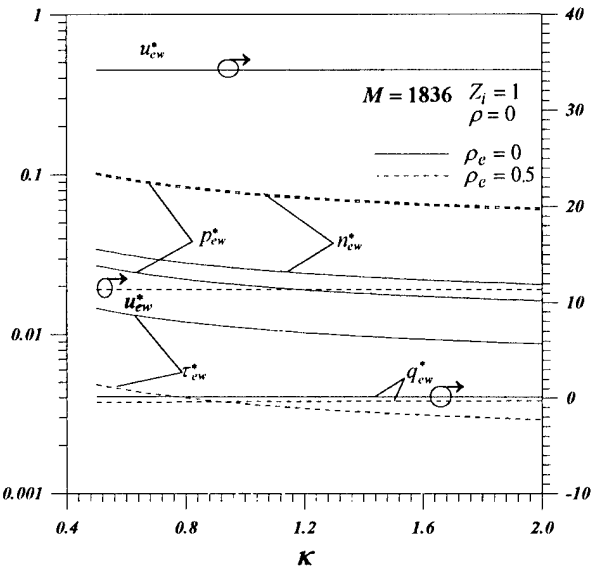


Fig. 12. Dimensionless electron density (n_{ew}^*), fluid speed (u_{ew}^*), mean pressure (p_{ew}^*), and fluid-like viscous stress (τ_{ew}^*) and conduction (q_{ew}^*) at wall versus electron-to-ion temperature ratio at presheath edge (κ) for different electron reflectivities (ρ_e).

of the electrons at the wall with ion-to-electron mass ratio for different electron reflectivities. In contrast to fluid speed, electron density, mean pressure, and fluid-like viscous stress decrease with increasing ion-to-electron mass ratio. The effect of ion-to-electron mass ratio on conduction is insignificant. However, the directions of fluid-like conduction are, respectively, positive and negative for electron reflectivities of 0 and 0.5. The variations in dimensionless transport variables of the electrons at the wall with electron-to-ion temperature ratio at the presheath edge for different electron reflectivities are shown in Fig. 12. Fluid speed, mean pressure, and fluid-like viscous stress gradually decreases with increasing electron-to-ion temperature ratio at the presheath edge. Interestingly, fluid speed is independent of the variation of electron-to-ion temperature ratio at the presheath edge (51). The effect of electron-to-ion temperature ratio at the presheath edge on fluid-like conduction is slight.

Comparisons of the ratios of transport variables at a location in the sheath and sheath edge versus electrostatic potential predicted from Schwager and Birdsall [9] and this work for a completely absorbing wall are shown in Fig. 13. Curves cannot be distinguished by choosing grid points of 100 and 400. It can be seen that agreement is good, except the results near the wall. Similar results for the electrons are shown in Fig. 14. The present work, therefore, provides consistent predications for the

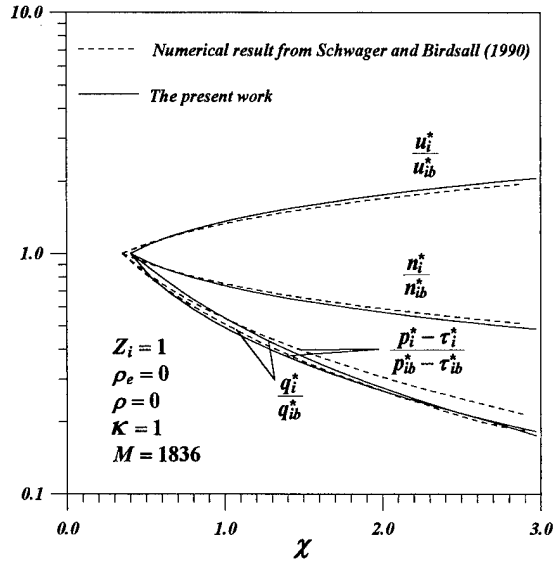


Fig. 13. Comparisons of ratios of ion densities (n_i^*/n_{ib}^*), fluid velocities (u_i^*/u_{ib}^*), fluid-like conduction (q_i^*/q_{ib}^*), and differences between mean pressure and fluid-like viscous stress $((p_i^* - \tau_i^*)/(p_{ib}^* - \tau_{ib}^*))$ at locations in sheath and sheath edge versus potential obtained from numerical result [9] and this work.

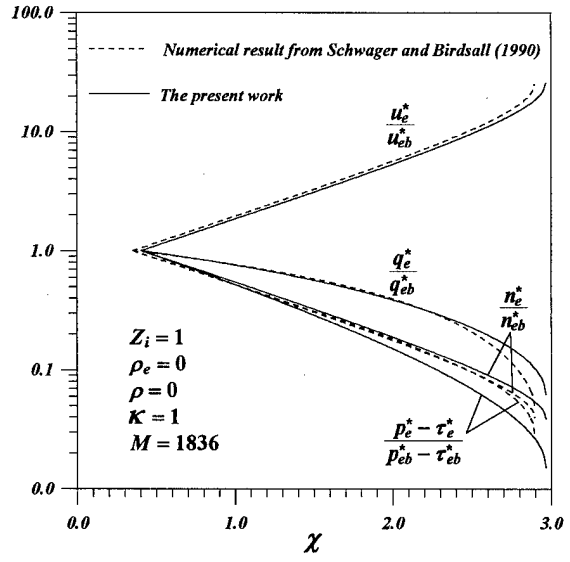


Fig. 14. Comparisons of ratios of electron densities (n_e^*/n_{eb}^*), fluid velocities (u_e^*/u_{eb}^*), fluid-like conduction (q_e^*/q_{eb}^*), and differences between mean pressure and fluid-like viscous stress $((p_e^* - \tau_e^*)/(p_{eb}^* - \tau_{eb}^*))$ at locations in sheath and sheath edge versus potential obtained from numerical result [9] and this work.

transport variables of the ions and electrons from the presheath edge, across the presheath and sheath, and to the wall.

IV. Conclusion

In this work, accurate prediction of transport processes in the plasma comprising the presheath and sheath near a wall can be revealed from the successful model of Emmert *et al.* [10], experimental verifications for the ion distribution functions from Bachet *et al.* [22], and computed results from Schwager and Birdsall [9], respectively. The conclusions drawn are as follows.

1) Independent dimensionless parameters controlling transport processes in the plasma near a wall partially reflecting ions and electrons are reflectivities of ions (ρ) and electrons (ρ_e), ion-to-electron mass ratio (M), charge number (Z_i), and electron-to-ion temperature ratio at the presheath edge (κ).
2) Understanding the moments of a highly non-Maxwell–Boltzmann distribution is necessary to interpret transport processes near the wall. All transport variables near a wall partially reflecting ions and electrons are independent of spatial variations in ion source and temperature, etc., by choosing potential as an independent variable. Dimensionless sheath edge potential, which is independent of ion and electron reflectivities and ion-to-electron mass ratio, only increases with the product of charge number and electron-to-ion temperature ratio at the presheath edge. Dimensionless wall potential increases with decreasing charge number and electron reflectivity and increasing ion reflectivity, electron-to-ion temperature ratio at the presheath edge, and ion-to-electron mass ratio.
3) Ion density as a function of potential is independent of ion reflectivity. Irrespective of ion reflectivity, ion density decreases and fluid velocity increases in the direction toward the wall. Mean pressure decreases in the forward direction, except for a slight increase in the sheath near the wall with an ion reflectivity of 0.5. An increase in ion reflectivity reduces fluid velocity and increases fluid-like mean pressure. Fluid-like viscous stresses are, respectively, driving and retarding forces for ion reflectivities of 0 and 0.5. Regardless of ion reflectivity, fluid-like conduction of the ions near the presheath edge is toward bulk plasma. Fluid-like conduction at the sheath edge directs toward the wall and bulk plasma for ion reflectivities of 0 and 0.5, respectively. Fluid-like conduction to the completely absorbing wall is small.
4) The wall conditions of the ions affected by dimensionless parameters are summarized as follows.

   a) An increase in charge number reduces ion density. Increases of ion reflectivity, ion-to-electron mass ratio, and electron-to-ion temperature ratio at the presheath edge slightly decrease ion density.

   b) Fluid speed is increased by decreasing ion reflectivity and electron-to-ion temperature ratio at the presheath edge, and increasing charge number and ion-to-electron mass ratio.

   c) Mean pressure decreases with increasing charge number and electron-to-ion temperature ratio at the presheath edge and with reducing ion reflectivity. An increase in ion-to-electron mass ratio increases and decreases mean pressure for ion reflectivity of 0.5 and 0, respectively.

   d) Fluid-like viscous stress for a wall having small ion reflectivity acts as a driving force with magnitude increasing with decreasing charge number, ion reflectivity,

ion-to-electron mass ratio, and electron-to-ion temperature ratio at the presheath edge. Otherwise, viscous stress is a retarding force with magnitude increasing with reducing charge number and electron-to-ion temperature ratio at the presheath edge and with increasing ion reflectivity and ion-to-electron mass ratio.

(e) Fluid-like conduction is in forward direction for ion reflectivities near zero. The effects of other dimensionless parameters on fluid-like conduction are insignificant. Conduction toward the plasma increases and then decreases in magnitude with increasing ion reflectivity. The maximum value occurs at ion reflectivity around 0.3. An increase in ion-to-electron mass ratio and a decrease in electron-to-ion temperature ratio at the presheath edge increases the magnitude of conduction toward the plasma. The effect of charge number on conduction is slight.

5) Electron density, mean pressure, and fluid-like viscous stress decrease, whereas fluid speed increases in the direction toward the wall. The fluid-like viscous stress becomes a driving force. The wall conditions of the electrons affected by dimensionless parameters are summarized as follows.

a) Electron density and mean pressure increase with decreasing ion-to-electron mass ratio and electron-to-ion temperature ratio at the presheath edge and with increasing electron reflectivity and charge number.

b) Fluid speed decreases with increasing electron reflectivity and with decreasing ion-to-electron mass ratio. Fluid speed is independent of the variation in electron-to-ion temperature ratio at the presheath edge.

c) Fluid-like viscous stress decreases with increasing ion-to-electron mass ratio, electron reflectivity, and electron-to-ion temperature ratio at the presheath edge and with decreasing charge number.

d) Fluid-like conduction is negligibly small. Except for small electron reflectivities, fluid-like conduction is toward the plasma. The effects of other dimensionless parameters on fluid-like conduction are insignificant.

APPENDIX

The following integrals are used for integration:

$$\int_0^a e^{b\xi}\,\mathrm{erf}\left(\sqrt{b\xi}\right)\frac{d\xi}{\sqrt{c-\xi}} = \frac{4}{\sqrt{\pi b}}\,e^{bc}\left[-\frac{\pi}{4}\,\mathrm{erf}\left(\sqrt{ab}\right)\mathrm{erf}\left(\sqrt{bc-ab}\right) - \frac{1}{2}\,e^{-bc}\sin^{-1}\sqrt{\frac{a}{c}} + \frac{\pi}{4} - \frac{1}{2}\,N_1\left(ab, \sin^{-1}\sqrt{\frac{a}{c}}\right)\right] \tag{A1}$$

$$\int_0^a D\left(\sqrt{\xi}\right)\frac{d\xi}{\sqrt{b-\xi}} = 2e^{-b}\left[\frac{1}{2}\,e^{b}\sin^{-1}\sqrt{\frac{a}{b}} - \frac{\pi}{4} + \frac{1}{2}\,N_2\left(a, \sin^{-1}\sqrt{\frac{a}{b}}\right) - e^{b}D\left(\sqrt{b-a}\right)D\left(\sqrt{a}\right)\right] \tag{A2}$$

$$\int_{a-b}^a \mathrm{erf}\left[\sqrt{c(a-\xi)}\right]e^{c(a-\xi)}\sqrt{\xi}\,d\xi = -c^{-(3/2)}\left[\frac{1}{\sqrt{\pi}}\left(\sqrt{cb}\sqrt{ca-cb} + ca\sin^{-1}\sqrt{\frac{b}{a}}\right) - e^{ca}\left(\frac{\sqrt{\pi}}{2} - \frac{1}{\sqrt{\pi}}\sin^{-1}\sqrt{\frac{b}{a}}\,e^{-ca} - \frac{N_1}{\sqrt{\pi}}\right) + \gamma\left(\frac{3}{2}, ca-cb\right)\mathrm{erf}\left(\sqrt{cb}\right)e^{ca}\right] \tag{A3}$$

$$\int_{a-b}^a D\left(\sqrt{a-\xi}\right)\sqrt{\xi}\,d\xi = \frac{\sqrt{b}\sqrt{a-b}}{2} + \frac{a}{2}\sin^{-1}\sqrt{\frac{b}{a}} - \sqrt{a-b}\,bD\left(\sqrt{b}\right) - e^{-a}\left(\frac{1}{2}\sin^{-1}\sqrt{\frac{b}{a}}\,e^{a} - \frac{\pi}{4} + \frac{N_2}{2}\right) + D\left(\sqrt{a-b}\right)D\left(\sqrt{b}\right) \tag{A4}$$

$$\int_0^a D\left(\sqrt{\xi}\right)(b-c\xi)\,d\xi = \left(b - c - \frac{ac}{3}\right)\sqrt{a} + (ac - b + c)D\left(\sqrt{a}\right) \tag{A5}$$

$$\int_0^a e^{b\xi}\,\mathrm{erf}\left(\sqrt{b\xi}\right)(c-s\xi)\,d\xi = \left(\frac{s}{b} + c - sa\right)\frac{1}{b}\,e^{ab}\,\mathrm{erf}\left(\sqrt{ab}\right) + 2\left(\frac{sa}{3} - c - \frac{s}{b}\right)\sqrt{\frac{a}{\pi b}} \tag{A6}$$

$$\int_0^1 e^{-s\omega}\gamma(b, s-s\omega)\omega^{a-b-1}\,d\omega = s^{b-a}\frac{\Gamma(b)\Gamma(a-b)}{\Gamma(a)}\,\gamma(a,s) \tag{A7}$$

$$\int_a^c N_1\left(ab, \sin^{-1}\sqrt{\frac{a}{\xi}}\right)e^{b\xi}\,d\xi = \frac{1}{b}\left[e^{bc}N_1\left(ab, \sin^{-1}\sqrt{\frac{a}{c}}\right) - \frac{\pi}{2} + \sin^{-1}\sqrt{\frac{a}{c}}\right] \tag{A8}$$

$$\int_a^b N_2\left(a, \sin^{-1}\sqrt{\frac{a}{\xi}}\right)e^{-\xi}\,d\xi = -e^{-b}N_2\left(a, \sin^{-1}\sqrt{\frac{a}{b}}\right) + \frac{\pi}{2} - \sin^{-1}\sqrt{\frac{a}{b}}. \tag{A9}$$

REFERENCES

[1] F. F. Chen. *Introduction to Plasma Physics*. New York: Plenum Press, 1974.

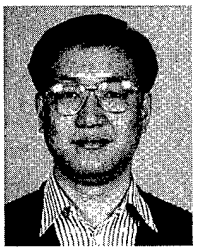
[2] D. Bohm, "Minimum ionic kinetic energy for a stable sheath," in *The Characteristics of Electrical Discharges in Magnetic Fields*, A. Guthrie and R. Wakerling, Eds. New York: McGraw-Hill, 1949, pp. 77–86.

[3] S. Chapman and T. G. Cowling, *The Mathematical Theory of Non-Uniform Gases*. Cambridge: Cambridge Univ. Press, 1952.

[4] S. I. Braginskii, "Transport processes in a plasma," in *Reviews of Plasma Physics*, M. A. Leontovich, Ed. New York: Consultants Bureau, 1965, vol. 1, pp. 205–311.

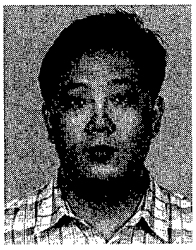
[5] E. Zawaideh, F. Najmabadi, and R. W. Conn, "Generalized fluid equations for parallel transport in collisional to weakly collisional plasmas," *Phys. Fluids*, vol. 29, pp. 463–474, 1986.

[6] R. C. Bissell, P. C. Johnson, and P. C. Stangeby, "A review of models for collisionless one-dimensional plasma flow to a boundary," *Phys. Fluids B*, vol. 1B, pp. 1133–1140, 1989.
[7] J. T. Scheuer and G. A. Emmert, "A fluid treatment of the plasma presheath for collisionless and collisional plasmas," *Phys. Fluids B*, vol. 2B, pp. 445–451, 1990.
[8] R. Chodura, "Plasma flow in the sheath and the presheath of a scrape-off layer," in *Physics of Plasma Wall Interactions in Controlled Fusion*. New York: Plenum, 1986, pp. 99–134. Proc. NATO Adv. Study Inst., July 30–Aug. 10, 1984, Val-Morin, QC, Canada.
[9] L. A. Schwager and C. K. Birdsall, "Collector and source sheaths of a finite ion temperature plasma," *Phys. Fluids B*, vol. 2B, pp. 1057–1068, 1990.
[10] G. A. Emmert, R. M. Wieland, A. T. Mense, and J. N. Davidson, "Electric sheath and presheath in a collisionless, finite ion temperature plasma," *Phys. Fluids*, vol. 23, pp. 803–812, 1980.
[11] E. R. Harrison and W. B. Thompson, "The low pressure plane symmetric discharge," *Proc. Phys. Soc. Lond.*, vol. 74, pp. 145–152, 1959.
[12] C. A. Ordonez, "Fully kinetic plasma-sheath theory for a cold-electron emitting surface," *Phys. Fluids B*, vol. 4B, pp. 778–783, 1992.
[13] P. S. Wei, F. B. Yeh, and C. Y. Ho, "Distribution functions of positive ions and electrons in a plasma near a surface," *IEEE Trans. Plasma Sci.*, vol. 28, pp. 1244–1253, Aug. 2000.
[14] B. Chapman, *Glow Discharge Processes, Sputtering and Plasma Etching*. New York: Wiley, 1980.
[15] B. J. Lee and J. D. Callen, "Fluidlike modeling of the plasma-material interaction," *Phys. Fluids B*, vol. 5, pp. 1647–1655, 1993.
[16] M. Abramowitz and I. A. Stegun, Eds., *Handbook of Mathematical Functions with Formulas, Graphs, and Mathematical Tables*. Washington, D.C.: National Bureau of Standards, 1970.
[17] A. Erde'lyi, Ed., *Higher Transcendental Functions*. New York: McGraw-Hill, 1953, vol. 2.
[18] I. S. Gradshteyn and I. M. Ryzhik, *Table of Integrals, Series, and Products*, A. Jeffrey, Ed. U.K.: Scripta Technica, 1980.
[19] W. G. Vincenti and C. H. Kruger, Jr., *Introduction to Physical Gas Dynamics*. New York: Wiley, 1970.
[20] R. J. Procassini, C. K. Birdsall, and E. C. Morse, "A fully kinetic, self-consistent particle simulation model of the collisionless plasma-sheath region," *Phys. Fluids B*, vol. 2, pp. 3191–3205, 1990.
[21] J. T. Scheuer and G. A. Emmert, "A collisional model of the plasma presheath," *Phys. of Fluids*, vol. 31, pp. 1748–1756, 1988.
[22] G. Bachet, L. Cherigier, and F. Doveil, "Ion velocity distribution function observations in a multipolar argon discharge," *Phys. Plasmas*, vol. 2, pp. 1782–1788, 1995.



Peng-Sheng Wei (M'00) received the M.S. degree in power mechanical engineering department from National Tsing Hua University, Hsinchu, Taiwan, R.O.C., in 1978, and the Ph.D. in mechanical engineering department from University of California at Davis in 1984.

He has been a Professor of mechanical engineering department in National Sun Yat-Sen University, Kaohsiung, Taiwan, R.O.C., since 1989. His research interests are heat transfer, fluid mechanics, phase change, and metals processing including processes and defects of welding, casting and surface heat treatment.



Feng-Bin Yeh received the B.S. degree in aerospace engineering department from Tamkang Univeristy, Taipei, Taiwan, R.O.C., in 1988, and the M.S. degree in mechanical engineering from NSYSU in 1990.

He is currently a Ph.D. student in mechanical engineering, NSYSU, and is also an engineer in the quality control division of Tang Eng Stainless Steel Plant, Kaohsiung. His research interests are heat transfer, fluid mechanics, and rapid solidification in metals processing.

Distribution Functions of Positive Ions and Electrons in a Plasma Near a Surface

Peng-Sheng Wei, *Member, IEEE*, Feng-Bin Yeh, and Ching-Yen Ho

***Abstract*—In this study, the velocity distribution functions of the ions and electrons in a collisional presheath and collisionless sheath of a plasma near a wall emitting and reflecting ions and electrons are systematically determined. The collisions in the presheath are modeled by a relaxation time approximation (namely, Bhatnagar–Gross–Krook model, or simply BGK model). To find the variation in electrostatic potential with position, the model and analysis from Emmert *et al.* are used. Distribution functions of the ions and electrons in a collisionless presheath and sheath on a wall partially reflecting ions and electrons, therefore, can be exactly obtained. The reflections of the ions and electrons by a wall play important roles in studying heat transfer from a plasma sheath to a workpiece surface, and sputter etching and deposition, ion implantation, and ion scattering spectroscopy. Irrespective of ion and electron reflectivities, velocities of the ions in the presheath and sheath are of highly non-Maxwell–Boltzmann distributions. The electrons in the presheath are close to Maxwell–Boltzmann distributions, whereas those in the sheath are non-Maxwell–Boltzmann distributions. Even though the wall partially reflects ions and electrons, the Bohm's criterion is marginally satisfied at the sheath edge. The computed distribution functions for a completely absorbing surface agree with theoretical results provided in the literature. Good comparison of the resulted transport variables with available analytical work is presented in the companion paper.**

***Index Terms*—Kinetic analysis of plasma, plasma materials processing, plasma-wall interactions, space charge.**

NOMENCLATURE

c	Particle thermal speed, $c^* = c/(k_B T_{e0}/m_i)^{1/2}$.
c_0	$(-2Z_i e\phi/m_i)^{1/2}$.
c_0'	$[2Z_i e(\phi_b - \phi)/m_i]^{1/2}$.
D	Dawson function, as defined in (40).
e	Electron charge.
f, F, g	Ion distribution function, $F^* = F(k_B T_{e0}/m_i)^{1/2}/n_{e0}$.
H	Heaviside function, $H(x) = 1$ for $x > 0$; $H(x) = 0$ for $x < 0$.
I, K	Function defined in (37) and (32).
k_B	Boltzmann constant.
m	Particle mass.
n	Particle density, $n^* = n/n_{e0}$.
S	Ion source, defined in (30).
T	Temperature.
x, y, z	Cartesian coordinate.
Z	Charge number.

Greek Letters

β	Collision parameter.
ε	Total energy.
κ	T_{e0}/T_{i0}.
ρ	Reflectivity.
σ	$c_x/\lvert c_x\rvert$.
ϕ, χ	Dimensional and dimensionless potential, $\chi = -e\phi/k_B T_{e0}$.
χ_t	$-\varepsilon/(Z_i k_B T_{e0}) = -m_i c_x^2/(2Z_i k_B T_{e0}) + \chi$.
ε_t	$Z_i e\phi$.
λ	Mean free path.

Superscript

$*$	Dimensionless quantity.

Subscript

b	Boundary between sheath and presheath.
e, i	Electron and ion.
t	Turning point.
w	Wall.
0, 1	Coordinate origin at $\phi = 0$ and sheath edge, as illustrated in Fig. 1.

Manuscript received April 16, 1999; revised March 14, 2000. This work was supported by the National Science Council, R.O.C., under Grant NSC 87-2212-E-110-029.

P.-S. Wei and F.-B. Yeh are with the Department of Mechanical Engineering, National Sun Yat-Sen University, Kaohsiung, Taiwan 80424, R.O.C. (e-mail: pswei@mail.nsysu.edu.tw).

C.-Y. Ho is with the Hwa Hsia College of Technology and Commerce, Taipei, Taiwan, R.O.C.

Publisher Item Identifier S 0093-3813(00)07248-9.

I. INTRODUCTION

THE plasma induced in metals processing is usually accompanied by strong momentum and energy transport near the workpiece surface. Owing to different thermal speeds of the ions and electrons, a sheath or space-charge region in a thin layer exists on the surface [1]. The function of the sheath is to form a potential barrier so that the flux of electrons that have enough energy to go over the barrier to the wall is just equal to the flux of ions reaching the wall. Regardless of the Debye shielding, small electrostatic potential in the presheath between the sheath and bulk plasma still accelerates the ions up to and beyond sonic speed before entering the sheath, as first explicitly pointed out by Bohm [2].

An accurate study of transport processes for a plasma near a wall requires a kinetic analysis, that is, to solve velocity distribution functions of the ions and electrons from Boltzmann's equations coupled with Poisson's equation. One of the earliest kinetic analyzes of a bounded, quasineutral, collisionless plasma for a gaseous discharge was performed by Tonks and Langmuir [3]. An integrodifferential plasma equation for a planar, cylindrical, and spherical plasma consisting of warm electrons

0093–3813/00$10.00 © 2000 IEEE

($T_e \neq 0$) and cool and cold ions ($T_i/T_e \ll 1$ and $T_i = 0$) by choosing different ion source functions was derived. The solutions were found in series of infinitesimal Debye length for various ratios of ion mean-free path to characteristic length of the plasma [4]. The collision-free low-pressure column was experimentally confirmed by the free fall of the ions originating from ionization of the cold neutrals.

Harrison and Thompson [5] solved exactly the plasma equation obtained from Tonks and Langmuir [3] by introducing an ion source function indicating that all ions were generated with zero speed. Interestingly, the resulted potential and current density at the sheath edge were found to be independent of spatial variations in ion sources. Rather than the monoenergetic distribution at ion temperature $T_i = 0$ as used by Bohm [2], they found a generalized Bohm's criterion, which was valid for any velocity distribution of ions at the sheath edge.

The first model to study warm ions in a presheath was proposed by Hu and Ziering [6], who assumed that velocities of the ions at the plasma–sheath interface were of accelerated, cutoff, and drifted Maxwell–Boltzmann distributions. The results lead to another generalized Bohm sheath criterion, which reduced to the Bohm's original inequality in the limit $T_{i0}/T_{e0} \rightarrow 0$. Emmert *et al.* [7] extended the analysis of Hu and Ziering [6] to obtain a more realistic noncutoff ion distribution function in a collisionless presheath near a completely absorbing and floating wall. The ion source function was chosen such that the ions would be of a Maxwell–Boltzmann distribution in the absence of electrostatic field. Because no ions were produced with zero speed in this model, this study first successfully confirmed that the ions were satisfied by a finite electrostatic field and generalized Bohm criterion at the sheath edge [8], [9]. Physically speaking, the ions must be accelerated from their initial speeds by the electric field. Provided that the ions were generated with zero speed under charge neutrality, the electric field at the sheath edge would become infinitely large to force the ions to reach a sonic speed [8]. Surprisingly, in the limit of infinitesimal ratio of the Debye length to macroscopic length of the system, the resulting "warm" plasma equation by a transformation became the "cold" plasma equation treated by Harrison and Thompson [5]. Potential ion and total energy fluxes at the sheath edge, therefore, were analytically and exactly found. Aside from the potential curve cutoff at a new sheath edge, the predicted mass and total energy fluxes were different from those obtained from a half-space Maxwell–Boltzmann distribution.

Bachet *et al.* [10] measured the ion distribution functions of an argon plasma at pressures of 0.08 and 0.013 Pa and densities between 10^{14} and 10^{15} particles/m^3 with a laser-induced fluorescence. The experimental findings showed good agreement with the solutions of Emmert *et al.* [7] by adjusting ion temperatures between 2000 and 43 000 K in a trend decreasing with distance from the wall. It was observed that the ion distribution function at any location in the presheath can be divided by three parts agreeing with the prediction made by Emmert *et al.* [7]. The first part was referred to the ions coming from the presheath edge and the ions created in the presheath. The middle part was for the low-energy ions generated with positive velocities in the backward region and negative velocities in the entire presheath. The left part was composed of high-energy ions originated with negative velocities in the forward region. Although the ion distribution functions were consistent, temperatures of ions should be around the ambient temperature as presented by Goeckner *et al.* [11]. One possible reason for this discrepancy is a neglect of ion-neutral collisions.

In this study, general velocity distribution functions of the ions and electrons in a collisional presheath and collisionless sheath of a plasma near a wall emitting and reflecting ions and electrons are derived. Extending the model and analysis from Emmert *et al.* [7] to find the variation in electrostatic potential with position, distribution functions of the ions and electrons in a collisionless presheath and sheath on a wall partially reflecting ions and electrons can be obtained. The reflections of the ions and electrons play important roles in studying heat transfer from a plasma sheath to a workpiece [12] and sputter etching and deposition, ion implantation, and a technique known as ion scattering spectroscopy [13]. Transport variables of ions and electrons in the plasma near the wall can be accurately obtained from the moments of the distribution functions in the companion paper [14].

II. Kinetic Model and Analysis

The plasma comprising the bulk plasma, presheath, and sheath near walls is illustrated in Fig. 1. The origin of the coordinate is conveniently set at the edge of the presheath or bulk plasma, where electrostatic potential is zero. The quasineutral presheath is an ionization zone to supply ions lost to walls. Because electrostatic potential decreases, the ions in the positive x-direction are accelerated, whereas backward-moving ions are decelerated. The decelerated ions with total energy less than zero experience turning. On the other hand, the electrons in the positive direction need to overcome potential. An electron with the total energy less than wall potential turns to the presheath before hitting the wall. In this study, the major assumptions made are as follows.

1) Transport processes in the presheath and sheath can be considered in a quasisteady state [1], [7], [13]. In reality, this is only the average result of the many detailed interactions among particle–particle, wave–particle, and wave–wave, such as plasma oscillations, oscillations of kinetic, two-stream and parametric decay instabilities, and the effects of Landau damping, and so on [1]. The electrostatic potential can also have spatial and temporary oscillations and trap particles. In practice, dissipative processes tend to destroy oscillations.
2) The ion collisions are simulated a relaxation time approximation as first proposed by the Bhatnagar–Gross–Krook (BGK) model [15] to replace the complicated collision integral. The BGK model treating a binary collision simplifies the mathematical manipulation but retains many of the features of the true collision integral. The collision model needs to satisfy conservation of particle, momentum, and energy. When a charged particle undergoes a large number of small deflections in the force field of many charged particles, a more realistic and complicated Fokker–Planck collision term can be used.

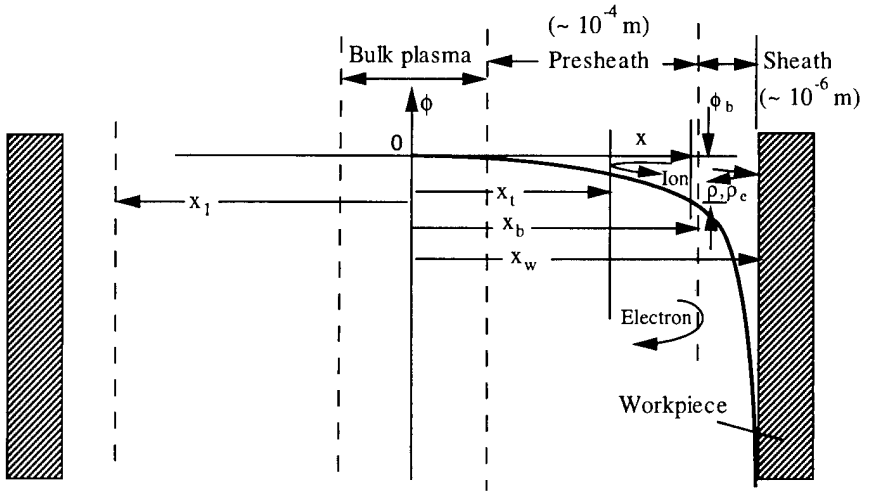


Fig. 1. System model and coordinates.

3) Electromagnetic force (namely, Lorentz force) is ignored. This is valid for the cases in which magnetic field is negligible or the direction of magnetic lines is parallel to the ion flow. Neglect of the magnetic field is due to a greater Larmor radius than the thickness of the presheath. Larmor radius is a measure of the radius of the helical path of a charged particle. For a typical magnetic flux density less than 0.1 tesla [16], Larmor radius is greater than 5×10^{-3} m.
4) Reflectivities of electrons and ions are constant and independent of energy.

A. Ion Distribution Functions

With the above assumptions, the Boltzmann equation integrated over velocity component c_y and c_z yields

$$c_x \frac{\partial F_i}{\partial x} - \frac{Z_i e}{m_i} \frac{d\phi}{dx} \frac{\partial F_i}{\partial c_x} = S_i(x, c_x) + \nu(F_{i0} - F_i) \quad (1)$$

where the ion distribution function and source terms are

$$F_i(x, c_x) = \int_{-\infty}^{\infty} f_i \, dc_y \, dc_z$$
$$S_i(x, c_x) = \int_{-\infty}^{\infty} S_i \, dc_y \, dc_z. \quad (2)$$

The last term on the right-hand side of (1) represents collisions simulated by the BGK model [15], [17], where ν is collision frequency, and distribution function F_{i0} is the Maxwell-Boltzmann distribution function. Equation (1) can be conveniently expressed by independent variables of position x and total energy ε

$$\frac{\partial}{\partial x} [\sigma |c_x| g(x, \varepsilon, \sigma)] = S_i(x, \varepsilon, \sigma) + \frac{\nu}{\sigma m_i c_x} (F_{i0} - F_i) \quad (3)$$

where the total energy is

$$\varepsilon = \tfrac{1}{2} m_i c_x^2 + Z_i e \phi(x) \quad (4)$$

Because energy is a scalar, the quantity $\sigma \equiv c_x/|c_x|$ is introduced to account for the direction of velocity. The velocity distribution function and source function of ions in (3) are, respectively, defined as

$$g(x, \varepsilon, \sigma) \equiv \frac{\sigma F_i(x, c_x)}{m_i c_x}$$
$$S_i(x, \varepsilon, \sigma) = S_i(x, c_x) \frac{dc_x}{d\varepsilon} = \frac{S_i(x, c_x)}{\sigma m_i c_x}. \quad (5)$$

B. Presheath

To determine ion distribution functions in the presheath, (3) can be written as

$$\frac{\partial}{\partial x} [\sigma |c_x| g(x, \varepsilon, \sigma)] = A(x, \varepsilon, \sigma) - \nu g(x, \varepsilon, \sigma) \quad (6)$$

where the ion source function $A \equiv S_i + \nu F_{i0}/(m_i|c_x|)$ is symmetric with respect to zero velocity, namely, $A(x, \varepsilon, +1) = A(x, \varepsilon, -1)$ [17]. Boundary conditions of (6) are $g(x_1, \varepsilon, +1) = g_1(\varepsilon, +1)$, and $g(x_b, \varepsilon, -1) = g_b(\varepsilon, -1)$. Equation (6) can be readily integrated to obtain the ion distribution function. Because the ion distribution function also depends on if positive ions moving in the negative direction experience turning, two different cases are considered as follows.

1) Ion distribution functions for total energy $\varepsilon > 0$. The distribution function of the ions moving in the forward direction yields

$$|c_x| g(x, \varepsilon, +1) = g_1(\varepsilon, +1) \, |c_{x_1}| \, e^{-(\beta x - \beta_1 x_1)} + \int_{x_1}^{x} A(x', \varepsilon, +1) e^{-(\beta x - \beta' x')} \, dx' \quad (7)$$

where variable β represents the mean value of collisions or the reciprocal of ion mean-free path within a distance x. Equation (7) indicates that the ion distribution at location x is determined by the ions of a distribution function g_1 at the boundary x_1 and the ions generated between x_1 and x. The distribution function for negative velocities is

$$|c_x| g(x, \varepsilon, -1) = g_b(\varepsilon, -1) \, |c_{x_b}| \, e^{-(\beta_b x_b - \beta x)} + \int_{x}^{x_b} A(x', \varepsilon, -1) e^{-(\beta' x' - \beta x)} \, dx' \quad (8)$$

which is determined by the ions of a distribution function $g_b(\varepsilon,-1)$ at the sheath edge and the ion generated between x and x_b, respectively.

2) Ion distributions functions for total energy $\varepsilon < 0$. The positive ions moving in the negative direction experiences turning. Ion distribution function for negative velocities is the same as (8), wheras that in the forward direction is

$$|c_x|g(x,\varepsilon,+1) = g[x_t(\varepsilon),\varepsilon,+1]\,|c_{x_t}|\,e^{-(\beta x-\beta_t x_t)} + \int_{x_t(\varepsilon)}^{x} A(x',\varepsilon,+1)e^{-(\beta x-\beta' x')}\,dx'. \tag{9}$$

Conservation of the positive ion at the turning point is

$$|c_{x_t}|\,g[x_t(\varepsilon),\varepsilon,-1] = |c_{x_t}|\,g[x_t(\varepsilon),\varepsilon,+1]. \tag{10}$$

Equation (9), by introducing (10) and (8) evaluated at the turning point, leads to

$$\begin{aligned}|c_x|g(x,\varepsilon,+1) &= g_b(\varepsilon,-1)\,|c_{x_b}|\,e^{-(\beta_b x_b+\beta x-2\beta_t x_t)} \\ &\quad + \int_{x_t(\varepsilon)}^{x_b} A(x',\varepsilon,-1)e^{-(\beta' x'+\beta x-2\beta_t x_t)}\,dx' \\ &\quad + \int_{x_t(\varepsilon)}^{x} A(x',\varepsilon,+1)e^{-(\beta x-\beta' x')}\,dx'\end{aligned} \tag{11}$$

where the first two terms on the right-hand side refer to the ions moving in the negative direction and experiencing a turn at x_t. This can be clearly seen from the first term, in which dimensionless distance for collisions between x_b and x is $\beta_b x_b+\beta x-2\beta_t x_t = (\beta_b x_b-\beta_t x_t)+(\beta x-\beta_t x_t)$. The last term on the right-hand side of (11) is for the ions created in the upstream locations and directed in the positive direction. Regardless of total energy, distribution functions of the ions moving in the forward direction governed by (7) and (11) can be combined into one equation

$$\begin{aligned}|c_x|g(x,\varepsilon,+1) &= H(\varepsilon)\left[g_1(\varepsilon,+1)\,|c_{x_1}|\,e^{-(\beta x-\beta_1 x_1)} + \int_{x_1}^{x} A(x',\varepsilon,+1)e^{-(\beta x-\beta' x')}\,dx'\right] \\ &\quad + H(-\varepsilon)\left[g_b(\varepsilon,-1)\,|c_{x_b}|\,e^{-(\beta_b x_b+\beta x-2\beta_t x_t)} + \int_{x_t(\varepsilon)}^{x_b} A(x',\varepsilon,-1)e^{-(\beta' x'+\beta x-2\beta_t x_t)}\,dx' + \int_{x_t(\varepsilon)}^{x} A(x',\varepsilon,+1)e^{-(\beta x-\beta' x')}\,dx'\right].\end{aligned} \tag{12}$$

The distribution function of the ions moving in the negative direction is (8). Combining ion distribution functions in both directions yields

$$\begin{aligned}\frac{F_i(x,c_x)}{m_i} &= H(c_x-c_0)\left[g_1(\varepsilon,+1)\,|c_{x_1}|\,e^{-(\beta x-\beta_1 x_1)} + \int_{x_1}^{x} A(x',\varepsilon,+1)e^{-(\beta x-\beta' x')}\,dx'\right] \\ &\quad + H(c_x)H(c_0-c_x) \times \left[g_b(\varepsilon,-1)\,|c_{x_b}|\,e^{-(\beta_b x_b+\beta x-2\beta_t x_t)} + \int_{x_t(\varepsilon)}^{x_b} A(x',\varepsilon,-1)e^{-(\beta' x'+\beta x-2\beta_t x_t)}\,dx' + \int_{x_t(\varepsilon)}^{x} A(x',\varepsilon,+1)e^{-(\beta x-\beta' x')}\,dx'\right] \\ &\quad + H(-c_x)\left[g_b(\varepsilon,-1)\,|c_{x_b}|\,e^{-(\beta_b x_b-\beta x)} + \int_{x}^{x_b} A(x',\varepsilon,-1)e^{-(\beta' x'-\beta x)}\,dx'\right]\end{aligned} \tag{13}$$

where the relations $H(\sigma)H(\varepsilon) = 1$ for $c_x > c_0$ and $H(\sigma)H(-\varepsilon) = 1$ for $0 < c_x < c_0$ are substituted.

C. Sheath

The solution of (6) without source terms in the sheath yields $|c_x|g(x,\varepsilon,\sigma) = b(\varepsilon,\sigma)$. Hence, for a given total energy ε and direction, the ion distribution function is conserved. The boundary condition at the wall is

$$g(x_w,\varepsilon,-1) = g_w(\varepsilon,-1) + \rho g(x_w,\varepsilon,+1) \tag{14}$$

where ρ is the ion reflectivity. The other condition is the distribution function at the sheath edge g_b, which is obtained from the solution in the presheath. Because the ions experience turning in the sheath for total energy less than sheath edge potential, different ion distribution functions are presented as follows.

1) Total energy $\varepsilon \geq Z_i e\phi_b$. Owing to conservation of distribution functions, the ion distribution function in the forward direction is

$$\begin{aligned}|c_x|g(x,\varepsilon,+1) &= |c_{xw}|\,g(x_w,\varepsilon,+1) \\ &= |c_{xb}|\,g_b(\varepsilon,+1).\end{aligned} \tag{15}$$

The ion distribution function for the negative velocities by substituting (14) yields

$$\begin{aligned}|c_x|g(x,\varepsilon,-1) &= |c_{xw}|\,[g_w(\varepsilon,-1)+\rho g(x_w,\varepsilon,+1)] \\ &= |c_{xb}|\,g(x_b,\varepsilon,-1).\end{aligned} \tag{16}$$

2) Total energy $\varepsilon < Z_i e\phi_b$. Conservation of the ion distribution function in a given direction and at the turning point leads to

$$|c_x|g(x,\varepsilon,+1) = |c_x|g(x,\varepsilon,-1) = |c_x|g(\varepsilon), \qquad \varepsilon < Z_i e\phi_b. \tag{17}$$

Irrespective of directions and locations, ion distribution functions in the sheath, therefore, are the same for a given total energy. Introducing (14) into (17) gives

$$|c_x|g(x,\varepsilon,+1) = |c_{xw}|\,[g_w(\varepsilon,-1) + \rho g(x_w,\varepsilon,+1)]. \tag{18}$$

Evaluating at the wall, (18) becomes

$$g(x_w,\varepsilon,+1) = \frac{1}{1-\rho}\, g_w(\varepsilon,-1). \tag{19}$$

Combining (15), (16), (17), and (19), ion distribution functions in the forward and backward directions in the sheath are, respectively,

$$\begin{aligned}|c_x|g(x,\varepsilon,+1) &= H(\varepsilon - Z_i e\phi_b)\,|c_{xb}|\,g_b(\varepsilon,+1) \\ &\quad + H(Z_i e\phi_b - \varepsilon)\,\frac{1}{1-\rho}\,|c_{xw}|\,g_w(\varepsilon,-1) \qquad (20)\\ |c_x|g(x,\varepsilon,-1) &= H(\varepsilon - Z_i e\phi_b)\,[|c_{xw}|\,g_w(\varepsilon,-1) \\ &\quad + \rho\,|c_{xb}|\,g_b(\varepsilon,+1)] + H(Z_i e\phi_b - \varepsilon) \\ &\quad \times \frac{1}{1-\rho}\,|c_{xw}|\,g_w(\varepsilon,-1). \qquad (21)\end{aligned}$$

Ion distribution function $F_i = H(\sigma)m_i|c_x|g(\varepsilon,+1) + H(-\sigma)m_i|c_x|g(\varepsilon,-1)$ by substituting (20) and (21) leads to

$$\begin{aligned}\frac{F_i(x,c_x)}{m_i} &= H(c_x - c_0')\,|c_{xb}|\,g_b(\varepsilon,+1) + H(c_x)H(c_0' - c_x) \\ &\quad \times \frac{1}{1-\rho}\,|c_{xw}|\,g_w(\varepsilon,-1) + H(-c_x)H(c_0' + c_x) \\ &\quad \times \frac{1}{1-\rho}\,|c_{xw}|\,g_w(\varepsilon,-1) + H(-c_0' - c_x) \\ &\quad \times [|c_{xw}|\,g_w(\varepsilon,-1) + \rho\,|c_{xb}|\,g_b(\varepsilon,+1)], \qquad (22)\end{aligned}$$

where the relations $H(\sigma)H(\varepsilon - Z_i e\phi_b) = 1$ for $c_x > c_0'$, $H(\sigma)H(Z_i e\phi_b - \varepsilon) = 1$ for $0 < c_x < c_0'$, $H(-\sigma)H(\varepsilon - Z_i e\phi_b) = 1$ for $c_x < -c_0'$, and $H(-\sigma)H(Z_i e\phi_b - \varepsilon) = 1$ for $-c_0' < c_x < 0$ are introduced.

D. Coupling Between Presheath and Sheath

Evaluating (21) at the sheath edge gives

$$\begin{aligned}&|c_{xb}|\,g_b(\varepsilon,-1) \\ &\quad = H(\varepsilon - Z_i e\phi_b)\,[\rho\,|c_{xb}|\,g_b(\varepsilon,+1) + |c_{xw}|\,g_w(\varepsilon,-1)]\end{aligned} \tag{23}$$

where the first term on the right-hand side is determined by evaluating (12) at the sheath edge. Equation (23), therefore, yields

$$\begin{aligned}&|c_{xb}|\,g_b(\varepsilon,-1) \\ &\quad = \frac{1}{1 - H(-c_{xb})\,H(c_{0b} + c_{xb})\,\rho e^{-(2\beta_b x_b - 2\beta_t x_t)}} \\ &\qquad \times \Bigg\{ H(-c_{xb} - c_{0b})\,\rho \Bigg[g_1(\varepsilon,+1)\,|c_{x_1}|\,e^{-(\beta_b x_b - \beta_1 x_1)} \\ &\qquad\quad + \int_{x_1}^{x_b} A(x',\varepsilon,+1) e^{-(\beta_b x_b - \beta' x')}\,dx' \Bigg] \\ &\qquad + H(-c_{xb})\,H(c_{0b} + c_{xb})\,\rho \\ &\qquad \times \Bigg[\int_{x_t(\varepsilon)}^{x_b} A(x',\varepsilon,-1) e^{-(\beta' x' + \beta_b x_b - 2\beta_t x_t)}\,dx' \\ &\qquad\quad + \int_{x_t(\varepsilon)}^{x_b} A(x',\varepsilon,+1) e^{-(\beta_b x_b - \beta' x')}\,dx' \Bigg] \\ &\qquad + H(-c_{xb})\,|c_{xw}|\,g_w(\varepsilon,-1) \Bigg\}\end{aligned} \tag{24}$$

where the relations $H(-\sigma)H(\varepsilon - Z_i e\phi_b)H(\varepsilon) = 1$ for $c_{xb} < -c_{0b}$, $H(-\sigma)H(\varepsilon - Z_i e\phi_b)H(-\varepsilon) = 1$ for $-c_{0b} < c_{xb} < 0$, and $H(-\sigma)H(\varepsilon - Z_i e\phi_b) = 1$ for $c_{xb} < 0$ are used.

E. Ion Density in Presheath

Ion density can be determined by

$$\begin{aligned}n_i(x) &= \int_0^\infty F_i(x,-c_x)\,dc_x + \int_0^\infty F_i(x,c_x)\,dc_x \\ &= \sum_\sigma \int_{\varepsilon_t(x)}^\infty g(x,\varepsilon,\sigma)\,d\varepsilon.\end{aligned} \tag{25}$$

It is useful to reverse the order of integration $dx'\,d\varepsilon$ to $d\varepsilon\,dx'$. Because the domain should be the same, domain surrounded by $x_t(\varepsilon)H(-\varepsilon) \le x' \le x_b$ and $\varepsilon_t(x) \le \varepsilon \le \infty$ can also be represented by $\varepsilon_{\min}(x') \le \varepsilon < \infty$ and $0 \le x' \le x_b$, where $\varepsilon_{\min}(x') \equiv \text{greater}[Z_i e\phi(x), Z_i e\phi(x')]$. Substituting $A(-x',\varepsilon,-1) = A(x',\varepsilon,-1) = A(x',\varepsilon,+1)$ [17], $\beta \equiv 0$ and $\rho = 0$, $g_w \equiv 0$ in an symmetric system (25) leads to the ion density equation provided by Scheuer and Emmert [17].

F. Electron (or Negative Ion) Distribution Function in the Sheath

The electrons experience turning in the sheath for a total energy less than the potential at the wall. The electron distribution function yields

$$\begin{aligned}F_e(x,c_x) &= H(c_x)m_e|c_x|g_e(x,\varepsilon,+1) \\ &\quad + H(-c_x)m_e|c_x|g_e(x,\varepsilon,-1)\end{aligned} \tag{26}$$

where distribution functions

$$\begin{aligned}|c_x|g_e(x,\varepsilon,+1) &= H(\sigma)\,|c_{xb}|\,g_{eb}(\varepsilon,+1)\end{aligned} \tag{27}$$

$$
\begin{aligned}
&|c_x| g_e(x, \varepsilon, -1) \\
&\quad = H(-\sigma)\left\{H(\varepsilon + e\phi_w)\left[|c_{xw}|\, g_{ew}(\varepsilon, -1)\right.\right. \\
&\qquad + \rho_e\, |c_{xb}|\, g_{eb}(\varepsilon, +1)] \\
&\qquad \left.\left. + H(-e\phi_w - \varepsilon)\, |c_{xb}|\, g_{eb}(\varepsilon, +1)\right\}. \qquad (28)
\end{aligned}
$$

Substituting (27) and (28) into (26) leads to

$$
\begin{aligned}
F_e(x, c_x) &= H(c_x + c'_{e0}) m_e\, |c_{xb}|\, g_{eb}(\varepsilon, +1) \\
&\quad + H(-c_x - c'_{e0})\left[m_e\, |c_{xw}|\, g_{ew}(\varepsilon, -1)\right. \\
&\quad \left. + \rho_e m_e\, |c_{xb}|\, g_{eb}(\varepsilon, +1)\right] \qquad (29)
\end{aligned}
$$

which the relations $H(-\sigma)H(\varepsilon + e\phi_w) = 1$ for $c_x < -c'_{e0}$ and $H(-\sigma)H(-\varepsilon - e\phi_w) = 1$ for $-c'_{e0} < c_x < 0$ are used. Equation (29) indicates that the electrons with velocities greater than critical velocity c'_{e0} result from the electrons across the sheath edge, whereas those greater than c'_{e0} in the negative direction are from the wall emission and reflection after contacting the wall.

G. Electrostatic Potential Versus Position—An Extension of Emmert et al.'s Model

The variation of electrostatic potential with position can be obtained by following the model and analysis from Emmert *et al.* [7]. This work further accounts for the wall partially reflecting ions and electrons. Aside from a quasisteady state and ignorance of electromagnetic force, as mentioned previously, the assumptions made are as follows.

1) The ion source function in the presheath is chosen to be that provided by Emmert *et al.* [7]. This model is based on the fact that the ions would be a Maxwell–Boltzmann distribution in the absence of an electrostatic field at the symmetric point in a plasma or far from the wall.
2) The presheath is collisionless. The results can also apply to the ion–ion collisions [17]. Collisionality in the presheath, unfortunately, is often marginal. That is, mean-free paths between the electrons and ions can be of the same magnitude as the thickness of the presheath. Modeling different kinds of atomic or molecular collisions is complicated and inaccurate.
3) Thermal, field, and secondary emissions of electrons from the wall are ignored. For copper or tungsten having a work function of 4.5 eV, emitted electrons evaluated from a T–F equation [18] are 10^6 A/m^2 for a typical temperature of 3000 K and electric field intensity 10^7 V/m. Current density is, therefore, one-tenth to one-hundredth of the total current predicted by Hsu and Pfender [19]. The secondary electron emission can be observed for bombardment by ions, electrons, and neutrals. Provided that the incident energies of ions, electrons, and neutrals are less than 1 eV or much greater than 10^5 eV, the surface of the wall is covered by a monolayer, or the microstructure exhibits crystalline directions, the secondary electron coefficient, or yield, indicating the number of electrons ejected per incident particle can be much less than unity [13]. Ion emission can be found by a similar equation [20].
4) Electron density in the presheath is of Maxwell–Boltzmann distribution. The error induced is within 1%, as discussed by Self [21] and Emmert *et al.* [7].

The ion source function in (3) proposed by Emmert *et al.* [7] is

$$
S_i(x', \varepsilon) = \frac{S_0 h(x')}{2k_B T_{i0}} \exp\left[-\frac{\varepsilon - Z_i e\phi(x')}{k_B T_{i0}}\right] \qquad (30)
$$

where the unknown function $h(x')$ includes spatial variations of temperature (in a local equilibrium sense), potential, and concentrations of ions, electrons, or neutrals. Temperature T_{i0} is the temperature at the location where potential $\phi = 0$ and fluid velocity $u = 0$. Substituting (30) and symmetric condition $g_1 = g_b$, ion distribution function in the presheath from (13) is simplified to

$$
\begin{aligned}
F_i(x, c_x) &= \frac{n_{e0}}{(1+\rho)Z_i}\sqrt{\frac{m_i}{2\pi k_B T_{i0}}} \exp\left(-\frac{\varepsilon}{k_B T_{i0}}\right) \\
&\quad \cdot \{H(c_x - c_0)\{K(\chi_b) + K(\chi) \\
&\quad + \rho[K(\chi_b) - K(\chi)]\} \\
&\quad + H(c_x)H(c_0 - c_x)\{K(\chi_b) - 2K(\chi_t) \\
&\quad + K(\chi) + \rho[K(\chi_b) - K(\chi)]\} \\
&\quad + H(-c_x)H(c_0 + c_x)\{K(\chi_b) - K(\chi) \\
&\quad + \rho[K(\chi_b) - 2K(\chi_t) + K(\chi)]\} \\
&\quad + H(-c_0 - c_x)\{K(\chi_b) - K(\chi) \\
&\quad + \rho[K(\chi_b) + K(\chi)]\}\}, \qquad (31)
\end{aligned}
$$

where function K is defined as [7]

$$
K(\chi) \equiv \frac{\pi B(Z_i\kappa + 1)}{\sqrt{\pi Z_i \kappa}} \int_0^{\chi} h(\chi') e^{-Z_i \kappa \chi'} \frac{dx'}{d\chi'}\, d\chi'. \qquad (32)
$$

In (31), the critical velocity c_0 is defined as a particle released from $x = 0$ has speed c_0 at location x. Evidently, four regions of the ion distribution function exist at location x. Equation (31) reduces to the ion distribution function of Emmert *et al.* [7] for a completely absorbing wall ($\rho = 0$). To find electrostatic potential in (32), electrical neutrality, $n_e = Z_i n_i$, in the presheath is needed. The ion and electron densities are, respectively

$$
n_i = \int_{-\infty}^{\infty} F_i\, dc_x, \qquad n_e = \int_{-\infty}^{\infty} F_e\, dc_x. \qquad (33)
$$

Substituting (13), (25) gives

$$
n_i(x) = \frac{2(1+\rho)}{1-\rho} \int_0^{x_b} \int_{\varepsilon_{\min}(x')}^{\infty} \frac{S_i(x', \varepsilon)}{|c_x|}\, d\varepsilon\, dx'. \qquad (34)
$$

Electron density is of a Maxwell–Boltzmann distribution

$$
n_e = n_{e0} \exp\left(\frac{e\phi}{k_B T_{e0}}\right). \qquad (35)
$$

Substituting (30) into (34), performing integration, and applying electrical neutrality by introducing (35) lead to a plasma equation

$$
e^{-\chi} = B\sqrt{\frac{\pi}{Z_i\kappa}}\,(Z_i\kappa + 1) \int_0^{\chi_b} h(\chi') I(\chi - \chi') \frac{dx'}{d\chi'}\, d\chi' \qquad (36)
$$

where B is a constant and function I is defined as

$$I(\chi-\chi') \equiv e^{Z_i\kappa(\chi-\chi')}\{H(\chi-\chi')\operatorname{erfc}[\sqrt{Z_i\kappa(\chi-\chi')}] + H(\chi'-\chi)\}. \tag{37}$$

Equation (36) by substituting (37) and differentiating with respect to χ leads to

$$e^{-\chi} = B\int_0^{\chi} \frac{h(\chi')}{\sqrt{\chi-\chi'}}\frac{dx'}{d\chi'}\,d\chi' \tag{38}$$

which is the well-known Abel's integral equation [22]. The solution of (38), therefore, yields

$$\frac{dx'}{d\chi'} = \frac{1}{\pi B h(\chi')}\left[\frac{1}{\sqrt{\chi'}} - 2D\left(\sqrt{\chi'}\right)\right] \tag{39}$$

where the Dawson function [23] is defined as

$$D\left(\sqrt{\chi'}\right) = e^{-\chi'}\int_0^{\sqrt{\chi'}} e^{t^2}\,dt. \tag{40}$$

The Dawson integral defined by (40) is slightly different from that of Emmert *et al.* [7]. The Bohm criterion is automatically satisfied by differentiating (36) with respect to χ to obtain (38), as proved by Bissell [8]. A detailed derivation will be presented later. Substituting (39) into (32) and performing integration lead to

$$K(\chi)e^{Z_i\kappa\chi} = K(\chi_b)e^{Z_i\kappa\chi}\operatorname{erf}\left(\sqrt{Z_i\kappa\chi}\right) + \frac{2}{\sqrt{\pi Z_i\kappa}}D(\sqrt{\chi}). \tag{41}$$

Interestingly, K function is independent of unknown functions h and S_0. Emmert *et al.* [7] obtained the same results for a completely absorbing wall. Substituting (37) and (39) into (36) and integrating lead to

$$\frac{2}{\sqrt{\pi Z_i\kappa}}D(\sqrt{\chi_b}) = \operatorname{erfc}\left(\sqrt{Z_i\kappa\chi_b}\right)e^{Z_i\kappa\chi_b} \tag{42}$$

which is the same equation as obtained by Emmert *et al.* [7], even though ion reflection is taken into account. Equation (42) is also independent of potential and unknown function h appearing in (30). Equation (41) leads to $K(0) = 0$ and $K(\chi_b) = 1$. The latter is obtained by substituting (42) into (41) evaluated at the sheath edge.

H. The Bohm Criterion

Equation (31) at the sheath edge reduces to

$$\begin{aligned} F_{ib}(c_x) = {} & \frac{2n_{e0}}{(1+\rho)Z_i}\sqrt{\frac{m_i}{2\pi k_B T_{i0}}} \\ & \times \exp\left(-\frac{\varepsilon}{k_B T_{i0}}\right)\{H(c_x-c_0) \\ & + H(c_x)H(c_0-c_x)[1-K(\chi_t)] \\ & + H(-c_x)H(c_0+c_x)\rho[1-K(\chi_t)] \\ & + H(-c_0-c_x)\rho\}. \end{aligned} \tag{43}$$

Substituting (43) and conducting integration, the following identity is obtained:

$$\int_{-\infty}^{\infty}\frac{F_{ib}(c_x)}{c_x^2}\,dc_x = \frac{n_{e0}m_i}{Z_i^2 k_B T_{e0}}e^{-\chi_b} \tag{44}$$

which is the Bohm criterion satisfied marginally, irrespective of ion and electron reflectivities. Equation (44) can also be represented by

$$\frac{Z_i^2 e}{m_i}\int_{-\infty}^{\infty}\frac{F_{ib}(c_x)}{c_x^2}\,dc_x = \left(\frac{dn_e}{d\phi}\right)_{\phi=\phi_b} \tag{45}$$

which is the marginal form provided by Chen [1] and Bissell [8].

I. Distribution Functions in Sheath

The ion distribution function at location x can be readily obtained from (22) by ignoring wall emission

$$\begin{aligned} \frac{F_i(x,c_x)}{m_i} = {} & H(c_x-c_0')\,|c_{xb}|\,g_b(\varepsilon,+1) \\ & + H(-c_0'-c_x)\rho\,|c_{xb}|\,g_b(\varepsilon,+1) \end{aligned} \tag{46}$$

where the first term on the right-hand side represents the distribution function of the ions moving in the positive direction and the last term is the distribution function for the ions in the negative direction after hitting the wall. The distribution function of the forward-moving ions at the sheath edge from (31) yields

$$\begin{aligned} |c_{xb}|\,g_b(\varepsilon,+1) = {} & \frac{2n_{e0}}{m_i(1+\rho)Z_i}\sqrt{\frac{m_i}{2\pi k_B T_{i0}}}\exp\left(-\frac{\varepsilon}{k_B T_{i0}}\right) \\ & \times\{H(c_{xb}-c_0)\,K(\chi_b) + H(c_{xb}) \\ & \times H(c_0-c_{xb})[K(\chi_b)-K(\chi_t)]\} \end{aligned} \tag{47}$$

where the first term on the right-hand side is referred to high-energy ions ($\varepsilon > 0$) coming from the presheath edge and the ions ionized with positive velocities in the presheath, and the last term represents low-energy ions ($Z_i e\phi_b < \varepsilon < 0$) generated with positive velocities and negative velocities experiencing turning in the presheath.

Without wall emission, the electron distribution function in the sheath from (29) yields

$$\begin{aligned} F_e(x,c_x) = {} & H(c_x+c_{e0}')m_e\,|c_{xb}|\,g_{eb}(\varepsilon,+1) \\ & + H(-c_x-c_{e0}')\rho_e m_e\,|c_{xb}|\,g_{eb}(\varepsilon,+1) \end{aligned} \tag{48}$$

where the distribution function at the sheath edge

$$\begin{aligned} & m_e\,|c_{xb}|\,g_{eb}(\varepsilon,+1) \\ & = n_{eb}\sqrt{\frac{m_e}{2\pi k_B T_{e0}}}\exp\left(-\frac{\varepsilon+e\phi_b}{k_B T_{e0}}\right). \end{aligned} \tag{49}$$

The error and Dawson functions were numerically integrated by a Simpson's rule. Errors were less than 10^{-6} by comparing grids of 1000 and 500.

III. Results and Discussion

In this study, distribution functions of the ions and electrons in the presheath and sheath are determined from the Boltzmann equation. The electric field in the presheath is found by applying the condition of electrical neutrality and introducing the ion source model proposed by Emmert *et al.* [7]. The effects of ion reflectivity on dimensionless ion distribution functions in the presheath and sheath are shown in Fig. 2. Dimensionless potential, which is an increasing function of x-coordinate, is used to represent position, to avoid specifications of unknown function

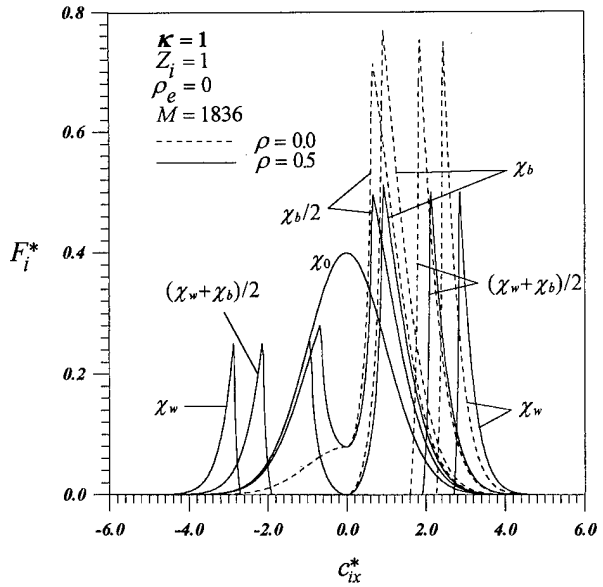


Fig. 2. Dimensionless distribution function (F_i^*) versus velocities (c_{ix}^*) of ions at different locations in presheath or sheath for different ion reflectivities of the wall (ρ).

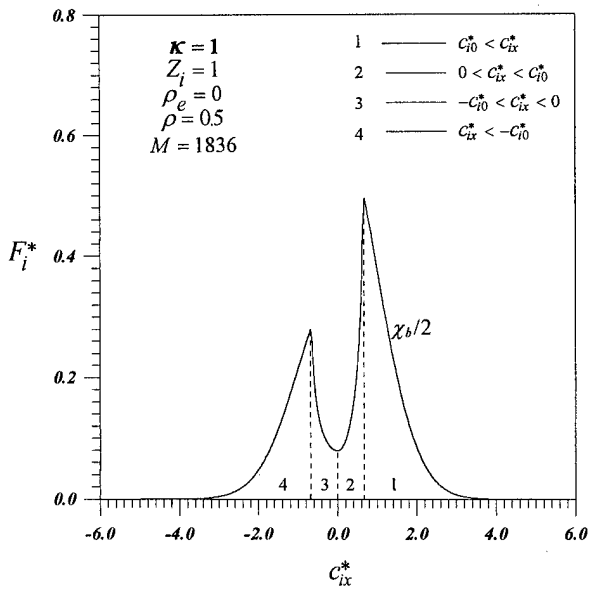


Fig. 3. Dimensionless distribution function (F_i^*) versus velocities (c_{ix}^*) of ions composed of the ions coming from different regions at location $\chi = \chi_b/2$ in presheath.

h [see (30)] and variations in temperature and ion source, and so on. Irrespective of ion reflectivity, the ions near the presheath edge or at the center of bulk plasma obey a Maxwell–Boltzmann distribution. This is because the effect of ion reflectivity on ion flow in the backward direction decays because of the retarding electric field. In the case of zero ion reflectivity, ion distribution functions in the presheath and sheath are found to be identical to those of Emmert *et al.* [7]. For a nonzero ion reflectivity, distribution functions in both the presheath and sheath exhibit two peaks, which are associated with positive and negative velocities, respectively. The ions near the peak with positive velocity are similar to those for zero ion reflectivity. The ions are composed of those coming from the presheath edge and the ions created with positive velocities in the backward region of the presheath, and the low-energy ions generated with negative velocities in the entire presheath. The ions close to the other peak come from the ions reflected by the wall and ions generated with negative velocities in the forward region. In the sheath, two peaks are separated by a gap, which is attributed to the ions having minimum energy equal to sheath edge potential. The gap widens because of an increase in ion speed in the forward direction. It is found that ion distribution functions at the sheath edge vanish at zero speed for different reflectivities. This is the requirement to avoid infinite potential [5]. If two-stream instability is accounted for, distortion of the distribution function can be ignored because of a local energy transport between the wave and particles having thermal velocities near the phase velocity or the wave having the phase velocity lying far in the tail of the distribution [1]. A systematic study of the relationships between different kinds of instabilities and distribution function is crucial.

The dimensionless distribution function at a typical location $\chi = \chi_b/2$ in the presheath can be divided into four parts, as shown in Fig. 3. The ions in part 1 have positive velocities $c_{ix}^* > c_{i0}^*$ (or $\varepsilon > 0$). They are the ions coming from the presheath edge and ions created with high positive velocities in the presheath. The ions in part 2 have low-energy with positive velocities $c_{ix}^* < c_{i0}^*$ (or $Z_i e\phi < \varepsilon < 0$). They are composed of ions created with positive velocities from the backward region and negative velocities experiencing turning in the presheath. Part 3 is for low-energy ions moving with negative velocities $c_{ix}^* > -c_{i0}^*$ (or $Z_i e\phi < \varepsilon < 0$). The ions include those created with positive velocities after reflection by the wall and those ionized with negative velocities in the forward region. Part 4 is for high-energy ions with negative velocities $c_{ix}^* < -c_{i0}^*$ (or $\varepsilon > 0$). They are composed of the ions reflected by the wall and created with high negative velocities in the forward region. The former includes the ions streaming into the presheath from the bulk plasma and ions generated with high positive velocities in the presheath.

The dimensionless ion distribution function at a given location in the sheath can be divided into six parts, as shown in Fig. 4. The ions in part 1 are composed of the ions coming from the bulk plasma and ions generated with high positive velocities in the presheath. Part 2 is for the ions created with total energy $Z_i e\phi_b < \varepsilon < 0$ in the presheath. No ions presented in parts 3 and 4, because no ions are generated in the sheath. In other words, ions across the sheath have the minimum energy equal to sheath edge potential. The ions in parts 5 and 6 are, respectively, those reflected by the wall from regions 2 and 1. Referring to Figs. 3 and 4, it is concluded that using Maxwell–Boltzmann distributions for ions to study transport process near a wall reflecting ions is inaccurate.

Spatial variations of electron distribution functions in the presheath and sheath for different electron reflectivities are presented in Fig. 5. It can be seen that electron distribution functions gradually become Maxwell–Boltzmann distribution in the backward direction toward the bulk plasma. Hence, for different electron reflectivities, electron distribution functions in the presheath ($0 < \chi < \chi_b$) can be considered as

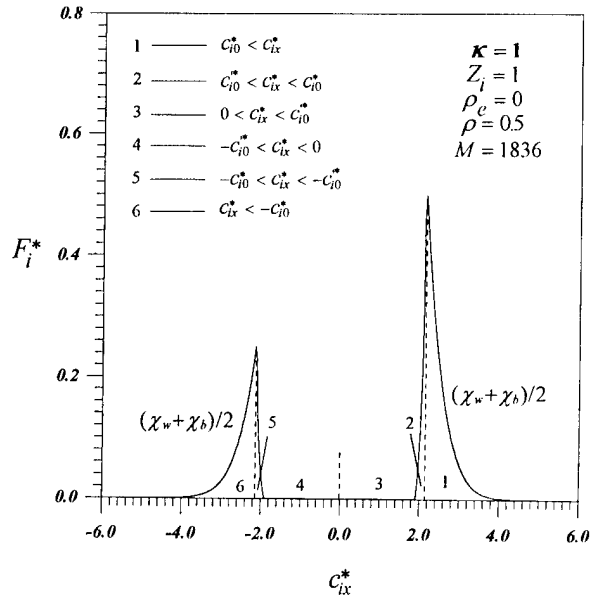


Fig. 4. Dimensionless distribution function (F_i^*) versus velocities (c_{ix}^*) of ions composed of the ions coming from different regions at location $\chi = (\chi_b + \chi_w)/2$ in sheath.

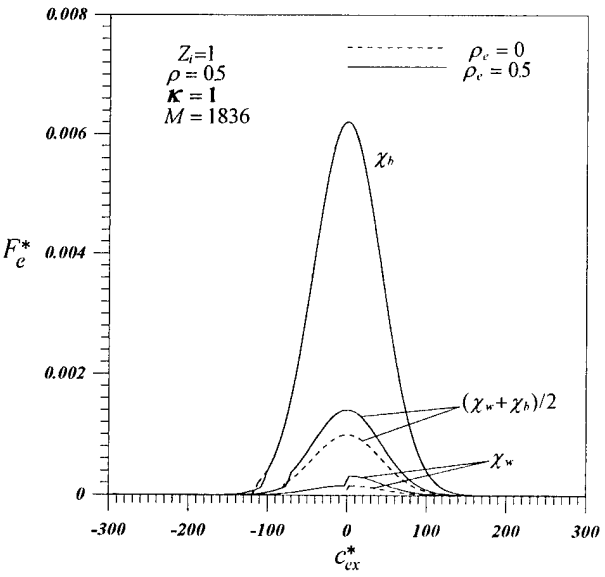


Fig. 5. Dimensionless distribution function (F_e^*) versus velocities (c_{ex}^*) of electrons at different locations in sheath for different electron reflectivities of the wall (ρ_e).

Maxwell–Boltzmann distributions. The distribution function at the sheath edge deviates slightly from a Maxwell–Boltzmann distribution in the tail region (for $c_{ex}^* < -100$). Because only the electrons that have high energy to overcome potential can hit the wall, the electrons in the tail region are those rebound by the wall and accelerated to high speeds. Errors induced for transport variables, which are obtained by integrating a distribution function, are therefore negligibly small. It is noted that for a wall emitting electrons, the distribution function also depends on surface conditions of the wall. Strong wall emission results in a significant deviation from a Maxwell–Boltzmann distribution. For a wall reflecting ions and electrons, the assumption of Maxwell–Boltzmann distributions for the electrons in the presheath is still relevant. On the other hand, electrons in the sheath ($\chi_b \leq \chi < \chi_w$) deviate significantly from the Maxwell–Boltzmann distribution, because the tail region, as discussed previously, causes a large error (namely, the drop in the range of negative velocity) for a wall partially reflecting ions. Regardless of electron (and ion) reflectivity, the forward-moving electrons still obey a half part of the Maxwell–Boltzmann distribution.

The predicted transport variables, such as densities, fluid velocity, fluid-like conduction heat, difference between mean pressure and fluid-like viscous stress of the ions and electrons in the sheath from the moment equations of the ion and electron distribution functions provided by this work agree well with the available theoretical work from Schwager and Birdsall [24]. The results are shown in the companion paper [14].

IV. Conclusion

The conclusions drawn are as follows:

1) General solutions of the ion and electron distribution functions in a collisional presheath and collisionless sheath of a plasma in contact with a wall reflecting and emitting electrons and ions are presented. The collisions are simulated by the BGK model. To obtain the relationship between electrostatic potential with position, the successful ion source model from Emmert *et al.* is used. The ion and electron distribution functions in the presheath and sheath on a wall partially reflecting ions and electrons, therefore, can be exactly obtained.
2) Velocities of the ions near the wall partially reflecting ions are of highly non-Maxwell–Boltzmann distributions having two peaks associated with positive and negative velocities, respectively. The two peaks in the sheath are separated by a gap, which widens as the wall is approached.
3) Velocities of the electrons in the presheath can be of Maxwell–Boltzmann distribution, even though the wall reflects electrons and ions. In the sheath, the electron distribution drops sharply in a range of negative velocity because of the wall partially reflecting electrons.
4) The generalized Bohm criterion is derived and satisfied marginally (namely, with the equality sign), even though ion and electron reflectivities are accounted for.

References

[1] F. F. Chen, *Introduction to Plasma Physics*. New York: Plenum, 1974.
[2] D. Bohm, "Minimum ionic kinetic energy for a stable sheath," in *The Characteristics of Electrical Discharges in Magnetic Fields*, A. Guthrie and R. Wakerling, Eds. New York: McGraw-Hill, 1949, ch. 3, pp. 77–86.
[3] L. Tonks and I. Langmuir, "A general theory of the plasma of an arc," *Phys. Rev.*, vol. 34, pp. 876–922, 1929.
[4] K.-U. Riemann, "The influence of collisions on the plasma sheath transition," *Phys. Plasmas*, vol. 4, pp. 4158–4166, 1997.
[5] E. R. Harrison and W. B. Thompson, "The low pressure plane symmetric discharge," *Proc. Phys. Soc. Lond.*, vol. 74, pp. 145–152, 1959.
[6] P. N. Hu and S. Ziering, "Collisionless theory of a plasma sheath near an electrode," *Phys. Fluids*, vol. 9, pp. 2168–2179, 1966.
[7] G. A. Emmert, R. M. Wieland, A. T. Mense, and J. N. Davidson, "Electric sheath and presheath in a collisionless, finite ion temperature plasma," *Phys. Fluids*, vol. 23, pp. 803–812, 1980.

[8] R. C. Bissell, "The application of the generalized Bohm criterion to Emmert's solution of the warm ion collisionless plasma equation," *Phys. Fluids*, vol. 30, pp. 2264–2265, 1987.
[9] K.-U. Riemann, "The Bohm criterion and sheath formation," *J. Phys. D: Appl. Phys.*, vol. 24, pp. 493–518, 1991.
[10] G. Bachet, L. Chèrigier, and F. Doveil, "Ion velocity distribution function observations in a multipolar argon discharge," *Phys. Plasmas*, vol. 2, pp. 1782–1788, 1995.
[11] M. J. Goeckner, J. Goree, and T. E. Sheridan, "Laser-induced fluorescence characterization of a multidipole filament plasma," *Phys. Fluids B*, vol. 3, pp. 2913–2921, 1991.
[12] S. Takamura, M. Y. Ye, T. Kuwabara, and N. Ohno, "Heat flows through plasma sheaths," *Phys. Plasma*, vol. 5, pp. 2151–2158, 1998.
[13] B. Chapman, *Glow Discharge Processes, Sputtering and Plasma Etching*. New York: Wiley, 1980.
[14] P. S. Wei and F. B. Yeh, "Fluidlike transport variables in a kinetic, collisionless plasma near a surface with ion and electron reflections," *IEEE Trans. Plasma Sci.*, vol. 28, pp. 1233–1243, Aug. 2000.
[15] P. L. Bhatnagar, E. P. Gross, and M. Krook, "A model for collision processes in gases. I. Small amplitude processes in charged and neutral one-component systems," *Phys. Rev.*, vol. 94, pp. 511–525, 1954.
[16] G. H. Kim, N. Hershkowitz, D. A. Diebold, and M. H. Cho, "Magnetic and collisional effects on presheaths," *Phys. Plasmas*, vol. 2, pp. 3222–3233, 1995.
[17] J. T. Scheuer and G. A. Emmert, "A collisional model of the plasma presheath," *Phys. Fluids*, vol. 31, pp. 1748–1756, 1988.
[18] E. L. Murphy and R. H. Good, Jr., "Thermionic emission, field emission, and the transition region," *Phys. Rev.*, vol. 102, pp. 1464–1473, 1956.
[19] K. C. Hsu and E. Pfender, "Analysis of the cathode region of a free-burning high intensity argon arc," *J. Appl. Phys.*, vol. 54, pp. 3818–3324, 1983.
[20] L. P. Smith, "The emission of positive ions from tungsten and molybdenum," *Phys. Rev.*, vol. 35, pp. 381–395, 1930.
[21] S. A. Self, "Exact solution of the collisionless plasma-sheath equation," *Phys. Fluids*, vol. 6, pp. 1762–1768, 1963.
[22] N. N. Lebedev, I. P. Skalskaya, and Y. S. Uflyand, *Worked Problems in Applied Mathematics*. New York: Dover, 1965.
[23] M. Abramowitz and I. A. Stegun, Eds., *Handbook of Mathematical Functions with Formulas, Graphs, and Mathematical Tables*. Washington, D.C.: National Bureau of Standards, 1970.
[24] L. A. Schwager and C. K. Birdsall, "Collector and source sheaths of a finite ion temperature plasma," *Phys. Fluids B*, vol. 2B, pp. 1057–1068, 1990.



Peng-Sheng Wei (M'00) received the M.S. degree in power mechanical engineering department from National Tsing Hua University, Hsinchu, Taiwan, R.O.C., in 1978, and the Ph.D. in mechanical engineering department from University of California at Davis in 1984.

He has been a Professor of mechanical engineering department in National Sun Yat-Sen University, Kaohsiung, Taiwan, R.O.C., since 1989. His research interests are heat transfer, fluid mechanics, phase change, and metals processing including processes and defects of welding, casting and surface heat treatment.



Feng-Bin Yeh received the B.S. degree in aerospace engineering department from Tamkang Univeristy, Taipei, Taiwan, R.O.C., in 1988, and the M.S. degree in mechanical engineering from NSYSU in 1990.

He is currently a Ph.D. student in mechanical engineering, NSYSU, and is also an engineer in the quality control division of Tang Eng Stainless Steel Plant, Kaohsiung. His research interests are heat transfer, fluid mechanics, and rapid solidification in metals processing.



Ching-Yen Ho received the B.S. degree in mechanical engineering department from National Chung-Hsing University, Taichung, Taiwan, ROC, in 1985, and the M.S. and Ph.D. degrees in mechanical engineering department from NSYSU in 1988 and 1997, respectively.

He was a faculty of mechanical engineering department in Wu Feng College of Technology and Commerce during 1988–1997. He has been an associate Professor of mechanical engineering department in Hwa Hsia College of Technology and Commerce, Taipei, since 1997. His current research interests are laser and electron beam machining, conduction, convection and radiative heat transfer, and solidification.

Temporal Characteristics of Runaway Electrons in Electron-Neutral Collision–Dominated Plasma of Dense Gases. Monte Carlo Calculations.

Konstantin I. Bakhov, Leonid P. Babich, and Igor M. Kutsyk

***Abstract*—Electron runaway rates, and runaway delay time, runaway threshold energies were obtained from Monte Carlo (MC) simulations in the field domains 35–400 kV/cm and 240–400 kV/cm, respectively, for helium and nitrogen at 1 ATM. MC simulations disprove all available analytical theories that ignore angular scattering of electrons, with the sole exception of Gurevich's theory for helium, in which angular scattering is relatively weak.**

***Index Terms*—Dense gas, electron-neutral collisions, Monte Carlo, runaway electrons.**

I. Introduction

THE phenomenon of runaway electrons (REs) in electron-neutral collision dominated plasma was observed in a variety of laboratory experiments and in nature (see [1]–[4], [23], [5]–[8], [24], [9], and the literature cited therein). It is a consequence of decreasing probabilities of electron interactions with atomic particles for electron energies ε in the range from $\sim$100 eV up to $\sim$1 MeV [10]. The microscopic description of REs is conducted on the basis of effective cross sections in terms of a time-dependent distribution function $f(\vec{v}, \vec{r}, t)$ obtained from MC simulations or from a kinetic equation (KE). It is essentially stochastic and does not allow us to introduce accurate runaway criterion. Adequate stochastic definition of REs was formulated by Kunhardt *et al.* [6], who stated that "an electron is runaway if it does not circulate through all energy states available to it at a given E/N, but on average moves toward high-energy states."

The macroscopic description, being deterministic, generally is based on equations of moments for $f(\vec{v}, \vec{r}, t)$, including an effective drag force $\vec{F}(\varepsilon)$. The force is a continuous function of the energy ε behaving similar to the cross sections. In the low-energy domain, it hits a maximum $F_{\max}$ (Fig. 1) equal in nitrogen to 270 kV/cm/atm at $\varepsilon \approx 110$ eV and in helium 51 kV/cm/atm at $\varepsilon \approx 60$ eV [1]. To become runaway, an electron should overcome a threshold ε_{th} (Fig. 1), defined as the second root of the equation

$$F(\varepsilon_{th}) = eE. \tag{1}$$

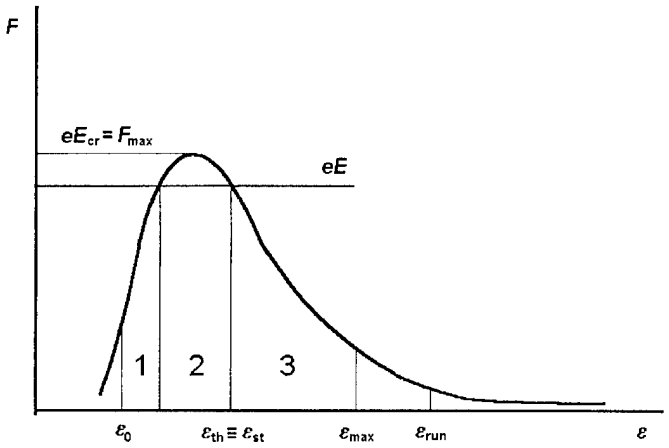


Fig. 1. Scheme for transition of low-energy electrons to the runaway mode.

In the framework of the deterministic approach, all electrons with energies above ε_{th} are runaways. Actually, it is not the case. In the framework of the stochastic description, there is no accurate runaway threshold, because $f(\vec{v}, \vec{r}, t)$ in a strong electric field only enlarges its high-energy tail in the course of time. The stochastic definition allows us to introduce only an artificial low boundary of high-energy domain. If electron collisions with neutral particle dominate, it is reasonable to choose the boundary as the onset of the energy range with decreasing cross sections, which is well above the ionization threshold ε_i.

The problem of simulation of gas discharges with REs is difficult because in this case electron distribution in essence is nonlocal and nonstationary, so that the conventional approaches, useful when electron assembly as a whole is equilibrium with a local electric field, appear to be inadequate. The necessity to consider a very wide range of energies tremendously complicates simulations. Tentatively, we can consider the three energy sections illustrated in Fig. 1, each of which differs by electron kinetics. In section 1, electrons are equilibrium with the field. Here, elastic scattering affects electron distribution very much, making it isotropic. In section 2, inelastic interactions dominate, forcing electrons to decelerate to section 1. The high-energy section 3 can be defined as the acceleration (runaway) domain. Combined approaches were attracted to describe electron kinetics (see [5], [7], [8], and [24] and the literature cited therein). They are sophisticated and incorporate rather arbitrary approximations not allowing us even to estimate an accuracy of the results obtained.

Manuscript received May 17, 1999; revised June 13, 2000. This work was supported by ISTC, under Project 490.

The authors are with the Russian Federal Nuclear Center-VNIIEF, 607188 Sarov, Russia (e-mail: babich@expd.vniief.ru).

Publisher Item Identifier S 0093-3813(00)09161-X.

0093–3813/00$10.00 © 2000 IEEE

Analytical studies of REs allow us to understand fundamentals of the phenomenon; however, their accuracy is absolutely uncertain. In this sense, numerical simulations are more illuminating, especially those, in which MC techniques were used. MC techniques presenting an opportunity to simulate a stochastic motion of a single tested electron, are the most powerful method to study kinetics of REs. The focus of the present work is to compute by means of MC such temporal characteristics of REs as runaway rate, runaway delay time, and so on to compare them with those calculated from available analytical formulas and to estimate the accuracy of the formulas. It is important to check the formulas, because they are rather frequently applied to laboratory discharges [7]–[9], [24] and to natural phenomena [11].

II. Review of Analytical Theories

The first analytical formula for REs in electron-neutral collision–dominated plasma was deduced by Gurevich in his pioneer work [10]. Gurevich obtained a stationary, spatially uniform electron distribution function over velocities $f(v)$ valid in the domain between $v_0 \approx (5\varepsilon_i/m)^{1/2}$ and v_{st} determined by equation $F(v_{st}) = eE$ similar to (1). Bethe's drag force was adopted for $F(v)$. Gurevich considered a case of a weak electric field, namely, $E < E_{cr} = F_{\max}/e$. Angular scattering of electrons was not taken into account. Electrons were assumed to move along the electric force. Time-dependent distribution of REs was not calculated, so that the approach was not consistently stochastic. The bulk of electrons was considered as a large reservoir with a "hole" at v_{st}. A leakage of particles away through the hole with the inherent rate $\nu_{\rm run}$ constitutes the RE flux estimated as

$$\Gamma = -\frac{dN_e}{dt} = \nu_{\rm run} \times N_e \approx \frac{eE}{mv_{st}} v_T^3 f(v_0) \times \exp\left\{\frac{mv_0^2}{\overline{d}\varepsilon_i}\left[1 - \frac{E}{E_{cr}}\right]\right\} \times \exp\left[-\frac{E_{cr}}{4E}\cdot A\right]. \quad (2)$$

The distribution $f(v_0)$ at the lower boundary was adopted to be Maxwellian with the temperature T. Here, $v_T = \sqrt{2T/m}$, $A \approx 5.4\,(\overline{\varepsilon}/\varepsilon_i\overline{d}) \times \ln\left[(0.35)mv_{st}^2/\overline{\varepsilon}\right]$, $\overline{\varepsilon}$ is the average excitation energy in Bethe's formula, and $\overline{d}$ is close to unity ($\overline{d} = 0.99$ in helium [10]). To verify if $\overline{d}$ is close to unity in nitrogen as well, the function $d(\varepsilon)$ defined in [10] was calculated using elementary cross sections. It was found that in the domain from $\varepsilon_0 \approx 40$ eV to $\varepsilon_{st}(E) \approx 110$–$190$ eV for $E = 270$–240 kV/cm, $d(\varepsilon)$ varies from 0.923 to 0.985. So, in nitrogen, $\overline{d}$ is also close to unity. Owing to $A/4 > 1$, the RE flux is strongly decreasing the function of the ratio $E_{cr}/E > 1$. The quantity $\nu_{\rm run}$, used in (2), is "a rate for runaway electron production" [12]. Actually, it was introduced much later by Sizykh as a fraction of electrons acquiring per unit time an energy higher than the runaway threshold at a given field intensity [12].

Later, Kremnev and Kurbatov put $v_{st} = v_0$ in (2) and rather arbitrarily extended it to the domain of strong fields $E/E_{cr} > 1$ as follows [8], [24], [13]

$$\Gamma = \nu_{\rm run} \times N_e \approx \frac{eE}{mv_0} v_T^3 f(v_0). \quad (3)$$

Sizykh calculated $\nu_{\rm run}$ proceeding from stationary KE [12]. Electrons were assumed to move in the direction of the electric force. The problem was considered in terms of the total interaction cross section $\sigma(\varepsilon)$ for which the following approximation was adopted:

$$\sigma(\varepsilon) = \begin{cases} \sigma_0, & \varepsilon \le \varepsilon_0 \\ \sigma_0\varepsilon_0/\varepsilon, & \varepsilon \ge \varepsilon_0 \end{cases} \quad (4)$$

with $\sigma_0 = 1.5 \times 10^{-15}$ cm^2 and $\varepsilon_0 = 200$ eV for nitrogen. Actually, for $F(\varepsilon)$, a rough approximation $N\sigma(\varepsilon)\varepsilon^*$ was used. For the runaway rate, Sizykh deduced the following formula valid for $E < E_{cr}$:

$$\nu_{\rm run} \approx \frac{eEv_{th}}{2\varepsilon^*}\sqrt{\frac{\varepsilon_{th}}{\varepsilon^*}} \times \exp\left[-\frac{E_0}{E_{cr}}\left(1 - \frac{E^2}{E_{cr}^2}\right)\right] \quad (5)$$

where $v_{th} = \sqrt{2\varepsilon_{th}/m}$, $E_0 = (\varepsilon_0/\varepsilon_i) \times E_{cr}$, and $E_{cr} = \sigma_0 N\varepsilon^*/e$. Here, for nitrogen, $\varepsilon_i = 15.6$ eV and "average excitation energy" $\varepsilon^* = 10$ eV were adopted [12]. Sizykh estimated $E_{cr} = 400$ kV/cm [12]. It is expedient to note that $E_0 \approx 8$ MV/cm in the paper of Sizykh can only be obtained if $\varepsilon_i = \varepsilon^*$.

Slavin and Sopin [7] defined the runaway rate as

$$\nu_{\rm run} = eE/mv(\varepsilon_p) \times Q \quad (6)$$

with ε_p chosen to be the energy at which the elastic scattering cross section equals to the inelastic one. Specifically, for nitrogen, $\varepsilon_p = 100$ eV was adopted. To calculate the probability Q for an electron to achieve the energy ε without collisions, they used the formula

$$Q(\varepsilon/\overline{\varepsilon}) = \exp\left[-q + q\,\frac{\ln(1+\varepsilon/\overline{\varepsilon}) + 1}{1+\varepsilon/\overline{\varepsilon}}\right], \quad q = \sigma_0 N\overline{\varepsilon}/eE \quad (7)$$

deduced by Kozyrev *et al.* [8], [24], by employing the theory of branching processes and the following approximation for the total interaction cross section:

$$\sigma(u) = \sigma_0\,\frac{\ln(1+\varepsilon/\overline{\varepsilon})}{(1+\varepsilon/\overline{\varepsilon})^2} \quad (8)$$

where $\overline{\varepsilon}$ and σ_0 were calculated to be 38 eV and 4.34×10^{-16} cm^2 for helium and 150 eV and 8×10^{-16} cm^2 for nitrogen, so that $E_{cr}/P = 550$ V/cm/Torr for helium and $E_{cr}/P = 4000$ V/cm/Torr for nitrogen [8], [24]. These E_{cr}/P are highly overestimated, even if compared with $F_{\max}$, cited in Section I. Slavin and Sopin instead of $q = \sigma_0 N\overline{\varepsilon}/eE$ used $q = E_{cr}/E$ with $E_{cr}/P = 4000$ V/cm/Torr for nitrogen.

III. Computation Approach

MC techniques being consistently stochastic seem to be the most adequate to the stochastic nature of REs because these techniques are free from approximations of mathematical origin. They are especially convenient in those cases when the number of REs is so small that continuous distribution functions are inadequate. MC techniques are extremely computer time-consuming. This, however, is the only basic shortcoming limiting a simulated temporal interval and therefore an accuracy of results obtained. In the most of published works, where MC was employed (see, e.g., [14], [25]–[27]), REs appeared on a background of the total electron population and were studied in a manner not allowing us to obtain their fundamental characteristics. Here, the MC technique was realized in a sufficiently

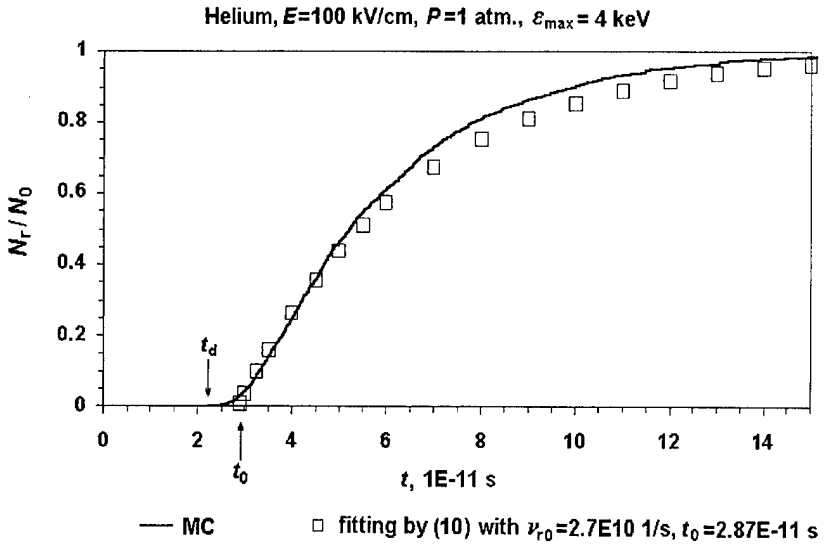


Fig. 2. Fitting by (10) of typical MC time dependence of the fraction of electrons achieved $\varepsilon_{\max} = 4$ keV until the moment t ($N_0 = 5000$, $t_{\max} = 3 \cdot 10^{-10}$ s).

general manner, so that results obtained enable us to single out REs and estimate their deposition to discharge processes more accurately than available analytical formulas allow.

The following approach was adopted. It was supposed that in a dense gas with a strong electric field, there is an assembly of N_0 electrons with initial energy of 1 eV and initial velocities unidirectional with the electric force. Electron trajectories were followed up to some upper energy $\varepsilon_{\max}$ (a variable parameter) during some fixed time $t_{\max}$ large enough for a considerable number of electrons to achieve $\varepsilon_{\max}$. In the event the individual electron achieved the energy $\varepsilon_{\max}$ earlier, simulation of its history was terminated. For every field intensity, a specific value $\varepsilon_{\max} = \varepsilon_{\text{run}}$ exists high enough to satisfy strong inequality $F(\varepsilon_{\max}) \ll eE$, guaranteeing the probability of electrons to move through ε_{run} backward to low energies to be negligibly small. Therefore, electrons with energies above ε_{run} can be considered as REs, and ε_{run} is possible to define as a stochastic runaway threshold analogous to the deterministic one ε_{th}. Such formulation is similar to Gurevich's reservoir of low-energy electrons N_0 with a leakage caused by the action of the electric field [10]. Unlike analytical formulas obtained from stationary KE written for one variable, either v or ε, with $\mu = 1$, MC computations were performed in the space of three variables (ε, μ, t), where μ is the cosine of the angle relative to the electric force. To simulate electron trajectories, the MC code realizing an individual collision scheme with a "null collision" approach [15] was employed.

Computations were carried out for nitrogen as the main component of the atmosphere and for helium, the gas with the simplest structure of atomic levels. Atmospheric number density N was assumed. The field intensity was varied in the domains 35–400 kV/cm and 240–400 kV/cm for helium and nitrogen, respectively. $E_{cr}/P = 270$ kV/cm/atm for nitrogen and $E_{cr}/P = 51$ kV/cm/atm for helium were adopted to be close to $F_{\max}/e$ [1]. The other values were as follows: $\bar{\varepsilon} = 80$ eV for nitrogen and 44 eV for helium [8], [24] in (2), 150 eV and 38 eV [7] in (7), $\varepsilon_i = 15.6$ eV for nitrogen and 23.42 eV for helium [16], and in (5), for nitrogen, $\varepsilon^* = 10$ eV exactly, as Sizykh stated [12]. Electron temperature in (2) and (3) was calculated as $T = (2/3) \times \langle \varepsilon(0\text{–}200\ \text{eV}) \rangle$, where $\langle \varepsilon(0\text{–}200\ \text{eV}) \rangle$ is the average energy of low-energy electrons obtained from MC computations (see Table I).

TABLE I
MC GROUP TEMPERATURE OF ELECTRONS WITH ENERGIES BELOW 200 eV VERSUS ELECTRIC FIELD INTENSITY

Nitrogen		Helium	
E, kV/cm	T, eV	E, kV/cm	T, eV
400	17.87	400	42.86
375	16.73	300	39.57
350	15.52	200	34.39
325	14.34	150	29.89
300	13.16	100	22.89
270	11.81	75	18.01
260	11.39	60	14.72
250	10.97	50	12.56
240	10.54	45	11.54
235	10.36	40	10.61
200	9.02	35	9.75
150	7.28		
100	5.65		

The following set of cross sections for elementary processes was employed. In the domain of energies above 1 keV, the evaluated electron data library (EEDL) was used for elastic scattering of electrons and impact ionization [16]. Integral excitation cross sections from Phelps's and Pitchford's library [17], [28] were employed. A total ionization cross section below 1 keV was taken from the paper of Rapp and Englander-Golden [18]. The remaining integral and differential cross sections were chosen from [19], [29], [30] for helium and [20], [31] for nitrogen. For differential cross sections of excitation of electronic states in nitrogen, below 50-eV data of Cartwright *et al.* [32] were used.

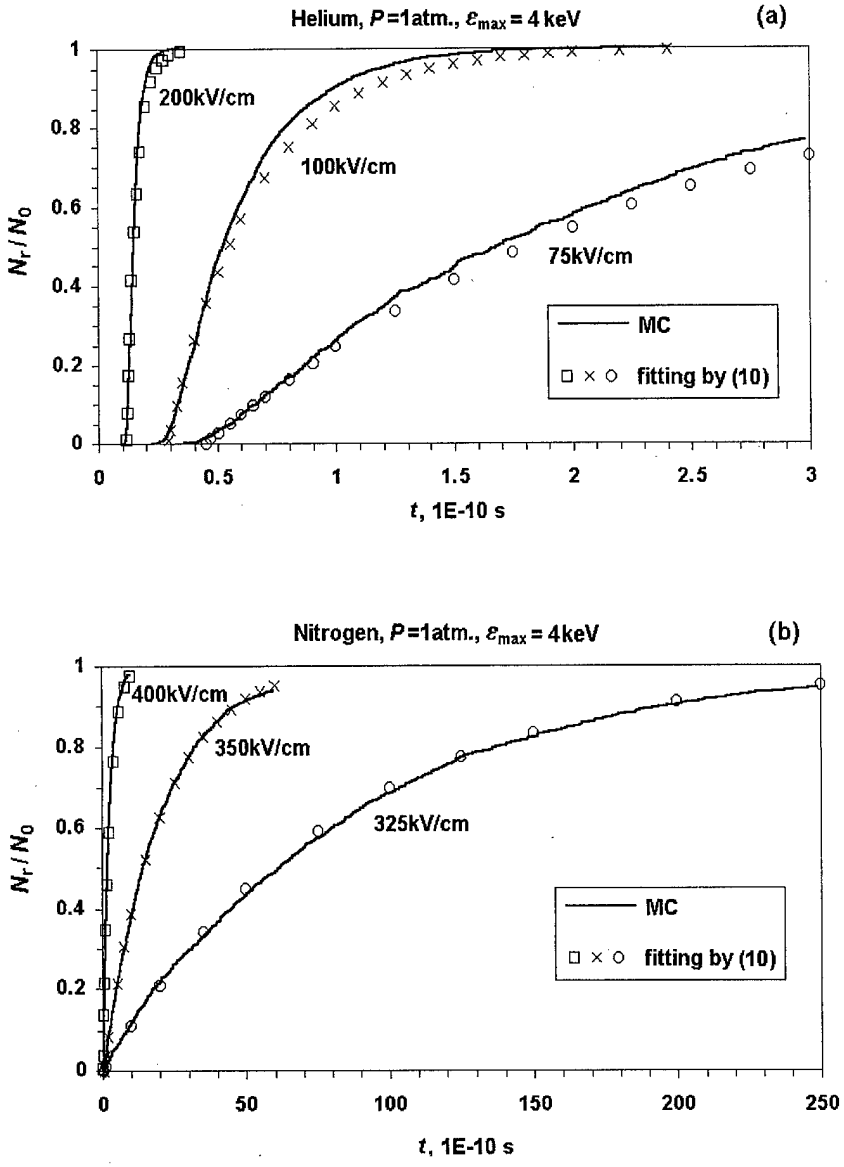


Fig. 3. Temporal dependencies of the fraction of electrons achieved $\varepsilon_{\max} = 4$ keV until the moment t for a number of field intensities.

At higher energies, electrons after excitation collisions were adopted to move forward. The following nitrogen electronic states were taken into account: $A^3\Sigma_u^+$ ($\nu = 5$–$9, \varepsilon_{ex} = 7$ eV and $\nu = 10 - \infty$, $\varepsilon_{ex} = 7.8$ eV), $B^3\Pi_g$ ($\varepsilon_{ex} = 7.35$ eV), $W^3\Delta_u$ ($\varepsilon_{ex} = 7.36$ eV), $B'^3\Sigma_u^-$ ($\varepsilon_{ex} = 8.16$ eV), $C^3\Pi_u$ ($\varepsilon_{ex} = 11.03$ eV), $w^1\Delta_u$ ($\varepsilon_{ex} = 8.89$ eV), $a^1\Pi_g$ ($\varepsilon_{ex} = 8.55$ eV), and the integral cross section of all remaining singlet states with the excitation threshold $\varepsilon_{ex} = 13$ eV. The following excitation states of helium were included separately: $2^1P(\varepsilon_{ex} = 21.21$ eV), $2^1S(\varepsilon_{ex} = 20.61$ eV), $2^3P(\varepsilon_{ex} = 20.96$ eV), $2^3S(\varepsilon_{ex} = 19.82$ eV), along with effective state $3SPD(\varepsilon_{ex} = 22.97$ eV) uniting states 3^1S, 3^1P, 3^1D, 3^3S, 3^3P, 3^3D with close excitation thresholds.

IV. Results and Discussion

Preliminary calculations proved that for the considered fields, almost all electrons above 4 keV proceed to gain energy further because the deceleration effect of collisions above 4 keV appeared to be negligible. Fig. 2 illustrates typical temporal MC dependence of the fraction $N_r(t)/N_0$ in helium for one field intensity. Here, $N_r(t)$ is the number of electrons achieved $\varepsilon_{\max} = 4$ keV until the moment t. The runaway process can be described by the following set of equations by fitting parameters t_0 and ν_{r0}:

$$\begin{cases} \dfrac{\partial N_r(t')}{\partial t} = \nu_{r0} \times N_e(t'), \quad t' = t - t_0 \\ N_r(t') + N_e(t') = N_0 \\ N_r(t_0) = 0. \end{cases} \tag{9}$$

Its solution

$$N_r(t') = N_0 \times (1 - \exp[-\nu_{r0} t']) \tag{10}$$

is close to linear dependence at $t \sim t_0$ and asymptotically tends to constant N_0 at large t. Here, ν_{r0} defines a production rate of electrons with energy $\varepsilon_{\max}$. MC results for all fractions $N_r(t)/N_0$ were fitted by (10), as is illustrated in Fig. 2. A discrepancy seen near t_0 is caused by the number of electrons with

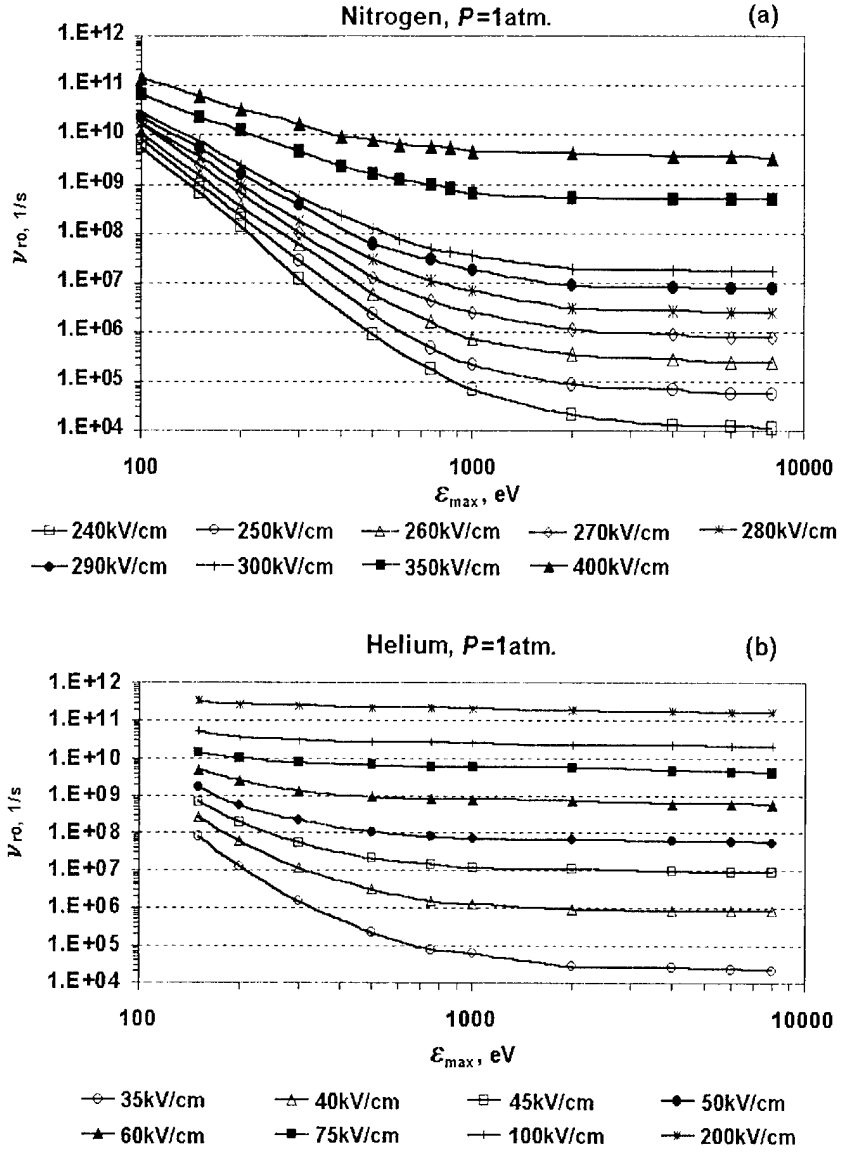


Fig. 4. Dependencies of the production rate ν_{r0} of electrons with maximum simulated energy $\varepsilon_{\max}$ on $\varepsilon_{\max}$ for a number of field intensities.

$\varepsilon_{\max}$ in the vicinity of t_0 is too small. Actual delay time t_d, namely, the time necessary for the production of the first electron with $\varepsilon_{\max}$, is less than t_0. MC simulations of evolution of electron assembly with large N_0 performed during sufficiently short $t_{\max} \sim 2 \times t_0$ proved that actually t_0 is close to t_d. Fig. 3 illustrates MC dependencies of $N_r(t)/N_0$ for a number of field intensities. All curves are similar to each other and are satisfactory fitted by (10).

Fig. 4 displays the dependence of the production rate ν_{r0} of electrons with the energy $\varepsilon_{\max}$ on $\varepsilon_{\max}$. Each $\nu_{r0}(\varepsilon_{\max}, E)$ in Fig. 4 was obtained by fitting (10) to the corresponding MC dependence $N_r(t)/N_0$ for a given E and selected $\varepsilon_{\max}$, as is demonstrated in Figs. 2 and 3. At sufficiently large $\varepsilon_{\max} = \varepsilon_{\rm run}(E)$, every curve $\nu_{r0}(\varepsilon_{\max}, E)$ for either gas species practically terminates to decrease, achieving almost a constant value $\nu_{run0}(E)$. So it is reasonable to define $\nu_{run0}(E)$ as an actual runaway rate and $\varepsilon_{\rm run}(E)$ as a stochastic runaway threshold for a given E. At $\varepsilon_{\max} = 4$ keV, ν_{r0} really achieves almost a constant value, even for the lowest field considered. As for the deterministic threshold ε_{th} (Fig. 1), the weaker the field, the higher $\varepsilon_{\rm run}$. At one and the same E, however, $\varepsilon_{\rm run}$ is higher than ε_{th}. Therefore, an actual flux of REs is less than can be predicted basing on ε_{th}. Formulas (2), (3), (5)–(7) imply that for a given E/P and P different from 1 atm, the rate can be scaled as $\nu_{\rm run}(E/P) = P \times \nu_{run0}(E/P)$.

MC field dependencies of the runaway rate $\nu_{run0}(E)$ are presented in Fig. 5 along with $\nu_{run0}(E)$ calculated from (2), (3), (5), and (6). Statistical accuracy of MC results is better than 15%. The rates obtained from (2) for helium [Fig. 5(a)], appeared to be amazingly close to MC rates in vicinity and below the adopted E_{cr}. Formula (3) gives $\nu_{\rm run}$ by the order of magnitude lower than MC results in the upper domain of the tested field intensities. In comparison with MC results, (6) highly overestimates $\nu_{\rm run}$ in the domain of weaker fields. At high E, it tends to predict the runaway rate coincident with MC calculations. In general, (2) combined with (3), predicts the behavior

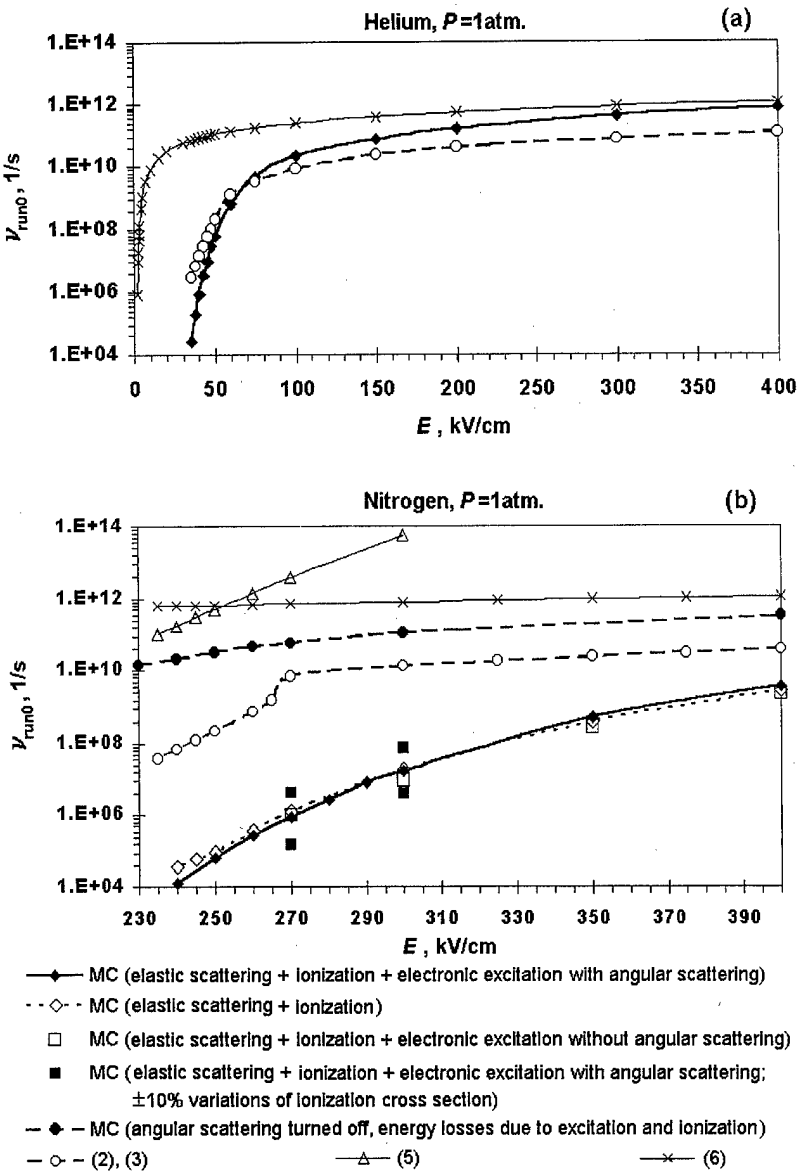


Fig. 5. Field dependencies of the runaway rate obtained from MC simulations and from analytic formulas.

of $\nu_{\rm run}(E)$ similar to that computed by MC. The dependence $\nu_{\rm run}(E)$ predicted by (6), in general, also is similar to that computed by MC; however, it is strongly shifted to the low energies. For nitrogen [Fig. 5(b)], all formulas give runaway rates much higher than MC ones throughout the tested field domain, with (2) and (3) giving the lowest discrepancy. In extremely strong fields, (3) tends to give $\nu_{\rm run}$ coincident with MC rates. Formula (5) gives the largest discrepancy with MC in the domain of small fields. As for helium, the curve calculated from (6) for nitrogen displays a decreasing section in the range of low energies not shown in Fig. 5(b). Actually, however, all formulas highly overestimate the runaway rate in nitrogen. This is explained by the disordering effect of angular scattering in nitrogen being stronger than in helium. All formulas entirely discount angular scattering. Turning off both elastic and inelastic angular scatterings increased MC rates above those calculated from (2) and (3) [Fig. 5(b)].

MC computations for nitrogen were carried out to study the effect of excitation interactions and inaccuracies of ionization cross section. In Fig. 5(b), plotted points are calculated with $\pm 10\%$ variation of the ionization cross section, most likely corresponding to the accuracy of the available data. Obviously, neither incorporation of the excitation nor variation of the ionization cross section can account for the discrepancy between the rates calculated by MC and from the formulas. So, the discrepancy is inherent to analytical theories because of the approximations adopted. Fig. 5(b) illustrates the effect of angular scattering of electrons caused by excitation collisions. We can see that within the accuracy of the present MC computations, they do not affect significantly the results. On the contrary, the elastic scattering makes the main contribution to the formation of the angular distribution of low-energy electrons. It was simulated as accurate as possible by using complete differential cross section taking into account

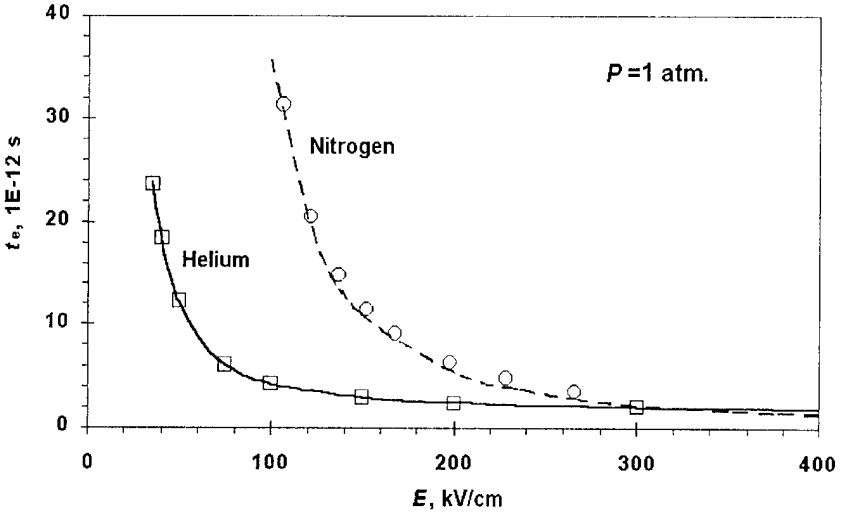


Fig. 6. Field dependencies of the time scale for e-fold increase of the total electron number obtained from MC simulations (curves) and calculated from experimental data (markers).

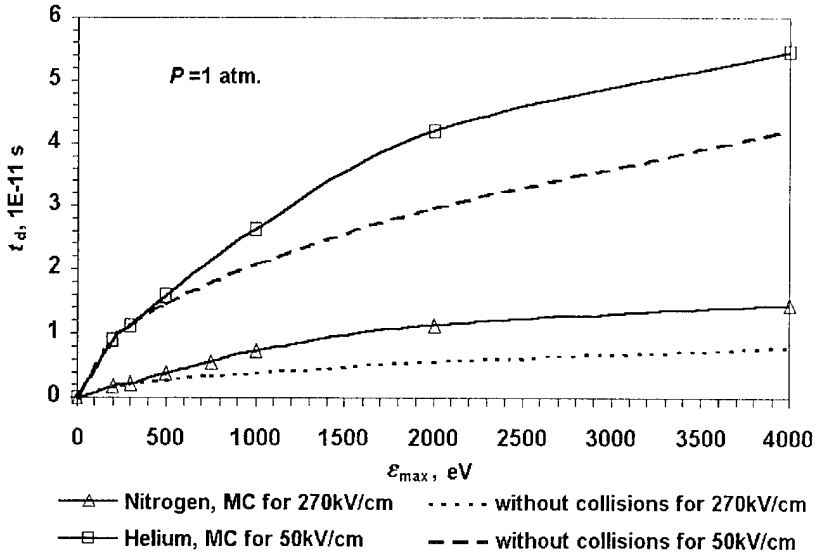


Fig. 7. MC dependencies of the delay time of production of electrons with maximum simulated energy ε_{max} on ε_{max}.

anisotropy of the elastic scattering below 50 eV according to Trajmar *et al.* [32].

To check the MC technique used, it was applied to compute field dependencies of the time $t_e(E)$ necessary for an e-fold increase of the total electron population, to be compared with $t_e = 1/(\alpha \times w)$ calculated by employing measured data for ionization coefficient α and drift velocity w [21], [33], [34]. Evolution of an assembly consisting primarily of $N_0 = 10^3$ electrons was simulated during reasonable time $t_{\max}(E)$ guaranteeing sufficient multiplication, limited actually to hundreds times. For instance, in nitrogen, $N(t_{\max} = 9 \times 10^{-12}\ \text{s})/N_0 = 800$ for $E = 400$ kV/cm and $N(t_{\max} = 2 \times 10^{-10}\ \text{s})/N_0 = 250$ for $E = 100$ kV/cm. The portion of REs produced during $t_{\max}$ was so small that they did not deposit multiplication. Fig. 6 demonstrates good agreement between MC results and experimental data, thus, testifying to the validity of MC code in general. According to Figs. 5 and 6, a general condition $\nu_{run0} \times t_e \ll 1$ is satisfied. It means that the number of secondary low-energy electrons always is larger than RE number.

In the framework of the deterministic description, $E = F_{\max}/e$ is the critical value of the field intensity ensuring that all electrons, including those with zero initial energy, are involved in the mode of permanent acceleration [1]. Results of the above consistently stochastic computations proved that actually it is not the case because the fraction of REs is determined not by the runaway rate, but by the product $\nu_{run0} \times \Delta t$. Here, the characteristic runaway time is $\Delta t = \min[\Delta t_E, t_e(E)]$, where Δt_E is the duration of the existence of the field strong enough to guarantee electron runaway.

The delay time t_d necessary for the first electron with the energy $\varepsilon_{\max}$ to appear naturally depends on $\varepsilon_{\max}$, as illustrated in Fig. 7, along with t_d calculated with all collisions turned off.

As an illuminating example, it is interesting to apply the obtained results to analysis of d'Angelo, who considering a possibility of electron acceleration in front of a return stroke, estimated that at $P = 1$ atm, the field $E = 100$ kV/cm with duration 10 ns guarantees 100 kA/cm^2 for RE current in the head of a return stroke [22]. This would mean that REs constitute the total current in the head. However, according to $\nu_{run0} \times t_e \ll 1$, the number of low-energy electrons far exceeds the RE number. Therefore the low-energy electrons, not REs, carry most of the current in the head of the return stroke, and hence, 100 kA/cm^2 is too large for RE current in the lightning.

V. Conclusion

Field dependencies of the runaway rate, runaway delay time, and stochastic runaway threshold were calculated for helium and nitrogen. In addition, there were calculated field dependencies of the time necessary for an e-fold increase of the total electron number. The results are rather general within the tested domains of E, namely, 35–400 kV/cm for helium and 240–400 kV/cm for nitrogen. It was senseless to descend to the lower E because of a very low runaway rate and in view of extremely time-consuming computations. Under certain limitations, the obtained results can be applied to discharges with REs at pressures other than 1 atm and in fields varying in space and time. Excitation interactions, inaccuracies of ionization cross section, and angular scattering of electrons caused by inelastic collisions do not affect significantly the runaway rate.

Unlike the generally accepted opinion, the runaway threshold appears in the framework of the stochastic description as well. The production rate of electrons with the upper energy $\varepsilon_{\max}$, to which electron trajectories were simulated, almost ceases to decrease with increasing $\varepsilon_{\max}$. The energy $\varepsilon_{\rm run}$, above which this rate is practically constant, can be defined as the stochastic runaway threshold. The field dependence $\varepsilon_{\rm run}(E)$ is similar to the dependence $\varepsilon_{th}(E)$. The stochastic threshold is higher than ε_{th} predicted by (1) and more justified physically. Unlike the rigorous deterministic threshold ε_{th} not incorporating a number of REs, the stochastic one, however, is somewhat artificial because 1) electrons with energies below $\varepsilon_{\rm run}$ have nonzero probability to become runaways during a time interval longer than the adopted maximum simulation time $t_{\max}$, and 2) actually the production rate of electrons with $\varepsilon_{\max}$ higher than adopted $\varepsilon_{\rm run}$ proceeds weakly to decrease with a $\varepsilon_{\max}$ increase (see Fig. 4).

Dependencies of the runaway rate on the field intensity calculated from analytical formulas, were compared with MC ones. The results convincingly proved that Gurevich's formula (2) in the domain of its validity, $E < E_{cr}$ in helium gives runaway rates practically coinciding with MC rates obtained by employing a complete set of cross sections, provided that, however, the electron temperature available from MC computations is inserted in the formula. This is remarkable in view of approximations, in the framework of which the formula has been deduced. At high fields, the formula of Slavin and Sopin (6) incorporating theory of Kozyrev *et al.* [8], [24] fits MC results for helium best of all. For nitrogen, all formulas give a strong discrepancy because angular scattering of electrons was not taken into account. Gurevich's formula (2) combined with its rather arbitrary extrapolation to the range of strong field (3) proposed by Kremnev and Kurbatov fits MC rates best of all.

Naturally an MC technique realizing an individual collision scheme is free from limitations inherent to any analytical approach, and therefore, its results are much reliable. What is important is that the MC technique allows us at least to estimate the accuracy of the results. The performed MC simulations proved that even in a very strong field, a consistently stochastic description of low-energy electrons is necessary to obtain correct results. However, computations by analytical formulas are by far less time-consuming. Therefore, it would be reasonable to employ them with a preliminary fitting to MC results.

Were computations performed by the formulas with $E_{cr}/P = 550$ V/cm/Torr for helium and $E_{cr}/P = 4000$ V/cm/Torr for nitrogen available in [8], [24] and used for nitrogen by Slavin and Sopin [7], they would give that almost all electrons are runaways in absolute disagreement with MC computations. Sizykh's statement that "runaway electrons can exist at *any value of the field intensity* E on account of energy losses decrease along with the decrease of all cross sections for all collision processes" perhaps in general is valid, provided, however, that the considered time interval is extremely long. The weaker the field, the longer the time interval necessary for at least one RE to appear. However, within the framework of a particular experiment, the number of REs is limited by the duration of the process studied and the field intensity, so that REs never will appear if the field is too weak. This was strictly shown by extremely strong dependence of $\nu_{\rm run}$ on E in the domain of weaker fields.

Acknowledgment

The authors are pleased to express their gratitude to S. Voss and Dr. S. Gitomer for their invaluable work in establishing collaboration between LANL and RFNC-VNIIEF, and to A. Gurevich, Dr. R. Roussel-Dupre, Dr. E. Symbalisty, Prof. K. Zybin, and to Corresponding Member of Russian Academy of Science A. Gurevich for fruitful collaboration. They are also grateful to Dr. E. Donskoy and Dr. B. Shamraev for a number of useful discussions.

References

[1] L. Babich, T. V. Loiko, and V. A. Tsukerman, "High-voltage nanosecond discharge in a dense gas at high overvoltage with runaway electrons," *Sov. Phys. Usp.*, vol. 33, no. 7, pp. 521–539, 1990.

[2] L. M. Vasilyak *et al.*, "Highspeed ionizing waves at electrical breakdown" (in Russian), *Uspekhi Phys. Nauk*, vol. 164, no. 3, pp. 263–286, 1994.

[3] A. Gurevich, G. Milikh, and R. Roussel-Dupre, "Runaway electron mechanism of air breakdown and preconditioning during a thunderstorm," *Phys. Lett. A*, vol. 165, no. 5, 6, pp. 463–468, 1992.

[4] R. Roussel-Dupre, A. Gurevich, T. Tunnel, and G. Milikh, "Kinetic theory of runaway air breakdown," *Phys. Rev. E*, vol. 49, no. 3, pp. 2257–2271, 1994.

[5] L. Babich and I. Kutsyk, "Numerical simulation of a nanosecond discharge at atmospheric pressure, developing in the mode of runaway electrons," *High Temp.*, vol. 33, pp. 190–197, 1995.

[6] E. E. Kunhardt, Y. Tzeng, and J. P. Boeuf, "Stochastic development of an electron avalanche," *Phys. Rev. A*, vol. 34, no. 1, pp. 440–449, 1986.

[7] B. B. Slavin and P. I. Sopin, "Breakdown in neutral gas by ionizing waves of negative potential gradients," *Teplofiz. Vys. Temp.*, vol. 30, pp. 1–11, 1992.

[8] Yu. D. Korolev and G. A. Mesyats, *Physics of Pulse Breakdown in Gases*. Moscow: Nauka, 1991.
[9] R. E. Beverly III, "Modeling of X-ray generation during the breakdown phase of surface discharges," *J. Appl. Phys.*, vol. 60, pp. 1753–1757, 1986.
[10] A. V. Gurevich, "On the theory of runaway electrons," *Sov. Phys. JETP*, vol. 12, p. 904, 1961.
[11] B. Chang and C. Price, "Can gamma radiation be produced in the electrical environment above thunderstorms?," *Geophys. Res. Lett.*, vol. 22, no. 9, pp. 1117–1120, 1995.
[12] S. Sizykh, "Runaway production rate in gas discharges," *High Temp.*, vol. 31, no. 1, pp. 1–6, 1993.
[13] V. V. Kremnev and Yu. A. Kurbatov, "Study of X-rays from gas discharge in high electric fields," *Sov. Phys. Tech. Phys.*, vol. 17, p. 626, 1972.
[14] Y. Tzeng and E. E. Kunhardt, "Effect of energy partition in ionizing collisions on the electron-velocity distribution," *Phys Rev. A*, vol. 34, no. 3, pp. 2148–2157, 1986.
[15] S. L. Lin and J. N. Bardsley, "The null-event method in computer simulation," *Comput. Phys. Commun.*, vol. 15, no. 3–4, pp. 161–163, 1978.
[16] S. T. Perkins and D. E. Cullen, "ENDL type formats for the LLNL evaluated atomic data library, EADL, for the evaluated electron data library, EEDL, and for the evaluated photon library EPDL, LLNL," UCRL-ID-117796, Livermore, CA, July 1994.
[17] A. Phelps and L. Pitchford, "Anisotropic scattering of electrons by N_2 and its effect on electron transport," *Phys Rev. A*, vol. 31, pp. 2932–2949, 1985.
[18] D. Rapp and P. Englander-Golden, "Total cross sections for ionization and attachment in gases by electron impact. I. Positive ionization," *J. Chem. Phys.*, vol. 43, no. 5, pp. 1464–1479, 1965.
[19] I. Shimamura, "Cross sections for collisions of electrons with atoms and molecules," *Sci. Papers I.P.C.R.*, vol. 82, pp. 1–51, 1989.
[20] D. Dill and J. L. Dehmer, "Total elastic electron scattering cross section for N_2 between 0 and 1000 eV," *Phys. Rev. A*, vol. 16, no. 4, pp. 1423–1431, 1977.
[21] S. Haydon and O. Williams, "Combined spatial and temporal studies of ionization growth in nitrogen," *J. Phys. D: Appl. Phys.*, vol. 9, no. 3, pp. 523–536, 1976.
[22] N. D'Angelo, "On X-rays from thunderclouds," *Ann. Geophys.*, vol. 5B, no. 2, pp. 119–122, 1987.
[23] R. Roussel-Dupre and A. Gurevich, "On runaway breakdown and upward propagating discharges," *J. Geophys. Res.*, vol. 101, no. A2, pp. 2297–2311, 1996.
[24] A. Kozyrev, Yu. Korolev, G. Mesyats, and Yu. Novoselov, "Model of the continuos electron acceleration in gas discharge" (in Russian), in *Proc. 6th All Union Conf. Phys. Low-Temp. Plasma*, vol. 2, Leningrad, 1983, pp. 228–230.
[25] E. E. Kunhardt and Y. Tzeng, "Role of electron-molecule angular scattering in shaping the electron-velocity distribution," *Phys. Rev. A*, vol. 34, no. 3, pp. 2158–2166, 1986.
[26] V. A. Shveigert, "Evolution of electron distribution function in strong electric fields" (in Russian), *Teplofiz Vys. Temp.*, vol. 28, no. 1, pp. 35–39, 1990.
[27] V. A. Shveigert, "Development of an electron avalanche in strong electric fields" (in Russian), *Fiz. Plasmy*, vol. 14, no. 5, pp. 633–636, 1988.
[28] B. Jelenkovic and A. Phelps, "Excitation of N_2 in dc electrical discharges at very high E/n," *Phys Rev. A*, vol. 36, no. 11, pp. 5310–5326, 1987.
[29] J. P. Boeuf and E. Marode, "A Monte Carlo analysis of an electron swarm in a nonuniform field: The cathode region of a glow discharge in helium," *J. Phys. D: Appl. Phys.*, vol. 15, pp. 2169–2187, 1982.
[30] D. V. Fursa and I. Bray, "Calculation of electron-helium scattering," *Phys. Rev. A*, vol. 52, no. 2, pp. 1279–1297, 1995.
[31] S. Trajmar, D. F. Register, and A. Chutjian, "Electron scattering by molecules II. Experimental methods and data," *Phys. Rep.*, vol. 97, no. 5, pp. 219–356, 1983.
[32] D. C. Cartwright, A. Chutjian, S. Trajmar, and W. Williams, "Electron impact excitation of the electronic states of N_2. I. Differential cross sections at incident energies from 10 to 50 eV," *Phys. Rev. A*, vol. 16, no. 3, pp. 1013–1040, 1977.
[33] A. Von Engel, *Handbuch der Physik*. Berlin: Springer-Verlag, 1956.
[34] H. Hasegawa, H. Date, Y. Ohmori, P. Ventzek, M. Shimozuma, and H. Tagashira, "Measurements of the drift velocity of electrons in mixtures of nitrogen and carbon dioxide from 100 to 1000 Td," *J. Phys. D: Appl. Phys.*, vol. 31, no. 5, pp. 737–741, 1998.

Konstantin I. Bakhov was born June 3, 1966, in Arzamas-75 (presently Sarov), Russia. He received the undergraduate Diploma degree in the field of physics of accelerators and charged particle beams from Moscow Engineering Physics Institute in 1989.

Since 1989 he has been with the Russian Federal Nuclear Center—VNIIEF (formerly, All Union Scientific Research Institute), Sarov. Presently, he is a Scientific Researcher in the Plasma Physics Laboratory. His research interests include low-temperature plasma physics, physics of charged particle beams, atmospheric electrical phenomena, and numerical simulation of electron kinetics.

Leonid P. Babich was born in Kiev, Ukraine, in the former USSR, December 2, 1944. He received the undergraduate Diploma degree in nuclear engineering from the Moscow Engineering Physics Institute in 1968, Moscow, Russia, the Candidate of Science (Ph.D.) degree in theoretical physics from All Union Scientific Research Institute, Arzamas-16 (Sarov), Russia in 1974, and the Doctor of Science degree in plasma physics in 1987.

Since 1968, he has been with the Russian Federal Nuclear Center—VNIIEF, Sarov. Presently, he is Head of the Plasma Physics Laboratory. His research interests include nuclear weapons, acceleration of charged particles in dense gases, discharges for pumping of high-power gas lasers, high-power plasma electronics, nuclear synthesis in super high magnetic fields, nanosecond neutron and X-ray sources, ultrasonic for nondestructive testing, and atmospheric electricity. He delivered lectures for the XXII International Conference on Phenomena in Ionized Gases (USA, 1995) and the NATO Advance Research Workshop (Russia, 1997).

Igor M. Kutsyk was born June 11, 1957, in Jaroslavl', Russia. He received the Diploma degree in the field of quantum electronics from Moscow Engineering Physics Institute, Moscow, Russia, in 1980 and the Candidate of Science (Ph.D.) degree in theoretical physics from All Union Scientific Research Institute, Arzamas-16 (Sarov), Russia, in 1993.

Since 1980 he has been with the Russian Federal Nuclear Center—VNIIEF (formerly, All Union Scientific Research Institute), Sarov. He is a Senior Researcher in the Plasma Physics Laboratory. His research interests include gas lasers, gas-discharge physics, plasma chemistry, nonequilibrium electron kinetics, and atmospheric electrical phenomena.

Current Sheath Dynamics and X-Ray Emission Studies from Sequential Dense Plasma Focus Device

Ruby Gupta, S. R. Mohanty, R. S. Rawat, and M. P. Srivastava

Abstract—**A conventional dense plasma focus (DPF) device shows one or two compression phases. In the present paper, we report on a sequential DPF device with modified central electrode design to obtain more than two compression phases (i.e., multiple focusing). The sequential focusing was optimized by taking six different electrode designs for different filling gas pressures of argon. The optimization was inferred on the basis of intensity of spikes of voltage probe signals. The optimized central electrode design has then been used to study current sheath dynamics and X-ray emission using nitrogen laser shadowgraphy and diode X-ray spectrometer, respectively. Shadowgraphs show the breaking of current sheath during first focus as one part of it goes into radial collapse phase, and the other remains in axial acceleration phase. The one that remains in axial phase moves axially ahead in comparison to the other part of the current sheath. A bubble formation is observed after first focus phase. Shadowgraphs also show the formation of weak off-axis second focus. Finally, an on-axis third radial collapse is observed shadowgraphically (X-ray signals depict a multispike structure indicating hereby a sequential X-ray bursts from the sequential DPF device). The plasma electron temperatures have also been estimated using these X-ray signals.**

Index Terms—**Current sheath, dense plasma focus, electron temperature, sequential, shadowgraphy, X-ray emission.**

I. Introduction

THE dense plasma focus (DPF) device has been developed as a fusion device [1] with most of its studies being done in hydrogen and its isotopes. Because DPF is also a source of X-rays, energetic ions, and relativistic electrons, it has found its applications in other areas too. Use of energetic ions of DPF for phase changes of materials [2]–[5] and deposition of thin films [6], [7] has been reported. The relativistic electrons of this device have been used for microlithography [8]. The DPF device also emits soft X-rays during pinch and subsequent phases. There has been an increasing potential application of plasma X-ray sources in X-ray spectroscopy, X-ray cinematography, microfabrication, microscopy, laser pumping, and high-density microelectronic lithography [9]–[12]. However, X-ray cinematography requires a repetitive (sequential) pulsed source of X-rays and neutrons, for which many efforts are being made recently. Lee *et al.* [13] were the first to indicate the possibility of developing a sequential focus by placing a flat disk as an auxillary anode above the central electrode of the DPF device. Subsequently, Lee [14] proposed a theoretical model for sequential focusing. In another study, Nisar *et al.* [15] reported to achieve sequential focusing by placing a target disk being hung by two off-centered insulating supports instead of the single axially centered support used by Lee *et al.* [13]. Nisar *et al.* [15] interpreted sequential focusing due to the presence of two spikes in the voltage signal. However, two spikes in the voltage signal are easily seen, even in a conventional DPF device [16] without placing any target disk. Hence, the observation of only two spikes in a voltage signal cannot be taken as conclusive evidence of sequential focusing event in the DPF device.

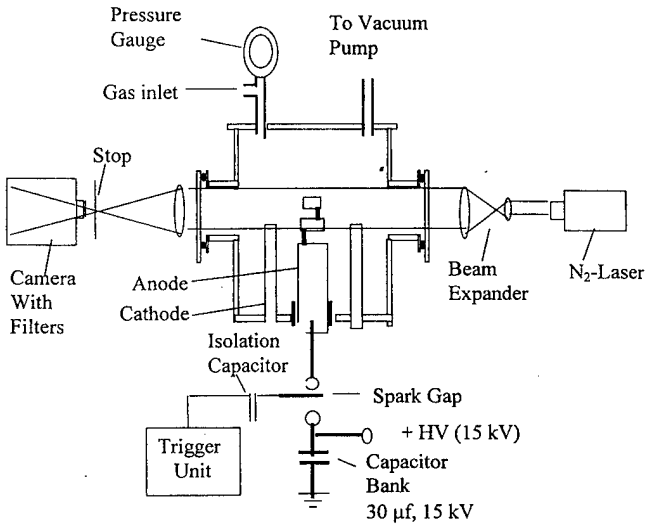


Fig. 1. Schematic of experimental setup.

In the present study, we tried several modified versions of anode design [17] to obtain sequential focusing in our DPF device. The voltage probe signals are used to optimize the best modified anode design for strong sequential focusing action. Such an optimized anode design has been used to study current sheath dynamics and X-ray emission. The subnanosecond N_2 laser shadowgraphic technique is used for assessing current sheath dynamics in the best optimized sequential focus device. The X-ray emission studies have been performed using a multichannel diode X-ray spectrometer. We have also estimated the plasma electron temperatures using these X-ray signals.

Manuscript received August 26, 1999; revised April 7, 2000. This work was carried out at Plasma Research Laboratory, Department of Physics and Astrophysics, University of Delhi.

R. Gupta and M. P. Srivastava are with the Department of Physics and Astrophysics, University of Delhi, Delhi-110 007, India.

S. R. Mohanty is with the Center of Plasma Physics, Dispur, Guwahati, Assam, India.

R. S. Rawat is with the Department of Physics/Electronics, SGTB Khalsa College, University of Delhi, Delhi-110 007, India.

Publisher Item Identifier S 0093-3813(00)07848-6.

0093–3813/00$10.00 © 2000 IEEE

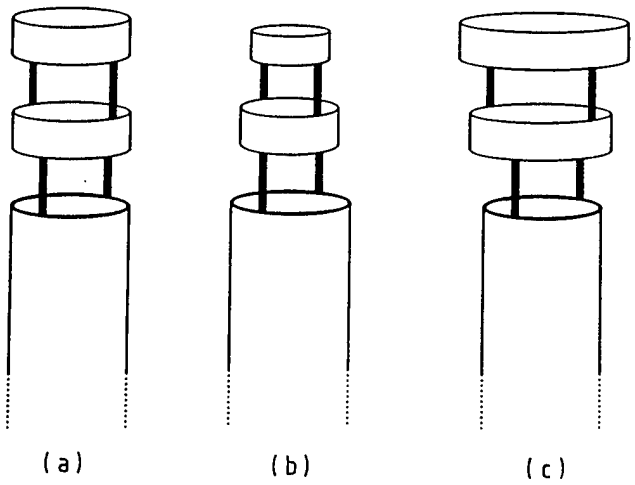


Fig. 2. Modified anode having cylindrical attachments with two supports: (a) each support length 12 mm; radii 9.5 and 9.5 mm; (b) each support length 12 mm; radii 8.5 and 7.5 mm; and (c) each support length 12 mm; radii 10.5 and 11.5 mm.

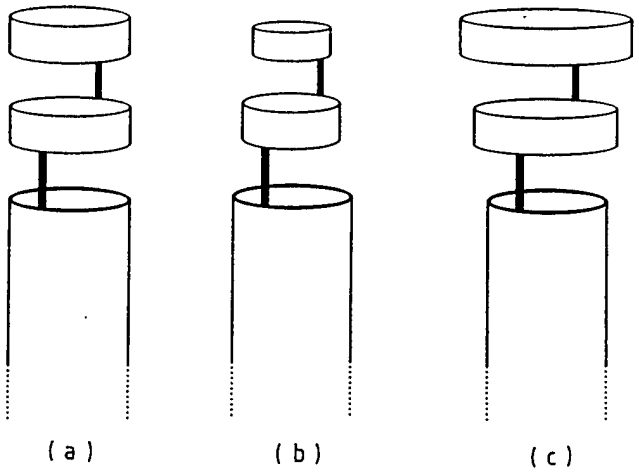


Fig. 3. Modified anode having cylindrical attachments with single support: (a) each support length 12 mm; radii 9.5 and 9.5 mm; (b) each support length 12 mm; radii 8.5 and 7.5 mm; and (c) each support length 12 mm; radii 10.5 and 11.5 mm.

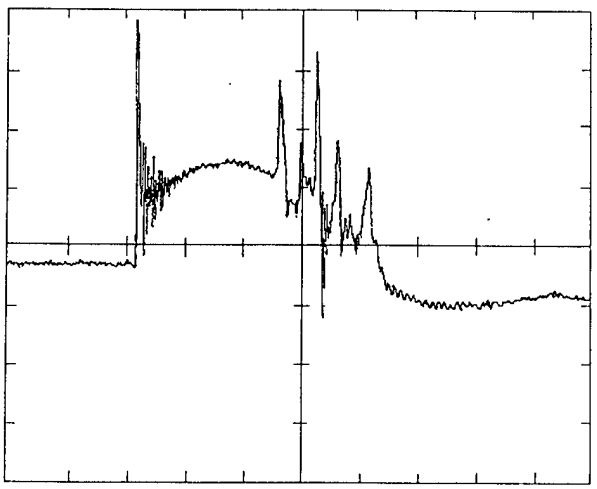
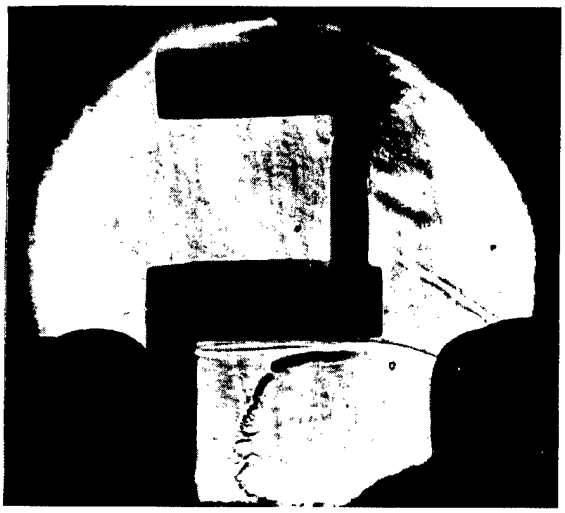
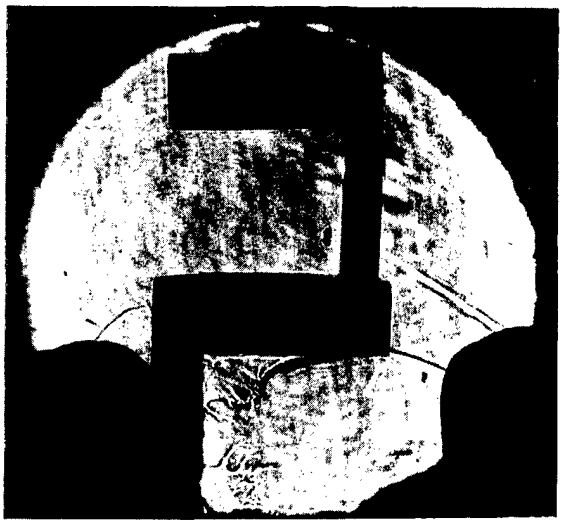


Fig. 4. Typical voltage probe signal for anode design of Fig. 3(b) at pressure = 80 Pa. Horizontal one division = 1 μs. Vertical one division = 1 V.



(a)



(b)

Fig. 5. Shadowgraphs of current sheath configurations showing first radial collapse. (a) $t_l = -16$ ns and (b) $t_l = +4$ ns, from first voltage spike.

II. Experimental Setup and Methodology

The DPF device used in this study is a 3.3-kJ Mather-type device with different modified anode designs whose schematic is shown in Fig. 1. The details of the device can be found elsewhere [18]. We have modified the conventional hollow cylindrical central electrode (anode) by taking several designs of anode, as shown in Figs. 2 and 3. We have taken the copper anode larger in length than the conventional DPF and have carved two cylindrical attachments on the top portion with either two supports or a single support, as shown in Figs. 2 and 3, respectively. The effective length and radii of the main part of the anode without supports and cylindrical attachments is 15.0 cm and 9.5 mm, respectively. Figs. 2(a) and 3(a) show that the cylindrical attachments have radii same as the main part of the anode, whereas Figs. 2(b) and 3(b) show that their radii decrease gradually with respect to the main part of the anode. On the other hand, Figs. 2(c) and 3(c) have their radii increasing gradually with respect to the main part of the anode. The common feature in all of these designs is that the length of support is a little more than the

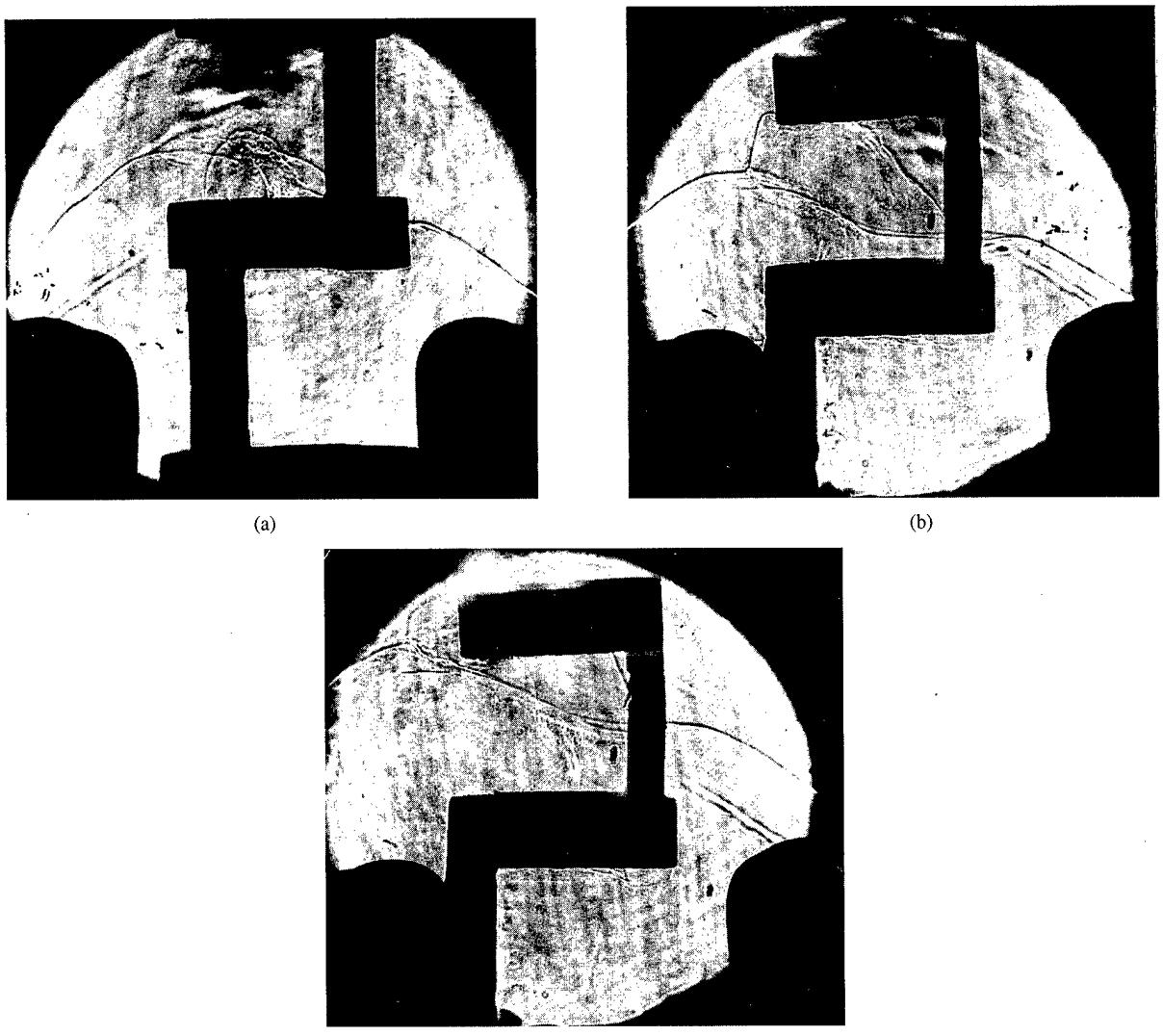


Fig. 6. Shadowgraphic sequence showing current sheath dynamics after first focus formation. (a) $t_l = +98$ ns, (b) $t_l = +168$ ns, and (c) $t_l = +220$ ns, from first voltage spike.

radius of the preceding part. We have done this because Lee *et al.* [13] observed that the focus formation gets hindered if there is any obstruction being placed at a distance less than the radius of central electrode. Nisar *et al.* [15] used a target disk that is not connected to the central electrode. The outer electrodes consist of six copper rods whose design was kept same throughout the study. The device is operated with argon as the filling gas in the pressure range of 50 to 160 Pa. The device is powered by a low-inductance 30-μF capacitor bank charged up to 14.2 kV. The Tektronix TDS 784 digital storage oscilloscope (located at Plasma Research Laboratory, Department of Physics and Astrophysics, University of Delhi) has been used for recording voltage probe, laser flash, and X-ray signals. The sequential focusing was optimized by taking different electrode designs tested for different filling gas pressures of argon. The anode design shown in Fig. 3(b) gave the strongest sequential focusing action, inferred on the basis of the voltage probe signal, which was then used for studying current sheath dynamics and X-ray emission. The plasma electron temperatures were estimated from X-ray signals.

We performed shadowgraphy to study the current sheath dynamics in different phases of sequential DPF. The shadowgraphic system used in the present study is similar to that of Lee *et al.* [19]. This shadowgraphic system uses a homemade nitrogen laser [20], with laser gap being operated at atmospheric pressure of commercially available N_2 gas. The laser pulse ($\lambda = 337$ nm) of fairly good beam quality and pulsewidth of about 1 ns (spatial resolution of 0.2 mm) may easily be obtained. High-speed polaroid film is used for shadowgraph recording. The instant of plasma focus is defined as the time instant of the peak of voltage spike on the voltage probe signal. The plasma focus times are found to vary from shot to shot, because of the jitter due to the parallel-plate swinging-cascade spark-gap and focus rundown time. The jitter in different focus time instants and laser flash time instant compel us to take a large number of shots to record the shadowgraphs of interest and to draw a meaningful current sheath dynamics sequence

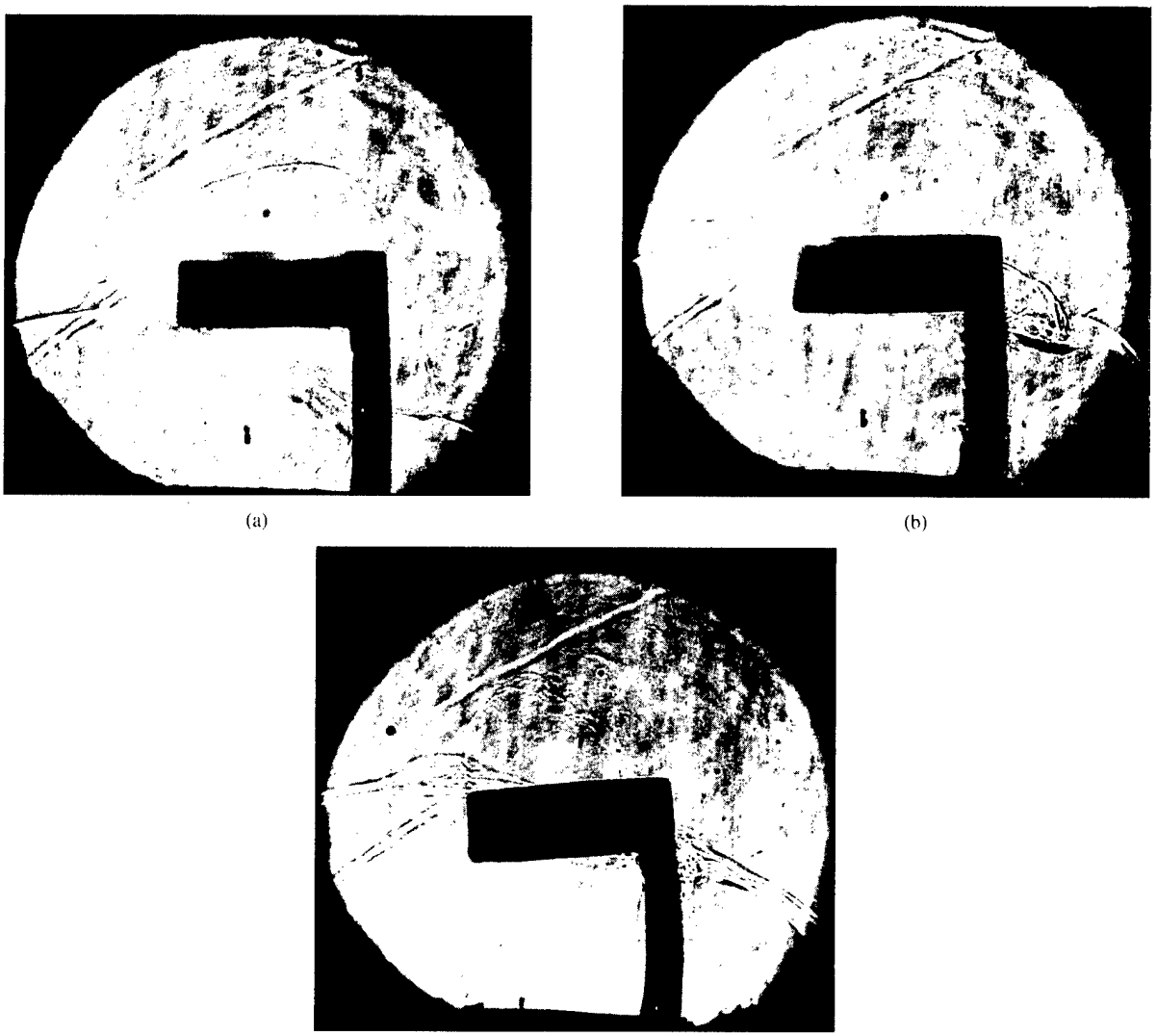


Fig. 7. Shadowgraphic sequence showing current sheath dynamics during second focus formation. (a) $t_1 = -86$ ns, (b) $t_1 = -34$ ns, and (c) $t_1 = +8$ ns, from second voltage spike.

for modified anode. It is important to mention here that the diagnostic viewport window, which is used for shadowgraphy in our device, is at such a height that it was not possible to record the main acceleration phase, i.e., the acceleration phase at the main anode before first focus.

X-ray emission from sequential plasma focus has been investigated and reported by us in one of our earlier papers [21]. The same multichannel diode X-ray spectrometer (DXS) [21] has been used to study X-ray signals.

III. Results and Discussion

The DPF device with modified anode design is operated at 14.2 kV. The voltage signals for all of the anode designs with filling pressure in the range of 60–80 Pa show three or more spikes. For gas pressures beyond 160 Pa no focus formation takes place for all of the anode designs. For operating pressures greater than 80 Pa, voltage peaks reduce in number and intensity with focusing being delayed. Moreover, for pressures below 60 Pa (in the present work up to 50 Pa), intensity of peaks on voltage signals decreases gradually.

It has been observed that the best sequential focusing is obtained for central electrode design shown in Fig. 3(b). The typical voltage probe signal for this central electrode design is shown in Fig. 4. All further studies of current sheath dynamics and X-ray emission were done only on the anode design shown in Fig. 3(b). Until specified, all results are for argon filling gas pressure of 80 Pa.

Voltage probe signals typically contain four to five voltage spikes for our sequential DPF device [17]. Presently, a more detailed and systematic study has been done for the voltage probe signals by taking many shots and presented here. The average time of occurrence, along with standard deviation, of each spike after the initial breakdown has been estimated over ten DPF shots from voltage probe oscillographs using simple statistical methods. The first spike has been found to occur at about 2.54 ± 0.30 μs after the initial breakdown at the glass insulator. This invariably is seen to follow by a relatively weak second spike occurring at about 2.82 ± 0.26 μs after the breakdown. The third one is the most intense of all and is found to occur at 3.23 ± 0.32 μs after the breakdown. This is followed

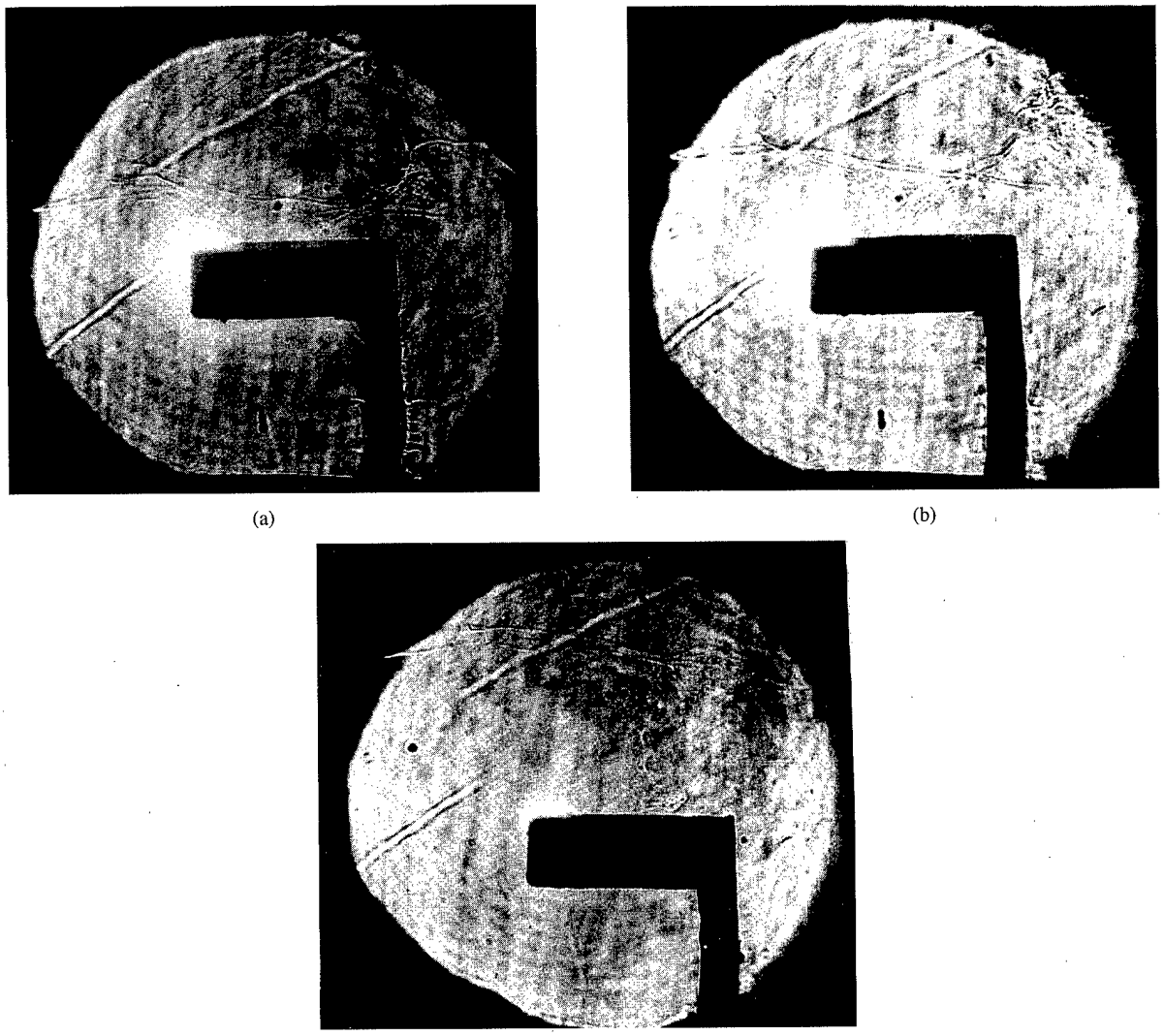


Fig. 8. Shadowgraphic sequence showing current sheath dynamics after second focus formation. (a) $t_l = +114$ ns, (b) $t_l = +144$ ns, and (c) $t_l = +176$ ns, from second voltage spike.

by one or two more spikes that are generally as intense as the first one. Voltage probe signals give us the crude idea of what is happening in sequential focusing device.

The shadowgraphs shown in Fig. 5(a) and (b) are taken at $t_l = -16$ and $+4$ ns with respect to the peak of the first spike on voltage probe signals. Both of these shadowgraphs show the collapse of current sheath at the top of the main part of the anode. It may be noted that the sheath from the nonsupport side has almost reached the center of the top of the anode, whereas the support-side plasma sheath is still continuing in the axial phase, as shown in Fig. 5(a) and (b). This is possibly due to the following reasons. First, the support acts like an obstruction in the usually followed path of the radially collapsing current sheath. Second, the support being off-axis sustains the current density also off-axis. This makes the magnetic field much stronger toward the support side, causing greater axial acceleration of the current sheath on the support side. The shadowgraph shown by Fig. 5(b) shows the nonuniform broken plasma focus column after the peak compression phase. It also shows the current sheath entering into the second axial acceleration phase on the first cylindrical attachment from the nonsupport side. The sheath from the support side, which is already in axial acceleration phase, is axially ahead in comparison to the nonsupport-side sheath.

The shadowgraph sequence shown in Fig. 6, taken at $t_l = +98$, $+168$, and $+220$ ns after the first focus peak, depicts the current sheath dynamics after first focus formation. The shadowgraph in Fig. 6(a) shows that the current sheath from the support side has climbed over the first cylindrical attachment and has entered into radial collapse phase, whereas the current sheath from the nonsupport side is still in the axial acceleration phase. This shadowgraph also shows a "bubble formation" in front of the axially moving current sheath [seen more clearly in Fig. 6(b)]. This "bubble formation" has taken place typically due to the strong focusing event (first focus) at the top of the main part of the anode. The radial collapse on the top of first cylindrical attachment is visible in Fig. 6(b) and (c). We can also observe the axial advancement of the bubble, which is formed after first focus in Fig. 6(b) and (c). It can be inferred from Fig. 6(b) and (c) that the current sheath collapses off-axis (not seen in the

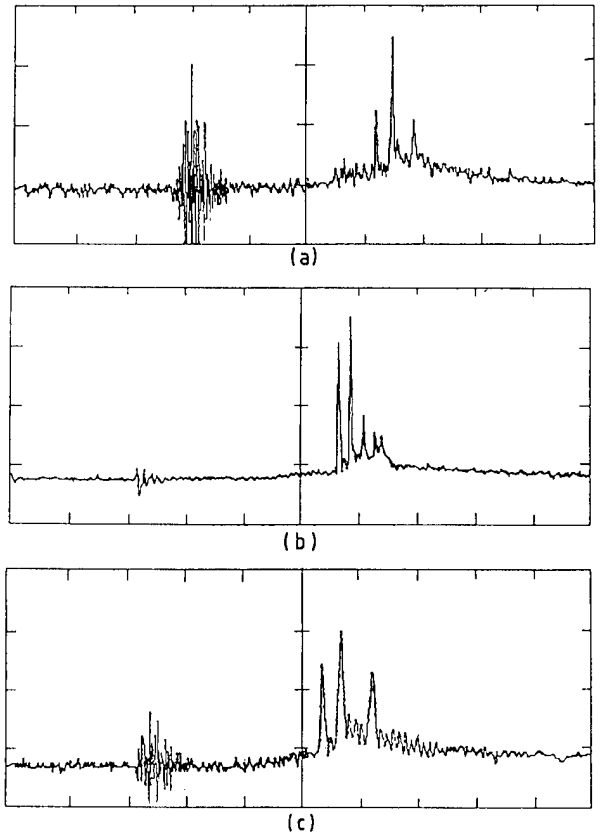


Fig. 9. Three typical X-ray signals at 60-, 100-, and 120-Pa filling gas pressure of argon. Horizontal one division = 1 μs. Vertical one division = 1 V.

shadowgraph). It may also be mentioned that these three shadowgraphs are occurring at a time instant between the first and second major spikes in the voltage probe signal.

The shadowgraphic sequence shown in Fig. 7 is seen to coincide with the second major voltage spike at time instants of -86, -34, and $+8$ ns, respectively, with respect to the peak of second voltage spike, and thus, it is related to the second focus formation at the top of first cylindrical attachment [e.g., see Fig. 7(c), where it is clear that the focus column happens to be just visible behind the vertical support of the second cylindrical attachment]. This set of shadowgraphs has much more prominent current sheaths in comparison to the shadowgraphic set of Fig. 6. We can also observe the axially moving bubble in front of these radially collapsing current sheathes. It can also be seen that the current sheath that was initially lagging behind (as far as axial position is concerned) is now trying to catch the other sheath. The reason being is that the second support for second cylindrical attachment is on the diametrically opposite side of the first one. Therefore, current density now becomes larger on the second support on the diametrically opposite side of the first support, thus, creating a stronger magnetic field toward this second support. This stronger magnetic field will push the second support-side current sheath to move faster so that the two sheaths now collapse cohesively on the axis of the anode.

The shadowgraphs in Fig. 8 shows the current sheaths from both sides entering into the third collapse phase after climbing over the second cylindrical attachment. These shadowgraphs show almost on-axis [slightly to the right of axis in Fig. 8(c)]

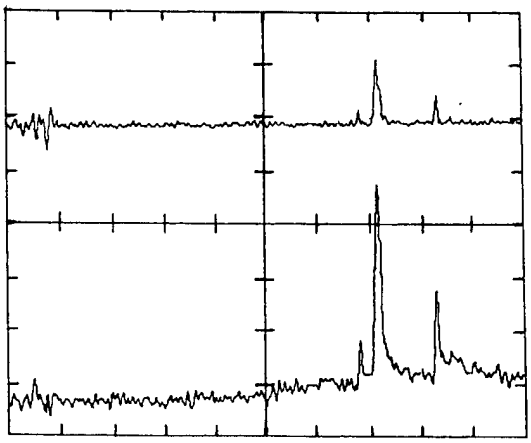


Fig. 10. Comparison of the X-ray signals for estimation of electron temperature. Upper signal is observed in pin diode window covered by 24-μm mylar + 10 μm Cu. Lower signal is observed in pin diode window covered by 24-μm mylar. Horizontal one division = 1 μs. Vertical one division = 1 V.

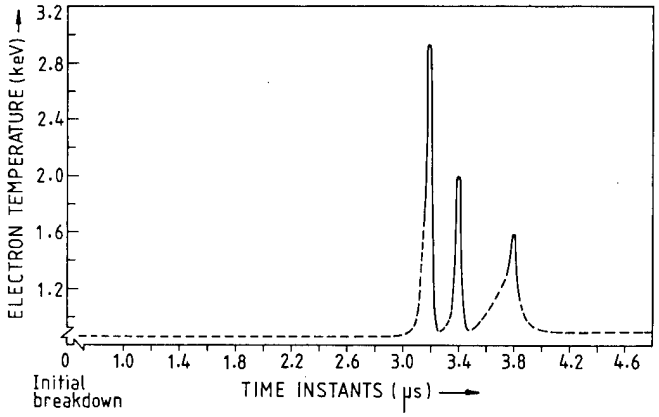


Fig. 11. Typical time history of electron temperature in plasma focus.

radial collapse, resulting in a strong third focus. This is also indicated by the fact that the third peak on the voltage probe signal is the sharpest one. The bubble can still be seen moving in front of current sheath.

X-ray emission from sequential plasma focus has been reported by us earlier [21]. In the present paper, we systematically analyze the quantitative measurements of time history of X-ray signals from many DPF shots, using that channel of DXS in which the PIN diode window is covered by 149-μm aluminized mylar. Three such typical X-ray signals taken at different filling gas pressure of argon are shown in Fig. 9. All of these signals show that there are about three to four X-ray spikes. It may be noted that X-ray spikes occur with a certain time delay with respect to voltage spikes. It has been estimated, averaged over ten DPF shots, with each one at 80 Pa, that the first, second, and third X-ray spikes occur at about 3.16 ± 0.11 μs, 3.37 ± 0.09 μs, and 3.82 ± 0.27 μs, respectively, after initial breakdown.

For estimating the plasma electron temperature, the X-ray signals are observed simultaneously in two channels 1 and 4 of the DXS. In channel 1 of DXS, the PIN diode window is covered by 24-μm mylar, whereas in channel 4, the PIN diode window is covered by 24-μm mylar + 10-μm Cu. The peak height of the spike in the X-ray emission from the channel 1 is more than

the channel 4. One such typical pair of X-ray signals is shown in Fig. 10. Adopting the method used earlier [17], plasma electron temperature during third, fourth, and fifth voltage spikes has been estimated to be 3.08 ± 0.64 keV, 2.28 ± 0.56 keV, and 1.77 ± 0.36 keV. These estimations are averaged over ten DPF shots at an argon-filling gas pressure of 80 Pa. Fig. 11 shows the typical time history of electron temperature in plasma focus. It is noteworthy to mention here that for obtaining the time history of plasma electron temperatures, we zoomed the pair of X-ray signals with a time resolution of 10 ns (one such typical pair being shown in Fig. 10 with 1-μs time resolution), along with voltage probe signal, and calculated the intensity ratio of X-ray signals after every 10 ns. The plasma electron temperature versus time data is simply compressed in time scale and is shown in Fig. 11 with respect to the initial breakdown.

IV. Conclusion

A sequential DPF device has been successfully developed by modifying the central electrode design of a conventional DPF device. Shadowgraphic studies on optimized sequential DPF show modification in plasma sheath structure and its dynamics in comparison to conventional DPF. It has been observed that the current sheath gets broken during first focus because of obstruction provided by the support to the first cylindrical attachment. One portion of the current sheath goes into radial collapse phase, whereas the other remains in axial phase resulting in first focus formation of modest strength. The current sheath that remains in axial phase moves ahead in comparison to the other portion and, thus, forms a weak off-axis second focus. A strong on-axis third focus is shadowgraphically seen to form because the current sheath collapses axisymmetrically. The multispike structure of X-ray signals establishes sequential DPF as a source of sequential X-ray pulses as well.

Acknowledgment

R. Gupta is grateful to the Council of Scientific and Industrial Research, India, for providing a Junior Research Fellowship, which has helped her in carrying out this investigation. The authors would like to thank Prof. S. Lee for providing the ICTP-UM collaboration for fabrication of the DPF at Delhi University.

References

[1] J. W. Mather, "Dense plasma focus," in *Methods of Experimental Physics*, R. H. Lovberg, Ed, London, U.K.: Academic, 1970, vol. 9, pp. 187–249.

[2] R. S. Rawat, M. P. Srivastava, S. Tandon, and A. Mansingh, "Crystallization of an amorphous lead zirconate titanate thin film with a dense-plasma-focus device," *Phys. Rev. B*, vol. 47, pp. 4858–4862, 1993.

[3] R. Sagar and M. P. Srivastava, "Amorphization of thin film of Cds due to ion irradiation by dense plasma focus," *Phys. Lett. A*, vol. 183, pp. 209–213, 1993.

[4] M. P. Srivastava, S. R. Mohanty, S. Annapoorni, and R. S. Rawat, "Diode like behavior of an ion irradiated polyanyline film," *Phys. Lett. A*, vol. 215, pp. 63–68, 1996.

[5] P. Agarwala, S. Annapoorni, M. P. Srivastava, R. S. Rawat, and P. Chauhan, "Magnetite phase due to energetic argon ion irradiation from a dense plasma focus on hematite thin film," *Phys. Lett. A*, vol. 231, pp. 434–438, 1997.

[6] C. R. Kant, M. P. Srivastava, and R. S. Rawat, "Thin carbon film deposition using energetic ions of a dense plasma focus," *Phys. Lett. A*, vol. 226, pp. 212–216, 1997.

[7] ——, "Dense plasma focus energetic ions based fullerene films on Si(111) substrate," *Phys. Lett. A*, vol. 239, pp. 109–114, 1998.

[8] P. Lee, X. Feng, G. X. Zhang, M. H. Liu, and S. Lee, "Electron lithography using a compact plasma focus," *Plasma Source Sci. Technol.*, vol. 6, pp. 343–348, 1997.

[9] J. S. Pearlman and J. C. Riordan, "X-ray lithography using a pulsed plasma source," *J. Vacuum Sci. Technol.*, vol. 19, pp. 1190–1193, 1981.

[10] R. Feder, J. S. Pearlman, J. C. Riordan, and J. L. Costa, "Flash X-ray microscopy with a gas jet plasma source," *J. Microscopy*, vol. 135, pp. 347–351, 1984.

[11] J. L. Porter, R. B. Spielman, M. K. Matzen, E. J. Mcguire, L. E. Ruggles, and M. F. Mvargas, "Demonstration of population inversion by resonant photopumping in a neon gas cell irradiated by a sodium Z pinch," *Phys. Rev. Lett.*, vol. 68, pp. 796–799, 1992.

[12] Y. Kato and S. H. Be, "Generation of soft X-rays using a rate gas-hydrogen plasma focus and its application to X-ray lithography," *Appl. Phys. Lett.*, vol. 48, pp. 686–688, 1986.

[13] S. Lee, M. A. Alabraba, A. V. Gholap, S. Kumar, K. H. Kwek, R. S. Rawat, and J. Singh, "Effect of targets on plasma focus dynamics," *IEEE Trans. Plasma Sci.*, vol. 18, pp. 1028–1032, 1990.

[14] S. Lee, "A cascading plasma focus," *IEEE Trans. Plasma Sci.*, vol. 19, pp. 912–919, 1991.

[15] M. Nisar, F. Y. Khattak, G. Murtaza, M. Zakaullah, and N. Rashid, "Sequential focusing in a Mather type focus," *Physica Scripta*, vol. 47, pp. 814–816, 1993.

[16] R. S. Rawat, M. P. Srivastava, and S. R. Mohanty, "Study of current sheath dynamics in dense plasma focus in the presence of axial magnetic field using laser shadowgraphic technique," *IEEE Trans. Plasma Sci.*, vol. 22, pp. 967–972, 1994.

[17] S. R. Mohanty, "X-ray studies from dense plasma focus and plasma processing," Ph.D. dissertation, Univ. Delhi, Delhi, India, 1997.

[18] S. Lee, T. Y. Tou, S. P. Moo, M. A. Eissa, A. V. Gholap, K. H. Kwek, S. Mulyodrono, A. J. Smith, S. Suryadi, W. Usada, and M. Zakaullah, "A simple facility for teaching of plasma dynamics and plasma nuclear fusion," *Am. J. Phys.*, vol. 56, pp. 62–68, 1988.

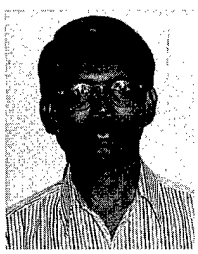
[19] S. Lee, M. A. Alabraba, A. V. Gholap, S. Kumar, K. H. Kwek, M. Nisar, R. S. Rawat, and J. Singh, "A simple shadowgraphic system and some results," *J. Phys. Malaysia*, vol. 11, pp. 1–11, 1990.

[20] K. H. Kwek, T. Y. Tou, and S. Lee, "A preionized nitrogen laser as a diagnostic light source for fast pulsed experiment," *IEEE Trans. Instrum. Meas.*, vol. 38, pp. 103–107, 1989.

[21] S. R. Mohanty, R. S. Rawat, and M. P. Srivastava, "X-ray emission from dense plasma sequential focus device," *J. Plasma Fusion Res. SERIES*, vol. 2, pp. 320–323, 1999.



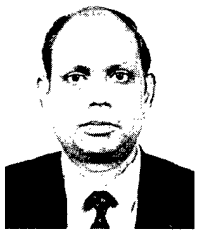
Ruby Gupta received the B.Sc. and M.Sc. degrees in physics from University of Delhi, India in 1994 and 1996, respectively. She is a Senior Research Fellow of CSIR and pursuing her research work for the last three years for a Ph.D. degree. She has published one paper.



S. R. Mohanty received the B.Sc. and M.Sc. degrees from Utkal University, India in 1986 and 1989, respectively. He received the Ph.D. degree from University of Delhi in 1998. He is presently an Assistant Professor at Centre of Plasma Physics (CPP), Guwahati, India. He visited University of Malaya in 1990. He has been actively engaged in experimental plasma research for the last ten years. He has published about ten research papers and is looking after the experimental Plasma Physics activities at CPP.



R. S. Rawat received the B.Sc., M.Sc., and Ph.D. degrees in physics from University of Delhi, India, in 1985, 1987, and 1994, respectively, and has been teaching for the last eight years. Presently, he is a Senior Lecturer in the Department of Physics and Electronics, SGTB Khalsa College, University of Delhi and visiting Nanyang Technological University, Singapore as a Research Fellow. As a Ph.D. student, he had visited University of Malaya in 1990. He had been actively engaged in experimental Plasma Research for the last twelve years and has published about twenty papers on basic plasma processes and plasma applications using dense plasma focus. He is an active young collaborator in the research group of Plasma Research Laboratory of Delhi University.



M. P. Srivastava, is a Professor in the Department of Physics and Astrophysics, University of Delhi, he received the B.Sc. and M.Sc. degrees in physics from University of Lucknow in 1963 and 1965, respectively. He received the Ph.D. degree from Indian Institute of Sciences, Bangalore in 1969. He has been teaching in the University of Delhi since 1970 and has been in active research since 1965. He is the author of about 85 research papers and has got two patents in the process. He has supervised a large number of students for their research work and sixteen students have been awarded Ph.D. degree under his supervision. A large number of students have also written their dessertation for M.Sc. and M.Phil. degree under his supervision. A number of Senior Research Associates, Lecturers, Senior Lecturers and Readers have also been associated with him in their research work. He nucleated and developed a full fledged Experimental Plasma Research group at the Department of Physics, University of Delhi. A very active research work in the Plasma Research Laboratory, University of Delhi, is going on under his leadership on basic plasma phenomena and plasma processing of materials particularly on phase change of materials and thin film deposition, using Dense Plasma Focus device. Plasma Research Laboratory at Delhi University is also networked with 33 member institution in 21 countries spread over Asia and Africa region.

He has lectured at various Universities/Institutes in USA, USSR, Europe, Japan and South East Asia, and has delivered invited lectures in a large number of international and national conferences. He has been Platinum Jubilee Lecturer of Physics Section of 87 Indian Science Congress Association in the year 2000. He is Vice President of Asian African Association for Plasma Training (AAAPT), with its headquarters at Malaysia, since 1988. He is looking after Delhi regional centre of AAAPT through which he has trained more than a dozen researchers in Experimental Plasma Physics. He is presently President of Plasma Science Society of India, 1999–2000 and remained vice-president during 1990–91. He has been Associate member of International Centre for Theoretical Physics in 1983, Trieste, Italy. He has been involved in the organization of various International and National Conferences in various capacities. He was member of the International Organizing Committee of 1987 ICPP (Kiev, USSR), Co-chairman of International Organizing Committee of 1989 International Conference of Plasma Physics ICPP (New Delhi, India), and member of International Advisory Committees of 1992 ICPP (Innsbruck, Austria), 1994 ICPP (Foz D Iguacu, Brazil), 1996 ICPP (Nagoya, Japan) and 2000 ICPP (Qubec, Canada). He has been member of American Physical Society, New York Academy of Sciences, American Geophysical Union and life members of National Academy of Sciences, Plasma Science Society of India and Indian Science Congress Association.

Fundamental Properties of Inert Gas Mixtures for Plasma Display Panels

Georgios Veronis, Umran S. Inan, *Senior Member, IEEE*, and Victor P. Pasko

***Abstract*—A fundamental kinetic model is used to compare the luminous efficiency of different compositions of Ne–Xe, He–Xe, and Ne–Xe–Ar mixtures in plasma display panels. A self-sustaining condition is used to estimate the breakdown electric field E_k, accounting also for Penning ionization. The excitation frequency of Xe states that emit UV photons is calculated for applied electric field values ranging from $0.2E_k$ to $5E_k$. Light generation efficiency, defined as the ratio of the energy spent in excitation of UV emitting states of Xe per unit volume and per unit time versus dissipated electrical power, is an increasing function of the Xe concentration N_{Xe} in both the Ne–Xe and He–Xe cases, although He–Xe mixtures were found to be somewhat less efficient. The fractional increase in efficiency is very small for $N_{\mathrm{Xe}} > 0.1N$. The addition of small amounts of Ar in Ne–Xe mixtures leads to insignificant changes in efficiency or breakdown voltage level. Results of a one-dimensional (1-D) self-consistent simulation of an ac plasma display cell are consistent with the conclusions derived based on the homogeneous unbounded kinetic analysis.**

***Index Terms*—Gas discharge, plasma display panel (PDP), Xe.**

I. Introduction

PLASMA display panels (PDPs) are one of the leading candidates in the competition for large-size, high-brightness flat panel displays, suitable for high-definition television (HDTV) monitors [1], [2]. Their advantages are high resolution, fast response, wide viewing angle, low weight, and simple manufacturing process for fabrication. The fact that they are expected to be the next generation of TV displays is evident in the remarkable recent progress of PDP technology development and manufacturing [3], [4].

One of the most critical issues in PDP research and technology development is the improvement of luminance and luminous efficiency [1], which is dependent on the gas mixture composition, phosphor efficiency, driving voltage characteristics, and cell geometry. PDP cells can operate only if the applied voltage is held within certain limits. The minimum and maximum values of the applied voltage define the margin of the panel [5]. These limits are determined by the breakdown voltage. In some PDP designs, reducing the breakdown voltage may be of higher priority than is increasing the efficiency, because of the high cost of high-voltage driving circuits [1]. In this article, we focus our attention on the effects of gas mixture composition on light generation efficiency and on the breakdown voltage.

Manuscript received October 29, 1999; revised March 14, 2000. This work was supported by the National Science Foundation under Grant ATM-9731170.

The authors are with the Space, Telecommunications, and Radioscience Laboratory, Department of Electrical Engineering, Stanford University, Stanford, CA 94305-9515 USA (e-mail: inan@nova.stanford.edu).

Publisher Item Identifier S 0093-3813(00)07374-4.

Typical plasma displays consist of two glass plates, each with parallel electrodes deposited on their surfaces. The electrodes are covered with a dielectric film. The plates are sealed together with their electrodes at right angles, and the gap between the plates is filled with an inert gas mixture. A protective MgO layer is deposited above the dielectric film. The role of this layer is to decrease the breakdown voltage caused by the high secondary electron emission coefficient of MgO. The discharge is initiated by applying a voltage pulse to the electrodes. Xenon gas mixtures are used to efficiently generate UV photons. The UV photons emitted by the discharge hit the phosphors deposited on the walls of the PDP cell and are converted into visible photons. Each cell contains phosphor that emits one primary color—red, green, or blue.

In this paper, we study different Xenon gas mixtures and theoretically investigate their efficiency in generating UV photons. In particular, we examine three different cases, i.e., Ne–Xe, He–Xe, and Ne–Xe–Ar. In each case, we investigate the effect of the variation of the percentage of the constituent gases on the efficiency of the mixture and on the breakdown voltage. In Section II, we describe our approach, based on the fundamental processes that determine the gas mixture efficiency. In Section III, we present the results of our model. In Section IV, a one-dimensional (1-D) self-consistent simulation is used to assess the validity of the conclusions derived from the homogeneous and unbounded kinetic model. Our conclusions are summarized in Section V.

II. Formulation

In this work, we investigate the effect of the gas mixture on PDP performance from the point of view of the fundamental inherent properties of the constituent gases. For this purpose, we rely on exact numerical solutions of the kinetic Boltzmann equation in a homogeneous, unbounded system while accurately accounting for all the known processes of excitation as well as ionization and other losses. Our chosen measure of comparison of different mixtures is the efficiency η, defined as the ratio of the energy spent in excitation of UV emitting states of Xe per unit volume and per unit time, over the dissipated power per unit volume.

The luminous efficiency of a PDP cell is a measure of the number of photons emitted per unit power dissipated in the discharge. In color PDPs, the purpose of the discharge is to produce UV photons that are then converted to visible light by means of phosphors. UV photons that excite the phosphors and produce visible light [6] are emitted by certain excited states of Xe [$Xe^*(^3P_1)$ (resonant state) at 147 nm, $Xe_2^*(O_u^+)$ at 150 nm,

0093–3813/00$10.00 © 2000 IEEE

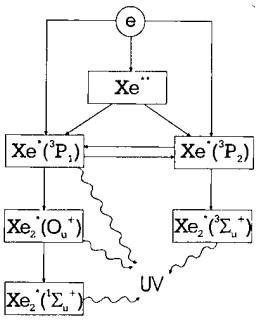


Fig. 1. Block diagram of reaction channels related to UV emitting excited states of Xe.

and $Xe_2^*(^3\Sigma_u^+)$ and $Xe_2^*(^1\Sigma_u^+)$ at 173 nm (excimer states)]. Although the duration of the discharge current pulse is on the order of 10 ns, emission of UV photons lasts for about 5 μs because of the lifetimes of some of the excited species [6]. Some excited states of Ne also radiate photons [7] [$Ne^*(^1P_1)$ at 736 Å, $Ne^*(^3P_1)$ at 743 Å], but these are not in the UV range and the visible orange glow actually deteriorates color purity [8]. Shown in Fig. 1 is a block diagram of reaction channels related to the excited states of Xe that produce UV photons [6]. Atoms in the $Xe^*(^3P_1)$, $Xe^*(^3P_2)$ (metastable), and Xe^{**} (sum of the $6s'$, $6p$, $5d$, $7s$ states) excited states are mainly produced by electron impact excitation reactions. Because stepwise ionization is negligible and no other important loss mechanisms exist, all of the energy going into these excited states leads to the production of UV photons [6]. As a result, for a given gas mixture, the number of UV photons emitted by excited Xe atoms per electron in the discharge is determined by the excitation frequency ν_{exc} of the $Xe^*(^3P_1)$, $Xe^*(^3P_2)$, and Xe^{**} excited states as a function of the reduced electric field E/N, where E is the electric field and N is the gas density. The energy spent on excitation of UV emitting states of Xe per unit volume and per unit time is

$$P_{\rm UV} = \nu_{exc} N_e \varepsilon_{\rm UV}$$

where N_e is the electron number density and $\varepsilon_{\rm UV}$ is the energy of an emitted UV photon, equal to the energy spent on the excitation of a Xe atom. (We consider 150-nm photons and do not take into account the frequency distribution of UV radiation, so that $\varepsilon_{\rm UV} \simeq 8.3$ eV). Although some UV emitting excited states of Xe have relatively long lifetimes, all of the energy spent on excitation of UV emitting states of Xe is eventually converted to UV photons. For our purposes, we can thus consider the efficiency η to be equal to the luminous efficiency.

The power dissipated in the discharge is determined by the voltage applied to the electrodes of the PDP cell and the discharge current. The driving voltage is related to the breakdown voltage, which depends on the gas mixture used. The dissipated power per unit volume caused by electron current is

$$P_{diss} = EJ_e = N_e q_e \mu_e E^2$$

where

J_e electron current density;
q_e electronic charge;
μ_e electron mobility.

Thus, the luminous efficiency is given as

$$\eta = \frac{\nu_{exc}\varepsilon_{\rm UV}}{q_e \mu_e E^2} = 8.3 \left[\frac{\nu_{exc}}{\mu_e E^2}\right]. \quad (1)$$

Both of the quantities ν_{exc} and μ_e in (1) exhibit highly nonlinear dependence on the electric field E, so that the luminous efficiency can only be evaluated numerically. In this paper, we determine η by numerically solving the full electron Boltzmann equation to compare the efficiency of different gas mixtures by calculating the breakdown voltage and excitation of Xe states that lead to the production of UV photons. It should be noted that η, as defined in (1), represents the efficiency of the electrons in exciting UV emitting states of Xe. In an actual PDP cell, a fraction of the input energy is dissipated by the ions. However, (1-D) self-consistent calculations (Section IV) indicate that the dependence of the actual discharge efficiency on gas mixture composition is nevertheless well represented by η.

A. Ne–Xe Mixtures

For our homogeneous and unbounded system, we use a breakdown voltage equivalent to that which would result in a self-sustaining condition in a 1-D parallel plate geometry, with plate separation $d = 100$ μm, corresponding to the gap length of a typical PDP cell. This assumption is appropriate because the actual voltage that must be applied to the electrodes of the PDP cell to cause breakdown in the gas is directly proportional to the voltage obtained from the self-sustaining condition. In the Ne–Xe mixture case, this condition can be written as [9], [10]

$$\frac{\alpha_{\rm Ne}\gamma_{\rm Ne} + (\alpha_{\rm Xe} + \alpha_P)\gamma_{\rm Xe}}{\alpha_{\rm Ne} + \alpha_{\rm Xe} + \alpha_P}\left[e^{(\alpha_{\rm Ne}+\alpha_{\rm Xe}+\alpha_P)d} - 1\right] = 1 \quad (2)$$

where $\alpha_{\rm Ne} = \nu_{\rm Ne}/v_d$ and $\alpha_{\rm Xe} = \nu_{\rm Xe}/v_d$ are the partial first Townsend ionization coefficients for Ne and Xe, respectively, $\nu_{\rm Ne}$ and $\nu_{\rm Xe}$ are the corresponding partial ionization frequencies caused by direct ionization of neutral atoms by electrons, v_d is the electron drift velocity, and $\gamma_{\rm Ne}$ and $\gamma_{\rm Xe}$ are, respectively, the secondary electron emission coefficients for Ne and Xe ions impingent on MgO. The quantity α_P is the effective partial first Townsend ionization coefficient per electron caused by ionization by metastable neon atoms (Penning ionization). Neon metastable atoms have a much longer lifetime than do the other excited states of Ne and have an energy of $\varepsilon_{\rm m} \simeq 16.6$ eV. Thus, they are capable of ionizing the atoms of other gases having an ionization energy less than 16.6 eV [11]. The process is highly efficient, if the energy difference between the levels concerned is small [12].

The pressure p and the gas temperature T are assumed, respectively, to be 500 Torr and 300 K, consistent with the usual operation conditions of PDPs [6]. The ionization frequencies $\nu_{\rm Ne}$ and $\nu_{\rm Xe}$, as well as the electron drift velocity v_d, are calculated as a function of the reduced electric field E/N by numerically solving the full electron Boltzmann equation, using the Boltzmann code ELENDIF [13]. Electron–atom collision cross sections for Ne and Xe are taken from the SIGLO series [14], whereas $\gamma_{\rm Ne} = 0.5$ and $\gamma_{\rm Xe} = 0.05$ are taken from Meunier *et al.* [6]. It should be noted that in many cases, there is a lack of data concerning secondary electron emission coefficients and guessed values are often used in PDP models [6]. The results of

the models are sensitive to the uncertainties in these coefficients [10].

In the Ne–Xe case, the energy of the metastable atom is $\varepsilon_m \simeq 16.6$ eV, whereas the ionization energy of Xe is $[\varepsilon_i]_{\mathrm{Xe}} \simeq 12.1$ eV, so that the energy difference is approximately 4.5 eV. Penning ionization is represented by the reaction [15]

$$\mathrm{Ne}^m + \mathrm{Xe} \longrightarrow \mathrm{Ne} + \mathrm{Xe}^+ + e$$

where Ne and Ne^m represent a ground-state and metastable Ne atom, respectively, Xe and Xe^+ represent a ground-state Xe atom and its positive ion, respectively, and e is an electron.

The steady-state Townsend condition [16], [17] does not hold in typical PDP operation conditions, because the discharge is quickly quenched as a result of the accumulation of charge on the dielectric walls covering the electrodes, inducing a potential opposing the applied voltage. The duration of the discharge current pulse is on the order of $t_0 \simeq 10$ ns [6]. During this short time, the concentration of Ne metastable atoms N_{Ne^m} increases because of electron impact excitation and is determined by

$$\frac{dN_{\mathrm{Ne}^m}}{dt} = \nu_{\mathrm{Ne}^m} N_e - \nu^P_{\mathrm{Ne}^m} N_{\mathrm{Ne}^m}$$

where $\nu^P_{\mathrm{Ne}^m}$ is the Penning ionization frequency per Ne metastable atom and ν_{Ne^m} is the excitation frequency of the Ne metastable state. The average metastable atom concentration is therefore given as

$$\begin{aligned}\langle N_{\mathrm{Ne}^m}\rangle &= \frac{1}{t_0}\int_0^{t_0} N_{\mathrm{Ne}^m}(t)\,dt \\ &= \frac{\nu_{\mathrm{Ne}^m}}{\nu^P_{\mathrm{Ne}^m}}\left(1 + \frac{e^{-\nu^P_{\mathrm{Ne}^m} t_0} - 1}{\nu^P_{\mathrm{Ne}^m} t_0}\right) N_e\end{aligned}$$

where N_e is assumed to be constant during the discharge current pulse. Although this approximation is rough, it allows us to make a first-order estimate of N_{Ne^m}, and it provides a good estimate of the effect of Penning ionization. Our kinetic model results, as well as the 1-D simulations (Section IV), show that the Penning effect is not very significant in all three cases considered and, thus, results in relatively small changes in the breakdown field. Thus, possible inaccuracies in the calculation of Penning ionization do not have a significant effect on our results. The effective Penning ionization frequency per electron is then given as

$$\begin{aligned}[\nu^P_{\mathrm{Ne}^m}]_{\mathrm{eff}} &= \frac{\nu^P_{\mathrm{Ne}^m}\langle N_{\mathrm{Ne}^m}\rangle}{N_e} \\ &= \left(1 + \frac{e^{-\nu^P_{\mathrm{Ne}^m} t_0} - 1}{\nu^P_{\mathrm{Ne}^m} t_0}\right)\nu_{\mathrm{Ne}^m} \qquad (3)\end{aligned}$$

where we note that $\nu^P_{\mathrm{Ne}^m}$ is proportional to the concentration of Xe atoms. The corresponding effective partial first Townsend ionization coefficient is $\alpha_P = [\nu^P_{\mathrm{Ne}^m}]_{\mathrm{eff}}/v_d$. The frequency ν_{Ne^m} as a function of the reduced electric field E/N is calculated using the Boltzmann code [13], whereas $\nu^P_{\mathrm{Ne}^m}$ is taken from Levin *et al.* [15]. Stepwise ionization and recombination processes, as well as Penning ionization by collisions between two Xe excited atoms, are not taken into account in our modeling, because their effect on typical operational conditions for PDPs is negligible [6].

In the Ne–Xe case, the total excitation frequency ν^{tot}_{exc} is equal to the excitation frequency caused by electron collisions with Xe atoms ν_{exc}, because no other important excitation mechanisms exist [15]. The excitation frequency is, thus, calculated as a function of E/N using the Boltzmann code [13].

B. He–Xe Mixtures

In the He–Xe case, the self-sustaining condition for the calculation of the breakdown field is similar to the corresponding in the Ne–Xe case

$$\frac{\alpha_{\mathrm{He}}\gamma_{\mathrm{He}} + (\alpha_{\mathrm{Xe}} + \alpha_P)\gamma_{\mathrm{Xe}}}{\alpha_{\mathrm{He}} + \alpha_{\mathrm{Xe}} + \alpha_P}\left[e^{(\alpha_{\mathrm{He}}+\alpha_{\mathrm{Xe}}+\alpha_P)d} - 1\right] = 1 \qquad (4)$$

where

- $\alpha_{\mathrm{He}} = \nu_{\mathrm{He}}/v_d$ partial first Townsend ionization coefficient for He;
- ν_{He} corresponding partial ionization frequency caused by direct ionization of neutral atoms by electrons;
- γ_{He} secondary electron emission coefficient for He ions on MgO;
- ν_{He} calculated as a function of E/N using the Boltzmann code [13].

Cross sections for He are taken from the SIGLO Series [14], whereas $\gamma_{\mathrm{He}} = 0.3$ is taken from Veerasingam *et al.* [18].

In the case of a He–Xe mixture, Penning ionization is represented by the reaction

$$\mathrm{He}^m + \mathrm{Xe} \longrightarrow \mathrm{He} + \mathrm{Xe}^+ + e$$

where He and He^m represent a ground-state and metastable He atom, respectively. In this case, the energy of the He metastable level is $\varepsilon_{\mathrm{m}} \simeq 20$ eV; so the energy difference with the Xe ionization level is approximately 7.9 eV. The effective Penning ionization frequency per electron is calculated in the same way as in the Ne–Xe case, and we obtain

$$[\nu^P_{\mathrm{He^m}}]_{\mathrm{eff}} = \left(1 + \frac{e^{-\nu^P_{\mathrm{He^m}} t_0} - 1}{\nu^P_{\mathrm{He^m}} t_0}\right)\nu_{\mathrm{He^m}} \qquad (5)$$

where

- $\nu_{\mathrm{He^m}}$ excitation frequency of the He metastable state;
- $\nu^P_{\mathrm{He^m}}$ Penning ionization frequency per He metastable atom taken from Rauf and Kushner [19];
- $\nu_{\mathrm{He^m}}$ calculated as a function of E/N using the Boltzmann code [13].

In addition, the total excitation frequency of the excited states of Xe that emit UV photons is equal to the excitation frequency caused by electron collisions with Xe atoms, because, as in the Ne–Xe case, no other important excitation mechanisms exist [19].

C. Ne–Xe–Ar Mixtures

In the case of the Ne–Xe–Ar mixture the breakdown field is calculated using the condition

$$\left[\frac{\alpha_{\rm Ne}\gamma_{\rm Ne}+(\alpha_{\rm Xe}+\alpha_{P1})\gamma_{\rm Xe}+(\alpha_{\rm Ar}+\alpha_{P2})\gamma_{\rm Ar}}{\alpha_{\rm Ne}+\alpha_{\rm Xe}+\alpha_{P1}+\alpha_{\rm Ar}+\alpha_{P2}}\right]\cdot\left[e^{(\alpha_{\rm Ne}+\alpha_{\rm Xe}+\alpha_{P1}+\alpha_{\rm Ar}+\alpha_{P2})d}-1\right]=1 \quad (6)$$

where

$\alpha_{\rm Ar}=\nu_{\rm Ar}/v_d$ partial first Townsend ionization coefficient for Ar;

$\nu_{\rm Ar}$ corresponding partial ionization frequency caused by direct ionization of argon atoms by electrons;

$\gamma_{\rm Ar}$ secondary electron emission coefficient for Ar ions on MgO;

$\nu_{\rm Ar}$ calculated as a function of E/N using the Boltzmann code [13].

Cross sections for Ar are taken from the SIGLO series [14], whereas $\gamma_{\rm Ar}=0.05$ is taken from Sahni *et al.* [7].

In this case, there are two Penning ionization reactions

$$\rm Ne^m + Xe \longrightarrow Ne + Xe^+ + e \quad (7a)$$

$$\rm Ne^m + Ar \longrightarrow Ne + Ar^+ + e \quad (7b)$$

where Ar and $\rm Ar^+$ represent a ground-state Ar atom and its positive ion, respectively. In the second reaction, the argon ionization energy is $[\varepsilon_i]_{\rm Ar}\simeq 15.8$ eV; so the energy difference with the Ne metastable state is ~0.8 eV. Because the energy difference is small, this process is highly efficient [12]. The effective Penning ionization frequencies per electron are calculated in the same way as in the Ne–Xe and He–Xe case, and we obtain

$$\nu_{P1}=\frac{\nu_{i1}}{\nu_{i1}+\nu_{i2}}\left[1+\frac{e^{-(\nu_{i1}+\nu_{i2})t_0}-1}{(\nu_{i1}+\nu_{i2})t_0}\right]\nu_{\rm Ne^m} \quad (8a)$$

$$\nu_{P2}=\frac{\nu_{i2}}{\nu_{i1}+\nu_{i2}}\left[1+\frac{e^{-(\nu_{i1}+\nu_{i2})t_0}-1}{(\nu_{i1}+\nu_{i2})t_0}\right]\nu_{\rm Ne^m} \quad (8b)$$

where ν_{i1} and ν_{i2} are the Penning ionization frequencies per Ne metastable atom, corresponding to reactions (7a) and (7b). Note that ν_{i1} is the same quantity that was denoted as $\nu^P_{\rm Ne^m}$ in Section II-A, and it is taken from Levin *et al.* [15], whereas ν_{i2} has been taken from Sahni *et al.* [7]. The excited states of Xe that emit UV photons are mainly produced by electron impact reactions, as in the case of Ne–Xe and He–Xe mixtures. However, in this case, a particular excitation mechanism caused by collisions of Ar excited atoms with Xe atoms does exist

$$\rm Ar^* + Xe \longrightarrow Ar + Xe^*$$

where Ar and $\rm Ar^*$ represent a ground-state and excited Ar atom, respectively, and Xe and $\rm Xe^*$ represents a ground-state and excited Xe atom, respectively [20]. In the Ne–Xe–Ar mixtures under consideration, this reaction is the dominant loss mechanism of Ar excited atoms. Thus, the total excitation frequency of the excited states of Xe that emit UV photons ν^{tot}_{exc} is equal to the direct excitation frequency $\nu^{\rm Xe}_{exc}$ caused by electron collisions with Xe atoms plus the excitation frequency $\nu^{\rm Ar}_{exc}$ caused by electron collisions with Ar atoms. Both $\nu^{\rm Xe}_{exc}$ and $\nu^{\rm Ar}_{exc}$ are calculated as a function of E/N using the Boltzmann code [13].

III. Results

Our stated goal in this paper is to compare the different gas mixtures by their breakdown voltage and efficiency defined as the ratio of the energy spent in excitation of UV emitting states of Xe per unit volume and per unit time, over the dissipated power per unit volume. However, the electric field E in the PDP cell during the discharge is spatially nonuniform because of space charges, with its spatial distribution being time dependent. In addition, Xe excitation, which has a highly nonlinear dependence on the electric field, occurs both in the high- and low-field regions. Accordingly, we evaluate the efficiency η for $E=0.2E_k$, E_k, $5E_k$, where E_k is the breakdown field for our conditions ($p=500$ Torr, $T=300$ K) calculated using (2), (4), and (6) in the case of Ne–Xe, He–Xe, and Ne–Xe–Ar mixtures, respectively. This range of electric field values, defined with respect to E_k, encompasses electric fields typically encountered in PDP cells, according to previous 1-D or two-dimensional (2-D) models [6].

In the following subsections, we separately examine each of the three gas mixtures.

A. Ne–Xe Mixtures

Fig. 2(a) shows the variation of the breakdown gap voltage $V_g\equiv E_k d$ as a function of the Xe concentration $N_{\rm Xe}$ in the mixture, calculated using (2). We observe that for $N_{\rm Xe}\geq 0.02N$, E_k is an increasing function of $N_{\rm Xe}$. The Penning effect is found to not be significant for this mixture, because $[\nu^P_{\rm Ne^m}]_{\rm eff}$ is found to be less than ~12% of the total ionization frequency ν^{tot}_{ion} for the full range of parameter values. Fig. 2(b) shows the excitation frequency ν_{exc} as a function of $N_{\rm Xe}$ for $E=0.2E_k$, E_k, $5E_k$, keeping in mind that E_k is also a function of the concentrations of the constituent gases. We observe that for small values of $N_{\rm Xe}$, ν_{exc} increases dramatically with small percentage increases in Xe concentration, whereas ν_{exc} increases at a much smaller rate for high Xe concentrations. We also observe that $\nu_{exc}(0.2E_k)\ll\nu_{exc}(E_k)\ll\nu_{exc}(5E_k)$, independent of $N_{\rm Xe}$, because at higher E, electron impact excitation reactions are more efficient. Fig. 2(c) shows the efficiency η as a function of $N_{\rm Xe}$, calculated in the way described above. We observe that the discharge is more efficient at low electric field values, although the number of UV photons emitted is higher at high electric field values [Fig. 2(b)]. Efficiency is also an increasing function of $N_{\rm Xe}$.

The numerical results given in Fig. 2 can be interpreted by the inherent kinetic behavior of Ne and Xe under applied electric fields. Fig. 2(d) shows the dynamic friction force of electrons, also known as the electron energy loss function, as a function of electron energy in a pure Ne gas, a pure Xe gas, and a 10% Xe–90% Ne gas mixture. In any given mixture, the loss function is defined as

$$F(\varepsilon)=\sum_i N_i\sigma_i(\varepsilon)\delta\varepsilon_i,$$

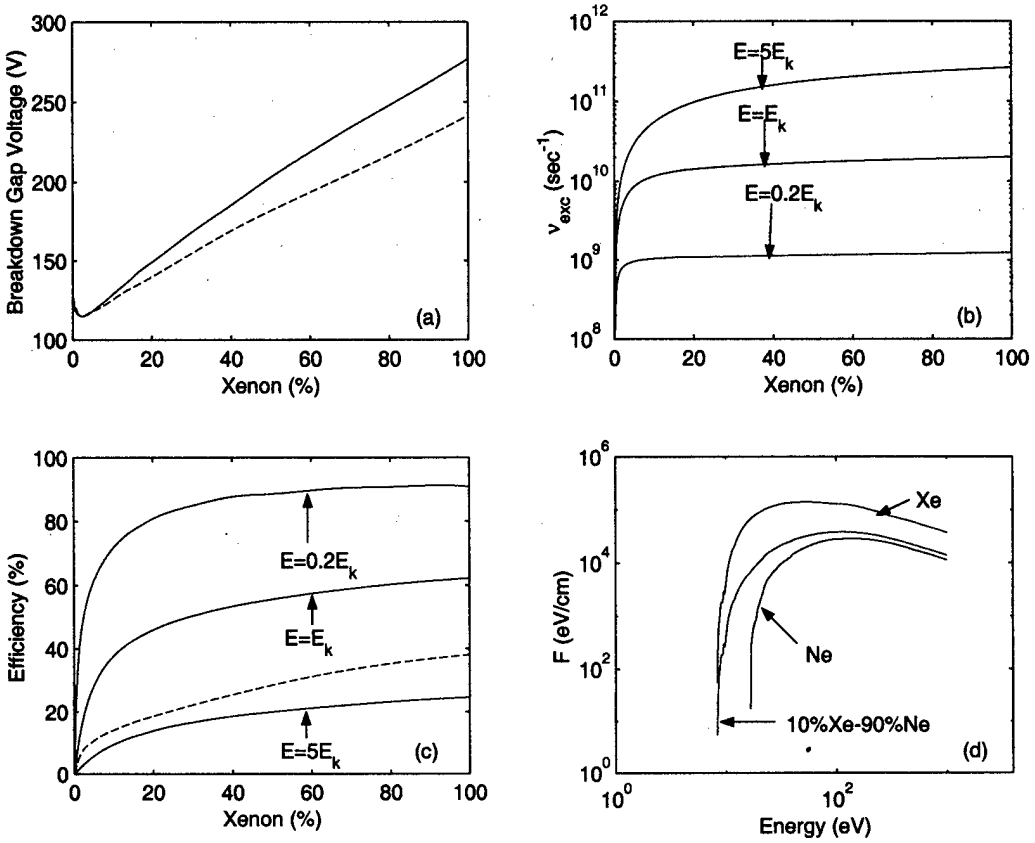


Fig. 2. (a) Breakdown gap voltage as a function of Xe concentration N_{Xe} in Ne–Xe mixtures, calculated using (2). The dashed line shows the mid-margin gap voltage, calculated using the 1-D model. (b) Excitation frequency ν_{exc} as a function of N_{Xe}. (c) Efficiency (%) η as a function of N_{Xe}. The dashed line shows the efficiency of the discharge, calculated using the 1-D model. (d) The loss function as a function of electron energy in a pure Ne gas, a pure Xe gas, and a 10% Xe–90% Ne gas mixture.

where the summation is over of all the collision cross sections of inelastic processes σ_i with corresponding energy loss $\delta\varepsilon_i$, and N_i is the number density of the corresponding target atoms. The dynamic friction force has units electronvolts/meters (energy loss per unit length), and it can be thought of as an effective force acting on electrons against the accelerating action of the electric field.

The breakdown field is much higher for Xe compared with Ne, as is evident from Fig. 2(a). That this is the case can be understood in terms of the corresponding loss functions. The ionization energy of Xe is $[\varepsilon_i]_{\mathrm{Xe}} \simeq 12.1$ eV, wheras $[\varepsilon_i]_{\mathrm{Ne}} \simeq 21.6$ eV. However, the dynamic friction for Xe is much higher than that for Ne, because the excitation and ionization cross sections of Xe are almost one order of magnitude higher [14] than are those of Ne. Thus, if the same electric field is applied at a pure Xe versus a pure Ne gas, the number of electrons above the corresponding ionization threshold is much higher in Ne, accounting for the fact that E_k is an increasing function of N_{Xe} [Fig. 2(a)] in Ne–Xe mixtures. This is also because the secondary electron emission coefficient γ_{Ne} for neon ions on MgO is an order of magnitude higher than is the corresponding coefficient γ_{Xe} for xenon ions. The loss function (or dynamic friction) also determines the electron energy distribution function that is attained in a gas for a given applied electric field. For small values of N_{Xe}, the loss function (and, thus, the electron energy distribution) does not vary significantly with increasing N_{Xe}, so that the dynamic friction at the excitation energy of Xe is relatively low, and many electrons have energies above this threshold, leading to the dramatic increase of Xe excitation frequency ν_{exc}. The corresponding partial ionization frequency of Xe (i.e., ν_{Xe}) increases dramatically for the same reason, whereas the corresponding partial ionization frequency ν_{Ne} of Ne slightly decreases, because the electron distribution function is only slightly perturbed by the addition of a small amount of Xe in Ne. Thus, E_k is a decreasing function of N_{Xe} for small N_{Xe} ($N_{\mathrm{Xe}} \leq 0.02\,N$).

The results presented in Fig. 2(a) and (c) should allow quantitative evaluation of the effects of Xe percentage in Ne–Xe mixtures in practice. In this context, it is desirable to have high luminous efficiency and low breakdown field (i.e., lower voltage operation). From Fig. 2(c), we note that although η increases rapidly with Xe percentage for low values of N_{Xe}, the rate of increase in η decreases with increasing N_{Xe}. Specifically, we note that although $\eta \simeq 70\%$ for $N_{\mathrm{Xe}} \simeq 0.1\,N$, it is only $\sim$10% higher for $N_{\mathrm{Xe}} \simeq 0.2\,N$, whereas the breakdown voltage is $\sim$25% higher. In Section IV, we show that the dependence of the actual discharge efficiency on N_{Xe} is very similar.

B. He–Xe Mixtures

Fig. 3(a) shows the breakdown gap voltage $V_g \equiv E_k d$ as a function of Xe concentration N_{Xe} in a He–Xe mixture, calculated using (4). The functional dependence of E_k on N_{Xe} is

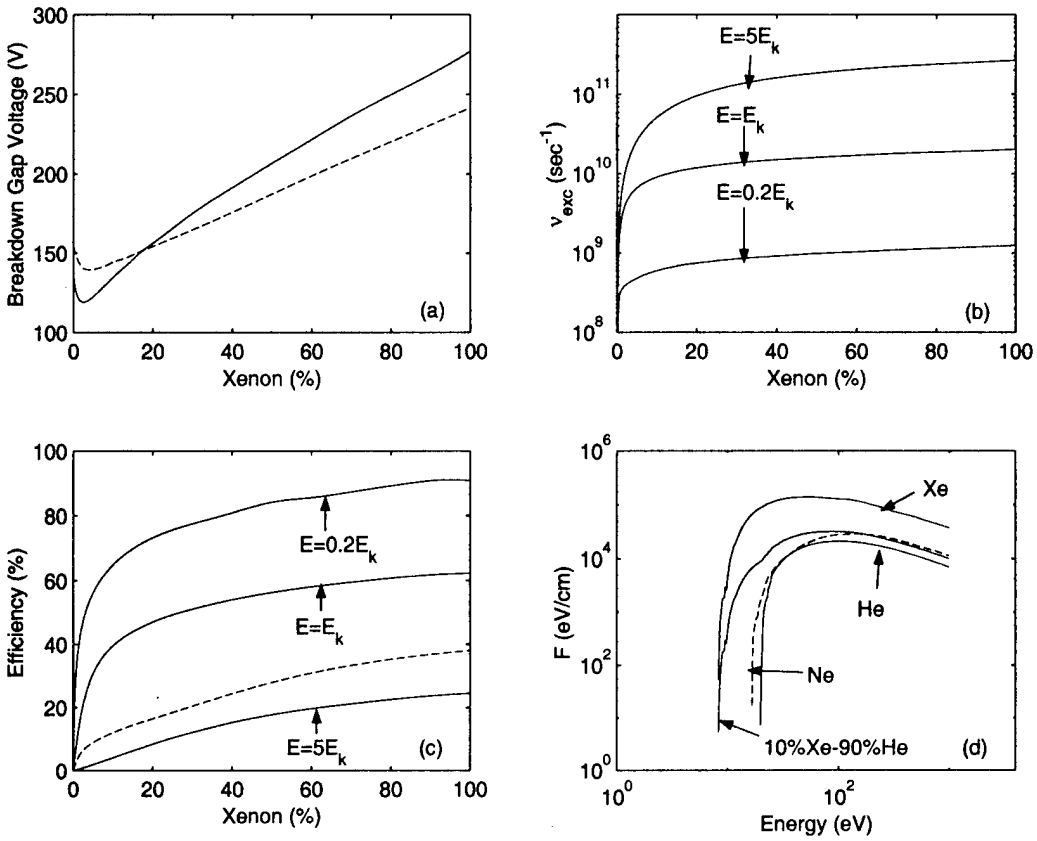


Fig. 3. (a) Breakdown gap voltage as a function of $N_{\rm Xe}$ in He–Xe mixtures, calculated using (4). The dashed line shows the mid-margin gap voltage, calculated using the 1-D model. (b) Excitation frequency ν_{exc} as a function of $N_{\rm Xe}$. (c) Efficiency (%) η as a function of $N_{\rm Xe}$. The dashed line shows the efficiency of the discharge, calculated using the 1-D model. (d) The loss function as a function of electron energy in a pure He gas, a pure Ne gas (dashed line), a pure Xe gas, and a 10% Xe–90% He gas mixture.

similar to the Ne–Xe case. However, E_k is slightly higher in a He–Xe mixture compared with a Ne–Xe mixture with the same Xe concentration. The contribution of the Penning effect is also not significant for this case, because $[\nu^P_{\rm He^m}]_{\rm eff}$ is found to be less than $\sim$7% of ν^{tot}_{ion} for the full range of parameter values considered. Fig. 3(b) shows the excitation frequency ν_{exc} of Xe as a function of $N_{\rm Xe}$ for $E = 0.2E_k$, E_k, $5E_k$. The results are similar to the Ne–Xe case, although ν_{exc} values are smaller. Because of the higher breakdown field and the smaller Xe excitation frequency, the efficiency is smaller, as shown in Fig. 3(c). However, it should be noted that He–Xe mixtures achieve better color purity, because the discharge does not produce visible light as in the Ne–Xe case [8].

In Fig. 3(d), we plot the loss function as a function of electron energy in a pure He gas, a pure Xe gas, and a 10% Xe–90% He gas mixture. For comparison, we also plot the loss function for pure Ne. We observe that the loss function for pure Ne has slightly higher values than that for pure He. Based on the discussion in Section III-A, we would expect slightly lower ionization and excitation frequencies in Ne–Xe mixtures in comparison with He–Xe mixtures. However, the ionization and excitation frequencies in He–Xe mixtures are actually lower compared with Ne–Xe mixtures with the same Xe concentration, resulting in higher breakdown field and lower efficiency. It was found that this unexpected result is mainly caused by the higher electron momentum transfer cross section of He compared with that of Ne [14]. Because the loss functions are almost equal, this effect dominates, resulting in lower ionization and excitation frequencies in He–Xe mixtures in comparison with Ne–Xe mixtures with the same Xe concentration [21]. The higher breakdown field in He–Xe mixtures is also because of the lower secondary electron emission coefficient $\gamma_{\rm He}$ of helium ions on MgO, compared with the coefficient $\gamma_{\rm Ne}$ of neon ions.

From a practical point of view, we note from Fig. 3(a) and (c) that the tradeoff between luminous efficiency and breakdown voltage level is similar for He–Xe mixtures as for Ne–Xe mixtures.

C. Ne–Xe–Ar Mixtures

In Section III-A, we saw that for Ne–Xe mixtures, the efficiency η is an increasing function of $N_{\rm Xe}$. However, the breakdown field E_k is also an increasing function of $N_{\rm Xe}$. In addition, in Section III-B, we saw that Ne–Xe mixtures are more efficient than are He–Xe mixtures. In this section, we investigate the effect of adding a small amount of Ar in Ne–Xe mixtures, as is done in some PDP designs.

Fig. 4(a) shows $V_g \equiv E_k d$ as a function of Ar concentration $N_{\rm Ar}$ in a mixture with $N_{\rm Xe}/N_{\rm Ne} = 5/95$. We observe that E_k decreases when small amounts of Ar are added, caused primarily by the Penning ionization reaction of Ar atoms with Ne metastable atoms, as described in (7b). By examination of

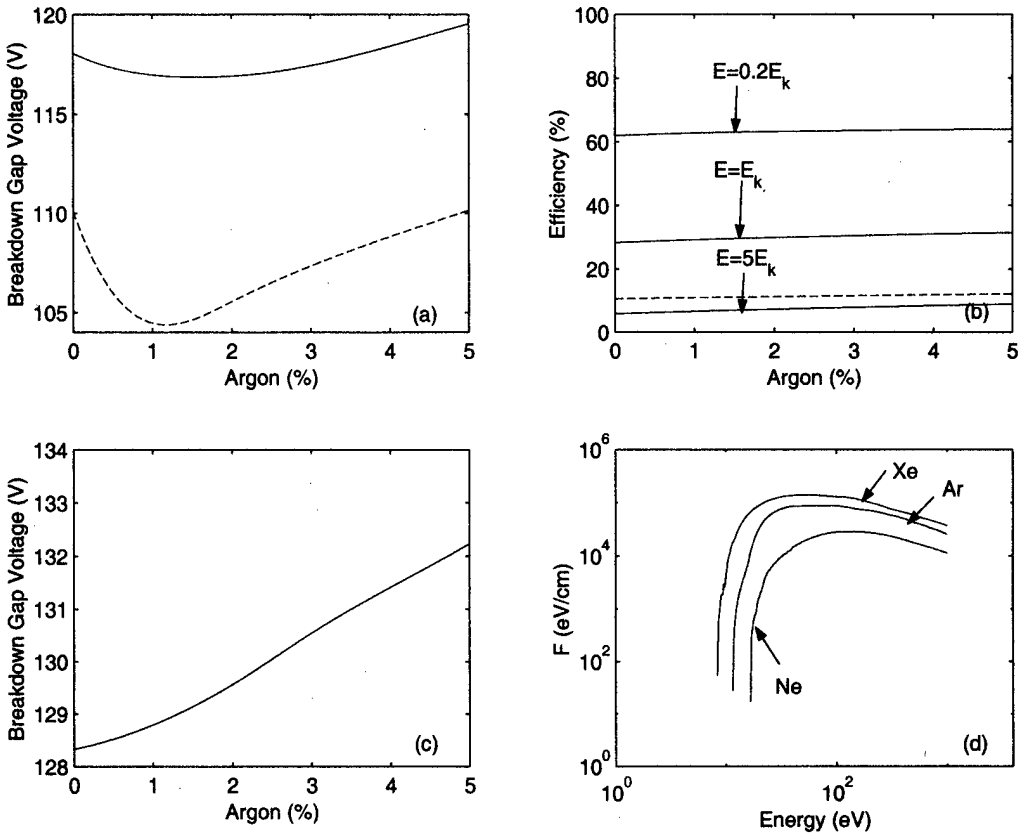


Fig. 4. (a) Breakdown gap voltage as a function of Ar concentration $N_{\rm Ar}$ in a mixture with $N_{\rm Xe}/N_{\rm Ne} = 5/95$, calculated using (6). The dashed line shows the mid-margin gap voltage, calculated using the 1-D model. (b) Efficiency (%) η as a function of $N_{\rm Ar}$ in a mixture with $N_{\rm Xe}/N_{\rm Ne} = 5/95$. The dashed line shows the efficiency of the discharge, calculated using the 1-D model. (c) Breakdown gap voltage as a function of $N_{\rm Ar}$ in a mixture with $N_{\rm Xe}/N_{\rm Ne} = 10/90$, calculated using (6). (d) The loss function as a function of electron energy in a pure Ne gas, a pure Xe gas, and a pure Ar gas.

the loss functions of Ne, Ar, and Xe, plotted in Fig. 4(d), we observe that the friction losses are higher in Ar than in Ne. Thus, when Ar is added to the mixture, the dynamic friction force on electrons increases, and we would ordinarily expect to see a corresponding increase in E_k. However, E_k actually decreases because of Penning ionization of Ar atoms by Ne metastables, which is very efficient, as mentioned above. We note from Fig. 4(a) that E_k is minimized at $N_{\rm Ar} \simeq 0.01\,N$. For $N_{\rm Ar} > 0.01\,N$ the increased losses dominate over the Penning ionization effect and E_k increases. Fig. 4(b) shows the luminous efficiency of the gas mixture as a function of $N_{\rm Ar}$. The efficiency slightly increases when small amounts of Ar are added. Thus, adding a small amount of Ar to a Ne–Xe mixture both decreases E_k and increases η. However, both of these improvements are relatively small, being less than $\sim$1%.

Fig. 4(c) shows $V_g \equiv E_k d$ as a function of $N_{\rm Ar}$ in a mixture with $N_{\rm Xe}/N_{\rm Ne} = 10/90$. The Penning effect is less important in comparison with the previous case because of the higher Xe concentration. As a result, the effect of the increased losses dominates and E_k increases when small quantities of Ar are added to the mixture.

Based on the results shown in Fig. 4, there does not seem to be any significant advantage in using small amounts of Ar in Ne–Xe mixtures, at least from the point of view of fundamental properties of the gases.

IV. Comparison with 1-D Simulation Results

In order to assess the validity of conclusions derived from our fundamental kinetic analysis of unbounded and homogeneous gas mixtures, we have developed a 1-D self-consistent simulation of an ac PDP cell, similar to those previously developed by Meunier *et al.* [6] and Punset *et al.* [22]. The space and time variation of the electric field within the gas is self-consistently determined by solving the fluid equations for ions and electrons together with Poisson's equation, subject to the boundary conditions imposed by the electrode boundaries. Ionization caused by Penning reactions is also included. The data used in the 1-D model, such as electron–atom collision cross sections, secondary electron emission coefficients, and reaction rates are identical to those used in the homogeneous and unbounded kinetic model. The gap length d, the pressure p, and the gas temperature T are also chosen to be the same as in the unbounded model. Other model parameters, such as length and relative permittivity of dielectrics, are identical to those used in Meunier *et al.* [6].

We use the 1-D model to calculate the voltage margin of stable operation of the cell by the voltage transfer curve method, introduced by Slottow and Petty [5] and described in Meunier *et al.* [6]. In each case, we use an applied voltage corresponding to operation in the middle of the calculated voltage margin to determine the efficiency of the discharge. The energy dissipated

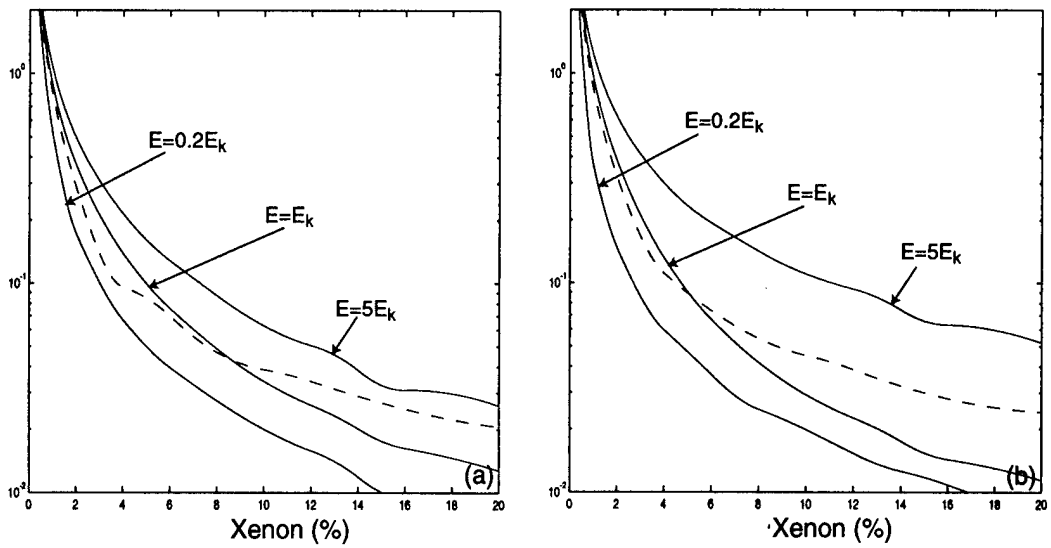


Fig. 5. (a) Normalized derivative of the efficiency η as a function of $N_{\rm Xe}$ in Ne–Xe mixtures. The dashed line shows the normalized derivative of the efficiency of the discharge, calculated using the 1-D model. (b) Normalized derivative of the efficiency η as a function of $N_{\rm Xe}$ in He–Xe mixtures. The dashed line shows the normalized derivative of the efficiency of the discharge, calculated using the 1-D model.

by electrons and ions, as well as the energy spent in excitation of UV emitting states of Xe are calculated. In other words, efficiency η is calculated as given by (1), except for the fact that $P_{diss} = E(J_e + J_{ion}) = (N_e q_e \mu_e + \sum_i N_i q_i \mu_i)E^2$.

The dashed line curve in Fig. 2(a) shows the variation of the mid-margin sustaining voltage in the gap V_{sg} as a function of the Xe concentration $N_{\rm Xe}$ in a Ne–Xe mixture. V_{sg} is given by

$$V_{sg} = \left[\frac{C_D}{C_D + C_g}\right] \frac{V_s^{\min} + V_s^{\max}}{2}$$

where

C_D equivalent capacitance of the dielectric layers;

C_g gas gap capacitance;

$V_s^{\min}$, $V_s^{\max}$ calculated minimum and maximum values of the sustaining voltage.

The dashed curve in Fig. 2(c) shows the variation of the discharge efficiency as a function of $N_{\rm Xe}$ in Ne–Xe mixtures for a middle-margin applied sustaining voltage. These 1-D results show that the sustaining voltage and the discharge efficiency of the PDP cell exhibit very similar dependence on $N_{\rm Xe}$ with the corresponding quantities of the unbounded homogeneous kinetic model. This similarity is further illustrated in Fig. 5(a), where we show the normalized derivative of the efficiency $(\eta^{-1} d\eta/d[N_{\rm Xe}/N])$ as a function of $N_{\rm Xe}$. The dashed line curve shows the normalized derivative of the discharge efficiency, calculated with the 1-D simulation. This plot illustrates that the fractional increase in η is very small for $N_{\rm Xe} > 0.1\,N$. It also illustrates that the dependence of the discharge efficiency on $N_{\rm Xe}$ is determined by the fundamental property η of the gas mixture.

The dashed lines in Figs. 3(a), 3(c), and Fig. 5(b) show similar results for He–Xe mixtures. In agreement with the unbounded and homogeneous kinetic model, it is found that V_{sg} is higher in a He–Xe mixture compared with a Ne–Xe mixture with the same Xe concentration and that the discharge efficiency is lower. It should be noted that He exhibits a very gradual rise in the slope of the voltage transfer curve [18]. We found that this is mainly from the high electron momentum transfer cross section of He. In agreement with Veeresingam *et al.* [18], we found that this effect results in disagreement between the actual $V_s^{\min}$, $V_s^{\max}$ and those calculated using the voltage transfer curve method for He–Xe mixtures with high helium concentrations. However, in the discharge efficiency calculation, we used an applied sustaining voltage that results in a stable discharge.

The dashed curves in Fig. 4(a) and (b) show V_{sg} and discharge efficiency as a function of Ar concentration $N_{\rm Ar}$ in a mixture with $N_{\rm Xe}/N_{\rm Ne} = 5/95$. In agreement with the results of the unbounded homogeneous model, V_{sg} is minimized at $N_{\rm Ar} \simeq 0.01\,N$ because of Penning ionization, and the efficiency slightly increases when small amounts of Ar are added. Although these improvements of $\sim$5% seem to have been underestimated by the unbounded homogeneous model, they are still small, confirming that there is no significant advantage in using small amounts of Ar in Ne–Xe mixtures.

V. Summary

We have considered the fundamental kinetic behavior under an applied electric field of homogeneous, unbounded inert gas mixtures to compare the breakdown field and UV photon generation efficiency of Ne–Xe, He–Xe, and Ne–Xe–Ar mixtures used in PDPs. Efficiency is an increasing function of Xe concentration in Ne–Xe and He–Xe mixtures, although He–Xe mixtures were found to be less efficient than were Ne–Xe mixtures with the same Xe concentration. The fractional increase in efficiency is very small for $N_{\rm Xe} > 0.1\,N$.

For Ne–Xe mixtures with $N_{\rm Xe}/N_{\rm Ne} = 5/95$, the addition of a small amount of Ar results in a slight minimum in the breakdown field at $N_{\rm Ar}/N \simeq 0.01$, whereas the efficiency increases only slightly. For Ne–Xe mixtures with $N_{\rm Xe}/N_{\rm Ne} = 10/90$, the addition of a small amount of Ar increases the breakdown

field. Based on these results, the addition of Ar to Ne–Xe mixtures does not lead to any significant improvement in PDP performance, either in terms of luminous efficiency or breakdown voltage level.

Using a 1-D model of an ac PDP cell, we confirmed the validity of the conclusions derived by the homogeneous and unbounded kinetic model.

REFERENCES

[1] A. Sobel, "Television's bright new technology," *Sci. Am.*, vol. 278, pp. 70–77, May 1998.

[2] S. Matsumoto, *Electronic Display Devices*. New York: Wiley, 1990, p. 131.

[3] Y. Sano, T. Nakamura, K. Numomura, T. Konishi, M. Usui, A. Tanaka, T. Yoshida, H. Yamada, O. Oida, and R. Fujimura, "High-contrast 50-in. color ac plasma display with 1365 × 768 pixels," *SID'98 Dig.*, pp. 275–278, 1998.

[4] H. Hirakawa, T. Katayama, S. Kuroki, T. Kanae, H. Nakahara, T. Nanto, K. Yoshikawa, A. Otsuka, and M. Wakitani, "Cell structure and driving method of a 25-in. (64-cm) diagonal high-resolution color ac plasma display," *SID'98 Dig.*, pp. 279–282, 1998.

[5] H. G. Slottow and W. D. Petty, "Stability of discharge series in the plasma display panel," *IEEE Trans. Electron Devices*, vol. ED-18, pp. 650–654, Sept. 1971.

[6] J. Meunier, Ph. Belenguer, and J. P. Boeuf, "Numerical model of an ac plasma display panel cell in neon-xenon mixtures," *J. Appl. Phys.*, vol. 78, pp. 731–745, July 1995.

[7] O. Sahni, C. Lanza, and W. E. Howard, "One-dimensional numerical simulation of ac discharges in a high-pressure mixture of Ne+0.1% Ar confined to a narrow gap between insulated metal electrodes," *J. Appl. Phys.*, vol. 49, pp. 2365–2375, Apr. 1978.

[8] M. Noborio, T. Yoshioka, Y. Sano, and K. Nunomura, "(He,Ne)–Xe gas mixtures for high-luminance color ac PDP," *SID'94 Dig.*, pp. 727–730, 1994.

[9] F. M. Penning, *Electrical Discharges in Gases*. New York: MacMillan , 1957, p. 29.

[10] J. P. Boeuf, C. Punset, and H. Doyeux, "Physics and modeling of plasma display panels," *J. Phys. IV*, vol. 7, pp. 3–14, Oct. 1997.

[11] F. M. Penning, *Electrical Discharges in Gases*. New York: Macmillan , 1957, p. 15.

[12] J. M. Meek and J. D. Craggs, *Electrical Breakdown of Gases*. New York: Wiley, 1978, p. 68.

[13] W. L. Morgan and B. M. Penetrate, "ELENDIF: A time-dependent Boltzmann solver for partially ionized plasmas," *Comput. Phys. Commun.*, vol. 58, pp. 127–152, 1990.

[14] [Online]http://www.sni.net/siglo/database/xsect/siglo.sec

[15] L. A. Levin, S. E. Moody, E. L. Klosterman, R. E. Center, and J. J. Ewing, "Kinetic model for long-pulse XeCl laser performance," *IEEE J. Quantum Electron.*, vol. QE-17, pp. 2282–2289, Dec. 1981.

[16] Y. Sakai, S. Sawada, and H. Tagashira, "Boltzmann equation analyzes of electron swarm parameters in Ar/Ne, Kr/Ne, Xe/Ne, Hg/Ar and Hg/Kr mixtures and derived effective excitation cross sections for metastable states of rare atoms," *J. Phys. D: Appl. Phys.*, vol. 24, pp. 283–289, 1991.

[17] F. M. Penning, "The starting potential of the glow discharge in neon argon mixtures between large parallel plates," *Physica*, vol. 1, pp. 1028–1044, 1934.

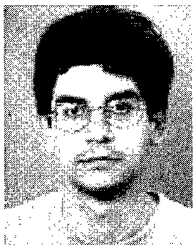
[18] R. Veerasingam, R. B. Campbell, and R. T. McGrath, "One-dimensional single and multipulse simulations of the ON/OFF voltages and the bistable margin for He, Xe, and He/Xe filled plasma display pixels," *IEEE Trans. Plasma Sci.*, vol. 24, pp. 1399–1410, Dec. 1996.

[19] S. Rauf and M. J. Kushner, "Dynamics of a coplanar-electrode plasma display panel cell. I. Basic operation," *J. Appl. Phys.*, vol. 85, no. 7, pp. 3460–3469, Apr. 1999.

[20] F. Kannari, A. Suda, M. Obara, and T. Fujioka, "Theoretical simulation of electron-beam-excited xenonchloride (XeCl) lasers," *IEEE J. Quantum Electron.*, vol. QE-19, pp. 1587–1600, Oct. 1983.

[21] S. Rauf and M. J. Kushner, "Dynamics of a coplanar-electrode plasma display panel cell. II. Cell optimization," *J. Appl. Phys.*, vol. 85, pp. 3470–3476, Apr. 1999.

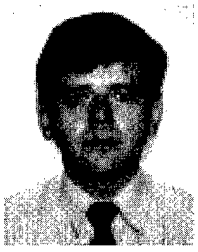
[22] C. Punset, J. P. Boeuf, and L. C. Pitchford, "Two-dimensional simulation of an alternating current matrix plasma display cell: Cross-talk and other geometric effects," *J. Appl. Phys.*, vol. 83, pp. 1884–1897, Feb. 1998.



Georgios Veronis was born in Greece on January 11, 1975. He received the B.S. degree from the National Technical University of Athens, Greece, in 1997 and the M.S. degree from Stanford University, Stanford, CA, in 1999, in electrical engineering. Since 1997, he has been a Research Assistant in the Space, Telecommunications, and Radioscience (STAR) Laboratory at Stanford University, where he is pursuing the Ph.D. degree. His research interests include plasma physics and applications, and computational electromagnetics.



Umran S. Inan (S'76–M'82–SM'99) was born in Turkey on December 28, 1950. He received the B.S. and M.S. degrees in electrical engineering from the Middle East Technical University in Ankara, Turkey in 1972 and 1973, respectively, and his Ph.D. degree in electrical engineering from Stanford University in 1977. He is currently a Professor of electrical engineering at Stanford University, where he serves as Director of the Space, Telecommunications, and Radioscience (STAR) Laboratory. He has received the 1998 Stanford University Tau Beta Pi Award for Excellence in Undergraduate Teaching, and actively conducts research in electromagnetic waves in plasmas, lightning discharges, ionospheric physics, and very low frequency remote sensing. Dr. Inan has served as the Ph.D. thesis adviser for 13 students and is a member of Tau Beta Pi, Sigma Xi, the American Geophysical Union, the Electromagnetics Academy, and currently serves as Secretary of US National Committee of the International Union of Radio Science (URSI).



Victor P. Pasko received his undergraduate and Candidate of Sciences degrees in theoretical physics and mathematics from Kiev University, Ukraine, in 1987 and 1990, respectively. He received his Ph.D. degree in electrical engineering from Stanford University in 1996. Dr. Pasko is currently an Engineering Research Associate in the Department of Electrical Engineering of Stanford University.

Dr. Pasko has published 32 peer-reviewed scholarly articles dealing with the theory of strong shock wave propagation in the interstellar medium, kinetic theory of collisionless electron beam-plasma relaxation with applications to active experiments in space, linear, and nonlinear theories of plasma stratification in cometary tails and in the auroral region, relaxation of transient lower ionospheric disturbances caused by lightning-whistler-induced electron precipitation, the nonlinear coupling of quasielectrostatic thundercloud fields to the mesosphere and lower ionosphere, diffraction effects of gravity waves generated by tropospheric convection, upward mapping and heating effects of electrostatic thundercloud fields, dynamics and spectroscopy of different types of electrical breakdown in air, and ELF radiation from sprites. He has reported his work in over 50 talks at national and international meetings. In 1996 Dr. Pasko was awarded an NSF (CEDAR) Post-Doctoral Award.

In 1996, he also received the Young Scientist Award of International Union of Radio Science (URSI). Dr. Pasko is a member of the American Geophysical Union and U.S. Comission H of URSI.

Experimental Investigation of Ion Parameters in a Cathodic Arc Plasma Operated with Nitrogen Gas

Diana Grondona, Héctor Kelly, Adriana Márquez, Fernando O. Minotti, and Jaroslaw Zebrowski

Abstract—**The ion kinetic energy and ion density was determined for the plasma generated in the outer region of the arc channel in a pulsed low-pressure cathodic arc. The device was operated with N_2 gas and with a Ti cathode within the pressure range $10^{-2} \div 150$ Pa, with a peak current of 520 A. A retarding field analyzer, a spherical Langmuir probe, and a calorimetric system were employed. The resulting kinetic energy for both Ti^+ and Ti^{++} ions was 40 ± 3 eV at the cathode spots. The obtained values for the ion density are in agreement with those predicted by hydrodynamic models with spherical symmetry if the ion current penetrating into the outer region is taken as 10% of the total discharge current. It was also found that the ion density increases (and the ion kinetic energy decreases) with the filling pressure, a fact that can be attributed to an ion slowing by elastic collisions with neutrals. This behavior cannot be explained with the presence of a shock wave separating a plasma region from an unperturbed neutral gas region.**

Index Terms—**Hydrodynamic model, ion diagnostics, ion–gas interaction, vacuum arc.**

I. Introduction

CATHODIC plasma arcs are characterized by the production of an intense metallic ion flux emerging from the cathode surface, which is commonly used for coating purpose [1]. For moderate values of the total discharge current (I), the emission comes from minute and mobile sites on the cathode surface known as cathode "spots." The kinetic energies of the ions are in the range 15–120 eV, depending on the cathode material and on the charge state of the ion [2]–[4], and with a total ion current (I_i) proportional to I. Under vacuum conditions, it has been found that $I_i/I \approx 0.08$–0.1 [5]. Although the angular distribution of the ion flux is peaked toward the anode, the ions are emitted within broad angles (measured with respect to the normal to the cathode plane), so that depending on the electrode geometry, a considerable fraction of the ion yield [6] flies away from the interelectrode region, penetrating into the otherwise empty outer space. During a short transient stage, of duration roughly given by the ion transit time along the discharge chamber (typically, $\sim 10\ \mu$s), these ions drag electrons from the interelectrode region, and hence, the outer space is filled with a neutral plasma.

In many experiments with plasma arcs operated in the abovementioned cathode-spot mode, an additional reactive neutral gas is also present in the discharge chamber, to promote chemical reactions for the production of complex films. Usual neutral gas pressures employed with continuous arcs are in the range 1–10 Pa [7], but in some works, neutral gas pressures (p) in the range 100–1000 Pa were used, either with the purpose of studying the attenuation of the metallic ion flux through the absorption by the neutral gas [8]–[10] or because in some pulsed high-current experiments with I in the range 500–1200 A, and with faced electrodes separated by a small gap (2–5 mm), the above-quoted high-pressure range resulted in good reactive coating production [11], [12].

The study of the outer region of the discharge when the arc is operated with neutral gas filling is important because in this region the ions lose their kinetic energy by elastic collisions with the neutral particles, and some of them are recombined through inelastic processes in the neutral gas. In addition, the knowledge of the plasma properties in this region can provide information on the plasma state in the arc channel.

Two different approaches have been proposed to describe the complex plasma–neutral gas structure developed in low-pressure arcs operating with p in the range $10 \div 1000$ Pa. Meunier [13] presented a snowplow fluid model to study the transient expansion of the plasma jet, based on previous detection [14] of a luminous plasma "ball" whose radius R was found to be dependent on p and I. Later on, Boxman and Goldsmith [15] presented a zero-order model for the plasma jet–background gas interaction, by equating the plasma jet momentum flux with the background pressure. This balance was produced at a certain radius, which the authors identified with R. In all of these studies, R was thought to represent an impermeable barrier (shockwave) separating two gas-like volumes, the metallic plasma and the neutral gas. The existence of the shock front was supported by a sudden delivery of the ion kinetic energy to the neutrals.

Following a different approach, Kelly *et al.* [16] presented a steady fluid model with spherical symmetry to describe the elastic interaction between metallic plasma and neutral gas in the outer region of the arc channel. The set of equations corresponded to a charge neutrality condition, ion continuity and momentum, electron momentum and energy, and neutral momentum and energy equations. The model gave the radial profiles of the ion density and velocity, the electron temperature, the plasma electrostatic potential, the neutral density, and temperature for given values of these quantities at the border of the arc channel. It was found that no shockwave was present in the steady state of the phenomenon, but instead the ions gradually delivered their kinetic energy into a strongly heated and rarefied gas.

Because the plasma–neutral gas structure generated in these low-pressure arcs is complex, and many physical quantities of the problem are not easily accessible to experimental study, the

Manuscript received November 22, 1999; revised February 24, 2000. This work was supported by the Buenos Aires University and the Consejo Nacional de Investigaciones Científicas y Tecnológicas (CONICET).

The authors are with the Instituto de Física del Plasma (CONICET), Departamento de Física, Facultad de Ciencias Exactas y Naturales (UBA), 1428 Buenos Aires, Argentina (e-mail: kelly@tinfip.lfp.uba.ar).

Publisher Item Identifier S 0093-3813(00)07247-7.

0093–3813/00$10.00 © 2000 IEEE

availability of theoretical profiles of several physical quantities is useful (and necessary) for the interpretation of experimental results. Conversely, the analysis of the experimental data in terms of a certain theoretical approach must substantiate the validity of that approach.

In this work, we will present a study of several plasma characteristics in the outer region of a pulsed cathodic arc operated at low-pressure values. Electrostatic probe, and calorimetric and retarding field analyzer diagnostics are employed. The obtained ion energy and ion density at different nitrogen pressures and distances of the arc channel are confronted with the theoretical predictions of previously published fluid models [16], [17], which predict smooth radial profiles of the physical quantities of the structure, because of a gradual delivery of the ion kinetic energy to a heated and rarefied neutral gas. Another possible interpretation of the experimental signals in terms of a shockwave model [15] is also discussed.

For a pulsed arc operated with $I \approx 500$ A (peak value), it is found that the ions are ejected from the cathode surface with a kinetic energy value close to that reported for arcs operated at $I \approx 100$ A. The plasma density values obtained from the probe are in good agreement with those predicted by the theoretical models, for an ion current of $\approx$10% of the total discharge current. Also, the ion energy as a function of the filling gas pressure at different radial positions (derived from the calorimetric measurements) is in reasonable agreement with the theoretical ion slowing by elastic collisions with the gas particles, predicted by hydrodynamic models, which do not include the presence of a shockwave.

II. Experimental Apparatus and Procedure

The arc was produced by discharging an electrolytic capacitor bank ($C = 0.075$ F) connected to a series inductor-resistor ($L = 2$ mH, $R = 0.33\ \Omega$) that critically damped the discharge (PROTO 1Z device). The vacuum chamber was a 25-cm long and 10-cm diameter stainless steel cylinder. The electrodes (of radii $a = 0.75$ cm) were introduced through the ends of the cylinder, facing each other. The gap between anode and cathode was set at 2 mm. The arcs were performed in N_2 gas with pressure (p) values in the range $10^{-2} \div 150$ Pa, using a Ti cathode. The arc was ignited by applying a short, high-voltage pulse to a trigger electrode contained in the cathode. The operating voltage was 260 V, giving a current pulse (measured through a low-value resistor, $R_2 = 0.008 \pm 0.001\ \Omega$) with an amplitude of 520 A and HAFW duration of 35 ms. More details on the device can be found elsewhere [18].

The diagnostics included a calorimetric system, a spherical electrostatic probe and an ion retarding field energy analyzer RFA [19]. For the first two diagnostics, it was possible to move the sensors in the radial direction perpendicular to the electrode axis. The calorimeter was composed of a thermally insulated cup-shaped Cu plasma collector, with a diameter of 6 mm, 19 mm length, and 20 μm thickness (total mass of 70 mg), in thermal contact with a thermocouple. By immersing the calorimeter in a thermal bath with controlled temperature, the sensitivity of the thermocouple was determined to be $25 \pm 5\ \mu$V/°C. The set was wrapped with a Teflon insulator and shielded with a brass tube of 18 mm diameter. The thermocouple signal was electronically amplified (250×) and then registered in a computer through a digital multimeter (with a 2-s/s sampling rate). The electrostatic probe electrode consisted of a spherical copper tip (0.94 mm of diameter), which was made by melting (and then quenching) a Cu wire. To avoid contamination of the probe insulator from the discharge products, the probe was wrapped with a double glass tube [20]. Several test shots were performed before the measurements to evaluate the influence of the coating on the probe-collecting head. It was found that after four shots, the amplitude of the signal began to be affected by the coating; so it was decided to clean the probe every two shots. The probe was biased by connecting it to a regulated dc power source (±50 V, 2 A) through a calibrated series resistor (R_p). The probe voltage (V_p), the voltage drop on R_p (which in turn is proportional to the probe current i_p), the voltage between the electrodes (V_A), and the total discharge current were simultaneously registered using a four-channel digitizing oscilloscope. To register the plasma potential (V_f), a series of shots with the probe simply connected to a high-impedance resistive voltage divider was also performed.

The RFA analyzer consisted of a housing subjected to differential pumping, with an entrance pinhole (0.8 mm of diameter), a metal grid (with a 40% transparency) located 8 cm from the pinhole, and a Cu circular collector of 1 cm of diameter, placed 2.5 cm far from the grid. The RFA was located perpendicular to the electrode axis (at an axial position corresponding to the middle of the interelectrode gap), with the pinhole at a radial position of 1.5 cm (measured with respect to the electrode axis). The metallic holder of the pinhole was grounded, whereas the grid was biased to -10 V, to separate ions from electrons in the grid-collector section of the RFA. The collector current I_c was registered for different bias collector voltages V_c, with V_c in the range $-40 \div 100$ V. During the measurements, the pressure inside the RFA was smaller than 10^{-2} Pa.

In Fig. 1, a scheme of the experimental arrangement is presented, showing also a discharge current waveform in the insert at the right top of the figure.

With the diagnostics described above, the following set of measurements was performed. For a fixed $p = 5$ Pa, a complete $I_c - V_c$ RFA collector characteristic was registered. This was done to get the ion energy distribution (following the procedure depicted in [19]) at a discharge current value of $\approx$500 A. On the other hand, varying p in the range $10^{-2} \div 150$ Pa, the electrostatic probe registered i_p and V_f at an axial position corresponding to the middle of the interelectrode gap and at a radial position $r_p = 1.75$ cm. The calorimeter registered the temperature increment at $r_c = 1.25$ cm and $r_c = 1.75$ cm. Occasionally, some measurements at $r_c = 3.65$ cm were also performed.

III. Results

A. Ion Energy Analysis

In Fig. 2, the $I_c - V_c$ RFA collector characteristic corresponding to $p = 5$ Pa is presented. Each experimental point corresponds to the average between three and five shots performed under identical conditions. As shown in [19], (minus)

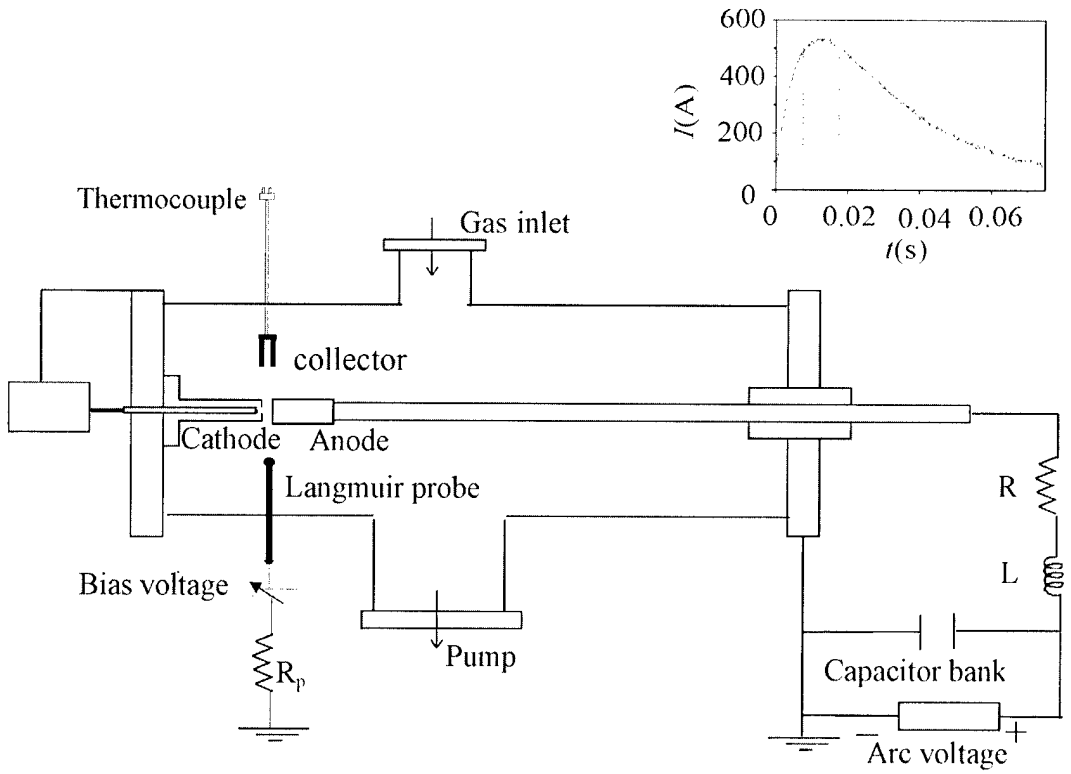


Fig. 1. Scheme of the experimental setup. The discharge current waveform is shown in the insert at the upper right of the figure. The time interval considered for the averaging procedure is shown between vertical dotted lines.

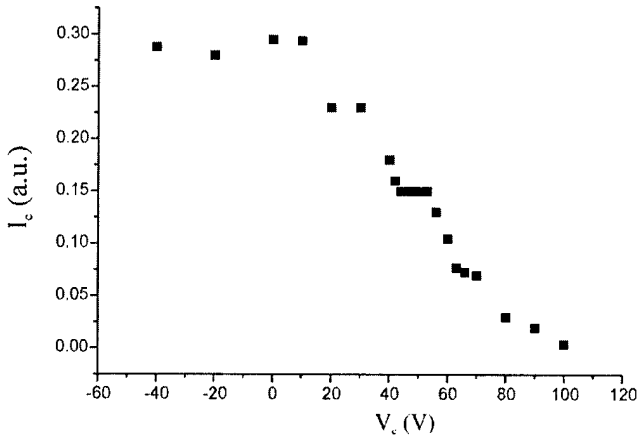


Fig. 2. I–V characteristic of the retarding field analyzer collector corresponding to $p = 5$ Pa.

the slope of this curve is proportional to the ion energy distribution function ($f(E)$). Within the experimental uncertainties, it was found that $f(E)$ presented two peaks at $V_c = 42 \pm 3$ V and $V_c = 60 \pm 3$ V, respectively. Taking into account that the ions are generated in a region (close to the spots) in which the plasma potential is close to the anode potential ($V_A = 21.5 \pm 0.25$ V, measured with a high-impedance resistive voltage divider), and that the entrance pinhole of the RFA is grounded, the two peaks were identified as corresponding to Ti^+ and Ti^{++} ions ejected from the cathode surface with an energy of 40 ± 4 eV for both kind of ions. This value is in agreement with that reported for vacuum arcs operated at current levels of 100 A [21].

B. Probe Measurements

The probe signals were noisy and consisted of a main signal (the ion register followed the total discharge current waveform), but with superimposed unidirectional spikes with characteristic frequencies in the range 0.05–0.5 MHz. These spikes are indicative of strong cathode spot activity and are usually found in low-pressure arc experiments [22], [23]. Because the spike pattern in the probe signals was completely irreproducible, showing changes from shot to shot in the amount, amplitude and temporal position of the spikes, it was decided to extract a mean behavior of the plasma by averaging the probe signals on a relatively large period of time. Hence, the mean probe floating voltage and current were defined as

$$\langle V_f \rangle = (1/\Delta t) \int V_f(t)\, dt$$

$$\langle i_p \rangle = (1/\Delta t) \int i_p(t)\, dt$$

where $\Delta t = t_1 - t_2$ and the limits of integration were taken to include a period of time during which the amplitude of $I(t)$ is considerable and its temporal variations are relatively small. In practice, $t_1 = 7.5$ ms and $t_2 = 17.5$ ms, measured with respect to the beginning of the discharge. Note that with the definitions quoted above, the effects of the spike irregularities are smoothed, but at the price of deriving mean plasma properties during the time interval considered. For simplicity in the notation, in what follows, we will use V_f and i_p for the time average of these quantities. In practice, even after the average-smoothing process described above, large uncertainties develop in the determination of the electron temperature T_e from the slope of the

$\ln i_p - V_p$ line. Taking into account that the last procedure is also time-consuming, in this work, we decided to obtain T_e (for each pressure value) from the floating potential equation. Because this method requires the knowledge of the plasma potential at the probe position (which is hard to obtain experimentally), it is necessary to get the plasma potential from a theoretical model. It is clear that this procedure does not lead to a proper determination of T_e, but aims to determine a value of T_e consistent with the adopted theoretical frame. In any case, we have checked for one value of p ($p = 50$ Pa) that the T_e value obtained from the floating potential equation is consistent with that obtained from the electron branch of the $i_p - V_p$ characteristic (with an uncertainty ≈100%).

For the interpretation of the probe measurements, the models of [16] (for high pressure, $p \geq 50$ Pa) and [17] (for lower pressures) were adopted. For all cases, it was found that the collision mean free path of electrons and ions was large compared with the probe size, so that collisionless theory can be applied. Because in this case the kinetic energy of the ions can be much larger than T_e, Lam's generalization of classic Langmuir's theory [24] (which takes into account ions of arbitrary kinetic energy) was employed.

According to Lam's theory, the ion saturation current (i_p^+) can be obtained from the relationship

$$-(V_p - \varphi) = (i_p^+)^{2/3}(m_I/2ez_r)^{1/3}F[(j/j_m)^{1/2}] \quad (1)$$

where φ is the plasma potential at the probe position, m_i and z_r are the ion mass and charge, respectively, $j = (i_p^+/n_i\pi R_p^2)[m_I/2(E_i + z_rT_e)]^{1/2}$ (n_i is the ion density, E_i the ion kinetic energy, and R_p is the probe radius), $j_m = j_m(\beta)$ (with $\beta = E_I/z_rT_e$) is a function tabulated in Lam's work that for large β values takes a value $j_m \approx 1$, and $F[(j/j_m)^{1/2}]$ is another function that can also be obtained from Lam's work for a spherical probe.

In Lam's work, an approximate expression for the floating probe potential is obtained as

$$V_f = \varphi - (T_e/e)\ln[(\pi^{1/2}/2j_m)(z_rm_e/m_i)^{1/2}(1+\beta)^{1/2}]. \quad (2)$$

For a measured V_f, T_e can be obtained from (2) if φ and E_i are known. On the other hand, for given values of V_p and i_p^+, (1) can be used for the determination of n_i if T_e is known. As previously quoted, we have resorted to the models of [17] and [16] to obtain the E_i and φ values at the probe position.

It was found that V_f was almost independent of p ($V_f = 14.5 \pm 0.5$ V), within the experimental uncertainties. Because the arc voltage drop was also constant ($V_A = 21 \pm 0.25$ V), and the plasma potential (as obtained from [16] and [17]) did not vary strongly with p (see Table I), the inferred electron temperature value was also approximately constant, with a value $T_e = 1.0 \pm 0.2$ eV.

In Table I, the experimental values of i_p^+ (corresponding to $V_p = -40$ V), the plasma density obtained from Lam's theory (1), and the theoretical values of E_i, φ, and the ion density ($n_{i\text{th}}$) are presented for the probe radial position $r_p = 1.75$ cm and for the different p values investigated. Each experimental value of i_p^+ in Table I represents the average of 3–5 experimental data. To obtain the theoretical values of E_i and φ, the following parameters and boundary values were employed in the model: $E_i(a) = 40$ eV (according to the results of the RFA diagnostic), $T_e(a) = 1.2$ eV, $\varphi(a) = V_A, n_{i\text{th}}(a)$ was fixed by selecting I_i equal to 10% of the total current ($I_i = 52$ A), and an average ion charge $z_r = 1.8$ (corresponding to Ti ions [21]). It can be seen from Table I that the experimental values of the plasma density are in good agreement with the theoretical ones. It must also be noted that, as long as $E_i > z_rT_e$, the n_i values obtained from (1) are almost independent of the T_e-value. The condition $E_i > z_rT_e$ is fulfilled in all of the pressure range investigated, except for the highest pressure point $p = 150$ Pa.

TABLE I
EXPERIMENTAL VALUES OF i_p^+ (CORRESPONDING TO $V_p = -40$ V) AND THE INFERRED VALUE OF n_i FROM PROBE MEASUREMENTS, AT $r_p = 1.75$ cm. THE THEORETICAL VALUES OF E_i, $n_{i\text{th}}$, AND φ ARE ALSO INCLUDED

p (Pa)	i_p^+ (mA)	E_i (eV)	φ (V)	n_i^{th} (10^{12}cm^{-3})	n_i (10^{12}cm^{-3})
$5\,10^{-2}$	20.0±0.5	45.7	18.9	7.0	7.5 ± 0.5
1	19.4±1.3	45.7	18.9	7.0	7.3 ± 0.5
5	20.6±1.0	45.7	18.9	7.0	7.7 ± 0.5
10	16.9±1.0	37.3	18.9	7.3	6.9 ± 0.5
50	14.6±0.5	17.4	19.2	10.3	8.3 ± 0.6
100	18.1±0.5	3.3	19.6	21.8	18.8 ± 1.2
150	18.7±1.0	1.0	19.9	23.0	23.9 ± 1.4

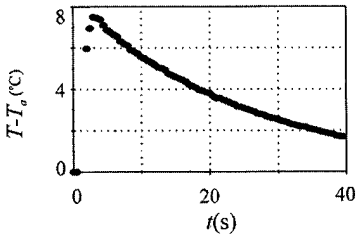


Fig. 3. Typical calorimetric signal.

C. Calorimetric Measurements

In Fig. 3, a typical calorimetric signal is shown. It can be seen that the signal reaches a peak value at a time of the order of the thermocouple rise time (≈0.5 s), followed by a decrease with a time scale of ≈30 s (the cooling time). The energy delivery time corresponds to the total arc duration (~0.1 s).

Designing with T_0 the peak temperature that should have been registered by the calorimeter if there was no thermocouple rise time or cooling effects, the time evolution of the temperature registered by the system can be written as

$$T(t) = T_a + (T_0 - T_a)\{1 - \exp(-t/\tau_1)\}\exp(-t/\tau_2) \quad (3)$$

where T_a is the ambient temperature and τ_1, τ_2 are the thermocouple rise time and cooling time, respectively. Equation (3) has a maximum ($T_{\max}$) for $t = t_{\max}$. They are given as

$$T_{\max} = T_a + (T_0 - T_a)[\tau_2/(\tau_1 + \tau_2)][\tau_1/(\tau_1 + \tau_2)]^{\tau_1/\tau_2}$$
$$t_{\max} = \tau_1 \ln[(\tau_1 + \tau_2)/\tau_1] \quad (4)$$

for $\tau_1 = 0.5$ s and $\tau_2 = 30$ s, (4) gives

$$T_{\max} - T_a = 0.9(T_0 - T_a). \quad (5)$$

On the other hand, the calorimetric balance gives

$$\Delta E = m_{\mathrm{Cu}} c_p (T_0 - T_a) \quad (6)$$

where ΔE is the energy input on the collector, m_{Cu} is the mass of the Cu target, and c_p is the Cu-specific heat. At low operating pressure values ($p < 50$ Pa), the ion kinetic energy losses are negligible [16]; so the main contribution to ΔE comes from the metallic ions impinging on the target surface, because the ion kinetic energy is much larger than the electron thermal energy (because the collector is at floating potential, the ion and electron fluxes arriving to its surface are equal). Hence

$$\Delta E = \int n_i(t) v_i E_i^* A \, dt \quad (7)$$

where v_i is the ion velocity, A is the collector surface, and E_i^* is the ion energy at the calorimeter collector position. Note that E_i^* is equal to the kinetic ion energy $E_i^{\exp}$ plus the energy acquired in the voltage drop from the plasma potential to the floating potential ($z_r(V_f - \varphi)$). In (7), the integral extends over the whole arc duration. Because E_i^* is assumed to be independent of t, $n_i(t)$ is proportional to the instantaneous value of the discharge current $I(t)$ (this result follows from the proportionality between $I(t)$ and the ion current [5]), and because the profile of $I(t)$ is known, the integral (7) can be solved in terms of n_i. After solving (7), combining with (5) and (6), and replacing the geometrical value of A, it results in

$$E_i^{*3/2}(\mathrm{eV}) = 7.4\ 10^{14}(T_{\max} - T_a)/k n_i(\mathrm{cm}^{-3}). \quad (8)$$

Equation (8) was employed to determine E_i^* for $r_c = 1.75$ cm, because n_i is known from the ion branch of the electrostatic probe (see Table I) and $T_{\max} - T_a$ from the calorimeter measurements. Note the presence of a nondimensional factor (k) in the left-hand side of (8). It was introduced because the numerical value of A employed in that equation corresponds to the bottom part of the cup-shaped collector of the calorimeter, and it is likely that some parts of its lateral area participate in the ion collection. The k-value (and, hence, the proper value of the collecting area) was derived by taking into account that under very low gas pressure values, there are practically no interactions between the ions and the background gas. In these conditions ($p = 5 \cdot 10^{-2}$ Pa), the ion kinetic energy at the calorimeter position can be simply calculated as the emitted energy (40 eV) at the cathode spots plus the energy gained under the voltage drop between the arc and the floating potential of the calorimeter

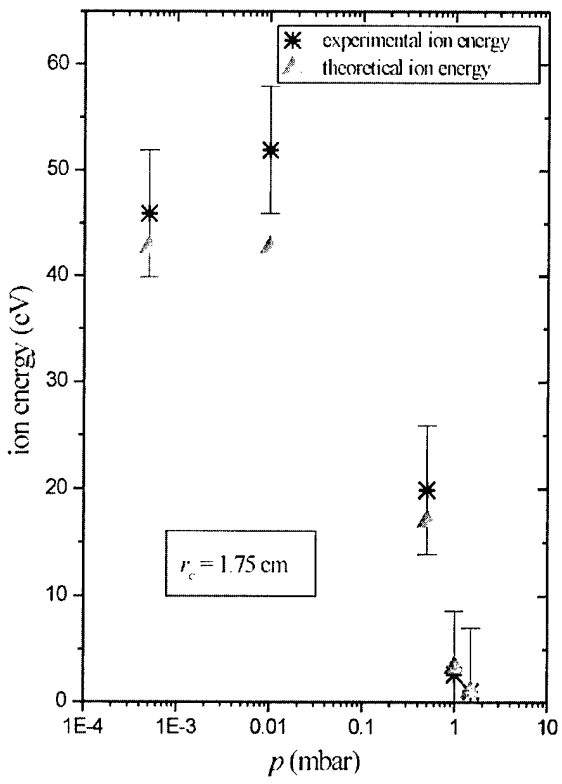


Fig. 4. Ion kinetic energy as a function of p determined from calorimetric measurements employing the experimental n_i values for $r_c = 1.75$ cm. The ion kinetic energies obtained from the theoretical model are also shown.

($V_{ca} - V_f(r_c) = 6.5$ V), resulting in $E_i^* = 51$ eV. At this radial position $n_i = 7.5 \cdot 10^{12}$ cm^{-3} and $T_{\max} - T_a = 7.8\,^{\circ}$C, thus, (8) gives $k = 2.0$. This value indicates that a considerable fraction of the lateral surface of the Cu collector contributes to the ion collection. Equation (8) gave the same value of k for the temperature increments obtained at other calorimeter positions ($r_c = 1.25$ and $r_c = 3.65$ cm) and at a low-pressure value ($p = 5\ 10^{-2}$ Pa), using in these cases the n_i-value obtained from the theoretical model [17].

In Fig. 4, the values of the ion kinetic energy inferred from (8) ($E_i^{\exp}$) for several values of p and for $r_c = 1.75$ cm are presented. The E_i^*-value was determined from (8), employing the experimental n_i values from Table I, and $E_i^{\exp}$ was obtained by subtracting from E_i^* the voltage drop in the positive sheath around the calorimeter ($z_r[\varphi(r_c) - V_f(r_c)]$). Note that E_i^* depends mainly on n_i [see (8)], and hence, it is independent of T_e, except for the point $p = 150$ Pa. For comparison purposes, the values of E_i obtained from the theoretical models (under the same boundary values of those used in Table I) are also shown.

In Fig. 5, the same quantities as those presented in Fig. 4 are shown, but for $r_c = 1.25$ cm. Because in this case no experimental data on n_i were available, the determination of $E_i^{\exp}$ from (8) was performed using the theoretical values of n_i ($n_{i\mathrm{th}}$) as given by the models of [16] and [17]. In all of the cases, the uncertainty in the $E_i^{\exp}$-values can be estimated in $\approx$5–6 eV. It can be seen that the agreement between the values of $E_i^{\exp}$ and E_i is good.

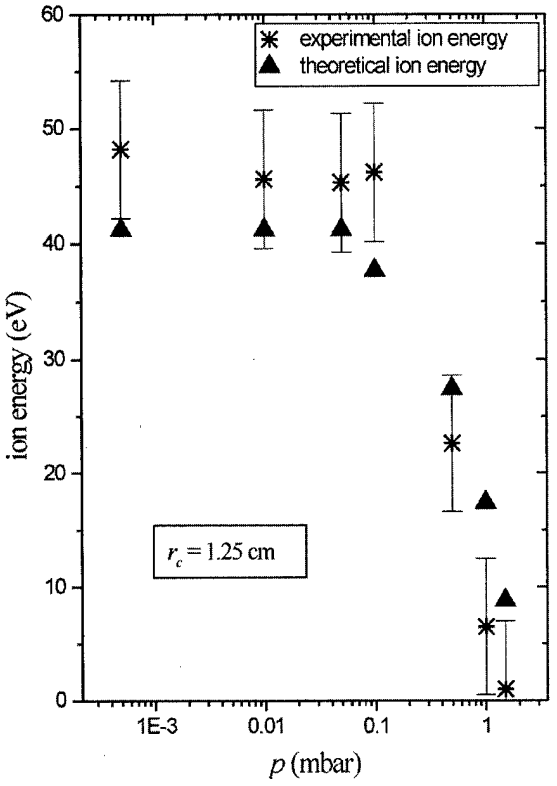


Fig. 5. Ion kinetic energy as a function of p determined from calorimetric measurements using the theoretical values of n_i (n_{ith}) for $r_c = 1.25$ cm. The ion energies obtained from the theoretical model are also shown.

IV. Discussion and Final Remarks

The inferred kinetic energies from the cathode spots for Ti^+ and Ti^{++} ions ($E_i^{exp}(a) = 40 \pm 3$ eV for both species) corresponding to an arc current of 520 A and $p = 5$ Pa are in good agreement with those reported for $I = 100$ A under vacuum conditions [21]. However, no evidence of the presence of Ti^{+++} ions was found in this experiment, which can be because of the uncertainty of the diagnostic (the reported fraction of Ti^{+++} ions is only about 6%). This energy has been employed as an input parameter to calculate the theoretical radial profile of E_i with the models of [16] and [17].

The results of the electrostatic probe measurements for the ion density show a good agreement with those predicted by the models, if an ion current of 10% of the discharge current is assumed. Although it must be considered that the reported value of T_e does not come from a direct experimental measurement, it has practically no influence on the behavior of n_i and E_i with p. The increase of the ion density with the filling pressure can be attributed to the ion slowing produced by elastic ion-neutral collisions. Within the pressure range investigated, the rarified neutral density between the arc channel and the probe position is not high enough to produce a significant ion absorption by inelastic processes.

The values of the kinetic ion energies obtained from the calorimetric measurements [with the knowledge of the ion density (8)], are also in fair agreement with the values predicted theoretically.

Let us assume the presence of a shockwave in the steady plasma–neutral gas structure, as proposed in [13]–[15]. If we express the radius R of the hypothetical shock as function of I and p according to the relationship presented in [15], it is obtained, in practical units, as R (cm) $= 3.7\{I_i\ (\mathrm{A})/p\ (\mathrm{Pa})\}^{1/2}$. In this case, $I_i = 52$ A; hence, for the pressure range investigated, the last relationship predicts that $R \geq 2.2$ cm. Because the calorimeter radial positions were both smaller than R for all of the p values, we can conclude that the E_i^{exp}-values should have remained independent of the pressure value, because the plasma "ball" was always outside of the calorimeter. We can argue that the value of I_i is only a theoretical value selected for a good fitting of the theoretical models [16], [17], and if the true value of I_i was somewhat smaller, the value of R would have been smaller, perhaps smaller than the calorimeter radius for some value of p. But if this was the case, the shock would have crossed the calorimeter position as the pressure decreased; so we should expect that E_i^{exp} versus p behaved as a kind of "step" function. In either case, this is not the behavior of E_i^{exp} shown in Figs. 4 and 5. For the above reasons, we think that the smooth decrease of E_i when the filling pressure increases (Figs. 4 and 5) cannot be explained with the presence of a shockwave separating a plasma region from an unperturbed neutral gas region.

To summarize, we think that the experimental behavior of the ion density and ion kinetic energy with the filling pressure presented in this work point to support the existence of a plasma–neutral gas structure characterized by a strongly perturbed neutral gas (heated and rarefied) interpenetrating the metallic plasma.

References

[1] R. L. Boxman, D. M. Sanders, and P. J. Martin, *Handbook of Vacuum Arc Science and Technology, Fundamentals and Applications*. Park Ridge, NJ: Noyes, 1995.

[2] A. A. Plyutto, V. N. Ryzhkov, and A. T. Kapin, "High speed plasma streams in vacuum arcs," *Sov. Phys. JETP*, vol. 20, pp. 257–260, 1965.

[3] W. D. Davis and H. C. Miller, "Analysis of the electrode products emitted by dc arcs in a vacuum ambient," *J. Appl. Phys.*, vol. 40, pp. 2212–2221, 1969.

[4] V. M. Lunev, V. G. Padalka, and V. M. Khoroshikh, "Plasma properties of a metal vacuum arc. II," *Sov. Phys.-Tech. Phys.*, vol. 22, pp. 858–861, 1977.

[5] C. W. Kimbling, "Erosion and ionization in the cathode spot regions of vacuum arcs," *J. Appl. Phys.*, vol. 44, pp. 3074–3081, 1973.

[6] J. Kutzner and H. C. Miller, "Ion flux from the cathode region of a vacuum arc," *IEEE Trans. Plasma Sci.*, vol. 17, pp. 688–694, 1989.

[7] H. Randhawa, "Cathodic arc plasma deposition technology," *Thin Solid Films*, vol. 167, pp. 175–185, 1988.

[8] C. W. Kimbling, "Cathode spot erosion and ionization phenomena in the transition from vacuum to atmospheric pressure arcs," *J. Appl. Phys.*, vol. 45, pp. 5235–5244, 1974.

[9] J. L. Meunier and M. D. de Acevedo, "Carbon cathode spot plasma flux distributions in low pressures of hydrogen: Some evidence for the $C^+ + H_2 \rightarrow CH^+ + H$ reaction," *IEEE Trans. Plasma Sci.*, vol. 20, pp. 1053–1059, 1992.

[10] D. Grondona, H. Kelly, and A. Márquez, "Ion-gas interaction in a vacuum arc at intermediate pressures," *Astrophys. Space Sci.*, vol. 286, pp. 511–515, 1998.

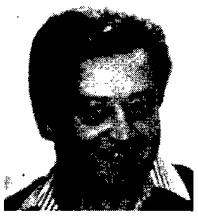
[11] R. L. Boxman, S. Goldsmith, S. Shalev, H. Yaloz, and N. Brosh, "Fast deposition of metallurgical coatings and production of surface alloys using a pulsed high current vacuum arc," *Thin Solid Films*, vol. 139, pp. 41–52, 1986.

[12] H. Bruzzone, H. Kelly, A. Márquez, D. Lamas, A. Ansaldi, and C. Oviedo, "TiN coatings generated with a pulsed plasma arc," *Plasma Sources Sci. Technol.*, vol. 5, pp. 582–587, 1996.
[13] J. L. Meunier, "Pressure limits for the vacuum arc deposition technique," *IEEE Trans. Plasma Sci.*, vol. 18, pp. 904–910, 1990.
[14] J. L. Meunier and M. G. Drouet, "Experimental study of the effect of gas pressure on arc cathode erosion and redeposition in He, Ar and SF_6 from vacuum to atmospheric pressure," *IEEE Trans. Plasma Sci.*, vol. 15, pp. 515–519, 1987.
[15] R. L. Boxman and S. Goldsmith, "Momentum interchange between cathode-spot plasma jets and background gases and vapors and its implications on vacuum-arc anode-spot development," *IEEE Trans. Plasma Sci.*, vol. 18, pp. 231–236, 1990.
[16] H. Kelly, A. Márquez, and F. Minotti, "A simplified fluid model of the metallic plasma and neutral gas interaction in a multicathode spot vacuum arc," *IEEE Trans. Plasma Sci.*, vol. 26, pp. 1322–1329, 1998.
[17] H. Kelly, A. Márquez, F. Minotti, and C. F. Fontan, "The plasma state in the surroundings of a multi-cathode-spot vacuum arc," *J. Phys. D: Appl. Phys.*, vol. 31, pp. 1737–1741, 1998.
[18] H. Bruzzone, H. Kelly, A. Márquez, D. Lamas, A. Ansaldi, and C. Oviedo, "TiN coatings generated with a pulsed plasma arc," *Plasma Sources Sci. Technol.*, vol. 5, pp. 582–587, 1996.
[19] C. Rusteberg, M. Lindmayer, B. Juttner, and H. Pursch, "On the ion energy distribution of high current arcs in vacuum," *IEEE Trans. Plasma Sci.*, vol. 23, pp. 909–914, 1995.
[20] M. Sakaki and T. Sakakibara, "Pressure dependence of plasma parameters in medium-vacuum nitrogen arc discharge with the titanium cathode," *IEEE Trans. Plasma Sci.*, vol. 19, pp. 25–28, 1991.
[21] J. Kutzner and H. C. Miller, "Integrated ion flux emitted from the cathode spot region of a diffuse vacuum arc," *J. Phys. D: Appl. Phys.*, vol. 25, pp. 686–693, 1992.
[22] S. M. Shkolnik, "Electrostatic probe measurements in a vacuum arc," *IEEE Trans. Plasma Sci.*, vol. 13, pp. 336–338, 1985.
[23] D. Grondona, H. Kelly, A. Márquez, and F. Minotti, "Electrostatic probe measurements in the outer region of a low pressure arc," *J. Phys. D: Appl. Phys.*, vol. 31, pp. 3358–3366, 1998.
[24] S. H. Lam, "Unified theory for the Langmuir probe in a collisionless plasma," *Phys. Fluids*, vol. 8, pp. 73–87, 1965.
[25] S. Goldsmith, "The interelectrode plasma," in *Handbook of Vacuum Arc Science and Technology*, R. L. Boxman, P. J. Martin, and D. M. Sanders, Eds. NJ: Noyes Publications, 1995, pp. 283–284.

Diana Grondona was born in Buenos Aires, Argentina, on July 23, 1964. She received the M.S. degree in 1989 and the Ph.D. degree in physics in 1994, both from Buenos Aires University.

She joined the Plasma Physics Institute of the Science Faculty of Buenos Aires University in 1987. Her current research interests include electrical discharges and plasma coatings based on electrical discharges. Since 1996, she has been with a Researcher at the Plasma Physics Institute.

Dr. Grondona was a Fellow of the National Research Council of Science of Argentina from 1989 to 1995.



Héctor Kelly was born in Mendoza, Argentina, on February 14, 1948. He received the M.S. degree in 1972 and the Ph.D. degree in physics in 1979 from Buenos Aires University.

Since 1973, he has worked as a Researcher at the Plasma Physics Institute of the Science Faculty of Buenos Aires University. His current research interests include electrical discharges, plasma modeling, and plasma coatings based on electrical arcs.

Dr. Kelly has been a member of the National Research Council of Science of Argentina since 1980.



Adriana Márquez was born in Buenos Aires, Argentina, on August 4, 1964. She received the M.S. degree in 1989 and the Ph.D. degree in physics in 1994 from Buenos Aires University.

She joined the Plasma Physics Institute of the Science Faculty of Buenos Aires University in 1987. Her current research interests include electrical discharges and plasma coatings based on electrical discharges. Since 1996, she has been working as a Researcher at the Plasma Physics Institute.

Dr. Márquez was a Fellow of the National Research Council of Science of Argentina.

Fernando O. Minotti was born in Buenos Aires, Argentina, on January 27, 1960. He received the M.S. degree in 1984 and the Ph.D. degree in physics in 1990 from Buenos Aires University.

He has worked as a Researcher at the Plasma Physics Institute of the Science Faculty of Buenos Aires University since 1984. His current research interests include fluid mechanics and turbulence.

Dr. Minotti has been a member of the National Research Council of Science of Argentina since 1993.



Jaroslaw Zebrowski was born in Warsaw, Poland, in 1955. He received the M.Sc. degree in electrical engineering from the Technical University of Warsaw in 1979.

He has been with the Andrzej Soltan Institute for Nuclear Studies (IPJ) in Otwock-Swierk, Warsaw, Poland, since 1981. During the past years, he was engaged in ion, X-ray, and neutron diagnostics at different plasma-focus and ion-implosion facilities of energy ranging from several kilojoules to about 300 kJ, as operated in Swierk. He was also engaged in the scientific collaboration with the Institut fuer Plasmaforschung at the Stuttgart University, Germany, the Institute of Plasma Physics at the NSC Kharkov Institute of Physics & Technology, Ukraine, the Czech Technical University in Prague, Czech Republic, and plasma research groups at the universities of Buenos Aires and Tandil, Argentina.

Electron Mobility in Mixtures of Optically Excited Sodium Vapor, Molecular Nitrogen, and Heavy Inert Gases

Nikolai A. Gorbunov, Olga V. Krylova, and Igor Smurov

Abstract—**A study is made of the processes of formation of a nonequilibrium electron energy distribution in mixtures of sodium, molecular nitrogen, and heavy inert gases. It is shown that in these mixtures, a local maximum on the electron energy distribution can form in the energy range corresponding to the Ramsauer minimum in the elastic collision cross section for inert gases. The question is discussed of whether the electron mobility can become negative during the resonant optical excitation of the 3S–3P transition in sodium. The electron distribution function is calculated parametrically to determine the critical plasma parameters for which negative electron mobility can be observed in experiments, specifically, the composition of the mixture, the concentration of resonantly excited sodium atoms, the temperature corresponding to the distribution of vibrationally excited molecules, the degree of ionization, and the electric field strength.**

Index Terms—**Conductivity, distribution function, plasma properties.**

I. Introduction

In OUR previous papers [1], [2], we considered the formation of the electron energy distribution function (EEDF) in a photoplasma in mixtures of sodium vapor with inert gases. We treated the mixtures containing heavy inert gases and showed that when the electron energy deviates from the thermal energy of the heavy particles because of superelastic collisions between electrons and resonantly excited sodium atoms, a nonequilibrium electron energy distribution can form with a local maximum in the energy range $\varepsilon > \varepsilon_{\min}$ above the Ramsauer minimum in the elastic scattering cross section $\sigma(\varepsilon)$ for heavy inert gases. We found that in order for the inverse EEDF such that $\partial f(\varepsilon)/\partial\varepsilon > 0$ to form in the above energy range, the following two conditions should be satisfied.

1) $\delta\nu_{ea}(\varepsilon) > \nu_{01}(\varepsilon)$, which indicates that the frequency of the energy losses caused by elastic electron–atom collisions $\delta\nu_{ea}(\varepsilon)$ (where $\delta = 2$ m/M is the energy transfer coefficient in the course of elastic collisions between an electron of mass m and a heavy particle of mass M) should exceed the frequency $\nu_{01}(\varepsilon)$ of the energy losses caused by inelastic collisions between electrons and sodium atoms in the near-threshold energy range $\varepsilon \geq \Delta E$ (where ΔE is the excitation threshold) for the excitation cross section for the resonant Na(3S–3P) transition in sodium by electron impact.
2) $\nu*(\varepsilon_{\min}) > \delta\nu_{ea}(\varepsilon_{\min})$, which indicates that the frequency $\nu*(\varepsilon)$ of superelastic collisions between electrons and resonantly excited sodium atoms Na(3P) should exceed the frequency of energy losses caused by elastic electron–atom collisions in the energy range $\varepsilon \approx \varepsilon_{\min}$ near the Ramsauer minimum in the elastic scattering cross section for inert gases.

We showed that the EEDF inversion causes the electron mobility to decrease substantially. The EEDF can lead to the absolute negative conductivity (ANC) effect in argon–sodium mixtures. Necessary conditions for the ANC effect to occur are as follows: 1) the population of resonantly excited sodium atoms Na(3P) should exceed a certain critical value close to the saturation level for the optical 3S–3P transition and 2) the degree of ionization ξ of a medium should be sufficiently low (lower than the critical value $\xi \leq 2 \cdot 10^{-11}$). These requirements are clearly in contradiction, which makes it difficult to achieve the ANC in experiments with a photoplasma in two-component mixtures.

In [1] and [2], we have shown that among the main obstacles to the formation of an inverse EEDF are collisions of the first kind between electrons and sodium atoms in the ground state Na(3S). These collisions reduce the efficiency with which fast electrons are produced in the course of superelastic impacts because of the reverse processes. Here, in order to make the EEDF inversion more pronounced, we propose to reduce the effect of electron–sodium-atom inelastic collisions by using molecular nitrogen as a third mixture component.

The formation of EEDFs with different shapes in nonself-sustained discharges in pure nitrogen was studied both theoretically and experimentally in a number of papers [3]–[9]. Summarizing the results obtained in those studies, we can draw the conclusion that the shape of the EEDF in nitrogen is governed by inelastic processes, including both the excitation and deexcitation of molecules in the ground electronic state $X^1\Sigma_g^+$ and collisions of electrons with electronically excited molecules ($A^3\Sigma_u^+$, etc.). A specific feature of the excitation of vibrational levels of the lowest electronic state of nitrogen molecules is that the cross section for excitation by electron impact depends strongly on energy. The vibrational excitation is most efficient in the energy range $\varepsilon_1 \leq \varepsilon \leq \varepsilon_2$ ($\varepsilon_1 \approx 1.5$ eV and $\varepsilon_2 \approx 3.7$ eV), the total cross section for excitation from the ground state being maximum at $\varepsilon_{\max} \approx 2.3$ eV (see Fig. 1). Analysis of the cited papers shows that, in nonself-sustained discharges, the shape of

Manuscript received December 7, 1999; revised May 24, 2000. This work was supported in part by INTAS, under Grant 93-3676-EXT.

N. A. Gorbunov and O. V. Krylova are with the Department of Optics, Physics Institute, St. Petersburg University, 198904 St. Petersburg, Russia.

I. Smurov is with the École National d'Ingénieurs de Saint-Etienne, 42032 Saint-Etienne Cedex, France.

Publisher Item Identifier S 0093-3813(00)09160-8.

0093–3813/00$10.00 © 2000 IEEE

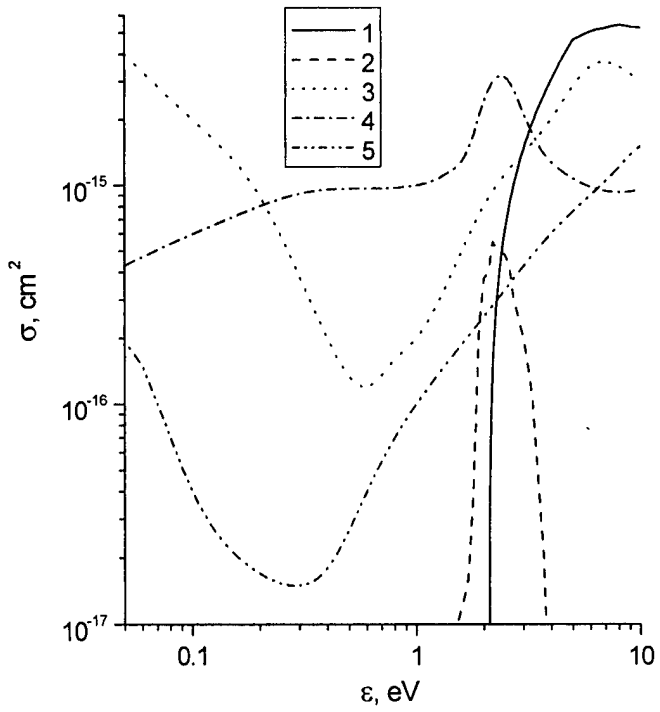


Fig. 1. Cross sections for the main processes responsible for the formation of the EEDF in the mixtures under consideration: (1) the cross section for the excitation of the resonant states Na(3S–3P) of sodium atoms; (2) the total cross section for the excitation of the first eight vibrational levels $X^1\Sigma_g^+$ of nitrogen molecules; and the transport cross section for elastic collisions of electrons with (3) Xe atoms, (4) N_2 molecules, and (5) Ar atoms.

the EEDF depends strongly on the molecular distribution over the vibrational levels of the ground state $X^1\Sigma_g^+(v)$, where v is the vibrational quantum number.

When the gas temperature T_a and the vibrational temperature T_v of the $X^1\Sigma_g^+$ state are both low, the electron flux into the energy range $\varepsilon_1 \leq \varepsilon \leq \varepsilon_2$ in energy space is governed by the relaxation of fast electrons produced in the range $\varepsilon > \varepsilon_2$ caused by superelastic collisions between thermal electrons ($\varepsilon \ll \varepsilon_1$) and electronically excited molecules. In the range $\varepsilon > \varepsilon_2$, the relaxation of fast electrons is governed by electron–electron collisions, elastic electron–molecule collisions, and the processes responsible for the excitation of the rotational levels of molecules. In the range $\varepsilon_1 \leq \varepsilon \leq \varepsilon_2$, the relaxation is also affected by the processes of the excitation of vibrational levels, which leads to the formation of a dip in the EEDF profile [3], [4], [6]. In this range, such a dip was observed in experiments with electron–beam-driven discharges in nitrogen at low pressures [5] and with cage discharges (which are a sort of beam-driven discharge) in helium with a small (about 0.03%) nitrogen admixture; in the latter case, fast electrons were produced in the course of chemi-ionization processes and superelastic collisions with metastable helium atoms [10].

The effect of the nonequilibrium character of the EEDF on the transport properties of a plasma in heavy inert gases with a small admixture of molecular gases (N_2, CO) characterized by the resonant nature of the cross section for the excitation of vibrational levels was studied in [11] and [12]. It was shown that in such mixtures, the effect of a negative differential plasma conductivity can manifest at certain electric field strengths. This effect is attributed to the combined action of the Ramsauer minimum in the transport cross section for heavy inert gases and the electron impact excitation of the vibrational levels of the molecules of admixtures.

Here, we propose to exploit such a property of molecular nitrogen as its ability to form a dip in the EEDF profile. The use of molecular nitrogen admixtures makes it possible to reduce the effective rate of inelastic collisions between electrons and sodium atoms. We chose nitrogen because the maximum cross section for the excitation of the vibrational levels of nitrogen molecules corresponds to the near-threshold energy range for the excitation cross section for the resonant Na(3S–3P) transition in sodium. Consequently, by varying the percentage of the components in mixtures containing heavy inert gases, sodium, and nitrogen, we can make the EEDF inversion more pronounced in the energy range around the Ramsauer minimum. This allows us to vary the electron mobility in a certain range in the desired fashion by forming a nonequilibrium EEDF in three-component mixtures.

Our aim here is to calculate the nonequilibrium EEDF and electron mobility in mixtures of an optically excited sodium vapor, molecule nitrogen, and heavy inert gases. We will analyze the conditions under which the inverse electron distribution forms in the energy range around the Ramsauer minimum and the effect negative electron mobility develops. We will parametrically determine the amount of the components that would be beneficial for the negative electron mobility in the mixtures of interest. We will calculate the critical parameters (the population of resonantly excited sodium atoms, the temperature corresponding to the molecular distribution over vibrational levels, the degree of ionization of a medium, and the electric field strength) for which the ANC can be achieved in experiments with photoplasmas.

II. Theoretical Model and Calculation Technique

The processes that involve sodium atoms and inert gases and are to be taken into account in our analysis were discussed in detail in [1] and [2]. Like in those papers, we use the two-level model of sodium atoms. In calculations, we incorporate the processes of the excitation of sodium atoms from the ground state and the relevant reverse processes. The kinetic Boltzmann equation for electrons and numerical algorithm for solving this equation were also described in [1] and [2]. Let us now consider the processes involving molecular nitrogen.

The transport cross sections for collisions between electrons and nitrogen molecules were taken from [13]. Under the conditions corresponding to low vibrational temperatures $T_v < 0.3$ eV (see below), the elastic scattering of electrons by molecules is governed by collisions between electrons and molecules in the lowest vibrational state. This circumstance enables us to neglect particular features of the transport cross section for electron scattering by vibrationally excited molecules. The processes of the excitation and deexcitation of the rotational levels of molecules are, as usual, incorporated in the Fokker–Planck approximation [6], [7], [14]. The effective cross section for the excitation of rotational levels and the rotational constant for molecular nitrogen were taken from [14]. The cross sections

for the excitation of the vibrational levels of molecules with the quantum number v ($v = 1, \ldots, 8$) from the ground state were taken from [14]. Fig. 1 presents the total cross section for the excitation of the first eight levels. The energies of the vibrational levels were taken from [15]. The cross sections for the electron impact excitation of the electronic states of nitrogen molecules were thoroughly analyzed in [16]. The cross section for the excitation of the electronic states of molecular nitrogen is three orders of magnitude smaller than the cross section for the excitation of resonant sodium atoms, whose excitation threshold $\Delta E \sim 2.1$ eV is much smaller than the threshold $\Delta\varepsilon \sim 6.2$ eV for exciting the electronic states of nitrogen molecules. For low vibrational temperatures, we can neglect both the lowering of the threshold for exciting the $A^3\Sigma_u^+$ molecular state via transitions from the vibrationally excited $X^1\Sigma_g^+(v)$ states and the stepwise excitation of vibrational levels from the states with $v > 1$. Consequently, under the conditions $[N_2] \sim [Na]$ and $T_v < 0.3$ eV (see below), the processes of exciting the electronic states of nitrogen molecules can be neglected compared with the excitation of sodium atoms. The results of our calculations carried out in the range $T_v > 0.3$ eV should be regarded only as estimates for the electron mobility.

We will characterize the total population of the resonantly excited doublet N^* of sodium atoms, $3P_{1/2}$ and $3P_{3/2}$, by the effective population temperature T^*

$$T^* = -\Delta E[\ln(N^* g_0/N_0 g^*)]^{-1} \qquad (1)$$

where g^* is the total statistic weight of the doublet and N_0 and g_0 are, respectively, the concentration and the statistic weight of sodium atoms in the ground state. Under the conditions considered below, the concentration of inert gases in the mixture exceeds the total concentration of admixtures by more than three orders of magnitude, so that the processes of vibrational-translational exchange between N_2 molecules and argon atoms cause the molecular distribution over the vibrational levels of the ground state to approach a Boltzmann-like distribution with temperature T_v [14]. On the other hand, the electron impact excitation of N_2 molecules as well as their excitation in collisions with Na(3P) atoms can influence the vibrational energy balance. Consequently, in our calculations, T_v was regarded as one of the input parameters ($T_v \geq T_a$). The gas temperature was varied in the range 450–600 K, which corresponds to the sodium atom concentration in the range 10^{12}–10^{15} cm^{-3}.

We neglected the population of those states of sodium atoms that lie above the 3P state along the energy scale and the population of the electronically excited states of N_2 molecules. This model corresponds to the conditions for resonant optical excitation of the Na(3S–3P) transition in sodium.

III. Calculation Results

A. *Effect of the Mixture Composition on the Electron Mobility*

1) Na–N_2–Ar Mixture: As an example, Fig. 2 shows the reduced electron mobility μN (where N is the total concentration of atoms and molecules in the mixture) and the electron temperature T_e as functions of the content of nitrogen in mixtures

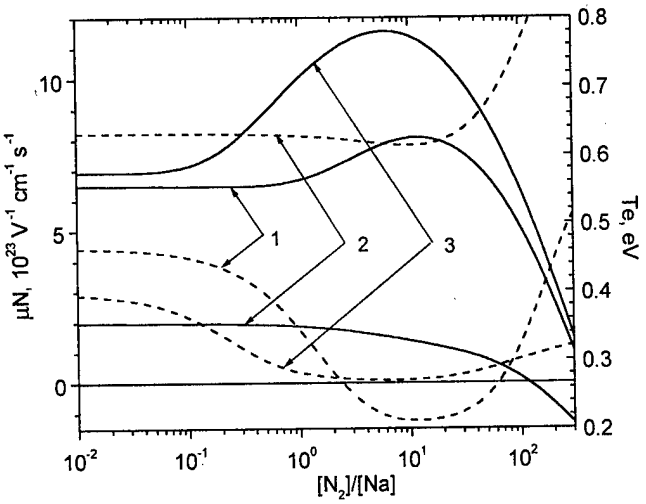


Fig. 2. Electron mobility (dashed curves) and the electron temperature (solid curves) as functions of the amount of nitrogen in a Na–Ar–N_2 mixture at $T^* = 0.6$ eV and $T_a = T_v = 0.047$ eV for different argon concentrations [Ar]/[Na] = (1) 10^4, (2) 10^5, and (3) 10^3.

with different argon concentrations. In the case of a nonequilibrium EEDF, the temperature T_e is regarded as $T_e = 2\langle\varepsilon\rangle/3$ with $\langle\varepsilon\rangle$ the mean electron energy. In calculations carried out for $T^* = 0.6$ eV and $T_v = T_a = 500$K, we neglected the effect of Coulomb collisions on the shape of the EEDF (this effect will be discussed below). From Fig. 2, we can see that both T_e and the electron mobility depend on the content of the mixture in a complicated manner. For sodium and argon in the ratio [Na]/[Ar] $= 10^{-4}$ (curves 1), increasing the nitrogen concentration in the mixture in the range $[N_2]/[Na] \sim 1$–10 leads to a significant increase in T_e, which is associated with the nonequilibrium character of the formation of the EEDF. In such a mixture, the rate $\nu_{0V}(\varepsilon)$ with which the vibrational levels of nitrogen molecules are excited becomes higher than the rate of inelastic collisions with sodium atoms $\nu_{0V}(\varepsilon_{\max}) > \nu_{01}(\varepsilon_{\max})$. Because the cross section for the excitation of vibrational levels decreases rapidly with the quantum number v, the dominant contribution to the excitation rate $\nu_{0V}(\varepsilon)$ comes from collisions such that the energy lost by an electron during each collision event is about the energy $\Delta\varepsilon_{01} = 0.29$ eV of the vibrational quantum of a molecule. Because $\Delta\varepsilon_{01} \ll \Delta E$, this effect reduces the total electron energy losses, thus, causing T_e to grow. The majority of electrons displace toward the energy range above the Ramsauer minimum; this is one of the conditions for achieving the ANC effect [17].

In fact, from Fig. 2, we can see that at $[N_2]/[Na] \sim$ (3–50), the electron mobility becomes negative. The reason is that the EEDF becomes inverse in the energy range near the Ramsauer minimum. The EEDF inversion is closely related to the dip that appears in the EEDF profile at an energy of $\varepsilon \sim 2$ eV caused by electron–molecule collisions. The shape of the EEDF in the vicinity of the point at which the absolute value of the negative electron mobility is maximum is shown in Fig. 3 (curve 1). For the above composition of the mixture, fast electrons produced in the course of superelastic collisions with excited sodium atoms relax toward the energy range $\varepsilon < \Delta E$ below the threshold, caused primarily by the excitation of the vibrational levels of

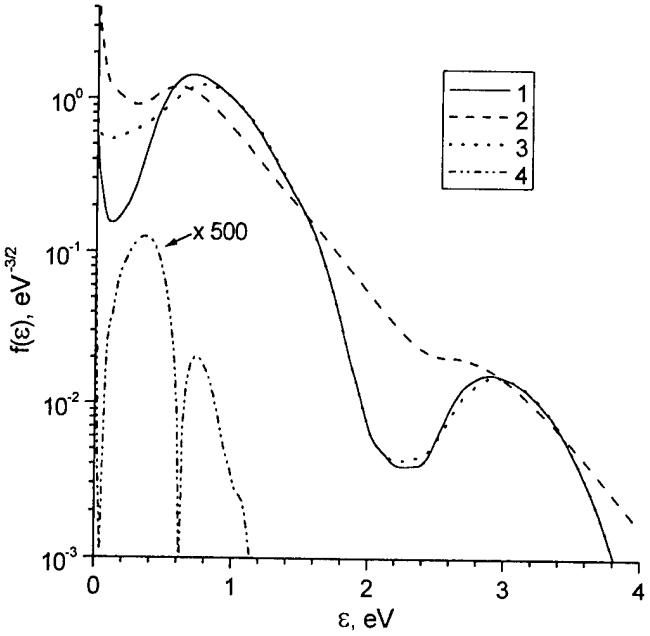


Fig. 3. EEDF in a Na–Ar–N_2 mixture at [Ar]/[Na] = 10^4, [N_2]/[Na] = 10, $\xi = 0$, $T_a = 0.047$ eV, $T^* = 0.6$ eV for (1) $T_v = T_a$ and $E = 0$, (2) $T_v = 0.4$ eV and $E = 0$, and (3) $T_v = T_a$ and $E/N = 0.02$ Td; (4) the left-hand side of inequality (2) at $T_v = T_a$ and $E/N = 0.02$ Td.

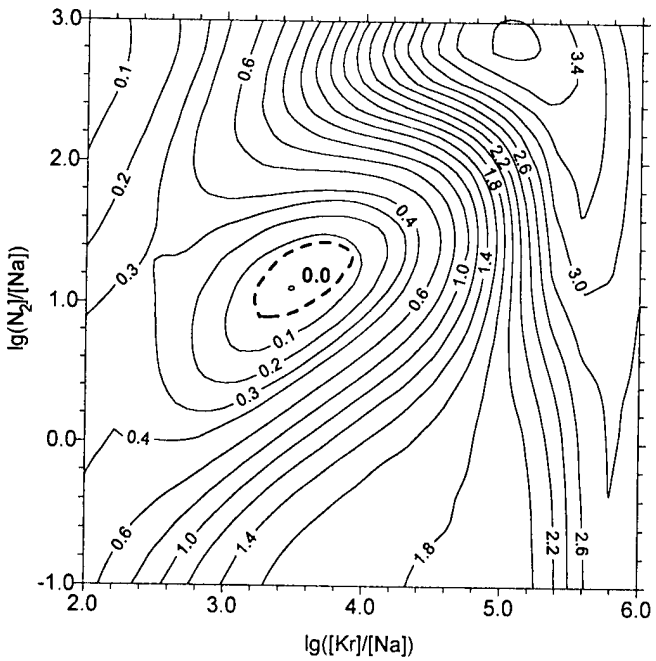


Fig. 4. Isocontours of the reduced electron mobility μN (in 10^{23} V^{-1} $cm^{-1}s^{-1}$) in a Na–Kr–N_2 mixture at $\xi = 0$ and $T_a = T_v = 0.047$ eV: the solid curves were calculated for $T^* = 1$ eV, and the dashed curve corresponds to $\mu N = 0$ at $T^* = 1.2$ eV.

nitrogen molecules. After leaving the range $\varepsilon < \varepsilon_1$ of the efficient vibrational excitation, the electrons continue to relax but because of elastic collisions with argon atoms. In the energy range close to the Ramsauer minimum, the electron energy relaxation rate decreases. The probability for the electrons to relax toward the thermal energy range is low, because under the conditions adopted, the rate of superelastic collisions between electrons and excited sodium atoms is higher than the energy relaxation rate caused by elastic collisions $\nu^*(\varepsilon_{\min}) > \delta\nu_{ea}(\varepsilon_{\min})$. After the electrons have undergone superelastic collisions, they acquire their energy and, thus, return to a higher energy range. As a result, the EEDF becomes inverse in the range near the Ramsauer minimum.

In mixtures with a higher nitrogen concentration (at [N_2]/[Na] > 50), the mean electron energy decreases, because the electron energy relaxation rate caused by electron–molecule collisions becomes higher. Most of the electrons relax toward the thermal energy range; so the extent to which the EEDF is inverse decreases and the electron mobility becomes positive.

In mixtures containing a smaller amount of sodium, [Na]/[Ar] = 10^{-5} (see curve 2 in Fig. 2), the electron mobility cannot be negative, because the relative concentration of the excited sodium atoms is too low. In such mixtures, the condition $\delta\nu_{ea}(\varepsilon_{\min}) > \nu^*(\varepsilon_{\min})$ always holds, under which only a weakly inverse EEDF can form.

For the electron mobility to become negative, not only the EEDF should be inverse, but also the inequality $\partial[\varepsilon^{3/2}/\nu_{tr}(\varepsilon)]/\partial\varepsilon < 0$ with $\nu_{tr}(\varepsilon)$ as the transport frequency of elastic collisions should be satisfied [17]. In the mixtures under consideration, this necessary condition, which holds only for such profiles of the transport cross sections that are peculiar to heavy inert gases in the range $\varepsilon > \varepsilon_{\min}$, sets a limit on the maximum possible amount of sodium and nitrogen admixtures for which the electron mobility can be negative. In a Na–N_2–Ar mixture, this condition fails to hold when [Na]/[Ar] > 10^{-3}, because, in the range $\varepsilon \approx \varepsilon_{\min}$, the dominant contribution to the total transport collision frequency comes from collisions between electrons and sodium atoms. In a mixture with the above composition, the EEDF inversion is pronounced, which causes the electron mobility to become lower than that in the case of an equilibrium distribution whose temperature is determined from the energy balance equation for an electron gas. However, curve 3 in Fig. 2 shows that under conditions at hand, the ANC effect cannot be achieved.

2) Na–N_2–Kr Mixture: Fig. 4 displays an isogram of the reduced electron mobility as a function of the mixture composition for $T^* = 1$ eV and $T_a = T_v = 0.047$ eV. We can see that according to our model, in a three-component Na–N_2–Kr mixture, a region exists in which the electron mobility can become negative. However, this region is too small, so in the figure it looks like a point with the coordinates lg([N_2]/[Na]) ~ 1 and lg([Kr]/[Na]) ~ 3.5. An increase in the population of excited atoms makes it possible to achieve $\mu < 0$ in mixtures in which the relative amount of admixtures can be varied in a wider range. Consequently, adding nitrogen to mixtures in which krypton is used as a buffer gas leads to a fundamentally new result, because in two-component mixtures containing sodium, the electron mobility cannot be negative. The reason is that in the presence of nitrogen admixtures, the EEDF inversion becomes more pronounced.

3) Na–N_2–Xe Mixture: Fig. 5 presents an isogram of the reduced electron mobility as a function of the mixture composition for $T^* = 1$ eV and $T_a = T_v = 0.047$ eV. We can see that it is possible to achieve negative electron mobility in mixtures in whichthe relative amount of admixtures can be varied in a wider

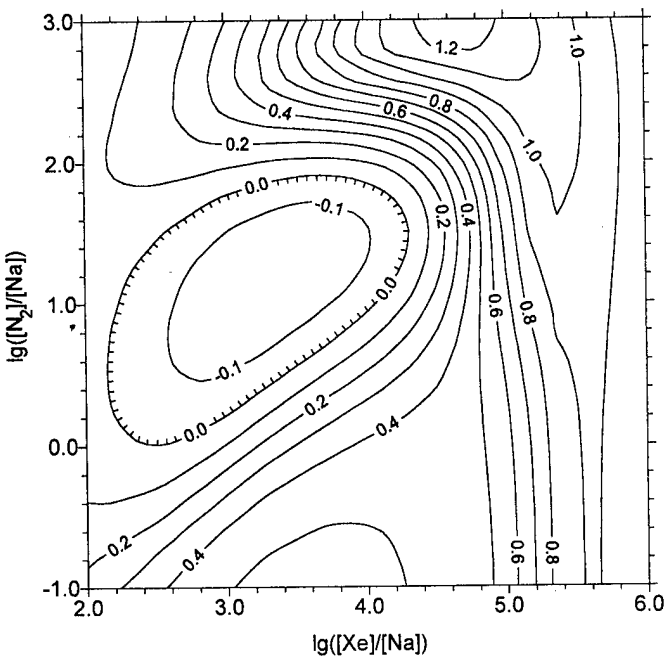


Fig. 5. Isocontours of the reduced electron mobility μN (in 10^{23} $V^{-1}cm^{-1}s^{-1}$) in a Na–Xe–N_2 mixture at $\xi = 0$, $T_a = T_v = 0.047$ eV, and $T^* = 1$ eV.

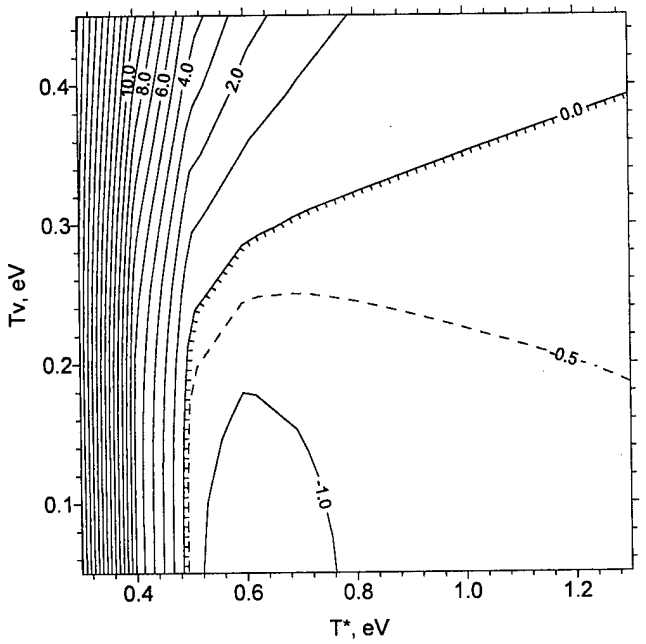


Fig. 6. Isocontours of the reduced electron mobility μN (in 10^{23} $V^{-1}cm^{-1}s^{-1}$) as a function of T^* and T_v in a Na–Ar–N_2 mixture at [Ar]/[Na] = 10^4, [N_2]/[Na] = 10, $\xi = 0$, and $T_a = 0.047$ eV.

range in comparison with the Na–N_2–Kr mixture, because the elastic scattering cross sections for xenon are several-fold larger than those for krypton. Consequently, in mixtures for which the condition $\partial[\varepsilon^{3/2}/\nu_{tr}(\varepsilon)]/\partial\varepsilon < 0$ holds, the total concentration of nitrogen and sodium can be substantially increased. Because, in such mixtures, the formation of a nonequilibrium EEDF is governed by collisions of electrons with nitrogen molecules and excited sodium atoms, the EEDF inversion becomes more pronounced in the energy range around the Ramsauer minimum. As a result, in the Na–N_2–Xe mixture, the region in which the electron mobility can be negative becomes less sensitive to the choice of the relative amount of admixtures compared with the case of a Na–N_2–Kr mixture.

Our calculations show that, in all of the mixtures under study, the region in which it is possible to achieve negative electron mobility narrows as T^* decreases. In this connection, it is important to determine the critical values of the internal plasma parameters at which the ANC effect can be observed.

IV. Critical Values of the Mixture Parameters

A. Populations of the Excited States of Atoms and Molecules

Fig. 6 presents the calculated mobility μN as a function of T^* and T_v for a Na–N_2–Ar mixture. The relative amount of the components in the mixture corresponds to the maximum absolute value of the negative electron mobility in Fig. 1. It is seen that the critical population temperature for which the electron mobility in the indicated weakly ionized mixture ($\xi = 0$) can be negative is $T^*_{cr} \sim 0.48$ eV, which corresponds to such relative populations of Na(3P) atoms that are an order of magnitude lower than those in a two-component Na–Ar mixture [1]. A further increase in T^* raises the absolute value of the negative electron mobility. However, in the range $T^* > 0.6$ eV, the absolute value of the negative electron mobility begins to decrease at $T_v = T_a$, because the range in which the EEDF inversion is maximum starts to displace from the vicinity of the Ramsauer minimum toward the range $\varepsilon > \varepsilon_{\min}$, in which the cross section for electron scattering in elastic collisions is an increasing function. This circumstance sets an upper bound on the range of T^* in which the absolute value of the negative electron mobility is maximum ($\mu N < -1$).

Fig. 6 also shows that, for each temperature $T^* > T^*_{cr}$, a critical vibrational temperature exists $T^{cr}_v < T^*$ above which the electron mobility cannot be negative. To explain this result, we turn to Fig. 2, in which curve 2 illustrates the EEDF calculated at $T_v = 0.4$ eV and $T^* = 0.6$ eV. We can see that an increase in T_v leads to an increase in the number of electrons in the range $\varepsilon \approx \varepsilon_{\max}$ caused by superelastic collisions with vibrationally excited molecules. This, in turn, raises the electron flux into the thermal energy range caused by inelastic collisions of electrons with sodium atoms. As a result, in the range around the Ramsauer minimum, the EEDF inversion disappears, and the electron mobility becomes positive.

In mixtures in which krypton and xenon were used as a buffer gas, the electron mobility as a function of T^* and T_v was found to behave in a similar manner. Here, we present the critical values of the parameters only for mixtures whose composition corresponds to the maximum absolute value of the negative electron mobility in Figs. 4 and 5. In Na–N_2–Kr and Na–N_2–Xe mixtures, the critical populations of excited sodium atoms correspond to $T^*_{cr} \sim 1.0$ eV and $T^*_{cr} \sim 0.8$ eV, respectively. Recall that in mixtures containing xenon, the EEDF inversion is most pronounced and, consequently, the electron mobility can be negative in a wider parameter range in comparison with krypton-containing mixtures.

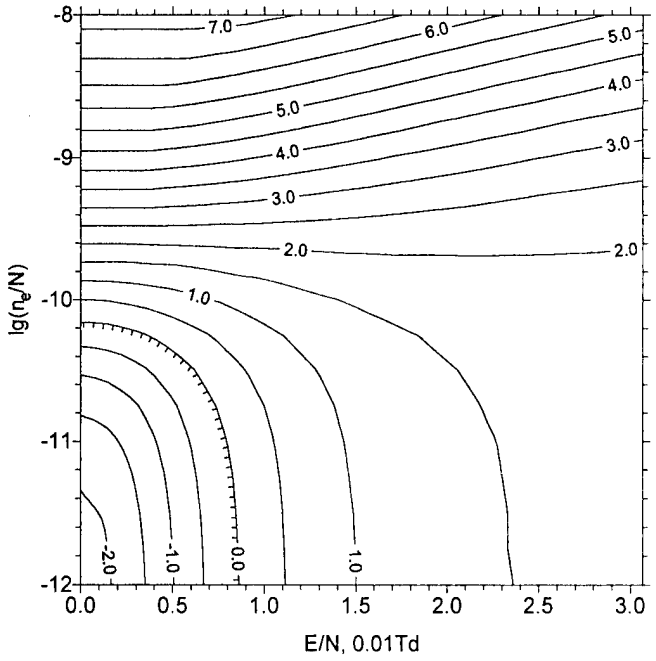


Fig. 7. Isocontours of the reduced electron mobility μN (in 10^{23} $V^{-1}cm^{-1}s^{-1}$) as a function of the degree of ionization n_e/N and of the reduced electric field E/N in a Na–Ar–N_2 mixture at [Ar]/[Na] = 8.3×10^1, [N_2]/[Na] = 3.3×10^1, $T^* = 1$ eV, and $T_a = T_v = 0.047$ eV.

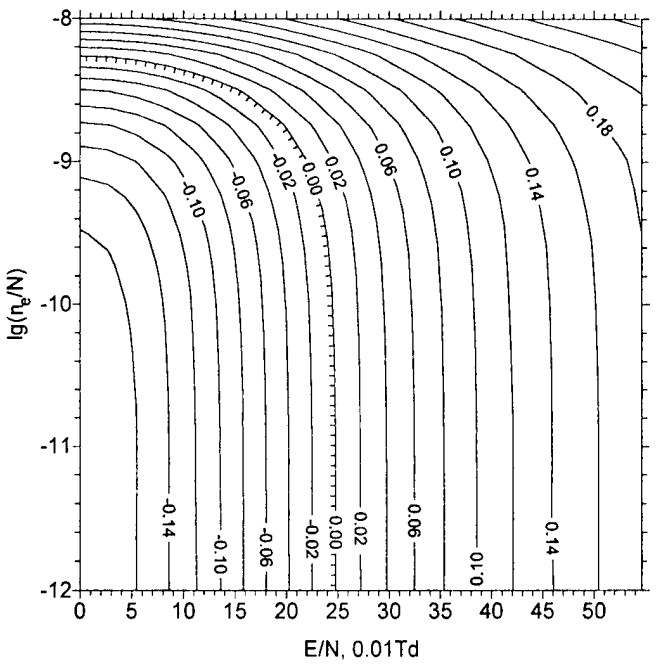


Fig. 8. Isocontours of the reduced electron mobility μN (in 10^{23} $V^{-1}cm^{-1}s^{-1}$) as a function of the degree of ionization n_e/N and of the reduced electric field E/N in a Na–Xe–N_2 mixture at [Xe]/[Na] = 1.8×10^3, [N_2]/[Na] = 13, $T^* = 1$ eV, and $T_a = T_v = 0.047$ eV.

B. Critical Degree of Ionization and Critical Electric Field

In order to address the ANC effect experimentally, it is necessary to determine the critical degree of ionization and the critical electric field. On the one hand, the electron concentration acts to increase the plasma conductivity $\sigma = en_e\mu(\xi, E/N)$, where e is the electron charge and n_e is the electron concentration. On the other hand, it is well known [14] that the electron–electron collisions tend to make the EEDF Maxwellian and, hence, to destroy the effect of negative electron mobility. An increase in the reduced electric field raises the diffusion in energy space, thus, reducing the EEDF inversion. Because the above analysis has revealed that the effect of negative electron mobility is most pronounced in mixtures with argon and xenon, we will focus on a comparison of these mixtures. We consider the mixtures whose composition corresponds to the points at which the absolute value of the negative electron mobility is maximum at $T^* = 1$ eV and $T_v = T_a = 0.047$ eV.

Fig. 7 shows the calculated electron mobility as a function of the degree of ionization and of the electric field strength in a Na–N_2–Ar mixture. The electron mobility becomes negative at $\xi_{cr} < 10^{-10}$. An increase in T^* causes ξ_{cr} to grow. This follows from an order-of-magnitude estimate for ξ_{cr}, which can be obtained from the approximate equality between the electron–electron collision frequency and the superelastic collision frequency at the Ramsauer minimum, $\nu_{ee}(\varepsilon_{\min}) \approx \nu^*(\varepsilon_{\min})$. In a three-component mixture, at $T^* = 1.3$ eV, ξ_{cr} is about two orders of magnitude higher than that in a Na–Ar mixture.

An order-of-magnitude estimate for the critical electric field strength can be obtained from the condition that the electric field weakly affects the mean electron energy, $eE\lambda(\varepsilon_{\min}) \approx \delta^{1/2}T_e$ [18], where $\lambda(\varepsilon)$ is the electron mean free path. Making the EEDF inversion more pronounced by means of nitrogen admixtures allows the critical electric field strength to be increased by almost an order of magnitude compared to that in a two-component mixture [1].

Fig. 8 displays an isogram of the electron mobility in a Na–N_2–Xe mixture. We can see that for the same ξ and E/N, the electron mobility in the xenoncontaining mixture is almost an order of magnitude lower than that in the mixture containing argon. The reason is that in the first mixture, the transport cross section at $\varepsilon_{\min}$ is almost an order of magnitude larger than that in the mixture with argon. This also explains why the critical electric field strength in a Na–N_2–Xe mixture is larger than that in a Na–N_2–Ar mixture by a factor of 20.

Fig. 8 also shows that the critical degree of ionization in the mixture with xenon is higher than that in the argon-containing mixture by a factor of 50. This stems from the following two circumstances.

1) Because the elastic scattering cross section for xenon is large, it is possible to use mixtures with a relatively high concentration of sodium atoms, and the criterion for the formation of an inverse EEDF, $\nu_{ee}(\varepsilon_{\min}) \leq \nu^*(\varepsilon_{\min})$, is valid for high degrees of ionization.
2) In mixtures with xenon, the energy corresponding to the Ramsauer minimum is higher than that in mixtures with argon. Because the Coulomb collision cross section decreases in inverse proportion to the squared energy, this criterion is valid for high electron concentrations.

Hence, in mixtures containing sodium vapor and molecular nitrogen, the use of xenon (instead of argon) as a buffer gas makes it possible to achieve the ANC effect over a significantly wider range of parameters. A similar conclusion was drawn in [19] in analyzing the processes of formation of the EEDF in pure inert gases: it was shown that in mixtures with xenon, the

effect of differential negative conduction can be achieved for larger values of ξ and E/N compared with argon-containing mixtures.

In our study, we use a two-term decomposition of the EEDF in Legendre polynomials. The question of how the above electric field strengths affect the applicability range of this decomposition requires separate consideration. Generally, this question is tackled by comparing the results from calculations of the EEDF and electron mobility carried out in a two-term approximation with those obtained with allowance for higher order Legendre polynomials or with the Monte Carlo simulation results [20]. Here, we restrict ourselves to checking the general criterion for the applicability of the two-term decomposition at arbitrary values of the energy. This criterion, which was derived in [21], has the form [22]

$$\frac{e^2E^2}{m\nu_{tr}^2(\varepsilon)\sqrt{\varepsilon}}\left|\frac{d}{d\varepsilon}\left(\varepsilon^{3/2}\frac{df(\varepsilon)}{d\varepsilon}\right)\right| \ll f(\varepsilon). \qquad (2)$$

Fig. 3 shows the EEDF and the left-hand side of (2), both calculated at $E/N > (E/N)_{cr}$ for argon and drawn to an enlarged scale (500 : 1). The quantitative criterion (2) is seen to be satisfied just in the range in which the EEDF is inverse; consequently, the two-term approximation, which was used to calculate the EEDF and to analyze the possibility for achieving negative electron mobility, is valid under the conditions adopted here. This results agrees with the qualitative criterion $eE\lambda(\varepsilon)/2\varepsilon \ll 1$ [22] for the applicability of the two-term approximation. According to this criterion, the energy acquired by an electron in an electric field over a distance equal to the mean free path should be lower than the energy of the electron. This criterion is less stringent than is the quantitative criterion, which reflects the influence of the electric field on the mean electron energy, except in the thermal energy range $\varepsilon \ll T_a$. However, the contribution from the thermal electron species to the integral electron mobility is small.

The accomplished parametric calculations just indicate the range of the relative content of the mixture components when the effect of negative mobility may be realized. The absolute values of the concentrations are determined by gas temperature of the mixture (T_a), which denounce the alkaline density as a function of metal vapor pressure. The actual value of T_a shall be chosen from the conditions of the concordance of the critical population of the excited atoms (T^*) and ionization degree of the media derived from the mobility calculations. Ionization degree of the plasma should be determined from the kinetics of ionization and recombination.

Let us carry out the qualitative analysis of the problem for the Na + N_2 + Ar mixture. To make the estimations, let us accept $T^* = 0.6$ eV by the relative density of the mixture components ([N_2]/[Na(3S)]= 13; [Ar]/[Na(3S)]= $4.2\cdot10^4$; $\xi_{cr} = 2\cdot10^{-11}$). Under these conditions, the maximum absolute value of the negative mobility is realized if the influence of interelectron impact on EEDF shape is neglected. The first problem to consider is a basic mechanism of ionization. To recover it, the computations were made of the direct ionization rate by electron impact from the ground state Na(3S) and resonant-excited state Na(3P), employing the cross-sections data from [23]. The corresponding ionization rates turned out to be $k_{i,\,3S} = 3.3\times10^{-13}$ cm^3/s and $k_{i,\,3P} = 7.7\times10^{-11}$ cm^3/s. This result proves that the ionization flow from the resonant excited state $j_i = k_{i,\,3P}\cdot$[Na(3P)] is for an order of magnitude greater than the one from the ground state $j_i = k_{i,\,3S}$ [Na(3S)]. The influence of nitrogen admixture leads to the fact that the corresponding ionization rates get considerably lower than those for the two-component mixture [1].

It shall be notified that the impact ionization produces the electrons in the low-energy region, which diminish the inversion on the EEDF. At the same time, this flow is for two orders of magnitude smaller than the flow caused by the first the kind of collisions Na(3S)+ e→Na(3P) + e ($k_{3S,\,3P} = 1.3\times10^{-9}$ cm^3/s—process rate); consequently, it cannot significantly affect EEDF shape. As result, we can neglect the influence of the ionization processes on the electron mobility.

Under considered conditions, the time of EDDF formation is determined, basically, by the excitation of nitrogen molecules and the second kind of collisions with excited atoms ($k_{3P,\,3S} \sim 10^{-8}$ cm^3/s). The efficiency of these processes are superior over the efficiency of the ionization collisions. The rate values indicate that the characteristic time of EEDF formation is smaller than is ionization time. It makes it principally possible to realize the transient effect of negative mobility, when the relevant ionization degree of the mixture (produced by the initial ionization pulse, for example) is superimposed at the definite moment by the resonant exciting radiation, forming the required resonant atoms density. The duration of negative mobility existence in this case will be determined by the time over which the critical ionization degree of the media is sustained.

The ionization rate of alkali atoms under conditions of laser saturation of a resonant transition was considered in [24]. It was shown that within the ionization dynamics, a certain "intermediate phase" exists when the ionization by electron impact from the resonant state is a basic mechanism of ionization. For pure metal vapors, this phase is unstable, but because of burn out ionization, it turns into the state with the high ionization degree when the major ionization mechanism is stepwise ionization from the high laying states. The duration of the transient phase depends on laser irradiance and on the initial density of metal vapor. The analysis of buffer gas influence performed in some following works took into account, mostly, the energy losses in electron energy balance and described the corresponding slowdown of the ionization rate [25]. To find out if the stable state can be realized while $T^* > T^*_{cr}$ by low ionization degree, we need to perform a detailed analysis of recombination processes involving molecules and atoms of the buffer gas.

The recombination process is greatly determined by the quenching of Rydberg state atoms. Using the quenching cross sections from [26], we carried out the computations of a three-body recombination rate within the model of modified diffusion approximation [14]. The calculation results showed that the "bottle-neck" for the recombination flow is formed by the states paced about $E_r \sim (2 \div 3)T_a$ from the continuum. It was also proven that the radiation–collision recombination caused by quenching of sodium excited states by argon cannot counterbalance direct ionization by electron impact by [Ar] $< 10^{20}$ cm^{-3}. The same is true for the mixture with xenon as a buffer gas. The ionization flow in this case can be counterbalanced by three-body recombination when

electron plays the role of the third body. Consequently, the recombination–ionization equilibrium may be realized by a high ionization degree of metal vapor; EEDF in this case has a Maxwellian shape. The charged particles balance under these conditions was considered in [27], for example.

The presence of nitrogen in the mixture can accelerate considerably the recombination of charged particles [14]. The first reason is the multiquantum change of the state of excited atom caused by the quenching followed by the excitation of vibration states. The second reason is the efficient formation of molecular ions in plasma-containing nitrogen, (for example, NaN_2^+ with binding energy ~0.33 eV) [28], followed by the dissociative recombination, which can significantly affect electron balance. Discussing the experimental results for the Cs+ N_2 mixture in [28], the authors came to the conclusion that the dissociative recombination of CsN_2^+ ions has a major influence on charged particle losses. The experimental results on the recombination in Na + N_2 mixture [29] available at the moment show a complicated dependence of plasma decay rate on the component relative concentration and allow just a qualitative interpretation.

Let us make some estimations to clear out the role of dissociative recombination in charged particles balance, taking NaN_2^+ ions as an example. The ion composition of the plasma will be determined by molecular ions, if atomic ions formation is counteracted by the process of their conversion into molecular ones $k_{i,3P}[\mathrm{Na(3P)}]n_e \sim \alpha_c[\mathrm{N_2}]\cdot[\mathrm{Ar}]\cdot n^+$, where α_c is the conversion constant. Using the data from [30] on N_2 and Ar polarization, we have got $\alpha_c \sim 9\cdot 10^{-31}(300/T_a)^{3/4}$ cm^6/s. It means that by [Ar] $\sim 7\cdot 10^{17}$ cm^{-3}, the molecular ions form the majority. This corresponds [31] to mixture temperature $T_a = 500$K. We can derive an approximate value of a direct dissociative recombination rate α_{DR}, which counterbalances the direct ionization from the resonant excited states, in accordance to the equation $\alpha_{DR}n_e n_2^+ = k_{i,3P}[\mathrm{Na(3P)}]n_e$, where molecular ions concentration $n_2^+ \sim n_e$ by $T_a > 500$K. The estimation gives $\alpha_{DR} > 2\cdot 10^6$ cm^{-3}/s. The obtained value is possible for the complex ions [30].

It is well known [14] that an effective dissociative recombination leading to the population of the high-laying excited state does not obligatory mean complete recombination. The recombination flow gets into the low-laying states, only if the dissociative recombination populates the states situated below the "bottle neck" of the radiation–collision recombination. In the opposite case, the part of the dissociative recombination flow returns to the continuum because of impact ionization from the excited states. It means the recombination–ionization equilibrium may be reached by a rather high electron concentration. Consequently, within this problem, a very important question is which particular states are populated by the dissociative recombination of molecular ions? The data of this kind are not available at the moment. As a result, to answer if ANC effect may be realized in stationary conditions, we need to study in detail recombination processes in three-components mixtures.

V. Conclusion

We have shown that in mixtures containing molecular nitrogen, the EEDF inversion is more pronounced in the energy range corresponding to the Ramsauer minimum in the cross section for elastic collisions between the electrons and the atoms of heavy inert gases. The addition of molecular nitrogen makes the parameter range that is favorable for achieving the ANC effect in a three-component plasma wider than that in two-component mixtures of alkaline metals with heavy inert gases. The critical population of resonantly excited sodium atoms decreases by an order of magnitude, the critical degree of ionization increases by two orders of magnitude, and the ANC effect can be achieved at larger electric field strengths compared with the case of two-component mixtures. The presence of nitrogen in the mixture decreases the rate of the direct ionization via electron impact and can accelerate considerably the recombination of charged particles.

In mixtures whose composition satisfies the inequalities $\nu_{cr}(\varepsilon_{\max}) > \nu_{01}(\varepsilon_{\max})$ and $\nu^*(\varepsilon_{\min}) > \delta\nu_{ea}(\varepsilon_{\min})$, the parameter range in which the electron mobility can be negative is less sensitive (in comparison with the case of a two-component Na–Ar mixture) to variations in the elastic collision cross sections for heavy inert gases. Also, it depends weakly on variations in the shape of the profile of the excitation cross section in the near-threshold energy range for the resonant transition in sodium. Varying all of these cross sections and the absolute value of the cross section for exciting the vibrational levels of nitrogen molecules in the range 20%–40% only leads to a corresponding change in the mixture composition for which the absolute value of the negative electron mobility is maximum.

Our calculations have shown that the shape of the EEDF and the value of the negative electron mobility are strongly influenced by the processes of the stepwise excitation of sodium atoms from the 3P state, predominantly by transitions to the nearest 4S and 3D states, which have the largest excitation cross sections. The stepwise excitation increases the electron flux into the energy range $\varepsilon < \varepsilon_{\min}$, which reduces the EEDF inversion. According to our calculations, the extent to which the EEDF is inverse depends on both the stepwise excitation cross sections (which were determined with limited accuracy, especially in the near-threshold energy range) and the populations of the 4S and 3D states.

Using the model in which the plasma is regarded as a self-consistent system would allow us to thoroughly analyze how the shape of the EEDF is influenced by both the stepwise excitation processes and the consistency between the critical degrees of ionization and the temperatures corresponding to molecular distributions over vibrational levels, on the one hand, and the critical populations of resonantly excited sodium atoms, on the other hand. Along with the free electron kinetics examined above, this model should include the vibrational-level molecular distributions and the kinetics of the excited sodium atoms, which makes it possible to determine the ionization and recombination rate constants in a plasma. However, this problem requires a separate study.

Acknowledgment

The authors are grateful to L. Tsendin, whose idea regarding "Plasma Engineering" gave impetus to this study. They are indebted to Dr. A. Melnikov for fruitful collaboration and to Dr. I. Movtchan for his comments.

REFERENCES

[1] N. A. Gorbunov, A. S. Melnikov, I. A. Movtchan, I. Smurov, and G. Flamant, "Conductivity of a photoplasma in sodium vapor–inert gas mixtures," *IEEE Trans. Plasma Sci.*, vol. 27, pp. 182–192, Feb. 1999.

[2] N. A. Gorbunov, Ph. E. Latyshev, and A. S. Melnikov, "Electron mobility in a weakly ionized sodium–inert gas plasma," *Plasma Phys. Rep.*, vol. 24, no. 10, pp. 885–890, Oct. 1998.

[3] F. Paniccia, C. Gorse, J. Bretagne, and M. Capitelli, "Electron energy distribution functions in molecular nitrogen: The role of superelastic electron collisions in discharge and post-discharge conditions," *J. Appl. Phys.*, vol. 59, pp. 4004–4006, June 1986.

[4] C. Gorse, M. Cacciatore, M. Capitelli, S. De Benedictis, and G. Dilecce, "Electron energy distribution functions under N_2 discharge and post-discharge conditions: A self-consistent approach," *Chem. Phys.*, vol. 119, pp. 63–70, Jan. 1988.

[5] H. Amemiya, S. Ono, and S. Teii, "Electron energy distribution in nitrogen plasma in various discharges," *J. Phys. Jpn.*, vol. 56, pp. 4312–4328, Dec. 1987.

[6] N. A. Gorbunov, N. B. Kolokolov, and A. A. Kudryavtsev, "Development of electron energy distribution in the plasma of a nitrogen afterglow in the local regime," *Sov. Phys. Tech. Phys.*, vol. 36, pp. 616–620, June 1991.

[7] N. A. Dyatko, I. V. Kochetov, and A. P. Napartovich, "Electron energy distribution function in decaying nitrogen plasmas," *J. Phys. D: Appl. Phys.*, vol. 26, pp. 418–423, Mar. 1993.

[8] G. Colonna, C. Gorse, M. Capitelli, R. Winkler, and J. Wilhelm, "The influence of electron–electron collisions on electron energy distribution functions in N_2 post discharge," *Chem. Phys. Lett.*, vol. 213, pp. 5–9, Oct. 1993.

[9] G. Delecce and De Benedictis, "Relaxation of the electron energy in the post-discharge of He–N_2 mixture," *Plasma Sources Sci. Technol.*, vol. 2, pp. 119–122, May 1993.

[10] R. A. Arslanbekov, A. A. Kudryavtsev, and I. A. Movtchan, "Cage discharge: Theory and experiment," *IEEE Trans. Plasma Sci.*, vol. 24, pp. 1–16, June 1996.

[11] W. H. Long, W. F. Bailey, and A. Garscadden, "Electron drift velocities in molecular-gas–rare-gas mixtures," *Phys. Rev. A*, vol. 13, pp. 471–475, June 1976.

[12] N. L. Aleksandrov, A. V. Dem'yanov, I. V. Kochetov, and A. P. Napartovich, "Possibility of negative differential plasma conductivity in two intervals of the electric field values," *Plasma Phys. Rep.*, vol. 23, pp. 610–615, Jul. 1997.

[13] L. G. Huxley and R. W. Crompton, *The Diffusion and Drift of Electrons in Gases*. New York: Wiley, 1974.

[14] L. M. Biberman, V. S. Vorob'ev, and I. T. Yakubov, *Kinetics of Nonequilibrium Low-Temperature Plasmas*. New York: Consultants Bureau, 1987.

[15] K. P. Huber and G. Herzberg, *Molecular Spectra and Molecular Structure. V. 4: Constants of Diatomic Molecules*. New York: Van Nostrand, 1979.

[16] N. A. Dyatko, M. Capitelli, R. Celiberto, and A. P. Napartovich, "Attachment rate constants in decaying air plasmas: The role of superelastic collisions from electronically excited states," *Chem. Phys. Lett.*, vol. 263, pp. 305–312, Dec. 1996.

[17] N. A. Dyatko, M. Capitelly, S. Longo, and A. P. Napartovich, "Negative electron mobility in a decaying plasma," *Plasma Phys. Rep.*, vol. 24, pp. 691–699, Aug. 1998.

[18] V. E. Golant, A. P. Zhylinsky, and I. E. Sakharov, *Fundamentals of Plasma Physics*. New York: Wiley, 1980.

[19] N. L. Aleksandrov, N. A. Dyatko, I. V. Kochetov, A. P. Napartovich, and D. Lo, "Negative differential conductivity in pure rare gases," *Phys. Rev. E*, vol. 53, pp. 2730–2734, Mar. 1996.

[20] Z. Petrovic, Z. Raspopovic, S. Sakadzic, N. A. Dyatko, and A. P. Napartovich, "Negative electron mobility in a decaying Ar : F_2 plasma. The correlation between Monte Carlo and Boltzmann equation calculations," in *Proc. XXIV ICPIG*, vol. 3, Warsaw, Poland, 1999, pp. 61–62.

[21] V. L. Ginzburg and A. V. Gurevich, "Nonlinear phenomenon in plasma is subjected to an alternating electromagnetic field," *Usp. Fiz. Nauk*, vol. 70, pp. 201–246, Feb. 1960.

[22] N. L. Aleksandrov and E. E. Son, "Energy distribution and electron kinetic coefficients in an electric field in gases," in *Khim. Plazmy*, B. M. Smirnov, Ed. Moscow: Energoatomizdat, 1980, pp. 35–75.

[23] I. Bray, "Calculation of electron impact total, ionization, and nonbreakup cross sections from the 3S and 3P states of sodium," *Phys. Rev. Lett.*, vol. 73, pp. 1088–1090, Aug. 1994.

[24] R. M. Measures and P. G. Cardinal, "Laser ionization based on resonance saturation—A simple model description," *Phys. Rev. A.*, vol. 23, pp. 804–815, Feb. 1981.

[25] W. T. Hill, "Quenching of resonant laser-driven ionization at high buffer gas pressures," *J. Phys. B: At. Mol. Phys.*, vol. 19, pp. 359–368, Feb. 1986.

[26] I. L. Beigman and V. S. Lebedev, "Collision theory of Rydberg atoms with neutral and charged particles," *Phys. Rep.*, vol. 20, pp. 95–328, Jan. 1995.

[27] R. Shuker, A. Gallagher, and A. V. Phelps, "Models of high-power discharges for metal–Xe excimer lasers," *J. Appl. Phys.*, vol. 51, pp. 1306–1320, Mar. 1980.

[28] A. T. Pritt, "Cs^+—Electron recombination in the presence of N_2, O_2, and CO_2 at 300K," *J. Appl. Phys.*, vol. 61, pp. 2795–2802, Apr. 1987.

[29] A. L. Kuranov, I. N. Skoblo, Yu. E. Skoblo, I. E. Suleimenov, and M. O. Chaika, "Effect of small alkaline additives on recombination processes in the positive column of a glowing nitrogen discharge," *Plasma Phys. Rep.*, vol. 24, pp. 1060–1065, Dec. 1998.

[30] B. M. Smirnov, *Ions and Excited Atoms in Plasma* (in Russian). Moscow: Atomizdat, 1974.

[31] N. Nesmejanov, *Vapor Pressure of the Elements*. New York: Academic, 1963.

Nikolai A. Gorbunov was born in Wladimir region, Russia, in 1960. He received the M.S. degree in 1985 and the Ph.D. degree in plasma physics and optics in 1989, both from the Leningrad State University, Leningrad, Russia.

Since 1990, he has been working at St. Petersburg State University in the Optics Department, Laboratory of Low Temperature Plasma Physics, St. Petersburg, Russia, as a Research Scientist. His research interests include photoplasma formation in resonant excited medium, electron kinetic in plasmas, probe, optical, and UHF diagnostic, and applications.

Olga V. Krylova was born on August 28, 1975, in Moldova, USSR. She received the M.D. degree in plasma physics and optics from the St. Petersburg State University, St. Petersburg, Russia, in 1999.

She is a Postgraduate Student at St. Petersburg State University, Faculty of Physics, Department of Optics. Her research interests include electron kinetic in plasma and optic and molecular spectroscopy of hydrogen plasma.

Igor Smurov was born on January 12, 1954, in Moscow, Russia. He received the Diploma from the Physical-Engineering Institute of Moscow in 1977 and the Ph.D. degree in 1982 from Baikov Institute of Metallurgy (IMET), USSR Academy of Sciences, Moscow.

From 1977 to 1991, he was with IMET. His last position was Vice-Head of the Laboratory of Laser Machining of Materials. Since 1991, he has been a Professor at Ecole Nationale d'Ingénieurs de St-Etienne (ENISE), France. His main research interest includes the interaction of energy fluxes (laser, plasma, electron beam) with materials. He has made important contributions in the fields of laser-induced heat and mass transfer involving phase transformations, pyrometry in energy beams applications, and laser-induced plasma. He has more than 200 publications, including one book, 15 invited articles in books, 38 articles in international journals, and approximately 70 proceedings of international conferences.

Feasibility Study on Frozen Inert Gas Plasma MHD Generator

Hiromichi Kobayashi and Yoshihiro Okuno

Abstract—**The feasibility of a magnetohydrodynamics (MHD) generator with frozen inert gas plasma (FIP) is examined numerically. The FIP is produced by pre-ionizing helium of inert gas without alkali metal seed at the generator inlet. Because the three-body recombination coefficient of helium ions is low at the electron temperature more than 5000 K, the ionization degree of inert gas is kept almost constant in the entire region of the generator channel and the relation between the electron temperature and the electron number density deviates from the Saha equilibrium. In a small-scale disk-shaped generator, the enthalpy extraction ratio of 22.7% and the isentropic efficiency of 54.8% are obtainable for the load resistance of 3.0 Ω and magnetic flux density of 4 T under the pre-ionization degree of 4.79×10^{-5}. The auxiliary power to sustain the pre-ionized plasma corresponds to about 2% of the thermal input. For high-magnetic flux density, the generator performance can be improved as well as a conventional-seeded plasma MHD generator.**

Index Terms—**Frozen inert-gas plasma, MHD power generation, nonequilibrium plasma, r-θ two-dimensional numerical simulation.**

I. Introduction

A magnetohydrodynamics (MHD) power generation directly converts the enthalpy of a high-temperature gas of about 2000 K to electric energy by applying a magnetic field to high-velocity plasma flow. To realize the high-energy conversion efficiency, a high electrical conductivity in the working medium is required, and for this purpose, a small amount of seed material is injected to the working gas. As the seed material, in general, an alkali metal or an alkali metal composition is used for a closed-cycle MHD power generation with inert gas or for an open-cycle MHD power generation with combustion gas, respectively. It is well known in the closed-cycle MHD generation that the nonequilibrium plasma with full ionization of seed material, such as cesium and potassium, provides a high generator performance [1]–[3]. Thus, the electron temperature in the range from 4000 K to 8000 K is suitable when helium is used as the working gas, because ionization instabilities attributed to seed and inert gas partial ionization are not caused and steady and uniform plasma is realized [4]. In the nonequilibrium seeded plasma above, the electron number density can be under the regime of Saha equilibrium at the electron temperature.

Manuscript received January 27, 2000; revised April 4, 2000.

H. Kobayashi is with the Department of Physics, Hiyoshi Campus, Keio University, Kouhoku-ku, Yokohama 223-8521, Japan (e-mail: hkobayas@phys-h.keio.ac.jp).

Y. Okuno is with the Department of Energy Sciences, Tokyo Institute of Technology, Midori-ku, Yokohama 226-8502, Japan.

Publisher Item Identifier S 0093-3813(00)07250-7.

The closed-cycle MHD power generation with the nonequilibrium-seeded plasma is attractive, and in fact, the high-power generation has been successfully demonstrated with several experimental facilities [5]–[7]. The ionization of seed material provides the sufficient electrical conductivity even under less Joule dissipation. From the viewpoint of the system operation, however, the injection and removal of the seed material can be one of the key techniques for a future commercial plant. Furthermore, the seed material should be injected uniformly in time and space, and the fraction should be controlled precisely.

As another candidate, a closed-cycle MHD power generation with nonequilibrium plasma without alkali metal seed can be offered. In fact, the concept of MHD generator working on the nonequilibrium ionization of pure inert gas has been already proposed and examined in Russia [8], [9]. This concept is based on the fact that the three-body recombination coefficient of inert gas ions is low at the electron temperature $T_e > 5000$ K because of the specific structure of the electronic level. Under this condition, the frozen inert gas plasma (FIP) is realized because the ionization degree of inert gas is maintained almost constant in the generator channel. For this kind of generator, the performance is affected mainly by the inlet electron number density (or electron temperature), and in order to obtain the high electron number density at the generator inlet where the electron temperature is about 10 000 K, a pre-ionization of inert gas is inevitable.

There can be two types of the FIP-MHD power generation. One is the system of the "P-layers" (conducting plasma clots), in which the inert gas is pulse-periodically pre-ionized [10], [11]. The plasma as current layer turns to be slowly recombining, and the high concentration of electrons remains in it when the plasma layer passes through the MHD channel. Thus, the electron number density is higher than that expected from the Saha equilibrium at the electron temperature. This pulse-periodically pre-ionized plasma can be suitable for the power generation with a linear-shaped MHD generator, because the plasma clots can act as "pistons" [12]. Another, which is suitable for a disk-shaped MHD generator, is the system of continuously produced FIP [9], [13]. If the uniform pre-ionization in time and space at the generator inlet is possible and the FIP is maintained in the generator channel, the generator with performance comparable to a conventional-seeded plasma MHD generator is feasible. In the disk generator, in comparison with the linear generator, the FIP may be maintained more successfully, because the influence of voltage drop near electrodes, which collapses the plasma easily, is considered to be negligible. It is obvious here that as a compensation for the elimination of seed material, the inlet plasma condition should be controlled precisely, and the auxil-

0093–3813/00$10.00 © 2000 IEEE

iary electric power to produce the pre-ionized plasma is necessary.

In the present study, the feasibility of an FIP disk MHD generator is examined with r-θ two-dimensional (2-D) numerical simulation. This 2-D code has been successfully used for the explanation of the plasma behavior and the performance of a conventional-seeded plasma MHD generator [14]. The effects of the pre-ionization degree of inert gas, the load resistance and the magnetic flux density on the plasma structure, and the generator performance, such as the enthalpy extraction ratio and isentropic efficiency, are revealed.

II. Basic Equations and Numerical Procedures

A. Governing Equations for the Charged Particles

Nonequilibrium MHD plasma consists of noble gas atoms, noble gas ions, and electrons. The governing equations for the charged particles are written as follows.

Ion Continuity Equation:

$$\frac{\partial n_n^+}{\partial t} + \nabla \cdot (n_n^+ \vec{u}) = k_f n_e n_n - k_r n_e^2 n_n^+ \qquad (1)$$

$$n_e = n_n^+$$

where

- n_n^+ number density of noble gas ions;
- n_n number density of noble gas atoms;
- n_e electron number density;
- u velocity;
- k_f ionization rate coefficient;
- k_r recombination rate coefficient.

The recombination rate as a function of electron temperature is shown in Fig. 1. In the present study, the recombination rate by Hinnov and Hirschberg [15] for the electron temperature less than 4000 K and the rate by Slavin [11] for more than 4000 K are used

$$k_r = 1.21 \times 10^{-35} \frac{e^{55300.0/T_e}}{T_e^2}, \quad (T_e > 4000\ \text{K}). \qquad (2)$$

The expression (2) of recombination is theoretically derived from the modified diffusion approximation by taking into account electron-atom collisions and radiative processes [16], and is compared with the experimental values for hydrogen and helium listed in [15]. According to the literature [16], good agreements between experiment and calculation for hydrogen were obtained in the range from 2000 to 16 000 K of electron temperature. The expression (2) of recombination for helium was derived by using the same technique adopted for hydrogen, although the experimental values were not indicated for high electron temperature. Two orders of magnitude lower recombination coefficient for inert gases of helium and argon are caused by the first exited state greater than 70% of the first ionization potential [17]. For argon plasma, two orders of magnitude lower recombination coefficient is obtained from the comparison with the experiment [18]. As mentioned later, the recombination rate by Slavin is adopted practically, because the electron temperature is maintained more than 4000 K all through the channel under the desirable FIP condition, except for strongly nonuniform plasma condition because of the ionization instability.

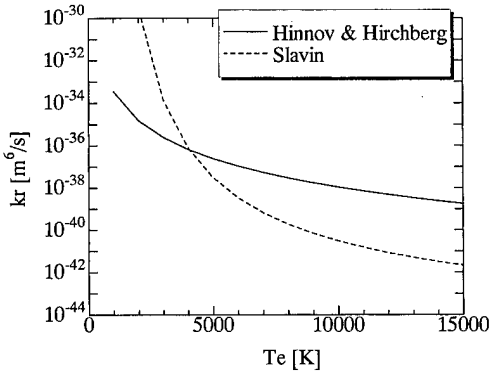


Fig. 1. The recombination rate as a function of electron temperature.

Generalized Ohm's Law:

$$\vec{j} + \frac{\beta}{|\vec{B}|}\vec{j} \times \vec{B} = \sigma(\vec{E} + \vec{u} \times \vec{B}), \qquad (3)$$

$$\sigma = \frac{e^2 n_e}{m_e \nu_e}, \qquad \beta = \frac{eB}{m_e \nu_e}, \qquad (4)$$

where

- j current density;
- E electric field strength;
- B magnetic flux density;
- e charge of electron;
- β Hall parameter;
- σ electrical conductivity;
- m_e mass of electron;
- ν_e averaged collision frequency for electron with the other particles

$$\nu_e = \sum_j n_j Q_{ej} c_e, \qquad (j = \text{atom, ion}) \qquad (5)$$

where $c_e = \sqrt{8kT_e/\pi m_e}$ is the mean electron velocity for a Maxwellian distribution.

The energy-averaged momentum transfer cross section Q_{ej} is obtainable experimentally [19] and theoretically [20]

$$Q_{e-H_e} = \frac{4}{3} \times 5.65 \times 10^{-20} \qquad (6)$$

$$Q_{e-\text{Ion}} = 6\pi \left(\frac{e^2}{12\pi\varepsilon_0 k T_e}\right)^2 \ln\left[12\pi \left(\frac{\varepsilon_0 k}{e^2}\right)^{3/2} \sqrt{\frac{T_e^3}{n_e}}\right] \qquad (7)$$

where ε_0 is the permittivity of free space.

Electron Energy Equation:

$$\frac{\partial U_e}{\partial t} + \nabla \cdot (U_e \vec{u_e}) = -p_e \nabla \cdot \vec{u_e} + \frac{|\vec{j}|^2}{\sigma} - 3 n_e m_e k (T_e - T_g) \sum_j \frac{\nu_{ej}}{m_j} \qquad (8)$$

$$(j = \text{atom, ion})$$

$$U_e = \frac{3}{2} n_e k T_e + \epsilon_n n_e$$

where

U_e energy for electrons;
u_e verocity for electrons;
p_e pressure for electrons;
k Boltzmann constant;
T_e electron temperature;
T_g static gas temperature;
ν_{ej} collision frequency for electron with jth particle;
ϵ_n ionization energy of noble gas.

In the electron energy equation (8), the two-temperature model [21] is adopted, and the radiation losses are neglected.

B. Governing Equations for the Heavy Particles

The Euler equation and the energy equation are given with including the Lorentz force and the Joule heating terms, respectively, as follows.

Continuity Equation:

$$\frac{\partial \rho}{\partial t} + \nabla \cdot (\rho \vec{u}) = 0 \tag{9}$$

where ρ is the mass density and u is the velocity.

Momentum Equation:

$$\frac{\partial}{\partial t}(\rho \vec{u}) + \nabla \cdot (\rho \vec{u}\vec{u}) = \vec{j} \times \vec{B} - \nabla p - \vec{P}_L \tag{10}$$

where p is the static gas pressure and P_L is the pressure loss [22].

Energy Equation:

$$\frac{\partial E_s}{\partial t} + \nabla \cdot [(E_s + p)\vec{u}] = \frac{|\vec{j}|^2}{\sigma} + \vec{u} \cdot (\vec{j} \times B) - Q_L$$
$$E_s = \rho \left(e_s + \frac{1}{2} |\vec{u}|^2 \right) \tag{11}$$

where

E_s total energy;
e_s internal energy;
Q_L thermal loss [22].

C. Maxwell Equations

The conventional MHD approximations of the charge neutrality and low magnetic Reynolds number are assumed. In these approximations, the Maxwell equations are reduced to as follows:

$$\nabla \times \vec{E} = \vec{0}, \qquad \nabla \cdot \vec{j} = 0. \tag{12}$$

D. Numerical Procedures

The ion continuity equation (1), the electron energy equation (8), the continuity equation (9), the momentum equation (10), and the energy equation (11) of the hyperbolic type are solved by the CIP method [23]. The time step in the present simulation is determined as $\Delta t = 0.02\ \mu$s from the condition of $\Delta t < \tau_{T_e} < \tau_{n_e}$, where τ_{T_e} and τ_{n_e} are relaxation times of electron temperature and electron number density, respectively. Grid numbers

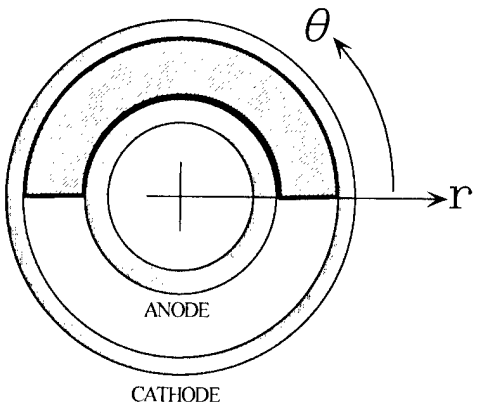


Fig. 2. The calculation region in r-θ-plane.

TABLE I
OPERATING CONDITIONS OF THE GENERATOR

Working gas	He
Thermal input	9.55 [MW]
Stagnation temperature	2000 [K]
Stagnation pressure	3.0 [*atm*]
Inlet pre-ionization degree	$3.58, 4.79, 6.39 \times 10^{-5}$
Inlet electron temperature	10000, 10200, 10400 [K]
Load resistance	$1.0 \sim 6.0$ [Ω]
Magnetic flux density	4.0 [T]
Inlet Mach number	2.0
Inlet radius of channel	160.0 [*mm*]
Outlet radius of channel	284.0 [*mm*]
Inlet height	15.0 [*mm*]
Outlet height	22.0 [*mm*]

and $\Delta r, \Delta\theta$ are decided on $(N_r, N_\theta) = (32, 50), \Delta r = 4.0$ mm, $\Delta\theta = \pi/50$ in accordance with the CFL restriction. The elliptic equation derived from (3) and Maxwell equations (12) as a function of the potential ϕ are solved by using the Galerkin method, one of the finite element methods.

The calculation region in r-θ-plane is shown in Fig. 2. The region is from the downstream edge of anode to the upstream edge of cathode for radial direction, and from $\theta = 0$ to $\theta = \pi$ for the azimuthal direction. On $\theta = 0$ and $\theta = \pi$, the periodical boundary condition is given. The ion number density determined from the Saha equilibrium equation under the assumption of a certain electron temperature is given as the inlet boundary condition for (1). The inlet condition of the mass density, the velocities, and the static gas temperature for (9)–(11) are determined from the isentropic relation for an assumed inlet Mach number. The values of the ion number density, the electron temperature, the mass density, the velocities, the static gas temperature, and their derivatives at the outlet boundary are decided as the free boundary condition, in which the value of the derivatives along the r-direction equals zero.

The boundary condition for the elliptic equation is given as $\phi = 0$ on anode and as $\phi = V_H$ on cathode, where $V_H = R_L \cdot I_H$, and V_H, R_L, and I_H are the Hall voltage, the external load resistance and the Hall current, respectively. Table I shows the operating conditions of the generator. Helium is selected for working gas, because the gas velocity is the fastest of all inert gases. The operating conditions and scale of analyzed generator are chosen on the basis of a conventional-seeded MHD generator for relatively small thermal input of the experimental scale [14], because the comparison between the conventional and the

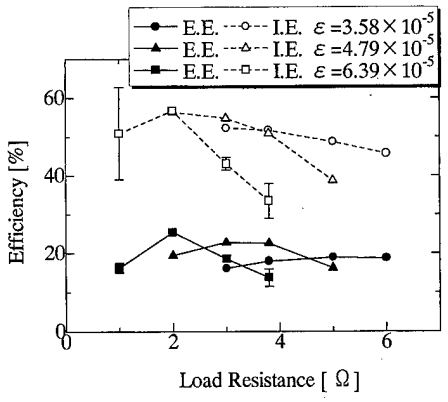


Fig. 3. The enthalpy extraction ratio (E.E.) and isentropic efficiency (I.E.) for pre-ionization degree of noble gas (ε) of 3.58, 4.79, and 6.39 $\times$ 10^{-5} as a function of load resistance.

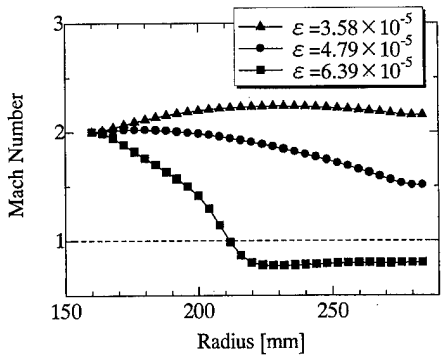


Fig. 4. The radial distributions of the Mach number for 3.0 Ω under the pre-ionization degree of noble gas (ε) of 3.58, 4.79, and 6.39 $\times$ 10^{-5}.

present generators is one of the purposes in the present study. The inlet electron temperature is determined from the similarity between the pre-ionization degree for the present generator and the seed fraction for a seeded MHD generator. In the present study, the channel height is assumed to expand linearly. The optimization of the channel shape, which is important for the high generator performance, will be made in the future study.

The calculating procedure is as follows:

1) The electron temperature is assumed initially as 10 000, 10 200, or 10 400 K in the whole region. The initial electron number density has a perturbation with normal distribution and the standard deviation of 2.5% from the mean value. This spatial perturbation is also applied to inlet grid points. The initial distributions for ρ, u_r, and T_g are determined from the isentropic relation. The initial distribution for u_θ is given as zero all through the channel.
2) The distributions of β and σ are calculated from (4), and then the distribution of ϕ is calculated. The distributions of E and j are obtained from $E = -\nabla\phi$ and (3).
3) The distributions of $n_e, T_e, \rho, u_r, u_\theta$, and T_g at the next time step are calculated by using (1), (8), (9), (10), and (11), then the calculations in 2) are carried out, and all properties at the next time step are calculated.

III. Results and Discussion

The pre-ionization degrees of noble gas are given as 3.58, 4.79, and 6.39 $\times$ 10^{-5} at the generator inlet from the Saha relation at the inlet electron temperatures of 10 000, 10 200 and 10 400 K, respectively. Fig. 3 shows the enthalpy extraction ratio (E.E.) and isentropic efficiency (I.E.) for pre-ionization degrees of noble gas (ε) of 3.58, 4.79, and 6.39 $\times$ 10^{-5} as a function of the load resistance. It is found first that the optimal loading condition exists for each pre-ionization degree, as well as a conventional-seeded plasma MHD generator. Under the optimal load resistance, the enthalpy extraction ratio above 20% and the isentropic efficiency above 50% are successfully obtained even for the simple linear-expand generator. The optimal load resistance shifts to the low value with increasing the pre-ionization degree, because the internal resistance of the generator becomes less. For the pre-ionization degrees of noble gas of 3.58 and 4.79 $\times$ 10^{-5}, the load resistance for the maximum isentropic efficiency is lower than that for the maximum enthalpy extraction ratio. This discrepancy is also confirmed in a seeded plasma MHD generator. Error bars in this figure refer to the fluctuation in time, which is attributed to the nonuniform and unsteady plasma structure.

The radial distributions of the Mach number for 3.0 Ω under the pre-ionization degrees of noble gas of 3.58, 4.79, and 6.39 $\times$ 10^{-5} are shown in Fig. 4, where the static pressure ratios ($p_{\text{out}}/p_{\text{in}}$) are 0.32, 0.53, 1.28, and the stagnation pressure ratios ($P_{0\text{out}}/P_{0\text{in}}$) are 0.40, 0.26, and 0.25, respectively. The outlet stagnation pressures are derived from the substitution of the outlet Mach number and static pressure into the isentropic relation. The supersonic flow is kept under the pre-ionization of 3.58 and 4.79 $\times$ 10^{-5}, but the flow in the downstream region becomes subsonic under that of 6.39 $\times$ 10^{-5}, because the MHD interaction becomes strong with increasing the pre-ionization degree of noble gas. It was confirmed that the fluctuation in the inlet electron number density of 1.01 and 1.46 $\times$ 10^{20} m^{-3} (ε = 3.58 and 4.79 $\times$ 10^{-5}) is acceptable until about ±5%. Because subsonic boundary condition in the present calculation is not used at the generator outlet, the efficiencies under the pre-ionization degree of 6.39 $\times$ 10^{-5} might lack in reliability. Under the supersonic condition all through the channel, as the best performance, the enthalpy extraction ratio of 22.7% and the isentropic efficiency of 54.8% for 3.0 Ω under the pre-ionization degree of 4.79 $\times$ 10^{-5} are obtained. In order to realize the pre-ionization degree of 4.79 $\times$ 10^{-5} at the generator inlet, the auxiliary power of 180 kW is necessary if the pre-ionized plasma with ring-shape and 1 cm width at the generator inlet is produced, where the volume is 1.56 $\times$ 10^{-4} m^3 and the inlet Joule heating is about 1.16 GW/m^3. This auxiliary power corresponds to about 2% of the thermal input. As one of several ways, a pre-ionization by the radiofrequency inductive coupling electromagnetic field can be useful to produce such a ring-shaped plasma [24].

The radial distributions of ionization degree and electron temperature for 2.0 Ω, 3.0 Ω, and 3.8 Ω under the pre-ionization degree of 4.79 $\times$ 10^{-5} are shown in Fig. 5. Fig. 6 shows the radial distributions of electron number density realized under the FIP condition and the electron number densities predicted from Saha relation at the electron temperature shown in Fig. 5. It is

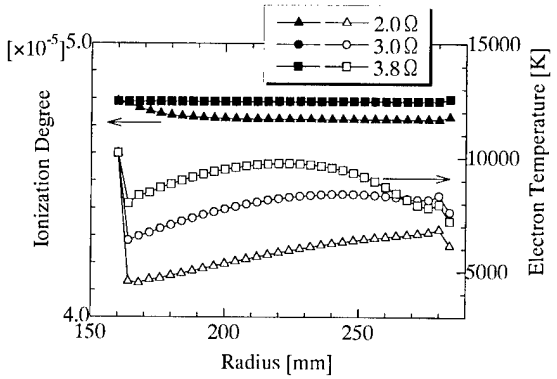


Fig. 5. The radial distributions of ionization degree and electron temperature for 2.0 Ω, 3.0 Ω, and 3.8 Ω under the pre-ionization degree of 4.79×10^{-5}.

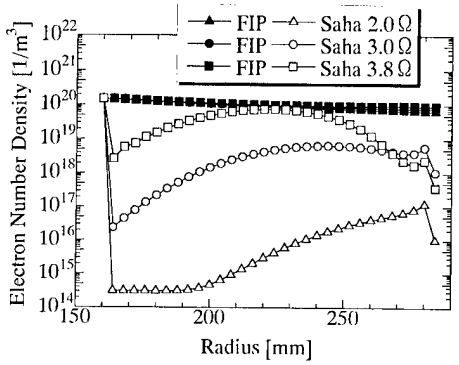


Fig. 6. The radial distributions of electron number density realized under the FIP condition and the electron number densities predicted from the Saha relation at the electron temperature shown in Fig. 5.

confirmed that the ionization degree of helium is maintained almost constant in the entire region of the generator. Although the high inlet electron temperatures are necessary to obtain the sufficient ionization degrees under the Saha equilibrium, the electron temperatures decrease in the generation channel. As mentioned before, the relaxation time of the electron temperature is shorter than that of the electron number density. Because the low external load resistances are connected under the present condition, the electron temperatures sharply decrease owing to the low Joule heating in the generation channel. In spite of the decrease in the electron temperature, the ionization degree and the electron number density are successfully frozen in the generator, because the plasma slowly recombines with the relaxation time longer than the residence time of gas in the generator. As shown in Fig. 6, the electron number density under the FIP condition considerably deviates from the Saha equilibrium. The electron temperature increases with increasing load resistance, because the Faraday current and the amount of the Joule heating become large.

The electron temperature distribution in the r-θ-plane for 3.0 Ω under the pre-ionization degree of 4.79×10^{-5} is shown in Fig. 7. The spoke-like nonuniform structure of plasma caused by the artificially given variation in the electron number density at the generator inlet is observed in the generator, because the three-body recombination coefficient of helium is low at

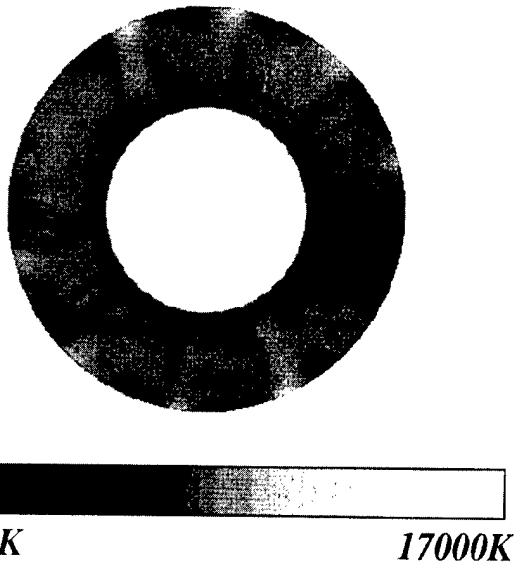


Fig. 7. The electron temperature distribution in r-θ-plane for 3.0 Ω under the pre-ionization degree of 4.79×10^{-5}.

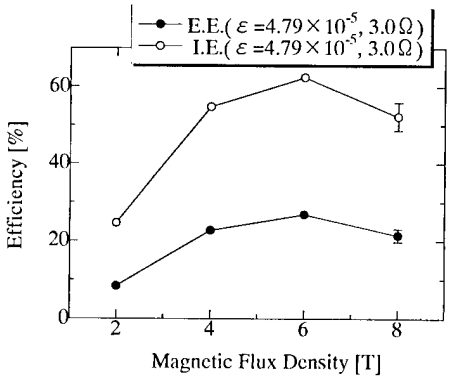


Fig. 8. The enthalpy extraction ratio (E.E.) and the isentropic efficiency (I.E.) as a function of the magnetic flux density for 3.0 Ω and the pre-ionization degree of noble gas (ε) of 4.79×10^{-5}.

electron temperature $T_e > 5000$ K. This structure of electron temperature has been indicated as the "standing azimuthal wave" in [25]. It should be noted here that this structure is steady and stable.

The enthalpy extraction ratio and the isentropic efficiency as a function of the magnetic flux density for 3.0 Ω and the pre-ionization degree of noble gas of 4.79×10^{-5} are shown in Fig. 8. The efficiencies can be improved with increasing the magnetic flux density. The enthalpy extraction ratio of 26.8% and the isentropic efficiency of 62.4% for 6 T are obtainable. For 8 T, however, both efficiencies decrease and periodically fluctuate. Under the condition, it has been confirmed that the flow becomes subsonic. The electron temperature distribution for 8 T in the r-θ-plane is shown in Fig. 9. The ionization instability occurs, and the nonuniformity in the electron temperature is caused in the generator. This structure of the electron temperature periodically rotates along θ direction and is unsteady. Under this situation, the FIP condition is no longer satisfied and the electron number density is almost given by the Saha relation. The reason of the deterioration in the performance for 8 T can

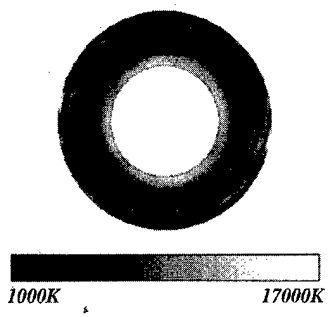


Fig. 9. The electron temperature distribution for 8 T in r-θ-plane.

be attributed to the fact that the inlet conditions of the pre-ionization degree and load resistance are not suitable. To obtain the higher efficiencies, therefore, it is necessary to optimize the inlet plasma conditions, as well as the channel shape.

IV. Conclusion

The feasibility of an FIP disk MHD generator has been examined numerically. The following conclusions can be drawn.

1) The frozen inert gas plasma is realized in the entire region of the generator even under the strong MHD interaction without any instability. The ionization degree is maintained almost constant, and the electron number density higher than that predicted from the Saha relation at the electron temperature is kept through the channel.
2) As typical values, the enthalpy extraction ratio of 22.7% and the isentropic efficiency of 54.8% for the load resistance of 3.0 Ω and magnetic flux density of 4 T under the pre-ionization degree of 4.79×10^{-5} can be obtained even for a small-scale and simple linear-expand channel. Then, the auxiliary electric power for the pre-ionization corresponds to about 2% of the thermal input if the ring-shaped plasma with 1 cm width is generated at the generator inlet.
3) The variation in the electron number density at the generator inlet with several percents provides the steady and stable spoke-like nonuniform structure of plasma in the generator. The nonuniformity, however, does not deteriorate the generator performance.
4) The generator performance such as the enthalpy extraction ratio and the isentropic efficiency can be improved with the increase in the applied magnetic flux density.

It has been confirmed through the present study that the FIP disk MHD generator is feasible as another candidate of the closed-cycle MHD power generation. The optimization of the channel shape and inlet plasma condition will be discussed in a future study.

References

[1] T. Nakamura and W. Riedmüller, "Stability of nonequilibrium MHD plasma in the regime of fully ionized seed," *AIAA J.*, vol. 12, no. 5, pp. 661–668, 1974.
[2] H. Yamasaki and S. Shioda, "MHD power generation with fully ionized seed," *J. Energy*, vol. 1, no. 5, pp. 301–305, 1977.
[3] R. J. Rosa, C. H. Kruger, and S. Shioda, "Plasmas in MHD power generation," *IEEE Trans. Plasma Sci.*, vol. 19, pp. 1180–1190, June 1991.
[4] H. Kobayashi, Y. Okuno, and S. Kabashima, "Three-dimensional structure of MHD flow in a disk generator," *IEEE Trans. Plasma Sci.*, vol. 26, pp. 1526–1531, May 1998.
[5] Y. Okuno, T. Okamura, K. Yoshikawa, T. Suekane, K. Tsuji, M. Okubo, T. Murakami, T. Maeda, S. Kabashima, H. Yamasaki, S. Shioda, and Y. Hasegawa, "High enthalpy extraction experiments with Fuji-1 MHD blow-down facility," *J. Energy Conversion Manage.*, vol. 40, pp. 1177–1190, 1999.
[6] H. Yamasaki, Y. Okuno, S. Torii, J. Masuda, M. Tsutsumi, N. Oda, U. Uchiyama, H. Kouka, T. Fujimoto, H. Suzuki, M. Suzuki, and K. Ohgaki, "Improvement of disk MHD generator performance by inlet swirl," in *AIAA Paper, 30th Plasmadynamics Laser Conf.*, AIAA-99-3658, 1999.
[7] H. Nakamura, T. Okamura, and S. Shioda, "Measurements of properties concerning isentropic efficiency in a nonequilibrium MHD disk generator," *IEEE Trans. Plasma Sci.*, vol. 24, pp. 1125–1132, Mar. 1996.
[8] A. L. Genkin, V. L. Goryachev, N. N. Dumenskii, and A. S. Remennyi, "Characteristics of the flow of a two-temperature plasma of inert gases in an MHD channel," *High Temp.*, vol. 18, pp. 663–667, 1981.
[9] R. V. Vasil'eva, A. V. Erofeev, D. N. Mirshanov, and T. A. Alekseeva, "Evolution of the ionization instability of a plasma with nonequilibrium ionization in an MHD channel," *Sov. Phys. Tech. Phys.*, vol. 34, no. 7, pp. 728–732, 1989.
[10] V. A. Derevyanko, V. A. Lyubochko, S. V. Kukhtetskii, O. G. Parfenov, and V. S. Sokolov, "Formation of current layers in the gas flow in a model MHD channel without using an alkaline additive," *High Temp.*, vol. 19, no. 4, pp. 642–646, 1981.
[11] V. S. Slavin, M. S. Lobasova, K. A. Finnikov, V. S. Slokolov, and V. V. Danilov, "Numerical simulation of MHD process in the planned experimental facility with nonuniform gas-plasma flow driving recombinated plasma clots," in *Proc. 12th Int. Conf. MHD Power Generator*, vol. 2, 1996, pp. 981–993.
[12] V. S. Slavin and K. A. Finnikov, "Ionization kinetics in the nonuniform flow of noble gas carrying T-layers in the faraday channel of MHD generator," in *Proc. Int. Conf. MHD Power Generation High Temperature Technol.*, vol. 2, 1999, pp. 539–550.
[13] A. Yu. Sokolov and Y. Okuno, "Consequent disk MHD generators with nonequilibrium ionization of inert gas," in *Proc. 34th Symp. Eng. Aspects Magnetohydrodynamics*, 1997, pp. 6.2.1–6.2.14.
[14] T. Murakami, H. Kobayashi, Y. Okuno, and S. Kabashima, "Plasma behavior in a nonequilibrium disk MHD generator with a spatially nonuniform seed fraction," in *Electrical Engineering in Japan*. New York: Wiley, 1999, vol. 126, pp. 48–54.
[15] E. Hinnov and J. G. Hirschberg, "Electron-ion recombination in dense plasmas," *Phys. Rev.*, vol. 125, no. 3, pp. 795–801, 1962.
[16] L. M. Biberman, V. S. Vorob'en, and I. T. Yakubov, "On the theory of ionization and recombination in a low-temperature plasma," *Sov. Phys. JETP*, vol. 29, no. 6, pp. 1070–1074, 1969.
[17] S. W. Simpson, "Ionization and recombination rates in argon plasmas," *J. Phys. D: Appl. Phys.*, vol. 22, pp. 1161–1167, 1990.
[18] T. G. Owano, C. H. Kruger, and R. A. Beddini, "Electron-ion three-body recombination coefficient of argon," *AIAA J.*, vol. 31, no. 1, pp. 75–82, 1993.
[19] D. E. Golden, "Comparison of low-energy total and momentum-transfer scattering cross sections for electrons on helium and argon," *Phys. Rev.*, vol. 151, no. 1, pp. 48–51, 1966.
[20] M. Mitchner and C. H. Kruger, *Partially Ionized Gases*. New York: Wiley, 1973, pp. 54–62.
[21] ——, *Partially Ionized Gases*. New York: Wiley, 1973, pp. 163–241.
[22] R. J. Rosa, *Magnetohydrodynamic Energy Conversion*. New York: McGraw-Hill, 1968.
[23] T. Yabe and T. Aoki, "A universal solver for hyperbolic equations by cubic-polynomial interpolation I. One-dimensional solver," *Comput. Phys. Commun.*, vol. 66, pp. 219–232, Feb. 1991.
[24] T. Murakami, Y. Okuno, and S. Kabashima, "Plasma stabilization and improvement in performance of a nonequilibrium disk MHD generator by a radio-frequency electromagnetic field," *IEEE Trans. Plasma Sci.*, vol. 27, pp. 604–612, Feb. 1999.
[25] A. Yu. Sokolov and S. Kabashima, "Numerical simulation of nonlinear ionization nonuniformities in nonequilibrium disk MHD generator," *IEEE Trans. Plasma Sci.*, vol. 25, pp. 15–26, Jan. 1997.



Hiromichi Kobayashi received the B.E., M.E., and D.E. degrees from the Tokyo Institute of Technology in 1994, 1996, and 1998, respectively.

He is presently an Assistant Professor at the Keio University, Yokohama, Japan.



Yoshihiro Okuno received the B.E. degree in electrical engineering from the Kyushu Institute of Technology in 1982 and the M.E. and D.E. degrees in energy sciences from the Tokyo Institute of Technology in 1984 and 1987, respectively.

He is presently Professor at the Tokyo Institute of Technology, Yokohama, Japan.

Technical Notes

Chopping Effect Observed at Cathodic Arc Initiation

André Anders, *Senior Member, IEEE*

***Abstract*—Chopping of current and induction of high-voltage spikes has been observed at the rising edge of cathodic vacuum arcs. It is argued that current chopping at the rising edge is similar to the current chopping effect that is well known for the arc current approaching current-zero. Current chopping can generate high-voltage spikes, and thus, cathodic arc equipment should be protected against voltage spikes that exceed the system's nominal voltage by an order of magnitude.**

***Index Terms*—Chopping current, vacuum arcs, vacuum interrupters, voltage spikes.**

I. Introduction

Cathodic arcs or "vacuum" arcs can be initiated by a variety of techniques. DC or quasicontinuous arcs often use a mechanically moved trigger electrode, and pulsed arcs are usually triggered by a high-voltage surface flashover across an insulator that separates the arc cathode from the high-voltage trigger electrode.

An alternative method of arc initiation that uses neither a mechanical electrode nor a very high pulsed voltage was dubbed the "triggerless" method [1]. It is based on explosive formation of a "hot spot" by ohmic heating of a contact point at the interface between the cathode and a conductive coating that is deposited on an insulator touching the cathode. The coating brings the anode potential to the contact point. The only power supply involved is the arc power supply. The coating is regenerated by plasma deposition. The "triggerless" arc initiation technique was successfully demonstrated in our laboratory for over 50 cathode materials and has been implemented in pulsed plasma sources for thin film deposition [1] and in a vacuum arc ion source [2]. In the following, we focus on a scheme with "triggerless" arc initiation, although the observed chopping effect may also occur with other arc initiation techniques.

The chopping effect has been well studied [3]–[5] because of its importance for vacuum interrupters. In essence, the vacuum arc develops instabilities and extinguishes when the arc current becomes smaller than a critical value: The current "chops off." The critical current value depends on the cathode material, the cathode surface condition, the electrode configuration, the magnetic field (if present), and the electric circuit parameters. The phenomenon is associated with the plasma-generating mechanism of the arc spot. When the arc current decreases and approaches current-zero, the number of current-carrying arc spots, or spot fragments [6], decreases, and the amplitude of noise in the arc voltage increases. When the arc current is further decreased, the conditions for the ignition of spot fragments deteriorate. For instance, cathode surface heating by ion bombardment decreases. If no new spot fragments are ignited, plasma production and electron emission at cathode spots ceases, the current transport is interrupted, and the arc extinguishes. The phenomenon can be harmful if it occurs at relatively high critical chopping current because high-voltage spikes can be induced that can be dangerous to personnel and equipment. Special electrode materials, such as CuW and CuCr, have been developed showing very low chopping currents.

Manuscript received March 6, 2000; revised May 24, 2000. This work was supported by the U.S. Department of Energy, under Contract DE-AC03-76SF00098.

The author is with the Lawrence Berkeley National Laboratory, University of California, Berkeley, CA 94720 USA (e-mail: aanders@lbl.gov).

Publisher Item Identifier S 0093-3813(00)07246-5.

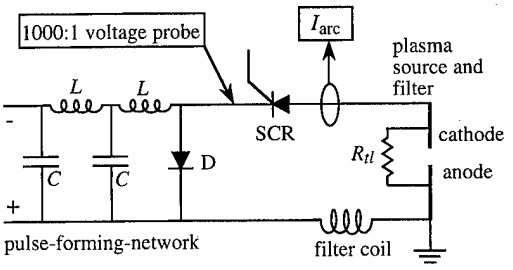


Fig. 1. Simplified electrical schematic of the experiment. The pulse-forming network had an impedance of 0.5 Ω, and the charging voltage could be varied up to 1 kV. The resistor R_{tl} represents the resistance of the conducting path used for "triggerless" arc initiation (typically, ~1 kΩ). The locations of current and voltage measurements are indicated.

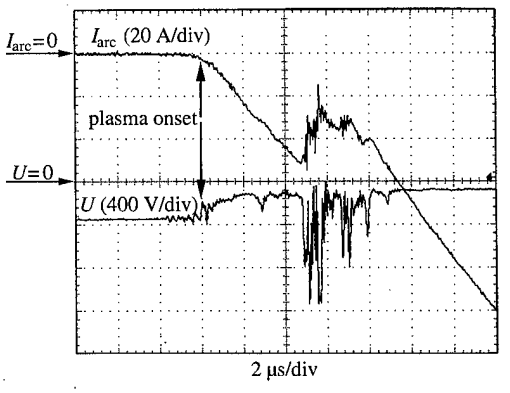


Fig. 2. Example of current and voltage measurements showing an instability that may be associated with the chopping effect. Note that the voltage spikes are about 1.4 kV, although the charging voltage is only 360 V.

The chopping effect is usually observed for *decreasing* arc current. In this publication, we report on the observation of the chopping effect with *increasing* current after arc initiation. As pointed out by a reviewer, the effect is not really new but often observed with AC vacuum arc interrupters after current-zero [7].

Fig. 1 shows the electrical schematic of the experiment. Cathodic arcs are initiated simply by applying the charging voltage of a 0.5-Ω pulse-forming-network to the arc electrodes (360 V in the example shown). The resistor R_{tl} ~ 1 kΩ in Fig. 1 symbolizes the resistance of the conducting path between the anode and cathode that is used for "triggerless" arc initiation. The cathode was an aluminum rod surrounded by an aluminum-coated ceramic tube (plasma source of the minigun type [8]). The vacuum pressure was about 10^{-4} Pa. The arc current, measured by a wideband current transformer of sensitivity 0.01 V/A, shows a current rise-time that is determined by the inductance of the arc circuit. In the example shown in Fig. 2, the thyristor's (SCR) switching time of about 1 μs is manifested by small voltage variations, although the current is still close to zero. The current flows initially through the conducting path, limited by the resistance of the conducting path. For most arc pulses, the current rise is smooth. However, some

0093–3813/00$10.00 © 2000 IEEE

arc pulses exhibit an instability, as shown in Fig. 2. The arc current is still small when the instability occurs, indicating that the underlying physical reasons are similar to what is known for the chopping effect at decreasing arc current. A statistical test of several hundred arc pulses showed that the instability occurred for about 10% of the pulses and, if present, occurred always at currents less than 60 A.

Although more studies are needed to prove that the mechanism of the chopping effect observed with increasing current is indeed identical to the mechanism for decreasing current, high-voltage spikes are induced in both cases. The amplitude of the spikes can exceed the charging voltage by a factor 3–5, and sometimes even higher spikes are observed. Power supplies and other equipment are often not adequately protected. Failure of equipment by overvoltage has been observed. Noteworthy, this type of failure occurred when operating with relatively low charging voltage, in agreement with the interpretation that the instability leading to current chopping and voltage generation is more likely to occur at low arc current.

The author would like to thank I. Brown for his continued support and encouragement.

REFERENCES

[1] A. Anders, I. G. Brown, R. A. MacGill, and M. R. Dickinson, "'Triggerless' triggering of vacuum arcs," *J. Phys. D: Appl. Phys.*, vol. 31, pp. 584–587, 1998.

[2] A. Anders, J. Schein, and N. Qi, "Pulsed vacuum-arc ion source operated with a 'triggerless' arc initiation method," *Rev. Sci. Instrum.*, vol. 71, pp. 827–829, 2000.

[3] R. P. P. Smeets, "The origin of current chopping in vacuum arcs," *IEEE Trans. Plasma Sci.*, vol. 17, pp. 303–310, 1989.

[4] ——, "Experimental characterization of arc instabilities and their effect on current chopping in low-surge vacuum interrupters," *IEEE Trans. Plasma Sci.*, vol. 20, pp. 439–446, 1992.

[5] A. Yamamoto, T. Okutomi, M. Homma, and M. Okawa, "Instability of vacuum arc in Ag-Cu contact alloys," *IEEE Trans. Plasma Sci.*, vol. 21, pp. 463–468, 1993.

[6] B. Jüttner, "The dynamics of arc cathode spots in vacuum," *J. Phys. D: Appl. Phys.*, vol. 28, pp. 516–522, 1995.

[7] R. P. P. Smeets, W. J. van der Ven, K. Watanabe, and M. Homma, "Vacuum arc lifetime extension at small gap length: Beneficial for low-surge circuit interruption," in *11th Int. Conf. Gas Discharges Their Applicat.*, Tokyo, Japan: Institute of Electrical Engineering, Sept. 11–15, 1995, vol. 1, pp. 82–85.

[8] R. A. MacGill, M. R. Dickinson, A. Anders, O. R. Monteiro, and I. G. Brown, "Streaming metal plasma generation by vacuum arc plasma guns," *Rev. Sci. Instrum.*, vol. 69, pp. 801–803, 1998.

A Note on the Possible Electrostatic Disruption of Bacteria

D. A. Mendis, M. Rosenberg, and F. Azam

***Abstract*—Recently published scanning electron and transmission electron photomicrographs of cells of the bacterium *Escherichia coli* exposed to plasma glow discharges at atmospheric pressure indicate physical disruption of their outer cell membranes. However, the mechanism of cell disruption was unclear. Here, we propose and model an electrophysical mechanism for this phenomenon, namely, the electrostatic disruption of the cell membrane, which takes place when it has acquired a sufficient electrostatic charge that the outward electrostatic stress exceeds its tensile strength. It also appears that surface roughness or irregularity would render it more sensitive to electrostatic disruption.**

***Index Terms*—Bacteria, electrostatic disruption, plasma, sterilization.**

I. INTRODUCTION

In a recent paper, Laroussi *et al.* [1] display scanning electron microscope (SEM) photographs of *Escherichia coli*, in a Luria-Bertani broth, undergoing sterilization by a glow discharge under atmospheric pressure (GDAP), wherein five orders of magnitude reduction in cell viability was achieved within exposure time of 20 min. The authors speculate that the bacteria were damaged and poisoned by their interaction at a molecular level, with energetic ions, UV radiation, and cytotoxic free radicals, the latter originating from the breaking of chemical bonds by electrons of energy 1–5 eV present in the discharge. The above authors also reported that the outer membrane of the cell was grossly disrupted and that there was an obvious loss of structural integrity. See addendum.

The purpose of this brief note is to suggest an alternative possibility for the demise of the bacteria in the discharge. We propose that the disruption of the cell structure is a physical process, namely, the electrostatic disruption of the cell membrane, which occurs when it has accumulated sufficient electric charge that the resulting (outward) electrostatic stress is sufficient to exceed its material tensile strength.

There have been many early studies, both theoretical and experimental, of the electrical properties of cell membranes. These are largely concerned with its current-voltage characteristics, including nonlinear effects such as dielectric breakdown (e.g., [2], [3]), the "Wien" field effect on the dissociation of ion pairs [4], and a compressive electrochemical instability leading to the breakdown of bimolecular lipid membranes [5]. In the latter work, the lipid bilayer membrane is idealized as a capacitor whose plates are separated by a uniform elastic medium, wherein the applied voltage leads to a compressive electric force that eventually leads to a catastrophic collapse of the membrane. The lethal effects of microsecond pulses of high electric fields (kilo-electronvolts/centimeter) in bacteria and yeast cells has also been reported [6].

Here, it is not our intention to critique this extensive earlier work on electrical effects on cell membranes. Rather, it is our limited aim to propose the new, above-mentioned, electrophysical mechanism (viz.

Manuscript received March 20, 2000; revised May 30, 2000. This work was supported by the Department of Energy, under Grant DE-FG03-97ER54444, by the IGPP/LANL, under a joint LANL/UCSD grant, and by the National Science Foundation, under Grant OCE-9819603.

D. A. Mendis and M. Rosenberg are with the Department of Electrical and Computer Engineering, University of California at San Diego, La Jolla, CA 92093 USA (e-mail: mendis@ece.ucsd.edu).

F. Azam is with the Marine Biology Research Division, University of California at San Diego, La Jolla, CA 92093 USA.

Publisher Item Identifier S 0093-3813(00)07237-4.

0093–3813/00$10.00 © 2000 IEEE

the electrostatic disruption of the outer cell membrane caused by surface charge accumulation) as an alternative for killing the bacteria, and explore its relevance to the experimental results of Laroussi *et al.* [1].

II. The Model

The electrostatic disruption of homogenous, solid, spherical [7], as well as conducting spheroidal [8] bodies caused by surface charging has previously been discussed. Here, we will follow a similar analysis, except that now the body is not a uniform solid; rather, it is a thin shell enclosing the protoplast of the bacterium. The cell envelope in the Gram-negative *E. coli* is multilayered with two membranes, an inner cytoplasmic membrane (~8 nm thick) and an outer lipopolysaccharide membrane (also ~8 nm thick) enclosing a very thin (~2-nm) layer of peptidoglycan (murein) embedded within a gel-like periplasm (e.g., [9], [10]). While the entire envelope is about 30 nm thick, it is the very thin murein layer with its N-acetylglucosamine and N-acetylmuramic acid polymeric chains cross-linked by peptide that provides both the strength and the rigidity to the bacterium. The SEM micrograph of the untreated *E. coli* [1 , Fig. 4(a)] shows it to be roughly spherical with some surface roughness, either real or caused by fixation and dehydration before SEM examination. In order to bring out the role of surface roughness, while keeping the analysis simple, we idealize the bacterium to be essentially a sphere of radius R, with a hemispherical irregularity (a "pimple") of radius r ($\ll R$). Also, we assume the outer membrane to have a thickness Δ ($\ll r, R$) and to have a uniform surface potential ϕ. Because disruption will take place across a section with minimum radius of curvature due to the larger electric fields there [8], in this case the base of the pimple, the condition for electrostatic disruption is that the component of total electric force along the axis joining the centers of the larger sphere and small hemisphere exceeds the total tensile force on the membrane along this axis

$$\int_0^r \left(\frac{E^2}{8\pi}\right) 2\pi\rho\, d\rho > F_t \cdot 2\pi r\Delta \tag{1}$$

where

ρ	cylindrical coordinate normal to this axis;
F_t	tensile strength of the membrane;
$E^2/8\pi$	electrostatic tension normal to the surface.

Since $E = \phi/r$ on the hemispherical surface, (1) leads to the condition

$$|\phi(V)| \geq 0.2\sqrt{r(\mu\text{m})R(\mu\text{m})}\sqrt{\frac{\Delta}{R}}F_t^{1/2} \tag{2}$$

where F_t is in dynes/cm^2.

If the bacterium had been idealized as a perfect sphere, the condition for disruption across the middle, into two hemispheres, is obtained from (2) by replacing r with R. So, it is clearly easier to disrupt or tear the membrane by breaking off the "pimple" than by breaking it into two more or less equal pieces.

For the present calculation, let us take $R = 1\,\mu$m and $\Delta = 0.008\,\mu$m (e.g., [9]) and $r = 0.02\,\mu$m. The actual measured value of the tensile strength F_t of the outer membrane is not available. However, since Gram-negative bacteria can maintain turgor pressure of 1–5 atm [11] and the purpose of the strong murein layer appears to be to help withstand such pressures (e.g., [9]), it seems to us that the tensile strength of the membranes (both inner and outer) could not exceed the above values. So, we assume that $F_t \approx (1\text{–}5) \times 10^6$ dynes/cm^2. If we assume the higher value, i.e., $F_t \sim 5 \times 10^6$ dynes/cm^2, we obtain $|\phi| \geq 6$ V as the condition for the disruption of the membrane by rupturing the pimple. The condition to break it in half (obtained by replacing r by R in (2) is $|\phi| \sim 40$ V. If we use the smaller value for F_t (~10^6 dynes/cm^2), the corresponding limits for $|\phi|$ are, respectively, ~3 V and ~18 V.

Incidentally, if we had assumed a more rod-like geometry, in particular, a right circular cylinder with hemispherical end caps each of radius R with an axial pimple of radius r on one of them, the above analysis would still apply.

In the experiment of Laroussi *et al.* [1], the plasma electron temperature $kT_e \approx 1$–5 eV, and the ions are largely He^+. If we assume that both electrons and ions are Maxwellian with $T_e = T_i$ (although T_e is significantly larger than T_i in this case), and solve the standard transcendental equation for the equilibrium potential obtained by equating the orbit limited electron and ion currents to the bacterium immersed in the plasma (e.g., [12]), we obtain $\phi \approx -15$ V if $kT_e \approx 5$ V. In such discharges, the plasma (particularly, the electrons) are not expected to be Maxwellian, having thicker tails at higher energies, and are better fit by generalized Lorentzian (kappa) distributions [13]. If we assume this to be the case, with $\kappa = 2$, we get $\phi \approx -20$ V. Although these values for the equilibrium potentials were obtained using the orbit limited currents, which are valid only when the currents are orbit limited (i.e., when the Knudsen number, $Kn = \ell/R \geq 1$, where ℓ is the collision mean-free path of the ions), it is expected that they will not be significantly changed even when $Kn < 1$, when the currents are diffusion limited. This is because in the latter case both currents are reduced approximately by the same factor, i.e., Kn [14]. The main difference is that the charging time would be increased by a factor ~$(1/Kn)$, in the latter case, when $Kn < 1$.

We thus see that the potential expected to be achieved by the *E. coli* bacterium in a glow discharge plasma could be sufficient to break the outer membrane in half if its tensile strength is low ($F_t \sim 10^6$ dynes/cm^2). If the tensile strength was higher ($F_t \approx 5 \times 10^6$ dynes/cm^2), the surface potential achieved is insufficient to break this membrane in half, but would be sufficient to tear it if it had a surface roughness on the scale of a few percent.

III. Discussion

Before concluding that the process of electrostatic disruption of the cell membrane, which we have discussed, is a plausible mechanism for killing bacteria in a GDAP, we need to check if the charging time of the bacteria is sufficiently small (i.e., smaller than the "kill times" that have been reported). By an analysis of the time-dependent charging equation, it is easy to see that there are in fact two relevant time scales. The first is essentially an e-folding time T_{ef}, during which the initially uncharged surface acquires most of its negative charge because of the larger mobility of the electrons. Following this, the surface approaches its equilibrium potential on a longer time scale T_{eq}. In the orbit limited case ($Kn > 1$), for an isothermal Maxwellian plasma, these times are given by

$$T_{ef} \sim \frac{\lambda_D}{\omega_{pe}} \cdot \frac{1}{R}; \quad T_{eq} \sim \frac{\lambda_D}{\omega_{pi}} \cdot \frac{1}{R} = \sqrt{\frac{m_i}{m_e}}\, T_{ef}$$

where λ_D is the plasma Debye shielding length and ω_{pe}, ω_{pi} are, respectively, the electron and ion plasma frequencies. In the case when $Kn \ll 1$, both of the above time scales should be increased by the multiplicative factor $(1/Kn)$.

While the electron density in the GDAP used by Laroussi *et al.* [1] is not available, we assume that it has a typical value of $n_e \approx 10^{10}$ cm^{-3} (e.g., [15]). Then, with $kT_e \sim 5$ eV and $R \sim 1\,\mu$m, we get $T_{ef} \sim 30$ ns and $T_{eq} \sim 3\,\mu$s. If we take $1/Kn \sim 16$, as is appropriate for air at atmospheric pressure, we get $T_{ef} \sim 0.5\,\mu$s and $T_{eq} \sim 50\,\mu$s. The appropriate value for $(1/Kn)$ to use for the Luria–Bertani broth in the Laroussi *et al.* experiment is probably ~10^3–10^4 larger than that of air, which gives $T_{ef} \sim 0.5$–5 ms and $T_{eq} \sim 50$–500 ms. Both of these times are much smaller than are their reported kill times viz. 2–20 min. Even if a decrease in n_e by one or two orders of magnitude should occur as the plasma penetrates into the broth, T_{ef} and T_{eq} would still be

smaller than the kill times. So, it seems that the bacteria had sufficient time to acquire the requisite surface charge.

In summary, we have used a simple physical model of the cell membrane of the *E. coli* to investigate if its electrostatic disruption caused by the accumulation of a sufficient surface charge could explain the recent observation [1] of bacterial mortality observed in a glow discharge under atmospheric pressure. Our conclusion is that it is possible, but more likely if the surface has some irregularity implying regions of higher local curvature. Considering the simplicity of our model and the uncertainties in several parameters that are used, our conclusion certainly remains tentative at this time. Our purpose here was to demonstrate its plausibility and thereby to stimulate further investigation. Perhaps a way of checking the efficacy of our proposed electrophysical mechanism over the alternative photochemical processes proposed for killing *E. coli* would be to use a plasma composed entirely of an inert gas ion as opposed to one that is only partially composed of an inert gas ion, as in the experiment of Laroussi *et al.* [1], while decreasing the UV emission as far as possible. This would at least greatly decrease, if not entirely eliminate the lethal photochemical effects. We would also like to point out that we expect our process to be more efficacious the more irregular the bacterial surface, as for instance appendaged and budding bacteria possessing long stalks and hyphae, as well as filamentous bacteria with long thin cells (e.g., see [9, Fig. 3.9]).

Indeed, the cell surfaces, especially those of Gram-negative cells, are typically rough and convoluted (e.g., see [9, Fig. 3.26]). Also, while not explicitly considered in our model, we note that viruses (typically, $R \sim 0.01$–0.1 μm, with pronounced surface irregularities, particularly tailed viruses) subject to electrostatic stress might suffer structural disruption and consequently loose their infectivity.

The physical mechanism that we propose for the structural disruption of bacteria is only effective for Gram-negative ones like *E-coli*, which possess thin outer membranes and a thin ($\sim$2 nm) murein layer. We do not expect it to work in the case of Gram-positive bacteria, which lack an outer membrane but have a thicker murein layer ($\sim$15–80 nm [10]), thereby providing it with higher strength and rigidity. If such Gram-positive bacteria (e.g., *Staphylococcus aureus*) are also killed in a GDAP, as has been reported recently by Kelly-Wintenberg *et al.* [15], the reason for that may be different.

In this latter study, in which Gram-positive as well as Gram-negative bacteria were killed, no SEM photographs are provided as in the Laroussi *et al.* [1] experiment. Thus, we do not know whether the loss of viability of Gram-positive bacteria in the study of Kelly-Wintenberg *et al.* [15] was caused by gross loss of structural integrity. We note that these authors expressed cell death as reduction in viable cell counts (i.e., the ability of bacteria to grow to form visible colonies on a nutrient-agar solid medium). Bacteria exposed to physical or chemical stresses can lose their ability to form colonies without suffering structural damage or death (viable but unculturable bacteria [16], [17]). We might hypothesize that exposure to electrophysical stress caused the relatively more robust Gram-positive bacteria to enter the viable, but unculturable state. If so, the apparent sterilization might be reversed under suitable physicochemical and nutritional conditions. This hypothesis can be tested by using culture-independent techniques (e.g., live-dead stains; Molecular Probes, Oregon) to determine bacterial mortality.

IV. Addendum

Dr. Laroussi [20] subsequently pointed out that this cell membrane disruption was merely a speculation because the resolution of the photographs was insufficient to demonstrate it. (See also the earlier work by Laroussi [18] on the Gram-negative bacterium *Pseudomonas fluorescens*.) However, a more recent experimental study by Kelly-Wintenberg *et al.* [19] that came to our attention since the acceptance of our paper supports this speculation. In this latter study, high-resolution transmission electron micrographs of *E. coli* subject to a GDAP are exhibited, which indeed seem to show cell membrane disruption. The authors state that "the continuity of the cellular envelope was interrupted and cellular contents were released to the surrounding medium within 30s." This study also included the sterilization of other microorganisms, including Gram-positive bacteria. But transmission electron micrographs are shown only in the case of *E. coli*.

Dr. Laroussi [20] has also kindly reported to us very recent, and as yet unpublished, data on the Gram-positive bacterium *Bacillus subtilis* undergoing sterilization in a GDAP. While reduction in cell viability is achieved, differential interference phase contrast microscopy indicate that the cell wall remains intact. This result is consistent with our proposal in this paper that structural disruption caused by electrostatic stress is ineffective for Gram-positive bacteria because of their greater structural strength.

Acknowledgment

The authors thank Dr. M. Laroussi for several useful discussions and for reporting to us his most recent and as yet unpublished data on Gram-positive bacteria.

References

[1] M. Laroussi, G. Sayler, and B. Battle *et al.*, "Images of biological samples undergoing sterilization by a glow discharge at atmospheric pressure," *IEEE Trans. Plasma Sci.*, vol. 27, p. 34, 1999.

[2] U. Zimmerman, G. Pilwat, and F. Rieman, "Dielectric breakdown in cell membranes," *Biophys. J.*, vol. 14, p. 1881, 1974.

[3] H. G. L. Coster and U. Zimmerman, "The mechanism for electrical breakdown in membranes of *Valonia utricularis*," *J. Membrane Biol.*, vol. 22, p. 73, 1975.

[4] B. Neumcke, D. Walz, and P. Länger, "Non-linear electrical effects in lipid bilayer membranes. III. The dissociation field effect," *Biophys. J.*, vol. 10, p. 172, 1970.

[5] J. M. Crowley, "Electrical breakdown of bimolecular lipid membranes as an electromechanical instability," *Biophys. J.*, vol. 13, p. 711, 1973.

[6] H. Hülsheger, J. Potel, and E.-G. Niemann, "Electrical field effects on bacteria and yeast cells," *Radiat. Environ. Biophys.*, vol. 22, p. 149, 1983.

[7] E. J. Öpik, "Interplanetary dust and terrestrial accretion of meteoric matter," *Irish Astron. J.*, vol. 4, p. 84, 1956.

[8] J. R. Hill and D. A. Mendis, "Electrostatic disruption of a charged conducting spheroid," *Can. J. Phys.*, vol. 59, p. 897, 1981.

[9] M. Madigan, J. M. Martinko, and J. Parker, *Brock Biology of Microorganisms*. 8th ed. Englewood Cliffs, NJ: Prentice-Hall, 1997, p. 53.

[10] J. L. Ingraham, O. Maaloe, and F. C. Neidhardt, *Growth of the Bacterial Cell*. Boston, MA: Sinauer Assoc., 1983, p. 26.

[11] F. C. Neidhardt, J. L. Ingraham, and M. Schaechter, *Physiology of the Bacterial Cell: A Molecular Approach*. Boston, MA: Sinauer Assoc., 1990, p. 240.

[12] C. K. Goertz, "Dusty plasmas in the solar system," *Rev. Geophys.*, vol. 27, p. 271, 1989.

[13] M. Rosenberg and D. A. Mendis, "A note on dust grain charging space plasmas," *J. Geophys. Res.*, vol. 97, p. 14773, 1992.

[14] J. S. Chang and J. G. Laframboise, "Probe theory for arbitrary shape in a large Debye length stationary plasma," *Phys. Fluids*, vol. 19, p. 25, 1976.

[15] K. Kelly-Wintenbe _, T. C. Montie, and C. Brickman *et al.*, "Room temperature sterilization of surfaces and fabrics with a one atmosphere uniform glow discharge plasma," *J. Indust. Microbio. and Biotech.*, vol. 20, p. 69, 1998.

[16] R. R. Colwell, P. R. Brayton, D. J. Grimes, D. H. Roszak, S. A. Huq, and L. M. Palmer, "Viable but nonculturable vibrio cholerae and related pathogens in the environment: Implications for release of genetically engineered microorganizms," *Biotechnology*, vol. 3, p. 817, 1985.

[17] J. J. Byrd, H. S. Xu, and R. R. Colwell, "Viable but nonculturable bacteria in drinking water," *Appl. Environ. Microbiol.*, vol. 57, p. 875, 1991.

[18] M. Laroussi, "Sterilization of contaminated matter with an atmospheric pressure plasma," *IEEE Trans. Plasma Sci.*, vol. 24, p. 1188, 1996.

[19] K. Kelly-Wintenberg, A. Hodge, and T. C. Montie *et al.*, "Use of one atmosphere uniform glow discharge plasma to kill a broad spectrum of microorganizms," *J. Vac. Sci. Technol. A*, vol. 17, p. 1539, 1999.

[20] M. Laroussi, private communication.

Pulsed Power/Plasma Science 2001 (PPPS-2001)

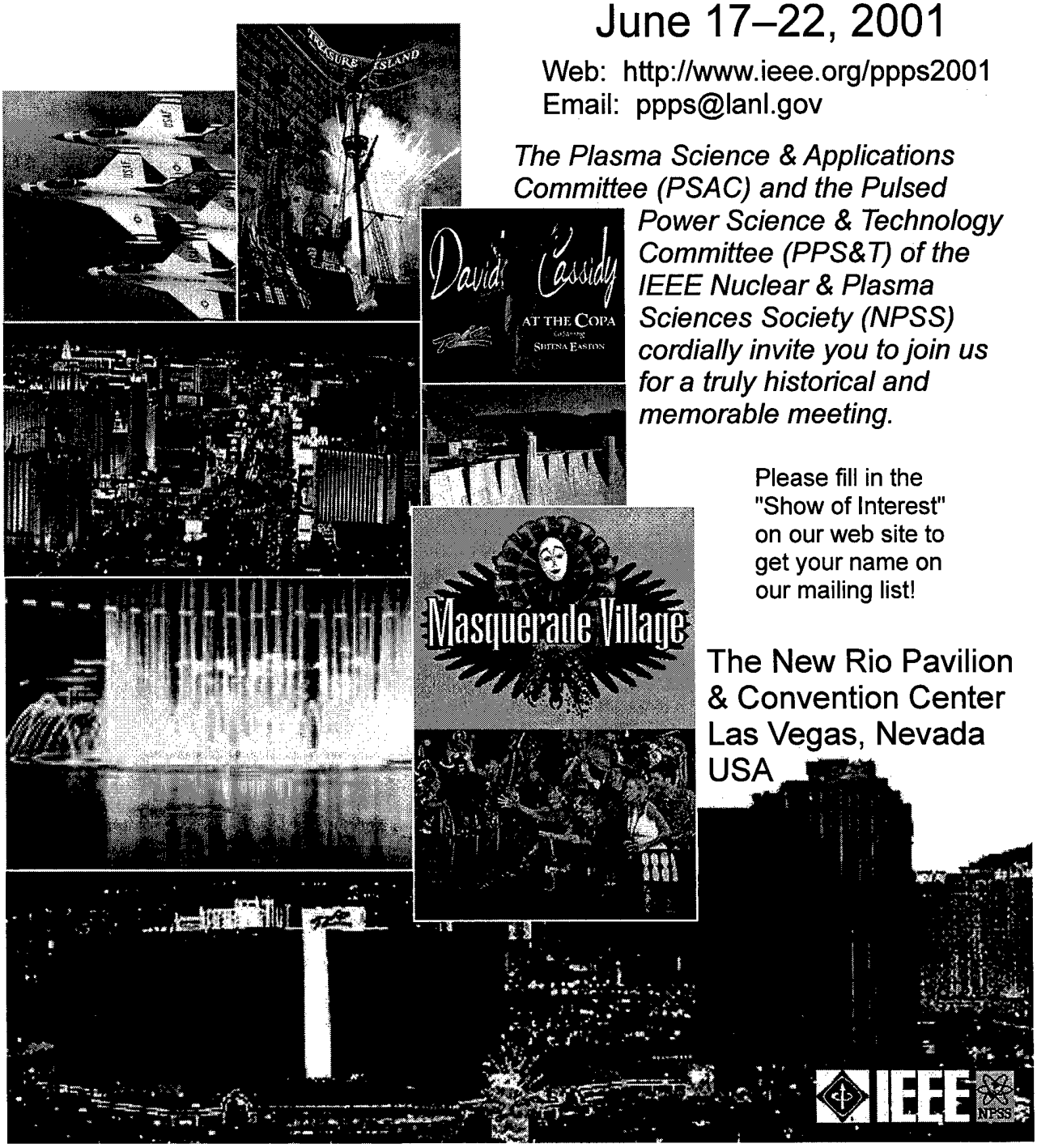
13th International Pulsed Power Conference (PPC)
28th International Conference on Plasma Science (ICOPS)

June 17–22, 2001

Web: http://www.ieee.org/ppps2001
Email: ppps@lanl.gov

The Plasma Science & Applications Committee (PSAC) and the Pulsed Power Science & Technology Committee (PPS&T) of the IEEE Nuclear & Plasma Sciences Society (NPSS) cordially invite you to join us for a truly historical and memorable meeting.

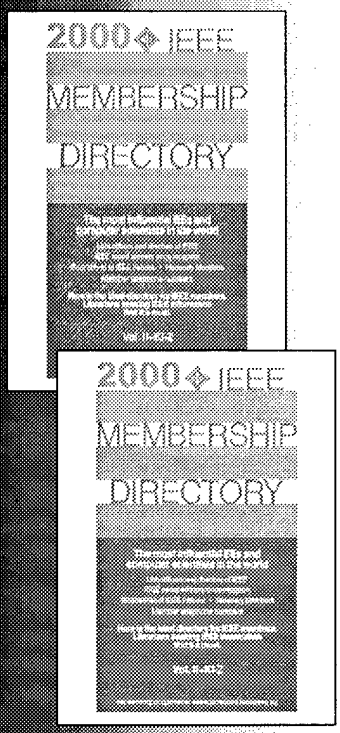
Please fill in the "Show of Interest" on our web site to get your name on our mailing list!



The New Rio Pavilion & Convention Center
Las Vegas, Nevada
USA

IEEE NPSS

Quick access to the world's top electronics and computing specialists! More than 350,000 strong!



THE IEEE MEMBERSHIP DIRECTORY

Do you need access to the world's leading electronics and computing engineers? The *IEEE Membership Directory*, published each May, gives you quick access to their names and current addresses, titles and (unless otherwise requested) phone numbers and e-mail addresses — now over 350,000 records in two volumes! Roughly 50% of all IEEE members change their addresses every 18 months, so it's essential to have the *Directory*. Plus, the *Directory* includes IEEE award winners and biographies of IEEE Fellows, making it a convenient way to contact the engineers who have the professional information you need.

List Price: $189.95
Member Price: $69.95
IEEE Product No. JP-507-0-52000-QBZ
ISBN 0-7803-9961-7

Subscribe to the *IEEE Membership Directory* and Save 15% every year — Guaranteed!

Do you use the *IEEE Directory* often? If so, why not get it fast, first, and at the lowest price available — 15% OFF the member or list price? Call IEEE Customer Service for more information.

4/00 937-y

Order 24 Hours a Day, 7 Days a Week!

Phone +1 800 678 IEEE (Toll-Free USA and Canada) or +1 732 981 0060
Fax +1 732 981 9667
email customer-service@ieee.org

IEEE

The Institute of Electrical and Electronics Engineers, Inc.
Member Services Dept. • 445 Hoes Lane • PO Box 1331 • Piscataway, NJ 08855-1331 U.S.A.

INFORMATION FOR AUTHORS

The IEEE TRANSACTIONS ON PLASMA SCIENCE is published bimonthly. Its scope includes all aspects of the theory and application of plasma science.

Manuscripts submitted for consideration should report on new results, although papers of a tutorial or historical nature are not excluded from consideration. Contributions for the Correspondence section are also welcome. Submission of material will be construed as indicating that it has not been copyrighted, published, submitted, or presented elsewhere, unless explicit notice to the contrary is given.

To avoid delay in processing, prospective authors should consult "Information for IEEE Transactions and Journal Authors," available upon request from the IEEE Transactions Department, 445 Hoes Lane, P.O. Box 1331, Piscataway, NJ 08855–1331 or by emailing "trans@ieee.org" or FAX at 732-562-0545.

The IEEE urges authors to submit the final version of their accepted manuscripts in electronic form (disks). All papers submitted on disks must be accompanied by three sets of hard copy. For further information see the "Editorial on Electronic Publishing" in the April 1991 issue of this TRANSACTIONS or contact the IEEE Transactions Department. Final approved manuscripts can be emailed to IEEE at t-ps@ieee.org.

Instructions for Paper Submission

1) Typewrite, using double spacing, on one side of letter-size white bond paper.

2) *Page Numbers:* The *first* manuscript page should contain the title, author's name, author's institution and address, abstract, and index terms. Succeeding manuscript pages should contain (in the following order): a) the body of the paper, b) acknowledgment, c) references, d) biography, e) tables, f) figure captions, g) figures, and h) photograph of author. All pages should be numbered with the first page being the title-abstract page.

3) A satisfactory abstract should be short (200 words maximum) and usually should answer the following:
What is the problem (or topic) being discussed, and what is the scope of its treatment?
What is the author's unique approach or important contribution, and is it primary information, a review, or tutorial material?
What is the solution, conclusion, principal result, or typical application?
(Fifty-word abstracts should accompany Correspondence items of archival value.)

4) *Organization of Material:* The longest section of a paper should be that treating the author's significant contribution; supporting or peripheral material should be condensed in shorter sections. This gives proper emphasis to the main subject of the paper and a high information density in the overall structure.

5) Refer to all illustrations and tables in the text.

6) Provide a separate sheet giving all figure captions. Captions lettered on figures will be blocked out in reproduction in favor of typeset captions.

7) Assure that all references are complete and in the following IEEE format:
For a paper: Initials and last name(s) of author(s), title of paper, name of journal, volume, number, inclusive page numbers, month, year.
For a book: Initials and last name(s) of author(s), and/or editor, book title, place of publication: publisher, year, chapter or page numbers.

8) Use *metric* units, more specifically, the International System of Units. If custom or convenience dictates British-American units for specific uses, the metric equivalent should be given also in parentheses. See "Information for IEEE Transactions and Journal Authors" (IEEE Recommended Practice for Units in Published Scientific and Technical Work).

9) Use only standard symbols and abbreviations unless defined when first used in the text.

10) Be sure that all subscripts, superscripts, Greek letters, and mathematical symbols are clearly identified.

11) To minimize the probability of error in typesetting, equations should be typed, not handwritten, whenever possible.

12) Avoid the use of trade and company names and proprietary terms whenever possible. Likewise, avoid "nationalisms," as in the following examples: our space program; power systems throughout the nation; research supported by the federal government.

13) Papers should be accompanied by a brief biography and photograph of the author. Papers with multiple authorship require a biography and photograph of each author.

14) Failure to follow the above instructions may delay publication of an otherwise acceptable manuscript.

Requirements for Illustrations

1) At least one complete set of the illustrations must consist of either the original line drawings in black ink on white paper or clear, high contrast, glossy prints of the line drawings.

2) All original line drawings, or sharp contrasting photographs of such drawings, must be no larger than 22 × 28 cm (8-1/2 × 11 in). The image area should not require reduction to final size in excess of a 5:1 ratio.

3) All lines and lettering should be black on white and heavy enough to remain legible after reduction to a column width.

4) Handwriting or freehand lettering is not acceptable on the line drawings; use a lettering set or some other suitable mechanism.

5) On graphs, show only the coordinate axes, or at most the major grid lines.

6) The author's name and figure number should be indicated in pencil on the back of each illustration, and the word TOP should appear at the top of the figure.

7) Figure captions should be typed on a separate sheet as indicated above in Instructions for Paper Submission.

8) Avoid photographs of laboratory experimental setups whenever possible.

9) Do not send xeroxes. Photos must be glossy prints with no screens. Laser prints are not acceptable in place of photos or where gray scale graphics are involved.

Technical Notes

This section of the IEEE TRANSACTIONS ON PLASMA SCIENCE is devoted to short communications describing either new research results for the first time or new findings which modify results already published in the technical literature. All submissions will be reviewed promptly, and acceptance will be based on the importance and timeliness of the results presented in the Technical Note. Each Technical Note must be accompanied by an abstract no longer than 50 words, and the main body of the text must clearly and concisely identify the technical objective of the Note, the approach used to meet this objective, and the significance of the results to the field of Plasma Science. The length of each Technical Note is limited to six typewritten, double-spaced pages, with each illustration being counted as equivalent to a half page. All relevant instructions cited on this page for the preparation and submission of full-length manuscripts should be followed in the preparation and submission of Technical Notes.

Submitting the Manuscript

1) Send the original and two copies (high quality office-duplicated copies are acceptable) of the complete manuscript to the Editor: Dr. Steven J. Gitomer, Center for International Security Affairs, Mail Stop K760, Los Alamos National Laboratory, P.O. Box 1663, Los Alamos, NM 87545. Telephone 505-667-4352, FAX 505-667-0966, e-mail sgitomer@lanl.gov. The transmittal letter should clearly state the name, address, telephone number, email address, and FAX number (if available) of the specific author to whom correspondence and page proofs should be sent.

2) Notify the Editor of any special circumstances, such as pending clearance or previous limited publication. It is understood that this submitted paper is not currently under consideration by another journal. The purpose of this requirement is to minimize duplication and waste of the valuable time of referees.

3) All papers will be reviewed by one or more referees.

4) A letter acknowledging receipt of the manuscript and an IEEE Copyright Form will be sent to the authors. The Copyright Form must be returned promptly since a paper cannot be accepted for publication without the receipt of a signed IEEE Copyright Form.

5) The IEEE Nuclear and Plasma Sciences Society adopted the following policy concerning page charges for the IEEE TRANSACTIONS ON PLASMA SCIENCE: *Papers will be reviewed on the basis of their technical merit, and decisions to publish will be made independently of an author's willingness or ability to pay page charges. Page charges of $110 per page will be requested for papers of five printed pages or less. Page charges of $110 per page are mandatory for each page in excess of five printed pages. A quota has been established for the number of pages printed in each issue of TRANSACTIONS ON PLASMA SCIENCE whose costs are not defrayed by payment of page charges. Papers not covered by page charges may need to be reduced in length to five printed pages and may be delayed until space in an issue is available. The Editor can waive the quota requirement for exceptional papers or because of other extenuating circumstances.* For purposes of estimating the number of printed pages use the following: The approximate number of printed typeset pages is equal to one-fourth the number of double-spaced regular typed manuscript pages plus one-fourth the number of figures. Count a table as equivalent to one figure.

Copyright

It is the policy of the IEEE to own the copyright to the technical contributions it publishes on behalf of the interests of the IEEE, its authors, and their employers and to facilitate the appropriate reuse of this material by others. To comply with the IEEE Copyright policy, authors are required to sign an IEEE copyright transfer form before publication. This form, a copy of which appears in the February 2000 issue of this TRANSACTIONS, returns to authors and their employers full rights to reuse their material for their own purposes. Authors must submit a signed copy of this form with their manuscripts.

AFFILIATE PLAN OF THE IEEE NUCLEAR AND PLASMA SCIENCES SOCIETY

The Affiliate Plan, established by the IEEE Board of Directors, enables individuals who are not members of the IEEE, but who have an interest in the field of plasma science, to join the IEEE Nuclear and Plasma Sciences Society. Admission as an affiliate requires only membership in a professional society listed below. Affiliates pay a special fee and have all Society privileges except that of holding elective office. Affiliates receive the IEEE TRANSACTIONS ON PLASMA SCIENCE.

AFFILIATE PLAN SOCIETIES

Acoustical Society of America
American Association for the Advancement of Science
American Association of Immunologists
American Association of Physics Teachers
American Chemical Society
American Institute of Chemcial Engineers
American Institute of Nutrition
American Institute of Physics
American Nuclear Society
American Physical Society
American Physiological Society
American Society of Bio-Chemistry
American Society of Experimental Pathology
American Society of Mechanical Engineers
American Society of Pharmacology & Experimental Therapeutics
British Institute of Radiology
Canadian Organization of Medical Physicists
Canadian Association of Physicists
Federation of American Societies for Experimental Biology
Health Physics Society
Institute of Physics of Great Britain
Institution of Electrical Engineers (Great Britain)
Instrument Society of America
Japanese Institute of Electrical Engineers
Norwegian Nuclear Society
Optical Society of America
Radiation Research Society
Scientific Research Society of America
Society of Nuclear Medicine
Society of Rheology
The Physical Society of Great Britain

HOW AN INDIVIDUAL MAY BECOME AN AFFILIATE OF THE IEEE NUCLEAR AND PLASMA SCIENCES SOCIETY

If you would like to become an Affiliate Member of the Nuclear and Plasma Sciences Society please contact IEEE Member Services at +1 800 678 IEEE (4333), +1 732 562 5539, Fax +1 732 981 0225 or e-mail "application-request@ieee.org" to request an Affiliate Brochure and application.